

---

# **OPTOELECTRONICS - MATERIALS AND TECHNIQUES**

---

Edited by **Padmanabhan Predeep**

**INTECHWEB.ORG**

## **Optoelectronics - Materials and Techniques**

Edited by Padmanabhan Predeep

### **Published by InTech**

Janeza Trdine 9, 51000 Rijeka, Croatia

### **Copyright © 2011 InTech**

All chapters are Open Access articles distributed under the Creative Commons Non Commercial Share Alike Attribution 3.0 license, which permits to copy, distribute, transmit, and adapt the work in any medium, so long as the original work is properly cited. After this work has been published by InTech, authors have the right to republish it, in whole or part, in any publication of which they are the author, and to make other personal use of the work. Any republication, referencing or personal use of the work must explicitly identify the original source.

Statements and opinions expressed in the chapters are these of the individual contributors and not necessarily those of the editors or publisher. No responsibility is accepted for the accuracy of information contained in the published articles. The publisher assumes no responsibility for any damage or injury to persons or property arising out of the use of any materials, instructions, methods or ideas contained in the book.

**Publishing Process Manager** Mirna Cvijic

**Technical Editor** Teodora Smiljanic

**Cover Designer** Jan Hyrat

**Image Copyright** Triff, 2010. Used under license from Shutterstock.com

First published September, 2011

Printed in Croatia

A free online edition of this book is available at [www.intechopen.com](http://www.intechopen.com)  
Additional hard copies can be obtained from [orders@intechweb.org](mailto:orders@intechweb.org)

Optoelectronics - Materials and Techniques, Edited by Padmanabhan Predeep

p. cm.

ISBN 978-953-307-276-0

**INTECH** OPEN ACCESS  
PUBLISHER

**INTECH** open

**free** online editions of InTech  
Books and Journals can be found at  
**[www.intechopen.com](http://www.intechopen.com)**



---

# Contents

---

## **Preface IX**

### **Part 1 Inorganic Optoelectronic Materials 1**

Chapter 1 **Optoelectronic Properties of Amorphous Silicon  
the Role of Hydrogen: from Experiment to Modeling 3**  
Franco Gaspari

Chapter 2 **Silicon-Rich Silicon Oxide Thin Films Fabricated  
by Electro-Chemical Method 27**  
Pham Van Hoi, Do Thuy Chi, Bui Huy and Nguyen Thuy Van

Chapter 3 **Silicon Oxide (SiO<sub>x</sub>, 0<x<2):  
a Challenging Material for Optoelectronics 55**  
Nicolae Tomozeiu

Chapter 4 **Gallium Nitride: An Overview of Structural Defects 99**  
Fong Kwong Yam, Li Li Low,  
Sue Ann Oh, and Zainuriah Hassan

Chapter 5 **Cuprous Oxide (Cu<sub>2</sub>O): A Unique System Hosting  
Various Excitonic Matter and Exhibiting Large  
Third-Order Nonlinear Optical Responses 137**  
Joon I. Jang

Chapter 6 **Optoelectronic Properties  
of ZnSe, ITO, TiO<sub>2</sub> and ZnO Thin Films 165**  
S. Venkatachalam, H. Nanjo, K. Kawasaki,  
H. Hayashi, T. Ebina and D. Mangalaraj

### **Part 2 Polymer Optoelectronic Materials 185**

Chapter 7 **Side-Chain Multifunctional  
Photoresponsive Polymeric Materials 187**  
Luigi Angiolini, Tiziana Benelli, Loris Giorgini,  
Attilio Golemme, Elisabetta Salatelli and Roberto Termine

- Chapter 8 **Ladder Polysiloxanes for Optoelectronic Applications** 211  
Zhongjie Ren, Shouke Yan and Rongben Zhang
- Chapter 9 **Synthesis of Aromatic-Ring-Layered Polymers** 235  
Yasuhiro Morisaki and Yoshiki Chujo
- Chapter 10 **Nanomorphologies in Conjugated Polymer Solutions and Films for Application in Optoelectronics, Resolved by Multiscale Computation** 261  
Cheng K. Lee and Chi C. Hua
- Part 3 Techniques and Characterization** 285
- Chapter 11 **Optoelectronic Techniques for Surface Characterization of Fabrics** 287  
Michel Tournonias, Marie-Ange Bueno and Laurent Bigué
- Chapter 12 **Optoelectronic Circuits for Control of Lightwaves and Microwaves** 313  
Takahide Sakamoto
- Chapter 13 **An Analytical Solution for Inhomogeneous Strain Fields Within Wurtzite GaN Cylinders Under Compression Test** 337  
X. X. Wei
- Chapter 14 **Application of Quaternary AlInGaN- Based Alloys for Light Emission Devices** 355  
Sara C. P. Rodrigues, Guilherme M. Sipahi, Luísa Scolfaro and Eronides F. da Silva Jr.
- Chapter 15 **Air Exposure Improvement of Optical Properties of Hydrogenated Nanostructured Silicon Thin Films for Optoelectronic Application** 375  
Atif Mossad Ali
- Chapter 16 **Fabrication and Characterization of As Doped p-Type ZnO Films Grown by Magnetron Sputtering** 393  
J.C. Fan, C.C. Ling and Z. Xie
- Chapter 17 **Light Intensity Fluctuations and Blueshift** 421  
Moon Kyu Choi
- Chapter 18 **Self-Similarity in Semiconductors: Electronic and Optical Properties** 435  
L. M. Gaggero-Sager, E. Pujals, D. S. Díaz-Guerrero and J. Escorcía-García

- Chapter 19 **Long-Term Convergence  
of Bulk- and Nano-Crystal Properties** 459  
Sergei L. Pyshkin and John Ballato
- Chapter 20 **Micro-Raman Studies  
of Li Doped and Undoped ZnO Needle Crystals** 477  
R. Jothilakshmi

*To my father; but for his unrelenting efforts I would not have made it to this day.*



---

## Preface

---

**Optoelectronics - Materials and Techniques** is the first part of an edited anthology on the multifaceted areas of optoelectronics contributed by a selected group of authors including promising novices to experts in the field, where are discussed related materials and techniques. Photonics and optoelectronics are making an impact multiple times the semiconductor revolution made on the quality of our life. In telecommunication, entertainment devices, computational techniques, clean energy harvesting, medical instrumentation, materials and device characterization and scores of other areas of R&D the science of optics and electronics get coupled by fine technology advances to make incredibly large strides. The technology of light has advanced to a stage where disciplines sans boundaries are finding it indispensable. In this context this book would be of importance to researchers from materials scientists to device designers and fabricators.

Photonics is to optics like electronics is to electricity. Photonics sculpts light like a sculptor does with granite. Light is beings squeezed, cut into the pieces, reconstructed back and the like. Currently optics is undergoing revolutionary changes and photonics is going to be the next centuries' technology. Globally, countries are vying with each other in formulating their technology initiatives so as to ensure that they should not miss the "Photonics Bus" as many of them missed the semiconductor revolution in the last century. Data transfer and communication technology are going to unimaginable heights by the idea of photonic crystals - the idea optical scientists copied from mother nature's work in nanotechnology in blooming beautiful colors and patterns on objects of desire like butterfly wings and peacock feathers

With the emergence of photonics and laser technology, optoelectronics seems to be losing its identity and is often mixed up with photonics. Photonics draws from and contributes to several other fields, such as quantum electronics and modern optics. In this era of great mix up of disciplines and multidisciplinary research, it is not surprising that such mix of closely connected players like electrons and photons refuses to be confined to narrow boundaries of sub disciplines. Naturally the articles in this anthology also have their boundaries diffused over the diverse optical phenomena of optoelectronics and photonics. Readers are advised to bear this in mind when looking for titles of this book.

I am proud to present this collection of carefully selected peer reviewed high quality articles on various optoelectronic and photonic materials and techniques and would like to thank to the authors for their wonderful efforts. Stake holders of the ongoing optoelectronic and photonics revolution such as researchers, academics and scientists are sure to find this collection of essays enormously useful.

July 2011

**P. Predeep**

Professor

Laboratory for Unconventional Electronics & Photonics

Department of Physics

National Institute of Technology Calicut

India





**Part 1**

**Inorganic Optoelectronic Materials**



# Optoelectronic Properties of Amorphous Silicon the Role of Hydrogen: From Experiment to Modeling

Franco Gaspari  
*University of Ontario Institute of Technology,  
Canada*

## 1. Introduction

Amorphous silicon, and its more useful alloy form, hydrogenated amorphous silicon (a-Si:H), has been the subject of investigation for more than three decades. A-Si:H is a low-cost, efficient material which is used extensively for electronic devices. Indeed, most recent electronic device textbooks contain a comprehensive review of the physics of amorphous materials and amorphous silicon in particular (Baranovski, 2006; Kasap, 2005; Street, 2000).

The advantages of a-Si:H are particularly evident when considering the photovoltaic application context for the preparation of solar cells: in fact, a-Si:H has a large optical absorption coefficient (about 0.5 micron of the material will absorb 90% of the incident sunlight); the energy gap can be modulated to allow for near optimum conversion efficiency for sunlight; it can be alloyed with other elements (carbon, germanium) to create multi-junction structures with increased energy conversion efficiency for sunlight. Finally, it is plentiful and can be deposited on a variety of materials (at low temperature, over large areas, and on flexible substrates).

However, the presence of metastable defects in a-Si:H adversely affects the performance of photovoltaic cells and thin film transistors. Electrical conductivity, photoconductivity and luminescence degradation have been linked to defect formation, such as dangling bonds (DBs) in the a-Si:H film (Akkaya & Aktas, 1995; Street, 1980).

Staebler and Wronski (1977) found that defects can be created by illuminating a-Si:H. The creation of these light-induced defects (LID) is therefore referred to as the Staebler-Wronski (SW) effect. The presence of these defects, or dangling bonds, is the major factor responsible for the deterioration of the optical and electronic properties of a-Si:H. On the other hand, these defects are metastable and can be cured. Indeed, we could define a SW process that can be described as a two-step reversible process:

- i. Exposure to sunlight leads to an increase in the density of states (dangling bonds) in the energy gap of a-Si:H; this represents the SW effect proper;
- ii. Subsequent annealing at elevated temperatures (150-200 °C) reduces the density of states back to the original value, thus restoring the optoelectronic properties.

It has been shown experimentally that both optical and electronic properties of amorphous silicon, such as refractive index, optical gap, absorption coefficient, electron and hole

mobility, etc., are strongly dependent on hydrogen content, in terms of both hydrogen concentration and hydrogen dynamics (diffusion) under various conditions - see, for instance, (Searle, 1998) and references therein. The investigation of such dynamics, including the relation with defect creation and annealing, is crucial for assessing the appropriate solutions to achieve better control of the defects and, consequently, better optoelectronic performances.

There exists a large amount of articles and review papers or books that address the basic properties of a-Si:H, including analysis of the structural, optical and electronic properties; description of a variety of experimental methods used for the growth of a-Si:H films; and correlation between growth parameters and film quality.

In this chapter a summary of the basic properties and historical issues related to a-Si:H and its applications in optoelectronics is presented in section 2. A more exhaustive description of the basic properties of a-Si:H is provided by the references in this section. Section 3 will focus on the role of hydrogen in relation to the optoelectronic properties and defect dynamics in a-Si:H, and will examine some of the prominent models of hydrogen diffusion also used to describe the SW process dynamics. Section 4 will describe the use of tritium, an isotope of hydrogen, as an experimental probe that can be used as a reference by such models. Finally, section 5 will present the results of an integrated experimental and theoretical approach aimed at developing a proper model of the dynamics inherent to a-Si:H and amorphous materials in general. Future work necessary to achieve a proper description of these dynamic processes will be indicated in the Conclusion section.

## 2. Properties of a-Si:H

There exist several preparation methods for a-Si:H films. Early work on evaporated and sputtered a-Si:H lead to poor quality films, and it is now widely accepted that Radio Frequency (RF) Glow Discharge produces the best quality material, although other more recent methods claim similar or better results. A comprehensive review of the advantages and disadvantages of the different methods employed to grow a-Si:H can be found in the books edited by Searle (1998) and Street (1991).

In general, it is desirable that a hydrogen plasma be employed to help the formation of Si-H<sub>n</sub> ion radicals; hence, methods based on plasma-enhanced chemical vapour deposition (PECVD) techniques are usually preferred. The ions produced in the plasma region are directed via an electric field towards a substrate, where film growth takes place. A common characteristic of these PECVD techniques is the possibility of tuning the system using several parameters, which might be mutually dependent on or independent of each other, like partial gas pressure, electrode bias, substrate bias, flow rates, gas mixtures, substrate temperature, and any other adjustable parameter. A review of plasma deposition of a-Si:H can also be found in (Bruno *et al.*, 1995).

If the goal of current research in this sector is the understanding and prediction of the properties of a-Si:H, it is crucial that the dependence of physical properties on preparation conditions be fully examined. This requires the development of experimental and predictive tools applicable to size scales ranging from the atomic to the macroscopic levels. Both Searle (1998) and Street (1991) provide an exhaustive review of the structural, optical and electronic properties of a-Si:H, and point out the still unresolved issues. In the following subsection, the basic properties of a-Si:H are presented, with a focus on the role of hydrogen.



## 2.1 Structure and Density of States (DOS)

In order to understand the implication of the amorphous structure of a-Si:H on its optoelectronic properties, it is useful to examine the structure of amorphous silicon in comparison to its crystalline form (c-Si). Crystalline silicon is characterized by the well known diamond (or tetrahedral) structure, with bond length of 23.3 nm and bond angle of  $109.5^\circ$ . As a matter of fact, the amorphous form shows very small changes from the crystalline parameters, with a  $\pm 10\%$  deviation in bond length, and a  $\pm 5\%$  deviation in bond angle. These small changes make it possible to maintain a relatively good short range order (within the first 2-3 nearest neighbours); however, the accumulation of structural stress, due to the progressive compounding of small deviations, eventually leads to bond breaking and the appearance of dangling bonds. Figure 1 shows simple 2-d schematics of the formation of dangling bonds: a 2-d square crystal (1a) is slightly distorted (1b, top, center atom). The distortions become more marked as the network is extended, and eventually a dangling bond (DB) appears to relieve the structural stress (top right quadrant of figure 1c: this is usually also accompanied by under-coordinated and over-coordinated bonds).

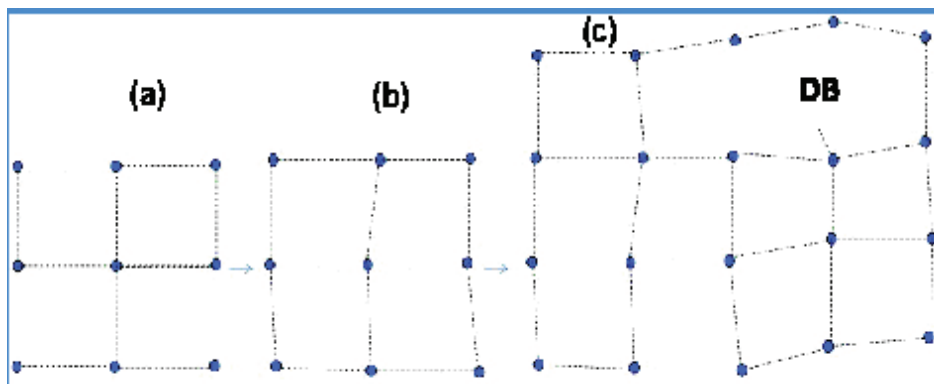


Fig. 1. (a to c) 2-d schematics of formation of dangling bonds due to long range disorder.

The negative effects of the dangling bonds on the opto-electronic properties of a-Si can be effectively removed by hydrogenation; that is, hydrogen atoms are introduced to passivate (bond to) the dangling bonds; see, for instance, (Kasap, 2005; Street 1991, 2000).

Hydrogen atoms incorporated into the films satisfy the covalent bonds at defects and microvoids and also allow the lattice to relax, thereby reducing the density of localized states by several orders of magnitude. Figure 2(b) show a 3-d representation of amorphous silicon with dangling bonds passivated by hydrogen atoms. A crystalline structure is also shown for comparison in figure 2(a).

The differences and similarities between the crystalline silicon and amorphous silicon structures are evident when we examine the radial distribution functions (RDF) for the two structures, as shown in Figure 3. The amorphous structure still shows ordered, crystalline features for the first 3 nearest neighbors. The first neighbor also maintains the crystalline sharpness for the peak, while the progressive deviations from the crystalline structure are evident in the spreading of the peaks for the second and third nearest neighbor.

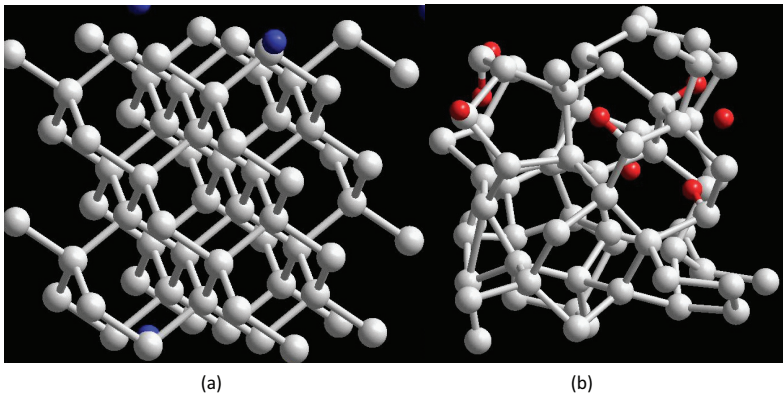


Fig. 2. A 3-d computer model representation of c-Si (a), and a-Si (b) with dangling bonds passivated by hydrogen atoms (red balls).

The role of hydrogen in determining the degree of disorder is also the subject of numerous studies. For instance, O'Leary *et al.* (1996), by using optical absorption data, and by investigating how the modeling parameters vary with the bonded hydrogen concentration, suggest that bonded hydrogen helps decreasing the amount of disorder, and has an impact on the optical absorption spectrum.

More recently, Ukpong (2007) studied the chemically-induced disorder-to-order transition in hydrogenated amorphous silicon as a function of hydrogen concentration,  $C_H$ . The author identifies three stages, associated with low  $C_H$ , medium  $C_H$ , and high  $C_H$ , that describe the changes in the stress and structure parameters. Rui *et al.* (2005) investigated the effect of hydrogen plasma annealing on the micro-structural transition from disorder to order in amorphous silicon films. They found that there exist two steps for the reaction between atomic hydrogen and Si network, and show that the hydrogen plasma treatment conditions strongly influence the microstructures of the amorphous Si films.

The disorder inherent in the amorphous structure and the presence of dangling bonds has a crucial impact also on the electronic density of states (DOS) of amorphous silicon. Figure 4 shows a simple schematic representation of the electronic DOS of a-Si:H.

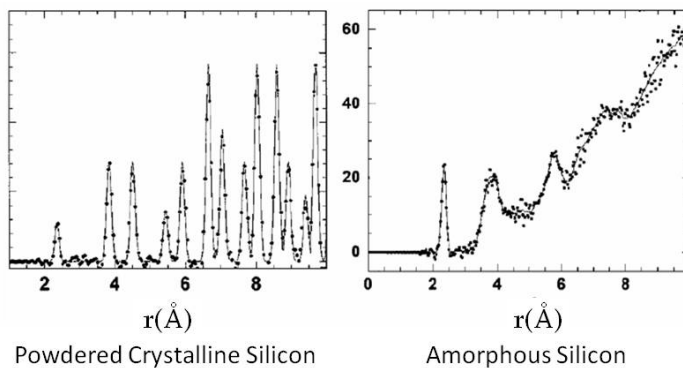


Fig. 3. Radial Distribution Function of crystalline silicon (left) and amorphous silicon (right) [From: Laaziri *et al.*, 1999]

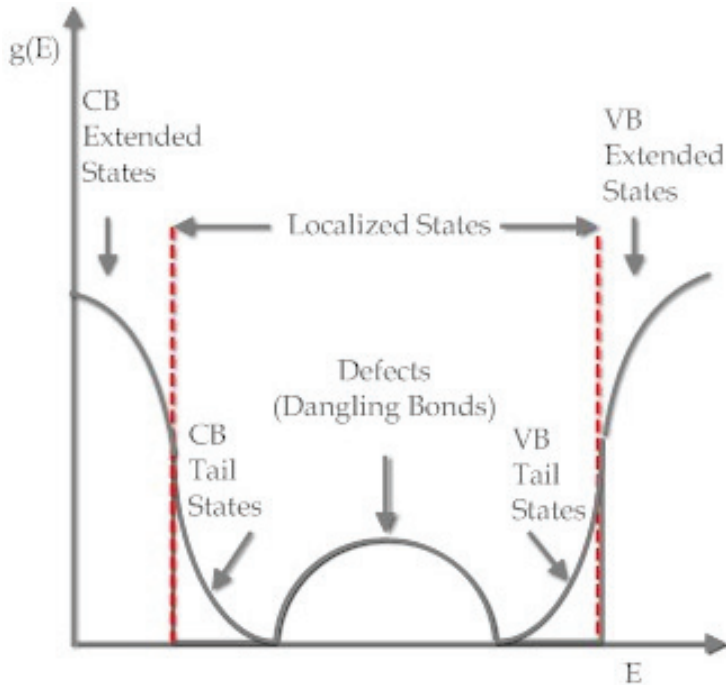


Fig. 4. A schematic representation of the electronic density of states,  $g(E)$ , of a-Si:H. VB indicates the valence band and CB the conduction band. The dashed, red, vertical lines show the mobility edges, which are defined as the energy level separating extended (non-localized) states from localized states.

The main features in Figure 4 can be summarized as follows:

- i. The localized tail states are a consequence of the disorder inherent to the amorphous structure. Several studies have examined the role and the extent of tails states in a-Si:H. In particular, a characteristic energy,  $E_U$ , or Urbach energy, gives the measure of the width of the tail states; hence, it is also referred to as the Urbach tail width - see, for instance, (Ley, 1983). The characteristic width for the band tail states is about 50 meV for the valence band tail states and about 25 meV for the conduction band tail states - see, for instance, (Cody, 1981) and the relevant articles cited in the reviews in (Street, 1991) and (Searle, 1998). Furthermore, the tail states width has been associated with a "degree" of disorder, with the implication that the optoelectronic properties of a-Si:H are also dependent on its value.
- ii. The localized defect states in the middle of the gap are associated with the formation of DBs. Different models have been proposed to identify the percentage and the energy levels of neutral DBs vs. the positive and negative DBs. Indeed, a DB is identified not only by the fact that the bond is unsatisfied, but also by its net charge, which is determined by the number of electrons sharing the dangling bond, i.e., no electrons imply a positive DB ( $D^+$ ), a single electron makes the bond a neutral one ( $D^0$ ), while the presence of two electrons lead to negative DBs ( $D^-$ ). One of the most interesting and

utilized models, describing the energy distribution of the three types of defects, is the so-called defect-pool model (Powell & Deane, 1996).

- iii. The localized states in the band tails become delocalized at a critical boundary called the mobility edge. A mobility gap is then defined as the energy separation between the two mobility edges of the conduction and valence bands.

## 2.2 Optical properties of a-Si:H

A-Si:H can be described as a direct band-gap semiconductor. The original study of Tauc *et al.* (1966), in which the distributions of electronic states are assumed to be exactly square-root in character, terminating abruptly at the respective band edges, leads to a simple analysis of optical absorption and luminescence experiments.

Optical absorption and luminescence occur by transition of electrons and holes between electronic states such as conduction and valence bands, tail states, and gap states. Tauc's relation (Tauc, 1966) describes the dependence of the optical absorption constant,  $\alpha$ , on the energy gap as:

$$\alpha\hbar\omega = B(\hbar\omega - E_G)^2 \quad (1)$$

Where B is a constant,  $\hbar\omega$  is the photon energy and  $E_G$  is the optical gap.

The empirical determination of the optical gap  $E_G$  can then be achieved by plotting  $\sqrt{\alpha\hbar\omega}$  vs.  $\hbar\omega$ , which is known as Tauc's plot (a schematic illustration of Tauc's plot is shown in Figure 5).

However, the presence of localized tail states extending from the conduction and valence bands into the energy gap makes the determination of an optical gap unclear. For instance, Malik & O'Leary (2004) and Thevaril & O'Leary (2010) have addressed the fact that in amorphous semiconductors considerable deviations from square-root distributions of electronic states occur. They claim that the presence of tail states introduces a corresponding tail in the imaginary part of the dielectric function,  $\epsilon_2(\hbar\omega)$ , which makes the optical gap difficult to determine, i.e., it introduces a considerable amount of uncertainty into the Tauc optical gap determination procedure.

Nevertheless, it is still a common procedure to determine the optical gap by using Tauc's relation, although two different methods have been used to obtain a value for the gap. The first simply extrapolates the high energy, linear section of the plot of  $\sqrt{\alpha\hbar\omega}$  vs.  $\hbar\omega$ , and takes the intercept with the x-axis as the value of the optical gap, as shown in Figure 5. The second chooses the photon energy at which the absorption coefficient is equal to  $10^4 \text{ cm}^{-1}$ , defined as  $E_{04}$ , as the optical gap.

The characteristic values for the band gap of a-Si:H determined from Tauc's plot range from  $\sim 1.7 \text{ eV}$  to  $\sim 1.9 \text{ eV}$ . The variations in gap value are due to preparation conditions, but it is well accepted that the main parameter responsible for the value of the optical gap is the hydrogen content ( $C_H$ ).

Indeed, there are numerous studies that have investigated the dependence of the optical gap and other optical parameters, like absorption coefficient and refractive index, on  $C_H$ . Earlier studies can be found in the references in (Searle, 1998) and (Street, 1991). In summary, it has been shown that the optical band-gap of a-Si:H tends to increase with hydrogen content; see also, for instance, (Daouahi *et al.*, 2001; Gaspari *et al.*, 1993).

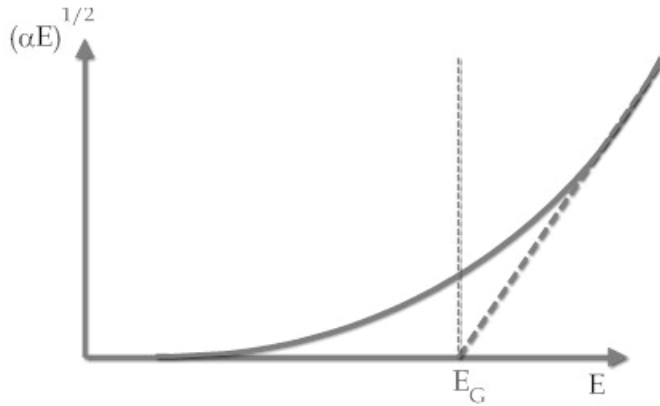


Fig. 5. A schematic illustration of a Tauc's plot. The extrapolation of the high energy linear portion is used to determine the optical gap  $E_G$

### 2.3 Electronic properties of a-Si:H

A-Si:H electronic properties also exhibit a strong dependence on the hydrogen bonding and content. For example, dark conductivity in a-Si:H can be described by two main processes. The first is the standard extended states conduction process, described by the relation (Mott, 1983)

$$\sigma = \sigma_0 \exp\left(-\frac{E_A}{k_B T}\right) \quad (2)$$

where  $\sigma$  and  $\sigma_0$  are the electrical conductivity and a prefactor, respectively, and  $E_A$ ,  $k_B$  and  $T$  are the activation energy, the Boltzmann constant and the temperature, respectively.  $E_A$  is given by either  $E_C - E_F$  or  $E_F - E_V$ , depending on whether electrons or holes are considered, with  $E_C$  and  $E_V$  being the conduction band and valence band edges respectively. The second conduction process is referred to as variable-range hopping (VRH) conduction, a well known process in amorphous materials in general. This conduction process is associated with hopping within tail states, and is characterized by the following temperature dependence (Mott, 1983):

$$\sigma_h = \sigma_{h0} \exp\left(-\frac{B}{T^{1/4}}\right) \quad (3)$$

where  $\sigma_h$  and  $\sigma_{h0}$  are the electrical conductivity and a prefactor, respectively, for variable range hopping.

It has been shown that tail states are also subject to the SW effect (Longeaud *et al.*, 2000). The authors also state that passivation of these DBs in the tail states is related to hydrogen reservoirs. As mentioned before, hydrogen will also influence tail states by reducing the amount of disorder, and by relaxing the structure; furthermore, defects states will tend to shift the Fermi level, thus influencing the activation energy in the dark conductivity. Therefore the hydrogen content plays a fundamental role in determining the conduction processes, as it does for the optical gap.

### 3. The role of hydrogen in a-Si:H

As previously indicated, the presence of hydrogen during the growth of a-Si:H has a dramatic effect on the optoelectronic properties of a-Si. It is a well established fact that the presence of hydrogen atoms reduces the DB density, both at the center of the gap and in the tail states, thus reducing also the  $E_U$  values. Furthermore, the optical gap increases with hydrogen content. However, several questions are still unanswered: for instance, it is still unclear whether there is a direct relation between hydrogen-content and optical gap, or whether such increase is also due to a structural reordering, leading to a less disordered structure, as indicated by the Urbach width.

More importantly, the role of hydrogen dynamics during the defect creation and defect passivation phases of the SW process is still a matter of debate. The nature of hydrogen bonds, the hydrogen distribution, and hydrogen mobility represent crucial parameters in addressing these issues.

#### 3.1 Hydrogen bonding

The most effective characterization of hydrogen content and hydrogen bonding is provided by the vibrational density of states (VDOS), obtained experimentally via transmission and Raman infrared spectroscopy. Fourier Transform Infrared Spectroscopy (FTIR) has become in fact one of the routine modes of investigation to determine the quality of the a-Si:H film (Searle, 1998; Street, 1991; and references therein).

Investigations on the correct interpretation of crucial features in the infrared (IR) spectrum, such as the nature of the stretching modes at about  $2000\text{ cm}^{-1}$ , the roles of chains and microvoids, the distinction among different poly-hydride bonds - i.e. Si-H<sub>2</sub> vs. Si-H<sub>3</sub> vs. (Si-H<sub>n</sub>)<sub>m</sub> - became crucial in order to achieve a better understanding of the role of hydrogen atoms both in the determination of the basic film properties (energy gap, Fermi level, etc.) and in the dynamics of creation and annealing of defects.

For instance, early infrared spectroscopy (Jeffrey *et al.* 1979; Knights & Lujan, 1979; Zanzucchi *et al.*, 1977), primarily of evaporated and sputtered a-Si:H, associated poly-hydride bonding with poor film properties, but Street & Tsai (1988) and Kato & Aoki (1985) showed that that was not the case. A model predicting the various modes of vibration for silicon and hydrogen atoms in a-Si:H was developed by Lucovski *et al.* (1989).

Recently, the correct interpretation of the various modes, in particular the stretching modes between  $1950$  and  $2150\text{ cm}^{-1}$ , has been questioned (Smets & van de Sanden, 2007); however the frequency assignments by Lucovski still provide an excellent reference for the investigation of a-Si:H.

#### 3.2 Hydrogen diffusion models

Several models have been proposed to describe the dynamics of hydrogen diffusion within the amorphous silicon network relative to the Staebler-Wronski effect. Furthermore, many techniques have been employed to generate a realistic computational model of a-Si:H. In particular, molecular dynamics (MD) has become one of the more powerful and frequently used tools for the correlation of the microscopic characteristic of materials with their macroscopic properties, observed experimentally. In order to underline the variety of models and approaches used to analyze hydrogen diffusion, a summary of some of the most

important models and experimental studies introduced over the past 20 years is presented below. It should be noted that the following summary represents only a fraction of the publications on this subject, and it is not intended to be exhaustive, but rather to provide a sense of the diversity in the approaches to the problem.

Santos *et al.* (1991, 1993) present first experimental evidence of light-induced hydrogen motion in undoped a-Si:H, obtained from diffusion experiments under illumination. A definite increase in diffusion was observed for the illuminated samples. The authors speculate that the recombination of e-h pairs releases energy and may induce excitation of hydrogen (H) from a Si–H bond. Another important conclusion is that there is an electronic nature to hydrogen motion in a-Si:H. Up to at least 275 °C, the H diffusion is not purely a thermal process but is dominated by the concentration of carriers.

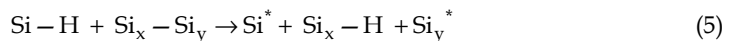
Jackson & Tsai (1992) consider hydrogen bonding in terms of a density of states. Bonding in a given configuration is equivalent to occupancy of the state. The barriers to configuration changes are equated with the energy required to reach transport energy. The main conclusions are that there is a range of possibilities: one extreme is the case in which hydrogen is predominantly bonded on void surfaces and the transport energy is substantially different in a-Si than in c-Si; the other extreme is that hydrogen predominantly resides in platelets structures and the transport energy is similar to c-Si. The actual case depends on deposition conditions. Also, Jackson *et al.* (1993) show that, at relatively high hydrogen concentration, hydrogen atoms reside mainly in clusters. The energy of the clusters depends on the number of hydrogen pairs within the cluster. Annealing has the effect to shift the hydrogen in more stable clusters.

Van de Walle & Street (1994, 1995) investigate, using first principle pseudo-potential calculations, the bonding energetics and the diffusion mechanism of Si–H bonds in general and in amorphous silicon. The main conclusions are as follows: i- it is favorable for a hydrogen atom to move from a DB site to a bond centered (BC) site (bond-centered between two silicon atoms); ii- not only is this a favorable path, but the energy levels which are introduced into the band-gap open the way for carrier-enhanced dissociation; iii- the main path is that by which H stays at approximately the same distance from the original silicon atom, i.e., it moves along the direction of its wagging mode into a BC site. Finally, the motion of hydrogen atoms through a-Si can be described by a diffusion coefficient:

$$D_H = D_0 \exp(-E_A / kT) \quad (4)$$

Where  $E_A$  is the activation energy of the diffusion process.

Biswas *et al.* (1998) agree that H diffusion involves some type of hydrogen interstitial state, but that the exact nature of the diffusion mechanism is not well identified. They propose a type of H diffusion motion more consistent with energetics calculations and experimental evidence. The authors use a tight-binding model to calculate the energy to break a Si–H bond and place the hydrogen atom at nearby or distant silicon sites. They find that hydrogen is very reactive, and can form a new Si–H bond by breaking a Si–Si bond. This is represented by:



These configurations typically consist of two DBs ( $\text{Si}^*$  and  $\text{Si}_y^*$ ). Remarkably, the energy of reaction is low even when the Si–H bond being broken is not a weak one. The authors

identify a manifold of transport states, which depends on the bond length deviation of Si–Si bonds, through the a-Si:H network. They propose that diffusion of hydrogen proceeds by the hydrogen atom breaking and reforming Si–Si bonds in the network, with the diffusing hydrogen carrying a transporting DB along. The basic conclusion is that hydrogen motion is very reactive and does not rely on the existing DBs in the network. It is also somewhat different from the hydrogen motion through bond-centered sites, which according to these authors is a less reactive process since it implies that the Si–Si bond must stretch outwards to accommodate the hydrogen atom. The calculation of the energy barriers is complex, but the authors set an upper limit of 0.8 eV and a likely value of 0.5 eV.

One of the most important and popular models for hydrogen diffusion is the one proposed by Branz (1999) with the Hydrogen Collision Model (HCM). In this model, DBs are created when recombination of light induced carriers stimulates emission of mobile hydrogen from Si-H bonds according to:



The basic process is described by the following steps:

1. The mobile hydrogen atom goes to a Si–Si bond
2. The bond is broken, forming a temporary Si-H and a DB
3. The hydrogen atom hops to another Si–Si bond, again breaking the bond, while the previous bond reconstructs itself.
4. The mobile hydrogen atom continues to hop (it can be proven that its binding energy to the various bonds it breaks on its way is weaker than regular Si-H).
5. Eventually, the mobile hydrogen atom re-traps to Si-H through one of two mechanisms, described below:

The first is a normal re-trapping to an immobile DB, given by  $\text{Si-H}/\text{DB} + \text{DB} \rightarrow \text{Si-H}$ , that is, the inverse process of eq. [6]. Basically, one can see this phenomenon as an H jumping to an ordinary DB, or as the formation of a bond between the mobile DB - that accompanies the mobile H - and the immobile DB. In both cases, no net DB results from the process.

The second mechanism can be described as a re-trapping process of the form  $\text{Si-H}/\text{DB} + \text{Si-H}/\text{DB} \rightarrow \text{M}(\text{Si-H})_2$ . This is far less frequent than normal re-trapping. It represents the collision of 2 mobile H atoms (and their accompanying mobile DBs) that associate into a metastable complex,  $\text{M}(\text{Si-H})_2$ , containing a pair of Si-H bonds in close proximity. The meaning of this process is that there is a net formation of 2 DBs (the ones left behind by the original Si-H bonds), thus resulting in the SW effect.

All this can be summarized by the following reaction:



Experimental studies by Cheong *et al.* (2000) examine one of the main and most controversial assumptions of the HC model, namely, that the photo-generated mobile hydrogen atoms can move a long distance at room temperature. They devised an experiment to observe hydrogen motion at room temperature, since detection with traditional methods such as IR and deuterium tracing is inadequate. By using the high sensitivity of the Raman spectrum of electro-chromic amorphous tungsten ( $\text{a-WO}_3$ ) to hydrogen insertion the authors were able to detect the long-range motion of hydrogen at room temperature.



The floating bond (FB) model as described, for instance, in (Biswas & Pan 2003), proposes an alternative explanation for the H diffusion process. To put it simply, compared with the hydrogen-collision model proposed by Branz, the creation of DBs is mediated by floating bonds rather than hydrogen atoms.

The proponents of the FB model point out that the emission rate of mobile hydrogen should be larger than the creation rate of a pair of DB and FB and that the mobility of movable hydrogen should be faster than that of FB, leading to the dominance of the Branz mechanism for DB creation. However, one should note that the possibility of the DB creation by the mobile hydrogen in the case of the HC model is very small, but DB-FB pair creation directly leads to the creation of DB.

As mentioned previously, the hydrogen distribution is also an important parameter in determining the dynamics of the SW effect. For instance, Tuttle & Adams (1997) show that the energetic and properties of H-atoms must be analyzed considering also their phases, i.e., dilute or clustered. According to the authors, the relative ratio of these phases and their distribution has an important role in determining the properties of a-Si:H. This is a fundamental fact that needs to be taken into account, if a model has to be used to simulate processes connected with hydrogen dynamics, including the testing of the models outlined above that have come to prominence as explanations of the Staebler-Wronski effect.

Gaspari *et al.* (2010) have examined the hydrogen distribution in simulated samples, obtained by *ab-initio* Molecular Dynamics (AIMD), by examining the H-H radial distribution function. It was noted that the H-structure and its distribution within the underlying silicon network is crucial in determining the properties of a-Si:H and for finding whether the sample possesses high quality characteristics for photovoltaic or micro-electronic applications. These findings are in agreement with results reported in (Tuttle & Adams, 1997), and indicate that the dilute vs. clustered distribution ratio, combined with a proper interatomic distance, plays a major role in determining the properties of a-Si:H.

More recent studies continue to refine old models and propose new ones; however the focus has now shifted on the computational aspect of the modeling and, in particular, the realism of the model structure. This topic will be discussed in section 5.

In the following section, a unique procedure providing a novel experimental and theoretical analysis regarding dangling bond formation and annealing in a-Si:H is presented. The approach employed is the incorporation of tritium into a-Si:H.

#### 4. Tritiated amorphous silicon

In order to shed light on the role of hydrogen in defect dynamics, it would be desirable to be able to control the evolution of DBs and correlate it with hydrogen dynamics. However, a quantitative study in which the density of DBs is changed usually involves changing deposition conditions, or high-temperature annealing, or damaging the material with high-energy particles or light (Danesh *et al.*, 2005; Schneider & Schröder, 1990; Sholz *et al.*, 1994). These procedures modify, to varying degree, other structural properties of the material, making it difficult to isolate the effect of DBs on the optoelectronic properties of a-Si : H.

An alternative approach to investigating the properties of a-Si:H has been to substitute hydrogen with one of its isotopes, tritium, and use the effects of the radioactive decay process of tritium as a means to follow the dynamics of defect creation and annealing, and their impact on the opto-electronic properties (Costea *et al.*, 2000; Gaspari *et al.*, 2000; Kherani *et al.*, 2008; Kostas *et al.*, 2000, 2003, 2005; Zukotynski *et al.*, 2002).

#### 4.1 Dangling bond formation due to tritium decay

Tritium decay is described by the formula:  $T \rightarrow {}^3\text{He}^+ + \beta^- + \bar{\nu}$ , where  $\beta^-$  is the beta-particle emitted by the Tritium atom and  $\bar{\nu}$  is an anti-neutrino. The half-life of tritium is 12.3 years and the mean energy of the beta particle is 5.69 keV. The bonding of tritium in amorphous semiconductors is stable at room temperature (Sidhu *et al.*, 1999).

Because of the direct-like nature of the energy gap in amorphous semiconductors, radiative recombination of electron-hole pairs is allowed. Furthermore, the nuclear decay process which leads to the emission of a  $\beta$  particle from a Si-T site will produce a  ${}^3\text{He}$  atom which will diffuse out and leave behind a dangling bond (or recombination center, as shown in Figure 6). This process has led to a novel way of investigating the properties of amorphous silicon and amorphous semiconductors in general; see, for instance, (Kosteski *et al.*, 2000, 2003; Zukotynski *et al.*, 2002).

It should be noted that tritium decay has side effects that might in turn have an impact on DB formation (i.e., He recoil, e-h pair recombination). These issues have been addressed and it was proven that the impact of the secondary effects is negligible. A detailed analysis of the relative impact of electron-hole pair recombination is presented in the following sub-section.

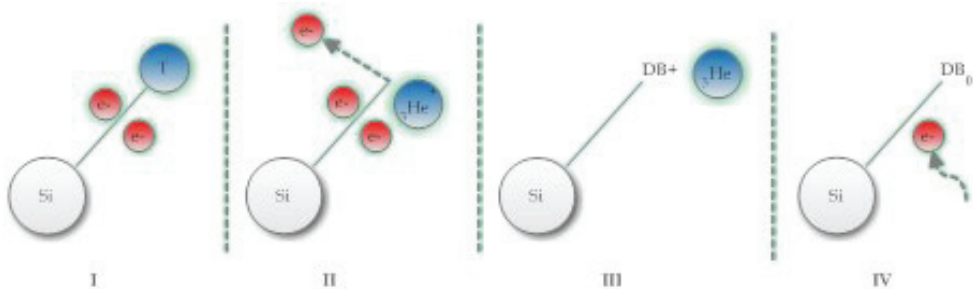


Fig. 6. The mechanism of tritium decay and dangling bond formation: I – Tritium is bonded to a Si atom and shares 2 covalently bonded electrons; II – Tritium decays into  ${}^3\text{He}^+$  and emits a high energy electron ( $\beta$  emission); III – The  ${}^3\text{He}^+$  ion captures both electrons shared with the Si atom and leaves behind a positive dangling bond ( $\text{DB}^+$ ); IV – The positive DB can become a neutral DB by capturing in turn an electron generated by collisions between the original  $\beta$  particle and the silicon matrix. An average of 1500 electron-hole pairs per  $\beta$  emission is generated via this process (Kosteski *et al.*, 2000).

#### 4.2 Effect of electron-hole pairs on dangling bonds

The tritium decay process results in the emission of a  $\beta$  particle with a mean energy of 5.7 keV. The  $\beta$  decay transforms the tritium atom into  ${}^3\text{He}^+$  with a, maximum, recoil energy of about 3 eV. Furthermore, electron-hole (e-h) pairs will be created in the material as the  $\beta$  particle transfers its energy to the silicon matrix.

It has been shown that electrons with keV energies are unlikely to produce atomic displacements (Dubeau *et al.*, 1996). They lose energy in collisions with electrons in the material, through which they pass, creating e-h pairs that thermalize by shedding 'Raman' phonons. In the case of a-Si:H, a pair is created for every 4.3 eV of energy lost. It can also be shown that Helium recoil is expected to create little damage (Street *et al.*, 1979; Stutzmann, 1991).

On the other hand, e-h pairs recombination has also been associated with the creation of DBs (Yelon *et al.*, 2000) and with the mechanism of hydrogen diffusion in a-Si:H (Branz *et al.*, 1993, 1999; Cheong *et al.*, 2000; Santos *et al.*, 1991, 1992). The relative impact of e-h pairs on DB formation can be estimated as follows:

An estimate of the number of e-h pairs generated by tritium decay in an a-Si:H:T film is given by the formula (Kosteski *et al.*, 2000):

$$G = \lambda n_{\text{Tv}} E_{\text{avg}} / \varepsilon \quad (8)$$

Where  $\lambda$  is the decay constant of tritium ( $\lambda = 1.78 \times 10^{-9} \text{ s}^{-1}$ ),  $E_{\text{avg}}$  is the average energy of a beta particle (5.7 keV) and  $\varepsilon$  is the energy needed to produce an electron-hole pair (4.3 eV);  $n_{\text{Tv}}$  is the volume density of atomic tritium. Assuming  $n_{\text{Tv}} \sim 5 \text{ at.}\%$ , as confirmed by IR measurements for standard tritiated samples used in the investigation (Gaspari *et al.*, 2000; Sidhu *et al.*, 1999), we obtain:

$$G = 5.9 \times 10^{15} \text{ cm}^{-3} \text{ s}^{-1} \quad (9)$$

The effects of electron beam irradiation on a-Si:H has been extensively investigated (Schneider & Schroder, 1990; Scholz *et al.*, 1994). In particular, the authors examined the effect of keV electrons - in the range 1 to 30 keV - and determined that metastable states were formed as a result of the irradiation. The results of their work can be summarized as follows:

- The annealing kinetics of these defects is the same as for those produced by light.
- The DB creation kinetics is linear with time over more than two decades in time.
- The approach to saturation goes from linear to saturated with a change of less than a factor of 2 in the total number of metastable defects.
- There is no sub-linear regime, in contrast to light-induced defect creation and annealing.
- The saturation defect density is independent of dose rate over three orders of magnitude and independent of primary electron energy from less than 1 to more than 30 keV .
- Finally, the defect creation rate and saturation are independent of temperature from 170 °C to room temperature.

Yelon *et al.* (2000) applied the hydrogen collision model developed by Branz to explain the origin of metastable states due to ion bombardment. Since the work by Schroder and co-workers deals in the most part with room temperature 20 keV irradiation, at 170 mW cm<sup>-2</sup>, of samples, d=0.6 μm thick, the authors have compared their model to the above-mentioned experimental conditions. The intensity of the e-beam corresponds to a flux of  $\Phi = 5.3 \times 10^{13} \text{ cm}^{-2} \text{ s}^{-1}$  electrons striking the sample. In this case, the initial *measured* creation rate of dangling bonds is  $R_0 = 2 \times 10^{15} \text{ cm}^{-3} \text{ s}^{-1}$ . They obtained for the volume-averaged pair generation rate the number:

$$R = \Phi N_p / d = 6 \times 10^{20} \text{ cm}^{-3} \text{ s}^{-1} \quad (10)$$

which is comparable to that of light degradation at the smaller intensities for which smaller DB creation rates and sub-linear ( $N_{\text{db}} \propto t^{1/3}$ ) kinetics are observed.

By applying Yelon's treatment to e-h pairs generated by beta particles originating from tritium decay, it can be shown that the number of dangling bond due to e-h recombination is 2 orders of magnitude less than the number due to the direct conversion of a Si-T bond into a DB. This is shown in Figure 7.

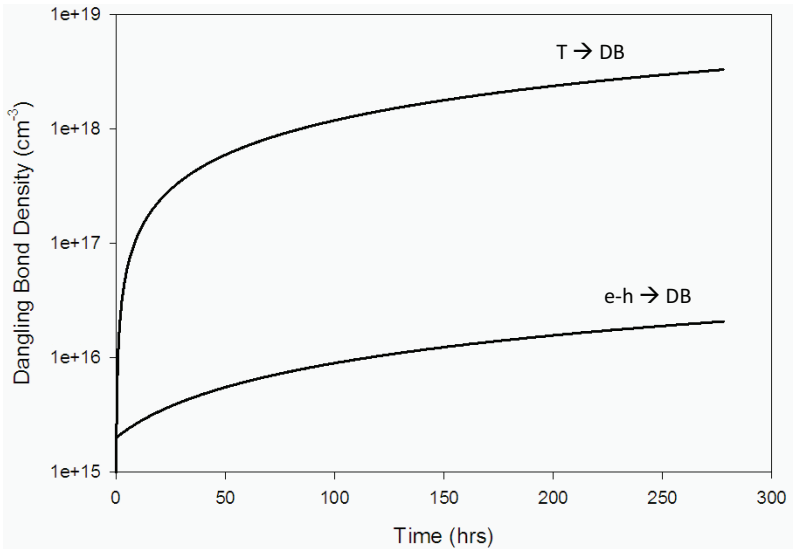


Fig. 7. DB generation rates due to direct conversion of a Si-T bond into a DB and to e-h pair recombination.

In summary, the studies of the properties of a-Si:H:T thin films have established the following:

Creation of DBs, or induced changes to the host structure, by other causes associated with Tritium decay (i.e., irradiation damage from  $\beta$  particles, e-h pair recombination, He recoil) is negligible. This is of particular relevance, since it makes it possible to eliminate any side effects of Tritium decay from the analysis, in particular electron irradiation. Calculations have shown that DBs due to electron irradiation caused by Tritium decay account for less than 1% of the total number of dangling bonds created by the release of the He atom from the Si bond.

Annealing recovers the photoluminescence (PL) and the electrical properties of the tritiated samples (see figures 8a and 8b). This is the fundamental aspect of the SW process in a-Si:H:T since the dangling bonds are created following a well known nuclear process, in which the Tritium atom is replaced by an Helium atom which diffuses away from the original bond. This clearly shows that the annealing process cannot be a simple reversal of the formation process of DBs. Therefore the passivation of DBs appears to be independent of the DB formation process and linked to the a-Si:H structure and bonding configuration.

The significance of point 2 should be emphasized: many models of the SW effect, in particular earlier ones (Adler, 1984; Stutzmann et al., 1985), are based on the assumption that the annealing mechanism is basically the reverse process of the dangling bond formation mechanism. Although some fundamental common aspect might be present in both phases of the SW process, it is possible to focus on each phase independently. In

particular, the objective is to establish the relationship between the structure of a-Si:H (i.e. void fraction, hydrogen bonding, etc.) and the curing process (i.e., is it due to H diffusion and/or a network readjustment during annealing? If H diffusion is involved, how is it mediated?). A number of fundamental issues remain unresolved: microscopic atom dynamics, for instance, influences atomic structure, chemical bonding, diffusion and vibrations, and are difficult to study both experimentally and theoretically. Furthermore, it is not clear why the number of DBs measured by electron spin resonance (ESR) is one order of magnitude less than expected, as noted by Whitaker *et al.* (2004) and Ju *et al.* (2007).

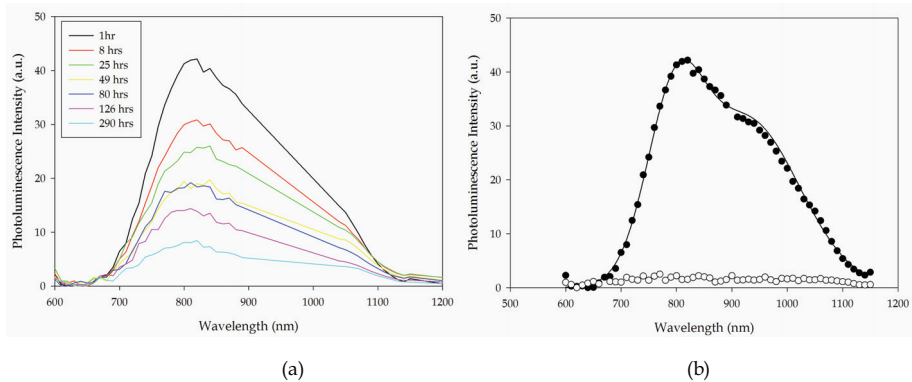


Fig. 8. (a) Decay of PL signal for a tritiated amorphous silicon film. The black curve was taken one hour after deposition, and the decay vs. time is shown by the coloured curves, labelled in the figure by the post-deposition times at which the spectra were recorded. (b) PL spectrum taken for the same sample after annealing. The open dots show the PL signal (almost completely quenched) approximately two weeks after deposition. The filled circles show the recovered PL signal after annealing at 150 °C for one hour.

### 4.3 The stretched exponential behaviour

One of the most interesting observations for tritiated a-Si:H is that the increase in DBs density can be described by a stretched-exponential function, as shown in figure 9 (Kosteski *et al.*, 2003). This indicates that the expected exponential growth of DBs due to tritium decay has a competing process of DB passivation that leads eventually to saturation and a steady-state distribution of DBs.

One hypothesis is that hydrogen atoms that diffuse from nearby sites annihilate the tritium induced defects. In this case, hydrogen detachment from such a site should not be accompanied by the creation of a new defect. This might be possible if the hydrogen atom comes from a large reservoir of paired hydrogen sites such as double-hydrogen complexes (Branz, 1999) or hydrogenated vacancies (Zhang & Branz, 2001). It should be noted that a similar concept has been proposed for DBs in tail states (Longeau, 2000).

The stretched exponential behaviour has been reported for a number of different conditions for a-Si:H, for instance: Danesh *et al.* (2005) have investigated a-Si:H degradation for 18 MeV electron beam bombardment. They observed that “the annealing kinetics obeys the stretched-exponential law which is known to be typical for a-Si:H films underwent the light-induced degradation.”

The stretched exponential behaviour has also been investigated, among others, by Morigaki & Hikita (2007) and Morigaki *et al.* (2008) for light-induced defects. Morigaki considers three possible annealing mechanisms, i.e., hydrogen dissociation from two closely located Si-H bonds, dissociation from a hydrogen molecule, and reconstruction of silicon network (Zukotynski *et al.*, 2002). Although the dissociation values for the first two processes are higher than the activation energy of thermal annealing ( $\sim 1$  eV), Morigaki argues that the values are still reasonable for activation energies higher than 1 eV.

It is not clear, however, why the same stretched exponential behaviour and similar saturation values are observed for tritiated samples, unexposed to light, or for high energy electron bombardment.

The stretched exponential behaviour observed for tritiated amorphous silicon is consistent with the reported values for light induced defects. The major difference between the defect re-equilibration dynamics in a-Si:H:T vs. illuminated a-Si:H is that in the former case there is no assistance from external excitation due to photons.

Yet, it appears that the a-Si:H:T structure still adjusts to the increase in the density of dangling bonds. As previously mentioned, this indicates that a common process, related to a combination of network reconstruction and H-diffusion, should be at the basis of the annealing phase, regardless of the DB formation mechanism.

The hydrogen bonding structure and the hydrogen diffusion process are linked by the activation energies required to bring a hydrogen atom into the mobility band, as indicated, for instance, in (Powell & Deane, 1996). As the above mentioned authors point out in their "defect pool" model, hydrogen transitions involve silicon DB defects, the defect energy and the Fermi energy. The hydrogen density of states (HDOS) is a crucial factor in this model, and is at the basis of the defect equilibration dynamics.

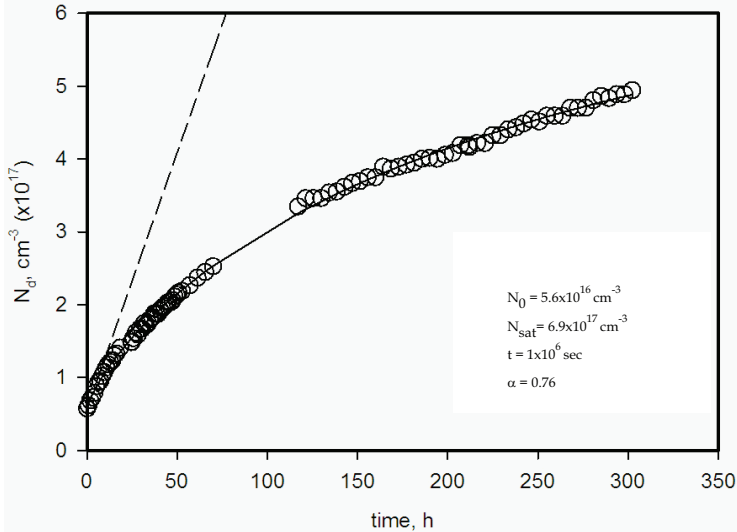


Fig. 9. Dangling bond rate of creation for a-Si:H:T measured by ESR (Kosteski, 2003). The dashed line is the theoretical prediction for one dangling bond per tritium decay. The solid line is a stretched exponential fit to the experimental data. The parameters in the inset refer to the stretched exponential formula:  $N_d = N_0 + (N_{sat} - N_0) \times \left[ 1 - \exp(-t/\tau)^\alpha \right]$ .

## 5. *Ab Initio* molecular dynamics

The main reason for the development of so many models and interpretations of hydrogen mobility is due to the difficulty of obtaining a clear microscopic picture of the dynamic processes via experimental techniques. The only way to investigate the trajectories of hydrogen atoms in a-Si:H is to extensively model it numerically.

Many theoretical techniques have been employed to generate a realistic model of a-Si:H, including classical MD (Ishimaru, 2002; Izumi *et al.*, 2005), tight-binding MD (Singh *et al.*, 2004; Tuttle & Adams, 1997), and *Ab-Initio* MD (Su & Pantelides, 2002). Molecular dynamics has become one of the more powerful and frequently used tools for the correlation of the microscopic characteristic of materials with their macroscopic properties, observed experimentally. Some authors (Abteu & Drabold, 2006) have applied the model to simulate the dynamics of hydrogen diffusion, in particular as a way of analyzing possible mechanisms behind the Staebler-Wronski (SW) effect. However, classical MD is not sufficiently accurate to describe the covalent bonding and forces in semiconductors, and a tight-binding approach; even DFT-LDA based MD (Singh *et al.*, 2004) is not sufficiently transferable to non-crystalline systems.

For amorphous Si, with no translational symmetry, presence of non-saturated Si bonds, hydrogen switching between host Si atoms and diffusion, the most accurate approach is first principles (or *ab-initio*) MD. Although AIMD has to be used with a smaller unit cell and the simulation time is shorter compared to, for instance, tight-binding, it is extremely accurate in the description of the interatomic potential, forces, and inharmonicity of the interaction.

We have seen that the microscopic details of disordering, hydrogen migration and bonding within the amorphous silicon network are crucial for the understanding of a-Si:H, and for the improvement of the overall quality of the material. However, hydrogen migration and other complex properties must be investigated within a realistic structure to obtain useful information. Kupchak *et al.* (2008) and Gaspari *et al.* (2009) have shown that the commonly used radial distribution function (RDF) is not a sufficient validation parameter, and that the recreation of physically consistent vibrational spectra does, on the other hand, represent a sound validation protocol.

The authors have used AIMD to model bulk a-Si:H under various conditions. At various key points in simulations, detailed pictures of measurable quantities related to the electronic structure have been calculated, assuring that the model remain close to nature. In AIMD one treats atoms classically, but the potential is calculated quantum mechanically using DFT. The solutions to the Schrödinger equation are approximated numerically. In terms of computing operations, these calculations involve mainly matrix operations and fast Fourier transforms (FFT). Details of this approach can be found in (Gaspari *et al.*, 2009; Kupchak *et al.*, 2008).

This approach has led to reproducing all the fundamental vibrational signals in a-Si:H. Computer visualization was used to demonstrate some of the most important features, like the existence of poly-hydride bonding. The vibrational spectra obtained for the “good” samples were consistent with experimental data and showed also time stability, as shown in Figures 10 and 11.

As previously mentioned, Gaspari *et al.* (2009) have examined the appropriateness of using RDF as a validation parameter for assessing the realism of a simulated structure. The authors compared a variety of a-Si:H samples with H content from 0 to 20%, and have found

that the RDF practically does not depend on the amount of hydrogen in the sample. Furthermore, all the calculated RDF agree reasonably well with the most recent and accurate RDF measurement for a-Si with no hydrogen. This reflects the fact that the most probable distance between neighboring atoms is equal to a sum of the atoms' covalent radii. Even when hydrogen passivates the dangling bonds, this does not modify the Si-Si bond length. On the other hand, atomic vibrations do depend on microscopic bonding (bonds), their angular distribution, distortion or breaking. In fact, the experimental measurements demonstrate a variety of spectral features that obviously require microscopic theoretical interpretation.

Furthermore, in order to further verify the validity of the model, the authors have also studied the special case of metastable Si-H-Si bonds, observed experimentally by Darwich *et al.* (1995), and have confirmed Darwich's claim within experimental error. Gaspari *et al.* (2009) indicate that the decrease in the vibrational frequency with respect to that of a stable mono-hydride bond is due to the sharing of the hydrogen electron density between two Si atoms. This decreases the Si-H bond strength, increases the bond length and results in reduction of the vibrational frequency. Therefore, the band in the 1500-1800  $\text{cm}^{-1}$  region can be interpreted as the signature of hydrogen metastable bonds, including the TCB bond, with variations in the frequency due to the different overlap between the H and the Si electron wave functions.

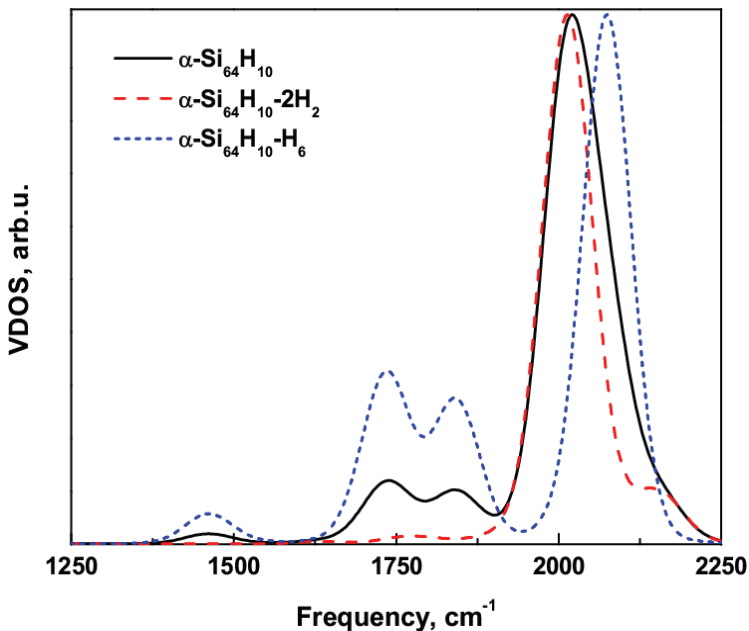


Fig. 10. Hydrogen stretch vibrations for a-Si<sub>64</sub>-H<sub>10</sub> system at high frequency (Kupchak *et al.*, 2008). The solid black line shows all H-associated stretching vibrations, including dihydride modes (blue, short dash) and monohydride modes (red, long dash). Note the very close agreement with data by Lucovsky *et al.* (1989).



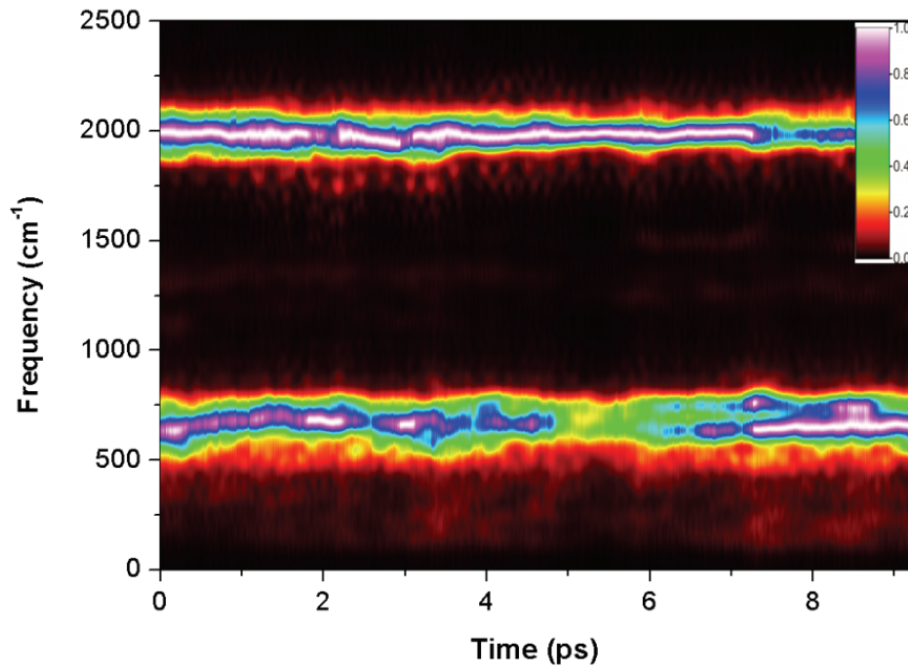


Fig. 11. Time dependent frequencies for a “good” sample. Note the absence of vibrations between the two main modes ( $2000\text{ cm}^{-1}$  and  $640\text{ cm}^{-1}$ ) indicating stability of the bonds. The colour scale is related to the peak intensity, that is, white represents the strongest signal (peak), while black represents no vibrational signal (Kupchak *et al.*, 2008).

The investigation led by this author has proven that in order to validate the simulation of complex structure, bonding, and diffusion, a protocol needs to be established for the verification of the “realism” of the simulated models. Using hydrogenated amorphous silicon as an example, Gaspari *et al.* (2009, 2010) have unambiguously demonstrated that reproduction of the radial distribution function, used commonly in numerical simulations, is not sufficient and must be complemented with verification of other, more complex, macroscopic properties. By focusing on the vibrational modes of the amorphous system, it was proven that the vibrational spectra represent a crucial testing tool for non-crystalline materials because of their complexity and sensitive link to structure and bonding configuration. Successful reproduction of all the experimentally observed vibrational features for a-Si:H has proven the validity of the algorithm and indicates that hydrogen structure and dynamics are extremely sensitive to the parameters of the model. In order to correctly apply a numerical model to extract such important macroscopic parameters as density of states, optical gaps, and migration dynamics, the accuracy should be verified first by the derivation of the standard vibrational modes and comparison with experimental observation.

Indeed, the importance of hydrogen distribution and its connection to hydrogen mobility is demonstrated by recent investigations, both experimental and theoretical, on the role of hydrogen in a-Si:H. For instance, Fehr *et al.* (2010) investigated the distribution of hydrogen

atoms around native dangling bonds in a-Si:H by electron-nuclear double resonance (ENDOR). The authors suggest that the hydrogen distribution is continuous and homogeneous and there is no indication for a short-range order between hydrogen atoms and dangling bonds. This is in contrast with current understanding that hydrogen is distributed as a succession of clustered and diluted phases (Gaspari *et al.*, 2010; Tuttle & Adams, 1997). Such controversies can only be addressed by using a rigorous, realistic model to simulate properties and dynamic processes.

## 6. Conclusions

Hydrogenated Amorphous Silicon (a-Si:H) has been the subject of intensive investigation for over 30 years. The main role of hydrogen in amorphous silicon is the passivation of the Si dangling bonds (DBs) to restore a proper energy gap and the semiconducting properties, thus enabling extensive application of a-Si:H in the microelectronics and the photovoltaic industry. Due to the importance of hydrogen, many experimental methods have been used to characterize the DBs passivation, bonding chemistry and related mechanisms of degradation of the material. Among the numerous experimental techniques used to study a-Si:H and the role of hydrogen, the Fourier Transform Infrared Spectroscopy (FTIR) is used extensively to analyze vibrational spectra of a-Si:H. Although FTIR represents one of the most common and powerful techniques, no microscopic links between the observed vibrational features of the hydrogen and the microscopic properties of a-Si:H can be yet established by any experimental means.

A number of other important fundamental issues remain unresolved for a-Si:H as well. Microscopic atom dynamics, for instance, influences atomic structure, chemical bonding, diffusion and vibrations, and are difficult to study both experimentally and theoretically. However, the microscopic details of disordering, hydrogen migration and bonding within the amorphous silicon network is crucial for the understanding of a-Si:H, and for the improvement of the overall quality of the material.

The Staebler-Wronski effect epitomizes this need. It is generally accepted that a-Si:H light-soaking degradation, observed by Staebler and Wronski, is caused by Si-H bonds breaking during illumination. However, the microscopic details of the SW effect are still controversial and it is not clear how to experimentally predict the stability of a-Si:H films, grown at particular temperature and hydrogen concentration, with respect to light induced degradation. Furthermore, a number of alternative techniques have been used to create dangling bonds, and the same dynamics has been observed in the curing (annealing) phase. That is, no matter how the dangling bonds were formed, a similar curing process occurs during annealing. This might be due to diffusion of hydrogen atoms, structural readjustment, or a combination of the two.

In this chapter I have briefly summarized how the optical and electronic properties of a-Si:H are dependent on the hydrogen content and pointed out that the challenge of uncovering the microscopic details of hydrogen bonding and distribution and their correlation with hydrogen dynamics cannot be answered by standard experimental techniques.

On the other hand, with the continuous improvement of computational capacity and software quality, the simulation of realistic structures is becoming ever more feasible. In particular, *Ab Initio* Molecular Dynamics (AIMD) allows highly accurate simulation of the dynamical properties of various systems, including amorphous materials.

The goal of such simulations is to be able to reproduce dynamic processes and follow the diffusion of hydrogen, the bond breaking processes, and the structural reorganization of the material, following external perturbations. The DB creation process in tritiated amorphous silicon can provide a simple and convenient source of experimental data that can be used as a basis for such simulations, since the tritium decay process is well understood, and its effect on a-Si:H can be treated as the simple removal of an hydrogen atom from an existing Si–H bond.

The main challenge is of course to make sure that the simulated structure is indeed a realistic one. The author of this chapter has shown that several models lack the necessary realism, since the validation of the model is based on the radial distribution function of the Si–Si bonds. The author has also shown that the reproduction of the vibrational modes of a-Si:H represents a much better validation test for a realistic structure. As the continuous advances in computational science will allow for the use of bigger simulated structures, the future direction of these studies should aim at reproducing other fundamental properties, such as the band-gap, the density of states, etc. By achieving this goal, it will be possible then to simulate dynamic processes too, such as the SW effect, and to shed light both on the formation phase of the dangling bonds and on the curing phase.

## 7. Acknowledgment

The work by the author was supported by the Shared Hierarchical Academic Research Computing Network (SHARCNET) and Natural Sciences and Engineering Research Council of Canada (NSERC).

The author would also like to thank Dr. A. Chkrebti for his invaluable contribution and leadership in the development of the AIMD algorithm. Thanks go also to Dr. J.M. Perz, Dr. S. Zukotynski, and Dr. N. P. Kherani for their support and helpful discussions spread over 20 years.

## 8. References

- Abtew, T.A., Drabold, D.A. (2006) *Phys. Rev. B*, Vol. 74, 085201.
- Adler D., (1984) *AIP Conference Proceedings*, n 120, 70-77.
- Akkaya, A., & Akta, G. (1995). *Mater. Lett.*, Vol. 22, 271.
- Baranovski, S. (2006). *Charge transport in disordered solids with applications in electronics*. John Wiley & Sons, ISBN: 9780470095041, New York.
- Biswas, R., Li, Q., Pan, B.C., Yoon, Y. (1998) *Phys. Rev. B*, Vol. 57, 2253.
- Biswas, R., Pan, B.C. (2003) *Solar Energy Materials and Solar Cells*, Vol. 78, 447.
- Branz, H.M., Asher, S.E., Nelson, B.P., (1993) *Phys. Rev. B* Vol. 47, 7061.
- Branz, H.M. (1999) *Phys. Rev. B* Vol. 59, 5498.
- Branz, H.M., Asher, S.E., Gleskova, H., Wagner S., (1999) *Phys. Rev. B* Vol. 59, 5513.
- Bruno, G., Capezzuto P., Madan A., (Eds.) (1995) *Plasma Deposition of Amorphous Silicon-Based Materials*. Academic Press, ISBN: 9780121379407, Burlington, MA.
- Cheong, H.M., Lee, S.H., Nelson, B.P., Mascarenhas, A., Deb, S.K., (2000) *App. Phys. Lett.* B Vol. 77, 2686.
- Cody, G.D., Tiedje, T., Abeles, B., Brooks B., Goldstein, Y. (1981) *Phys. Rev. Lett.* Vol. 47, 1480.

- Costea, S., Gaspari, F., Kostaschi, T., Zukotynski, S., Kherani, N. P., Shmayda, W.T. (2000) *Mat. Res. Soc. Symp. Proc.* Vol. 609, A27.4 (2000).
- Costea, S., Pisana, S., Kherani, N.P., Gaspari, F., Kostaschi, T., Shmayda, W.T., Zukotynski, S. (2005) *Fusion science and technology* Vol. 48, 712.
- Danesh, P., Pantchev, B., Vlaikova, A. (2005) *Nuclear Instruments and Methods in Physics Research B*, Vol. 239, 370.
- Daouahi, M., Ben Othmane, A., Zellama, K., Zeinert, A., Essamet, M., Bouchriha, H. (2001) *Solid State Communications* Vol. 120, 243.
- Darwich, R., Roca I. Cabarrocas, P., Vallon, S., Ossikovski, R., Morin, P., Zellama, K. (1995) *Phil. Mag. B*, Vol. 72, 363.
- Dubeau, J., Hamel, L.A., Pochet, T., (1996) *Phys. Rev. B* 53, 10 740
- Fehr, M., Schnegg, A., Teutloff, C., Bittl, R., Astakhov, O., Finger, F., Rech, B., Lips, K. (2010) *Physica Status Solidi A*, Vol. 207, 552.
- Gaspari, F., O'Leary, S.K., Zukotynski, S., Perz, J. (1993) *J. Non-Cryst. Solids* Vol. 155, 149.
- Gaspari, F., Kostaschi, T., Zukotynski, S., Kherani, N. P., Shmayda, W. (2000) *Phil. Mag. B*, Vol. 80, 561.
- Gaspari, F., Shkrebtii, A., Kupchak, I., Perz, J.M. (2009) *Phys. Rev. B* Vol 79, 224203.
- Gaspari, F., Shkrebtii, A., Kupchak, I., Teatro, T., Ibrahim, Z.A. (2010) *35th IEEE Photovoltaic Specialists Conference Proceedings*, Honolulu Hawaii, June 20-25, 003671-75.
- Ishimaru, M. (2002) *J. Appl. Phys.* Vol. 91, 686.
- Izumi, S., Hara, S., Kumagai, T., Sakai, S. (2005) *J. Cryst. Growth* Vol. 274, 47.
- Jackson, W.B., Tsai, C.C. (1992) *Phys. Rev. B*, Vol. 45, 6564.
- Jackson, W.B., Santos, P.V., Tsai, C.C. (1993) *Phys. Rev. B*, Vol. 47, 9993.
- Jeffrey, F.R., Shanks, H.R., Danielson, G.C. (1979) *Appl. Phys. Lett.* Vol. 50, 7034.
- Kasap, S. (2005) *Principles of Electronic Materials and Devices*. McGraw-Hill, retrieved from <http://Materials.usask.ca>.
- Kato, S., Aoki, T. (1985) *J. Non-Cryst. Solids* Vols. 77&78, 813.
- Kherani, N.P., Liu, B., Virk, K., Kostaschi, T., Gaspari, F., Shmayda, W.T., Zukotynski, S., Chen, K.P. (2008) *J. Appl. Phys.* Vol. 103, 024906.
- Knights, J.C., Lujan, R.A. (1979) *Appl. Phys. Lett.* Vol. 35, 244.
- Kostaschi, T., Gaspari, F., Hum, D., Costea, S., Zukotynski, S., Kherani, N.P., Shmayda, W.T. (2000) *Mat. Res. Soc. Symp. Proc.* Vol. 609, A30.1.
- Kostaschi, T., Stradins, P., Kherani, N.P., Gaspari, F., Shmayda, W.T., Sidhu, L., Zukotynski, S. (2003) *IEE Proc. Circuits, Devices and Syst.*, special issue on Amorphous and Microcrystalline Semiconductor Devices, Vol. 150 no. 4, 274.
- Kupchak, I. M., Gaspari, F., Shkrebtii, A. I., Perz, J. M. (2008) *J. Appl. Phys.* Vol. 104, 123525-1
- Laaziri, K., Kycia, S., Roorda, S., Chicoine, M. Robertson, J. L., Wang, J., Moss, S. C. (1999) *Phys. Rev. Lett.* Vol. 82, 3460.
- Ley, L. (1983) "Photoemission and Optical properties", in *The Physics of Hydrogenated Amorphous Silicon*, Vol II, Eds. J.D. Joannopoulos & G. Lucovski, Springer-Verlag, ISBN: 0387128077, New York.\
- Longeaud, C., Roy, D., Teukam Hangouan, Z. (2000) *App. Phys. Lett.* Vol. 77, 3604.
- Lucovski, G., Davidson, B.N., Parsons, G.N., Wang, C. (1989) *J. Non-Cryst. Solids* Vol. 114, 154.
- Malik, S. M., O'Leary, S. K. (2004) *J. Non Cryst. Solids*, Vol. 336, 64.

- Morigaki, K., Hikita, H. (2007) *Phys. Rev. B* 76, 085201
- Morigaki, K., Takeda, K., Hikita, H., Ogihara, C., Roca i Cabarrocas, P. (2008) *J. Non-Cryst. Solids*, Vol. 354, 2131.
- Mott, N. (1983) "Conductivity, Localization, and the Mobility Edge", in *The Physics of Hydrogenated Amorphous Silicon*, Vol II, Eds. J.D. Joannopoulos & G. Lucovski, Springer-Verlag, ISBN: 0387128077, New York.
- O'Leary, S.K., Sidhu, L.S., Zukotynski, S., Perz, J.M. (1996) *Canadian Journal of Physics*, Vol. 74, S256-9.
- Powell, M.J., Deane, S.C., (1996) *Phys. Rev. B*, Vol. 53, 10121.
- Rui, Y., Mei, J., Xu, J., Yang, L., Li, W., Chen, K. (2005) *Proceedings of SPIE - The International Society for Optical Engineering*, Vol. 5774, 279.
- Santos, P.V., Johnson, M.N., Street, R.A. (1991) *Phys. Rev. Lett.* Vol. 67, 2686.
- Santos, P.V., Johnson, N.M., Street, R.A., (1992) *Mat. Res. Symp. Proc.* Vol. 258, 353.
- Santos, P.V., Johnson, M.N., Street, R.A. (1993) *J. Non-Cryst. Solids* Vols. 164-166, Part I, 277.
- Schneider, U., Schröder, B. (1990) *Photovoltaic Specialists Conference. Conference Record of the Twenty First IEEE*, vol. 2, 1521.
- Searle, T. (Ed.) (1998) *Amorphous Silicon and its Alloys*, INSPEC, ISBN: 0852969228, London.
- Sholz, A., Schröder, B., Oechsner, H. (1994) *Mat. Res. Symp. Proc.* Vol. 336, 293.
- Sidhu, L. S., Kostas, T., Zukotynski, S., Kherani, N. P. (1999) *J. Appl. Phys.* Vol. 85, 2574.
- Singh, R., Prakash, S., Shukla, N., Prasad, R. (2004) *Phys. Rev. B* Vol. 70, 115213.
- Smets, A.H.M., van de Sanden, M.C.M. (2007) *Phys. Rev. B*, Vol. 76, 073202.
- Staebler, D.L., Wronski, C.R. (1977) *Appl. Phys. Lett.* Vol. 31, 292.
- Street, R.A., Biegelsen, D., Stuke, J., (1979) *Philos. Mag. B* Vol. 40, 451.
- Street, R.A. (1980) *Phys. Rev. B*, Vol. 21, 5775.
- Street, R.A. (1991) *Hydrogenated Amorphous Silicon*, Cambridge University Press, ISBN: 0521371562, New York.
- Street, R.A. (Ed.) (2000) *Technology and Applications of Amorphous Silicon*, Springer Verlag, ISBN: 3540657142, New York.
- Street, R.A., Tsai, C.C. (1988) *Philos. Mag.* Vol. B57, 663.
- Stutzmann M., Jackson W.B., Tsai, C.C. (1985), *Phys. Rev. B*, Vol. 32, n 1, 23-47
- Stutzmann M., (1991) in *Amorphous and Microcrystalline Amorphous Devices*, Vol. II, Ed. J. Kanicki, Atech House, Boston, p. 129.
- Tauc, J., Grigorovici, R., Vancu, A. (1966) *Phys. Status Solidi*, Vol. 15, 627.
- Thevaril, J.J., O'Leary, S.K. (2010) *J. Appl. Phys.*, Vol. 107, 083105.
- Tuttle, B., Adams, J. B. (1997) *Phys. Rev. B* Vol. 56, 4565.
- Ukpong, A.M. ((2007) *Turkish Journal of Physics*, Vol. 31, 317.
- Van de Walle, C.G., Street, R.A. (1994) *Phys. Rev. B*, Vol. 49, n 20, 14766-9.
- Van de Walle, C.G., Street, R.A. (1995) *Mat. Res. Soc. Symp. Proc.*, Vol. 377, 389.
- Yelon, A., Fritzsche, H, Branz, H.M., (2000) *J. Non-Cryst. Sol.* Vols. 266-268, 437.
- Ju, T., Whitaker, J., Zukotynski, S., Kherani, N., Taylor, P.C., Stradins, P. (2007) *Mat. Res. Soc. Symp. Proc.* Vol. 989, 9.
- Whitaker J., Viner, J., Zukotynski, S., Johnson, E., Taylor, P.C., Stradins, P. (2004) *Mat. Res. Soc. Symp. Proc.* Vol. 808, 153.
- Zanzucchi, P.J., Wronski, C.R., Carlson, D.E. (1977) *J. Appl. Phys.* Vol. 48, 5227.

- Zeman, M. (2006) "Advanced Amorphous Silicon Solar Cell Technologies", in *Thin Film Solar Cells: Fabrication, Characterization and Applications*, Eds. J. Poortmans & V. Arkhipov, John Wiley & Sons, New York.
- Zhang, S.B., Branz, H.M., (2001) *Phys. Rev. Lett.* Vol. 87, 105503
- Zukotynski, S., Gaspari, F., Kherani, N., Kostas, T., Law, K., Shmayda, W.T., Tan, C.M. (2002) *J. Non-Cryst. Solids* Vols. 299-302, 476.

# Silicon–Rich Silicon Oxide Thin Films Fabricated by Electro-Chemical Method

Pham Van Hoi, Do Thuy Chi, Bui Huy and Nguyen Thuy Van  
*Vietnam Academy of Science and Technology,  
Vietnam*

## 1. Introduction

Porous silicon (PS) has attracted increasing research interest in basic physics as well as applications since 1990 when Canham reported on the efficient visible photoluminescence (PL) of porous silicon (Canham, 1990). Structurally, PS consists of many pores and silicon residuals and usually can be described as a homogeneous mixture of silicon, air and, even silicon dioxide. Based on porosity, PS can be classified into three types: nano, meso- and macro-pores. In the case of PS nano-pores, the size of both the silicon residuals and the air voids (pores) can be in the range of few nanometers. The exciton Bohr radius in Si is around 4.3 nm, so that quantum confinement can occur and change the electronic structure of those silicon nanocrystals. On the other hand, because the value of porosity is directly linked to the effective index of refraction of the PS layer, this layer appears as an effective medium, where the refractive index has a tunable value between the index of refraction of bulk Si and that of the air (pores). Those changes in the electronic structure and refractive index of PS when compared with bulk Si make it fascinating as both a low-dimensional material and an optical one. The considerable and controllable changes in the electronic structure and refractive index of PS fabricated by electrochemical anodization make it a promising material for photonics in comparison with bulk silicon and/ or pure silica. Using the oxidation process in O<sub>2</sub> environment at high temperature, the PS samples become silicon-rich silicon oxides (SRSO), which has high chemical instability and avoids the aging of the PS that is important condition for optical devices such as planar optical waveguides, optical interference filters, micro-cavities, etc (Bettotti et al., 2002). During the last decade, Erbium (Er)-doped silicon-rich silicon oxide has attracted much interest due to its big potential application in Si-based optoelectronic devices for telecom and optical sensors. The Er-ions implanted in SRSO materials produce light emission at around wavelength range of 1540 nm, which corresponds to minimum light absorption in silica-based glass fibers. In this regard, a lot of studies have been carried out to improve the luminescence efficiency of this material. Such studies have revealed that co-implantation of Er and O<sub>2</sub> induce a strong enhancement in the Er-ions related emission at range of 1540 nm. In first case, samples were prepared by co-implanting Si and Er into silica thin films or co-sputtering Si, Er<sub>2</sub>O<sub>3</sub> and SiO<sub>2</sub> on the silicon substrate (Shin et al., 1995). In second case, samples were prepared by implanting Er-ions into SiO<sub>2</sub> films containing Si-nanocrystals (nc-Si) and/ or by Er-ion electrochemical deposition on silicon-rich oxide (SRSO) layers. The room temperature luminescence emission at the range of 1540 nm from Er-electrochemically doped porous

silicon was first reported by Kimura T. et al in 1994 (Kimura et al., 1994) and then followed by some other authors. The strong luminescence emission around 1540nm-range of Er-doped SRSO layers at room temperature can be explained by energy transfer from excitons confined in the nc-Si to Er-ions and the evidence of energy transfer had been revealed in photo-luminescent excitation spectra in visible and infrared region when the exciting wavelength was not equalized to resonant absorption wavelength of Er-ions. Up to now, there are very few evidences of energy transfer given in the case of Er-electrochemically doped SRSO layers.

In this book chapter, we will discuss the electrochemical method for preparing SRSO based on PS layers and Er-doped SRSO thin films for waveguide, optical filter and micro-cavity. In concentrating on the controllable changes in the refractive index of PS, we would like to use SRSO as a material for photonic devices such as optical interference filters, micro-cavities, etc. As an optical material, we present the fabrication method and properties of planar optical waveguides, active optical waveguides and optical interference filters operated in the range of infrared wavelengths. The advantage of optical waveguide amplifier based on Erbium-doped SRSO is the efficient energy transfer from electron-hole pairs generated in the Si nanocrystals to their neighbor erbium ions, which decay by emitting light at 1540nm (Bui Huy et al., 2008). The excitation cross-section of Er-ions in Er-doped SRSO is strongly increased in comparison of this one in the Er-doped silica glasses, so that the pump efficiency in Er-doped SRSO waveguides can be very high. The effect of energy transfer in elaborated Er-doped SRSO waveguides has also been explored. In order to design and predict the properties of the optical interference filters and micro-cavity based on SRSO multilayer, a simulation program based on the Transfer Matrix Method (TMM) was set up and the possible causes the difference in reflectivity spectra from this simulation and that from elaborated filters and/or cavity have been also given (Bui Huy et al., 2011). The structure and optical properties of SRSO layers are characterized by FE-SEM (Hitachi S-4800), M-line spectroscopy (Metricon 2010/M) and luminescent measurement. The energy transfer effect between silicon nanocrystals and Er ions in the SRSO layers has been obtained from experiments.

With the above-mentioned aim in mind, this chapter consists of the following sections: Section 2 presents the electrochemical method for preparing PS samples, Section 3 shows SRSO bi-layers based on PS annealed in oxygen environment at high temperature as a passive and active waveguides, Section 4 shows PS and/or SRSO multilayer with periodical refractive index change as an optical filter, Section 5 presents PS and/or SRSO multilayer with DFB configuration as micro-cavity, and Section 6 gives conclusions.

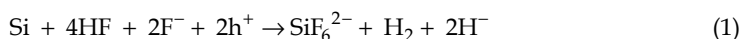
## **2. Electrochemical method for making SRSO thin films**

The porous silicon thin films were formed from silicon wafers by electrochemical etching in hydro-fluoric acid, without the necessity of any deposition process (Smith et al., 1992). During this anodization process a part of the silicon is dissolved and the remaining crystalline silicon forms a sponge-like structure with porosity between some tens percent up to more than 90%. The microstructure of the PS depends on the doping level of the silicon wafers: the use of low doped p-type substrates results in nanoporous silicon (with pore and crystallite size less than 2 nm) and the use of highly doped substrates in mesoporous silicon (size of 2-50 nm) (Herino et al., 1987). In the both cases the structures are much smaller than the wavelength of visible light and the materials appear as a homogenous, effective optical



medium. The effective refractive index of the porous silicon thin films is mainly determined by the porosity which can be varied by several anodization parameters. The most suitable way is changing the anodization current density, with high current densities resulting in high porosities and low refractive indices.

A porous silicon thin film consisting of void spaces in silicon is created as a result of the electrochemical dissolution process in hydrofluoric acid, which can be expressed as in Equation (Valance, 1997):



The mass transport of positive charge carriers ( $\text{h}^+$ ) in the substrate and reactant fluorine ions ( $\text{F}^-$ ) in the electrolyte are key components in the dissolution process. As described in the model by Lehmann and Gösele (Lehman & Gösele, 1991), dissolution begins when holes reach the silicon surface under anodic bias and enable a fluorine ion to replace a hydrogen atom bonded to silicon. Due to the polarizing influence of the bound fluorine ion, further reactions are initiated in which fluorine ions continue to bind to the silicon atom and hydrogen gas is formed. When all four silicon bonds are broken, the silicon atoms become soluble and leave behind an atomic size corrugation in the former atomically flat surface. Pore formation continues at the surface irregularity where the electric field is concentrated and holes are available. The interpore space is depleted of holes, inhibiting sidewall dissolution.

In general, the preparation process of Er-doped silicon-rich silicon oxide layers can be divided into 3 steps: making a porous silicon (PS) layer by anodic etching of a Si-crystalline wafer in a HF solution; Er-ion deposition on the PS layer in Er content solution; and using thermal annealing at high temperature in oxygen and/or inert gases to obtain SRSO materials. The PS sample preparation is carried out in two approaches: keeping the current and/or the potential at a constant value during the electrochemical deposition (ECD) process. The difference between these two methods is that in the constant potential ECD, an n-type Si-crystalline wafer is usually used without annealing steps while in the constant current ECD, p-type Si-wafers are used and need thermal annealing. In our work we used both ECD methods for making PS layers on n- and p-type Si-crystalline wafers.

## 2.1 Experimental procedure

In the electrochemical method for fabrication of porous silicon thin films, silicon wafer acts as the anode and is situated at the bottom of the Teflon cell. The silicon wafer was coated Au-thin film in back-side and contacted to HF-resistant metallic electrode in the form of the disk. This electrode disk enables a uniform contact on the whole area of silicon wafer. The electrolyte is a mixture of hydrofluoric acid and ethanol ( $\text{C}_2\text{H}_5\text{OH}$ ) at different concentrations and poured into the Teflon cell. The platinum wire, which is also chemically resistant to HF, acts as the cathode. The shape of the cathode is critical to ensuring homogeneous samples, because it must promote a uniform electric field while allowing hydrogen bubbles formed during the anodization process to escape. The Teflon cylindrical tube with diameters of 10-15mm was placed between the upper and lower parts of the Teflon cell. Finally, a stainless steel ring and nuts are used to hold the cell together. We can use either current or voltage source for the anodization process. In our experiments, we used the electrochemical system Autolab PGS-30 as the electric current source, which can control the current with the nano-Amper range. Figure 1 presents the experimental setup for

making porous silicon thin films. The computer-controlled electric source used for the electrochemical process, so precise control over current density and etching time were achieved, and then it is resulting in a good control of the refractive index and thickness over the individual layers forming the multilayer. The program is a LabView virtual instrument realized to control the fabrication process of monolayer and multilayer of porous silicon with a friendly interface. The program controls the different parameters of the electrochemical process via GPIB. Those parameters include two current steps (to form layers with different refractive indices), duration time of each step (to determine the thickness of each layer), delay time (time between two consecutive electrochemical currents), and number of period (number of multilayer structure).

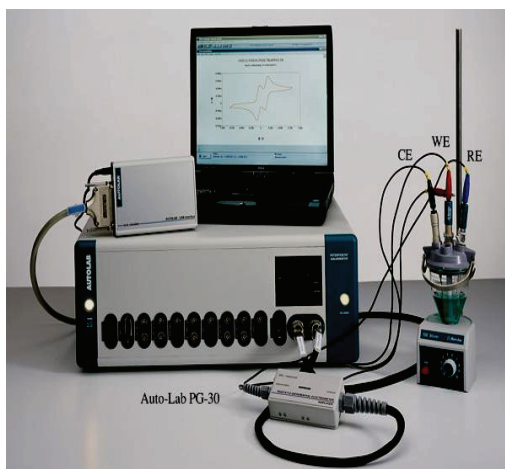


Fig. 1. Electrochemical etching setup for fabricating PS layers

## 2.2 Silicon samples

The initial Si-crystalline wafers, n-type with resistivities of 1-5  $\Omega\cdot\text{cm}$  and p-type with resistivities of 0.01-1  $\Omega\cdot\text{cm}$ , were used for constant potential and constant current ECD, respectively. For the case of n-type silicon substrates we need to illuminate the back side of silicon wafers. Resistivity of silicon wafer strongly affects on quality of porous silicon layers. High resistivity wafer often makes porous silicon layers with rough surface and easily peeled off from Si-substrate during fabrication or drying process, while the low resistivity sample have more flat surface of porous silicon layers. In order to form Ohmic contacts on the samples, we deposited pure gold (Au) and/or aluminum (Al) on the back faces of the n- and the p-type samples, respectively. The Si-crystalline wafers were anodic etched in a HF-ethanol solution with HF concentrations from 10% to 30% at a constant current density of 10-60  $\text{mA}\cdot\text{cm}^{-2}$  for time durations from some seconds to 15 minutes for controlling the refractive index of the PS layers. If the current density is modulated during the anodization, alternating layers of different porosities are formed as the silicon dissolution occurs primarily at the etched front PS/silicon substrates (Frohnhoff et al., 1995). Although the interface roughness between stacks is about 10-20nm, light scattering at these interfaces turned out to be very low. For this reason such layer stacks can act as optical waveguides and/or interference filters if the refractive indices are chosen properly (Krüger et al., 1998).

### 3. Active waveguide based on SRSO thin films

Initially, Canham proposed that the up-shift of the luminescence spectrum into the visible was due to quantum confinement in the silicon crystalline wire structure and that the hydride passivation of the Si wire was the reason for the high efficiency of the observed photoluminescence (PL). For a short time after that, spectroscopic studies conducted particularly on the polarization of the PL (Kovalev et al., 1996) and on features observed under conditions of resonant excitation (Calcott et al., 1993) have provided strong positive confirmation of the quantum confinement model. However, there were a lot of spectroscopic phenomena that can not be explained by the simple quantum confinement model. As such, numerous models have been put forward as alternative explanations for the PL from PS such as hydrogenated amorphous silicon, surface hydrides, defects, molecules, surface states (Amato & Rosenbauer, 1997). It is well known that in PS the surface to volume ratio is very large, so the surface effects are expected to have a significant influence on the material properties, especially optical ones (Kanemitsu et al., 1993). Because the Si atoms in Si nanocrystals are either at the surface or a few lattice sites away, the arrangement of interfacial atomic bonds, i.e. the passivation with Si-H or Si-O bonds, strongly affects the energy distribution of electronic states (Wolkin et al., 1999). In order to study PS as low-dimensional photonic materials, we elaborate on the effect of ageing on the spectral, intensity and lifetime of PL from the silicon nanocrystals in PS. Experimental results show that the effect of ageing on the spectral, intensity and PL lifetime of PS depends on the size of silicon nanocrystals. We focus our attention on strong emission properties and employ PS as a material for light emission sources, i.e. light emitting diodes and micro-cavity lasers operated in the visible region. In concentrating on the controllable changes in the refractive index of PS, we would like to use PS as a material for photonic devices such as planar optical waveguides, optical waveguide amplifier, optical interference filters, etc. As an optical material, we present the fabrication method for silicon rich silicon oxides (SRSO) thin films and properties of planar optical waveguides, active optical waveguides and optical interference filters operated in the range of infrared wavelengths. The advantage of optical waveguide amplifier based on Erbium doped SRSO is the efficient energy transfer from electron-hole pairs generated in the Si nanocrystals to their near erbium ions, which decay by emitting light at 1540nm. The excitation cross-section of Er-ions in Er-doped SRSO is increased more than two orders in comparison of this one in the Er-doped silica glasses (Friolo et al., 2001), so that the pump efficiency in Er-doped SRSO waveguides can be very high.

#### 3.1 Porous silicon as a low-dimension photonic material

In the first part of this section we explain the effect of surface states on the PL properties of PS based on the ageing process in air. In the last part, we present the reason for the intense and stable luminescence of blue region which has been of great interest in recent studies (Gorelkinskii et al., 2008). Previous studies on the interaction of oxygen in air on the as-prepared PS (Wolkin et al., 1999) show that: I) the as-prepared samples were well passivated by hydrogen and free of oxygen, ii) after exposure to air the samples were gradually passivated by oxygen, and the red-shift of PL spectral occurred as samples exposure to air and was nearly completed after ageing of 24 h. It was suggests that the ageing process can be divided into two periods: the first one in which the transition of the luminescence mechanism occurs after exposing the sample to air for a short time, and the second one in which the non-radiative center concentration is changed by oxygen passivation (Bui Huy et al, 2003).

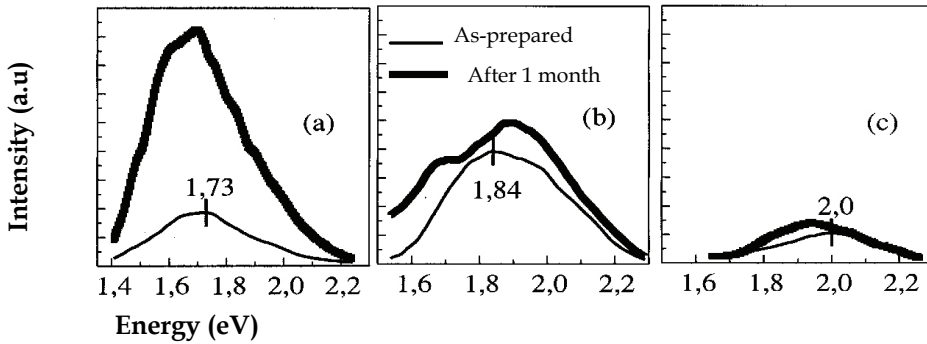


Fig. 2. PL spectra of the as-prepared samples and after exposure to air for 1-month; samples, denoted as 1, 2 and 3, were prepared by the anodic etching in 20%, 13% and 10% HF solution, respectively. (a) sample 1, (b) sample 2 and (c) sample 3

In order to investigate the effect of surface passivation on the size of Si nanocrystals, a series of PS samples denoted as 1, 2 and 3 were prepared by anodic etching in 20%, 13% and 10% HF solution respectively. As seen in figure 2, the PL peaks of the as-prepared samples 1, 2 and 3 have energy levels of 1.73, 1.84 and 2.00 eV respectively. This is related to a decrease of particle size in the considered samples. The figure also reveals that the ageing produces a pronounced increase in PL intensity in sample 1 and only a slightly increase in samples 2 and 3. As seen in figure 3, the decay rate of the as-prepared samples (the curves 1a, 2a and 3a) shows that the concentration of non-radiative centers in sample 1 is higher than those in samples 2 and 3. The pronounced increase in intensity (in figure 2) as well as the pronounced decrease in decay rate (in figure 3) of sample 1 could be caused by the oxygen passivation of non-radiative defects. In samples 2 and 3 containing smaller particles, the initial passivation degree is higher, therefore the ageing is expected to induce a small change both in intensity and decay rate. The data comparison from curves 2a and 2c in figure 3 reveals that the modification of emission mechanism has no effect on the decay rate as well as its energy dependence  $\tau^{-1}(E)$ . This result seems to indicate that the replacement of Si-H bond by a Si-O one acting as a radiative center has no effect on the lifetime.

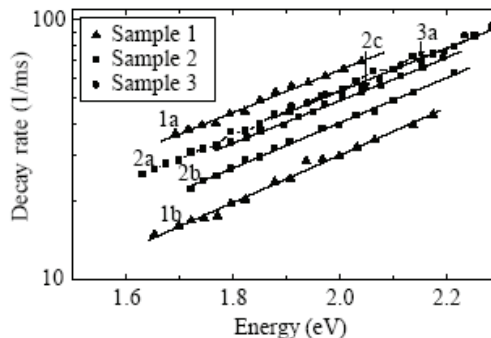


Fig. 3. Evolution of decay rate as a function of emission energy from samples after preparation, curves 1a, 2a, 3a and after exposure to air for 1-month, curves 1b, 2b. Curve 2c corresponds to sample 2 for 24 h (Bui Huy et al., 2003).

Figure 2 and 3 established the relation between the size of particle, intensity and decay rate during ageing. In the sample containing larger nanocrystals, the change in intensity and decay rate, i.e. the luminescence lifetime, is much larger compared with that of the smaller nanocrystals during ageing process.

Figure 4 shows the evolution of PL spectra, measured at the end of an excited pulse after different exposure times. The figure reveals that the blue zone with the PL emission peaked at 470 nm is only observed after 72 hours of exposure to air. Furthermore, the figure also reveals that the PL intensity increases with increasing air exposure time. These observations differ from those reported by Volkin et al. (Volkin et al., 1999) in which the intensity of blue emission from the as-prepared sample containing the small Si particles was shown to decrease as the exposure time increased. This result indicates that the blue-light emission observed in the present work does not originate from very small nanocrystals. Curve 4im shows the PL spectrum of a sample, which was exposed to air for 94 hours and then immersed in HF: ethanol solution. In comparing curves 4 and 4im, one can state that the blue zone in the PL spectrum observed for the sample after 94 hours of exposure to air is completely quenched. This quenching clearly relates to the fact that the silicon oxide layers in the exposed sample have been removed. The above results indicate that the intense and stable emission in the blue zone of the PL spectra observed in the considered samples relates to defects in silicon oxide layers.

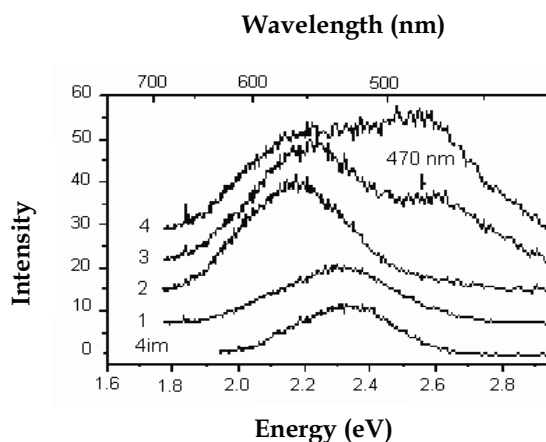


Fig. 4. Evolution of PL spectral measured at the end of excitation pulse from a PS sample after different exposure time (1): as-prepared, (2; 3; 4): after 26, 72 and 94 h of exposure to air, respectively, (4im): corresponding to sample exposed to air for 94 h. and then immersed in 5% HF: ethanol solution for 10 sec (Bui Huy et al., 2006).

### 3.2 Fabrication and characteristics of SRSO planar and active optical waveguides

In this section, before elaborating on the fabrication method and properties of planar optical waveguide, active optical waveguides, and optical interference filters based on SRSO thin films we explain the method of production for the PS multilayer which forms the basis for these devices.

The production of PS multilayer is possible because: (i) the etching process is self-limited (i.e. once porous layer is formed, the electrochemical etching of this layer stops); (ii) the

etching occurs mainly in correspondence between the pore tips; (iii) the porosity depends only upon the current density once the other etching parameters are kept fixed; and (iv) the refractive index of PS depends on its porosity (Mazzoleni & Pavesi, 1995). Therefore, by varying the current density during the etching process, it is possible to vary porosity in the etching direction. In this way, the formation of a stack of PS layers of different porosities (and hence, different refractive indices) results in a dielectric multilayer.

Our process for preparing an optical planar waveguide consists of 2 steps: making a PS film which contained a core layer and a cladding one, and stabilizing the waveguide structure by thermal annealing at high temperature in oxygen ambient for obtaining SRSO. In the process of fabricating an active optical waveguide, a step of deposition of Er ion into the PS film was carried out before thermal annealing. The high temperature treatment can cause an optical activation of Er ions in SRSO.

The PS films were formed by electrochemical etching of 1 $\Omega$ cm p-type Si wafers in 30%HF: ethanol solution. The top core layer was fabricated by applying current density of 15mA/cm<sup>2</sup> for 7 min. The cladding was formed in the same way, with current density of 65mA/cm<sup>2</sup> for 3 min. These conditions allowed the core and cladding to have a porosity of about 60% and 65%, respectively. For Er-deposition on the PS layer, the PS layers were immersed in an Er-content solution, and a negative bias, relative to a platinum electrode, was applied to the PS samples for a certain time so that Er-ions were drawn into the pores of the PS. In the constant current ECD method, an ErCl<sub>3</sub>-ethanol solution with an Er-concentration of 0.2 mol / liter was used, and the drift current was changed from 0.17mA.cm<sup>-2</sup> to 0.45mA.cm<sup>-2</sup> to obtain different Er-concentrations in the PS layers. To enable the optical activation of Er ions distributed in the pores of the PS layer, the sample was annealed at 400°C for 2 h. For making the SRSO layers, we thermally annealed the samples at 800° - 950°C in oxygen ambient for a short time (5-30 min.) and kept samples for a longer time in nitrogen gas at 1100°C.

Figure 5 presents the FE-SEM image of a two-layer SRSO with different refractive indices ( $n_{\text{core}} > n_{\text{clad}}$ ), which had been controlled by using current density of 20 and 30 mA.cm<sup>-2</sup> for the core and the cladding layers, respectively. Based on the contrast between the core and the cladding due to the difference in porosities, it is observed that the film consisted of two layers in which the core layer thickness is about 4.5  $\mu$ m, and the cladding about 7  $\mu$ m. The thickness of layers depended on the time duration of electrochemical process, and layers of up to tens of microns could be grown.

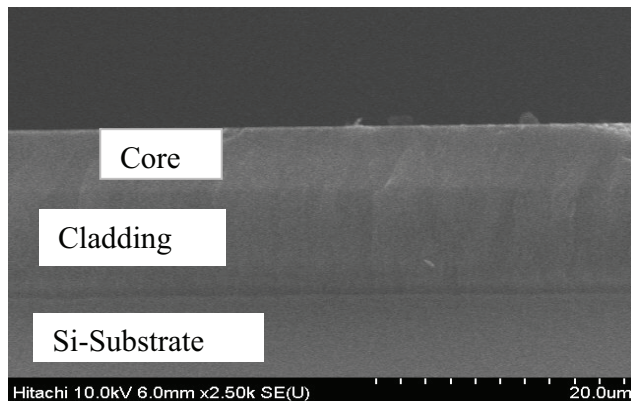


Fig. 5. FE-SEM image of bi-layer SRSO on a silicon substrate.

Figure 6 shows the HRSEM image of the surface of the core and cladding before (PS layer) and after (SRSO layer) of thermal annealing. As seen from Figures 6a and 6c, the difference in the density of the black area and the pores in the PS layer show that the porosity in the core layer is lower than that in the cladding. From this image we also observed the differences in density of the black area and the contrast between the black area and the white one from the PS layers (Figures 6a and 6c) and SRSO layers (Figures 6b and 6d). Those differences suggest that the treatment can cause a decrease in the size of pores and the porosity of SRSO layers. The prepared SRSO layers were dense and therefore the optical properties of the waveguides were stabilized.

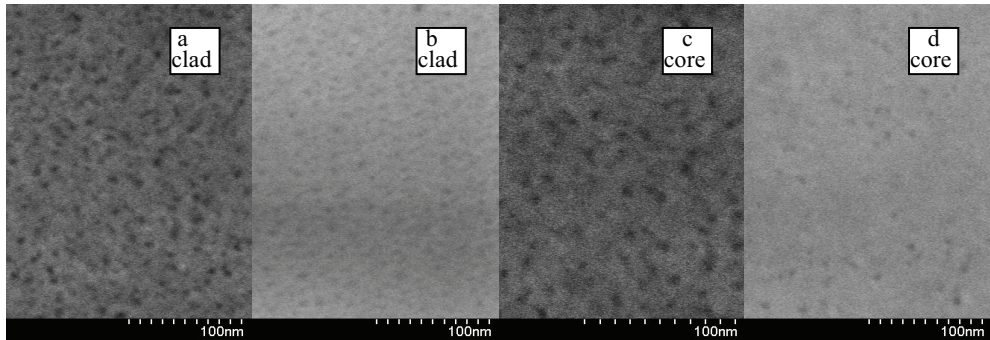


Fig. 6. FE-SEM image of surface of the core and cladding of PS layer (a, c), and of SRSO layer (b, d), which was obtained before (a, c) and after (b, d) thermal annealing in order to estimate their porosities.

Samples	Sample layers	Refractive index	Thickness ( $\mu\text{m}$ )
Series No.1	Core layer	1.4512	5.54
	Cladding layer	1.4275	3.35
Series No.2	Core layer	1.6088	1.908
	Cladding layer	1.5402	6.239

Table 1. Parameters of SRSO waveguide samples

The waveguide properties of the SRSO multi-layers were characterized by using M-line spectroscopy with the Prism-coupler method (Metricon 2010/M), which has the capacity to measure the thickness, the refractive index and the wave-guided modes in thin films with high accuracy ( $\pm 0.0005$  for index). The number of wave-guided modes in the SRSO waveguide strongly depended on the thickness of the core layer. Figure 7(a) shows that a single mode of 1310 nm in wavelength could be guided in a core layer with a thickness of 1.9 micron. The measured indices of this sample were 1.6088 and 1.5402 for the core and the cladding layers, respectively. Figure 7(b) demonstrated the measured indices and the two-mode waveguide at a 1310-nm wavelength for a core layer with a thickness of 5.54 microns. The measured indices were 1.4522 and 1.4275 for the core and the cladding, respectively. This result shows that, by changing the current density in the ECD process, we can obtain a planar layer with different indices that support the waveguide properties in the layer. The Er-ion distribution in the SRSO layer was characterized by using the EDX method with the SEM technique. The Er-ion concentration, which was doped into PS, could be controlled by using an Er-content solution

and by using the current density in the ECD method. For the purpose of obtaining high-concentration Er-doped SRO materials (more than 0.1 atomic % of Er) without Er clusters, which would be good candidates for planar-waveguide amplifiers, we carried out a very careful study of the distribution of Er ions along the depth of the SRSO layer.

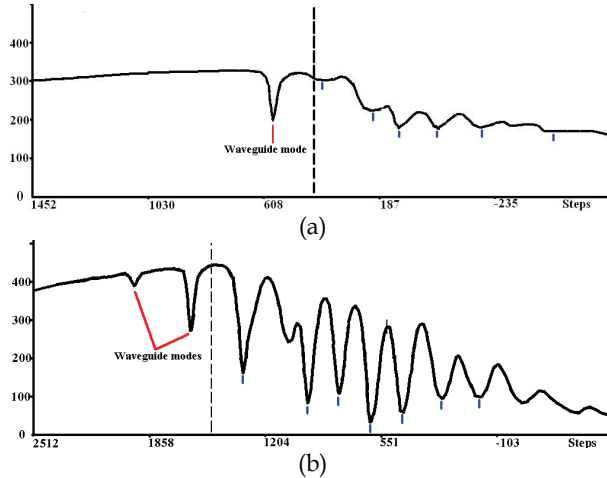


Fig. 7. Waveguide properties of the SRSO core/cladding layers. (a) Single-mode in the sample with core/cladding thickness of 1.90/6.24  $\mu\text{m}$  and indices of 1.6088/1.5402 (b) Multi-mode in the sample with core/cladding thickness of 5.54/3.35  $\mu\text{m}$  and indices of 1.4512/1.4275.

Samples	Type and resistivity	HF concentration (%)	Er-drift current ( $\text{mA}\cdot\text{cm}^{-2}$ )	Annealing ( $^{\circ}\text{C}$ )
BH-10	p-type, 1 $\Omega\text{cm}$	30	0.17	950
BH-11	p-type, 1 $\Omega\text{cm}$	25	0.20	950
BH-12	p-type, 1 $\Omega\text{cm}$	20	0.17	950
BH-13	p-type, 1 $\Omega\text{cm}$	30	0.20	820
BH-14	p-type, 1 $\Omega\text{cm}$	25	0.25	950
BH-15	p-type, 10 $\Omega\text{cm}$	30	0.17	950
BH-16	p-type, 1 $\Omega\text{cm}$	25	0.45	950

Table 2. Preparation conditions of Er-electrochemically-doped SRSO samples

Figure 8a shows a SEM image of the Er-doped SRSO wave-guide layer prepared by using the ECD method with a drift current density of  $0.2\text{mA}\cdot\text{cm}^{-2}$ . The measurement was carried out for an Er-doped SRSO thickness of 5 microns, and the Er-ion concentration was measured at points along the depth of the SRSO layer. The Er-ion concentration increased from 0.11 atom % at the top surface to 0.2 atom% at the depth of 3.5 micron from the top surface. The Er-ion concentration decreased with further increased in the depth inside the samples (see fig. 8b). For the characterization of optical properties of Er-doped SRSO layers, the Nitrogen gas laser (LN 1000,  $\lambda=337.1\text{nm}$ ) an Argon laser (Coherent Inova 300,  $\lambda=488\text{nm}$ ) and a 1-W continuous laser diode ( $\lambda=976\text{nm}$ ) were used as optical excitation sources. The



luminescent emission from the samples was collected by using two optical fibers located at 10 mm from the sample surface. The luminescence emission was analyzed by using a Jobin-Yvon spectrometer (HR460) with a multi-channel Charge-Coupled Device (CCD) detector and by Triax 320 spectrometer with a C7211 Hamamatsu CCD infrared detector for visible and infrared light, respectively.

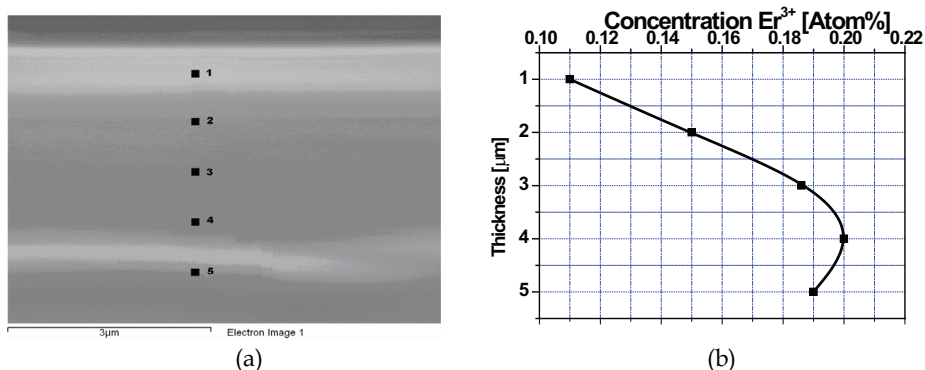


Fig. 8. FE-SEM image of Er-doped SRSO layers on a Si- substrate with the Er-concentration measured at points along the depth of the layer by using EDX method (a) and the Er-ion distribution inside the sample (b).

The first criteria for the Er-doped SRSO samples were that they could be in both optically activated centers: the Si-nanocrystal induced visible light and the Er ion induced infrared light. Our experiment shows that the samples without thermal annealing did not emit IR light, but after thermal annealing, they strongly emitted in the 1540-nm range. This fact shows that thermal annealing at high temperatures for obtaining Er-doped SRSO layers is an important condition for optical activation of Er ions.

In general, the intensity of luminescence emission at 1540 nm will be increase with increasing concentration of Er ions in the SRSO layer (Elhouichet & Oueslati, 2007), when the Er-ion concentration reaches its saturation value, the luminescence intensity at 1540 nm will be decreased due to the quenching effect from Er-ion clusters (Kit & Polman, 2000). Figure 9 presents the luminescence spectra at 1540 nm for samples with different drift currents from 0.17 to 0.45 mA.cm<sup>-2</sup> under excitation by 976-nm laser beam. The 1540-nm luminescence intensity of all the samples increased with increasing drift current density from 0.17 to 0.25 mA.cm<sup>-2</sup>, but when the drift current density was more than 0.25 mA.cm<sup>-2</sup> the luminescence decreased slightly with increasing drift current.

The evidence of energy transfer can be obtained by changing the wavelength of the excitation source. The pump at 976 nm only caused a direct excitement of Er ions (from <sup>4</sup>I<sub>15/2</sub> to <sup>4</sup>I<sub>11/2</sub> level), whereas the pump at 488 nm caused both a direct excitement of Er ions (from <sup>4</sup>I<sub>15/2</sub> to <sup>4</sup>F<sub>7/2</sub> level) and an indirect one related to the energy transfers from Si-nc to Er ions. As the effective Er excitation cross-section in the Er-doped SRSO layer is more than two orders of magnitude higher with respect to the Er resonant absorption of a photon, the pump at 976 nm causes a linear dependence of intensity on excited power (Najar et al., 2006) and the pump at 488 nm causes the non-linear one as seen in Figure 10. The photoluminescence intensity of samples irradiated by a 976-nm wavelength increased linearly with increasing excitation power when the PL emission of the sample pumped at a 488-nm wavelength has reached saturation at high power.

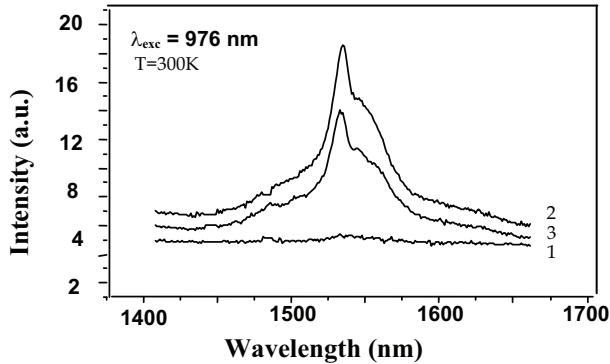


Fig. 9. Luminescence spectra from samples 1, 2 and 3 under drift current density of 0.17, 0.25, and 0.45 mA cm<sup>-2</sup>, respectively.

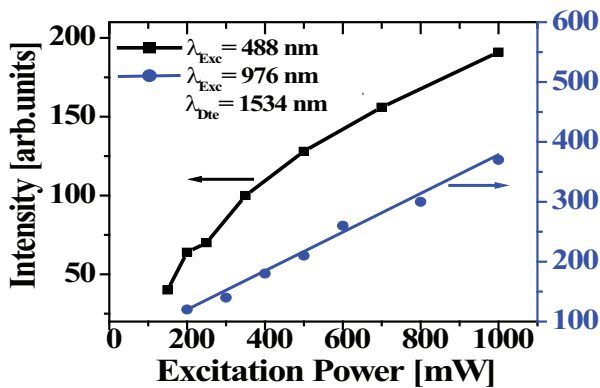


Fig. 10. Dependence of luminescence intensity of Er-ions at 1534 nm on the power of the excitation laser at wavelengths of 488 nm and 976 nm.

#### 4. Interference filters based on porous silicon and silicon-rich silicon oxide layers

Interference filters based on PS were realized for the first time in the last decade (Vincent, 2004). They are formed from silicon wafers by electrochemical etching in HF solution. Compared with other methods, the electrochemical etching method avoids the difficulty associated with the stacking and assembly of dielectric layers, eliminates the need for the lengthy deposition of thick films, and permits a wide range of refractive indices to be fabricated from a single silicon substrate. PS interference filters usually formed from different dept profiles of the refractive index of PS multi-layers which act as Bragg reflectors. The optical thickness of the high- ( $n_H$ ) and low-refractive index ( $n_L$ ) layers are 1/4 of the filter wavelength, so that these structures are usually called quarter-wave-stacks (Kruger et al., 1998). The effective refractive index of PS layer is mainly determined by the porosity which can be varied by several anodization parameters. The most suitable way is changing

the anodization current density, with high current densities resulting in high porosity and low refractive index. However, one of the main problems concerning the use of PS interference filters is the ageing of the PS: due to the large inner surface of the porous silicon the material oxidizes very fast compared to bulk silicon. This phenomenon is well-known from emitting PS layers, which was discussed in the section 3 of this chapter. For PS interference filters the natural oxidation is disturbing as well as it causes a change of the refractive index and of the PS layer thickness (Barla et al., 1986), which results in the following ageing effects: (i) a blue-shift of the filter wavelength; (ii) a decrease of the filter performance, if the change of the optical thickness is different for the  $n_H$  and  $n_L$  layers; (iii) a continuous decrease of reflectivity, which depends on the refractive index ratio  $n_H / n_L$ . The ageing effect of the PS quarter-wave-stacks could be strongly reduced by a thermal annealing process to obtain SRSO structure.

## 4.1 Simulation of the PS interference filters

### 4.1.1 Mathematical model

Before fabricating the interference filters based on multi-layer structure, a simulation program was set up in order to design and predict the optical properties of interference filter based on quarter-wave-stacks. Each quarter-wave stack system is characterized by the following basic parameters: number of layers, refractive indices, and optical thicknesses of layers. The computation of reflectivity and transmission spectrum from the above parameters has an important role in knowing thoroughly about multilayer system. There are many numerical methods for analyzing the multilayer system such as Transfer Matrix Method, Plane Wave Method, and Finite Difference Time Domain. In our work we use Transfer Matrix Method (TMM) for simulation of reflectivity and transmission of interference filters. The TMM can handle any number of layers in a multilayer structure. In addition, these layers can be ordered in any manner and there is no requirement that they should be periodic. Even if they are periodic, the unit cell that is repeated does not have to be composed of two layers only, but any number of layers. There is also no restriction on the thickness of any layer. The thickness and the refractive index of each layer can be defined independently. This makes the TMM most suitable for modeling structures formed by different periodic multi-layers stacked together, since they are not fully periodic. The TMM can also handle structures having a high index contrast between their two composite materials contrast material systems. This makes the TMM suitable for modeling multilayer structures, which usually have a high index contrast between their composite materials.

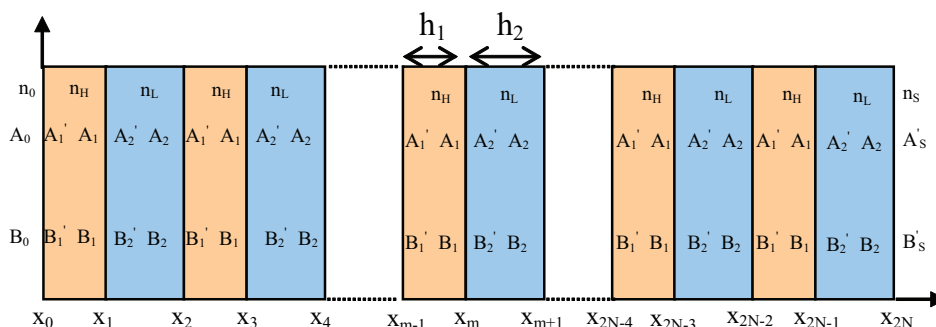


Fig. 11. Diagram of multi-layer interference filters.

We consider quarter-wave-stacks as a structure containing of  $N$  bi-layers of porous silicon with periodic refractive indices that are coupled with a medium with refractive index  $n_0$  at the interface and a substrate with refractive index  $n_s$  at the bottom. As can be seen from Fig.11, the configuration of interference filter is a periodic structure of two porous silicon layers ( $n_H | n_L$ ).  $A(x)$  represents the amplitude of the right-traveling-wave and  $B(x)$  is that of the left-traveling one and  $A(x)$  and  $B(x)$  are not continuous at the interfaces. The thickness of each layer is  $h_m$ ,  $n_m$  is the refractive index and  $\Lambda = h_m + h_{m+1}$  is a period of structure. The dielectric structure is defined by (Saleh & Teich, 1997):

$$n(x) = \begin{cases} n_0, x < x_0 \\ n_H, x_0 < x < x_1 \\ n_L, x_1 < x < x_2 \\ \dots \\ n_s, x_{2N} < x \end{cases} \quad (2)$$

Where  $n_0$ ,  $n_s$  are refractive indices of the incident medium (ambient) and of the substrate, respectively. With this structure, we have  $n(x) = n(x+\Lambda)$ . In general, for the  $m$ -th layer, the refractive index is  $n_m$  and thickness is  $d_m$  in which  $d_m = x_{m+1} - x_m$  ( $m=1:2N$ ). The electric field of a general plane-wave can be written as  $E = E(x) e^{i(\omega t - \beta z)}$  where  $E(x)$  is the electric field distribution and can write as:

$$E(x) = \begin{cases} A_0 e^{-ik_{0x}(x-x_0)} + B_0 e^{ik_{0x}(x-x_0)}, x < x_0 \\ A_m e^{-ik_{mx}(x-x_m)} + B_m e^{ik_{mx}(x-x_m)}, x_{m-1} < x < x_m \\ A_s e^{-ik_{sx}(x-x_{2N})} + B_s e^{ik_{sx}(x-x_{2N})}, x_{2N} < x \end{cases} \quad (3)$$

Where  $k_{mx}$  is the  $x$ -component of the wave vector,  $k_{mx} = \omega n_m \cos \theta_m / c$  and  $\theta_m$  is the ray angle in each layer.  $A_m$  and  $B_m$  are the amplitude of plane waves at interface  $x=x_m$ . If we write the two amplitudes of  $E(x)$  as a column vector, the plane waves at different layers can be related by:

$$\begin{pmatrix} A_{m-1} \\ B_{m-1} \end{pmatrix} = D_{m-1}^{-1} D_m \begin{pmatrix} A'_m \\ B'_m \end{pmatrix} = D_{m-1}^{-1} D_m P_m \begin{pmatrix} A_m \\ B_m \end{pmatrix}, \quad m=1, 2, \dots, 2N \quad (4)$$

Where the dynamical matrices  $D_m$  are written by:

$$D_m = \begin{cases} \begin{pmatrix} 1 & 1 \\ n_m \cos \theta_m & -n_m \cos \theta_m \end{pmatrix} & \text{for TE wave} \\ \begin{pmatrix} \cos \theta_m & \cos \theta_m \\ n_m & -n_m \end{pmatrix} & \text{for TM wave} \end{cases} \quad (5)$$

And the propagation matrix  $P_m$  can be written by:

$$P_m = \begin{pmatrix} e^{ik_{mx}h_m} & 0 \\ 0 & e^{-ik_{mx}h_m} \end{pmatrix} \quad (6)$$

Thus the relation between  $A_0$ ,  $B_0$  and  $A'_S$  and  $B'_S$  can be written as:

$$\begin{pmatrix} A_0 \\ B_0 \end{pmatrix} = D_0^{-1} \left[ D_1 P_1 D_1^{-1} D_2 P_2 D_2^{-1} \dots \right]^N D_S = \begin{pmatrix} M_{11} & M_{12} \\ M_{21} & M_{22} \end{pmatrix} \begin{pmatrix} A'_S \\ B'_S \end{pmatrix} \quad (7)$$

From the matrix elements, we can calculate the reflectance and transmittance of monochromatic plane waves through a multilayer structure. If the light is incident from medium  $n_0$ , the reflection and transmission coefficients can be calculated as:

$$r = \left( \frac{B_0}{A_0} \right)_{B'_S=0} \quad (8)$$

$$t = \left( \frac{A'_S}{A_0} \right)_{B'_S=0}$$

Using the matrix equation (7), we have:

$$r = \left( \frac{M_{21}}{M_{11}} \right) \quad (9)$$

$$t = \left( \frac{1}{M_{11}} \right)$$

$$R = \left| \frac{M_{21}}{M_{11}} \right|^2 \quad (10)$$

Then the reflectance is:

Where ambient with refractive index  $n_0$  is lossless.

#### 4.1.2 Simulation program

From the above-mention theory, we can set up a program for the simulation of multilayer structure by using Matlab. This program contains the following parameters:

- Refractive index of ambient is  $n_0$ : the medium from which the incident wave arrives to the surface of the first layer of multilayer structure.
- Refractive index of substrate is  $n_s$ : Substrate can be the silicon wafer or other medium.
- Incident angle ( $\theta$ ): The angle between the propagation direction of the incident wave and the normal to the surface of layers. This layer can vary from 0 to 90 degrees.
- Number of bi-layer (N): number of periodic multilayer of interference filter.
- Refractive indices ( $n_m$ ) and thickness ( $l_m$ ) of layers. They can be either  $n_{1L}$ ,  $d_1$  or  $n_{1L}$ ,  $d_2$ .
- Wavelength range: the range from the initial to the final values of wavelength for analyzing reflectivity spectra.

#### 4.1.3 Results of simulation

The refractive index ratio  $n_H/n_L$  of the interference filter strongly influences on the width and the sharpness of the filter wavelength band. Figure 12 shows the calculated reflection spectra of three filters with 12 periods and the thickness of one layer was calculated to obtain a centered reflection wavelength at 1550 nm. The calculated values of refractive

indices in the range of 1.5 to 2.5 are often obtained from prepared porous silicon layers. We surmised that the line-width and sharpness of the spectra are influenced by the ratio of  $n_1/n_2$  and the increase of  $n_1/n_2$  leads to the spectral broadening.

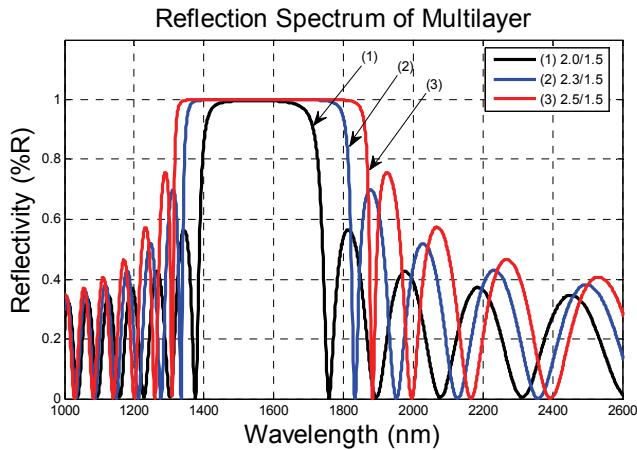


Fig. 12. Reflection spectra of multilayer structures with different ratio of  $n_H/n_L$

The influence of the number of periods ( $N$ ) of multilayer structure on the reflection spectra demonstrates in Figure 13. When  $N$  increases, the reflection spectra are sharper, narrower and the reflectivity tends to unity. The simulation results can be used for design interference filters based on both of PS and SRSO materials.

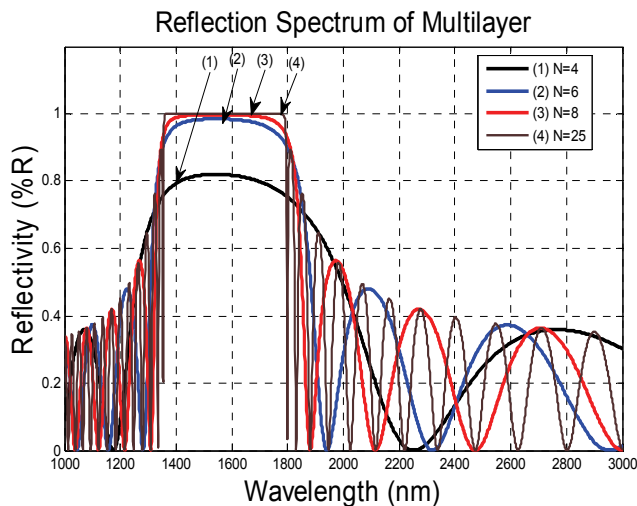


Fig. 13. Dependence of reflectivity upon period number of periods of multilayer structures with ratio  $n_H/n_L$  of 2.5/1.5, corresponding to period numbers 4, 6, 8 and 25, respectively.

#### 4.2 Fabrication of interference filters based on PS and SRSO multilayer

The porous silicon multilayer was fabricated using electrochemical etching of highly doped p-type (100) silicon wafers with resistivity of 0.01- 0.1 $\Omega$ .cm in 13%-20% hydrofluoric acid (HF): ethanol solution. The electrochemical process was carried out without illumination. The process was monitored by computer-controlled current source Autolab PGS-30, so precise control over current density and etching time was maintained, thus resulting in good control over the refractive index and thickness of the individual layers forming the multilayer. The multilayer was formed by periodically varying the applied current density between two levels ( $J_1$  and  $J_2$ ) of 64 and 19 mA/cm<sup>2</sup> respectively, as presented in Figure 14. The number of periods for each filter was from 6 to 18. The silicon pores and multilayer structures of the filter were analyzed by Field-Emission Scanning Electron Microscopy (FE-SEM). Figure 15 shows a FE-SEM-image of the completed porous silicon 12-period compose fabricated by ratio of current densities  $J_1/J_2 = 64/19$  and duration time of 6.33 and 12.3 seconds, respectively. As seen in Figure 15a, the typical sizes of the silicon residuals and air voids are about 50 nm. This allows us to describe the PS layers as "an effective medium", whereby its optical properties mainly depend on its porosity. The SEM-image of the multilayer displays different gray levels depending on the porosity of the layers (see Figure 15b). Because of this, the layers of the stack are distinguished and therefore the thickness of each layer can be experimentally determined.

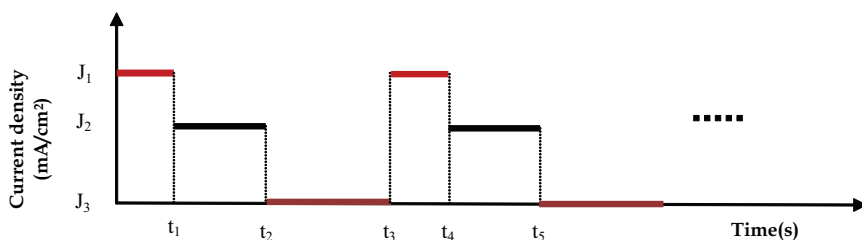


Fig. 14. Schematic of current density modulation versus anodization time

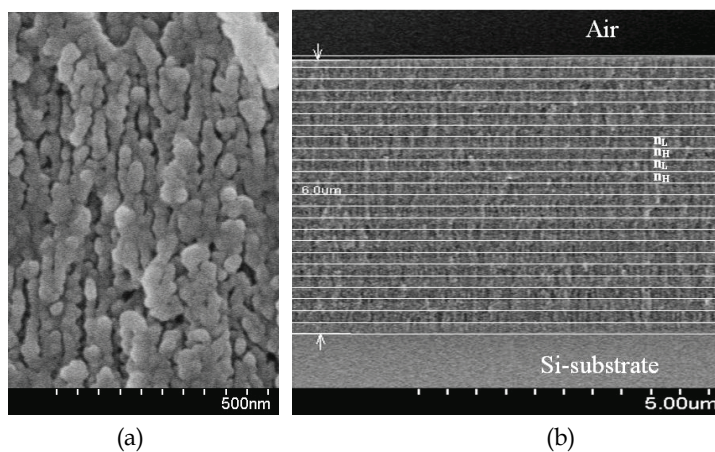


Fig. 15. Cross-sectional SEM images of silicon pores (a) and multilayer structure of the interference filter with period number  $N=12$  (b).

Figure 16 displays the reflection spectra of multilayer filters with different thickness levels. The curves (a), (b), (c) and (d) displays the reflection spectra of 12-period filters with a total thickness of 8.1 $\mu\text{m}$ , 6.0 $\mu\text{m}$ , 5.4 $\mu\text{m}$  and 4.5 $\mu\text{m}$ , respectively. The difference in the thickness of interference filters and therefore, the thickness of the layer in the stacks causes the shift of the center wavelength at which the reflectance would be maximal.

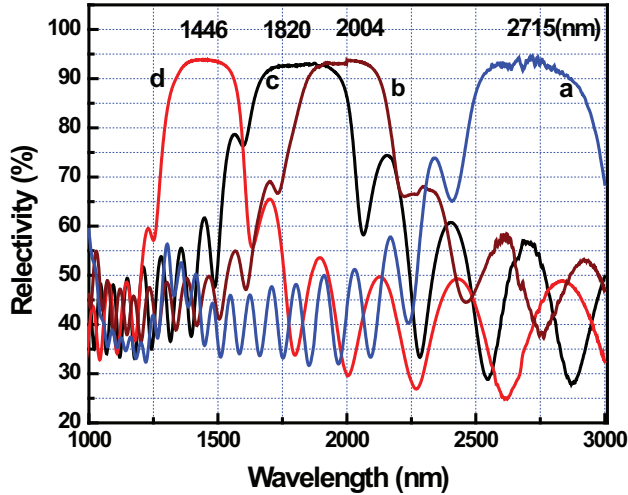


Fig. 16. Shifting the reflection spectra of 12-period filter by varying the thickness of the layers in the stacks: (a)  $h=8.1\mu\text{m}$ ; (b)  $h=6.0\mu\text{m}$ ; (c)  $h=5.4\mu\text{m}$ ; (d)  $h=4.5\mu\text{m}$ .

Figure 17 shows the reflection spectra from two filters, denoted as M5 and M4, fabricated at a ratio of current densities  $J_1/J_2 = 64/19$  and  $38/19$ , respectively. The refractive index of  $\text{PS}$  layer depends on anodization current density, so that the refractive index contrast between neighboring PS layers also depends on the ratio of current densities which created those layers. The increase in the FWHM (full-width at half-maximum) of the reflective spectrum from M5 filter compared with that from M4 one is due to the difference in the ratio of current densities ( $J_1/J_2$ ) forming those filters.

Figure 18 shows the reflection spectra at wavelength of 1550 nm-range from three filters with a different numbers of periods. As seen from this figure, when period number increases the spectra become shaper, narrower and the refractivity increased. This result relatively corresponds to our simulation as shown in Figure 12.

The difference in the characteristics of filter spectra from the simulation and experiment occurs in the filters having too few or too many periods ( $N$ ). In the case of filters having too few periods ( $N \leq 6$ ), reflection from the interfaces, especially from the interface between air and the top layer, becomes more important in those filters, so that the imperfections of interfaces created by electrochemical etching can cause a deformation of the reflective spectrum as seen in curve (a) of Figure 18. In the case of the filters having too many periods ( $N \geq 18$ ), the long anodization time causes a deformation of the nano-structure of surface layers whereas the nano- and micro-structure of the bottom layers can be affected by the slower transport of etching substances. All of these factors lead to a break in condition of the Bragg reflection in such layers and the decrease in reflectivity of the filter as shown in curve (b) of Figure 18.



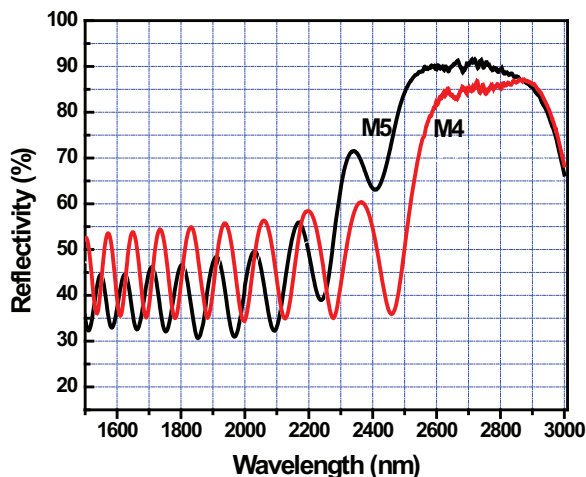


Fig. 17. Reflection spectra versus the refractive index ratio between nearest layers of PS interference filters.

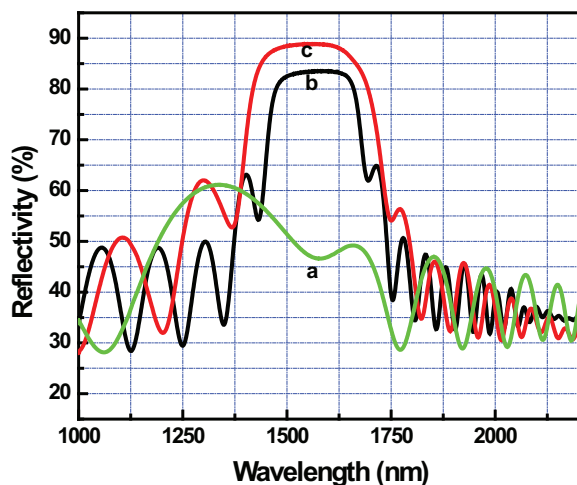


Fig. 18. Reflection spectra versus period numbers of stacks: curves a, b and c from multilayer filters with periods of 6, 18 and 12, respectively.

The interference filters have a big potential of applications not only for fiberoptic communication, but for bio-chemical sensory. The Table 3 shows an electrochemical etching process for making quarter-wave-stack filters operated at visible region, which is suitable for bio-chemical sensors. For making visible-range interference filters, we need decrease an etching time from tens seconds for IR region to some seconds for visible, while the current density is kept constantly.

Samples	Period numbers	Current density	Time (seconds)
Series No.1	12	$J_1 = 50 \text{ mA.cm}^{-2}$	2.857
		$J_2 = 15 \text{ mA.cm}^{-2}$	5.555
		$J_3 = 0$	8.0
Series No.2	12	$J_1 = 50 \text{ mA.cm}^{-2}$	3.625
		$J_2 = 15 \text{ mA.cm}^{-2}$	6.349
		$J_3 = 0$	8.0
Series No.3	12	$J_1 = 50 \text{ mA.cm}^{-2}$	2.653
		$J_2 = 15 \text{ mA.cm}^{-2}$	5.159
		$J_3 = 0$	9.5

Table 3. Electrochemical etching process for making interference filters at visible region

Figure 19 shows the reflection spectra of interference filters with reflection wavelength at 650nm-region, which prepared by etching process presented in table 1. When the etching time of electrochemical process increased, the reflection centered wavelength shifted to red-zone, i.e. the thickness of bi-layer stacks increased.

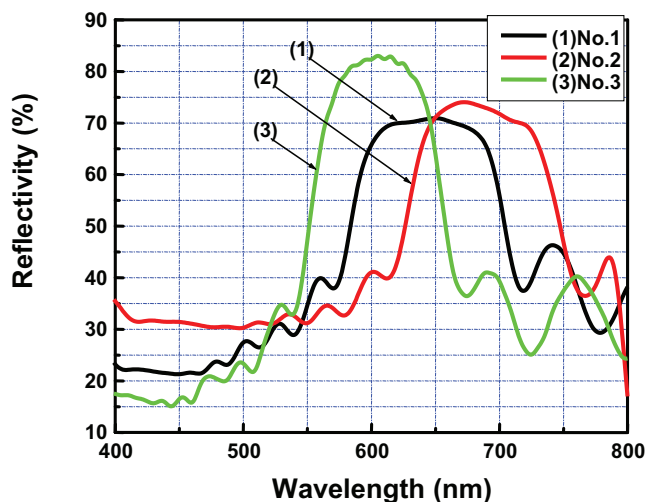


Fig. 19. Reflection spectra of red-light PS filters made by modulation of current density with different etching time.

We used thermal annealing process of samples for a stabilization of the optical properties of PS interference filters. The thermal annealing process of PS samples has three steps: i) first the PS samples were kept at 60°C for 60 min in air ambient to stabilize the PS structures; ii) the pre-oxidation of PS samples was performed at 300°C for different times varying from 20 to 60 min in oxygen ambient and iii) keeping the samples in Nitrogen ambient at the same temperature for 30 min and then the temperature decreased with very slow rate to room temperature.

Figure 20 shows the filter wavelength shift of as-prepared (PS) and pre-oxidized samples using the oxidation parameters 300°C/40min, respectively. The thermal annealing process caused a blue-shift of reflection wavelength of 42 nm and slightly increases a reflectance of

the filters (about 6%) in our case. At high temperature of annealing process (for example: at 900°C) filter wavelength still shifted to the shorter-wavelength zone the reflectance of filters would be strongly decreased. This can be explained as follows: the filter wavelength depends on the thickness of the bi-layer stacks which slightly decreased in the thermal annealing in oxygen ambient, while the reflectivity is determined by the refractive index ratio of the layers that may be decreased during oxidation process at high temperature.

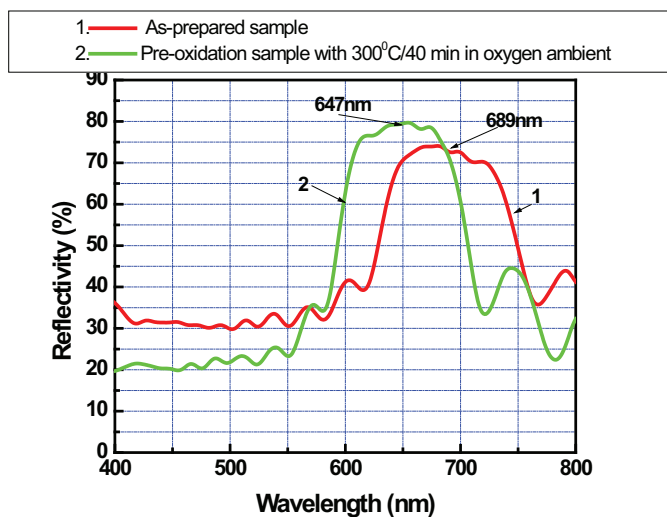


Fig. 20. Filter wavelength of as-prepared (1) and pre-oxidation (2) PS samples at 300°C in oxygen ambient. The blue-shift of filter wavelength of 42 nm was obtained.

## 5. Micro-cavity based on porous silicon and silicon-rich-silicon oxide multilayer

The structure of micro-cavities, also called Fabry-Perot filters, consists of two parallel Distributed Bragg Reflector (DBR) separated by a spacer layer, whose reflective index can be the same or different to the ones used for the DBRs. The optical thickness of the spacer layer can be  $\lambda$  or  $\lambda/2$  (Loni et al., 1996). The reflectivity spectrum of this structured material is characterized by a very narrow pass-band centered in a high reflectivity wavelength range. Micro-cavities can be used as band-pass filters with a tuned position of the peak (Weiss & Fauchet, 2003), tunable mirrors (Gao et al., 2002) and highly sensible detectors of substances like ethanol, methanol, acetone, chlorobenzene and nitrogen dioxide, among others (De Stefano et al., 2003; Volk et al., 2004; Anderson et al., 2003). They also have been used for optical sensor, biosensor and chemical sensor fabrication. In this section, we present the results of fabrication and investigate the wavelength-selective characteristics of DBR micro-cavity based on porous silicon multilayer structures. A simulation program for DBR micro-cavity based on the TMM has been developed from simulation program realized for interference filters that was shown in the subsection 4.1. Figure 21 shows the cross-sectional scheme of DBR micro-cavity with spacer of  $d_s$  between two interference filters consisting  $N$  periods for simulation.

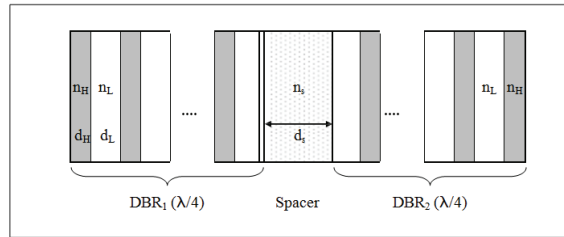


Fig. 21. Schematic of cross-section of DBR micro-cavity. The spacer layer with refractive index  $n_s$  and thickness  $d_s$  should be inserted between two symmetric DBRs.

### 5.1 Simulation results for DBR micro-cavity

Figure 22 shows the simulated reflectivity spectrum of DFB micro-cavity for selective wavelength of 650 nm, which consists the spacer layer thickness of  $\lambda/2$  and  $n_s=1.5$  between two multilayer stacks of 4 periods with  $n_H=2.3$  and  $n_L=1.5$  for high and low refractive indices of layers, respectively. These parameters result in wide reflectance with a high reflectivity (100%) and sharp transmission band in the spectra of Fabry-Perot filters.

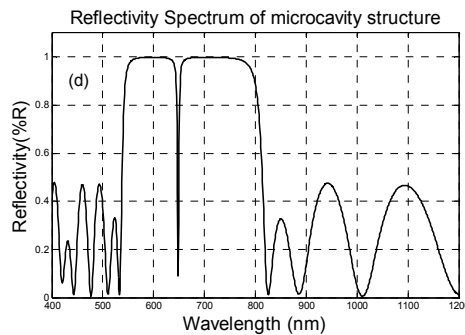


Fig. 22. Reflection spectrum of DBR micro-cavity with spacer thickness of  $\lambda/2$  and refractive index of 2.5 inserted in between two 4-period interference filters. The selective wavelength of cavity designed at 650 nm.

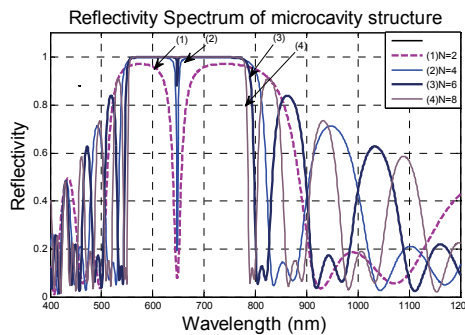


Fig. 23. Reflection spectra of a DBR micro-cavity at wavelength of 650 nm obtained by changing numbers of periods of DBR from 2 to 8.

The line-width of the transmission peak depends on the number of periods  $N$  of the DBR. When  $N$  increases, the transmission peak becomes narrower; the reflectivity of the band-gap increases and its edges become sharper. Simulation results show that the DBR micro-cavity has the band-pass width of 2 nm, the transmission of 90% at wavelength of 650 nm when the number of periods is more than 6 (see Figure 23).

## 5.2 Fabrication of PS and SRSO micro-cavity

Fabry-Perot PS micro-cavity has been formed by electrochemical etching of high doped  $p$ -type silicon wafers (resistivity of  $0.01 \pm 0.1 \Omega \cdot \text{cm}$ ) in an aqueous HF: ethanol electrolyte. The  $p$ -type silicon substrates yield the most favorable porous silicon morphology. The pores are large enough to allow infiltration of other species but interconnected and small enough to allow porous silicon to be treated as an optical medium for visible and infrared light. The electrolyte with concentration 16% HF and ethanol of ratio 1:2, respectively, is chosen because of the large porosity variation obtained by varying the etching current.

Description	Current density (mA/cm <sup>2</sup> )	Etching time (sec)
DBR on top (4.5 periods)	$J_1=15$	4.762
	$J_2=50$	2.857
Spacer layer (1 period)	$J_3=(10-50)$	5.714
DBR on bottom (5 periods)	$J_1=15$	4.762
	$J_2=50$	2.857

Table 4. Electrochemical etching conditions for making PS micro-cavities

Micro-cavity was formed by periodically varying the applied current density with two levels ( $J_1$  and  $J_2$ ) between 15 and 50 mA/cm<sup>2</sup> and one spacer layer ( $J_3$ ). PS micro-cavities are formed by first etching a top DBR with alternating  $\lambda/4$ -thickness layers of low and high porosities (high and low refractive indices, respectively), then etching a  $\lambda/2$ -thickness spacer layer with the designed refractive index, and finally etching a bottom DBR with the same conditions as the top DBR. Detailed electrochemical etching conditions are presented in Table 4. The PS micro-cavities used in our cases typically consist of 4.5/5 period upper/lower DBR. Each period has a pair of low and high porosity layers. The PS micro-cavity samples have been rinsed in methanol and isopropanol after anodization process and dried in nitrogen atmosphere.

The micro- and nano-structures of the prepared PS micro-cavity have been analyzed by using the Scanning Electron Microscopy (FE-SEM Hitachi S-4800). Figure 24 shows the SEM cross-section of a PS micro-cavity made by electrochemical etching condition shown in table 4. It can be observed in Figure 24a that the SEM image shows the dark and bright layers that have a low and high porosity, respectively. Based on this difference, the layers of the stack are distinguished and therefore the thickness of each layer can be determined of about 165 nm. As seen in Figure 24b, the typical sizes of the silicon residuals and air voids are less than 30 nm. The measured reflection spectrum of PS micro-cavity is shown in Figure 25. The spectrum is characterized by a transmission band at 643.3 nm in between two high reflection bands. The reflective distinction ratio of 40% and the Full-Width-Half-Maximum (FWHM) band-pass width of 20 nm were observed in PS micro-cavity based on symmetrical 5-period DBRs.

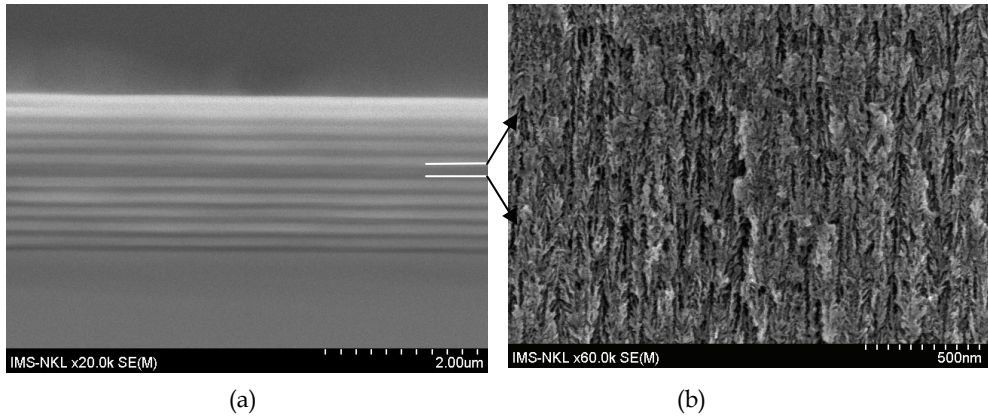


Fig. 24. SEM cross-section of PS micro-cavity with  $\lambda/2$ -wavelength thickness spacer for centered wavelength of 650 nm (a) and PS size in the spacer layer (b).

The preparation of PS structures composed by several layers for DBR micro-cavity with narrow band-pass width of 2 nm as a design by simulation is difficult in practice, because the line-width of transmission of micro-cavity was strongly affected by homogeneity of the layers. The anodization condition might drift as the sample thickness and refractive index of stacks, and the solution composition changes with the depth because of limited exchange through the pores, that caused the different of experimental results in comparison with simulation one. In general, the band-pass width of 20 nm at the visible region obtained from the PS micro-cavity based on electrochemical etching technique is good enable for applications in the optical sensor, biosensors and/or micro-cavity lasers.

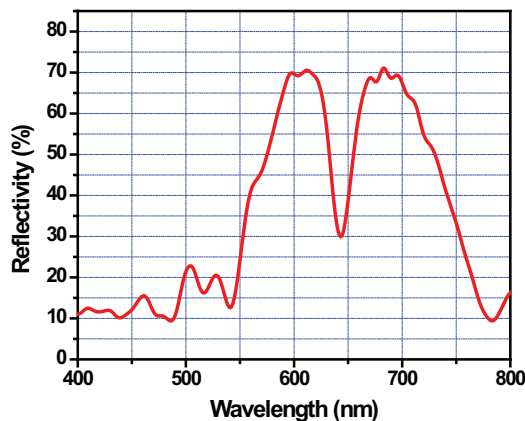


Fig. 25. Reflection spectrum of PS micro-cavity with transmission band of 650nm made by spacer of  $\lambda/2$ - thickness sandwiched between 5-period DBR.

For a prevention of ageing process of PS layers we used thermal annealing process of PS samples to obtain SRSO materials. The thermal annealing process used for SRSO has four steps: i) first the PS samples were kept at 60°C for 60 min in air ambient to stabilize the PS

structures; ii) the pre-oxidation of PS samples was performed at 300°C for different times varying from 20 to 60 min in oxygen ambient; iii) slowly increasing temperature up to 900°C and keeping samples for 5-10 min in oxygen ambient iv) keeping the samples in Nitrogen atmosphere at temperature of 900-1000°C for 30 min and then the temperature was decreased with very slow rate to room temperature. Table 5 presents the shift of transmission band in the spectra of Fabry-Perot filters based on the as-prepared and thermally annealed PS micro-cavity at 300°C and 900°C in oxygen ambient, respectively.

Samples	Centered wavelength of transmission (nm)	Line-width of transmission (nm)	Distinction ratio (%)
as-prepared sample	643.9	22.2	40
300°/40 min	565.6	22.6	34
300°/40 min + 900°C/5 min	472.5	19.2	25

Table 5. Shift of narrow transmission band in the spectra of Fabry-Perot PS filters (the anodization condition was shown in table 4)

The 900°C oxidation decreases the centered wavelength of transmission by more than 170nm and the reflective distinction ratio on 15%, while the line-width of transmission does not change. This can be explained as follows: the centered wavelength of transmission corresponds to the optical thickness of spacer layer that is the product of refractive index and layer thickness. During the oxidization process at high temperature the layer thickness and refractive index of spacer decreased, which causes the shift of transmission wavelength and decrease of reflective distinction ratio of micro-cavity.

## 6. Conclusions

We have demonstrated the electrochemical method combined with thermal annealing for making PS and SRSO layers. The advantages of electrochemical method compared with others to fabricate PS and SRSO layers are: low-cost fabrication and experimental setup; compatibility to silicon technology for optoelectronic devices; fast fabrication process and easily varying refractive index over wide range.

We showed that the ageing of PS by natural oxidation is disturbing as well as it causes a change of the emission wavelength of nc-Si, refractive index of PS layers by the change of Si nano-particle sizes. The experimental results indicate that the intense and stable emission in the blue zone of the PL spectra observed in the considered PS samples relates to defects in silicon oxide layers. For prevention of natural oxidation of PS layers we used thermal annealing to obtain SRSO layers, which have more stable optical properties in operations. Also, the Er-doped SRSO multi-layers with good waveguide quality fabricated by using the electrochemical method combined with thermal annealing are presented. The influence of the parameters of the preparation process, such as the resistivity of Si-substrate, the HF concentration, the drift current density, and the oxidation temperature, on the optical properties of the Er-doped SRSO waveguides was studied and discussed in detail. The luminescence emission of Er ions in the SRSO layers at 1540 nm was strongly increased in comparison with that of Er-doped silica thin film. The evidence for energy transfer between nc-Si and Er ions in Er-doped SRSO layer was obtained by changing the excitation wavelength.

Finally, we have demonstrated the electrochemical process for making interference filters and DBR micro-cavity based on PS and SRSO multi-layers with periodical change of refractive indices of the layer stacks. For the optimal parameters of interference filters and micro-cavities based on PS and SRSO multi-layers, we use Transfer Matrix Method for simulation of reflectivity and transmission of interference filters and DBR micro-cavity with the data obtained from experiments. We successfully fabricated the interference filters and DBR micro-cavity based on porous silicon multilayer which has the selectivity of wavelength in a range from visible to infra-red range with the reflectivity of about 90% and transmission line-width of 20nm. The spectral characteristics of those multi-layers such as desired centered wavelength ( $\lambda_0$ ), the FWHM line-width of spectrum, reflectance and transmission wavelength have been controlled. A good correspondence between simulation and experimental results has been received. The imperfection of interfaces of layers created by electrochemical etching was used to explain a deformation of reflective spectrum from filters having few periods. The SRSO thin films with single and multi-layer structures produced by electrochemical method have a big potential for applications in the active waveguide, optical filter, chemical and biosensors, DBR micro-cavity lasers.

## 7. Acknowledgements

This work was supported in part by the National Program for Basic researches in Natural Science of Vietnam (NAFOSTED) under contract No. 103.06.38.09. A part of the work was done with the help of the National Key Laboratory in Electronic Materials and Devices, Institute of Materials Science, Vietnam Academy of Science and Technology, Vietnam. The author would like to thank Pham Duy Long for his help with Autolab equipment.

## 8. References

- Amato, G., Rosenbauer, M. (1997). Absorption and photoluminescence in porous silicon, in Amato et al. (ed.), *Structure and Optical Properties of Porous Silicon Nanostructures*, Gordon and Breach Science Publishers, Amsterdam, 3-52
- Anderson, M.A., Tinsley-Brown, A., Allcock, P., Perkins, E.A., Snow, P., Hollings, M., Smith, R.G., Reeves, C., Squirrell, D.J., Nicklin, S., Cox, T.I. (2003). Sensitivity of the optical properties of porous silicon layers to the refractive index of liquid in the pores, *Phys. Stat. Sol. (a)* 197, 528-533
- Barla, K., Herino, R., Bomchil, G. (1986). Stress in oxidized porous silicon layers, *J. Appl. Phys.* 59, 439-441
- Bettotti, P., Cazzanelli, M., Dal Negro, L., Danese, B., Gaburro, Z., Oton, C.J., Vijaya Prakash, G., Pavesi, L. (2002). Silicon nanostructure for photonics, *J. Phys.: Condens. Matter.* 14, 8253- 8281
- Bui Huy, Pham Van Hoi, Phan Hong Khoi, Nguyen Thuy Van, Do Thuy Chi (2011). Porous silicon as a promising material for photonics, *Int. J.NanoTech.* 8, 360-370
- Bui Huy, Phi Hoa Binh, Bui Quang Diep, Phi Van Luong (2003). Effect of ageing on the luminescence intensity and lifetime of porous silicon: role of recombination centers, *Physica E* 17, 134-136
- Bui Huy, Pham Van Hoi, Phi Hoa Binh, Tran Thi Kim Chi, Le Quang Huy, Nguyen Quang Liem (2006). Effect of ageing on the statically and time-resolved photoluminescence spectra of porous silicon, *J. Phys. IV France* 132, 321-324



- Calcott, P.D.J., Nash, K.J., Canham, L.T., Kane, M.J., Brumhead, D. (1993) Spectroscopic identification of the luminescence mechanism of highly porous silicon, *J. Lumines.* 57, 257-269
- Canham, L.T. (1990). Si quantum wire arrays fabrication by electrochemical and chemical dissolution of wafer, *Appl. Phys. Lett.* 57, 1046-1048
- De Stefano, L., Rendina, I., Moretti, L., Rossi, A.M. (2003), Optical sensing of flammable substances using porous silicon microcavities, *J. Mater. Sci. and Eng. B100*, 271-274
- Elhouichet, H., Oueslati, M. (2007). Rare earth ions in porous silicon: optical properties, *J. Phys. Stat.Sol. (a)*, 204, No.5, 1497-1501
- Friolo, F., Franzo, G., Pacifici, D., Vinciguerra, V., Iacona, F., Irrena, A. (2001). Role of the energy transfer in the optical properties of undoped and Er-doped interacting Si nanocrystals, *J. Appl. Phys.* 89, 264-272
- Frohnhoff, S., Berger, M.G., Thönissen, M., Dicker, C., Vescan, L., Munder, H., Lüth, H. (1995). Formation techniques for porous silicon superlattices, *Thin Solid Films* 255, 59-62
- Gao, T., Gao, J., Sailor, M.J. (2002), Tuning the response and stability of thin film mesoporous silicon vapor sensors by surface modification, *J. Langmuir* 18, 9953-9957
- Gorelkinskii, Yu.V., Abdullin, Kh.A., Kalykova, G.K., Kikarin, S.M., Mukashev, B.N. (2008). Stable ultraviolet photoluminescence of nanoporous silicon, *J. Mater.Sci. & Eng.B* 147, 258-261
- Herino, R., Bomchil, G., Barla, K., Bertrant, C., Ginoux, J.L. (1987), Porosity and Pore size distributions of Porous silicon layers, *J. Electrochem. Soc.* 134, 1994-2000
- Huy. B., Cham T.T., Vinh H.X., Van D.K. and Hoi P.V. (2008). Erbium-doped silicon-rich oxide waveguides fabricated by using an electro-chemical method, *J. Korean Phys. Soc.* 53, 1397-1400
- Kanemitsu, Y., Uto, H., Masumoto, Y., Futagi, T., Mimura, H. (1993). Microstructure and optical properties of free-standing porous silicon films: Size dependence of absorption spectra in Si nanometer-sized crystallites, *Phys. Rev. B* 48, 2827-2830
- Kimura, T., Yokoi, A., Horiguchi, H., Saito, R., Ikoma, T., Saito, A. (1994). Electrochemical Er-doping of porous silicon and its room-temperature luminescence at 1.54  $\mu\text{m}$ , *Appl. Phys. Lett.* 65, 983-985
- Kit, P.G., Polman, A. (2000). Exciton-erbium interactions in Si nanocrystal-doped  $\text{SiO}_2$ , *J. Appl. Phys.* 88, 1992 (7 page)
- Kovalev, D., Averboukh, B., Benchorin, M., Koch, F., Efros, Al.L., Rosen, M. (1996). Optically induced polarization anisotropy in porous silicon, *Phys. Rev. Lett.* 77, 2089-2092
- Krüger, M., Hilbrich, S., Thönissen, M., Scheyen, D., Theiß, W., Lüth, H. (1998). Suppression of ageing effect in porous silicon interference filters, *Opt. Comm.* 146, 309-315
- Lehmann, V., Gösele, U. (1991). Porous silicon formation - a quantum wire effect, *Appl. Phys. Lett.* 58, 856-858
- Loni, A., Canham, L.T., Berger, M.G., Arens-Fischer, R., Munder, H., Lüth, H., Arrand, H.F., Benson, T.M. (1996), Porous silicon multilayer optical waveguides, *Thin Solid Films* 276, 143-146
- Mazzoleni, C., Pavesi, L. (1995). Application to optical components of dielectric porous silicon multilayer, *Appl. Phys. Lett.* 67, 2983-2985

- Najar, A., Charrier, J., Ajlani, H., Lorrain, N., Elhouichet, H., Oueslati, M., Haji, L. (2006). Optical properties of erbium-doped porous silicon waveguides, *J. Lumines.* 121, 245-248
- Saleh, B.E.A., Teich, M.C. (2007), *Fundamentals of Photonics*, 2nd Edition, Chapter 7, John Wiley&Son, Inc., NewYork.
- Shin, J. H., van d'Hoven, G. N., Polman, A. (1995). Origin of the 1.54  $\mu\text{m}$  luminescence of Erbium-implanted porous silicon, *Appl. Phys.Lett.* 66, 2379-2381
- Smith, R.L., Collins, S.D. (1992). Porous silicon formation mechanism, *J. Appl.Phys.* 71(8), R1 (21 pages)
- Valance, A. (1997). Theoretical model for early stages of porous silicon formation from n- and p-type silicon substrates, *Phys. Rev. B* 55, 9706-9715
- Vincent, G. (1994). Optical properties of porous silicon superlattices, *Appl. Phys. Lett.* 64, 2367 (3 page)
- Volk, J., Balazs, J., Tóth, A.L., Bársony, I. (2004), Porous silicon multilayers for sensing by tunable IR-transmission filtering, *J. Sensors & Actuators B100*, 163 -167
- Weiss, S.M., Fauchet, P.M. (2003), Electrical tunable porous silicon active mirrors, *Phys. Stat. Sol (a)* 2, 556-560
- Wolkin, M.V., Jorne, J., Fauchet, P.M. (1999). Electronic states and luminescence in porous silicon quantum-dots: the role of oxygen. *Phys. Rev. Lett.* 82,197-200

# Silicon Oxide ( $\text{SiO}_x$ , $0 < x < 2$ ): A Challenging Material for Optoelectronics

Nicolae Tomozeiu  
*R&D Department, Océ Technologies B.V.,  
The Netherlands*

## 1. Introduction

### 1.1 Why $\text{SiO}_x$ in optoelectronics

A complete integration of the silicon based optoelectronic devices was not possible, for many decades, to be made because the silicon is an inefficient emitter of light. Being a semiconductor with an indirect band-gap and having efficient free carrier absorption of the radiation, the crystalline silicon was considered an inadequate material for light emitter diodes (LED) and laser diodes to produce totally integrated optoelectronic devices. In the last two decades, special attention has been paid to the light-emission properties of low-dimensional silicon systems: porous silicon (Cullis & Canham, 1991; Wolkin et al., 1999), super-lattices of Si/SiO<sub>2</sub> (Zu et al., 1995), silicon nano-pillars (Nassiopoulos et al., 1996), silicon nanocrystals embedded in SiO<sub>2</sub> (Wilson et al., 1993) or in Si<sub>3</sub>N<sub>4</sub> (Cho et al., 2005). Both, the theoretical understanding of the physical mechanisms (quantum confinement of excitons in a nano-scale crystalline structure) and the technological advance to manufacture such structures have paved the path to produce a silicon based laser.

Pavesi et al (2000) have unambiguously observed modal and net optical gains in silicon nanocrystals. They have compared the gain cross-section per silicon nano-crystal with that the one obtained with A<sub>3</sub>B<sub>5</sub> (e.g. GaAs) quantum dots and it was found orders of magnitude lower. However, owing to the much higher stacking density of silicon nanocrystals with respect to direct band-gap A<sub>3</sub>B<sub>5</sub> quantum dots, similar values for the material gain are observed. In this way, the route towards the realization of a silicon-based laser, and from here, of a highly integrated silicon based optoelectronic chip, is open.

The silicon nano-crystals (Si-nc) embedded in various insulators matrix have been intensively studied in the last decade. Either the photoluminescence (PL) properties of the material or the emitted radiation from a LED/ diode laser structure was studied. A clear statement was made: the peak position of PL blue-shifts with decreasing the size of Si-nc. The nano-crystals interface with the matrix material has a great influence on the emission mechanism. It was reported that due to silicon-oxygen double bonds, Si-nc in SiO<sub>2</sub> matrix has localized levels in the band gap and emits light in the near-infrared range of 700–900 nm even when the size of Si-nc was controlled to below 2 nm (Wolkin et al., 1999; Puzder et al., 2002).

In the last decades, silicon suboxides (hydrogenated and non-hydrogenated) have been proposed as precursors for embedded silicon nano-crystals into silicon dioxide matrix. This material is a potential candidate to be used in laser diodes fabrication based on silicon technology. The need for such device was (and is) the main reason for theoretically (ab initio

theories) and experimentally investigations of  $\text{SiO}_x$ . This chapter dedicated to silicon suboxide as a challenging material for silicon based optoelectronics, begins in section two with a small (but comprehensive) discussion on the structural properties of this material. The implications of the  $\text{SiO}_x$  composition and its structural entities on the phonons' vibrations are shown in the third section. Here are revealed the IR spectra of various compositions of the  $\text{SiO}_x$  thin films deposited by rf reactive sputtering and the fingerprints related to various structural entities. The electronic density of states (DOS) for these materials is the subject of the fourth section. Here are defined the particularities of the valence- and conduction band with special attention to the structural defects as silicon dangling bonds (DB). Having defined the main ingredients to understand the optical and electrical properties of the  $\text{SiO}_x$  layers, these properties are discussed in the fifth and the sixth section, respectively. The investigations and their results on as deposited  $\text{SiO}_x$  materials are analyzed in this section. In the first part of this introduction it was mentioned that the material for optoelectronics is the silicon nano-crystals embedded in  $\text{SiO}_2$ . The physical processes in order to obtain the silicon nano-particles from  $\text{SiO}_x$  thin films are presented in section seven. The phase separation realized with post-deposition treatments as thermal annealing at high temperature, or ion bombardment or irradiation with UV photons is extensively discussed. This section ends with a brief review of the possible applications of the Si-nc embedded into a dielectric matrix as optoelectronic devices. Of course the main part is dedicated to the silicon-based light emitters.

## 2. The structure of $\text{SiO}_x$ ( $0 < x < 2$ )

### 2.1 Introductory notions

The structure of the silicon oxide, as the structure of other silicon-based alloys, is build-up from tetrahedral entities centered on a silicon atom. The four corners of the tetrahedral structure could be either silicon or oxygen atoms. Theoretically, this structural edifice appears as the result of the "chemistry" between four-folded silicon atoms and two-folded oxygen atoms, developed under specific physical conditions. It is unanimously accepted that an oxygen atom is bonded by two silicon atoms and never with another oxygen atom. The length of the Si-O bond is 1.62 Å while the Si-Si bond is 2.35 Å. The dihedral angle between two Si-Si bonds (tetrahedron angle) is  $109.5^\circ$  and the angle formed by the Si-O bonds in the Si-O-Si bridge is  $144^\circ$ . These data are the results of dynamic molecular computation (Carrier et al., 2002) considering the structure completely relaxed. In reality, the structure of the  $\text{SiO}_x$  thin films deposited by PVD or CVD techniques is more complicated. Both the bond length and the dihedral angle vary. Moreover, the picture of the structural design is complicated because the Si-O bond is considered partially ionic and partially covalent (Gibbs et al., 1998).

### 2.2 $\text{SiO}_x$ structure: theoretical assumptions

In order to obtain an elementary image of the  $\text{SiO}_x$  structure, we use a simple model. It is important to evaluate the main elements that define the material structure: the energy involved in keeping together the atoms within a specific structure and the number of each atom species from a defined alloy. The Si-Si and Si-O bonds are characterized by dissociation energy of 3.29 eV/bond and 8.26 eV/bond, respectively (Weast, 1968). The particles' density in crystalline silicon (c-Si) is  $5 \cdot 10^{28} \text{ m}^{-3}$  while for crystalline quartz (c- $\text{SiO}_2$ ) is  $6.72 \cdot 10^{28} \text{ m}^{-3}$ . Interpolating, it can be found for  $\text{SiO}_x$ :

$$N_{\text{SiO}_x}^{\text{at}} = 5 \cdot 10^{28} + 8.55 \cdot 10^{27} \cdot x \quad (\text{m}^{-3}), \quad (1)$$

where  $x = \text{O}/\text{Si}$ .

The silicon atoms' density is:

$$N_{\text{Si}} = N_{\text{SiO}_x}^{\text{at}} \cdot \frac{1}{1+x} \quad (2a)$$

and the oxygen atoms' density is:

$$N_{\text{O}} = N_{\text{SiO}_x}^{\text{at}} \cdot \frac{x}{1+x} \quad (2b)$$

Taking into account the fact that the silicon atom is four-coordinated and the oxygen is two-coordinated, the number of bonds can be easily calculated:

- O atoms are involved in Si-O-Si bridges<sup>1</sup>, which means two Si-O bonds:  $n(\text{Si-O-Si}) = 2 n(\text{Si-O}) = N_{\text{O}}$  (one oxygen atom contributes to two Si-O bonds);
- Si atoms will contribute to Si-Si and Si-O-Si bonds:  $n(\text{Si-Si, Si-O-Si}) = (4/2) N_{\text{Si}}$  (one silicon atom is shared by 4 Si-Si and/or Si-O bonds and it must be considered only once);

This means that for Si-Si bonds it is easy to write:  $n(\text{Si-Si}) = n(\text{Si-Si, Si-O-Si}) - n(\text{Si-O-Si})$ , where  $n(\text{A-B})$  is the number of bonds between atom specie A and atom specie B from an AB alloy, while  $N_y$ , with  $y = \text{Si, O}$  is the number of specie "y" atoms.

Having the number of bonds and the energy per bond, the energy involved in a SiO<sub>x</sub> material can be estimated. This represents practically the necessary energy to break all bonds between the atoms that form a structural edifice. Following the calculations presented above, the density of Si-Si and Si-O bonds versus silicon suboxide composition (x parameter from SiO<sub>x</sub>) is shown in figure 1a. Also, the values of the SiO<sub>x</sub> density energy (in J/m<sup>3</sup>) calculated for x ranging from 0 and 2 are displayed in figure 1b. The latter is an important parameter for experiments considering the structural changes of an already deposited (grown) SiO<sub>x</sub> material.

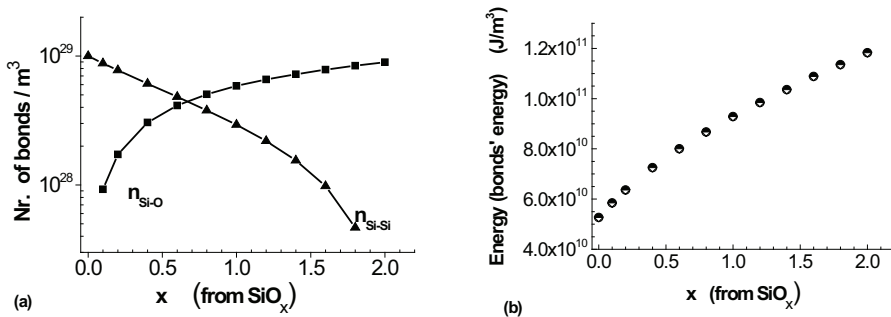


Fig. 1. (a) The calculated values of the Si-Si and Si-O bonds density as a function of x; (b) the dissociation energy per volume unit versus x parameter.

<sup>1</sup> The number of O-O bonds is considered as being equal to zero.

The interpretation of the data presented in figure 1b, is simple: for a sample with certain  $x$  value, if the corresponding value of the dissociation energy is instantaneously delivered, we can consider that for an extremely short time, the bonds are broken and the atoms can "look for" configurations thermodynamically more stable. With short laser pulses, such kind of experiments can be undertaken and structural changes of the material can be studied.

### 2.3 The main $\text{SiO}_x$ structural entities

Varying the number of oxygen atoms bonded to a silicon atom considered as the center of the tetrahedral structure, five entities can be defined. In a simple representation they are shown in figure 2. For a perfect symmetric structure (the second order neighboring atoms included), the Si-Si distance is 1.45 times the Si-O length. The nature of the Si-O bond makes the pictures shown in figure 2 more complicated. The electrical charge transferred to the oxygen neighbor charges positively the silicon atom. This means that a four-coordinated silicon can be noted as  $\text{Si}^{n+}$  where  $n$  is the number of oxygen atoms as the nearest neighbors. The length of a Si-Si or Si-O bond, as well as the angle between two adjacent bonds, is influenced by the  $n+$  value and the spatial distribution of those  $n$  oxygen atoms around the central silicon atom. Of course the  $4-n$  silicon atoms are also  $\text{Si}^{m+}$  like positions and they will influence the length of the  $\text{Si}^{n+} - \text{Si}^{m+}$  bond. Using first-principles calculations on Si/SiO<sub>2</sub> super-lattices, P. Carrier and his colleagues (Carrier et. al., 2001) have defined the interfaces as being formed by all  $\text{Si}^{1+}$ ,  $\text{Si}^{2+}$  and  $\text{Si}^{3+}$  entities. The super-lattice structure has been considered within a so-called *fully-relaxed model*. The main outcome of these calculations is that the bond-lengths of partially oxidized Si atoms are modified when compared with their counterparts from Si and SiO<sub>2</sub> lattice. As examples we mention: within a  $\text{Si}^{1+}$  structure the  $\text{Si}^{1+} - \text{Si}^{m+}$  bond is 2.39 Å for  $m=2$  and 2.30 Å when  $m=0$ . The  $\text{Si}^{n+} - \text{O}$  has a length of 1.65 Å when  $n=1$  and 1.61 Å for  $n=3$ . All these have influences on the structural properties of the material and from here on the density of states assigned to the phonons and electrons. The influence on physical properties (electrical, optical and mechanical) of the material deposited in thin films will be discussed in the next sections.

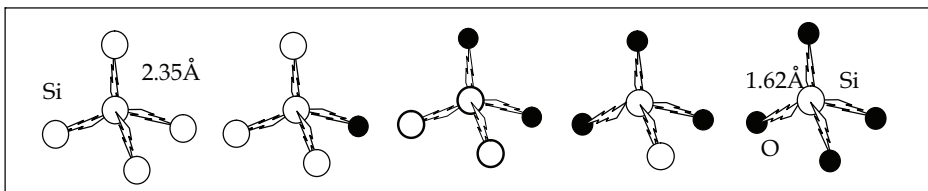


Fig. 2. The five structural entities defined as  $\text{Si}^{n+}$  in  $\text{SiO}_x$  alloys. The structures are build-up around a central Si atom from  $n$  oxygen atoms (the filled circles) and  $4-n$  silicon atoms (empty circles)

It should be noted that the differences in both the bond length and the dihedral angle of two adjacent bonds determine, for each structural entity, small electrical dipole with great impact on properties as electrical conductivity and dielectric relaxation. A contribution of the polarization field on the local electrical field will determine hysteresis - like effects, that could be used in some applications.

The multitude of possible connexions between various structural entities defines on macroscopic scale a  $\text{SiO}_x$  structure full of mechanical tensions which, speaking from a

thermodynamic perspective, provides an unstable character to the material. It is easy to see that a material formed from Si<sup>0+</sup> or Si<sup>4+</sup> structures without defects (e.g. dangling bonds) is thermodynamically stable.

### 3. The phonons' vibrations and SiO<sub>x</sub> structure

#### 3.1 Phonons' and molecular vibrations

Within the so-called Born - Oppenheimer adiabatic approximation, the general theory of solid state physics shows that the movement of the light particles-component of atoms (electrons) can be neglected or considered as a perturbation for the movement of the heavy parts of the atom (ions). In these conditions, for a crystalline material, the Schrödinger equation assigned to the system of heavy particles is:

$$\hat{H}_z \Psi(\{\vec{R}_\alpha\}) = E \Psi(\{\vec{R}_\alpha\}) \quad (3)$$

where the Hamiltonian  $\hat{H}_z$  is a sum of three terms:

- i. the first one describes the kinetic energy:  $\sum_\alpha \left( \frac{P_\alpha^2}{2M_\alpha} \right)$ , with  $\alpha$  the number of particles,  $M_\alpha$  and  $P_\alpha$ - the mass and the momentum of the ion;
- ii. the second one :  $\frac{1}{2} \sum_{\alpha, \beta (\alpha \neq \beta)} \hat{V}_{\alpha\beta}$  is the potential energy due to the interaction between ions;
- iii. and the third one defined as  $\hat{E}_e(\{\vec{R}_\alpha\})$  represents the electrostatic interaction between ions and electrons.

The equations (3) have been solved considering that the lattice vibrations involve small displacement from the equilibrium position of the ion: 0.1 Å and smaller. Under the so-called harmonic approximation, the problem is seen as a system of quantum oscillators with the solution:

- the eigenvector  $\Psi$  was found as

$$\Psi = \prod_\alpha \psi_\alpha \quad (4)$$

with  $\psi_\alpha = \frac{\exp(i\vec{k}\vec{R}_\alpha)}{\sqrt{V}} \cdot u_{\alpha\vec{k}}(\vec{R}_\alpha)$  given by the Bloch functions.

- the eigen-values for energy:

$$E = \sum_\alpha E_\alpha = \sum_\alpha \hbar \nu_\alpha \cdot \left( N_\alpha + \frac{1}{2} \right) \quad (5)$$

The relation (5) shows that  $\hbar \nu_\alpha$  is a quantum of energy assigned to the lattice oscillation. It represents the energy of a *phonon* - quasi-particle that describes the collective movement of the lattice constituents. The phonons are characterized by energy and momentum (impulse)

as long as the lattice and the collective movement of the atoms (ions) exists. Only under these conditions, the phonon can be understood as a particle that can interact with other particles (e.g. electrons, photons).

Let us consider a molecule formed from different atoms where the bond lengths and the bond angles represent the average positions around which atoms vibrate. At temperatures above absolute zero, all the atoms in molecules are in continuous vibration with respect to each other. If the molecule is consisting of  $N$  atoms, it has a total of  $3N$  degrees of freedom. For nonlinear molecules, 3 degrees of freedom describe the translation motion of entire molecule in mutually perpendicular directions (the X, Y and Z axes) and other 3 degrees correspond to rotation of the entire molecule around these axes. For a linear molecule, 2 degrees are rotational and 3 are translational. The remaining  $3n-6$  degrees of freedom, for nonlinear molecules, respectively  $3n-5$  degrees for linear molecules are *fundamental vibrations*, also known as *normal modes of vibration*.

Considering the adiabatic approximation and harmonic displacements of the atoms from their equilibrium positions, for each vibrational mode,  $q$ , all the atoms vibrate at a certain characteristic frequency,  $\nu_q$  called *fundamental frequency*. In this situation, for any mode the vibration energy states,  $E_{qv}$ , can be described by:

$$E_{qv}^{\text{harm}} = h\nu_q \left( n_q + \frac{1}{2} \right) \quad (6)$$

where  $h$  is Planck's constant,  $n_q$  is the vibrational quantum number of the  $q$ -th mode ( $n_q=0, 1, 2, \dots$ ). The ground state energy (that corresponds to  $n_q = 0$ ) is  $h\nu_q/2$  and each excited state, defined by the vibrational quantum number has an energy defined by the Rel. (6). The energy difference for transitions between two adjacent states is constant and equals  $h\nu_q$ .

The theoretical model of the harmonic displacement of the atoms helps to easily describe the atoms movement. In reality, the structural edifice of the molecule supposes atoms that belong to intra-molecule bonds or to inter-molecules bonds. This means that the character of harmonic oscillator disappears and a molecule is in fact an anharmonic oscillator. Introducing an anharmonicity parameter  $\gamma_q$  for each vibrational mode, the phonon energy can be expressed as:

$$E_{qv} = E_{qv}^{\text{harm}} + h\nu_q \gamma_q \left( n_q + \frac{1}{2} \right)^2 \quad (7)$$

where  $\gamma_q$  is dimensionless.

*How the length of the bond (the interatomic distance) influences the phonon energy?*

Considering a di-atomic molecule, its potential energy as a function of the distance between the atoms within an anharmonic oscillation is suggestively shown in figure 3. The minimum in the potential energy is reached when the distance between the two atoms equals the "bond length". As the inter-atomic distance increases, the potential energy reaches a maximum, which defines the bond dissociation energy.

An interesting observation is that the energy levels of the oscillator which represents the diatomic molecule are quantified (they have discrete values) and they become closer with increasing the interatomic distance. This means that the needed energy to excite the phonon on the nearest energy state,  $h\nu_q$ , is smaller when the distance between the atoms increases.



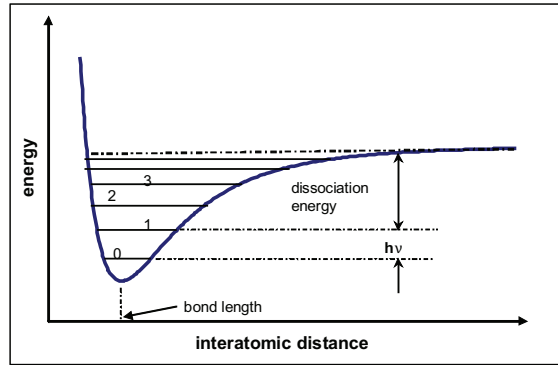


Fig. 3. The potential energy for a di-atomic molecule versus the interatomic distance, within the anharmonic oscillation model.

How the mass of the two atoms influences the phonon frequency? To answer this question, let's consider the simplest oscillator (a mechanical spring connecting two masses) and apply the classical Hooke's law. If  $m_1$  and  $m_2$  are the mass values for the two atoms, the frequency oscillation is:

$$\nu = \frac{1}{2\pi} \cdot \sqrt{\frac{k}{\mu}} \quad (8)$$

with the reduced mass,  $\mu$ , given by  $\mu = \frac{m_1 m_2}{m_1 + m_2}$ . The parameter  $k$  is called the elastic force constant of the bond and it defines the bond strength.

In most books of the IR spectroscopy the oscillation frequency is given in wave-number unit that is the inverse of the wavelength. In this condition the Rel. (8) becomes

$$\tilde{\nu} = \frac{1}{\lambda} = \frac{1}{2\pi c} \cdot \sqrt{\frac{k}{\mu}} \quad (\text{cm}^{-1}) \quad (8')$$

with  $c$  the speed of light,  $3 \cdot 10^{10}$  cm/s. Therefore, for the heavier atoms the vibration frequency is smaller. However the strength of the bond is also defining the vibrational frequency. In other words, the nature of the bond is important. We can conclude that the phonon spectrum is specific to each type of molecule and it could be utilized in identification of the atomic species.

We note that, within a multi-atomic molecule, the motion of two atoms cannot be isolated from the motion of the rest of the atoms in the molecule. Also, in such a molecule, two oscillating bonds can share a common atom. When this happens, the vibrations of the two bonds are coupled.

### 3.2 IR active vibrations - a theoretical approach

IR spectroscopy is one of the most utilized techniques in analyzing the compositional and structural properties of a molecular compound. When a radiation of IR optical range, with

energy  $h\nu$ , is sent on a molecular system whose vibration frequency is  $\nu$ , that radiation is absorbed, if the molecule has electrical dipole.

As a result of the interaction between the electrical field of the IR electromagnetic wave and the molecular dipole, the molecule will make a transition, in energy, between the states "i" and "j". The *transition moment*  $\mathfrak{S}$  is defined by:

$$\mathfrak{S} = \int \psi_i^* \mu \psi_j d\tau \quad (9)$$

where  $\psi$  and  $\psi^*$  are the eigen-function and its complex conjugate;  $d\tau$  is the integration over all space. In the relation (9)  $\mu$  is the *dielectric dipole moment* defined as:

$$\mu = q \cdot r \quad (10)$$

with  $q$  the charge of the dipole and  $r$  the distance between the charges.

Taking into account the vibrational motion of the atoms, the dielectric dipole changes, because the distance  $r$  changes:

$$\mu = \mu_0 + (r - r_e) \cdot \left( \frac{\partial \mu}{\partial r} \right)_0 + \frac{1}{2} \cdot (r - r_e)^2 \cdot \left( \frac{\partial^2 \mu}{\partial r^2} \right)_0 + \dots$$

In this situation the transition moment becomes:

$$\mathfrak{S} = \int \psi_i^* \left[ \mu_0 + (r - r_e) \cdot \left( \frac{\partial \mu}{\partial r} \right)_0 \right] \psi_j \cdot d\tau \quad (11)$$

When  $\mu_0$  is a constant, because of the orthogonality of the eigen-functions, ( $\int \psi_i^* \psi_j d\tau = 0$ ), the relation (11) remains:

$$\mathfrak{S} = \int \psi_i^* \left[ (r - r_e) \cdot \left( \frac{\partial \mu}{\partial r} \right)_0 \right] \psi_j \cdot d\tau \quad (12)$$

The transition probability is defined as  $\mathfrak{S}^2$ , and it scales the radiation absorption. With other words, the intensity of the IR absorption peak is proportional to the square of  $\mathfrak{S}$  and  $\left( \frac{\partial \mu}{\partial r} \right)$ . We can say that the *molecules with  $\left( \frac{\partial \mu}{\partial r} \right) = 0$  are IR inactive* because the absorption of the radiation is zero. We note that molecule with small dipole moment  $\mu$  may have large  $\left( \frac{\partial \mu}{\partial r} \right)$  and vice-versa. In both situations, according to Rel. (12), absorbing bands will appear in the IR spectrum.

Therefore, we can conclude that among the fundamental vibrations, those that produce a change in the dipole moment may result in an IR activity. Certain vibrations *give polarizability changes and they may give Raman activity*. Some vibrations can be both IR- and Raman-active.

### 3.3 The IR fingerprints of the $\text{SiO}_x$ structural entities

Does the  $\text{SiO}_x$  structure have an electrical dipole to interact with the incident IR radiation and to release an IR absorption spectrum?

Considering the structural entities presented in figure 2, all entities that contain at least one oxygen atom have such an electrical dipole. The tetrahedral structure build up around a silicon atom by its four neighbors will have a certain asymmetry concerning the "gravity center" of the positive charge vis-à-vis of that of the one of the negative charge. By molecular vibration a dipole is generated and, according to the theoretical explanation given in the previous section, energy of the IR electromagnetic field will be absorbed.

Calculations based on theoretical models (simpler or more sophisticated, modern) have produced the local density of vibrational states (LDOVS) for Si and O atoms (Lucovski and Pollard, 1963, Knights et al., 1980, Pai et al., 1986). The IR absorption spectrum specific to a  $\text{SiO}_2$  structure was calculated taking into account these LDOVS' and as it can be seen in figure 4 (after P.G. Pai et al., 1986) there are three vibrational bands which correspond to rocking, bending and stretching motions of the oxygen atoms. As a first observation, the dominant calculated peak in the IR absorption spectrum of  $\text{SiO}_2$  is associated with stretching motion of the oxygen atoms. The peak position and the shape of the peak absorption are greatly affected by the mixing of Si and O atoms.

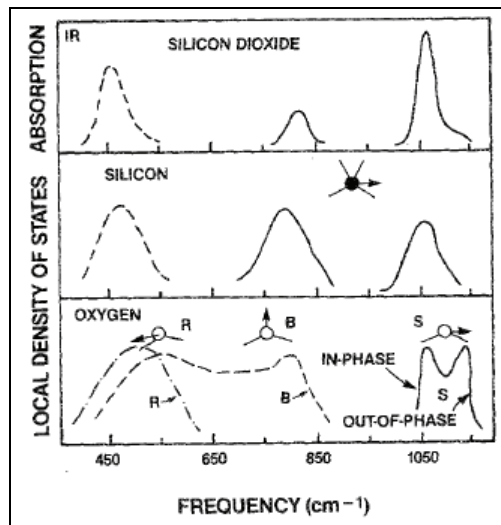


Fig. 4. Local density of vibrational states (LDOVS) for oxygen and silicon and, calculated IR response for silicon dioxide. Reprinted with permission from Pai et al., 1986; copyright 1986, American Vacuum Society.

According to the model proposed by Pai and his colleagues (Pai et al., 1986), this peak is an interesting example of coupled oscillations: the motion of the oxygen atom and that of the neighboring silicon atoms. The low frequency part of the spectrum peak is "imposed" by the silicon atoms' vibration (the motion of the oxygen atom is in phase). The high frequency edge of the same peak is dominated by oxygen; there is a little associated silicon motion, which is out of phase motion compared with the movement of the oxygen atoms. A broad shoulder centered at about  $1150\text{cm}^{-1}$  generally gives this part of the peak.

The IR vibrations of a Si-O-Si entity belonging to the  $\text{SiO}_x$  structure are briefly presented as following:

- a bond-stretching vibration,  $\nu_s$ , in which the O displacement is in a direction parallel to the line joining its neighboring silicon (in a-Si matrix, the peak absorption is placed at  $940\text{cm}^{-1}$  and in thermally growth a-SiO<sub>2</sub> is at  $1073\text{cm}^{-1}$ );
- bond-bending vibration,  $\nu_B$ , in which the O atom motion is along the bisector direction of the Si-O-Si bond angle ( $\nu_B=780\text{cm}^{-1}$ );
- out of plane rocking motion,  $\nu_R$ , with  $\nu_R=450\text{cm}^{-1}$ .

The majority of the published papers reveal the particularities of the stretching vibration peak. The oxygen atom is bonded to two adjacent silicon atoms by Si-O bonds. Considering the diatomic model described in the previous section, the movement of the oxygen atom is the result of the coupling of the two Si-O vibrations. The strength of the bond and the vibration frequency are dependent not only on the Si and O atoms partners in the bond, but also on the other neighbors of the silicon atom. Schematically, the Si-O-Si bridge is shown in figure 5.

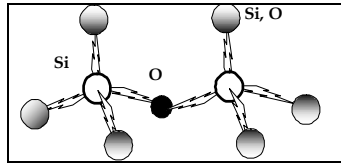


Fig. 5. A sketch of the Si-O-Si structural bridge with the other 6 atoms neighboring the two silicon atoms, which can be either oxygen atoms or silicon.

A measured IR spectrum of a  $\text{SiO}_x$  thin film deposited by reactive rf sputtering is shown in figure 6. The thickness of the layer was determined as being  $d=620\text{nm}$  and the composition corresponds to  $x=0.73$ . The rocking, bending and stretching modes of Si-O-Si are identified.

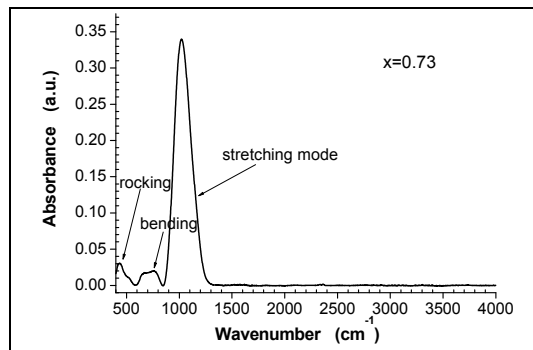


Fig. 6. The IR spectrum of  $\text{SiO}_x$  layer with  $x=0.73$ .

The peak position and the shape of the absorption peak assigned to the stretching vibration mode depend on the composition. This is well revealed in figure 7 where the normalized spectra are shown for  $\text{SiO}_x$  samples with  $x$  between 0.1 and 2. Increasing the oxygen content, the main peak position shifts towards larger wavenumber values, while its width becomes smaller. For larger  $x$  values, ( $x>1.2$ ), a shoulder appears on the  $1150\text{cm}^{-1}$ , which becomes more and more pronounced when the oxygen content increases. For  $x=2$  this shoulder is a characteristic feature for the  $\text{SiO}_2$  structural entities.

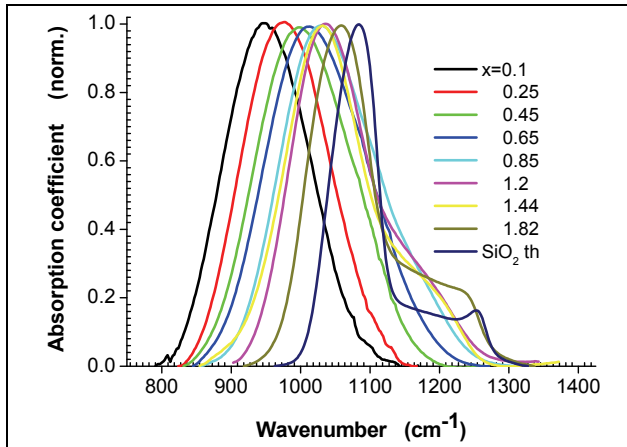


Fig. 7. The position and the shape of the absorption peak assigned to the stretching vibration mode of the Si–O–Si bridge are dependent on the oxygen content.

The shift in the peak position could be used to scale the oxygen content. This is applied when the samples have been deposited with the same technique, with well defined deposition conditions. A calibration curve between the oxygen content previously determined via other techniques (Rutherford back-scattering, or x-ray photoelectron spectroscopy, etc) and the IR peak position is needed. It must be mentioned that, although this method to determine the layer composition is used in many labs, the peak position is dramatically influenced by the deposition conditions (Tomozeiu, 2006). There is another model to determine the oxygen concentration from IR absorption measurements using the integrated absorption of the stretching mode peak. Also here, it is necessary to calibrate the method. This means that for some samples, the  $x$  parameter must be determined via other methods. The IR spectroscopy is set as a secondary standard in measuring the oxygen content.

The method was proposed by Zacharias and his colleagues to determine the concentrations of hydrogen and oxygen in a-Si:O:H thin films (Zacharias et al., 1994). It is based on the area of the IR absorption peak related to that atomic species and the connection with the concentration is:

$$c(i) = A(i) \int_{\tilde{\nu}_{\text{peak}(i)}} \frac{\alpha(\tilde{\nu})}{\tilde{\nu}} d\tilde{\nu} \quad (13)$$

where  $c(i)$  is the concentration of element  $i$  (H or O),  $\alpha(\nu)$  is the absorption coefficient in the peak region centered on  $\tilde{\nu}_{\text{peak}}$  and  $A(i)$  is the calibration factor. Writing this formula for SiO<sub>x</sub>, the oxygen concentration is:  $c(\text{O})=A(\text{O}) \cdot I(1080-960)$ , where  $I(1080-960)$  is the integrated absorption between  $\tilde{\nu} = 960 \text{ cm}^{-1}$  and  $\tilde{\nu} = 1080 \text{ cm}^{-1}$ .

For the spectra presented in figure 7 the calculated values of the integrated IR absorption are shown in figure 8. A good linearity between the integrated absorption and the  $x$  values is found for  $x < 1.3$ . For samples with oxygen content higher than the value corresponding to this point, there is a rapid increase of the integrated IR absorption. In other words, at  $x=1.3$  there is a kink point (Tomozeiu et al., 2003) in the plot shown in figure 8. This was evaluated as a signal that the SiO<sub>x</sub> structure changes from a random distribution of the Si–O bonds in

the material bulk (RBM model) to a random mixing model (RMM) which describes the material in terms of domains of fully oxidized silicon ( $\text{SiO}_2$ ) and low-oxygen silicon. Similar results have been reported by F. Stolz and his colleagues (Stolz et al., 1993) on  $\text{SiO}_x$  samples prepared under other conditions than those investigated in the figure 7. For the data presented in figure 8, the relation (13), in terms of  $x$  parameter, becomes:

$$x = 5.49 \cdot 10^{-4} \cdot I(1080 - 960), \quad \text{with } x < 1.3 \quad (13')$$

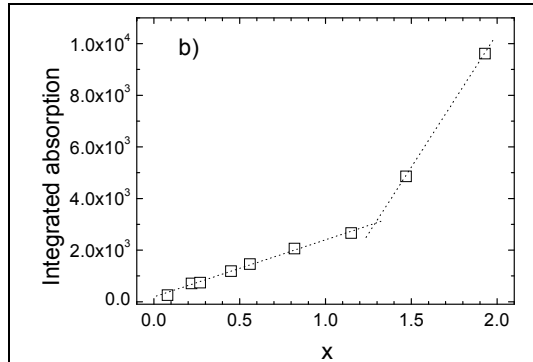


Fig. 8. The integrated IR absorption of the stretching mode near  $1000 \text{ cm}^{-1}$  versus the  $\text{SiO}_x$  oxygen content. A kink point is outstanding near  $x=1.3$

### 3.4 The material structure reflected in the IR absorption spectrum

Is the first part of the plot from figure 8 describing the  $\text{SiO}_x$  structure based on a random bonding model (RBM)?

The answer is based on a simpler theoretical model proposed by A Morimoto and his colleagues (Morimoto et al., 1987). They assumed a random distribution of the  $\text{Si-O-Si}$  bonds and they calculated the probability that " $n$ " oxygen atoms will neighbor a  $\text{Si-O-Si}$  bridge.

The probability to have " $n$ " O-atoms and " $6-n$ " Si-atoms around the  $\text{Si-O-Si}$  bridge (see the figure 6) is:

$$P_n(x) = C_6^n P(\text{Si})^{6-n} P(\text{O})^n \quad n = 0 \div 6 \quad (14)$$

where  $C_6^n$  gives the number of arrangements in which  $n$  sites are chosen from the total of 6 sites,  $P(\text{Si})$  and  $P(\text{O})$  being the presence probability of Si and O, respectively.

Considering the number of  $\text{Si-Si}$  bonds and the number of  $\text{Si-O}$  bindings as a function of the oxygen content, (see section 2.2) the  $P(\text{Si})$  and  $P(\text{O})$  probabilities are easy to calculate:

$$P(\text{Si}) = \frac{n(\text{Si-Si})}{n(\text{Si-Si}, \text{Si-O-Si})} = 1 - \frac{x}{2} \quad (15a)$$

and respectively:

$$P(\text{O}) = \frac{n(\text{Si-O-Si})}{n(\text{Si-Si}, \text{Si-O-Si})} = \frac{x}{2}. \quad (15b)$$

In this way, the probability to have the richest in silicon SiO<sub>x</sub> is given by Rel. (14) with n=0:

$P_0(x) = \left(1 - \frac{x}{2}\right)^6$  and the probability to have the richest in oxygen SiO<sub>x</sub> is obtained for n=6:

$P_6(x) = \left(\frac{x}{2}\right)^6$ . The probability to have Si-O-Si entities with “n” oxygen atoms around the

two silicon atoms, is naturally depending on the x value. For a SiO<sub>x</sub> structured as the RBM predicts, the P<sub>n</sub>(x) is shown in figure 9.

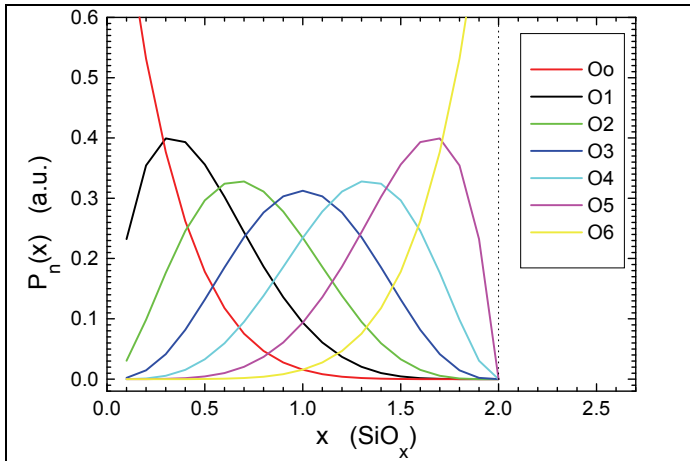


Fig. 9. The calculated probabilities to have n O-atoms bonded by Si-O-Si.

With this plot, a rough estimation of the number of the oxygen atoms and how they are bounded can be made for materials with known  $x$  parameter values. Such kind of maps are shown in figure 10 for different  $x$  values of SiO<sub>x</sub> samples deposited via reactive sputtering. We mention that this is a theoretical estimation within the RBM approximation.

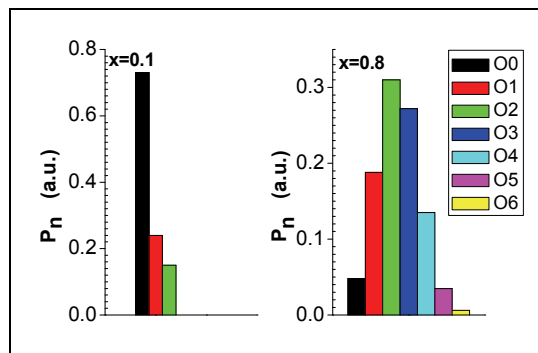


Fig. 10. The maps of the oxygen bounding probability on Si-O-Si structural bridge.

*How much this model represents reality?* This is a very important question for the applications of the SiO<sub>x</sub> material and the answer will be found in the section 7.

## 4. Electronic density of states (DOS) in SiO<sub>x</sub>

### 4.1 Introductory notions about DOS of amorphous semiconductors

In crystalline semiconductors the periodic variations of the lattice potential give rise to parabolic edges in  $\vec{k}$ -space for the electronic energy bands (Ashcroft and Mermin, 1988). The conduction band is separated, in energy scale, from the valence band by the so-called "band - gap". In amorphous semiconductors there is no periodicity of the lattice. Both, the bond length and the angle between two adjacent bonds vary with small amounts around what the crystalline counterparts reveal. Considering the example of amorphous silicon, the nearest neighbors (the first coordination sphere) are the same as for the crystalline silicon, but a difference appears when we speak of near neighboring (e.g. the second coordination sphere) where deviations of about  $\pm 5^\circ$  versus the crystallization direction appear. This gives rise to the existence of tails attached to valence- and conduction- band that penetrate into the band-gap. They are formed from localized states assigned to the carrier (electron). Generally, it is assumed that the density of states in the tail decreases exponentially into the gap.

Very often it happens that one bond is missing and the atom is sub-coordinated. Defects represented in amorphous semiconductors by "coordination defects", such as *dangling bonds*, (DB), give rise to electronic states around midgap. Dangling bonds show an amphoteric behavior, which means that a dangling bond can have three different charge states: *positively charged* when unoccupied, *neutral* when singly occupied by electron and *negatively charged* when doubly occupied. Such a defect is represented by two electronic states. There are several approaches to model the distribution of defect states within the gap of amorphous material. A standard model for the defect-state distribution assumes two symmetrical Gaussian distributions separated by the so-called correlation energy (Street, 1991) (see figure 11).

Normally, such a defect has one unbounded electron and electrically the defect is neutral, D<sup>0</sup>. But according to the Pauli's rule, on the same energy level, another electron can be accommodated (with unparallel spin) and the defect will become negatively charged, D<sup>-</sup>. The energy level of D<sup>-</sup>, in comparison with D<sup>0</sup> will be raised due to electron-electron interaction. The existence of D<sup>-</sup> defects implies the existence of positively charged defects, D<sup>+</sup>, - dangling bonds where the electron is missing. The energy states assigned to DB are localized and they form narrow bands near the mid-gap. The Fermi level is pinned between them. Due to their electronic states placed deep into the band-gap, around Fermi level, the defects control the optical and electrical properties of the amorphous material.

It is unanimously agreed that the energy bands (valence- and conduction-band) are formed in amorphous semiconductors from extended states (their contribution to the transport phenomena is similar to the homologous states in crystalline materials) and localized states that form the tail. The delimitation between these two types of states is made by the *mobility edge* levels; this name derives from the fact that the electron mobility is higher when extended states are involved than the mobility of localized electrons (4 to 6 order of magnitude). It is important to mention that the mobility edges in disordered materials play the same role as the energy band edges in crystalline counterparts.

Structural disorder (deviations in bond length and bond angle) is represented in the density of states distribution by localized states in the bands' tails. Figure 11 shows the



representation for density of electron states,  $N(E)$ , as a function of energy,  $E$ , according to the Mott and Davis model (Mott and Davis, 1979). The mobility edges of both the conduction- and valence-band are depicted by  $E_C$  and  $E_V$  respectively. The tails of these bands are considered as exponentially decaying into the band gap. In the case of bi- or multi-component amorphous alloy local variations in stoichiometry (composition) may appear. This means that the mobility edges will have a "sophisticated" spatial distribution.

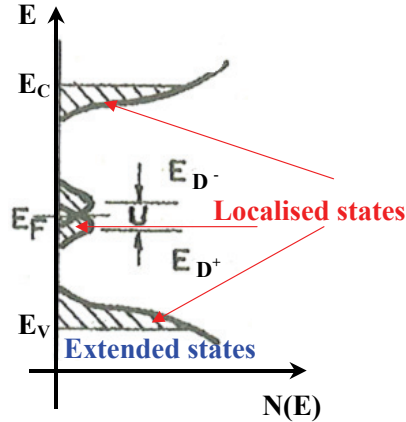


Fig. 11. Mott-Davis model for density of states (DOS) in disordered materials.

The DB density in amorphous materials depends on the quality of the material and on the technology used for layer preparation. Typical values for sputtered a-Si are  $10^{19}$  spin/cm<sup>3</sup> while in  $\text{SiO}_x$  could reach  $10^{22}$  spin/cm<sup>3</sup>. Thermal treatment (annealing) will help relax the lattice and therefore variations in DB's have been observed. Adding hydrogen during layer deposition, the DB's density will drastically decrease. The Si-H bonding energy lies deep in the valence band (VB). Therefore, defects from mid-gap are removed through hydrogenation.

#### 4.2 Particularities of $\text{SiO}_x$ density of states

In the last decades, silicon suboxides have been theoretically (ab initio theories) and experimentally investigated to better understand their electronic density of states (DOS). It is well known that this parameter defines both the optical and the electrical properties of the material. According to the random bonding model of the  $\text{SiO}_x$  structure, clusters of  $\text{Si}_n\text{O}_m$  have been theoretically investigated at the quantum-mechanic level (Zhang et al., 2001a) and it was found that:

- energetically the most favorable small silicon-oxide clusters have O atomic ratios at around 0.6;
- remarkably high reactivity at the Si atoms exists in silicon suboxide  $\text{Si}_n\text{O}_m$  clusters with  $2n > m$ .

The total density of states (TDOS) was theoretically calculated (Zhang et al., 2001b) and projected onto the constituent atoms to deduce the contribution of the individual atoms to the total electronic structures. Such a treatment was used to find the atoms in which the

highest occupied molecular orbital - HOMO (to be assigned to the valence band edge from crystalline semiconductors) and the lowest unoccupied molecular orbital - LUMO (similar to the conduction band edge) reside. The difference LUMO-HOMO is an indication of the material band-gap. The closest molecular orbital to the gap contains a significant contribution from the Si and O atoms, as  $\text{HOMO}_{\text{Si}}$ ,  $\text{HOMO}_{\text{O}}$ ,  $\text{LUMO}_{\text{Si}}$ , and  $\text{LUMO}_{\text{O}}$ , respectively. In figure 12 are shown the results of the calculations as a function of the relative oxygen content into the layer. Zhang and his colleagues (Zhang et al., 2001a) have used fourth-order polynomials fit, and in figure 12 are shown  $\text{LUMO}_{\text{Si}}$  (upper) and  $\text{HOMO}_{\text{Si}}$  (lower) with solid curves, while dashed curves represent  $\text{LUMO}_{\text{O}}$  (upper) and  $\text{HOMO}_{\text{O}}$  (lower). Therefore, considering a defect-free  $\text{SiO}_x$  material, its band gap is determined by the orbital of the atomic silicon for silicon-rich material and by the orbital of atomic oxygen for silicon-poor materials. Increasing the oxygen content, the LUMO position remains at about the same energy position, while the HOMO decreases.

Taking into account the localized states induced by dangling bonds in the region of mobility band gap, the energy distribution of the density of states, can be penciled (Singh et al., 1992; van Hapert, 2002) as in figure 13. This model is inspired by the data published till 2002 and it is successfully utilized to understand the physical properties of  $\text{SiO}_x$  thin films. As main conclusions we point out:

- the conduction band is formed by Si-Si and/or Si/O antibonding states;
- the valence band is formed by Si-Si bonding states for  $\text{SiO}_x$  with  $x < 1.3$  and by Si-O bonding states for  $\text{SiO}_x$  with  $x > 1.3$ ;
- the silicon dangling bonds (DB) states form a band of localized electronic states at 0.7 eV below the conduction band edge.

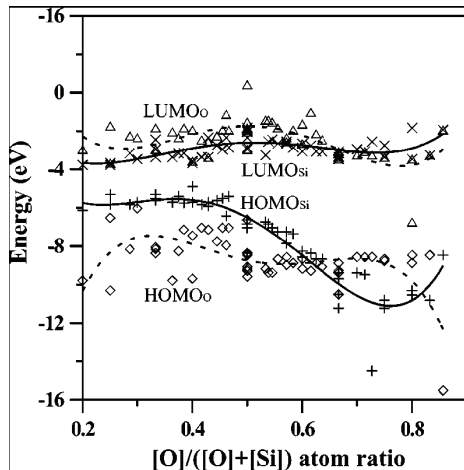


Fig. 12. Computed  $\text{LUMO}_{\text{Si}}$  ( $\times$ ),  $\text{LUMO}_{\text{O}}$  ( $\Delta$ ),  $\text{HOMO}_{\text{Si}}$  (+) and  $\text{HOMO}_{\text{O}}$  ( $\diamond$ ) of  $\text{Si}_n\text{O}_m$  clusters. Reprinted figure with permission from Zhang et al., 2001a<sup>2</sup>. Copyright (2001) by American Physical Society. <http://link.aps.org/abstract/PRB/v64/p113304>.

<sup>2</sup> Zhang, R. Q.; Chu, T. S.; Cheung, H. F.; Wang, N. & Lee, S. T. Phys. Rev. B64, pp. 113304 - 113308 (2001)

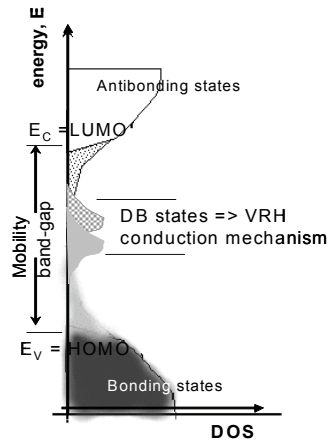


Fig. 13. Model for  $\text{SiO}_x$  density of states distribution.

### 4.3 The nature of the paramagnetic defects in $\text{SiO}_x$

In the section 4.1 it was shown that the structural defects defined by dangling bonds can be electrically neutral and positively or negatively charged. Defects' type and their density influence also the film structure. The *electron paramagnetic resonance* (EPR<sup>3</sup>) measurements will reveal the paramagnetic defects. These are the so-called neutral defects. Although later only this type of defects will be discussed, the presence of the positively and negatively charged defects has to be noted. These are defects with none electron or with two electrons placed on the energy level. Because of lack of the investigation methods for these defects' types, we will focus on EPR data. This technique measures the splitting of energy levels of unpaired electrons when placed in a magnetic field. The unpaired electrons essentially behave as small magnets whose orientation can be flipped by a microwave signal. The frequency at which the orientation can be flipped is determined by the strength of the applied magnetic field. This interaction between the unpaired electron and the microwave field assigned is maximized in condition of resonant oscillations of the electron. In other words, the electron absorbs energy from the microwave oscillations. The derivative absorption of microwave power is measured as a function of the magnitude of an external magnetic field. In figure 14 are shown EPR spectra of two  $\text{SiO}_x$  layers: one silicon rich, with  $x=0.45$  and the other one oxygen rich sample, with  $x=1.47$ .

From such measurements, the important information that can be obtained is the number of paramagnetic defects and the type of these defects. The first parameter needs a standard MnO oxide sample with known number of spins. The second parameter is found by evaluating the Landé's factor (the so called g factor). For the data hereunder presented the calibration MnO sample had  $3 \pm 1 \cdot 10^{15}$  spins. Comparatively to it, the paramagnetic defects' density in  $\text{SiO}_x$  layers was calculated. One has to mention that all  $\text{SiO}_x$  samples have been deposited via sputtering. The number of the EPR active defects found in  $\text{SiO}_x$  thin films as a function of layer composition (the x parameter) is shown in figure 15. As it can be seen, the

<sup>3</sup> The ERP measurements have been made and the results analyzed together with Dr. Ernst van Faassen at Utrecht University, The Netherlands. The fruitful discussions with him are acknowledged.

spin density is about  $10^{20}$   $\text{cm}^{-3}$  and increases with  $x$  values. For  $\text{SiO}_x$  samples with  $x$  very close to  $x=2$ , the spin density decreases.

The random distribution of the defects with various neighboring sides produces inhomogeneous line broadening. In figure 14 the differences in the plots' shape are really large when we compare the silicon rich  $\text{SiO}_x$  with the oxygen-rich one. This is related to the structural type of the paramagnetic defect. The  $g$  value will help in identification the defect type, and its values have been calculated and plotted against  $x$ , as figure 16 shows.

Generally, the Landée factor lies between 2.0057 - value assigned to dangling bond amorphous silicon defects (DB a-Si) and 2.001 - the value that reveals the so-called  $E'$  centers from  $\text{SiO}_2$ . Increasing the oxygen content in sample, the  $g$  values slightly decrease down to 2.004 when  $x$  varies between 0.2 and 1.2. For alloys with a larger concentration of oxygen,  $x > 1.2$ , the values of the  $g$  factor steeply diminish.

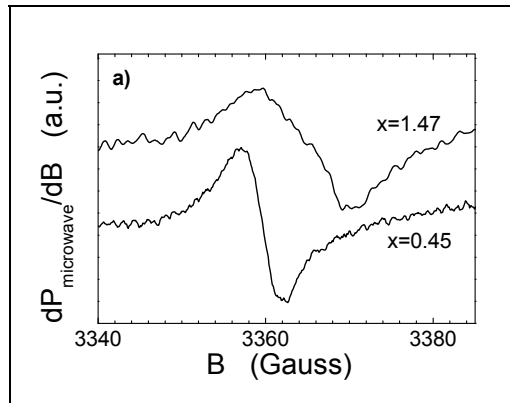


Fig. 14. Example of derivative absorption of microwave power in EPR measurements.

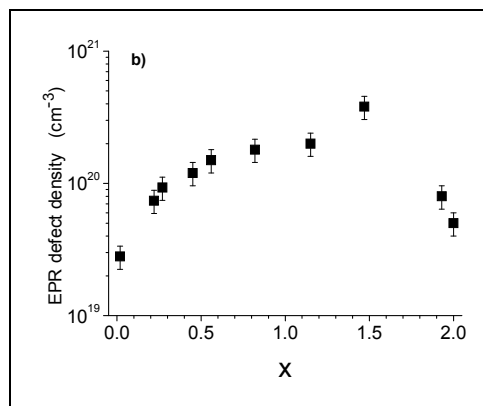


Fig. 15. The density of paramagnetic defects as a function of oxygen content in  $\text{SiO}_x$ .

In order to identify the defects types, experiments which reveal the defect saturation were carried out. The microwave magnetic field at the resonator of the EPR setup is proportional to the square root of the applied microwave power. Measuring the interaction of the spins

with the magnetic field by area of the resonant signal, a non-saturated signal is linear with  $\sqrt{P}$ , with  $P$  the microwave power. Studying the sample with  $x=1.47$ , at room temperature, the variation of the microwave power has emphasized two types of defects: one saturates very rapidly and the second one is practically non-saturated (see figure 17). The first type is characterized by  $g=2.0013$  and it is identified as  $E'$  like defect, while the second has  $g=2.0047$  and it is assigned to DB a-Si. Therefore, the a-Si dangling bonds paramagnetic defects do not saturate when the microwave power is varied up-to 30 mW, in this experiment.

No defects' saturation effect was observed for the sample with  $x=0.45$ , when the same experiment has been done. This indicates a single type of defects. According to the  $g$ -value, it is DB a-Si paramagnetic defect.

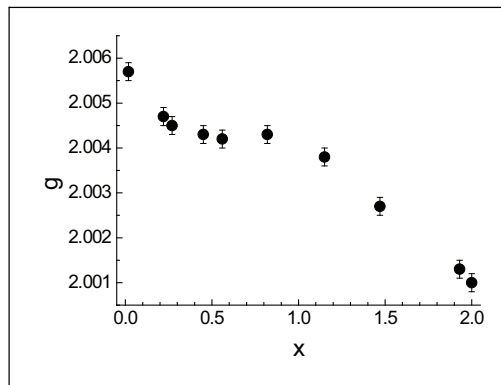


Fig. 16. The calculated values of the Landé factor is function of the oxygen content in  $\text{SiO}_x$ . In other words, the type of the paramagnetic defects is determined by the oxygen amount.

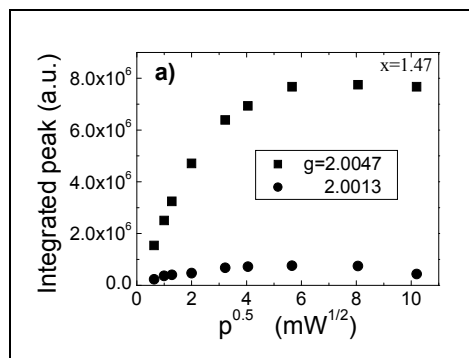


Fig. 17. The results of the saturation experiments for sample  $\text{SiO}_{1.47}$ . The absorption peak versus the square root of the microwave power reveals two types of paramagnetic defects in this material.

The difference between the two studied samples from this point of view is visible with the naked eyes in figure 14. The EPR registered plot for sample  $\text{SiO}_{0.45}$  is sharper than that of  $\text{SiO}_{1.47}$ .

## 5. Optical properties of SiO<sub>x</sub> thin films

### 5.1 Refractive and absorption index; optical band-gap

When an electromagnetic radiation interacts with a semiconductor, the optical properties of the material are revealed. If the radiation is in the UV-VIS range (the wavelength is 400 - 900 nm), the optical properties utilized to describe semiconductors are the refractive index,  $n$ , the absorption index,  $k$ , and the band-gap,  $E_g$ . We note that these physical amounts are dependent between them, according to various theories and models proposed to explain them. For example, the refractive index and the absorption index are connected between them via the Kramer-Krönig relation (Hutchings et al., 1992). Moreover, the modern theories in physics define the complex refractive index by its real part,  $n$ , and imaginary part,  $k$ , as:

$$n^*(\omega) = n(\omega) - ik(\omega) \quad (16)$$

where  $\omega = 2\pi\nu$  measures the electromagnetic field frequency,  $\nu$ , and "i" is the unit imaginary number ( $i^2 = -1$ ).

The optical band gap, which is the separation in energy between the minimum of the conduction band and the maximum of the valence band (in other words the difference between the LUMO and the HOMO levels - see the section 4.2), can be calculated following different optical models, either from the dispersion of the refractive index  $n(\omega)$ , or from the spectral dependence of the absorption coefficient. In all these models, the response of the investigated material (SiO<sub>x</sub> in our case) to the interaction with an electromagnetic wave (light) is described.

In order to reveal the optical band gap of the SiO<sub>x</sub>, mechanisms of photon absorption are invoked. The quantum mechanic treatment of this absorption is based on, and it explains, the electronic transitions induced by the electromagnetic field in semiconductor. The main issue is the interaction between the electron belonging to the SiO<sub>x</sub> electronic density of states and the incident photon. This interaction might have as result the transition of the electron from its initial state  $|i\rangle$  to a final state  $|f\rangle$ , transition that happens with the probability,  $w_{if}$ , given by the golden rule of the quantum mechanics:

$$w_{if} = \frac{2\pi}{\hbar} |\langle i|H'|f\rangle|^2 \delta(E_f - E_i - \hbar\omega) \quad (17)$$

In the Rel. (17),  $H'$  is the hamiltonian that describes the interaction between the electron and the electrical field assigned to the electromagnetic wave (visible light). Without getting into details (for more see Madan and Shaw, 1988) in the so-called dipole approximation, this interaction is described by:

$$H'(r,t) = q\vec{E}_0\vec{r} \cdot \exp(-i\omega t) + q\vec{E}_0\vec{r} \cdot \exp(i\omega t) \quad (18)$$

where  $q$  is the electronic charge,  $\vec{E} = \vec{E}_0 \exp(-i\omega t) + \vec{E}_0 \exp(i\omega t)$  is the electrical field assigned to the electromagnetic wave and  $\vec{r}$  is the electron displacement due to the electrical field.

With the probability of transition given by Rel. (17) and considering that for one transition the electronic system of the material absorbs energy that amounts  $\hbar\omega$  - the photon energy - the absorption coefficient,  $\alpha$ , can be calculated. By definition,  $\alpha$  is the energy absorbed per volume unity divided to the incident flux of energy:

$$\alpha(\omega) = \frac{\sum_{i,f} w_{if}(\omega) \cdot \hbar\omega}{(c/n)\bar{W}} \quad (19)$$

where  $\bar{W} = n^2 \bar{\mathcal{E}}_0^2$  is the averaged density of electromagnetic energy.

Introducing (17) in (19), after some calculations, following the model proposed by Tauc, Grigorovici and Vanco (Tauc et al., 1966), the absorption coefficient can be written as:

$$\alpha(\omega) \cdot (\hbar\omega)^\xi \approx \int_0^{\hbar\omega} g_i(-E) \cdot g_f(\hbar\omega - E) \cdot dE \quad (20)$$

with  $g_i(E)$  and  $g_f(E)$  as the density of electronic states for the initial and final state. The power parameter  $\xi$  can be  $\xi=1$  when in Rel. (19) are used the momentum matrix elements, or it can be  $\xi=-1$  when elements of the dipole matrix are used. The formula (20) is important because it helps to determine the dispersion law for the absorption coefficient. Moreover, it makes the connection between this optical parameter and the distribution of density of electronic states (see section 4). For example, when  $\xi=1$  in the Rel. (20) and the shape of the density of states is considered parabolic, the Rel. (20) will result in the so-called Tauc formula (Tauc et al., 1966):

$$\alpha(\omega) \cdot \hbar\omega = B \cdot (\hbar\omega - E_{gT})^2 \quad (21)$$

where  $E_{gT}$  is the "Tauc band-gap" and B is a coefficient.

On the other hand, solving in the same conditions the Rel. (20), but considering  $\xi=-1$ , the result will be the Cody formula (Cody et al., 1981), which will generate the so-called "Cody band-gap",  $E_{gC}$ :

$$\frac{\alpha(\omega)}{\hbar\omega} = C \cdot (\hbar\omega - E_{gC})^2 \quad (22)$$

with C the Cody coefficient.

From relations (21) and (22) the band gap of the semiconductor can be easily determined. However, for amorphous semiconductors there are many definitions for the optical band gap. Besides  $E_{gT}$  and  $E_{gC}$  a much utilized definition is the photon energy that corresponds to the absorption coefficient equal to  $10^4 \text{ cm}^{-1}$ ,  $E_{04}$ . In the next section, we will present the so-called OJL model specially designed for amorphous materials with density of states similar to that showed in the figure 11. Up to now, it is clear that in determining the value of the optical band-gap, the dispersion of the absorption coefficient is vital.

The absorption index, k, is related to the absorption coefficient as:

$$k(\omega) = \frac{c}{2 \cdot \omega} \cdot \alpha(\omega) \quad (23a)$$

while the refractive index is correlated to the absorption coefficient via the Kramer-Krönig (Hutchings et al., 1992) relation:

$$n(\omega) - 1 = \frac{c}{\pi} \wp \int_0^{\infty} \frac{\alpha(\omega')}{\omega'^2 - \omega^2} d\omega' \quad (23b)$$

where  $\wp$  denotes the Cauchy principal value.

## 5.2 The optical properties of the SiO<sub>x</sub> thin films

A method to investigate the optical properties is based on the experimental measurement of the spectral transmittance and reflectance of the material. Schematically, the experiment of measuring the transmittance and the reflectance of a SiO<sub>x</sub> thin film is shown in the figure 18. An optical radiation with intensity  $\mathfrak{S}_0(\lambda)$  is sent on the surface of the sample. By using two spectrometers, the intensities of the reflected light,  $\mathfrak{S}_R(\lambda)$  and that of the transmitted light,  $\mathfrak{S}_T(\lambda)$  are measured. In this way, the reflectance  $\mathfrak{R}(\lambda) = \mathfrak{S}_R(\lambda)/\mathfrak{S}_0(\lambda)$  and the transmittance  $T(\lambda) = \mathfrak{S}_T(\lambda)/\mathfrak{S}_0(\lambda)$  are measured as a function of the utilized wavelength light. As a result of the interaction with the electronic system of the SiO<sub>x</sub> material, part of the radiation can be absorbed by electronic excitations (intraband and/or interbands). In this way, the third physical quantity, called absorbance,  $A(\lambda)$ , is defined<sup>4</sup>:

$$A(\lambda) = 1 - T(\lambda) - R(\lambda) \quad (24)$$

These three physical parameters are defined in terms of radiation energy.

Measuring the reflectance and the transmittance on different SiO<sub>x</sub> samples and using the method of computer simulation proposed by Wolfgang Theiss in his Scout cod program (Theiss, 2005), the refractive and the absorption index, together with the layer thickness can be determined. In figure 19 the spectral distributions of the transmittance and reflectance measurements on SiO<sub>x</sub> layers are shown. We mention that the thickness of the samples is around 600 nm and the changes in the shape of the spectra are due to the optical properties of the material.

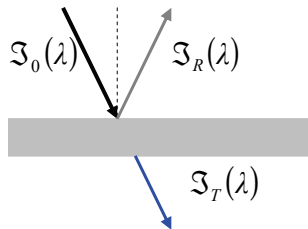


Fig. 18. When an optical radiation interacts with a solid thin film, part of it is reflected, part of it is emergent through the thin film and the rest is absorbed into the material.

The model utilized in this section to simulate the measured spectra is the so-called OJL model (O'Leary et al., 1997). The edges of the valence band and conduction band are

<sup>4</sup> It has to be noted that in chemistry, generally, the reflection is neglected and the absorbance is defined as:  $A(\lambda) = 1 - \mathfrak{S}_T(\lambda)/\mathfrak{S}_0(\lambda)$



considered to be parabolic in the  $\bar{k}$  space, but modulated with exponential decays. The first part (parabolic behavior) is specific to the Tauc or Cody models and they describe the extended states in both, the valence - and the conduction band. The second part (the exponential decay) represents the tails of the valence - and conduction - band formed from localized states due to the structural and compositional disorder (see figure 11 in section 4). Based on this figure, without considering the localized bands developed towards the middle of the band-gap, the definitions for the optical band gap and the DOS distribution is shown in the figure 20. Generally, the exponential tail of the valence band into the band-gap could be different than that of the conduction band ( $\gamma_{\text{VB}} \neq \gamma_{\text{CB}}$ ). In many simulations, for simplicity and in order to have a small number of the fit parameters, they are considered equal,  $\gamma_{\text{VB}} = \gamma_{\text{CB}} = \gamma$ . The bigger this parameter is, the larger is the material disorder.

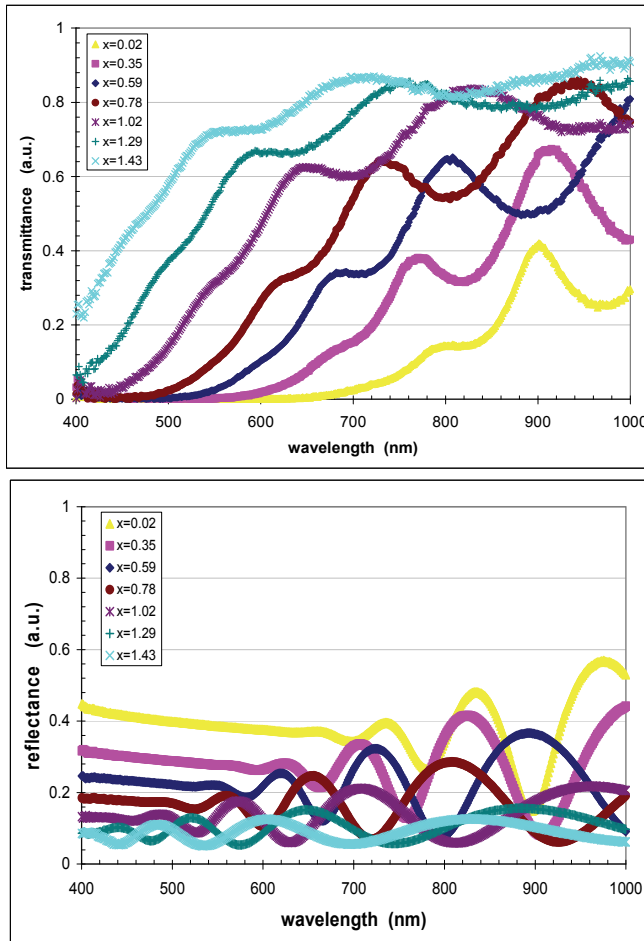


Fig. 19. The transmittance (up) and the reflectance (down) spectra of different  $\text{SiO}_x$  compositions, versus the light wavelength.

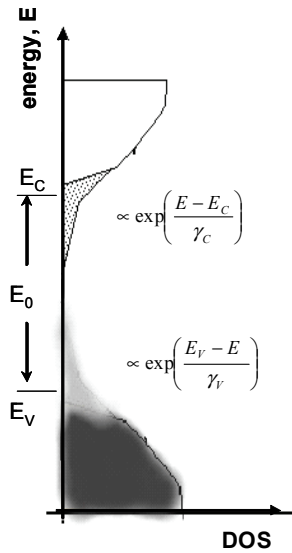


Fig. 20. The density of states for the valence band and for the conduction band in the OJL model (see the Rel. (25)). The optical band-gap,  $E_0$  means something more than the mobility gap. The difference is made by the exponential decays of the bands' tails formed from localized electronic states.

When comparing with the density of states given in figure 13, one can see that the localized states due to the defects (placed in the center of the band gap) are missing. This is an approximation needed for an easy simulation. The DOS function describing a band structure with localized states exponentially distributed from the band edge towards the middle of the band-gap is, according to O'Leary et al., 1997:

$$g_C(E) = \frac{\sqrt{2} \cdot m_e^{3/2}}{\pi^2 \hbar^3} \cdot \begin{cases} \sqrt{E-E_C} & E \geq E_C + \frac{\gamma}{2} \\ \sqrt{\frac{\gamma}{2}} \cdot \exp\left(-\frac{1}{2}\right) \cdot \exp\left(\frac{E-E_C}{\gamma}\right) & E < E_C + \frac{\gamma}{2} \end{cases}$$

$$g_V(E) = \frac{\sqrt{2} \cdot m_h^{3/2}}{\pi^2 \hbar^3} \cdot \begin{cases} \sqrt{E_V-E} & E < E_V - \frac{\gamma}{2} \\ \sqrt{\frac{\gamma}{2}} \cdot \exp\left(-\frac{1}{2}\right) \cdot \exp\left(\frac{E_V-E}{\gamma}\right) & E \geq E_V - \frac{\gamma}{2} \end{cases} \quad (25)$$

where  $m_e$ ,  $m_h$  is the effective mass of a charge carrier and  $E_C$ ,  $E_V$  are identical to the mobility edge. The mobility band-gap is  $E_0 = E_C - E_V + \gamma$ . In the OJL model, the refractive index, the damping constant  $\gamma$ , the mobility band-gap and the thickness of the layer are parameters of the model.

As an example, the simulations of the transmittance and reflectance spectra for  $\text{SiO}_x$  with  $x=1.43$  are shown in figure 21.

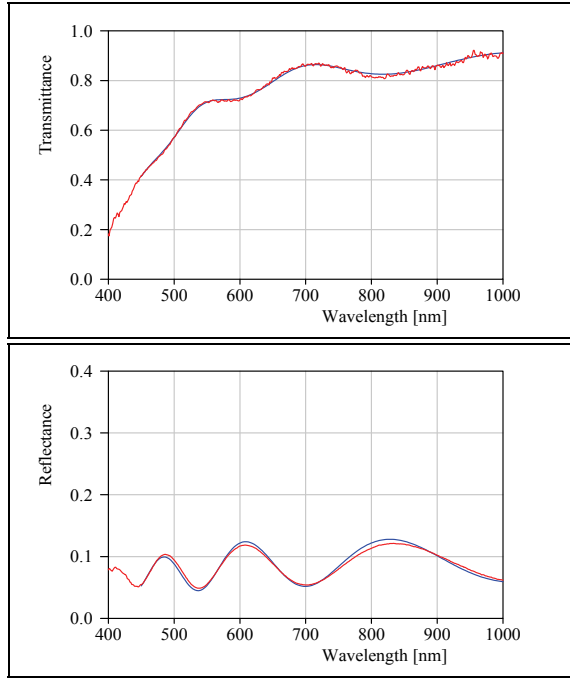


Fig. 21. The measured (in red color) and the simulated (in blue) transmittance and reflectance spectra for the  $\text{SiO}_{1.43}$ . The simulation was made with the Scout program using the OJL model.

The values of the fit parameters are:  $\gamma=0.47$  eV, band-gap = 2.98 eV and thickness=620.1 nm.

In a similar way the spectra of all  $\text{SiO}_x$  samples have been simulated. A curve of the refractive index versus the oxygen content can be plotted (see the figure 22).

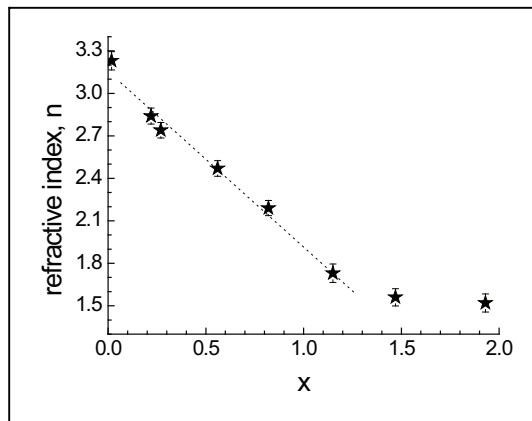


Fig. 22. The refractive index versus the oxygen content in  $\text{SiO}_x$  samples.

Increasing the oxygen content, the refractive index decreases. For  $x=1.3$  there is a kink point, the same as the one found for the IR peak position (figure 8, section 3.3). In our opinion this is due to structural transformations that occur for highly oxygenated  $\text{SiO}_x$  layers. More on this issue, in section 7.

*What about the optical band-gap determined within the OJL model? And with the Tauc band gap?*

These questions are answered hereunder. Because the Tauc gap needs a special representation, this question will be treated first. The absorption coefficient was calculated from the transmittance data considering the layer thickness obtained via the OJL model. According to the theory of the model presented in the previous section, the intercept with the Ox axis of the linear region of  $\sqrt{\alpha \cdot \hbar\omega} = f(\hbar\omega)$  plot is the Tauc optical band-gap,  $E_{gT}$ . The modality to obtain it and, automatically the  $E_{gT}$  values are shown in the figure 23 for  $\text{SiO}_x$  samples.

Analyzing the optical-gap values plotted in figure 24, we can say that increasing the oxygen content, the band-gap increases. This is in good agreement with the trend observed for the refractive index:  $\text{SiO}_x$  with smaller refractive index is characterized by larger band-gap. This is a general feature of the semiconductor materials (Ravindra et al., 1979). Moreover, speaking of the similarities between the determined band-gap and the refractive index, a kink around  $x=1.3$  appears. This is like a breaking in the physical properties of the  $\text{SiO}_x$  material.

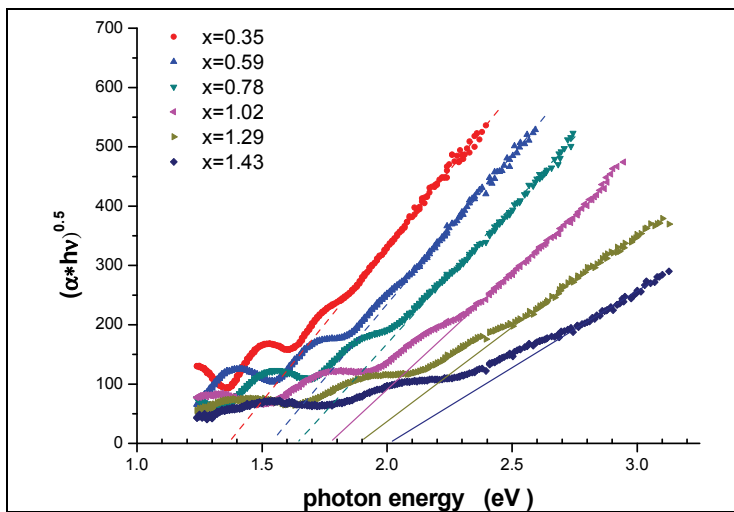


Fig. 23. The Tauc plots (see the Rel. (21)) and the corresponding Tauc band-gap values for various  $\text{SiO}_x$  layers' compositions.

The optical band-gap in the OJL model,  $E_0$ , and the exponential decay  $\gamma$  of the localized electronic states are obtained from simulation as fit parameters. In figure 24 these parameters are given as a function of the oxygen content.

When the variation of the  $\gamma$  parameter is considered, this increases with the oxygen content and the kink seems to be at  $x=0.6$ . This is not yet well understood up to now and we highlight the fact that the simulation is made considering the same decay of the localized electronic density of states for the valence band and for the conduction band, which is a strong approximation.

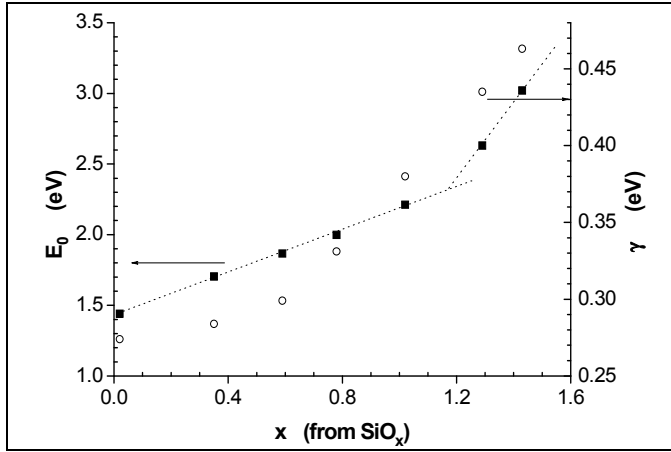


Fig. 24. The band gap,  $E_0$  and the  $\gamma$  parameter that describes the exponential decay of the localized states into the band-gap, as a function of the oxygen content.

## 6. Electrical properties via electronic transport

### 6.1 Electronic transport in sputtered SiO<sub>x</sub>

The energy and spatial distributions of the electronic density of states define the response of the material when an external electrical field is applied. The conductivity is, of course, the first electrical property that is immediately interesting for applications. A systematic research on the main conduction mechanism in SiO<sub>x</sub> electronic transport was made by van Hapert (van Hapert, 2002). He showed that, the variable range hopping (VRH) is the theoretical model that describes better the current - voltage characteristics measured on SiO<sub>x</sub> samples. A crucial role in understanding this mechanism is played by the localized electronic states that, spatially, are represented by the dangling bonds (DB) defects. As a function of the applied electrical field,  $\vec{E}$ , the electron can jump from one position to another. The hopping probability,  $w_{km}$ , between two DB sites, "k" and "m", is described by a contribution of a tunneling term and a phonon term:

$$w_{km} \sim \exp(-2\alpha|\vec{R}_k - \vec{R}_m| - |\varepsilon_k - \varepsilon_m|/k_B T) \quad (26)$$

where  $\vec{R}_i$  and  $\varepsilon_i$  with  $i=k,m$  represent the position vector of the site "i" and the electron energy on that site,  $\alpha$  is the localization parameter and  $k_B$  is Boltzmann's constant.

The hopping distance and the difference in energy between the initial state and the final state can be "chosen" such that the exponent from Rel. (26) is minimum: this is the so-called "R- $\varepsilon$  percolation" theory. If the current-voltage characteristic has an Ohmic behavior the result of this model is the well-known Mott "T<sup>-1/4</sup>" formula (Mott and Davis, 1979). But, for some disordered semiconductors, especially in the cases of the medium- and high-electrical field, the I-V curves become non-Ohmic. This situation has been studied within the VRH model (Brottger and Bryksin, 1985). They have defined the concept of the "directed percolation" and averaged the hopping probability as:

$$\tilde{w} \sim \exp\left(-2\alpha \cdot R + \frac{\varepsilon}{k_B T} + \frac{|e|\mathcal{E} \cdot R}{2k_B T} \cdot \cos\theta\right) \quad (27)$$

where  $\theta$  is the angle between the hopping direction  $\vec{R} = \vec{R}_k - \vec{R}_m$  and the electric field,  $\vec{\mathcal{E}}$ , and  $\varepsilon = \varepsilon_m - \varepsilon_k$  is defined in the absence of the electrical field. Working with these assumptions, Pollak and Riess have found, for medium - and high electrical field, the current density,  $j$ , expressed as (Pollak and Riess, 1976):

$$j \sim U \cdot \exp\left[-2\alpha \cdot R_c + \frac{3}{16} \cdot \frac{\mathcal{E} \cdot R_c}{k_B T}\right] \quad (28)$$

with  $R_c$  the critical percolation radius. Without getting too much into details, considering the electrical field  $\mathcal{E}$  as a function of the applied voltage, it is easy to see that, in Rel. (28) the current intensity has a complicated dependence on the applied voltage. We mention that this model was successfully utilized by van Hapert to describe the  $\text{SiO}_x$  current - voltage characteristics (van Hapert, 2002).

We have to note that, in VHR, the hopping implies a DB's path that contains "returns" and "dead ends" for electrons' transfer. The carriers that arrive on the "dead ends" will have no contribution to the electrical current for that specific electrical field value. This is equivalent with a reduction of the electron density in the percolation path and an enhancement of the trapped electrons.

After this introduction into the method let's see some experimental data and how the model works. For this we propose the electrical measurements on  $\text{SiO}_x$  samples deposited via rf magnetron sputtering. The voltage has been varied between 0.01 V and 100V. A delay of 10s was considered for each experimental point between the moment of the voltage application and the current measurement. As it will be shown in the next section, for high oxygen content samples, this delay time is important.

The dc current - voltage characteristics are given in the figure 25. Every investigated  $\text{SiO}_x$  sample shows a non-Ohmic character when  $U > 1\text{V}$ , ( $\mathcal{E} > 2 \cdot 10^4 \text{ V/cm}$ ). For these values the effect of the electrical field on the hopping processes has to be considered (see the Rel. (27)). For simplicity, the Pollak and Riess formula can be expressed in terms of experimental data (current intensity and applied voltage) as:

$$\ln\left(\frac{I}{U}\right) = a + b \cdot U \quad (28')$$

where the slope  $b = \frac{3}{16} \cdot \frac{R_c}{\delta} \cdot \frac{1}{k_B T}$  can be used to determine the reduced critical percolation

path  $\left(\frac{R_c}{\delta}\right)$  and the term "a" contains information about the localization parameter,  $\alpha$ . In

this expression,  $\delta$  is the sample thickness that equals the distance between electrodes.

Figure 26 reveals the Pollak and Riess model applied to the investigated samples using the graphical representation inspired by the Rel. (28'). The linearity of the plots is evident and, from the slope "b" some interesting information can be obtained: a) the critical percolation path is depending on the oxygen content, as the amount and the distribution of the DB

defects; b) the silicon rich  $\text{SiO}_x$  samples are characterized by a higher conductivity and, this is consequence of less “dead ends” for carriers; c) the reduced critical percolation path,  $(R_c/\delta)$ , varies within about 15% when  $x > 1$ .

From both, figures 25 and 26 we can observe that the  $\text{SiO}_x$  electrical conductivity is function of the applied electrical field. Also, it was already noted, the oxygen content in  $\text{SiO}_x$  plays an important role in tuning the electrical properties. Considering two representative samples - one for the silicon rich  $\text{SiO}_x$  and another one for the oxygen rich material - the calculated electrical resistance for  $U=50\text{V}$  varies from  $4.15 \cdot 10^9 \Omega$  for  $\text{SiO}_{1.43}$  to  $2.3 \cdot 10^4 \Omega$  for  $\text{SiO}_{0.01}$ .

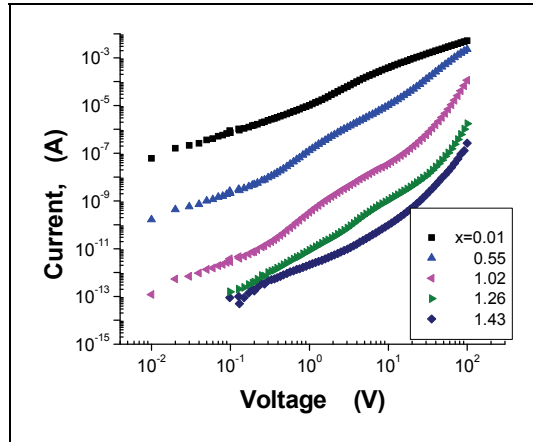


Fig. 25. The dc current-voltage characteristics measured on  $\text{SiO}_x$  samples with different oxygen content. The applied voltage was varied between 0.01 V and 100 V. The non-Ohmic feature of these I -V curves is clearly revealed.

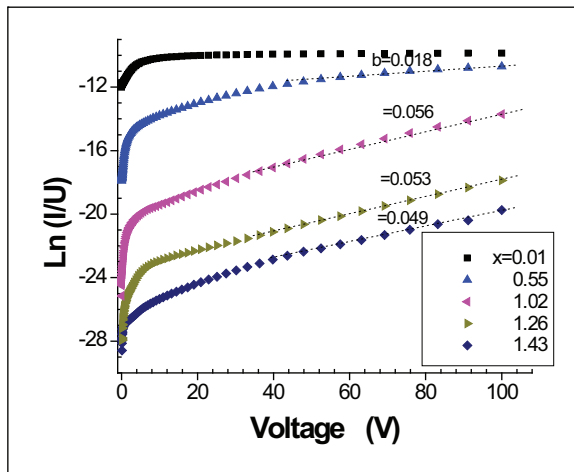


Fig. 26. The Pollak and Riess model of the VHR in current - voltage characteristics under high electrical field values is well shown for  $\mathcal{E} > 10^6 \text{ V/cm}$ .

## 6.2 Dielectric relaxation in $\text{SiO}_x$ materials: models of investigation

The existence of the “dead ends” along the percolation path of the electrical carriers in  $\text{SiO}_x$  implies a dielectric character for the material. A “dead end” means a structural defect where one (or two) electron(s) is/are trapped a longer time than the relaxation time that defines the conductivity. This is specific to a certain electrical field value; increasing this value, the percolation path changes and the status of the “dead ends” can also change.

How can we reveal the existence of these “dead ends”? For this we propose two experiments:

### a. Constant voltage pulse measurements

The application of a constant voltage pulse has the advantage that it renders the electrical field between the electrodes well known. The time variation of the electrical current through the sample gives information on the transported and trapped in “dead ends” charge carriers. In figure 27 are shown the current - time plots for the investigated samples, when a rectangular pulse voltage of 5 V was applied. For a nonzero applied voltage ( $t_1 < t < t_2$ ), the current decreases from a maximum value (determined by the voltage and the material conductivity) to a certain level that is a function of the  $x$  value. The decrease in time of the current could be easily explained if a capacitive character for the  $\text{SiO}_x$  material is considered: *the charging of this capacitor is equivalent with the diminishing of the flowing electronic flux.*

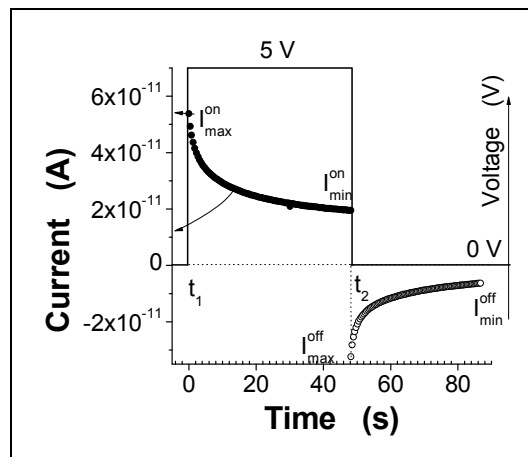


Fig. 27. The constant voltage pulse ( $U=5\text{V}$ ) measurement reveals the charging of the capacitor assigned to the  $\text{SiO}_x$  through the resistor represented by the same material (the plot with full symbols). Moreover, when the voltage becomes zero at the end of the pulse, the capacitor is discharging through the same resistor (the open symbol).

From figure 27 some values of the current are of interest: the maximum and minimum values of the current through the sample during the voltage-on and voltage-off experiments. They depend, of course on the applied voltage.

When the voltage pulse is on, the measured current shows an exponential decay in time from  $I_{\text{max}}^{\text{on}}$  towards a constant value,  $I_{\text{min}}^{\text{on}}$ . As we have said already, the decay reveals the capacitor charging;  $I_{\text{min}}^{\text{on}}$  is the current passing through the sample when the assigned capacitor is fully charged. The difference in electrical charges that define the  $I_{\text{max}}^{\text{on}}$  and  $I_{\text{min}}^{\text{on}}$  values is captured within the sample on the “dead ends” sites. These are silicon DB's that



can accommodate maximum two electrons and therefore becoming negatively charged. Such sites will influence the percolation path of the other electrons participating in the transport mechanism. The spatial distribution of these occupied “dead ends” has a larger density nearby the receiver electrode. We note that, the  $I_{\min}^{om}$  value is depending on the  $x$  value and the applied voltage.

When the applied pulse voltage is off, as figure 27 shows, a reverse current will flow in the sample. The driving force for this current is the gradient of the fully occupied “dead ends” density. For reverse transport, these sites are not anymore “dead ends” for the charge carriers. After a while, the reverse current reaches its  $I_{\min}^{off}$  value. The released charge in this time can be easily calculated by integrating the current of discharging experiments over the measurement time:

$$Q_{rel} = \int_{t_2}^{\infty} i(t) \cdot dt \quad (29)$$

In practice, the upper limit of this integral is finite to the time when  $I_{\min}^{off} / I_{\max}^{off} < 10\%$ . Considering the investigated samples with  $x > 1$ , and the experimental situation when the applied voltage was  $U = 5V$ , the calculated values for the charge trapped on the DB’s sites distributed in the bulk of the SiO<sub>x</sub> material are given in table 1. As a remark, increasing the amount of the oxygen in the sample, the amount of the trapped charge diminishes.

Knowing the charging voltage,  $V$ , the  $Q=f(V)$  plot reveals the layer capacity. As an example, the results for the SiO<sub>1.43</sub> sample are shown in figure 28. The slope of the  $\log(Q_{rel})=\log(V)$  plot is 0.59. This means that the capacity is voltage dependent:  $C = C_0 V^{\beta}$ , with  $\beta < 1$  and  $C_0$  as functions of the layer oxygen content (see the table 1). We note that increasing the oxygen content in the layer, the  $\beta$  parameter increases dramatically (from 0.05 for SiO<sub>1.01</sub> to 0.41 for SiO<sub>1.43</sub>). The  $C_0$  factor will be practically the voltage independent value of the capacity and is higher for the silicon richer samples. This could be macroscopically assigned to a larger value of the dielectric constant.

Of interest for applications is the dynamic of the charge releasing process from DB sites. Modeling with an exponential decay, the RC-time assigned to this phenomenon can be easily fitted. The results shown in table 1 prove that a more silicon rich sample has a smaller releasing time of the trapped charge: 1.32s for SiO<sub>1.02</sub> in comparison with 4.05s for SiO<sub>1.43</sub>. These results are understandable, considering the much smaller electrical resistance of the samples with less incorporated oxygen.

$x$	$Q_{rel}$ (C)	$C_0$ (F)	$\beta$	$\tau_{RC}$ (s)
1.02	-2.84E-09	4.26E-10	0,04	1.38
1.26	-1.50E-09	4.13E-10	0.25	2,94
1.43	-7.11E-10	1.99E-10	0.41	4.05

Table 1. The trapped charge in the so-called “dead ends”,  $Q_{rel}$ , the capacity parameters ( $C_0$  and  $\beta$ ) and the assigned RC-time for various SiO<sub>x</sub> samples when  $U = 5V$  constant voltage pulse is applied

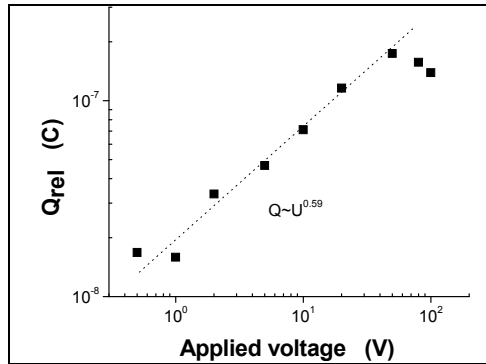


Fig. 28. Applying constant voltage pulses of different amplitude values and measuring the variation in time of the current through the sample, the chargeability of the layer can be calculated by using the Rel (29). The electrical charge versus the applied voltage defines the layer electrical capacity.

*b. the hysteresis measurements*

This type of measurements has been inspired by the study of the materials' magnetic properties. In fact here we apply a cycles of voltages varying in well known steps, and measure the corresponded current intensity. There is a defined delay time between applying the voltage and measuring the current. If charge is not trapped (stored) for a longer time than this delay time, the current values measured when decreasing the voltage must follow the same values as when the voltage increases. When a certain amount of charge is captured (trapped) an interesting hysteresis curve is obtained. Such an example is shown in figure 30 for two  $\text{SiO}_x$  samples:  $\text{SiO}_{1.02}$  and  $\text{SiO}_{1.43}$

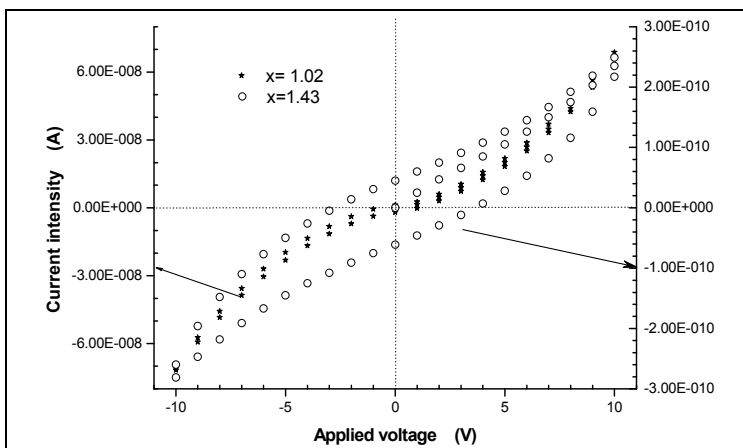


Fig. 29. The hysteresis curves current intensity versus the applied voltage for  $\text{SiO}_x$  samples with  $x=1.02$  (full symbols) and  $x=1.43$  (empty circles). The more resistive  $\text{SiO}_x$  showed a wider hysteresis loop.

We note the different scales for the measured current intensity through the two samples. Also, before any comment on the plots, we have to mention that the delay time between the

applying the voltage and the measuring the current was the same for both samples. The SiO<sub>1.02</sub> sample has a larger electrical conductivity and the hysteresis loop is narrower. Increasing the voltage, the occupation of the localized states is changed more rapidly because of the higher conductivity. When the oxygen content is increased, the material resistivity increases. The trapped charge needs more time to be released and this is well revealed by a larger hysteresis loop. During the cycle, when the current passes through zero, the voltage has a certain value, called the coercive voltage. The values for this parameter are given in the table 2. For both samples, there is an asymmetry when looking at the negative values versus the positive ones.

Sample	U <sub>coercive</sub> (V)		I <sub>remnant</sub> (A)	
SiO <sub>1.02</sub>	-0.67	1.15	-2.01 10 <sup>-9</sup>	1.18 10 <sup>-9</sup>
SiO <sub>1.43</sub>	-2.65	3.74	-6.12 10 <sup>-11</sup>	4.56 10 <sup>-11</sup>

Table 2. The main parameters of a hysteresis loop: the coercive voltage and the remnant current

Following the cycle in varying the voltage, we reach the situation when the voltage is null (zero), but the current intensity has a non-zero value called the remnant current. The value of this current reflects the electrical conductivity of the material, while the values of the coercive voltage is a measure of the dielectric properties. We can conclude from these experiments that the trapped charge is difficultly released from SiO<sub>x</sub> with higher oxygen content (in the as deposited sample!).

## 7. From SiO<sub>x</sub> thin films to silicon nano-crystals embedded in SiO<sub>2</sub>

### 7.1 Phase separation: structural changes, thermodynamics and technology design

Most of the physico-chemical properties of a material are determined by the internal structure of that material. It is well known that models used to study the electrical, optical, thermal and magnetic properties of semiconductors are based on the density of states (DOS) distribution (electrons and/or phonons). In the last decades, many published papers emphasized the connection between the deposition conditions and the properties of the deposited SiO<sub>x</sub> thin films. Modern and sophisticated methods of investigation revealed the structural differences for these layers.

*What if a certain SiO<sub>x</sub> material is subjected to post-deposition treatment? Is its structure changed?*

For answering these questions, we review the knowledge points from section 2. The elemental structural entity in SiO<sub>x</sub> was considered a tetrahedron with a silicon atom in the centre. The four corners of the tetrahedron are occupied by either silicon or oxygen atoms. Any type of bond is characterized by a bond energy that will define the bond length. The whole structure is formed from such tetrahedral structures interconnected. Based on calculations of the Gibbs free energy (Hamann, 2000) it was shown that tetrahedra as Si-(Si<sub>4</sub>) and Si-(O<sub>4</sub>) are stable, while Si-(Si<sub>n</sub>O<sub>4-n</sub>), with n=1, 2, 3 are in- or unstable. From a thermodynamics point of view the latter structures can change into a stable configuration via spinodal decomposition (van Hapert et al., 2004). The most unfavorable structural entity is Si-(Si<sub>2</sub>O<sub>2</sub>); the chemical bond between the central silicon atom and the oxygen ones is much stressed (disturbed) and, if conditions for migration of an oxygen atom are satisfied, the so called phase decomposition will take place. This means:

- $\text{Si}-(\text{Si}_2\text{O}_2) + \text{Si}-(\text{Si}_2\text{O}_2) \rightarrow \text{Si}-(\text{Si}_1\text{O}_3) + \text{Si}-(\text{Si}_3\text{O}_1)$ , or
- $\text{Si}-(\text{Si}_2\text{O}_2) + \text{Si}-(\text{Si}_2\text{O}_2) \rightarrow \text{Si}-(\text{O}_4) + \text{Si}-(\text{Si}_4)$ .

We note that the number of atoms of each species is conserved. Also, it is imperiously necessary to remark the need for intermediary structures to make the transition between the "stable" entities of amorphous silicon ( $\text{Si}-(\text{Si}_4)$ ) and quartz ( $\text{Si}-(\text{O}_4)$ ). In other words structures such as  $\text{Si}-(\text{Si}_1\text{O}_3)$  will make the transition between the two stable structural entities.

The easiest way to check for the structural changes is to follow, by IR measurements, the peak position and the shape of the Si-O-Si stretching vibrational mode. These parameters are sensitive to the compositional and structural arrangements. We note that, in order to prove the structural changes, the experiments must be made in such a way that the composition of the layer (the x parameter from  $\text{SiO}_x$ ) remains unchanged.

Without going into experimental details, as-deposited  $\text{SiO}_x$  samples have been structurally transformed by:

- annealing (Hinds et al., 1998) at 740°C, or
- ion bombardment (Arnoldbik et al., 2005), or
- irradiating with UV photons (mode details in the next section).

This is revealed by a new peak position that can be scaled up to the value that corresponds to  $\text{SiO}_2$ . In the figure 30 are shown some experimental results.

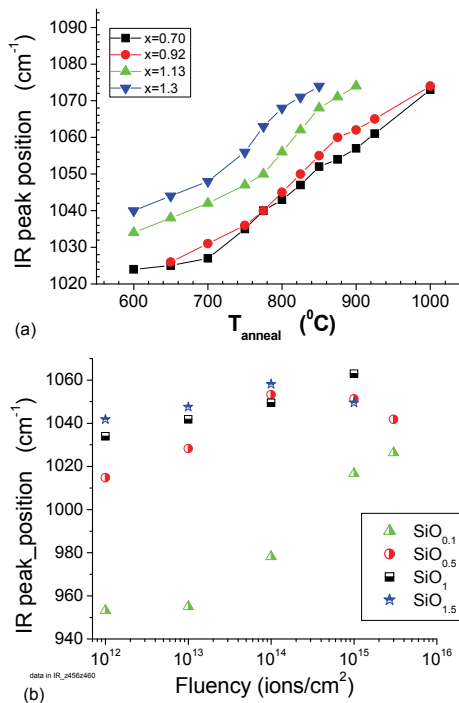


Fig. 30. The structural changes in  $\text{SiO}_x$  generated by post-deposition treatment as annealing (a) and ion bombardment (b) revealed by IR spectroscopy. The peak position of the stretching vibration is shifted towards higher wavenumber values when more energy is put into the  $\text{SiO}_x$  system. For more about this, see Hinds et al., 1998; and Arnoldbik et al., 2005, respectively.

In figure 30a it is showed that starting with  $\text{SiO}_x$  ( $x=0.7, 0.92, 1.13$  or  $1.3$ ), via annealing at temperatures higher than  $600^\circ\text{C}$ , structures where the silicon atoms are surrounded by a larger number of oxygen atoms than initially, are formed. The averaged  $x$  value remains unchanged (there are not added new atoms in the structure) but rearrangements of the oxygen atoms will provide structures characterized by a higher IR peak position. In sections 3.3 and 3.4 it was demonstrated that a larger value for the peak position means a larger  $x$  value. This applies also in these experiments: the changes in oxygen richer regions automatically mean formation of silicon rich domains. In other words the contribution of the signal assigned to the  $\text{Si}^{3+}$  and  $\text{Si}^{4+}$  sites to the total IR absorption signal is larger (see the section 3.4). We note that the  $\text{Si}^0$  sites do not have an IR absorption signal, but they are more visible in the Raman measurements and in the XPS spectra.

The larger the annealing temperature is, the more material suffers the phase transformation and, as a consequence, the peak position is more shifted. At high temperature ( $T > 950^\circ\text{C}$ ) the material becomes more "oxide thermally growth" like and the peak position is shifted towards  $1081\text{ cm}^{-1}$ , which is the position corresponding for this material.

Similar transformations can be seen in figure 30b where the experimental data are the result of the ion bombardment ( $50\text{ MeV } ^{63}\text{Cu}$  ions). This is another manner to create the conditions for phase decomposition in  $\text{SiO}_x$ . Increasing the fluency of the ions on the studied material has a similar effect as increasing the annealing temperature. The advantage on this experiment is the less time consumed, but as applicability at industrial scale it is less feasible. However for fundamental research and understanding of the processes involved, the method is valuable and highly appreciated.

As a result of the phase separation, islands of nano-crystalline silicon (Si-nc) embedded in a  $\text{SiO}_2$  matrix are obtained. Such a structure is shown in figure 31, using a TEM spectrum (Inokuma et al., 1998). As it was proved in this section, this new material can be obtained from silicon sub-oxides  $\text{SiO}_x$  ( $0 < x < 2$ ) as predecessors, and special post-deposition treatments.

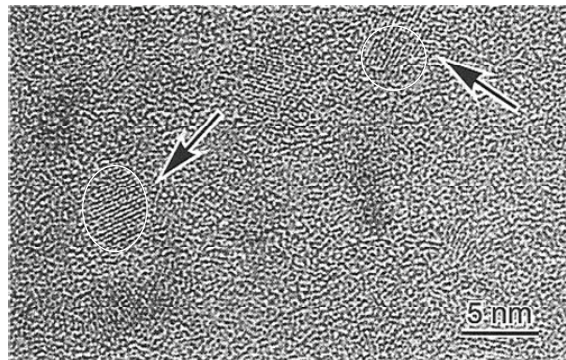


Fig. 31. Islands of Si nano-crystals embedded into a sea of  $\text{SiO}_2$  material. This new material was obtained from  $\text{SiO}_{1.3}$  annealed at  $1100^\circ\text{C}$ . The dimension and the concentrations of these nano crystals are very important for applications in optoelectronics. *Reprinted with permission from Inokuma et al., 1998; copyright 1998, American Institute of Physics.*

## 7.2 Phase separation induced by UV photons irradiation

Besides annealing and ion bombardment, another post deposition technique based on laser irradiation of the  $\text{SiO}_x$  thin films has been proposed to study the phase separation process (Tomozeiu, 2006). This technique has been successfully utilized to change the structure of the various amorphous materials (carbon nitride (Zhang and Nakayama, 1997) or amorphous silicon (Aichmayr et al., 1998)). Thin films of various  $\text{SiO}_x$  compositions have been irradiated with different fluxes of UV laser photons ( $\lambda=274 \text{ nm}$ ).

In figure 32 are shown the IR spectra of the as deposited samples and of the laser irradiated samples with various amount of UV photons. The peak position of the IR stretching vibration mode measured on irradiated samples is shifted towards higher wave-number values. For a better understanding, we mention the peak position for sputter deposited  $\text{SiO}_2$  at  $1054 \text{ cm}^{-1}$  (Tomozeiu, 2002). The as deposited  $\text{SiO}_{1.2}$  samples are characterized by a peak position at  $1027.7 \text{ cm}^{-1}$ . After the laser irradiation, the main peak has its maximum at  $1068.2 \text{ cm}^{-1}$ , when the laser energy is  $55 \text{ mJ}$  (which means  $103.4 \text{ mJ/mm}^2$ ). The full width at half-maximum (FWHM) - an indicator of the structural homogeneity - was also changed by UV irradiation. For the as deposited sample, the width of the peak was found  $146.4 \text{ cm}^{-1}$  and for the UV irradiated sample  $106.1 \text{ cm}^{-1}$  ( $55 \text{ mJ}$ ).

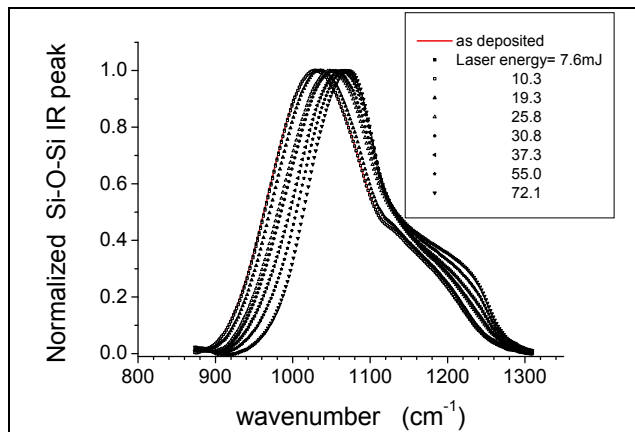


Fig. 32. The normalized IR absorption spectra of the stretching vibration mode for as deposited (full line) and UV irradiated samples with various laser energy (symbols). The energy delivered during the laser treatment is a measure of the number of the incident photons

Other issues related to the changing of the peak shape are:

- i. the IR spectra of the laser treated samples have the main peak placed nearer the peak position of the thermally grown  $\text{SiO}_2$ ,  $1073 \text{ cm}^{-1}$  (red shifted in comparison with the sputter deposited  $\text{SiO}_2$ );
- ii. the spectrum of the irradiated sample has a shoulder at  $1250 \text{ cm}^{-1}$  that is specific to the  $\text{SiO}_2$  structure;
- iii. the shift in the peak position is dependent on the energy transferred to the  $\text{SiO}_x$  via photon impacts.

Generally, the shift in the peak position and the changes in the peak shape show the structural changes in material. Figure 33 reveals the shift in the peak position and its dependence on the incident photons' energy.

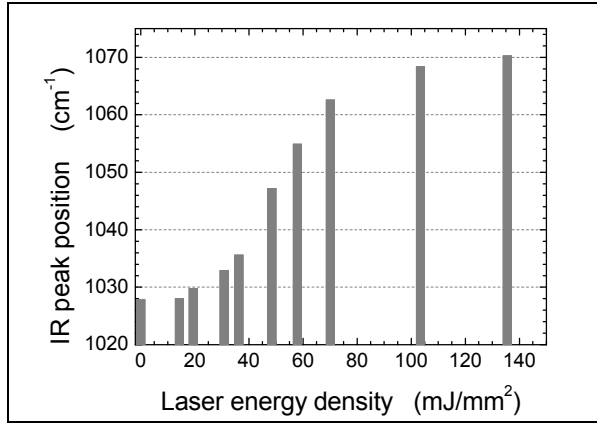
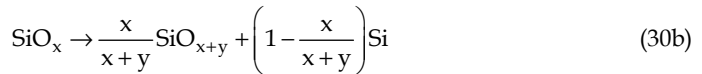


Fig. 33. The shift of the peak position assigned to the Si-O-Si stretching oscillation mode with increasing the UV photon's energy.

Considering the conservation of the silicon and oxygen atoms into the samples, the phase separation revealed by IR peak position in the figures 30 and 33 can be equated as:



with intermediary steps, depending on the incident energy:



The peak shape is drastically changed when more energy is added in the layer, especially when the corresponding value of the SiO<sub>x</sub> dissociation energy is exceeded. Having a calibration curve IR peak position versus oxygen content for 0<x<2 (see the section 3), the value of the y parameter can be calculated. In this way, the formation of oxygen rich regions in SiO<sub>x</sub> can be revealed.

*What about the silicon islands?* Spectroscopically, they can be emphasized with Raman spectroscopy. For amorphous silicon the Raman signature is a wide peak centered on 480 cm<sup>-1</sup>. If the material is crystalline, the Raman spectrum has a very sharp peak (Hayashi and Yamamoto, 1996) at 520 cm<sup>-1</sup>. Figure 34 shows the Raman spectra of SiO<sub>1.2</sub> as deposited and laser treated samples. Increasing the laser energy, the peak centered at 480 cm<sup>-1</sup> increases in intensity. This means that the amount of Si-Si bonds has been increased by the UV photon irradiation.

Therefore, IR spectroscopy revealed the increasing of the Si-O bonds' number and the Raman investigations showed the increase of the Si-Si number when the SiO<sub>x</sub> sample has been laser irradiated. Increasing the energy delivered to the material, more oxygen-rich and silicon-rich material has been detected. Increasing more the energy delivered to the SiO<sub>x</sub> it is possible to induce the phase separation (silicon and SiO<sub>2</sub>) together with the phase transformation: *from amorphous into crystalline silicon*. The sharp peak centered on 520 cm<sup>-1</sup>, which is the fingerprint for crystalline silicon, increases in intensity with increasing the

energy above a certain threshold value. Fitting the Raman spectrum with two gaussians – one for amorphous phase and the other for crystalline phase – the amount of the silicon transformed in crystalline silicon can be evaluated: 15.9% and 28.3% for incident UV energy of 70.1 mJ/mm<sup>2</sup> and 103.4 mJ/mm<sup>2</sup>, respectively. This proves the possibilities of the method to obtain Si-nc embedded into SiO<sub>2</sub> matrix.

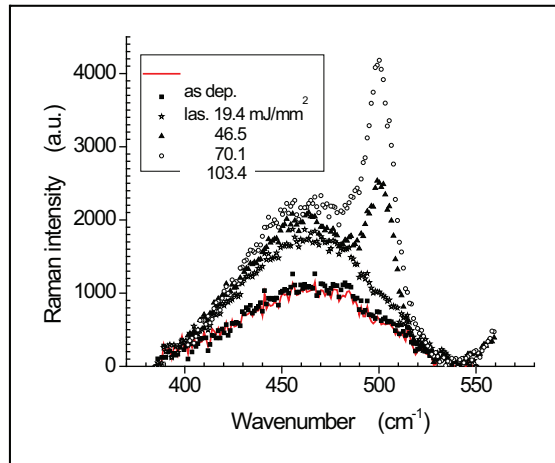


Fig. 34. The Raman spectra provide information regarding the increasing of Si-Si bonds when the photons' energy increases. The spectra of the samples irradiated with 70.1 and 103.4 mJ/mm<sup>2</sup> show the development of crystalline silicon from amorphous phase.

Also, the EPR measurements made on as-deposited and laser-treated samples, have revealed changes in the type of the structural defects. It was seen that, increasing the number of the incident photons, the amount of D<sup>0</sup> defect-like increases. Taking into account the influence of these defects on electrical conductivity, on capturing and trapping the electrical carriers and from here on the recombination electron-hole mechanisms, a real picture on the phase separation and its applicability in optoelectronics can be penciled. Such new materials as Si-nc embedded into a SiO<sub>2</sub> matrix (ore other dielectric matrix) are intensively studied and much required for silicon based light emitters in integrated optoelectronics.

### 7.3 Applications in optoelectronics

The Light Emitting Diodes (LED-s) represent together with the laser diodes the photonic devices that convert electrical energy into optical radiation. In the last half century the needs for such devices increased exponentially; new research sectors and industries have been developed due to these light producing devices. Optoelectronics, optronics and integrated optics have been developed and gained an important place in our daily life. However, as it is well known, silicon as material utilized in microelectronics devices is a poor light emitting material because of its indirect band-gap. But, silicon nano-crystals offer a solution because of their tunable indirect band-gap and more efficient electron-hole recombination. This is why, the discovery of visible light emission from silicon nano-structures has stimulated great interest for both the theoretical studies to understand the emission mechanisms, and the experimental approaches to obtain these nano-crystals. Also, the integration of such light sources within the optoelectronic devices is highly desirable.



As general knowledge, we note that the luminescence is the emission of an optical radiation due to the electronic excitation within a material. In LED the excitation of the carriers is the result of the electrical field or the current over/through the device. The photons' emission is the result of the recombination processes, which are favored by the creation of non-equilibrium states where the density of the minority carriers becomes much larger than the value corresponding to the equilibrium. We also note that within solid state devices, there are non-radiative recombination mechanisms that will reduce (cancel) the efficiency of the radiative ones.

Silicon nanocrystals can be considered low-dimensional structures with size of few nanometers. The structure of the electronic density of states is dramatically changed when theoretically we pass from three dimensional structures to one- or zero- dimensional structures. When the nanocrystals are structures with size comparable to the exciton Bohr radius (1-3 nm), the confinement induces a localization of the produced exciton. In many publications, the proposed model for the luminescence mechanisms is based on quantum confinement effects in silicon nano-crystals embedded in  $\text{SiO}_2$  or other dielectric materials. The transition between the Si-nc and the  $\text{SiO}_2$  matrix is a region with dangling bonds defects which appears because of the mismatch in the structural lattice of the two materials. These defects act as traps for the electrons and/or holes and, as a consequence, they quench the luminescence. Their passivation by hydrogen or oxygen atoms have been proved as being effective. According to the quantum confinement effect model, the photoluminescence in visible is observed when the band-gap of the nano-silicon is large enough due to the size reduction of the silicon nano-crystals. This together with a very well passivated surface by Si-H or Si-O bonds are the ingredients for a high efficiency in light emission from silicon nano-crystals embedded in  $\text{SiO}_2$ .

We mention that some publications suggest that surface states at the interface between the Si-nc and the composition of this intermediate layer are the principal mechanisms leading to photoluminescence (Koch et al., 1993). This model opened a new perspective on approaching the emission mechanisms. Moreover, in some situations researchers invoked both models to explain the photoemissions on two different optical wavelength ranges: the emitted light at 1.8-2.1 eV is explained via the quantum confinement effects, while the band at 2.55 eV is related to localized surface states at the  $\text{SiO}_x/\text{Si}$  interface (Chen et al., 2003).

Without getting into the details of these models (this is not the purpose of this work) we consider necessary to discuss two issues: a) the influence of the nanocrystals' size on the light emission, and b) the light amplification in silicon nanocrystals.

Concerning the first subject, the spatial dimension of the silicon nanocrystals is the key factor in tuning the electronic density of states in silicon and, in the theory of the quantum confinement. Moreover the size of the nano-crystals is important in obtaining the right emission spectrum. This is revealed in figure 35 where the peak maximum of the photoluminescence is plotted against the mean crystal size according. The data are from literature (Inokuma et al, 1998; Kahler and Hofmeister, 2002) and reveal the photoluminescence (PL) spectra in  $\text{SiO}_x$  films subjected to thermal annealing between 750°C and 1100°C.

This study shows that there is a remarkable increase in the PL intensity after annealing at temperature above 1000°C. Both, the composition of the as-deposited  $\text{SiO}_x$  and the annealing temperature value play an important role in the dimension of the crystals and, from here on the photoluminescence spectrum. Depending on the deposition method for the  $\text{SiO}_x$  precursor thin film and on the post-deposition treatment in order to obtain the phase

separation, the silicon nanocrystals result in different sizes. The higher is the annealing temperature, the larger are the obtained nano-crystals. From the data plotted in figure 35, a correlation between the PL peak and the mean crystal size can be penciled:

$$\lambda_{\text{PL max}}(\text{nm}) = 77.53 \cdot \text{mean cryst. size (nm)} + 552.6 \quad (31)$$

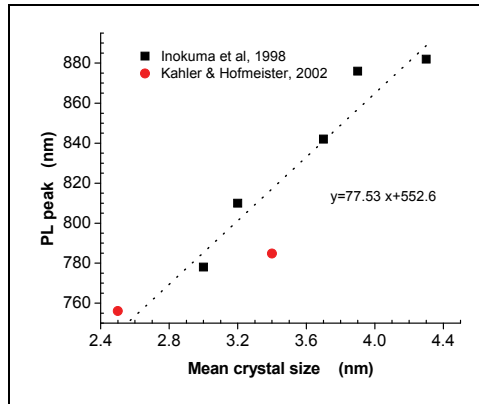


Fig. 35. The size of the silicon nanocrystals does matter in the light emission. This experimental data from literature show the importance of the post-deposition annealing in PL.

We mention that this relation was obtained from studies of  $\text{SiO}_x$  samples post-deposition annealed. Concerning the issue of silicon nanocrystals as light amplification, this is a step further from LED towards the laser diode. The works of Pavesi et al (e.g. Pavesi et al, 2000) have already penciled the main model for this new function of the silicon nanocrystals embedded into  $\text{SiO}_2$  matrix. Their energy diagram for a nano-crystal that works in lightemission regime represents a pioneering work in this field. The diagram consists of three energy levels, where two are the HOMO and LUMO nano-crystal bands' edges and the third level is an instable energy level placed into the band-gap region (between LUMO and HOMO levels). Let it to be called inversion level. Via an external pumping mechanism the electrons are transferred from the valence band edge (HOMO level) to the conduction band edge (LUMO level) and from here, via a fast transition (time-scale of  $10^{-9}$ s) the electrons will populate the inversion level. This is an instable energy level and the electrons will radiatively recombine with the holes from the valence band. This schematic energy diagram (see figure 7 of Pavesi et al., 2000) shows how the stimulated emission can be obtained from silicon nano-crystals embedded into  $\text{SiO}_2$ . More work is in course and we are confident that the laser light obtained from silicon-based materials, compatible with the silicon technology will be a reality in the nearest future.

In the last years, solar cells research and production have been much revigorated. Silicon based solar cells (mono-crystalline and amorphous) are the main candidates for this industry. The efficiency of a solar cell is defined by the carriers' generation per incoming photon. For photons with energy larger that the optical band-gap, it is considered that one pair of electron hole is generated by one photon. In 2000 a group of researchers at National Renewable Energy Laboratory (NREL) has found hat solar cells made with silicon nanocrystals could produce several electrons from one photon from the UV part of the

sunlight. The mechanism proposed was called “multiple exciton generation” and the calculations showed that these nanocrystals theoretically convert more than 40% of the light energy into electrical power. In a typical solar cell the energy in blue and UV light serves to produce one electron and the rest is transformed in heat. When silicon nanocrystals are used as solar cells material, this “lost” energy is converted via quantum-mechanical effects using the multiple exciton generation processes into electrons (Bullis, 2007). Although this technology is at the beginning, it is considered as the main step in obtaining a super efficient solar cell and studies are made in collecting these new generated electrons with a short lifetime.

Silicon nanocrystals are seen as promising biophotonics materials (Li and Ruckenstein, 2004; Michalet et al., 2005). In fact they can be used as luminescent markers for biological samples, having a low level of toxicity. Of great interest it is now the surface passivation of the water-dispersed Si-nc with organic compounds; in this way the luminescence is stabilized and their function as markers is more accurate. Moreover, considering the high surface-to-volume ratio of these nanocrystals, another function for them is foreseen: as therapeutic and diagnostic (theranostic) agent (Ho and Leong, 2010). There many conditions that an inorganic nanocrystal must accomplish for a complete compatibility with the *in vivo* organic material. According to this mini-review paper, the quantum dots have become a widely used research tool for diagnostics, cell and molecular biology studies and *in vivo* bioimaging. We mention that the authors have discussed only about the nano-particles as 5-50 nm of  $\text{A}_2\text{B}_6$  (e.g. CdTe and CdSe) and  $\text{A}_3\text{B}_5$  (e.g. InAs and InP) group of materials. A problem that must be solved is related to the toxicity of these elements for the living cell. It seems that the silicon nanocrystals are characterized by a low toxicity level and their use for these applications is in study.

As it was seen from this section the applications for the silicon nanocrystals embedded into a dielectric matrix are multiple and very actual. A better understanding of the processes that enable their formation and growth, and of their role within an optoelectronic (of biophotonic) application will end up into a high quality and more efficient devices.

## 8. Acknowledgements

The author is grateful to the group headed by Prof. Dr. FHPM Habraken from Utrecht University for support and interesting discussions. The permanent support offered by R&D Océ Technologies B.V. is acknowledged.

## 9. References

- Aichmayr, G.; Toet, D.; Mulato, M.; Santos, P.V.; Spangenberg, A.; Christiansen, S.; Albrecht, M. & Strunk, H.P., (1998), *Lateral grain growth during the laser interference crystallization of a-Si*, Phys. Status Solidi, A166, pp. 659 - 666.
- Arnoldbik, W.M.; Tomozeiu, N.; van Hattum, E.D.; Lof, R.W.; Vredenberg, A.M. & Habraken, F.H.P.M., (2005), *High-energy ion-beam-induced phase separation in  $\text{SiO}_x$  films*, Phys. Rev. B71, pp. 125329-125336
- Ashcroft, N.W. & Mermin, N.D. (1988). *Solid State Physics*, ISBN0-03-049346-3, ch. 17
- Brottger, H. & Bryksin, V.V. (1985). *Hopping conduction in solids*, Akademie-Verlag Berlin, ISBN-10 - 0895734818, pp. 236
- Bullis, K. (2007), *Silicon Nanocrystals for Superefficient Solar Cells* paper published on 15

- Augusts 2007, in <http://www.technologyreview.com>
- Carrier, P.; Abramovici, G.; Lewis, L.J. & Dharma-Wardana, M.W.C. (2001). *Electronic and Optical Properties of Si/SiO<sub>2</sub> Superlattices from First Principles : Role of Interfaces*. Mat. Res. Soc. Symp. Proc. vol. 677, pp. AA4.10.1 - AA4.10.6
- Carrier, P.; Lewis, L.J. & Dharma-Wardana, M.W.C. (2002). *Optical properties of structurally relaxed Si/SiO<sub>2</sub> superlattices: The role of bonding at interfaces*, Phys. Rev. B65, pp. 165339-165350
- Chen, X.Y.; Lu, Y.F.; Wu, Y.H.; Cho, B.J.; Liu, M.H.; Dai, D.Y. & Song, W.D. (2003), *Laser annealing of silicon nanocrystal films prepared by pulsed-laser deposition*, J. of Appl. Phys. 93, no.10, pp. 6311 - 6316
- Cho, K.S.; Park, N-M.; Kim, T-Y.; Kim, K-H.; Sung, G. Y. & Shin, J. H. (2005), *High efficiency visible electroluminescence from silicon nanocrystals embedded in silicon nitride using a transparent doping layer*, Appl. Phys. Lett. 86, pp.909-071911
- Cody, G. D.; Tiedje, T.; Abeles, B.; Brooks, B. & Goldstein, Y. (1981). *Disorder and the Optical-Absorption Edge of Hydrogenated Amorphous Silicon*, Phys. Rev. Lett. 47, pp. 1480-1483
- Cullis, A.G. & Canham, L.T. (1991). *Visible light emission due to quantum size effects in highly porous crystalline silicon*, Nature 353 pp. 335-338
- Gibbs, G.V.; Boisen, M.B.; Hill, F.C.; Tamada, O. & Downs, R.T. (1998). *SiO and GeO bonded interactions as inferred from the bond critical point properties of electron density distributions*, Phys Chem Minerals 25, 574-584
- Hamann, D.R., (2000), *Energetics of silicon suboxides*, Phys. Rev., B61 pp.9899-9901
- Hayashi, S. & Yamamoto, K. (1996) *Optical properties of Si-rich SiO<sub>2</sub> films in relation with embedded Si mesoscopic particles*, J. Lumin. 70 no. 1-6, pp. 352 - 363.
- Hinds, B.; Wang, F.; Wolfe, D.; Hinkle, C. & Lucovsky, G. (1998), *Investigation of postoxidation thermal treatments of Si/SiO<sub>2</sub> interface in relationship to the kinetics of amorphous Si suboxide decomposition*, J. Vac. Sci. Technol. B16, pp. 2171-2177
- Ho, Y.P. & Leong, K.W. (2010), *Quantum dot-based theranostics*, Nanoscale, 2, pp. 60 -68
- Hutchings, D.C.; Sheik-Bahae, M.; Hagan, D.J. & van Stryland, E.W. (1992). *Kramers-Kronig Relations in Nonlinear Optics*, Optical and Quantum Electronics 24 , pp. 1-30 (and the first two references of this paper)
- Inokuma, T.; Wakayama, Y.; Muramoto, T.; Aoki, R.; Kurata, Y. & Hasegawa, S. (1998), *Optical properties of Si clusters and Si nanocrystallites in high-temperature annealed SiO<sub>x</sub> films*, J.of Appl. Phys. 83, nr 4, pp. 2228 - 2234
- Kahler U. & Hofmeister, H. (2002), *Size evolution of silicon nanocrystallites in evaporated thin films of SiO<sub>x</sub> upon thermal processing*, Appl. Phys. A74, pp. 13 - 17
- Knights, J.C.; Street, R.A. & Lucovsky, G. (1980). *Electronic and structural properties of plasma-deposited a-Si:O:H - The story of O<sub>2</sub>*, J. Non-Cryst. Solids, 35-36 pp. 279 - 284
- Koch, F.; Petrova-Koch, V. & Muschik, T. (1993), *The luminescence of porous Si: the case for the surface state mechanism*, J. of Luminescence 57, pp. 271 - 281
- Li, Z.F. & Ruckenstein, E. (2004), *Water-soluble poly(acrylic acid) grafted luminescent silicon nanoparticles and their use as fluorescent biological staining labels*, Nano Letters, 4, no. 8, pp. 1463 -1467
- Lu, Z.H.; Lockwood, D.J. & Baribeau, J.M. (1995). *Quantum confinement and light emission in SiO<sub>2</sub>/Si superlattices*, Nature 378, pp. 258-260
- Lucovsky, G. & Pollard, W.B. (1983). *Local bonding of oxygen and hydrogen in a-Si:H:O thin films*, J. Vac. Sci. Technol. A 1, pp. 313 - 317

- Madan, A. & Shaw, M. (1988). *The physics and applications of amorphous semiconductors*, Academic Press Inc. ISBN-10: 9780124649606
- Michalet, X.; Pinaud, F.F.; Bentolila, L.A.; Tsay, J.M.; Doose, S.; Li, J.J.; Sundaresan, G.; Wu, A.M.; Gambhir, S.S. & Weiss, S. (2005), *Quantum Dots for Live Cells, in Vivo Imaging, and Diagnostics*, Science, 307, no 5709, pp. 538-544
- Morimoto, A.; Nariyama, H. & Shimizu, T. (1987). *Structure and Defects in Amorphous Si-O Films*, Jap. J. of Applied Phys. 26, no. 1, pp. 22-27
- Mott, N.F. & Davis, E.A. (1979). *Electronic processes in non-crystalline materials*, Oxford University Press, second edition, ch 2
- Nassiopoulos, A.G.; Grigoropoulos, S. & Papadimitriou, D. (1996). *Electroluminescent device based on silicon nanopillars*, Appl. Phys. Lett. 69, pp. 2267-2269
- O'Leary, S.K.; Johnson, S.R. & Lim, P.K. (1997). *The relationship between the distribution of electronic states and the optical absorption spectrum of an amorphous semiconductor: An empirical analysis*, J. Appl. Phys., 82, no 7, pp. 3334 - 3341
- Pai, P.G.; Chao, S.S.; Takagi, Y. & Lucovsky, G. (1986). *Infrared spectroscopic study of SiO<sub>x</sub> films produced by plasma enhanced chemical vapor deposition*, J. Vac. Sci. Technol. A 4 (3), pp. 689-695
- Pavesi, L.; Dal Negro, L.; Mazzoleni, C.; Franzo, G. & Priolo, F. (2000). *Optical gain in silicon nanocrystals*, Nature 408, pp. 440-444
- Pollak, M. & Reiss, I. (1976). *A percolation treatment of high-field hopping transport*, J. Phys. C 9 pp. 2339 - 2352
- Puzder, A.; Williamson, A. J.; Crossman, J. C.; & Galli, G. (2002). *Surface Chemistry of Silicon Nanoclusters*, Phys. Rev. Lett. 88, pp. 097401 - 04
- Ravindra, N.M.; Auluck, S. & Srivastava, V. K. (1979). *On the Penn gap in semiconductors*, Phy. Stat. Sol B 93, no. 2, pp. K155 - K160
- Singh, A.; Bayliss, S.C.; Gurman, S.J. & Davis, E.A. (1992), *The amorphous SiO<sub>x</sub>: H<sub>y</sub> thin film system. III. Structure and bonding*, J. Non-Cryst. Solids 142, pp. 113 - 125
- Stolze, F.; Zacharias, M.; Schippel, S. & Garke, B. (1993). *Compositional investigation of sputtered amorphous SiO<sub>x</sub>:H*, Solid State Communications, 87, no. 9 pp. 805-808
- Street, R.A. (1991). *Hydrogenated amorphous silicon*, Cambridge University Press, ch. 4.
- Tauc, J.; Grigorovici, R. & Vancu, A. (1966). *Optical Properties and Electronic Structure of Amorphous Germanium*, Phys. Stat. Sol. 15, pp. 627- 637
- Theiss, W. (2002). Scout program in <http://www.wtheiss.com>
- Tomozeiu, N.; van Hapert, J.J.; van Faassen, E.E.; Arnoldbik, W.M.; Vredenberg, A.M. & Habraken, F. H. P. M. (2002), *Structural properties of a-SiO<sub>x</sub> layers deposited by reactive sputtering technique*, J. of Optoelectronics and Advance Materials, 4, no. 3, pp. 513 - 521
- Tomozeiu, N.; van Faassen, E.E.; Habraken, F.H.P.M. (2003). *Structural transition in silicon suboxides at critical oxygen content*, Annals of West University of Timisoara, Series Chemistry 12, no. 3, pp 1039 - 1046
- Tomozeiu, N. (2006). *Effects of UV photon irradiation on SiO<sub>x</sub> (0<x<2) structural properties*, Applied Surface Science 253, pp. 376-380
- Tomozeiu, N. (2006). *SiO<sub>x</sub> thin films deposited by rf magnetron reactive sputtering: structural properties designed by deposition conditions*, J. of Optoelectronics and Advance Material, 8, no. 2 pp. 769 -775

- van Hapert, J.J. (2002). *Hopping conduction and chemical structure - a study on silicon suboxides*, PhD Thesis, Utrecht University ISBN 90-393-3063-8, ch 3 and 4
- van Hapert, J.J.; Vredenberg, A.M.; van Faassen, E.E.; Tomozeiu, N.; Arnoldbik, W.M. & Habraken, F. H. P. M., (2004), *Role of spinodal decomposition in the structure of SiO<sub>x</sub>*, Phys. Rev. B 69 pp. 245202-245210
- Zacharias, M.; Drusedau, T.; Panckow, A.; Freistedt, H. & Garke, B. (1994). *Physical properties of a-SiO<sub>x</sub> : H alloys prepared by dc magnetron sputtering with water vapour as oxygen source*, J. of Non-Crystalline Solids 169, pp. 29-36
- Zhang, M. & Nakayama, Y. (1997), *Effect of Ultraviolet Light Irradiation on Amorphous Carbon Nitride Films*, J. Appl. Phys. 82, no. 10, pp. 4912- 4015.
- Zhang, R. Q.; Chu, T. S.; Cheung, H. F.; Wang, N. & Lee, S. T. (2001). *High reactivity of silicon suboxide clusters*, Phys. Rev. B64, pp. 113304 - 113308
- Zhang, R. Q.; Lee, C. S. & Lee, S. T. (2001). *The electronic structures and properties of Alq<sub>3</sub> and NPB molecules in organic light emitting devices: decompositions of density of states* J. Chem. Phys. 112, pp. 8614-8620
- Weast, R.C. (1968). editor of *Handbook of Chemistry and Physics*, the 48-th edition, The Chemical Rubber Publishing Co., F149
- Wilson, W.L.; Szajowski, P.F. & Brus, L.E. (1993). *Quantum Confinement in Size-Selected, Surface-Oxidized Silicon Nanocrystals*, Science 262, pp. 1242-1244
- Wolkin, M.V.; Jorne, J.; Fauchet, P.M. Allan, G. & Delerue, C. (1999). *Electronic states and luminescence in porous silicon quantum dots*, Phys. Rev. Lett. 82, pp. 197-200

# Gallium Nitride: An Overview of Structural Defects

Fong Kwong Yam, Li Li Low, Sue Ann Oh and Zainuriah Hassan  
*School of Physics, Universiti Sains Malaysia,  
Malaysia*

## 1. Introduction

### 1.1 Foreword

The III-V nitrides have long been viewed as promising semiconductor materials for their application in the blue and ultraviolet wavelengths optical devices, as well as high power and high temperature electronic devices. In the absence of a suitable gallium nitride (GaN) substrate, GaN, and related III-V materials are heteroepitaxially grown on sapphire or other substrates. GaN grown on sapphire normally contains a high density of threading dislocations in the range of  $10^{10}$  cm<sup>-2</sup> (Lester, 1995; Qian, 1995a; Hong & Cho, 2009) due to lattice constant and thermal expansion coefficient mismatches between GaN and sapphire. Besides threading dislocations, there are many other structural defects, such as, inversion domain, stacking mismatch boundaries, micropipes/nanopipes or voids, and surface pits. These defects will cause the periodicity of the crystal to be disrupted over distances of several atomic diameters from the defect and affect the optoelectronic properties of the devices. For example, threading dislocations have been found to act as nonradiative centers and scattering centers in electron transport that is detrimental to the performance of light emitting diodes and field-effect transistor (Ng et al., 1998). Dislocations defects cause rapid recombination of holes with electrons without conversion of their available energy into photons, i.e., nonradiative recombination, which causes heating up of the crystal and making optoelectronic devices malfunction (Hong & Cho, 2009; Garni et al., 1996). With the advancement of crystal growth technology, crystal defects in GaN have been reduced tremendously. The threading dislocations density in the GaN films has been reduced from the range of  $10^{10}$  cm<sup>-2</sup> to  $10^5$  cm<sup>-2</sup>. However, effort to further reduce the density of structural defects in GaN is strongly driven by the growth of high crystal quality thin films for fabrication of high performance optoelectronic devices.

### 1.2 The properties of GaN

Table 1 summarizes some of the most important properties of GaN. GaN shows many others superior properties compared to other semiconductor materials, such as high breakdown field of approximately  $5 \times 10^6$  V/cm as compared to  $3 \times 10^5$  and  $4 \times 10^5$  V/cm for silicon (Si) and gallium arsenide (GaAs) (Morkoc et al., 1994). GaN is also a very stable compound. Its chemical stability at elevated temperatures coupled with wide bandgap has made GaN an attractive material for device operation in high temperature and caustic environments.

<b>Wurtzite GaN</b>	
Bandgap energy	$E_g(200\text{K}) = 3.39\text{eV}$ ; $E_g(1.6\text{K}) = 3.50\text{eV}$
Temperature coefficient	$dE_g/(dT) = -6.0 \times 10^{-4} \text{ eV/K}$
Pressure coefficient	$dE_g/(dP) = 4.2 \times 10^{-3} \text{ eV/kbar}$
Lattice constant	$a = 3.189\text{\AA}$ ; $c = 5.185\text{\AA}$
Thermal expansion	$\Delta a/a = 5.59 \times 10^{-6} \text{ K}$ ; $\Delta c/c = 3.17 \times 10^{-6} \text{ K}$ ;
Thermal conductivity	$k = 1.3 \text{ W/cm K}$
Index of refraction	$n(1 \text{ eV}) = 2.33$ ; $n(3.38 \text{ eV}) = 2.67$
Dielectric constants	$\epsilon_0 = 8.9$ ; $\epsilon_\infty = 5.35$
<b>Zincblende GaN</b>	
Bandgap energy	$E_g(330\text{K}) = 3.2 - 3.3 \text{ eV}$
Lattice constant	$a = 4.52\text{\AA}$
Index of refraction	$n(3 \text{ eV}) = 2.9$

Table 1. The properties of GaN (Edgar, 1994).

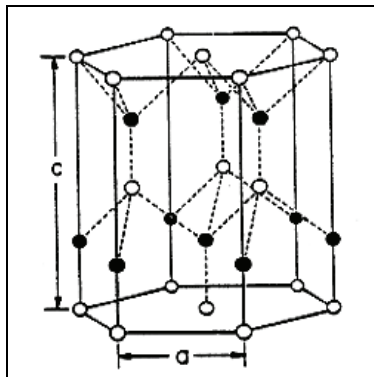


Fig. 1. The wurtzite crystal structure. The full circles are N, and open circles are Ga atoms. Adapted from ref. (Edgar, 1994).

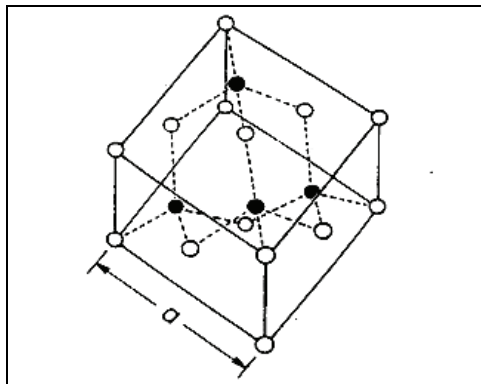


Fig. 2. The zincblende crystal structure. The full circles are N, and open circles are Ga atoms. Adapted from ref. (Edgar, 1994).



GaN can exist in 2 different structures, which are hexagonal wurtzite ( $\alpha$ -GaN) as shown in Fig. 1 and cubic zincblende ( $\beta$ -GaN) in Fig. 2 (Edgar, 1994). The former is the stable structure whereas the latter is the metastable structure.

For other technical data, readers are advised to refer to references (Morkoc et al., 1999a; Edgar & Liu, 2002; Parmer, 2008; Harima, 2002; Levinshtein et al., 2001; Nakamura & Chichibu, 2000; Henini & Razeghi, 2005).

## 2. Crystal defects

### 2.1 General classification of defects

The formation of defects during growth is unavoidable and can be classified by their dimensionality as (Spitsyn et al., 1993):

- a. Zero-dimensional defects or point defects, which are associated with a single atomic site (e.g. vacancies, interstitials and substitutional atoms).
- b. One-dimensional defects or line defects, which are associated with a direction (e.g. dislocations).
- c. Two-dimensional defects or planar defects, which are associated with a plane or area (e.g. grain boundaries, stacking faults, twins and inversion domain boundaries). Planar defects refer to the boundary between two orderly regions of a crystal. In other words, they are separate regions having different crystallographic orientations.
- d. Three-dimensional defects or volume defects, which are associated with a volume (e.g. voids, cracks and nanpipes)

#### 2.1.1 Point defects

In general, there are three main types of point defects: vacancies, interstitials and substitutional atoms.

An unoccupied regular crystal site is called a vacancy (Fig. 3). For a binary compound semiconductor, vacancies can either be cation or anion vacancies.

If an atom which does not occupy a regular crystal site but a site between regular atoms, it is called an interstitial impurity atom (Fig. 3). In order for an impurity atom to stay at an interstitial site, it must have sufficiently low energy there. This will be satisfied for interstitial sites which either have high local symmetry or which lie on a bond between two atoms. The incorporation of impurity atoms on interstitial sites is especially likely when the impurity atom deviates relatively strongly from the atoms of the host crystal.

However, interstitials may also come from atoms of the crystal itself. If a chemically compatible atom of the crystal occupies an interstitial site rather than a regular one, a self-interstitial is produced. For this type of point defect to develop in a crystal, there must be enough space between the host atoms, i.e. the crystal should not be packed too densely.

When an impurity atom substitutes an atom of the host crystal (Fig. 3), it is referred to as a substitutional impurity. In a binary compound semiconductor, the substitutional incorporation occurs on the lattice site which corresponds to the most chemically similar of the two atoms of the compound. Substitutional impurity can be introduced into the crystal either intentionally (controlled doping) or unintentionally (contaminants). Examples of common unintentional substitutional impurities in GaN are oxygen and carbon. Oxygen occupies N sites. As for carbon, calculations show that carbon is an amphoteric impurity in

GaN (Boguslavski et al., 1996) although however, the incorporation of carbon on nitrogen sites is preferable since the formation energy is lower.

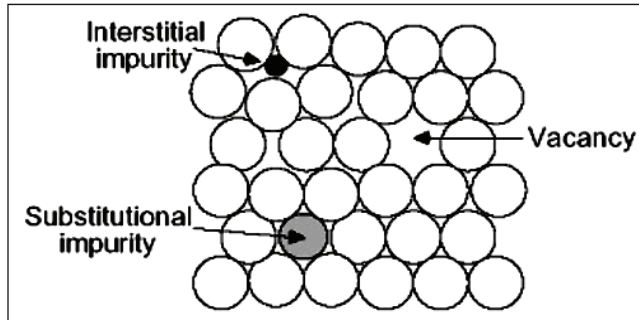


Fig. 3. Schematic representation of common point defects.

Substitution may also come from atoms of the crystal itself. In a binary semiconductor which consists of two different chemical elements, an atom of the first may occupy a regular site of the second, and vice versa. Such point defects are called antisite defects.

From the explanation above, it is apparent that point defects can be categorized as intrinsic or extrinsic. Intrinsic point defects encompass vacancies, self-interstitials and antisites, since they come from the crystal itself. Meanwhile extrinsic point defects, which involve foreign atoms, comprise of substitutional, impurities and interstitial impurities.

### 2.1.2 Dislocations

Dislocations are defined as abrupt changes in the regular ordering of atoms along a dislocation line in the solid. Dislocations are mostly due to misalignment of atoms or presence of vacancies along a line. The interatomic bonds are significantly distorted only in the immediate vicinity of the dislocation line called the dislocation core. Dislocations also create small elastic deformations of the lattice at large distances that cause lattice distortion centered around a line. They are characterized by the Burgers vector  $\vec{b}$ , which describes the unit slip distance in terms of magnitude and direction. The classification for dislocations are as follows:

1. Edge dislocation;
2. Screw dislocation; or
3. Mixed dislocation, which contains both edge and screw dislocation components.

An edge dislocation (Fig. 4(a)) may be described as an extra plane of atoms squeezed into a part of the crystal lattice, resulting in that part of the lattice containing extra atoms and the rest of the lattice containing the correct number of atoms. The part with extra atoms would therefore be under compressive stresses, while the part with the correct number of atoms would be under tensile stresses. In an edge dislocation, the Burgers vector is perpendicular to the dislocation line. Screw dislocations (Fig. 4(b)) result when planes are displaced relative to each other through shear. In this case, the Burgers vector is parallel to the dislocation line (W.F. Smith, 1996). In real crystals, however, most dislocations have mixed edge/screw character.

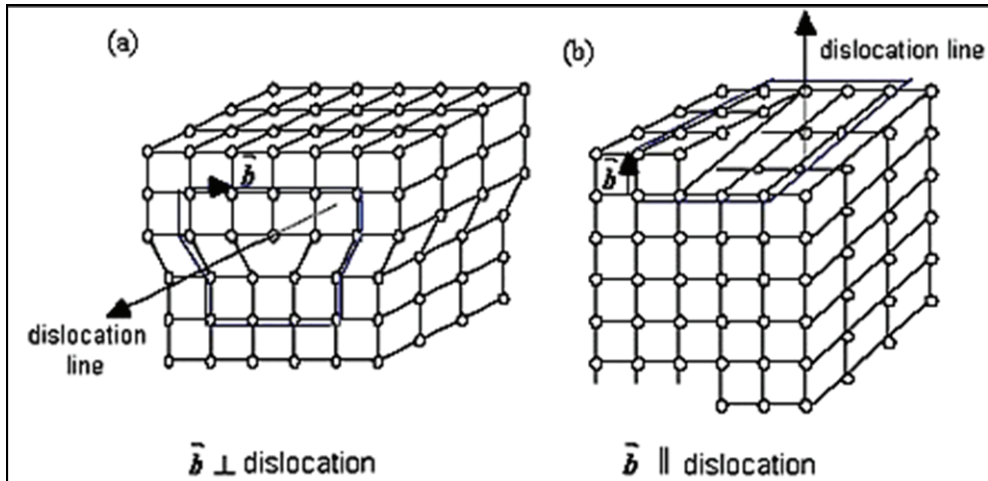


Fig. 4. Schematic representation of (a) edge dislocation (b) screw dislocation.

### 2.1.3 Stacking faults

Stacking faults, as the name implies, are partial displacements which upset the regular sequence in the stacking of lattice planes. For example, in the zinc blended packing sequence, ABCABC..., one of the lattice planes may be out of sequence due to a stacking fault, and become ..ABABCABC.... The result is then a mixture of zinc blende and wurtzite stacking.

In wurtzite structure, there are two types of stacking faults: basal stacking faults and prismatic stacking faults. Basal stacking faults consists of intrinsic ( $I_1$  and  $I_2$ ) types and an extrinsic ( $E$ ) type. They can be treated as thin layers of cubic stacking.  $I_1$ ,  $I_2$  and  $E$  correspond to 3 (e.g. ABC), 4 (e.g. ABCA) and 5 (e.g. ABCAB) bi-atomic layers of cubic structure, respectively. Prismatic stacking faults form on prismatic  $\{1210\}$  planes with a displacement vector of  $\frac{1}{2} [0111]$ . When the sample is viewed in cross-section along the  $[0001]$  zone axis, prismatic stacking faults are seen as zig-zags formed on  $(2110)$  and  $(1210)$  planes (Hull & Bacon, 1984). It was found that prismatic stacking faults terminate  $I_1$ -type basal stacking faults and therefore sometimes their presence can be beneficial. Star-rod dislocations are expected at the intersection of prismatic stacking faults and basal stacking faults when their displacement vectors are not equal. Theoretical calculations predict high formation energy for prismatic stacking faults (Northrup, 1998) of about 30 times higher than that calculated for  $I_2$  basal stacking faults (Zakharov et al., 2005).

### 2.1.4 Stacking mismatch boundaries

Stacking mismatch boundaries originate at substrate/film interface. Stacking mismatch boundaries are created by surface steps on substrates which cause nucleation and growth of separate III-nitrides domains at different levels: stacking disorder must occur across the domain boundaries. The formation of these domains is believed to account for the relaxation of the large lattice and thermal mismatches between nitrides and substrate. These stacking irregularities are also known as double positioning boundaries.

### 2.1.5 Grain boundaries

Polycrystalline materials comprise of grains of single crystals with different crystallographic orientation. Each grain is surrounded by a layer of interconnecting boundary atoms in amorphous phase, called grain boundary (Fig. 5).

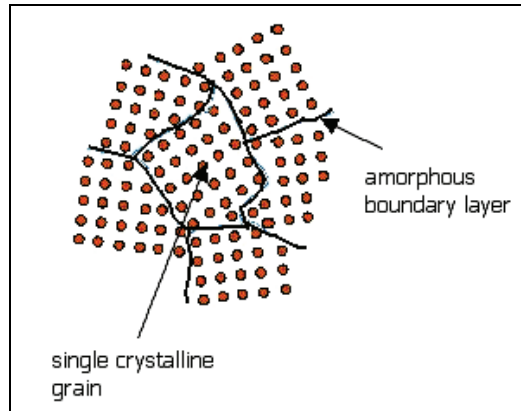


Fig. 5. Schematic representation of a polycrystalline surface.

### 2.1.6 Twins

A twin (Fig. 6) is an area defect in which a mirror image of the regular lattice is formed, where the twin boundary is the mirror plane of the twin formation. The atomic displacements during twinning increase with distance from the twin boundary.

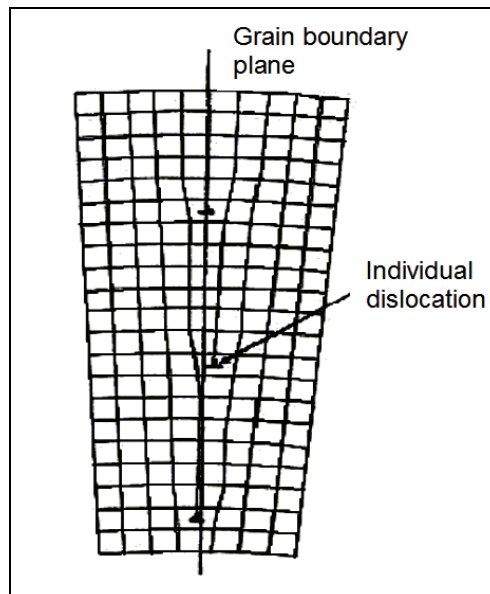


Fig. 6. Schematic diagram of a twin.

### 2.1.7 Inversion domains

This defect originates from the nucleation layer and has a filamentary nature. Inversion domains may not be easily distinguished from pure dislocations (Ponce et al., 1997).

### 2.1.8 Nanopipes

They are tunnel-like defects which are aligned along the growth direction of the crystal and penetrate the film. Like inversion domains, they have a filamentary nature and may not be easily distinguished from pure dislocations (Ponce et al., 1997).

## 2.2 Crystal defects caused by strain

One of the causes of defects is the strain due to lattice and thermal mismatch between film and substrate. The lattice and thermal mismatch induce residual strain in the III-V nitrides films (the term “residual” emphasizes the fact that the stress remains after all external forces are removed). When speaking of strain generated due to mismatch with the substrate, it is usually in reference to the biaxial strain in the plane of the layer (i.e. along the a-axis) (Fig. 7). In the perpendicular direction (i.e. along the c-axis), there will be a corresponding strain. Because strain in thin films is governed by both lattice and thermal mismatch, the dominating strain contribution will be determined by growth conditions such as growth temperature and the degree of the mismatch.

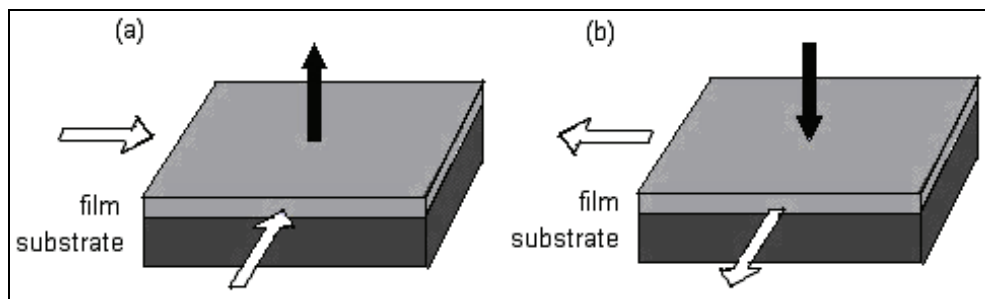


Fig. 7. Biaxial strain (white arrows) in a film grown on a lattice and thermally-mismatched substrate: (a) compressive strain (black arrow indicates the corresponding tensile strain in the perpendicular direction); (b) tensile strain (black arrow indicates the corresponding compressive strain in the perpendicular direction).

### 2.2.1 Lattice mismatch

When a film is grown on a substrate of different lattice constant, the film will expand (tensile strain) or contract (compressive strain) to accommodate the different lattice constant of the substrate. The type of strain which the film will be subjected to depend on whether the lattice constant is larger or smaller than that of the substrate. If the lattice constant of the film is larger than that of the substrate, the film will be subjected to compressive strain but if the lattice constant of the film is smaller than that of the substrate, the film will be under tensile strain (Fig. 8). Technically, a compressive strain in the film should go hand in hand with a tensile strain in the substrate, and vice versa. However, the substrate experiences negligible expansion or contraction due to its much larger thickness in comparison to the film. As a note, the lattice constant value of III-V nitrides is influenced by the growth conditions, impurity concentrations and film stoichiometry.

### 2.2.2 Thermal mismatch

The thermal expansion coefficient describes the change in length (linear thermal expansion coefficient) or volume (volume thermal expansion coefficient) of a material. With regard to GaN growth, it is the linear thermal expansion coefficient that is usually referred to, and it is defined as (Ibach & Lüth, 1996)

$$\alpha_L = \frac{1}{L} \frac{dL}{dT} \quad (1)$$

where  $L$  is length and  $T$  is temperature.

When a sample is cooled down after growth, a difference in the thermal expansion coefficient between substrate and film may cause strain to develop, to a degree dependent on the cool down procedure and if any defect formed during the cool-down is not sufficient to cause complete relaxation.

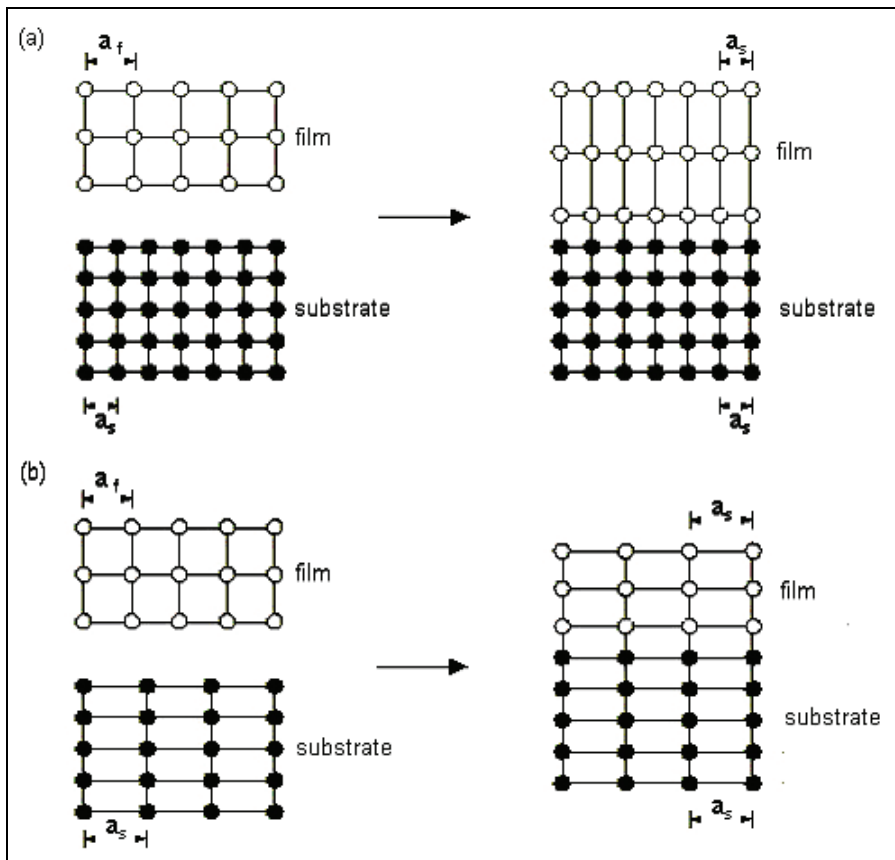


Fig. 8. Strain induced in a film grown on a substrate of different lattice constant: (a) for  $a_f > a_s$ , compressive strain in the plane of the film, with corresponding tensile strain in the direction perpendicular to the plane of the film; (b) for  $a_f < a_s$ , tensile strain in the plane of the film, with corresponding compressive strain in the direction perpendicular to the plane of the film.

### 2.2.3 Effect of strain on properties of III- nitrides

Certain properties of III-nitrides will be affected by the presence of strain. It has been found that strain in the film during growth can alter the surface mobility of Ga ad-atoms and consequently the growth mode, thereby vastly influencing the surface morphology (Fujii, 1997)

Also, strain has been known to cause the lattice constant of a crystal to increase (tensile strain) or decrease (compressive strain). The change in lattice constant from the unstrained value, or in other words, strain measurement, is typically investigated using x-ray diffraction.

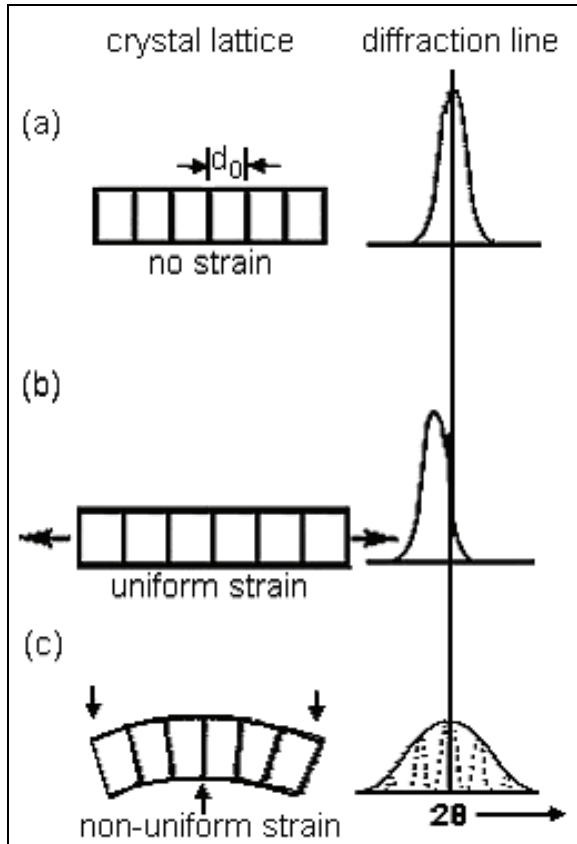


Fig. 9. Effect of lattice strain on x-ray diffraction peak width and position: (a) no strain; (b) uniform strain; (c) non-uniform strain. The vertical lines in the drawing for the crystal lattice represent the diffracting planes, and  $d_0$  is the equilibrium (strain-free) plane spacing. After ref (Cullity, 1967).

Basically, there are two types of strain - the uniform type and the non-uniform type. Therefore, there are two types of diffraction effects, i.e. peak shift and peak broadening, as illustrated in Fig. 9 (b and c). Fig. 9(a) shows the strain-free condition for comparison. Note that the crystal lattice shown in Fig. 9 represents a portion of a grain.

If the strain is uniform over large distances, it is called macrostrain and the equilibrium plane spacing  $d_0$  will become either larger (tensile strain) or smaller, (compressive strain) resulting in a shift in the diffraction peaks in the pattern. If  $d_0$  increases due to tensile strain as shown in Fig. 9(b), the diffraction peak will shift to lower angles. Conversely, if compressive strain acts on the grain instead, causing a reduction in  $d_0$ , the peak will shift to higher angles. Macrostrain is usually the result of biaxial strain caused by the substrate.

On the other hand, if strain varies from one grain to another or from one part of a grain to another part on a microscopic scale, it is called microstrain. Microstrain is produced by a distribution of tensile and compressive strain which causes the grain to be bent (Fig. 9(c)). On the top (tension) side, the plane spacing exceeds  $d_0$ ; on the bottom (compression) side, it is less than  $d_0$ ; somewhere in between, it equals  $d_0$ . This grain can be imagined to be composed of a number of small regions in each of which the plane spacing is substantially constant but different from the spacing in adjoining regions. These regions cause the various sharp diffraction peaks indicated in Fig. 9(c). The sum of these sharp peaks, each slightly displaced from the other, is the broadened diffraction peaks shown by the full curve, which is the only one experimentally observable. The common causes of microstrain are defects (grain boundaries, dislocations, point defects, shear planes, etc). Point defects introduce an internal strain that can be compressive or tensile depending on the size of the involved impurities. The effect will generally be a distribution of peaks around the unstressed peak location, and a crude broadening of the peak in the resultant pattern.

Actually, both kinds of strain are usually superimposed in the material and diffraction peaks are both shifted and broadened.

The change in interatomic distance due to strain field is also known to have a strong effect on the band gap energy for a semiconductor. In films subjected to compressive strain, an increase in band gap and excitonic energies are frequently observed while in films experiencing tensile strain, there would be a decrease in band gap and excitonic energies (Morkoc, 1999a; Monemar, 1997).

Phonon frequencies are also affected by strain. In general, compressive strain causes an upshift in phonon frequencies while tensile strain causes a downshift.

Strain in the film due to the thermal and lattice mismatch may also induce defects such as dislocations, which act as a form of strain relief. Such defects may be detrimental to the film quality. Conversely, the presence of defects can also induce strain. For instance, grain boundaries in polycrystalline materials may produce compressive strain on the surface of the film. Meanwhile, point defects introduce strain which depends on the size and type of the defect (vacancies and substitutional impurities smaller than the substituted host atom introduce compressive strain; interstitials and substitutional impurities larger than the substituted host atom introduce tensile strain). Therefore, the presence of strain in III-Nitrides films is generally undesirable as it usually corresponds to the presence of defects.

### 3. Substrates

The high melting temperature and dissociation pressure are the main obstacles in obtaining large single GaN crystal, which can serve as substrate for homoepitaxial growth. Therefore single crystalline film has to be grown heteroepitaxially on a number of substrates that share more or less similar lattice constants and thermal expansion coefficient of GaN.

The density of threading dislocation defects in GaN films is always in the range of  $10^{10}$  cm<sup>-2</sup>. These defects originate from the substrate/GaN interface and propagate into the epilayer.



The large difference of lattice constant and thermal expansion coefficient between the substrate and GaN is considered to be the major factor attributing to the high density of this defect.

Table 2 shows the lattice constant and thermal expansion coefficient for some prospective substrates (Edgar, 1994;).

Substrate material	Lattice Parameters (Å)	Thermal Conductivity (W/cm-K)	Coef. of Thermal Expansion (10 <sup>-6</sup> /K)
Wurtzite GaN	a = 3.189	1.3	5.59
	c = 5.185		3.17
Wurtzite AlN	a = 3.112	2	4.2
	c = 4.982		5.3
*6H-SiC	a = 3.08	4.9	4.2
	c = 15.12		4.68
$\alpha$ -Al <sub>2</sub> O <sub>3</sub>	a = 4.758	0.5	7.5
	c = 12.99		8.5
Si	a = 5.4301	1.5	3.59
GaAs	a = 5.6533	0.5	6

Table 2. Properties of some prospective nitride substrates. \*6H refers to stacking sequence: ABCACB (Pearnton, 1997a).

Sapphire exhibits a higher thermal expansion coefficient relative to GaN, and for silicon carbide (6H-SiC), the thermal expansion coefficient is smaller than GaN. At cool down after growth, the GaN films grown on sapphire and 6H-SiC will experience compressive and tensional biaxial strain respectively (Pearnton, 1997b). However, with the formation of threading dislocations, the strain in the GaN epilayer will be released.

Although sapphire (Al<sub>2</sub>O<sub>3</sub>) possesses a substantially different lattice constant and thermal expansion coefficient from GaN, it is still the most commonly used substrate for GaN growth because of its wide availability, hexagonal symmetry, and ease of handling and pregrowth cleaning. Sapphire is also stable at high temperature (~1000°C), which is normally required for GaN film grown by metalorganic chemical vapor deposition method. Si is another potential substrate due to the low price, high quality and wide availability as well as easy integration with the current silicon technology. Both Si (110) and (111) are employed for wurtzitic GaN growth (Yokouchi et al., 1996). However, GaN grown on Si (001) is predominantly cubic (Pearnton, 2000).

6H-SiC exhibits a closer lattice constant and thermal expansion coefficient to GaN, however, this substrate is very expensive. GaAs has been used as substrate despite its poor compatibility. This is mainly due to its widely availability and familiarity of the researchers. Other uncommon substrates such as MgO (Powell et al., 1990), ZnO (Sitar, 1990), MgAl<sub>2</sub>O<sub>4</sub> (Tempel et al., 1975) etc., also have been used as substrate, however, the use of these substrates need to be further developed and explored.

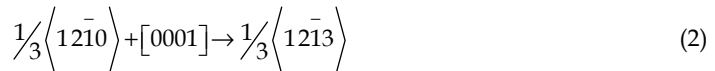
To obtain the highest quality of GaN substrates in term of dislocation density, advances dislocation elimination by the epitaxial growth with inverse-pyramidal pits procedure was developed by Sumitomo Electric Industries (Japan) (Motoki, 2010). The substrates contain 400-mm-wide stripes of very low dislocation density GaN (10<sup>5</sup> cm<sup>-2</sup>) separated by dislocated areas of GaN with inversed polarity. It is about five-order of magnitude lower than the typical reported value.

## 4. Defects in GaN films and formation mechanisms

### 4.1 Threading dislocation

D. Kapolnek (Kapolnek et al., 1995) proposed that in GaN films grown by metalorganic chemical vapor deposition on sapphire, the source for dislocation is the nucleation layer itself. During island coalescence, edge threading dislocation segments may be generated when misfit edge dislocations between adjacent island are spatially out of phase. The generation of screw dislocations appears to be more complex, they found out that pure screw or mixed threading dislocations do decrease with the film thickness, due to the ease of cross slip of screw dislocations.

Kyoyeol Lee (Lee & Auh, 2001) studied the dislocation density of GaN on sapphire grown by hydride vapor phase epitaxy. They found that the reduction of threading dislocation sites occurred with increasing GaN films thickness. Similarly, F. R. Chien (Chien et al., 1996) also investigated growth defects in GaN films grown by metalorganic chemical vapor deposition on 6H-SiC substrate, and reported that dislocation density decreases rapidly with the increase of GaN film thickness from the interface. The predominant defects in GaN films grown on 6H-SiC with aluminium nitride (AlN) buffer layer are edge type threading dislocations along [0001] growth direction with Burgers vector  $1/3 \langle 12\bar{1}0 \rangle$ . The reduction in dislocation density is due to the formation of half-loops. Besides this, dislocation reaction also plays a role, for example, two dislocations interact and merge to produce one dislocation, according to the reaction:



These dislocations originated at AlN/SiC interface to accommodate the misorientation of neighboring domains formed from initial island nuclei, which are twisted and tilted with respect to the substrate surface.

### 4.2 Stacking faults

There have been reported that stacking faults formed in GaN layers grown on polar and non-polar substrates are different. For the growth in polar direction, stacking faults are formed on the basal plane (c-plane) since their formation energy is the lowest on this plane. If growth is taking place on the c-surface, these faults will be located on planes parallel to the substrate (Fig. 10(a)). While for the growth in non-polar direction, stacking faults are formed on basal planes (c- planes) that are along growth direction (Liliental-Weber, 2008), since their formation energy on these planes is the lowest and they will be arranged perpendicular to the substrate (Fig. 10(b)).

On the other hand, F. Gloux (Gloux et al., 2008) studied the structural defects of GaN implanted with rare earth ions at room temperature and 500°C. The crystallographic damage induced in GaN by 300 keV rare earth ions implantation has been investigated as a function of the implantation temperature. It consists of point defect clusters, basal and prismatic stacking faults. The majority of basal stacking faults is  $I_1$ . The density of stacking faults after 500°C implantation is significantly smaller than after implantation at room temperature.

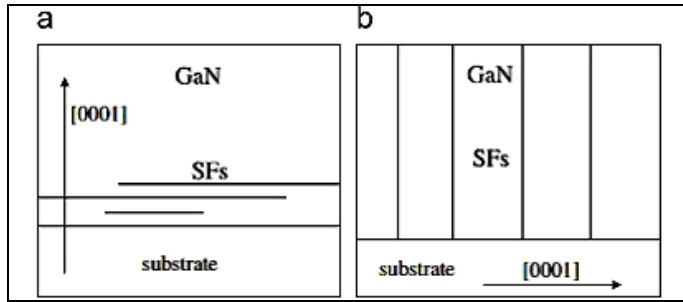


Fig. 10. Schematic of the arrangement of basal stacking faults (long lines) in GaN grown on: (a) polar surface and (b) non-polar surface. After ref (Liliental-Weber, 2008).

### 4.3 Stacking mismatch boundaries

Stacking mismatch boundaries have been observed by B. N. Sverdlov (Sverdlov et al., 1995). By using the same growth method on 6H-SiC substrate, they showed that the defects originate at substrate/film interface. The boundaries between differently stacked hexagonal domains are called stacking mismatch boundaries. Stacking mismatch boundaries are created by surface steps on substrates. Fig. 11 shows the cross-section atomic model of wurtzite GaN grown on 6H-SiC in (0001) direction. It explains how the stacking mismatch boundary is formed in the GaN/SiC interface.

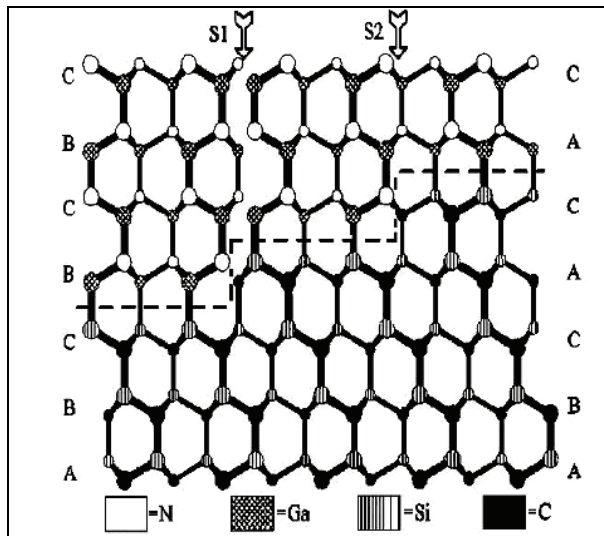


Fig. 11. Cross-section atomic model of wurtzite GaN grown on 6H SiC in the (0001) direction. Steps on the SiC surface are likely to create stacking mismatch boundaries as indicated by arrow S1, although certain steps do not lead to stacking mismatch boundaries as indicated by arrow S2. The circle sizes and line widths are used to give a three-dimensional effect and have no relation to atomic size or bond strength. The cross section is a bilayer where the large circles and lines are raised out of the plane above the small circles and lines. After ref (Sverdlov et al., 1995).

D. J. Smith (D.J. Smith et al., 1995) reported that the defects in wurtzite GaN grown on 6H SiC using plasma enhanced molecular beam epitaxy can be identified as double-position boundaries, which originate at the substrate-buffer and buffer-film interfaces. The density of these defects seems to be related to the smoothness of the substrate.

#### 4.4 Grain boundaries

H. Z. Xu and co-workers (Xu et al., 2001) studied the effect of thermal treatment on GaN epilayer on sapphire substrate grown by metalorganic chemical vapor deposition. They found that GaN crystal grains formed during high temperature growth are not perfectly arranged, and misorientation of crystal grains occur in both a- and c- axes due to fast surface migration and clustering of atoms. The stacking faults, edge and mixed dislocations will be generated at grain boundaries to compensate the misorientation during coalescence of laterally growing crystal grains.

Table 3 summarizes the source of threading dislocations/stacking mismatch boundaries and grain boundaries discovered/shown by different researchers. From the summary, we can observe that the source of the defect is closely linked to substrates and growth techniques used. Different growth technique but same substrate or vice-versa could induce different defect formation mechanisms.

Growth method	Substrate	Type of Defect	Source of Defect	Ref.
MOCVD	Sapphire	Threading dislocations	<ul style="list-style-type: none"> <li>Nucleation layer</li> </ul>	Kapolnek et al., 1995
MOCVD	6H-SiC	Threading dislocations	<ul style="list-style-type: none"> <li>The tilt of misaligned island nuclei with respect to the substrate surface</li> </ul>	Chien et al., 1996
PE-MBE	6H-SiC	Stacking mismatch boundaries	<ul style="list-style-type: none"> <li>Substrate/buffer and buffer/film interfaces</li> <li>Steps on substrate Nonisomorphic with wurtzite GaN.</li> </ul>	Sverdlov et al., 1995
PE-MBE	6H-SiC	Stacking mismatch boundaries	<ul style="list-style-type: none"> <li>Substrate/buffer and buffer/film Interfaces.</li> </ul>	D.J. Smith et al., 1995
MOCVD	Sapphire	Grain boundaries	<ul style="list-style-type: none"> <li>Misorientation of crystal grains.</li> </ul>	Xu et al., 2001

Table 3. Source of threading dislocations/stacking mismatch boundaries and grain boundaries defects from different substrates and growth techniques. (MOCVD: metalorganic chemical vapor deposition; PE-MBE: plasma enhanced molecular beam epitaxy)

#### 4.5 Inversion domain

Inversion domains consist of region of GaN with the opposite polarity to the primary matrix as schematically depicted in Fig. 12, where the section on the left is of Ga polarity and the

section on the right is of N polarity. The boundaries between them are called inversion - domain boundaries (F. Liu et al., 2007). When inversion domains happen, the alternating nature of anion-cation bonds can not be fully maintained. Inversion domains combined with any strain in nitride-based films lead to flipping Piezo Electric (PE) field with untold adverse effects on the characterization of nitride-based films in general and the polarization effect in particular, and on the exploitation of nitride semiconductor for devices. Pendeo-epitaxy also causes much decreased scattering of carriers as they traverse in the *c*-plane (Morkoc et al., 1999b).

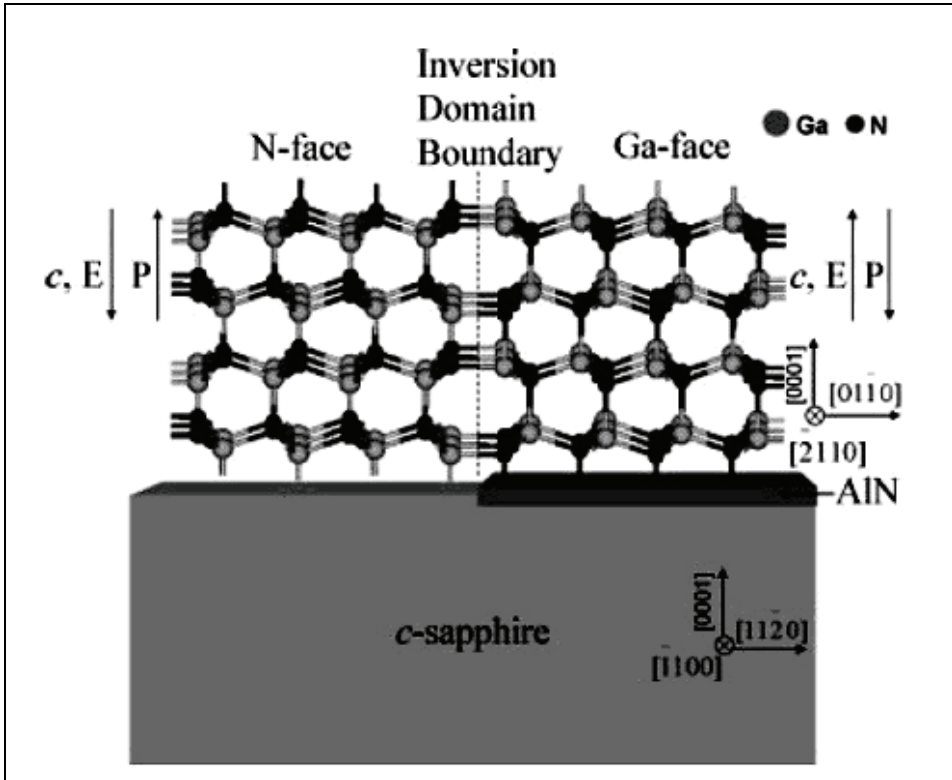


Fig. 12. Schematic view of the widely cited GaN inversion domain boundary structure on a sapphire substrate (not drawn to scale). A thin AlN layer ( $>5$  nm) is often applied to invert the polarity of GaN. On the left side, the GaN lattice has N-face polarity, the crystallographic *c*-axis and the internal electric field *E* point toward the interface with the substrate, and the macroscopic polarization *P* points toward the surface. On the right side, the directions are inverted. After ref (F. Liu et al., 2007).

Romano (Romano et al., 1996; Romano & Myers, 1997) reported that the nucleation of inversion domains may result from step related inhomogeneities of GaN/sapphire interface. The possible cause of this defect is inhomogeneous nitridation on the sapphire substrate due to remnant high energy ion content in the nitrogen flux from rf-plasma source. Fig. 13 shows that an inversion domain boundary nucleates at a step on the sapphire substrate. The

density of this defect depends on the growth technique and substrate pre-treatment prior to the growth. For GaN films grown by electron cyclotron resonance-molecular beam epitaxy on substrates nitrified before growth of the GaN buffer layer, the density of inversion domains was reduced to approximately 50%.

Differences in surface morphology were directly linked to the presence of inversion domains, which originated in the nucleation layer. Nitrogen-rich growth and growth under atomic hydrogen enhanced the growth rate of inversion domains with respect to the surrounding matrix.

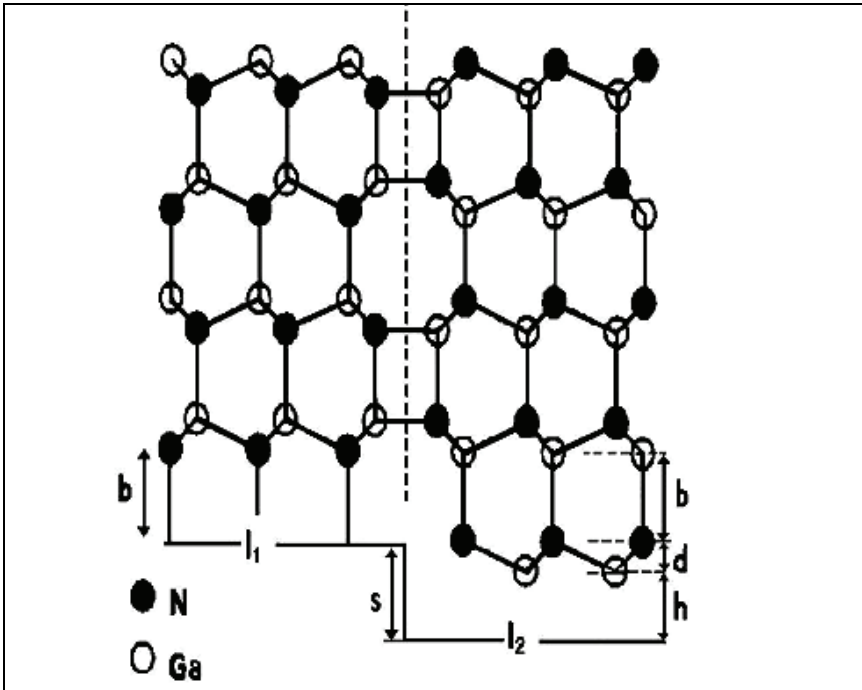


Fig. 13. Schematic  $[11\bar{2}0]$  projection of an inversion domain boundary which has nucleated at a step on sapphire. Two different interfaces,  $I_1$  and  $I_2$ , form on the upper and lower terraces. The Ga-N bond length is  $b=1.94 \text{ \AA}$ , the sapphire step height is  $s=2.16 \text{ \AA}$ , and  $h=s-d=1.5 \text{ \AA}$ . After ref (Romano et al., 1996).

J. L. Weyher and co-workers (Weyher et al., 1999) studied morphological and structural characteristic of homoepitaxial GaN grown by metalorganic chemical vapor deposition. They found that GaN grown on N-polar surface of GaN substrate exhibits gross hexagonal pyramidal features. The evolution of pyramidal defects is dominated by the growth rate of an emergent core of inversion domain. The inversion domains nucleate at a thin band of oxygen containing amorphous material, which are contaminated from the mechano-chemical polishing technique used to prepare the substrate prior to growth.

Inversion domains were also believed to be linked to the formation of columnar structure with a faceted surface and stacking faults. T. Araki (Araki et al., 2000) studied GaN grown on sapphire by hydrogen-assisted electron cyclotron resonance-molecular beam epitaxy,

and found that GaN layer change from 2-dimension to 3-dimension growth by adding hydrogen to nitrogen plasma. They assumed that the inversion domains of polarity existed on the buffer layer, which led to the formation of this defect.

The origin of inversion domains in Ga polar on GaN is not well defined. In the paper (Łuczniak et al., 2009), it showed that most probably they were formed because of some technical reasons (e.g imperfect substrate preparation). According to J.L. Weyher (Weyher et al., 2010), the simple methods to recognize the present of inversion domains are hot KOH water solution, molten eutectic of KOH/NaOH and photo-etching.

B. Barbaray (Barbaray et al., 1999) reported inversion domains were generated at substrate steps in GaN/(0001) Al<sub>2</sub>O<sub>3</sub> layers. Steps of height  $c$ -Substrate/3=0.433 nm were found to give rise to extended defects in the epitaxial layer. These defects were inversion domains whose boundary atomic structure was found to be described by the Holt model. The investigation of steps on the substrate showed that discontinuities of the substrate surface create defects in the deposited layers. They proposed that inversion domains can be due to the mismatch along  $c$  between the substrate and the deposit. A geometrical analysis showed that the formation of Holt or inversion domain boundaries minimizing the shift along the growth axis.

A.M. Sańchez (Sańchez et al., 2002) studied the AlN buffer layer thickness influence on inversion domains in GaN/AlN/Si(111) heterostructures grown by plasma assisted molecular beam epitaxy. Inversion domains density inside the GaN epilayers, is higher in the sample with a smaller buffer layer thickness. The N-polarity leads to a higher inversion domains density when reaching the GaN surface.

#### 4.6 Nanopipes

Another type of defect found in GaN films is nanopipes, also called micropipes by some researchers. This defect has the character of open core screw dislocation. The oxygen impurity is considered to be closely linked with the formation of this defect by poisoning the exposed facet walls thereby preventing complete layer coalescence. There is evidence from the observation of void formation along dislocations. Speculation is made on a generalized pipe diffusion mechanism for the loss of oxygen from GaN/sapphire interface during growth. This leads to the poisoning of  $\{10\bar{1}0\}$  side walls that allows nanopipes to propagate, or to the formation of void (Brown, 2000).

W. Qian (Qian, 1995b) reported similar type of defect in GaN film on  $c$ -plane sapphire grown by metalorganic chemical vapor deposition. Tunnel-like defects are observed and aligned along the growth direction of crystal and penetrate the epilayer. This provides evidence that the nanopipes occur at the core of screw dislocation. However they did not elaborate clearly about the formation mechanism of this structural defect.

Elsner (Elsner et al., 1998) studied the effect of oxygen on GaN surfaces grown by vapor phase epitaxy on sapphire. They found that oxygen has a tendency to segregate to the  $(10\bar{1}0)$  surface and identified the gallium vacancy surrounded by 3 oxygen (where 3 nitrogen atoms were replaced) impurities  $[V_{Ga}-(O_N)_3]$  to be a stable and inert complex. These defects increase in concentration when internal surfaces grow out. When a critical concentration of the order of a monolayer is reached further growth is prevented. A schematic defect complex model was proposed (Fig. 14) based on the calculation of the defect formation energy.

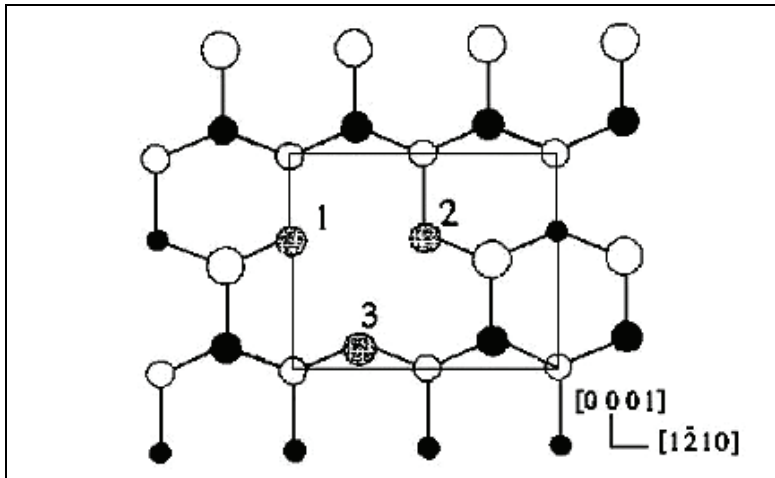


Fig. 14. Schematic top view of the  $V_{Ga}-(O_N)_3$  defect complex at the  $(10\bar{1}0)$  surface of wurtzite GaN. White (black) circles represent Ga (N) atoms and large (small) circles top (second) layer atoms. Atoms 1 and 2 are threefold coordinated second layer O atoms each with one lone pair, atom 3 is a twofold coordinated first layer O with two lone pairs. After ref (Elsner et al., 1998).

Elsner also proposed another possible nanopipe formation mechanism. They suggested that oxygen atoms constantly diffuse to the  $(10\bar{1}0)$  surface. Within the frame work of island growth, the internal  $(10\bar{1}0)$  surfaces between GaN islands are shrinking along with the space colliding GaN islands (Fig. 15).

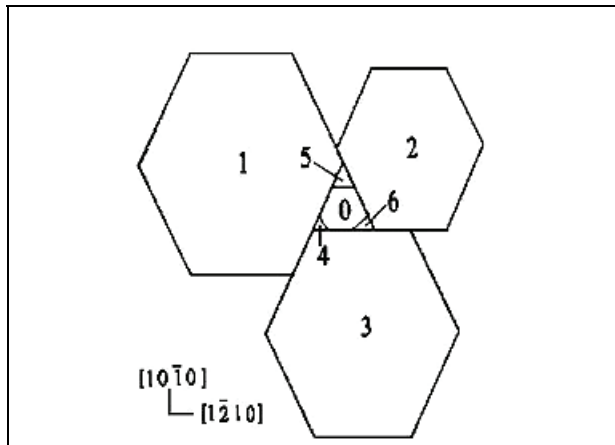


Fig. 15. Schematic view (in  $[0001]$ ) of the formation of a nanopipe (area No. 0). Three hexagons (Nos. 1, 2, and 3) are growing together. As the surface to-bulk ratio at ledges (Nos. 4, 5, and 6) is very large, they grow out quickly leaving a nanopipe (area No. 0) with  $\{10\bar{1}0\}$ -type facets. After ref. (Elsner et al., 1998).



E. Valcheva (Valcheva et al., 2002) studied the nanopipes in thick GaN films grown at high growth rate. They are observed to behave like screw component threading dislocations, terminating surface steps by hexagonal pits, and thus leading to the possibility of spiral growth. The mechanism of formation of nanopipes is likely due to the growth kinetics of screw dislocations in the early stages of growth of highly strained material.

## 5. Effect of defects on properties of GaN

As already mentioned in section 2.2.3, defects may introduce strain in GaN films, which consequently leads to effects such as change in the lattice constant and band gap energy.

Apart from that, defects form donor or acceptor levels in the band gap which are otherwise forbidden. For example, the nitrogen vacancy manifests itself as a shallow donor in GaN (Jenkins et al., 1992). Although yet to be established unequivocally, the nitrogen vacancy is considered to be the most plausible cause of the native n-type behaviour of most as-grown GaN (Jenkins et al., 1992; Maruska & Tietjen, 1969; Perlin et al., 1995; Boguslavski et al., 1995; Kim et al., 1997). However, there are conflicting arguments from some researches. For instance, Neugebauer and Van de Walle (Neugebauer & Van de Walle, 1994) suggested that the formation of the nitrogen vacancy in n-type material is highly improbable based on their first-principles calculations, by reason of high formation energy. Instead, impurities such as silicon and oxygen were suggested as possible sources of the autodoping. Nevertheless, nitrogen vacancies are the source of n-type doping in GaN, since it is the most commonly accepted argument.

The defect-related levels in the band gap may be the source of radiative recombination centres in devices, leading to below gap optical emission. Such emission is usually broad and is generally dominant except in very pure material or in thin layer structures that exhibit quantum confinement (Stradling & Klipstein, 1991). A common defect-related emission in n-type GaN is the infamous yellow emission which occurs at  $\sim 2.2$  eV. According to first principles calculations by Neugebauer et al. (Neugebauer & Van de Walle, 1996), the gallium vacancy is the most likely source of the yellow emission. Ponce et al. (Ponce et al., 1996) found that the yellow band is associated with the presence of extended defects such as dislocations at low angle grain boundaries or point defects which nucleate at the dislocation. However, its origin is still not well understood and more research would be required to firmly establish the source of this luminescence.

On the other hand, defects such as dislocations may act as non-radiative centres that may decrease device efficiency. For example, dislocations can form non-radiative centres and scattering centres in electron transport that limits the efficiency of light emitting diodes and field-effect transistors (Ng et al., 1998). Meanwhile, Nagahama (Nagahama et al., 2000) found that the lifetime of the laser diode is dependent on the dislocation densities in GaN.

In general, the presence of structural defects is undesirable as it could lead to poor device quality such as low mobility and high background carrier concentrations, and poor optoelectronic properties.

## 6. Common techniques used to reduce structural defects

### 6.1 Reduction of threading dislocations by intermediate layer

Quite a number of reports have been published to improve the threading dislocations by using intermediate temperature buffer layer. Motoaki Iwaya and co-workers (Iwaya et al.,

1998) showed a reduction of structural defect in metalorganic chemical vapor deposition grown GaN on sapphire by insertion of low temperature deposited buffer layer between high temperature grown GaN. They developed two-buffer layer sequence, which was reported to be effective in eradicating the etch pits. They assumed that the origin of etch pit was in the microtubes, and the origin of microtubes was believed to be in the screw dislocations.

H. Amano (Amano et al., 1999) showed that by inserting a series of low temperature deposited GaN interlayers or AlN interlayers grown at 500°C between high temperature grown GaN layers, the quality of GaN film is improved due to the reduction of the threading dislocation density. A further reduction in threading dislocations density was observed with the increased number of low temperature interlayers. Fig.16 schematically shows the structure of the sample. They reported that one interlayer could reduce threading dislocation density by about 1 order of magnitude. And 2 orders of magnitude reduction was found by using 5 interlayers. However, a high number of low temperature deposited GaN interlayers would increase the level of stress in material that will lead to film cracking. On the contrary, no cracks are observed in high temperature GaN grown using low temperature deposited AlN interlayers.

E. D. Bourret-Courchesne (Bourret-Courchesne et al., 2000, 2001) reported that a dramatic reduction of the dislocation density in GaN was obtained by insertion of a single thin interlayer grown at an intermediate temperature after initial growth at high temperature by metalorganic chemical vapor deposition. A large percentage of the threading dislocations present in the first GaN epilayer were found to bend near the interlayer and did not propagate into the top layer which grows at higher temperature in a lateral growth mode. They observed that the dislocation density was reduced by 3 orders of magnitude, from  $10^{10}$  cm<sup>-2</sup> in the first high temperature GaN to  $8 \times 10^7$  cm<sup>-2</sup> in the second GaN.

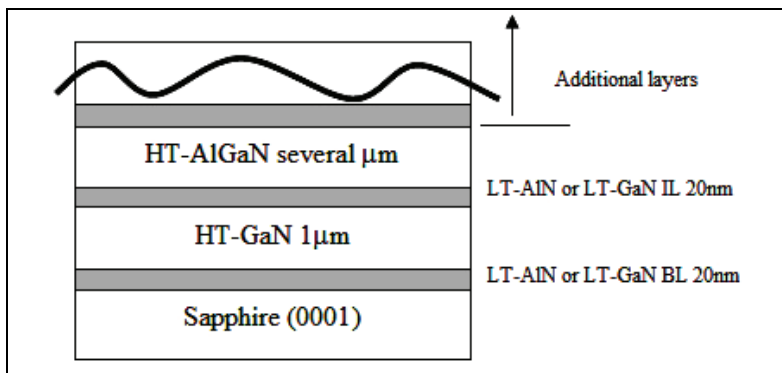


Fig. 16. Schematic drawing of the sample structure showing the use of intermediate layers in reducing the threading dislocations. After ref. (Amano et al., 1999). (LT: Low temperature; HT: High temperature; IL: interlayer; BL: Buffer layer)

Apart from that, similar result was also obtained by W. K. Fong (Fong et al., 2000). High quality GaN films were grown by molecular beam epitaxy on intermediate-temperature buffer layers. Here, the GaN epilayers were grown on top of a double layer that consisted of an intermediate-temperature buffer layer, which was grown at 690°C and a conventional low temperature buffer layer at 500°C. An improvement in the carrier mobility was also

reported. This was attributed to the reduction in threading dislocations, which an intermediate-temperature buffer layers in addition to the conventional buffer layer led to the relaxation of residual strain within the material. They explained that edge dislocations introduced acceptor centers along the dislocation lines, which captured electrons from the conduction band in an n-type semiconductor. The dislocation lines become negatively charged and a space charge is formed around it, which scatters electrons traveling across the dislocation and as a consequence, the electron mobility is reduced. They reported that electron mobility peaked at  $377 \text{ cm}^2\text{V}^{-1}\text{s}^{-1}$  for intermediate-temperature buffer layers thickness of 800nm. Further increase of intermediate-temperature buffer layers thickness results in degradation in electron mobility. However, no explanation was given for the degradation of electron mobility.

Yuen-Yee Wong (Wong et al., 2009) investigated the effect of AlN buffer growth temperatures and thickness on the defect structure of GaN film by plasma-assisted molecular beam epitaxy. When grown on a lower- temperature AlN buffer with rougher surface, the edge and total threading dislocation densities in GaN were effectively reduced. This phenomenon can be explained by the formation of inclined threading dislocation that promoted the reduction of both stress and edge threading dislocation in GaN. However, they observed the screw threading dislocation was increased with the use of lower-temperature AlN buffer. In addition, buffer thickness affects the stress and edge threading dislocation but not screw density in GaN. For the AlN buffer thinner or thicker than the optimum value, more stress and higher edge threading dislocation density were generated in GaN film. In this study, GaN film grown on a 15-nm-thick buffer grown at  $525^\circ\text{C}$  has a smooth surface (root mean square,  $\text{rms}=0.56\text{nm}$ ) and relatively low total threading dislocation density ( $5.8 \times 10^9 \text{ cm}^{-2}$ ).

Beside the conventional methods of using low temperature GaN or AlN nucleation layer as buffer layer, the  $\text{Si}_x\text{N}_y$  buffer layers or  $\text{Si}_x\text{N}_y/\text{GaN}$  buffer layers and  $\text{Mg}_x\text{N}_y/\text{GaN}$  buffer layer are possible solutions to reduce threading dislocation density in GaN.

S. Sakai (S. Sakai et al., 2000) also reported threading dislocation reduction in GaN with  $\text{Si}_x\text{N}_y$  layer by metalorganic chemical vapor deposition. The threading dislocation density is dramatically decreased from  $7 \times 10^8 \text{ cm}^{-2}$  in the conventional method to almost invisible in the observing area of the TEM. Fig. 17 shows schematic illustration of proposed growth mechanism in GaN on SiN buffer layer.

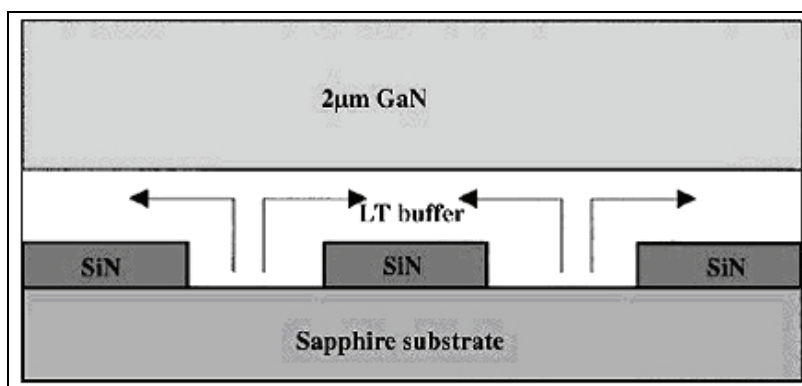


Fig. 17. The schematic illustration of the proposed mechanism GaN in SiN buffer layer. After ref (Sakai et al., 2000).

Growth technique	Interlayer	Improvement	Ref.
MOCVD	2-buffer layer	<ul style="list-style-type: none"> <li>Etch pits eradicated</li> </ul>	Iwaya et al., 1998
MOCVD	1 interlayer	<ul style="list-style-type: none"> <li>Threading dislocations reduced by 1 order magnitude</li> </ul>	Amano et al., 1999
	5 interlayers	<ul style="list-style-type: none"> <li>Threading dislocations reduced by 2 orders of magnitude</li> </ul>	
MOCVD	Single interlayer	<ul style="list-style-type: none"> <li>Threading dislocations reduced to <math>8 \times 10^7 \text{ cm}^{-2}</math></li> </ul>	Bourret-Courchesne et al., 2000, 2001
MBE	Double layer (intermediate-temperature buffer layers + low temperature buffer layer)	<ul style="list-style-type: none"> <li>Carrier mobility improved</li> </ul>	Fong et al., 2000
PA-MBE	buffer layers were deposited at different growth temperatures (from 450 to 840 °C) and thicknesses (from 4 to 30nm)	<ul style="list-style-type: none"> <li>GaN film grown on a 15-nm-thick buffer grown at 525°C has a smooth surface (rms=0.56nm).</li> <li>Relatively low total threading dislocation density (<math>5.8 \times 10^9 \text{ cm}^{-2}</math>).</li> </ul>	Wong et al., 2009
MOCVD	$\text{Si}_x\text{N}_y$ interlayer	<ul style="list-style-type: none"> <li>Reduction in threading dislocation</li> </ul>	S. Sakai et al., 2000
MOCVD	in situ $\text{Si}_x\text{N}_y$ interlayers	<ul style="list-style-type: none"> <li>Threading dislocation density have been reduced from mid <math>10^9 \text{ cm}^{-2}</math> in the GaN template to <math>9 \times 10^7 \text{ cm}^{-2}</math> with a coalescence thickness of 6 nm.</li> </ul>	Kappers et al., 2007
MOCVD	2-buffer layers ( $\text{Mg}_x\text{N}_y/\text{AlN}$ )	<ul style="list-style-type: none"> <li>Exhibits smaller x-ray diffraction FWHM of peak.</li> <li>Higher electron mobility, lower background concentration.</li> <li>Less etching pit density.</li> </ul>	Wong et al., 2009

Table 4. Improvement of crystal quality using insertion of interlayers by various research groups. (MOCVD: metalorganic chemical vapor deposition; MBE: molecular beam epitaxy; PA-MBE: plasma assisted molecular beam epitaxy; FWHM: full width at half maximum)

M.J. Kappers (Kappers et al., 2007) showed that by using in situ  $\text{Si}_x\text{N}_y$  interlayers in the metalorganic chemical vapor deposition of c-plane GaN epilayers, threading dislocation density have been reduced from mid  $10^9 \text{ cm}^{-2}$  in the GaN template to  $9 \times 10^7 \text{ cm}^{-2}$  with a coalescence thickness of 6 nm. The threading dislocation reduction mechanism is based on the change in growth mode to 3D island formation on the  $\text{Si}_x\text{N}_y$ -treated GaN surface and

the half-loop formation between the bent-over threading dislocations that occurs during the lateral overgrowth. The threading dislocation density can be lowered by increasing the  $\text{Si}_x\text{N}_y$  coverage and delaying intentionally the coalescence of the GaN islands at the cost of greater total film thickness.

C.W.Kuo (Kuo et al., 2009) reported dislocation reduction in epitaxial layer grown on double  $\text{Mg}_x\text{N}_y/\text{AlN}$  buffer layers. Bicyclopentadienylmagnesium (Cp2Mg) was used to grow  $\text{Mg}_x\text{N}_y$  buffer layer. Fig. 18 shows schematic illustration of proposed growth mechanism in GaN on  $\text{Mg}_x\text{N}_y/\text{AlN}$  buffer layer. The optimal growth time of  $\text{Mg}_x\text{N}_y$  is 15ps. With increasing growth time, more and more nanometer-sized holes are formed. However, if growth time is over a critical value, nanometer-sized holes disappear, which results in a degraded crystal quality. Epitaxial layer grown on double  $\text{Mg}_x\text{N}_y/\text{AlN}$  buffer layers exhibits smaller x-ray diffraction full width at half maximum of (002) and (102) peak, higher electron mobility, lower background concentration and less etching pit density.

Table 4 summarizes the improved results after inserting the interlayers. It can be seen that the degree of improvement is different from one researcher to another.

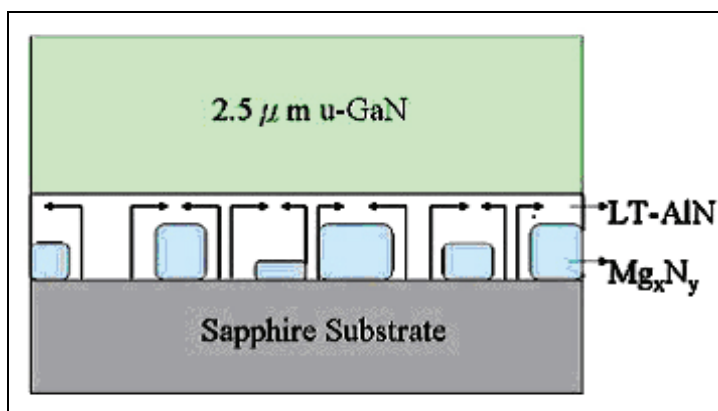


Fig. 18. The schematic illustration of the proposed growth mechanism in GaN on  $\text{Mg}_x\text{N}_y/\text{AlN}$  buffer layer. After ref (Kuo et al., 2009).

## 6.2 Nitridation

Nitridation, has been another aspect which researchers are studying intensively in order to improve the structural defects.

S. Keller (Keller et al., 1996) reported that the properties of GaN grown on sapphire by metalorganic chemical vapor deposition were significantly influenced by sapphire substrate to ammonia exposure time prior to the GaN growth initiation.

N. Grandjean (Grandjean et al., 1996) investigated effect on the optical properties of GaN layers grown by gas-source molecular beam epitaxy on sapphire substrate. They found that nitridation led to formation of AlN relaxed layer on substrate, which promoted the GaN nucleation. They also gave a similar account of the GaN epilayers quality, which found to be closely related to the nitridation time.

Similarly, Gon Namkoong and co-workers (Namkoong et al., 2000) also studied low temperature nitridation combined with high temperature buffer annealing of GaN grown on sapphire substrate by plasma assisted-molecular beam epitaxy. A strong improvement in the GaN crystal quality was observed at 100°C nitridation temperature. The nitridation

enhances the grain size due to the promotion of the lateral growth, this leads to higher quality GaN epilayers and larger grain sizes.

They (Namkoong et al., 2002) further investigated the impact of nitridation temperature on GaN/sapphire interface modifications, which were grown by plasma assisted molecular beam epitaxy. Nitridation at 200°C produces a very thin, homogenous and smooth AlN layer with 90% coverage, while high temperature nitridation leads to inhomogenous and rough AlN layer with 70% coverage and presence of nitrogen oxide.

Maksimov (Maksimov et al., 2006) demonstrated that crystalline quality of GaN films grown on [001] GaAs substrates was extremely sensitive to nitridation conditions. Nitridation has to be performed at low temperature (400°C) to achieve c-oriented wurtzite GaN. Higher substrate temperature promoted formation of mis-oriented domains and cubic zincblende GaN inclusions.

Masashi Sawadaishi (Sawadaishi et al., 2009) did a study on the effect of nitridation of (111)Al substrates for GaN growth by molecular beam epitaxy. Pre-nitridation cleanings like chemical etching for surface oxide removal by using buffered hydrogen fluoride (BHF) (Higashi et al., 1991) and thermal treatment ~660°C were carried out on Al substrate. The chemically cleaned Al substrates were gone through nitridation under pre-heated ammonia (700°C, 6ccm) for 1 hour. The GaN layers were then grown by compound-source molecular beam epitaxy on (111) aluminum (Al) substrates with and without nitridation. Reflection high-energy electron diffraction patterns of the layers indicated that nitridation improves the crystalline quality of the layers. Their reflection high-energy electron diffraction patterns are shown in Fig. 19. It was observed that the photoluminescence intensity of the GaN layer grown on the Al substrate with nitridation was higher than the case without nitridation. This was due to the following:

1. The improvement of crystalline quality, and
  2. The blocking of excited carriers, which prevents their diffusion to the substrate.
- At present, the main reason is still under investigation.

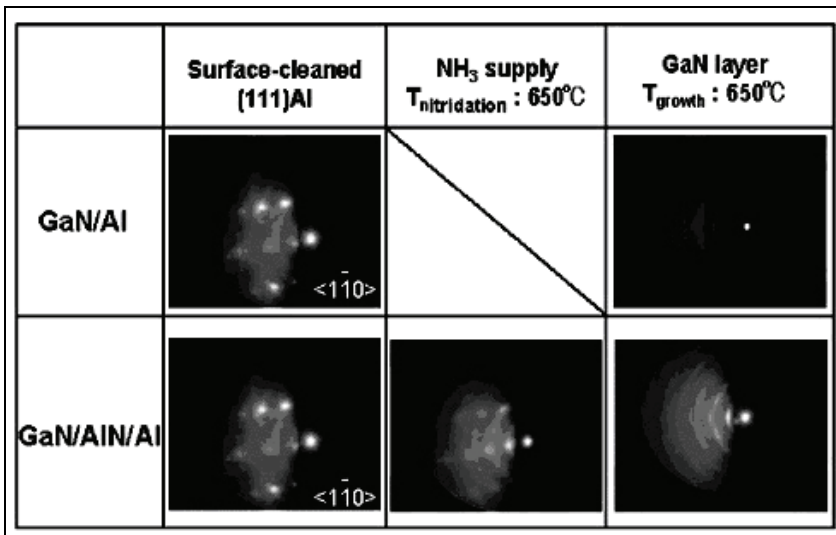


Fig. 19. Reflection high-energy electron diffraction patterns of GaN layer on Al substrates with and without nitridation. After ref. (Sawadaishi et al., 2009).

Table 5 summarizes the results on the nitridation process that have been discussed. It can be seen clearly that the optimum nitridation temperature and time were so much different from one researcher to another even though nitridation was proven to give a positive result in the improvement of the GaN film quality. The discrepancy may be attributed to different growth techniques, growth conditions and other pretreatment procedures.

Growth Technique	Nitridation Temperature (°C) [Optimum]	Exposure time (min) [Optimum]	Findings	Ref.
MOCVD	1050°C (Fixed)	1	<ul style="list-style-type: none"> <li>Reduction of dislocation density to <math>4 \times 10^8 \text{ cm}^{-2}</math></li> </ul>	Keller et al., 1996
CS-MBE	850°C (Fixed)	10	<ul style="list-style-type: none"> <li>Formation of AlN relaxed layer, promotes GaN nucleation</li> </ul>	Grandjean et al., 1996
PA-MBE	100°C	60 (Fixed)	<ul style="list-style-type: none"> <li>Enhancement of lateral growth &amp; larger grain size</li> </ul>	Namkoong et al., 2000
PA-MBE	200°C	60 (Fixed)	<ul style="list-style-type: none"> <li>200°C nitridation produces homogenous AlN layer with 90% coverage</li> <li>High temperature leads to inhomogenous AlN layer containing NO</li> </ul>	Namkoong et al., 2002
CS-MBE	650°C	60	<ul style="list-style-type: none"> <li>Reflection high-energy electron diffraction patterns indicated that nitridation improves the crystalline quality of the layers.</li> <li>Photoluminescence intensity of the GaN layer grown on the Al substrate with nitridation is higher than that in the case without nitridation</li> </ul>	Sawadaishi et al., 2009

Table 5. Different findings obtained by nitridation. (MOCVD: metalorganic chemical vapor deposition; CS-MBE: compound-source molecular beam epitaxy; PA-MBE: plasma assisted molecular beam epitaxy)

### 6.3 Epitaxial lateral overgrowth

In epitaxial lateral overgrowth, GaN film is grown on a sapphire substrate masked with SiO<sub>2</sub> strips. From the openings between the SiO<sub>2</sub> strips, GaN layer is regrown first vertically and then laterally over the SiO<sub>2</sub> strips until the lateral growth fronts coalesce to form a

continuous layer (Chen et al., 1999). Epitaxial lateral overgrowth and its derivatives pendeo-epitaxy and facet-controlled epitaxial lateral overgrowth, have been proven to significantly reduce threading dislocation density in GaN or AlGaIn to a range  $10^6$ -  $10^7$  cm<sup>-2</sup>. A drawback of epitaxial lateral overgrowth and pendeo-epitaxy methods is that one needs to perform epitaxial growth twice.

Both Akira Sakai and A. Usui (A. Sakai et al., 1997; Usui et al., 1997) have demonstrated similar reduction of threading dislocation density in thick GaN films by means of hydride vapor-phase epitaxy. The method consists of a selective homoepitaxial growth on GaN layers grown by metalorganic vapor-phase epitaxy or metalorganic chemical vapor deposition through windows formed in a SiO<sub>2</sub> mask. Fig. 20 shows the detail substrate structure.

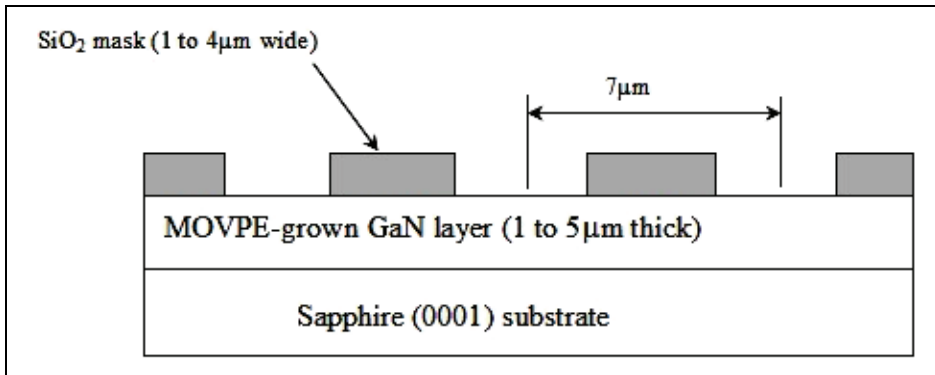


Fig. 20. Schematic diagram of the substrate structure used to reduce the threading dislocation density in thick GaN films grown by hydride vapor phase epitaxy. After ref (A. Sakai et al., 1997).

The threading dislocation reduction in hydride vapor phase epitaxy grown film is due to a change of the dislocation propagation directions during the selective growth of GaN. This change of the propagation direction prevented the dislocations from crossing the film to the surface region and led to a drastic reduction in the threading dislocation density in thicker films.

H. Marchand reported (Marchand et al., 1998) that epitaxial lateral overgrowth of GaN by metalorganic chemical vapor deposition has reduced the mixed character threading dislocation by 3-4 orders of magnitude. In this technique, the threading dislocations are reduced not only by mask blocking the vertically-propagating dislocation, but also by changing the propagation direction of some dislocations at the epitaxial lateral overgrowth growth front.

Similarly, X. Zhang (Zhang et al., 2000) also reported that there was an improvement of the GaN film if epitaxial lateral overgrowth technique is used.

Z. Liliental-Weber and coworkers (Liliental-Weber, 2008; Liliental-Weber et al., 2008) studied the structural defects in laterally overgrown GaN layers grown on polar [0001] and non-polar [2100] direction on sapphire substrate. For the overgrown layers grown in polar direction, a decrease in defect density by at least two to three orders of magnitude was



observed. Dislocation density in the wings was in the range of  $5 \times 10^6 \text{ cm}^{-2}$  to  $1 \times 10^7 \text{ cm}^{-2}$ . Areas of the wings close to the sample surface had only a small density of defects. These bent dislocations occasionally stopped at the wing areas at some obstacles or other dislocations, which started from the SiO<sub>2</sub> mask.  $0.5^\circ$ - $2^\circ$  of tilt/twist was observed at the meeting front between Ga - and N-wings<sup>104</sup>. For overgrown layers in non-polar direction, the (1120) a-plane GaN layers were grown on the (1102) r-plane of Al<sub>2</sub>O<sub>3</sub>. A 1.5  $\mu\text{m}$  thick GaN with a low-temperature nucleation layer was used as a template. Then SiO<sub>2</sub> layer was grown on the a-GaN template using plasma enhanced chemical vapor deposition, which was patterned using conventional photolithography oriented along the [1100] direction of GaN (Liliental-Weber et al., 2007; Ni et al., 2006). The density of defects in the seeds was much higher than in similar seeds grown in polar orientation. The density of dislocations was reduced by more than two orders of magnitude from  $\sim 4.2 \times 10^{10} \text{ cm}^{-2}$  in 'seed' areas to  $\sim 1.0 \times 10^8 \text{ cm}^{-2}$  in 'wing' areas. The density of basal stacking faults decreased from  $1.6 \times 10^6 \text{ cm}^{-1}$  in the seeds to  $1.2 \times 10^4 \text{ cm}^{-1}$  in the wings and the density of prismatic stacking faults decreased from  $0.7 \times 10^2 \text{ cm}^{-1}$  to about  $0.1 \times 10^2 \text{ cm}^{-1}$ . Some  $0.31^\circ$  tilt and  $0.11^\circ$  twist was observed at the meeting front between Ga - and N-wings (Liliental-Weber et al., 2008; Ni et al., 2007). They observed the growth rate difference (Ga-and N-polarity) in lateral epitaxial overgrown layers along the [1120] direction which often leads to crack formation due to the different height of the wings, as schematically shown in Fig. 21. To equalize the wing height, a two-step growth was explored (two different growth temperatures; lower at the beginning of growth and higher for the second part of growth). In this way the Ga- to N-polar wing ratio decreased further to from 6:1 to 2:1 and the surface of the coalesced layer was almost flat.

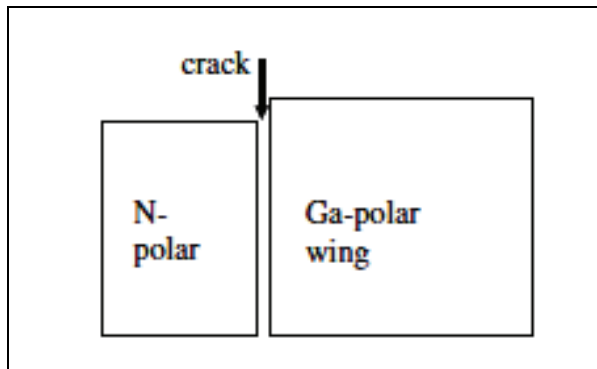


Fig. 21. Schematic showing a typical arrangement of two opposite wings with a crack between them. After ref (Liliental-Weber, 2008).

Due to its advantage of a single epitaxial process with no interruption, patterned sapphire substrate is another alternative method to reduce the dislocation density (Tadatomo et al., 2001; Yamada et al., 2002; W.K.Wang et al., 2005; Hsu et al., 2004). A combination of epitaxial lateral overgrowth and patterned sapphire substrate was successfully demonstrated to reduce the defect density to a level of  $10^5 \text{ cm}^{-2}$  (D.S. Wu et al., 2006). This significantly improves the internal quantum efficiency and light output power.

Furthermore, based on the studies by researchers (Tadatomo et al., 2001; Yamada et al., 2002; W.K.Wang et al., 2005; Hsu et al., 2004; Pan et al., 2007; Gao et al., 2008; J. Wang et al., 2006; Kang et al., 2007), the different patterns (shapes or sizes) of the patterned sapphire substrate were found to be able to influence the growth behavior and dislocation distribution of the GaN epilayers.

The epitaxial lateral overgrowth growth by hydride vapor phase epitaxy of GaN on patterned metalorganic vapor-phase epitaxy GaN/sapphire and sapphire substrates was investigated by Tourret (Tourret et al., 2008). High-quality uniform GaN films about 10 nm thick were successfully grown after epitaxial lateral overgrowth and coalescence on sapphire substrates.

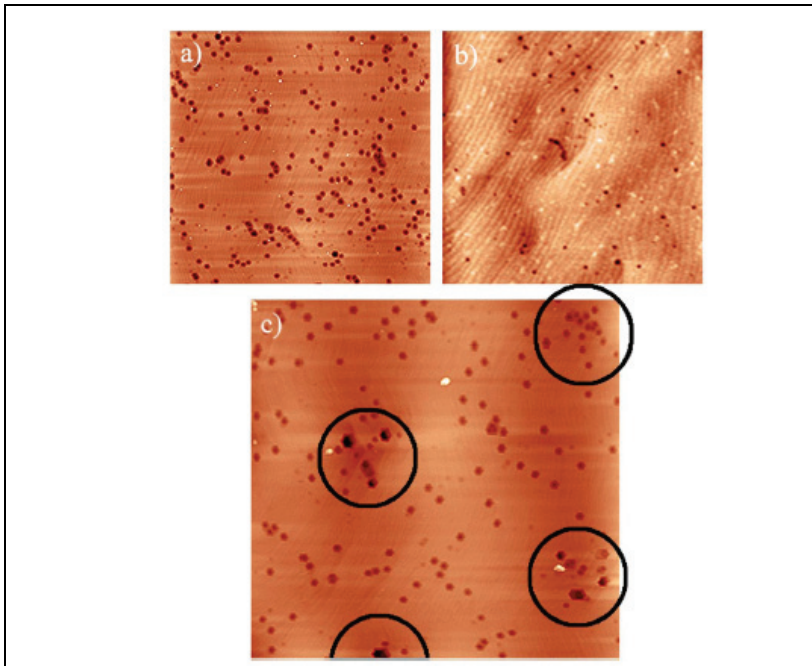


Fig. 22.  $10 \times 10 \mu\text{m}^2$  AFM etching pit density scans from the (a)reference sample, (b)GaN film on HS substrate, and (c)GaN film on PS substrate. It can be noted that the references ample has the highest threading dislocation density. In the substrate case there are concentration points of the threading dislocations. These circulated points follow the periodicity of the pillars on the PS substrate. After ref (Törmä et al., 2009).

Törmä (Törmä et al., 2009) also reported decreased in threading dislocation density when GaN film grown on patterned sapphire substrates by metalorganic vapor-phase epitaxy. Two patterns were investigated. The first pattern had etched hexagonal holes on sapphire (denoted as HS) and second pattern had pillars on the sapphire (denoted as PS). Both patterns showed reduction in threading dislocation as compared to conventional sapphire. The HS had the highest crystals quality. While PS showed relieved strain, which due to PS contains two lattice constants (the one with lattice constant similar to relieved strain and

other one with lattice constant nearly similar to standard GaN grown on a conventional substrate. Threading dislocation density in PS followed the period of the sapphire pattern and mostly concentrated on top of the pillars. The lesser threading dislocation around the pillars area is possibly caused by the dislocation bending (Hiramatsu et al., 2000; Bougrov et al., 2006) on the inclined facets during GaN growth. Fig. 22 (a), (b) and (c) show the  $10 \times 10 \mu\text{m}^2$  AFM etching pit density scans from the GaN surface grown on the conventional substrate, HS and PS substrates, respectively.

A similar result was obtained by Dong-Sing Wu (Wuu et al., 2009). The GaN epilayers on recess/hole -patterned substrate had the highest quality (less defects density) and exhibited a regular distribution of threading dislocation. Table 6 summarizes the structural properties of GaN epilayers on conventional sapphire (flat surface) and patterned sapphire (protruding and recess type) substrates.

Sample	FWHM (arcsec)		Dislocation density ( $\text{cm}^{-2}$ )		Etch pit density ( $\text{cm}^{-2}$ )
	(002)	(302)	Screw-type	Edge-type	
Conventional sapphire	224	486	$1.0 \times 10^8$	$1.6 \times 10^9$	$1.4 \times 10^9$
Protruding patterned sapphire substrate	245	422	$1.2 \times 10^8$	$1.2 \times 10^9$	$8.2 \times 10^8$
Recess patterned sapphire substrate	225	388	$1.0 \times 10^8$	$1.0 \times 10^9$	$6.8 \times 10^8$

Table 6. The structural properties of GaN epilayers on conventional sapphire and patterned sapphire. After ref. (Wuu et al., 2009). (FWHM: full width at half maximum)

Apart from that, Zheleva (Zheleva et al., 1999) proposed a pendeo-epitaxial approach for the lateral growth of GaN films from the side walls of sequential and parallel GaN columns. Fig. 23(a) shows the schematic of the pendeo-epitaxial lateral growth of GaN. The nearly defect-free pendeo-epitaxial GaN region can be associated with the free-standing lateral growth of GaN from the vertical  $\{11\ 2\ 0\}$  side walls of the GaN column, and (b) cross-sectional transmission electron microscope (TEM) micrograph of a pendeo-epitaxial GaN/AlN/6H-SiC (0001) multilayer structure. The region within the column has a  $10^9$ – $10^{10}$   $\text{cm}^{-2}$  dislocation density; the pendeo-epitaxial-GaN region contains a dislocation density of  $10^4$  to  $10^5$   $\text{cm}^{-2}$ . A four- to five-order decrease in the dislocation density was observed in the free-standing laterally grown GaN relative to that in the GaN columns.

Thomas Gehrke (Gehrke et al., 2000) also reported reduction of threading dislocation densities by pendeo-epitaxial method via the use of silicon nitride masks, intermediate high-temperature AlN(0001) buffer layers and 3C-SiC (111) transition layers. Tilting in the coalesced GaN epilayers of  $0.2^\circ$  was confined to areas of mask overgrowth, no tilting was observed in the material suspended above the trenches.

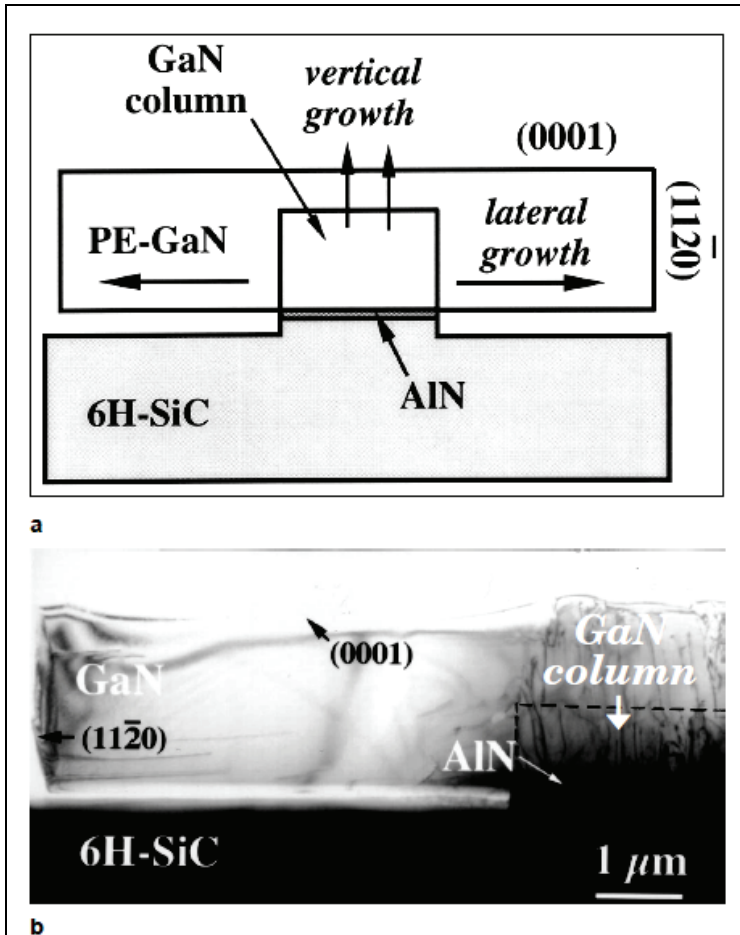


Fig. 23. (a) A schematic of the pendeo-epitaxial lateral growth of GaN. The nearly defect-free pendeo-epitaxial GaN region can be associated with the free-standing lateral growth of GaN from the vertical  $\{11\bar{2}0\}$  side walls of the GaN column, and (b) cross-sectional TEM. After ref (Zheleva et al., 1999).

## 7. Conclusion

In summary, various types of structural defects found in GaN such as threading dislocations, stacking faults, stacking mismatch boundaries, grain boundaries, inversion domains and nanopipes have been reviewed. The general classification of defects and effect of strain on defects were briefly introduced in this chapter. An in-depth discussion of the defects origin in GaN films and their formation mechanism models has been presented. Apart from that, the effects of structural defects on properties of GaN were described. Structural defects have long been known to have detrimental effect on the optoelectronic properties; therefore research and study are intensively focused on the reduction of

structural defects in order to obtain reliable GaN-based devices. In view of this, several different techniques i.e. intermediate temperature layer, nitridation and epitaxial lateral overgrowth that are commonly used to minimize the structural defects in GaN films, have also been compiled and discussed. Generally, the causes of the defects are found to be closely related to substrates, growth conditions, growth techniques and impurities.

## 8. Acknowledgement

This work was conducted under RU grant (grant no.: 1001/PFIZIK/811155). The support from Universiti Sains Malaysia is gratefully acknowledged.

## 9. References

- Amano, H., Iwaya, M., Hayashi, N., Kashima, T., Katsuragawa, M., Takeuchi, T., Wetzel, C., & Akasaki, I., (1999). *MRS Internet J. of Nitride Semicond.*, Vol. Res. 4S1, No. G10.1 .
- Araki, T., Chiba, Y., Nobata, M., Nishioka, Y., & Nanishi, Y., (2000). Structural characterization of GaN grown by hydrogen-assisted ECR-MBE using electron microscopy. *J. Crystal Growth*, Vol. 209, pp. 368-372.
- Barbaray, B., Potin, V., Ruterana, P., & Nouet, G., (1999). Inversion domains generated at substrate steps in GaN/(0001) Al<sub>2</sub>O<sub>3</sub> layers. *Diamond and Related Materials*, Vol. 8, No. 2-5, pp. 314-318.
- Boguslavski, P., Briggs, E.L., & Bernholc, J., (1995). Native defects in gallium nitride. *Phys. Rev. B*, Vol. 51, pp. 17255.
- Boguslavski, P., Brigs, E.L., & Bernholc, J., (1996). Amphoteric properties of substitutional carbon impurity in GaN and AlN. *Appl. Phys. Lett.*, Vol. 69, pp. 233.
- Bougrov, V.E., Odnoblyudov, M.A., Romanov, A.E., Lang, T., & Konstantinov, O.V., (2006). Threading dislocation density reduction in two-stage growth of GaN layers *Phys. Status Solidi (a)*, Vol. 203, No. 4, pp. R25-R27.
- Bourret-Courchesne, E.D., Kellermann, S., Yu, K.M., Benamara, M., Liliental-Weber, Z., & Washburn, J., (2000). Reduction of threading dislocation density in GaN using an intermediate temperature interlayer. *Appl. Phys. Lett.*, Vol. 77, No. 22, Pp. 3562.
- Bourret-Courchesne, E.D., Yu, K.M., Benamara, M., Liliental-Weber, Z., & Washburn, J., (2001). *J. Electron. Mat.*, Vol. 30, No.11, pp. 1417-1420.
- Brown, P.D., (2000). TEM assessment of GaN epitaxial growth. *J. Crystal Growth*, Vol. 210, pp. 143 - 150.
- Chen, Y., Schneider, R., Wang, S.Y., Kem, R.S., Chen, C.H., & Kuo, C.P., (1999). Dislocation reduction in GaN thin films via lateral overgrowth from trenches. *Appl. Phys. Lett.*, Vol. 75, No. 14, pp.2062.
- Chien, F. R., Ning, X. J., Stemmer, S., Pirouz, P., Bremser, M. D., & Davis, R. F., (1996). Growth defects in GaN films on 6H-SiC substrates. *Appl. Phys. Lett.* Vol. 68, pp. 2678.
- Cullity, B.D., (1967). *Elements of X-Ray Diffraction*, Addison-Wesley, United States of America.
- Edgar, J. H. (1994). *Properties of Group III Nitrides*, INSPEC, London, U.K.

- Elsner, J., Jones, R., Haugk, M., Gutierrez, R., Frauenheim, Th., Heggie, M. I., Oberg, S., & Briddon, P. R., (1998). Effect of oxygen on the growth of (100) GaN surfaces: The formation of nanopipes. *Appl. Phys. Lett.*, Vol, 73, pp. 3530.
- Fong, W.K., Zhu, C.F., Leung, B.H., & Surya, C., (2000). *MRS Internet J. of Nitride Semicond.*, Vol. Res. 5, No. 12.
- Fujii, H., Kisielowski, C., Krüger, J., Leung, M. S. H., Klockenbrink, R., Rubin, M., & Weber, E. R., (1997). Impact of growth temperature, pressure, and strain on the morphology of gan films. III-V Nitrides MRS Proceedings, Vol. 449, pp. 227.
- Gao, H., Yan, F., Zhang, Y., Li, J., Zeng, Y., & Wang, G., (2008). Fabrication of nano-patterned sapphire substrates and their application to the improvement of the performance of GaN-based LEDs. *J. Phys. D: Appl. Phys.*, Vol. 41, No. 11, pp. 115106.
- Garni, B., Ma, J., Perkins, N., Liu, J., Kuech, T.F., & Lagally, M.G. (1996). Scanning tunneling microscopy and tunneling luminescence of the surface of GaN films grown by vapor phase epitaxy. *Appl. Phys. Lett.*, Vol. 68, No. 10, pp. 1380.
- Gehrke, T., Linthicum, K.J., Preble, E., Rajagopal, P., Ronning, C, etl., (2000). Pendeo-epitaxial growth of gallium nitride on silicon substrates. *Journal of electronic materials*, Vol. 29, No. 3, pp. 306-310.
- Gloux, F., Ruterana, P., Lorenz, K., & Alves, E., (2008). A comparative structural investigation of GaN implanted with rare earth ions at room temperature and 500 °C. *Materials Science and Engineering B*, Vol. 146, pp. 204-207.
- Grandjean, N., Massies, J., & Leroux, M., (1996). Nitridation of sapphire. Effect on the optical properties of GaN epitaxial overlayers. *Appl. Phys. Lett.*, Vol. 69, No. 14, pp. 2071.
- Harima, H. (2002). Properties of GaN and related compounds studied by means of Raman scattering. *J. Phys.: Condens. Matter*, Vol. 14, pp. 967-993.
- Henini, M., & Razeghi, M. (April 6, 2005). *Optoelectronic Devices: III Nitrides* (1st edition), pp. 3, Elsevier Science.
- Higashi, G.S., Becker, R.S., Chabal, Y.J., & Becker, A.J., (1991). Comparison of Si(111) surfaces prepared using aqueous solutions of NH<sub>4</sub>F versus HF. *Appl. Phys. Lett.*, Vol. 58, No. 15, pp. 1656.
- Hiramatsu, K., Nishiyama, K., Onishia, M., Mizutania, H., Narukawaa, M., Motogaitoa, A., Miyakea, H., Iyechikab, Y., & Maedaet, T., (2000). Fabrication and characterization of low defect density GaN using facet-controlled epitaxial lateral overgrowth (FACELO). *J. Crystal Growth*, Vol. 221, No. 1-4, pp. 316.
- Hong, S. K. & H. K. Cho, (2009). Oxide and Nitride Semiconductors Processing, Properties, and Applications. *Advances in Materials Research*, Vol. 12, pp. 261-310, DOI 10.1007/978-3-540-88847-5\_6
- Hsu, Y.P., Chang, S.J., Su, Y.K., Sheu, J.K., Lee, C.T., Wen, T.C., Wu, L.W., Kuo, C.H., Chang, C.S., & Shei, S.C., (2004). Lateral epitaxial patterned sapphire InGaN/GaN MQW LEDs *J. Cryst. Growth*, Vol. 261, No. 4, pp. 466.
- Hull, D., & Bacon, D.J., (1984). *Introduction to Dislocations*, Pergamon Press, Oxford.
- Ibach, H., & Lüth, H., (1996). *Solid State Physics: An Introduction to Principles of Materials Science* (2<sup>nd</sup> edition), Springer-Verlag, Berlin Heidelberg, Germany.
- Iwaya, M., Takeuchi, T., Yamaguchi, S., Wetzels, C., Amano, H., & Akasaki, I., (1998). Reduction of Etch Pit Density in Organometallic Vapor Phase Epitaxy-Grown GaN

- on Sapphire by Insertion of a Low-Temperature-Deposited Buffer Layer between High-Temperature-Grown GaN. *Jpn. J. Appl. Phys.* Vol. 37, pp. L316-L318.
- Jenkins, D.W., Dow, J.D., Tsai, & M.-H., (1992). N vacancies in  $\text{Al}_x\text{Ga}_{1-x}\text{N}$ . *J. Appl. Phys.*, Vol. 72, pp. 4130.
- Kang, D.H., Song, J.C., Shim, B.Y., Ko, E.A., Kim, D.W., Kannappan, S., & Lee, C.R., (2007). Characteristic Comparison of GaN Grown on Patterned Sapphire Substrates Following Growth Time. *Jpn. J. Appl. Phys.* Vol. 46, pp. 2563.
- Kapolnek, D., Wu, X. H., Heying, B., Keller, B. P., Mishra, U. K., DenBaars, S. P., & Speck, J. S., (1995). Structural evolution in epitaxial metalorganic chemical vapor deposition grown GaN films on sapphire. *Appl. Phys. Lett.*, Vol. 67, pp. 1541.
- Kappers, M.J., Datta, R., Oliver, R.A., Rayment, F.D.G., Vickers, M.E., & Humphreys, C.J., (2007). Threading dislocation reduction in (0 0 01) GaN thin films using  $\text{SiN}_x$  interlayers. *Journal of Crystal Growth*, Vol. 300, No. 1, pp. 70-74.
- Keller, S., Keller, B.P., Wu, Y.F., Heying, B., Kapolnek, D., Speck, J.S., Mishra, U.K., & DenBaars, S.P., (1996). Influence of sapphire nitridation on properties of gallium nitride grown by metalorganic chemical vapor deposition. *Appl. Phys. Lett.*, Vol. 68, No. 11, pp. 1525.
- Kim, W., Botchkarev, A.E., Salvador, A., Popovici, G., Tang, H., & Morkoc, H., (1997). On the incorporation of Mg and the role of oxygen, silicon, and hydrogen in GaN prepared by reactive molecular beam epitaxy. *J. Appl. Phys.*, Vol. 82, pp. 219.
- Kuo, C.W., Fu, Y.K., Kuo, C.H., Chang, L.C., Tun, C.J., Pan, C.J., & Chi, G.C., (2009) Dislocation reduction in GaN with double  $\text{Mg}_x\text{N}_y/\text{AlN}$  buffer layer by metal organic chemical vapor deposition. *Journal of Crystal Growth*, Vol. 311, No. 2, pp. 249-253.
- Lee, K., & Auh, K., (2001). *MRS Internet J. of Nitride Semicond.* Vol. Res. 6, No. 9.
- Lester, S. D., Ponce, F. A., Crawford, M. G., & Steigerwald, D. A., (1995). High dislocation densities in high efficiency GaN-based light-emitting diodes. *Appl. Phys. Lett.*, Vol. 66, pp. 1249.
- Levinshtein, M.E., Rumyantsev, S.L., & Shur, M.S. (February 21, 2001). *Properties of Advanced Semiconductor Materials: GaN, AlN, InN, BN, SiC, SiO<sub>2</sub>* (1 edition), pp. 1, Wiley-Interscience, New York.
- Liliental-Weber, Z., Zakharov, D.N., (2007). Defects formed in nonpolar GaN grown on SiC and  $\text{Al}_2\text{O}_3$ : Structural perfection of laterally overgrown GaN layers, In: *Nitrides with Nonpolar Surfaces: Growth, Properties and Devices*, Paskova, T., (Ed.), Wiley-VCH Verlag.
- Liliental-Weber, Z., (2008). TEM studies of GaN layers grown in non-polar direction: Laterally overgrown and pseudo-epitaxial layers. *Journal of Crystal Growth*, Vol. 310, pp. 4011- 4015.
- Liliental-Weber, Z., Ni, X., & Morkoc, H., (2008). Structural perfection of laterally overgrown GaN layers grown in polar- and non-polar directions. *J. Mater. Sci.: Mater. Electron.* Vol. 19, No. 8-9, pp. 815-820.
- Liu, F., Collazo, R., Mita, S., Sitar, Z., Pennycook, S.J., & Duscher, G., (2008). Direct Observation of Inversion Domain Boundaries of GaN on c-Sapphire at Sub-ångstrom Resolution. *Advanced Materials*, Vol. 20, No. 11, pp. 2162-2165.

- Liu, L., & Edgar, J.H. (2002). Substrates for gallium nitride epitaxy. *Materials Science and Engineering*, Vol. 37, pp. 61-127.
- Łuczniak, B., Pastuszka, B., Kamler, G., Weyher, J.L., Grzegory, I., & Porowski, S., (2009). Bulk GaN crystals and wafers grown by HVPE without intentional doping. *Phys. stat. sol. (c)*, Vol. 6, No. S2, pp. S297-S300.
- Maksimov, O., Fisher, P., Skowronski, M., & Heydemann, V.D., (2006). Effect of nitridation on crystallinity of GaN grown on GaAs by MBE. *Materials Chemistry and Physics*, Vol. 100, No. 2-3, pp. 457-459.
- Marchand, H., Ibbetson, J.P., Kozodoy, P., Keller, S., DenBaars, S., Speck, J.S., & Mishra, U.K., (1998). *MRS Internet J. of Nitride Semicond.*, Vol. Res. 3, No. 3.
- Maruska, H.P., & Tietjen, J.J., (1969). The preparation and properties of vapor-deposited single-crystal-line GaN. *Appl. Phys. Lett.*, Vol. 15, pp. 327.
- Monemar, B., Bergman, J.P., & Buyanova, I.A., (1997). Optical Characterization of GaN and Related Materials, In: *GaN and Related Materials*, Pearson, S.J., pp. 85-139, Gordon and Breach Science Publications, The Netherlands.
- Morkoc, H., Strite, S., Gao, G. B., Lin, M. E., Sverdlov, B., & Burns, M. (1994). Large-band-gap SiC, III-V nitride, and II-VI ZnSe-based semiconductor device technologies. *J. Appl. Phys.*, Vol. 76, No. 3, pp. 1363.
- Morkoc, H., Series Editors, (1999a). *Nitride Semiconductor and Devices*, Springer-Verlag, ISBN 3-540-64038-x, Berlin, Heidelberg, New York, pp. 11-16.
- Morkoc, H., & Series Editors, (1999b). *Nitride Semiconductor and Devices*, Springer-Verlag, Berlin, Heidelberg, New York, pp. 149
- Motoki, K., (2010). Development of Gallium Nitride Substrates. *SEI Technical review*, No. 70, pp. 28-35.
- Nagahama, S., Iwasa, N., Senoh, M., Matsushita, T., Sugimoto, Y., Kiyoku, H., Kozaki, T., Sano, M., Matsumura, H., Umemoto, H., Chocho, K., & Mukai, T., (2000). High-Power and Long-Lifetime InGaN Multi-Quantum-Well Laser Diodes Grown on Low-Dislocation-Density GaN Substrates. *Jpn. J. Appl. Phys.*, Vol. 39, pp. L647-650.
- Nakamura, S., & Chichibu, S.F (2000). Introduction, In: *Introduction to nitride semiconductor blue lasers and light emitting diodes*, Taylor & Francis, London, New York.
- Namkoong, G., Doolittle, W.A., Sa, H., Brown, A.S., Stock, S.R., (2000). *MRS Internet J. of Nitride Semicond.*, Vol. Res. 5, No. 10.
- Namkoong, G., Doolittle, W.A., Brown, A.S., Losurdo, M., Capezzuto, P., & Bruno, G., (2002). Role of sapphire nitridation temperature on GaN growth by plasma assisted molecular beam epitaxy: Part I. Impact of the nitridation chemistry on material characteristics. *J. Appl. Phys.*, Vol. 91, No. 4, pp. 2499.
- Neugebauer, J., & Van de Walle, C.G., (1994). Atomic geometry and electronic structure of native defects in GaN. *Phys. Rev. B*, Vol. 50, pp. 8067.
- Neugebauer, J., & Van de Walle, C.G., (1996). Gallium vacancies and the yellow luminescence in GaN. *Appl. Phys. Lett.*, Vol. 69, No. 4, pp. 503.
- Ng, T. B., Han, J., Biefeld, R. M., & Weckwerth, M. V. (1998). In-situ reflectance monitoring during MOCVD of AlGaIn. *J. Electron. Mat.*, Vol. 27, pp. 190.



- Ni, X., Özgür, U., Fu, Y., Biyikli, N., Xie, J., Baski, A.A., Morkoç, H., & Liliental-Weber, Z., (2006). Defect reduction in (110) *a*-plane GaN by two-stage epitaxial lateral overgrowth. *Appl. Phys. Lett.*, Vol. 89, No. 26, pp. 262105.
- Ni, X., Ozgur, U., Morkoc, H., Liliental-Weber, Z., & Everitt, H.O., (2007). Epitaxial lateral overgrowth of *a*-plane GaN by metalorganic chemical vapor deposition. *J. Appl. Phys.*, Vol. 102, No. 5, pp. 53506.
- Northrup, J.E., (1998). Theory of the (1210) prismatic stacking fault in GaN. *Appl. Phys. Lett.*, Vol. 72, pp. 2316.
- Ohtani, A., Stevens, K. S., & Beresford, R., (1994). Growth and characterization of GaN on Si(111). Diamond, SiC and Nitride Wide Bandgap Semiconductors MRS Proceedings, Vol. 339, pp. 471-476.
- Pan, C.C., Hsieh, C.H., Lin, C.W., & Chyi, J.I., (2007). Light output improvement of InGaN ultraviolet light-emitting diodes by using wet-etched stripe-patterned sapphire substrates. *J. Appl. Phys.*, Vol. 102, No. 8, pp. 84503.
- Pearton, S.J., (1997a). Volume 2- GaN and Related Materials, In: *Optoelectronic properties of semiconductors and superlattices*, Manasreh, M.O., & Series editors, pp. 149, Gordon and Breach Science Publishers, Amsterdam.
- Pearton, S.J., (1997b). Volume 2- GaN and Related Materials, In: *Optoelectronic properties of semiconductors and superlattices*, Manasreh, M.O., & Series editors, pp. 96-98, Gordon and Breach Science Publishers, Amsterdam.
- Pearton, S.J., (2000). Volume 7- GaN and Related Materials II, In: *Optoelectronic properties of semiconductors and superlattices*, Manasreh, M.O., & Series editors, pp. 134, Gordon and Breach Science Publishers, Amsterdam.
- Perlin, P., Suzuki, T., Teisseyre, H., Leszczynski, M., Gregzory, I., Jun, J., Porowski, S., Boguslavski, P., Bernholc, J., Chervin, J.C., Polian, A., & Moustakas, T.D., (1995). Towards the Identification of the Dominant Donor in GaN. *Phys. Rev. Lett.*, Vol. 75, pp. 296.
- Ponce, F.A., Bour, D. P., Götz, W., & Wright, P.J., (1996). Spatial distribution of the luminescence in GaN thin films. *Appl. Phys. Lett.*, Vol. 68, No. 1, pp. 57.
- Ponce, F.A., Young, W.T., Cherns, D., Steeds, J.W., & Nakamura, S., (1997). Nanopipes and inversion domains in high quality GaN epitaxial layers. III-V Nitrides MRS Proceedings, Vol. 449, pp. 405
- Powell, R.C., Tomasch, G.A., Kim, Y.W., Thornton, J.A., & Greene, J.E., (1990) Growth of high-resistivity wurtzite and zincblende structure single crystal GaN by reactive-ion molecular beam epitaxy. Diamond, Boron Nitride, Silicon Carbide and Related Wide Bandgap Semiconductors MRS Proceedings, Vol. 162, pp. 525.
- Qian, W., Rohrer, G.S., Skowronski, M., Doverspike, K., Rowland, L.B., & Gaskill, D.K., (1995b). Open-core screw dislocations in GaN epilayers observed by scanning force microscopy and high-resolution transmission electron microscopy. *Appl. Phys. Lett.*, Vol. 67, pp. 2284.
- Qian, W., Skowronski, M., De Graef, M., Doverspike, K., Rowland, L. B., & Gaskill, D. K., (1995a). Microstructural characterization of  $\alpha$ -GaN films grown on sapphire by organometallic vapor phase epitaxy. *Appl. Phys. Lett.*, Vol. 66, pp. 1252.

- Romano, L.T., Northrup, J.E., & O'Keefe, M. A., (1996). Inversion domains in GaN grown on sapphire. *Appl. Phys. Lett.* Vol. 69, pp. 2394.
- Romano, L.T., & Myers, T.H., (1997). The influence of inversion domains on surface morphology in GaN grown by molecular beam epitaxy. *Appl. Phys. Lett.*, Vol. 71, pp. 3486.
- Sakai, A., Sunakawa, H., & Usui, A., (1997). Defect structure in selectively grown GaN films with low threading dislocation density. *Appl. Phys. Lett.*, Vol. 71, No. 16, pp. 2259.
- Sakai, S., Wang, T., Morishima, Y., & Naoi, Y., (2000). A new method of reducing dislocation density in GaN layer grown on sapphire substrate by MOVPE. *J. Crystal Growth*, Vol. 221, No. 1-4, pp. 334.
- Sánchez, A.M., Pacheco, F.J., Molina, S.I., Ruterana, P., Calle, F., Palacios, T.A., Sánchez-García, M.A., Calleja, E., & García, R., (2002). AlN buffer layer thickness influence on inversion domains in GaN/AlN/Si(111). *Materials Science and Engineering B*, Vol. 93, pp. 181-184.
- Sawadaishi, M., Taguchi, S., Sasaya, K., & Honda, T., (2009). Nitridation of (1 1 1) Al substrates for GaN growth by molecular beam epitaxy. *Journal of Crystal Growth*, Vol. 311, No. 7, pp. 1994-1996.
- Sitar, Z., Paisley, M.J., Yan, B., & Davis, R.F., (1990). Structural defects in GaN epilayers grown by gas source molecular beam epitaxy, Diamond, Boron Nitride, Silicon Carbide and Related Wide Bandgap Semiconductors. *MRS Proceedings*, Vol. 162, pp. 537.
- Smith, D.J., Chandrasekhar, D., Sverdlov, B., Botchkarev, A., Salvador, A., & Morkoc, H., (1995). Characterization of structural defects in wurtzite GaN grown on 6H SiC using plasma-enhanced molecular beam epitaxy. *Appl. Phys. Lett.*, Vol. 67, pp. 1830.
- Smith, W.F., (1996). *Principles of Materials Science and Engineering* (3<sup>rd</sup> edition), pp. 141, McGraw-Hill, New York.
- Spitsyn, B.V., Popovici, G., & Prelas, M.A. (1993). 2<sup>nd</sup> Int. Conf. On the Applications of Diamond Films and Related Materials, edited by Yoshikawa, M., MY, Tokyo.
- Stradling, R.A., & Klipstein, P.C., (1991). *Growth and Characterization of Semiconductors*, Adam Hilger, New York.
- Sverdlov, B.N., Martin, G. A., Morkoc, H., & Smith, D.J., Formation of threading defects in GaN wurtzite films grown on nonisomorphic substrates. *Appl. Phys. Lett.*, Vol. 67, pp. 2063.
- Tadatomu, K., Okagawa, H., Ohuchi, Y., Tsunekawa, T., Imada, Y., Kato, M., & Taguchi, T., (2001). High Output Power InGaN Ultraviolet Light-Emitting Diodes Fabricated on Patterned Substrates Using Metalorganic Vapor Phase Epitaxy. *Jpn. J. Appl. Phys.* Vol. 40, pp. L583.
- Tempel, A., Seifert, W., Hammer, J., & Butter, E., (1975). *Krist. Technol.*, Vol.747.
- Törmä, P.T., Ali, M., Svensk, O., Sintonen, S., Kostamo, P., Suihkonen, S., Sopenan, M., Lipsanen, H., Odnoblyudov, M.A., & Bougrov, V.E., (2009). An investigation of structural properties of GaN films grown on patterned sapphire substrates by MOVPE. *Physica B : Condensed Matter*, 404 (2009) 4911-4915 .

- Touret, J., Gourmala, O., Trassoudaine, A., Andre, Y., Gil, E., Castelluci, D., & Cadoret, R., (2008). Low-cost high-quality GaN by one step growth. *Journal of Crystal Growth*, Vol. 310, No. 5, pp. 924-929.
- Usui, A., Sunakawa, H., Sakai, A., & Yamaguchi, A.A., (1997). Thick GaN Epitaxial Growth with Low Dislocation Density by Hydride Vapor Phase Epitaxy. *Japn. J. Appl. Phys.*, Vol. 36, pp. L899.
- Valcheva, E., Paskova, T., Persson, P.O.Å., & Monemar, B., (2002). Nanopipes in Thick GaN Films Grown at High Growth Rate. *Phys. stat. sol. (a)*, Vol. 194, No. 2, pp. 532-535.
- Wang, J., Guo, L.W., Jia, H.Q., Xing, Z.G., Wang, Y., Yan, J.F., Yu, N.S., Chen, H., & Zhou, J.M., (2006). Investigation of characteristics of laterally overgrown GaN on striped sapphire substrates patterned by wet chemical etching. *J. Cryst. Growth*, Vol. 290, No. 2, pp. 398
- Wang, W.K., Wu, D.S., Lin, S.H., Han, P., Horng, R.H., Hsu, T.C., Huo, D.T.C., Jou, M.J., Yu, Y.H., & Lin, A., (2005). Efficiency improvement of near-ultraviolet InGaN LEDs using patterned sapphire substrates. *IEEE J. Quantum Electron*, Vol. 41, No. 11, pp. 1403.
- Weyher, J.L., Brown, P.D., Zauner, A.R.A., Muller, S., Boothroyd, C.B., Foord, D.T., Hageman, P.R., Humphreys, C.J., Larsen, P.K., Grzegory, I., & Porowski, S. (1999). Morphological and structural characteristics of homoepitaxial GaN grown by metalorganic chemical vapour deposition (MOCVD). *J. Crystal Growth*, Vol. 204, pp. 419-428.
- Weyher, J.L., Lucznik, B., Grzegory, I., Smalc-Koziorowska, J., & Paskova, T., (2010). Revealing of extended defects in HVPE-grown GaN, *Journal of Crystal Growth*, Vol. 312, pp. 2611-2615.
- Wong, Y.Y., Chang, E.Y., Yang, T.H., Chang, J.R., Chen, Y.C., Ku, J.T., Lee, C.T., & Chang, C.W., (2009). The effect of AlN buffer growth parameters on the defect structure of GaN grown on sapphire by plasma-assisted molecular beam epitaxy. *Journal of Crystal Growth*, Vol. 311, No. 6, pp. 1487-1492.
- Wuu, D.S., Wang, W.K., Wen, K.S., Huang, S.C., Lin, S.H., Huang, S.Y., Lin, C.F., Horng, R.H., (2006). Defect reduction and efficiency improvement of near-ultraviolet emitters via laterally overgrown GaN on a GaN/patterned sapphire template *Appl. Phys. Lett.*, Vol. 89, No. 16, pp. 161105.
- Wuu, D.S., Wu, H.W., Chen, S.T., Tsai, T.Y., Zheng, X., & Horng, R.H., (2009). Defect reduction of laterally regrown GaN on GaN/patterned sapphire substrates. *Journal of Crystal Growth*, Vol. 311, No. 10, pp. 3063-3066.
- Xu, H.Z., Takahashi, K., Wang, Z.G., Wang, C.X., Okada, Y., Kawabe, M., Harrison, I., & Foxon, C.T., (2001). Effect of in situ thermal treatment during growth on crystal quality of GaN epilayer grown on sapphire substrate by MOVPE. *J. Crystal Growth*, Vol. 222, pp. 110-117.
- Yamada, M., Mitani, T., Narukawa, Y., Shioji, S., Niki, I., Sonobe, S., Deguchi, K., Sano, M., & Mukai, T., (2002). InGaN-Based Near-Ultraviolet and Blue-Light-Emitting Diodes with High External Quantum Efficiency Using a Patterned Sapphire Substrate and a Mesh Electrode. *Jpn. J. Appl. Phys.*, Vol.41, pp. L1431-L1433.

- Yokouchi, K., Araki, T., Nagatomo, T., & Omoto, O., (1996). Epitaxial growth of GaN films on silicon substrates by MOVPE. *Inst. Phys. Phys. Conf. Ser.*, Vol. 142, pp. 867.
- Zakharov, D.N., Liliental-Weber, Z., Wagner, B., Reitmeier, Z.J., Preble, E.A., & Davis, R.F., (2005). Structural TEM study of nonpolar *a*-plane gallium nitride grown on (112 $\bar{0}$ ) 4H-SiC by organometallic vapor phase epitaxy. *Phys. Rev. B*, Vol. 71, pp. 235334.
- Zhang, X., Li, R.R., Dapkus, P.D., & Rich, D.H., (2000). Direct lateral epitaxy overgrowth of GaN on sapphire substrates based on a sparse GaN nucleation technique. *Appl. Phys. Lett.*, Vol. 77, No. 14, pp. 2213.
- Zheleva, T.S., Smith, S.A., Thomson, D.B., Linthicum, K.J., Rajagopal, P., & Davis, R.F., (1999). Pendeo-epitaxy: A new approach for lateral growth of gallium nitride films. *Journal of Electronic materials*, Vol.28, No.4, pp. L8-L5.

# Cuprous Oxide (Cu<sub>2</sub>O): A Unique System Hosting Various Excitonic Matter and Exhibiting Large Third-Order Nonlinear Optical Responses

Joon I. Jang

*Department of Physics, Applied Physics and Astronomy, State University  
of New York at Binghamton  
USA*

## 1. Introduction

Owing to its unique crystal and coupled electronic structures, a dipole-forbidden direct-gap semiconductor cuprous oxide (Cu<sub>2</sub>O) has gained considerable attention for studying fundamental exciton physics and relevant coherent phenomena, ultimately aiming at excitonic Bose-Einstein condensation (BEC) [Wolfe *et al.* (1995)]. Despite tremendous experimental efforts, however, excitons in Cu<sub>2</sub>O undergo mysterious collisional loss at high densities, resulting in a loss rate given by  $\tau_A^{-1} = An$ , where  $A$  is an empirical coefficient for collisional Auger-type loss and  $n$  is the exciton gas density [Hulin *et al.* (1980); O'Hara *et al.* (1999a,b); O'Hara & Wolfe (2000)]. Detailed analysis based on time- and space-resolved photoluminescence (PL) studies suggested formation of *optically inactive* excitonic molecules (biexcitons) [Jang & Wolfe (2005; 2006a,c)]. The existence of such "dark matter" seems to explain the long-standing difficulties in achieving BEC of excitons in Cu<sub>2</sub>O, which severely limits the experimental gas density far below the critical BEC density ( $n_c \simeq 10^{17} \text{ cm}^{-3}$  at 2 K) and the goal remains still elusive.

An exciton polariton (hereafter polariton) has emerged as a new candidate and condensation of polaritons in two-dimensional (2D) quantum-well microcavity structures was recently reported where multilayer Bragg mirrors confined the optical components [Balili *et al.* (2007); Christopoulos *et al.* (2007); Deng *et al.* (2003; 2010); Kasprzak *et al.* (2006); Lagoudakis *et al.* (2008); Lai *et al.* (2007); Utsunomiya *et al.* (2008)]. Even under strong cavity confinement, however, this "nonequilibrium" polariton BEC lasts only for several picoseconds, basically due to the short-lived excitonic component undergoing efficient dipole transitions in host semiconducting materials. The polariton lifetimes of this time scale is difficult to utilize for future optoelectronic applications.

*Quadrupole* polaritons in Cu<sub>2</sub>O may offer an alternative route to "long-lived" BEC. Unlike well-studied excitons in this semiconductor, a quadrupole polariton is relatively unexplored since its first discovery using coherent quantum beat spectroscopy [Frohlich *et al.* (1991); Langer *et al.* (1995)]. The measured lifetime of quadrupole polaritons is about 2 ns and this much longer lifetime arises from the above noted dipole-forbidden nature of Cu<sub>2</sub>O. Being a coherent quantum superposition of a quadrupole exciton and a photon, this

quasiparticle can be selectively created via resonant excitation. We have recently shown its unique half-matter/half-light characteristics such as scattering by atomic-scale impurities [Jang & Ketterson (2007)], significantly reduced Auger-type collisional loss [Jang & Ketterson (2008); Mani *et al.* (2010)], and resonantly enhanced reflection [Jang *et al.* (2008b)] at the crystal boundary, as demonstrated by the series of low-temperature PL experiments under resonant two-photon excitation. Together with dephasing times of several nanoseconds, these findings suggest that high-density quadrupole polaritons can be effectively confined to achieve polariton lasing and possibly “thermodynamic” BEC of polaritons.

Renewed interest in  $\text{Cu}_2\text{O}$  has been generated with thermal-oxidation-based fabrication of high-quality synthetic crystals with various morphologies [Mani *et al.* (2009a)] and observation of a very strong third-order optical nonlinearity supported by both Z-scan and third harmonic generation (THG) at room temperature [Mani *et al.* (2009b)]. Considering that the first-leading nonlinear term is the third order due to the centrosymmetric crystal structure of  $\text{Cu}_2\text{O}$ , this semiconductor, when engineered into unconventional structures, can be a very attractive system for optoelectronic applications involving various third-order nonlinear optical processes especially in the mid-IR range. Emerging practical examples involving coherent mid-IR applications are sensing for organic and inorganic molecules for environmental issues [Pestov *et al.* (2008); Pushkarsky *et al.* (2006)], minimal invasive medical surgery [Serebryakov *et al.* (2010)], and direct imaging of biological structures [Zipfel *et al.* (2003a)]. Also,  $\text{Cu}_2\text{O}$  has been considered an active material for solar cell applications [Olsen *et al.* (1982)].

This chapter is organized as follows: In Sec. 2 we describe fundamental properties of excitonic matter in  $\text{Cu}_2\text{O}$ . In Sec. 3 we describe the preparation method for high-quality synthetic  $\text{Cu}_2\text{O}$  crystals and the experimental setup for the measurements. In Sec. 4 typical two-photon generation of quadrupole polaritons is examined based on the relevant selection rules. In Sec. 5 we report on unique properties of quadrupole polaritons arising from their half-matter/half-light characters. In Sec. 6 we discuss quadrupole polariton generation under external mechanical stress and separate two-beam techniques. In Sec. 7 various nonlinear optical processes in  $\text{Cu}_2\text{O}$  are investigated and we propose a new direction for polariton-based BEC in this semiconductor. Section 8 gives our summary and conclusions.

## 2. Properties of excitonic matter in $\text{Cu}_2\text{O}$

The “cuprite” crystal structure of  $\text{Cu}_2\text{O}$  consists of interpenetrating bcc (O) and fcc (Cu) sublattices [see Fig. 1(a)]. The Bravais lattice is simple cubic with a lattice constant of 0.43 nm [Dahl & Switendick (1966)]. Due to the *center of inversion* around each copper atom site, both the lowest conduction band ( ${}^2\Gamma_6^+$ ) built from Cu 4s levels and the highest valence band ( ${}^2\Gamma_7^+$ ) from Cu 3d levels have a positive parity at zone center, causing a *dipole-forbidden energy gap* of  $E_g = 2.17$  eV [Grun *et al.* (1961)]. The next highest valence band ( ${}^4\Gamma_8^+$ ) lies 130 meV lower due to the spin-orbit interaction. The second lowest conduction band ( ${}^4\Gamma_8^-$ ), lying 450 meV above the lowest conduction band, serves as an intermediate state for various optical-phonon-assisted recombination processes. Figure 1(b) schematically illustrates the band structure of  $\text{Cu}_2\text{O}$  at zone center when considering only two conduction and two valence bands that form the visible exciton series. Therefore, there are four possible exciton series referred to as “yellow” ( ${}^2\Gamma_6^+ \otimes {}^2\Gamma_7^+$ ), “green” ( ${}^2\Gamma_6^+ \otimes {}^4\Gamma_8^+$ ), “blue” ( ${}^4\Gamma_8^- \otimes {}^2\Gamma_7^+$ ), and “indigo” ( ${}^4\Gamma_8^- \otimes {}^4\Gamma_8^+$ ). Our primary concern is *dipole-forbidden yellow* exciton ( ${}^2\Gamma_6^+ \otimes {}^2\Gamma_7^+$ ), which is the bound state of an

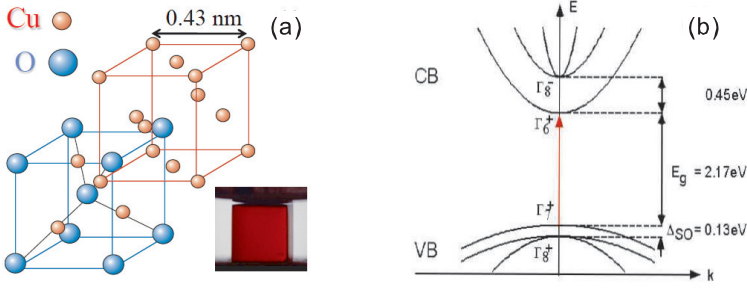


Fig. 1. (a) Crystal structure of Cu<sub>2</sub>O. Inset: natural-growth bulk Cu<sub>2</sub>O crystal. (b) Schematic of the Cu<sub>2</sub>O band structure near zone center. The red arrow denotes quadrupole transition.

electron in the lowest conduction band ( ${}^2\Gamma_6^+$ ) and a hole in the highest valence band ( ${}^2\Gamma_7^+$ ), and shows a hydrogenic Rydberg series in the optical absorption spectrum [Hayashi & Katsuki (1952)]. Including so-called central cell corrections [Kavoulakis *et al.* (1997)], a spectroscopic fit to the observed Rydberg series reveals a tightly bound  $1s$  excitonic state with a binding energy of 153 meV, corresponding to Bohr radius of 0.7 nm. The measured translational mass of the exciton is about  $2.7m_e$ , where  $m_e$  is the electron mass [Yu & Shen (1975)].

Since both the conduction and valence bands each have a simple spin-up/spin-down degeneracy, an exciton has a four-fold degeneracy, which is split into a triply-degenerate “ $J = 1$ ” *orthoexciton* ( ${}^3\Gamma_{25}^+$ ) and a nondegenerate “ $J = 0$ ” *paraexciton* ( ${}^1\Gamma_2^+$ ) by the electron-hole exchange interaction. The measured exchange splitting energy is 12 meV, the paraexciton level lying lowest [Kuwabara *et al.* (1977)]. Direct transition to the orthoexciton state is quadrupole allowed, but strictly forbidden for the paraexciton state because the process requires spin flip. Spin exchange between these two exciton states is possible via emission or absorption of a single transverse acoustic (TA) phonon [Jang *et al.* (2004); Wolfe & Jang (2005)]. Recently, Dasbach *et al.* (2004) performed high-resolution spectroscopy and observed the fine splitting of the triplet orthoexciton levels into the so-called “dark” and “bright” states depending on the wavevector direction inside the crystal. Although the relevant splitting is very small (several  $\mu\text{eV}$ ), this fine structure of orthoexciton states crucially affects both one- and two-photon selection rules [Dasbach *et al.* (2004); Inoue & Toyozawa (1965); Jang *et al.* (2008a); Yoshioka & Kuwata-Gonokami (2006)].

Near the light cone ( $k \simeq 2.63 \times 10^5 \text{ cm}^{-1}$ ), only a bright orthoexciton quadrupole couples to the electromagnetic field, resulting in a quadrupole polariton. This is a coherent quantum superposition of a bright orthoexciton (matter) and a photon (light) field. The corresponding modes involve two branches which, depending on the wavevector, are either exciton-like or photon-like. This quasiparticle can be most simply described by coupled exciton-photon wave equations in momentum-energy ( $\mathbf{k}, \omega$ ) space [Hopfield (1958)]:

$$\hbar\omega\hat{a}_{\mathbf{k}} = \hbar v k \hat{a}_{\mathbf{k}} + \eta^* \hat{b}_{\mathbf{k}}, \quad (1)$$

$$\hbar\omega\hat{b}_{\mathbf{k}} = \left( \frac{\hbar^2 k^2}{2m} + E_0 - i\Gamma \right) \hat{b}_{\mathbf{k}} + \eta \hat{a}_{\mathbf{k}}, \quad (2)$$

where  $\hat{a}_{\mathbf{k}}$  and  $\hat{b}_{\mathbf{k}}$  ( $\propto e^{-i\omega t}$ ) are the photon and exciton annihilation operators,  $v$  is the velocity of light in the medium,  $m$  is the exciton mass,  $E_0$  is the internal energy of an exciton, and

$\Gamma$  is a phenomenological damping rate. Equations (1) and (2) denote the photonic and excitonic parts of a polariton wave, where the coupling coefficient  $\eta$  is proportional to  $k$  for a quadrupole exciton. The solution to the above equations yields the quadrupole polariton dispersion [see Fig. 12(b)]. The propagating nature of the quadrupole polariton was first observed in the variation of the beat period using coherent quantum beat spectroscopy under resonant one-photon excitation [Frohlich *et al.* (1991); Langer *et al.* (1995)]. By contrast, a dark orthoexciton does not directly couple to the radiation field. When both excitonic matter species are generated under resonant excitation, the initial coherence of the laser light is essentially carried by them. These resonantly created dark orthoexcitons and quadrupole polaritons are potentially important in semiconductor-based coherent quantum information science [Yoshioka & Kuwata-Gonokami (2006)].

Excitons in  $\text{Cu}_2\text{O}$  can be created by conventional one-photon over-the-gap excitation. Under this excitation condition, electron-hole ( $e$ - $h$ ) pairs are initially generated which subsequently combine to form excitons via a screened Coulomb interaction. This “nonresonant” excitation results in excitons that initially have an excess kinetic energy and the exciton gas temperature can be much higher than the lattice temperature. Both orthoexcitons and paraexcitons can recombine via *indirect* phonon-assisted processes [Elliot (1961); Petroff *et al.* (1975)], but only the bright orthoexciton states can radiatively recombine by *direct* quadrupole transition, displaying a sharp Lorentzian peak.<sup>1</sup> Due to the flat dispersion relation of optical phonons, the phonon-assisted PL line can sample excitons having all possible kinetic energies, yielding a kinetic energy distribution of excitons [Beg & Shapiro (1976)]. At temperatures lower than about 20 K, the lifetime of orthoexcitons is basically limited by down-conversion into lower-lying paraexcitons, which is on the order of several nanoseconds [Jang *et al.* (2004); Wolfe & Jang (2005)]. Paraexcitons can have a lifetime up to several milliseconds in high-purity natural-growth samples but is extrinsically limited by the impurity concentration, i.e., the sample quality [Jang *et al.* (2006)]. Most of the previous experiments directed at excitonic BEC in  $\text{Cu}_2\text{O}$  were carried out using one-photon excitation [Fortin *et al.* (1993); Hulin *et al.* (1980); Snoke *et al.* (1987; 1990); Snoke & Negoita (2000); Wolfe *et al.* (1995)].

In contrast, quadrupole polaritons can be generated using *resonant* excitation involving either one or two photons [Frohlich *et al.* (1991); Goto *et al.* (1997); Ideguchi *et al.* (2008); Jang & Ketterson (2007); Jang *et al.* (2008a); Langer *et al.* (1995); Sun *et al.* (2001); Tayagaki *et al.* (2006)]. Rather than trying to cool the highly nonequilibrium state which follows nonresonant excitation, thermalization of the system under resonant excitation involves a subsequent *heating* induced by acoustic phonon absorption. Once resonantly generated, the lifetime (total coherence time) of quadrupole polaritons is basically limited by various elastic and inelastic dephasing processes [Takagahara (1985)]. Inelastic energy relaxation processes include irreversible damping arising from radiative recombination, thermalization to orthoexcitons, down-conversion to paraexcitons, and capture by ambient impurities, whereas elastic processes are caused by pure transverse dephasing mechanisms, affecting the phase only. All excitons and quadrupole polaritons undergo a *density-dependent* Auger-type decay process at high densities [Jang & Ketterson (2008); Tayagaki *et al.* (2006)]. According to the recent model [Jang & Wolfe (2005; 2006a;c)], it seems to arise due to formation of *optically inactive* biexcitons though their existence has not been confirmed spectroscopically yet.

---

<sup>1</sup> Details on various relaxation processes of excitons in  $\text{Cu}_2\text{O}$  are discussed in Jang (2005).



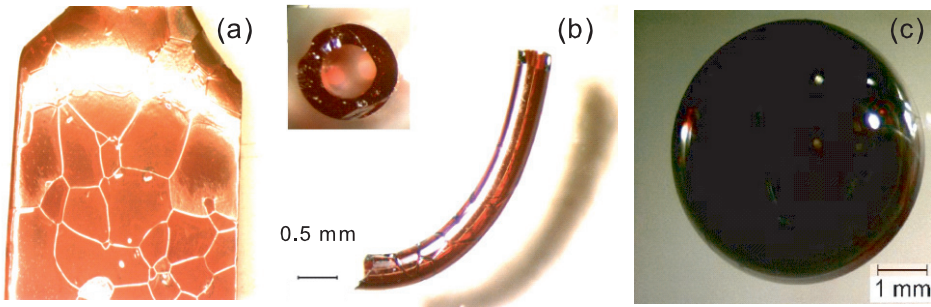


Fig. 2. High-quality synthetic crystals of  $\text{Cu}_2\text{O}$  grown by thermal oxidation with various structures: (a) Platelet with macroscopic grain boundaries, (b) hollow cylinder (inset: cross section), and (c) spheroid.

### 3. Experimental methods

In order to obtain shiny, ruby-red colored, large-area single crystals of  $\text{Cu}_2\text{O}$ , we utilize conventional thermal oxidation of metallic Cu with platelet, wire, and shot structures followed by a high-temperature annealing protocol. The oxidation parameters and annealing procedure are obtained from Toth *et al.* (1960) and carefully adjusted to refine the  $\text{Cu}_2\text{O}$  crystal quality. During the growth process, we carefully maintain  $\text{O}_2$  pressure and temperature to lie within the middle of the  $\text{Cu}_2\text{O}$  phase in the Cu– $\text{Cu}_2\text{O}$ –CuO phase diagram [Schmidt-Whitley *et al.* (1974)]. It is noted that elevated annealing temperatures near the melting temperature of  $\text{Cu}_2\text{O}$  and slower rates of oxidation, annealing, and cooling of the samples play key roles in diminishing the concentration of macroscopic defects such as voids and CuO precipitates.<sup>2</sup> Figure 2 shows as prepared, (a) platelet, (b) hollow tube, and (c) spherical structures of  $\text{Cu}_2\text{O}$ , respectively. It is interesting that the oxidation of Cu wire at high temperatures leads to the formation of *hollow* tubules of  $\text{Cu}_2\text{O}$ . Together with a spheroid form, such unconventional structures could be utilized to confine propagating quadrupole polaritons within a whispering gallery mode [Vollmer & Arnold (2008)]. Our natural-growth samples used in the experiments were donated by the Smithsonian Institute.

Our one- and two-photon experiments are performed on both natural-growth and synthetic  $\text{Cu}_2\text{O}$  crystals. For resonant two-photon excitation, the samples are properly oriented relative to the laser polarization ( $\mathbf{E}$ -field direction) to maximize optical transition. The cryogenic temperatures are produced with a Janis variable-gas-flow optical cryostat and an accompanying temperature controller. We use the frequency-tripled output of a mode-locked Nd:YAG laser (EKSPILA PL 2143 series) with a pulse width of about 30 ps and a repetition rate of 10 Hz in order to synchronously pump an optical parametric amplifier (OPA). The OPA generates vertically polarized pulses in the range of 400 - 2000 nm. At the two-photon resonance energy  $\epsilon_{2p} = 1016.5$  meV (1219.4 nm), the spectral bandwidth of the laser light from the OPA is rather broad, about 8 meV full width at half maximum. However, the phase space compression phenomena [Kuwata-Gonokami *et al.* (2002)] ensure an effective creation of quadrupole polaritons or dark orthoexcitons since the lower energy portions ( $\epsilon_{2p} - \delta\epsilon_{2p}$ ) are exactly compensated by higher parts ( $\epsilon_{2p} + \delta\epsilon_{2p}$ ), thereby satisfying both energy and

<sup>2</sup> See Mani *et al.* (2009a) for detailed growth procedures and X-ray and optical characterizations.

Table 1: Selection rules along (100)

State	1-photon	2-photon
$O_{xy}$	$\cos^2\theta$	0
$O_{yz}$	0	$\sin^2 2\theta$
$O_{zx}$	$\sin^2\theta$	0

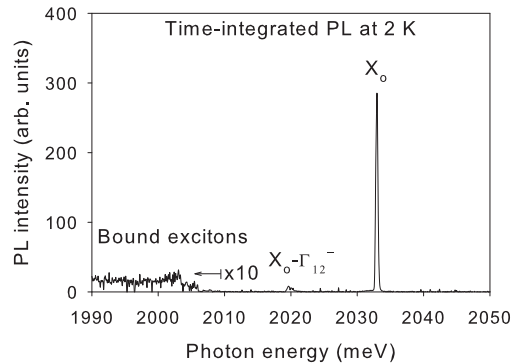


Fig. 3. Time-integrated PL spectrum at 2 K under resonant two-photon excitation along a (100) direction that initially generates dark orthoexcitons. The bound exciton PL is  $\times 10$  magnified.

momentum conservations. In order to verify the one- and two-photon selection rules, a pair of polarization analyzers is placed in front of and behind the samples. The incident laser pulse is focused onto a spot  $500 \mu\text{m}$  in diameter using a 15 cm focal-length lens. The PL from excitonic matter is collected and focused onto a fiber optic bundle mounted on a goniometer, thereby allowing us to measure the angular dependence ( $\phi$ ) of the PL. The output of the fiber optic bundle is coupled to the entrance slit of a Spex Spec-One 500 M spectrometer and detected using a nitrogen-cooled CCD camera. The collection efficiency of our optical system as a function of the collection angle  $\phi$  is explained in Jang & Ketterson (2007).

The Z-scan technique is traditionally employed to probe the third-order nonlinearity  $\chi^{(3)}$  by translating a test sample through the beam waist of a focused Gaussian-laser profile and measuring the corresponding variation of the transmitted beam intensity in the far field [Sheik-Bahae *et al.* (1990; 1991)]. For our Z-scan experiments [Mani *et al.* (2009b; 2010)], the laser pulses from the OPA is first *spatially* filtered using a  $100 \mu\text{m}$  pinhole, insuring transmission of only the  $\text{TEM}_{00}$  Gaussian mode. This Gaussian beam is focused on  $\text{Cu}_2\text{O}$  using a converging lens with a 7.5 cm focal length, which is mounted on a computer-controlled stage that is translated relative to the window of the optical cryostat. This allows us to continuously change the input irradiance  $I$  as a function of the lens position  $Z$ ;  $I$  can be varied more than a factor of 400 simply by translating  $Z$  in our 1-inch scan range. The change in the far-field image of the transmitted beam with  $Z$  is minimized by using a combination of collection lenses prior to entering a photomultiplier tube (PMT). The output of the PMT is fed into a boxcar integrator and read out using a data acquisition system.

#### 4. Resonant two-photon excitation and selection rules

According to  $\mathbf{k}$ -dependent exchange interactions [Dasbach *et al.* (2004)], two-photon excitation along highly symmetric crystal orientations does not generate quadrupole polaritons but dark orthoexcitons. For example, Table 1 shows the selection rules for a (100) direction, ensuring that two-photon excitation along this direction initially creates dark orthoexcitons, the  $O_{yz}$  state, whose one-photon transition is not allowed. This can be a crucial issue for achieving a polariton-based whispering gallery mode, where the direction of the

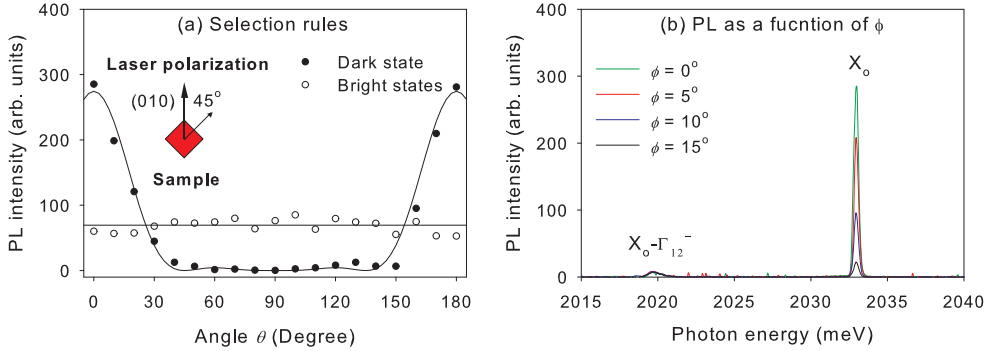


Fig. 4. (a) Dots (circles) correspond to the observed polarization dependence of the  $X_o$  line obtained using analyzers in front of (behind) the sample. Superimposed solid curve (line) is the two-photon (one-photon) selection rules. Inset: schematic of the excitation geometry. (b) Time-integrated PL spectra at 2 K as a function of the collection angle  $\phi = 0, 5, 10,$  and  $15^\circ$ .

polariton propagation is arbitrarily reflected and guided by curved interfaces. However, quadrupole polaritons can be *indirectly* generated although dark states are initially created. Figure 3 shows a typical time-integrated PL spectrum under resonant two-photon excitation at 2 K along a (100) direction. Considering that optically inactive “singlet”  $O_{yz}$  dark orthoexcitons are initially generated in this excitation geometry, it seems rather surprising to observe several PL lines. Once created, however, these excitons undergo various relaxation processes and can recombine accompanied with the emission of a single photon. For example, they can: (i) inelastically scatter from optical phonons, causing the phonon replica ( $X_o - \Gamma_{12}^-$ ), (ii) be captured by ambient impurities, where the symmetry of an exciton is broken and the parent selection rules do not apply, resulting in the broad bound exciton PL, and (iii) convert into the bright orthoexciton states that directly recombine, yielding a sharp  $X_o$  line. They also can either nonradiatively decay due to phonon cascade or down-convert into the lower-lying paraexcitons. Compared with other inelastic energy relaxation processes that cause irreversible damping of dark orthoexcitons, we find that the conversion into the bright state is the most dominant mechanism based on the observed strong  $X_o$  line.

In order to verify that the direct  $X_o$  line arises from two bright “doublet”  $O_{xy}$  and  $O_{zx}$  states, which are subsequently converted from the dark “singlet” state, we examine the one- and two-photon selection rules using two analyzers. The dots in Fig. 4(a) correspond to the observed two-photon selection rules for dark orthoexcitons inferred from the bright-state PL ( $X_o$  line) obtained with the analyzer in front of the sample. Considering that the sample orientation is  $45^\circ$  as shown in the inset of Fig. 4(a), the overall two-photon polarization dependence is shown as the solid curve and is given by  $P_{2p} \propto \sin^2[2(\theta - 45^\circ)] \cos^4 \theta$ , where the extra  $\cos^4 \theta$  term accounts for two-photon excitation of the incident laser intensity that decreases with  $\cos^2 \theta$ , as the analyzer rotates from  $\theta = 0^\circ$ . The circles correspond to the observed one-photon selection rules for bright orthoexcitons, converted from dark orthoexcitons, obtained with the analyzer behind the sample. Note that the measured  $X_o$  intensity barely depends on the analyzer angle. Considering the total polarization of the two bright states,  $O_{xy} \propto \cos^2 \theta$  and  $O_{zx} \propto \sin^2 \theta$ , this implies that the two-fold degenerate bright states are *equally* populated:  $P_{1p} \propto \cos^2 \theta + \sin^2 \theta = \text{constant}$  [solid line in Fig. 4(a)]. Clearly,

the observed polarization dependencies support that the strong direct PL line arises from *dark-to-bright conversion*.

This dark-to-bright conversion was first observed by Yoshioka & Kuwata-Gonokami (2006) using two-photon absorption along the (110) direction, and the measured conversion rate was about  $5 \text{ ns}^{-1}$ . The contribution to this conversion rate due to phonon scattering can be estimated by the deformation potential theory [Trebin *et al.* (1981); Waters *et al.* (1980)]:<sup>3</sup>

$$\gamma(T) = \frac{\Xi_{xy}^2 m^2 \delta}{3\pi\rho v_T \hbar^4} \left( 1 + \frac{2k_B T}{v_T \sqrt{2m\delta}} \right), \quad (3)$$

where  $\Xi_{xy} = 0.18 \text{ eV}$  is the shear deformation potential,  $m = 2.7m_e$  is the exciton mass,  $\rho = 6.1 \text{ g/cm}^3$  is the mass density of  $\text{Cu}_2\text{O}$ , and  $v_T = 1.3 \text{ km/s}$  is the TA-phonon velocity. With the measured splitting  $\delta = 2 \text{ } \mu\text{eV}$  along this direction [Dasbach *et al.* (2004)], Eq. (3) yields a conversion rate  $\gamma \simeq 0.7 \times 10^{-4} \text{ ns}^{-1}$  at 2 K. This implies that dark-to-bright conversion via phonon scattering is negligible. Therefore, it most likely arises from state mixing caused by the so-called *cross relaxation*, where two dark states *elastically* scatter to equally populate two bright states by satisfying angular momentum conservation. Although the dark orthoexcitons may lose their initial coherence, this implies that their phase information can be partially carried by subsequently generated bright states, because elastic scattering only induces a phase shift in the total ensemble coherence [Takagahara (1985)]. This cross relaxation mechanism is currently under investigation using two-photon quantum beat spectroscopy as a function of the incident laser intensity.

Figure 4(b) shows the PL spectra under the same conditions for several collection angles  $\phi$  in the range of  $0 - 15^\circ$ , where  $\phi$  is the angle between the laser beam direction and the PL collection direction. Note that the direct PL intensity sharply depends on  $\phi$  and is well correlated with the laser-propagation direction, whereas the indirect phonon line does not; i.e. it is essentially isotropic. This clearly indicates that the initial momentum of a dark orthoexciton inherited from the laser is nearly conserved after the conversion. This leads the momentum of a subsequently generated bright orthoexciton being near the light cone to form a quadrupole polariton, which propagates along the initial laser direction. Based on highly directional PL properties, this strongly indicates that propagating quadrupole polaritons are *indirectly* generated. This implies that two-photon excitation in  $\text{Cu}_2\text{O}$  eventually generates quadrupole polaritons regardless of the crystal orientation.

## 5. Half-matter/half-light characteristics of quadrupole polaritons

Near the quadrupole resonance in  $\text{Cu}_2\text{O}$ , light propagating through the medium is accompanied by quadrupolar polarization through the excitonic component. Ideally, the angular distribution of the quadrupole polariton PL should be same as the angular divergence for the incident laser because its propagation direction is inherently determined by the incident laser direction. However, these quadrupole polaritons can lose their initial coherence because the excitonic component of the mode, a tightly bound *e-h* pair, is subject to wide-angle scattering by atomic-scale imperfections within the crystal. Therefore, we employ angle-resolved spectroscopy to examine scattering by ambient impurities, which results in decoherence, and monitor the angular divergence of quadrupole polaritons generated

<sup>3</sup> See, for example, Jang & Wolfe (2006b) for the derivation of the rate due to off-diagonal shear scattering.

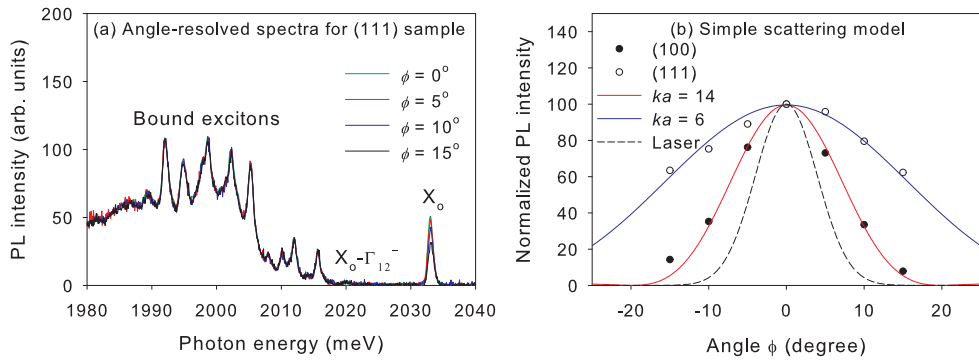


Fig. 5. (a) Time-integrated PL spectra at 2 K as a function of  $\phi = 0, 5, 10,$  and  $15^\circ$  obtained from the (111) oriented sample. (b) Angular distributions of the  $X_o$  intensities from the (100)-cut (dots) and (111)-cut (circles) samples, respectively. The solid red and blue curves correspond to our simplified model for  $ka = 14$  and  $6$ . The dashed curve denotes the angular distribution of the transmitted laser measured just below the quadrupole resonance.

by resonant two-photon transition. In fact, Fig. 4(b) displays such angle-resolved spectra obtained from a (100)-cut sample for several collection angles. This angle dependence can differ from sample to sample.

Figure 5(a) plots time-integrated spectra obtained from a (111)-cut sample<sup>4</sup> under the same conditions as Fig. 4(b). For this direction, the observed  $X_o$  line is caused by quadrupole polaritons both directly and indirectly generated by two-photon absorption. The series of peaks in a range from 1980 to 2015 meV arise from excitons bound to ambient impurities that are essentially isotropic (no  $\phi$  dependence). Considering much enhanced bound exciton PL intensity, this sample apparently contains more impurities and the  $X_o$  intensity from quadrupole polaritons remaining after transmission through the sample is strongly attenuated due to ambient impurity scattering. This is clearly indicated by much more gradual drop in the  $X_o$  intensity as  $\phi$  changes from  $0^\circ$ , compared with that in Fig. 4(b). This implies that the photonic character (straight propagation with a definite  $\mathbf{k}$ ) of a quadrupole polariton is obstructed by impurities, significantly affecting its excitonic component and thus deflecting its initial path which, in turn, affects the photonic component by the exciton-photon coupling terms in Eqs. (1) and (2).

From the fact that this wide-angle impurity scattering originates from the *particle nature* of a quadrupole polariton, our problem reduces to a “propagating” (not diffusive<sup>5</sup>) exciton that is most likely scattered by ambient *charged* impurities. The  $1s$  exciton is uncharged and has no higher multipole moments. However, a charged impurity can induce a dipole moment in the excitonic part of a quadrupole polariton. The potential between an *induced* dipole and an ion has the form  $V(r) = -\alpha e^2/2r^4$  for large  $r$ , where  $\alpha$  is the polarizability [Landau & Lifshitz (1977)]. But the scattering amplitude calculated with this potential is divergent due to the behavior of  $V(r)$  at small  $r$ . To avoid this problem we assume the interaction approaches a

<sup>4</sup> This sample contains high impurity levels and was used for studying bound excitons [Jang *et al.* (2006)].

<sup>5</sup> Highly diffusive nature of excitons in Cu<sub>2</sub>O are described in Trauernicht & Wolfe (1986).

constant at small  $r$ . Including a phenomenological “cutoff radius”  $a$ , the model potential is

$$V(r) = -\frac{\alpha e^2}{2r^4} \quad (r > a) \quad \text{and} \quad V_0 \equiv -\frac{\alpha e^2}{2a^4} \quad (r < a). \quad (4)$$

Since the observed angular divergence depends on the impurity concentration, the trajectory of a quadrupole polariton is mainly determined by successive small-angle scattering, leading to a Gaussian-like distribution. In order to obtain the angular distribution due to multiple scattering, one needs to numerically add each stochastic process considering many parameters [Amsel *et al.* (2003)]. In the absence of information on the nature and distribution of the scattering centers we model the behavior as arising from single scattering events which are parameterized by a cutoff radius  $a$ . By neglecting the long-range contribution, which is very small compared with the one for  $r < a$ , the quantum mechanical scattering amplitude produced by Eq. (4) is given in the first-order Born approximation by

$$f(\Omega) = -\frac{2m'}{\hbar^2} \frac{V_0}{q} \int_0^a r \sin(qr) dr = -\frac{2m'}{\hbar^2} \frac{V_0}{q^3} \{\sin(qa) - qa \cos(qa)\}, \quad (5)$$

where we take  $m'$  to be the effective mass of a quadrupole polariton and  $q = |\mathbf{k} - \mathbf{k}'| = 2k \sin(\theta/2)$  is the associated momentum transfer with the incident wavevector  $\mathbf{k}$ . Since the interaction potential is spherically symmetric, the scattering amplitude  $f(\Omega) = f(\theta)$  does not contain any azimuthal-angle dependence. The corresponding differential cross section is analytic and given by the absolute square of the scattering amplitude. The observed angular distribution is then proportional to this differential cross section.

In Fig. 5(b), we plot the angular distributions of the quadrupole polariton PL intensities from Figs. 4(b) (dots) and 5(a) (circles), where these intensity distributions are normalized at  $\phi = 0^\circ$  for comparison. The superimposed fits are generated using our model potential with  $ka = 14$  (red) and 6 (blue), respectively. The dashed curve is the angular divergence of the incident laser. Note that the only adjustable parameter is the effective screening radius  $a$  since the wavevector of a quadrupole polariton is given by  $k \simeq 2.63 \times 10^5 \text{ cm}^{-1}$  with a minor spreading  $\Delta k$ , which is a measure of the polariton bottleneck. Although our model might oversimplify the light character of a quadrupole polariton that actually undergoes multiple scattering, therefore affecting macroscopic ensemble coherence in a complicated way, we believe that it captures the essence of the dominant polariton-impurity scattering mechanism, where the charged-impurity concentration is parameterized by a cutoff radius  $a$ . Obviously, a stronger  $X_o$  signal with a narrower angular distribution would occur for samples containing lower impurity level. This also implies that the total coherence time can be extrinsically limited by scattering from impurities. Minimizing such extrinsic effects is crucial for preserving coherence. This angle-resolved technique can also be used as a sensitive path-averaged (and by some deconvolution perhaps a local) impurity detector allowing some degree of optimization for the coherence time of propagating quadrupole polaritons.

Another striking effect<sup>6</sup> arising from the dual character of quadrupole polaritons is anomalous Fresnel coefficients at the quadrupole resonance, resulting in resonantly enhanced reflection of quadrupole polaritons at crystal boundaries [Jang *et al.* (2008b)]. As originally suggested by

<sup>6</sup> Unlike polaritonic effects discussed in this section, which result from the half-matter character, suppressed collisional loss of quadrupole polaritons arises basically due to their half-light character and this is discussed in Sec. 7.

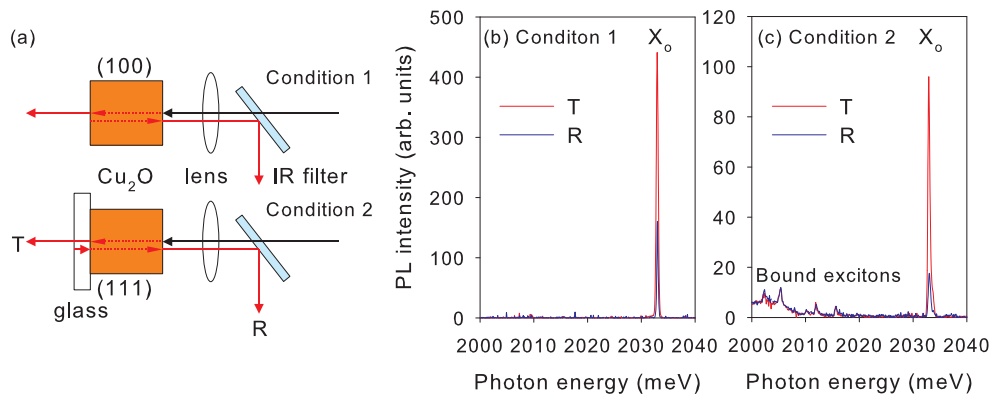


Fig. 6. (a) Schematic diagram of the PL collection geometry for two different boundary conditions. The incident IR beam (solid arrows) excites  $\text{Cu}_2\text{O}$  to create a traveling quadrupole polariton wave (red dashed arrows) inside the medium via two-photon absorption. As this wave leaves  $\text{Cu}_2\text{O}$ , it converts into photons (red solid arrows), yielding PL signals that we detect. The time-integrated PL measured from the incoming surface  $R$  (blue trace) and the opposite surface  $T$  (red trace) under (b) condition 1 and (c) condition 2, respectively.

Hopfield & Thomas (1963), polariton propagation in a dielectric medium is rather different from classical light propagation. The complexity basically arises from the fact that there are two propagating modes in the crystal associated with upper- and lower-branch polaritons. Therefore, the usual Maxwell boundary conditions are not enough to determine the field amplitudes for these two modes, requiring so-called *additional boundary conditions*. The special case of quadrupole polaritons was theoretically studied by Pekar *et al.* (1981) assuming a Frenkel-type excitation that vanishes at the vacuum-crystal boundary. However, the correction to the “effective” index of refraction at the quadrupole resonance is predicted to be negligible due to relatively small quadrupole coupling. In order to check this resonance effect, we experimentally investigate the “total” reflectance ( $R$ ) and transmittance ( $T$ ) of traveling quadrupole polaritons arising from multiple internal reflections at the sample surfaces. In our excitation geometry, we define  $R$  and  $T$  as the  $X_o$  intensities collected from the incoming and the opposing (outgoing) surfaces, respectively [see Fig. 6(a)]. Surprisingly, our principal finding indicates that the experimental value of  $T/R$  at the quadrupole resonance differs significantly from the prediction of Pekar *et al.* (1981).

Figure 6(a) shows a schematic diagram for measuring  $R$  and  $T$  for the two boundary conditions using (100)- and (111)-oriented natural-growth samples, respectively. Since we use resonant two-photon excitation in which the excitation energy is the half of the quadrupole polariton energy, the measured PL is decoupled from the incident laser. In order to measure  $R$  we use a dichroic mirror, which is an efficient IR filter transmitting the excitation light but reflecting visible light. The measured reflectivity in our observation range (1980 – 2040 meV) is about 0.485. Two-photon generated quadrupole polaritons propagate through the crystal along the incident laser direction. Therefore, the *opposite surface* is the first boundary encountered. For condition 2, the sample is attached to a glass slide to impose a different boundary condition. In this case, there is one more interface formed by the

glass and the superfluid He bath. When the quadrupole polariton wave leaves Cu<sub>2</sub>O, it is converted into transmitted light and a portion of that is reflected from this extra boundary by satisfying *usual* Fresnel relations. These reflected photons will resonantly excite Cu<sub>2</sub>O via *one-photon* excitation at the glass and Cu<sub>2</sub>O interface, thereby producing a counterpropagating quadrupole polariton wave in Cu<sub>2</sub>O.

In Fig. 6(b) we plot the observed PL spectrum (red trace) for condition 1 as collected from the opposite surface, corresponding to  $T$ . The blue trace shows the light transmitted at the incoming surface (corrected for the reflectivity of the IR filter), corresponding to  $R$ . The measured  $T/R$  is about  $2.75 \pm 0.05$ . Considering multiple internal reflections, this ratio can be analytically calculated and is given by

$$\frac{T}{R} = \frac{(te^{-\gamma})[1 + (re^{-\gamma})^2 + \dots]}{(re^{-\gamma})(te^{-\gamma})[1 + (re^{-\gamma})^2 + \dots]} = \frac{1}{re^{-\gamma}}, \quad (6)$$

where  $e^{-\gamma}$  is a phenomenological damping factor which includes all irreversible losses during a “one-way trip”, and  $r$  and  $t$  are the reflection and transmission coefficients at the Cu<sub>2</sub>O and superfluid He interface, which are approximately given by

$$r = \left(\frac{n-1}{n+1}\right)^2 \quad \text{and} \quad t = \frac{4n}{(n+1)^2}. \quad (7)$$

Note that  $R$  in Eq. (6) contains  $t$  because of transmission at the incoming surface. Also, Eq. (6) shows that the measured  $T/R$  is only affected by a *single* damping factor because the accumulative damping due to multiple internal reflections exactly cancels out in this ratio. In fact,  $e^{-\gamma}$  is negligible for our relatively thin samples ( $d < 1$  mm) considering a much longer decoherence length  $l = v_g \tau \simeq 2 - 20$  mm, where  $v_g$  is the quadrupole polariton group velocity (on the order of  $10^6 - 10^7$  m/s) and  $\tau \simeq 2$  ns is the measured decoherence time [Frohlich *et al.* (1991)]. Assuming  $e^{-\gamma} = 1$  and using  $n = 2.65$  for Cu<sub>2</sub>O, the simple Fresnel prediction yields  $T/R = 4.89$ , which does not agree with our measurement. Note that this damping factor, if significant, induces a larger discrepancy between the theoretical and measured  $T/R$ .

Figure 6(c) plots the measured  $R$  and  $T$  for condition 2 in which the sample attached to the glass contains a higher impurity concentration as indicated by the bound exciton PL. The isotropic bound exciton PL from two different collections overlap each other, verifying the scaling factor introduced by the IR filter. Because of an extra boundary formed by the glass and superfluid He, there are numerous combinations of multiple reflections and transmissions. In our analysis, we consider up to the 4th order, involving 8 combined reflections and transmissions at the boundaries. Using the measured index of refraction for the glass,  $n_g = 1.48$ , the calculation yields  $T/R = 9.77$ . However, the measured  $T/R$  for the condition 2 is about  $5.46 \pm 0.15$ , again significantly different from the classical Fresnel prediction.

The present theory [Pekar *et al.* (1981)] based on the additional boundary conditions predicts a *slight* modification in the effective index of refraction  $n_{eff}$  for a propagating quadrupole polariton wave depending on the wavevector direction. For example,  $n_{eff}$  for normal incidence is given by

$$n_{eff} = \sqrt{\varepsilon + \frac{2m'}{\hbar^2} \frac{4\pi q^2}{\Omega}} \equiv \sqrt{\varepsilon + \frac{1}{\zeta}}, \quad (8)$$



where  $\varepsilon = 7$  is the background dielectric constant,  $m'$  is the effective mass for a quadrupole polariton that depends on the wavevector direction,  $q$  is the exciton quadrupole moment, and  $\Omega$  is the unit-cell volume. The microscopic calculation yields  $1/\zeta \simeq -0.46$  and  $-0.17$  for (100) and (111) directions, respectively. Therefore, the predicted index of refraction at the quadrupole resonance is about  $n_{eff} = \sqrt{7-0.46} \simeq 2.56$  for the (100) direction. This negligible correction apparently does not explain our measurements and  $n_{eff}$  must be significantly larger than  $n = 2.65$ . Based on the series of experiments, we have confirmed that our experimental results can be explained by introducing the effective index of refraction  $n_{eff} = 4.0 \pm 0.1$  for the boundary conditions we employed. This increased index of refraction in turn implies a significantly enhanced reflection of quadrupole polaritons at the crystal boundary.

The failure of the present theory might result from assuming localized Frenkel excitons, whereas Cu<sub>2</sub>O is well known for hosting weakly bound Mott-Wannier excitons. Alternatively, the amplitude of the orthoexciton may not vanish at the boundary as discussed below. This significantly enhanced reflection arises most likely from the behavior of the matter component (exciton). Although thermal excitons may break down at the crystal boundary, the quasi-ballistic excitonic component of moving quadrupole polaritons will most likely be reflected at the surface with minimal surface recombination, presumably hindering quadrupole polaritons from exiting Cu<sub>2</sub>O and thus causing enhanced reflection. In the absence of a proper theory, we propose that the phase shift associated with this reflection be regarded as a free parameter. It may be that the behavior can be Fresnel-like, however with a modified index of refraction. We believe that this anomalous reflection is universal, arising from the half-matter/half-light property of polaritons, regardless of host materials. Our results have implications for the optoelectronic design of polariton waveguides and resonators in which a larger (effective) index of refraction implies a larger angle of total internal reflection which in turn affects the cutoff wavelength and with it the confinement of polaritons inside the medium.

## 6. Efficient quadrupole polariton generation with unconventional approaches

As a bound state of an electron and a hole, an exciton in Cu<sub>2</sub>O is electrically neutral and only weakly magnetic.<sup>7</sup> Therefore, conventional electromagnetic external perturbations do not cause a significant modification in its electronic properties. But, mechanical strain affects the electronic states of Cu<sub>2</sub>O in two ways: (i) it induces a bandgap shift and, more important, (ii) it lowers the crystal symmetry, resulting in splitting of orthoexciton levels depending on the stress direction. Although numerous studies on excitons under external stress were performed [Jang & Wolfe (2006b); Lin & Wolfe (1993); Liu & Snoke (2005); Mysyrowicz *et al.* (1983); Naka & Nagasawa (2002); Snoke & Negoita (2000); Trauernicht & Wolfe (1986)], the effect of external stress on quadrupole polaritons is essentially a virgin territory, potentially full of unexplored interesting physics.

Under spatially inhomogeneous Hertzian stress [Snoke & Negoita (2000)], a strain well forms a potential minimum for excitons inside the crystal. This technique has been extensively used in attempts to create trapped high-density excitons. Figures 7(a) and (b) illustrate the potential well formed in a Lucite crystal under Hertzian contact stress and a schematic of

<sup>7</sup> One needs more than 10 T to observe noticeable exciton-level splitting in Cu<sub>2</sub>O induced by external magnetic field [Fishman *et al.* (2009)].

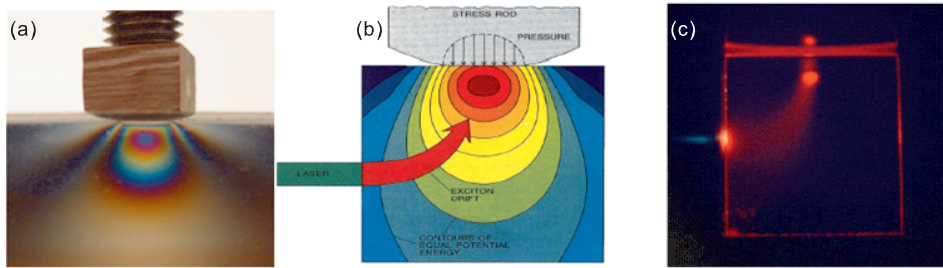


Fig. 7. (a) Hertzian contact at Lucite showing potential minimum and equipotential contours monitored by cross polarizer. (b) Schematic of potential-trap experiments and (c) image of excitons in  $\text{Cu}_2\text{O}$  effectively confined by a potential well just below the stressor after fast drift from the excitation spot (left).

stress experiments at low temperatures, respectively. Exciton drift into such a potential well in  $\text{Cu}_2\text{O}$  at 2 K is clearly shown in Fig. 7(c). One can then ask how this harmonic potential well affects the propagating quadrupole polaritons. They could be attracted by the well due to the excitonic component, as shown in Fig. 7(c), or not because the photonic component is little affected. It will be interesting to study the influence of the potential well on the quadrupole polariton propagation.

As a preliminary, we first conduct a rather simple experiment using *uniaxial* stress along a (001) direction and collect the PL from a (110) surface of a natural-growth  $\text{Cu}_2\text{O}$  sample.<sup>8</sup> Surprisingly, our results indicate that the quadrupole polariton PL ( $X_0$  line) is significantly enhanced with external stress. Figures 8(a)–(c) plot the observed  $X_0$  intensities (red traces) as a function of stress in the range of  $\sigma = 0 - 0.3$  kbar. The heavy solid traces are fits using a single or double Gaussian function, considering the spectral resolution of our detection system. As we increase stress, the triply-degenerate quadrupole state splits into the singlet and doublet states where the latter lies lower [Jang & Wolfe (2006b)]. The measured splitting is consistent with our theoretical prediction. In Figs. 8(d)–(f), we plot the corresponding polarization dependence of the  $X_0$  intensities obtained using an analyzer behind the sample, indicating a significant modification of the one-photon selection rules. Most of all, it is very interesting that the quadrupole polariton PL rapidly increases with  $\sigma$  and its brightness at  $\sigma = 0.3$  kbar is more than 10 times that obtained under no stress. We have also performed the same experiments using one-photon over-the-gap excitation to check the *exciton* PL as a function of  $\sigma$  and confirmed that no such a strong enhancement is observed. It implies that this is solely related to either "coherent" polaritonic effects or enhanced two-photon excitation, arising from modification of the electronic structure (mixing between dark and bright states) induced by external stress. In order to clarify the underlying mechanism, one needs to time-resolve the population and relaxation dynamics of quadrupole polaritons as a function of  $\sigma$ . Clearly, this stress technique is promising for generating high-density quadrupole polaritons for BEC.

Previous experiments based on two-photon absorption were conducted using a single-beam laser tuned to the two-photon quadrupole resonance (1219.4 nm). However, quadrupole polariton generation can be also accomplished using two independent beam sources as long as (i) the sum of beam frequencies matches with the quadrupole resonance and (ii) the

<sup>8</sup> This sample was previously used for studying paraexcitons under stress [Trauernicht & Wolfe (1986)].

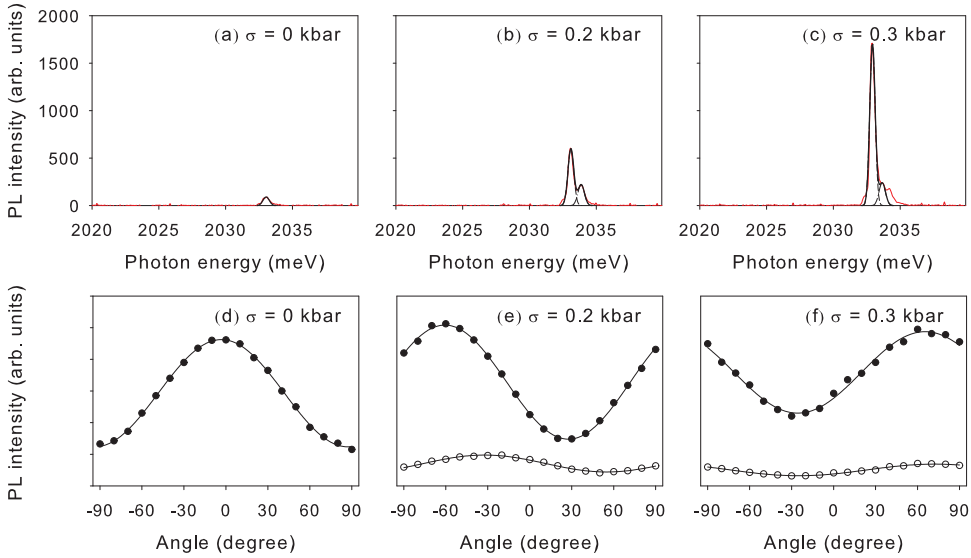


Fig. 8. Time-integrated quadrupole polariton PL (red traces) at (a)  $\sigma = 0$  kbar, (b) 0.2 kbar, and (c) 0.3 kbar, respectively, superimposed with Gaussian fits (heavy solid curves). (d) Measured polarization dependence (dots) under no stress, well explained by the one-photon selection rules (solid curve). The corresponding polarization dependence under external stress are plotted by dots (doublet) and circles (singlet) in (e) and (f). Superimposed are empirical fits.

conservation of momentum is fulfilled inside the crystal (phase matching). This two-beam technique has been initially triggered by the idea of mixing much stronger pulses from the pump YAG laser (1064 nm) and those from the OPA (tuned to 1428 nm) in order to generate high-density quadrupole polaritons. Moreover, we can independently control the polarizations of the two incident beams and their propagation directions, and therefore, the resulting wavevector of quadrupole polaritons inside the sample.

Unlike one-beam two-photon technique, however, there are number of issues to optimize two-beam two-photon excitation such as pulse synchronization, OPA wavelength tuning, and precise optical alignments, etc. For example, the dots in Fig. 9(a) correspond to the quadrupole polariton signal when the delay arm of the OPA is varied near the pulse synchronization position. The superimposed curve is a fit to the data, yielding a temporal overlap of 30 ps, which is consistent with the pulse widths of two beams. In Fig. 9(b), we plot the quadrupole polariton signal (dots) observed when we vary the wavelength of the OPA near 1428 nm. The solid curve is a fit that basically reflects the spectral linewidth of the OPA at this wavelength. These clearly show that two-beam two-photon efficiency strongly depends on both time and wavelength detuning of the OPA. The dots (and superimposed curve) in Fig. 9(c) show the relative polarization dependence of the two-beam two-photon efficiency when the polarization angle of the OPA is varied in the range from  $-90^\circ$  to  $90^\circ$ , indicating that orthogonal polarization is not favorable, as expected. Employing this two-beam two-photon technique, we can also study “impact ionization” of quadrupole polaritons by varying two incident beam powers independently, which arises from additional absorption

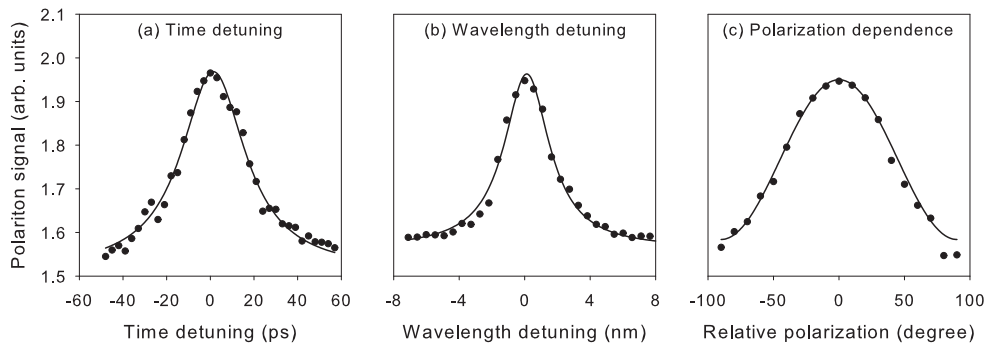


Fig. 9. Measured  $X_0$  intensity from quadrupole polaritons as a function of (a) OPA time detuning, (b) OPA wavelength detuning, and (c) OPA polarization relative to the fixed vertical polarization of the 1064 nm output from the YAG laser, respectively.

of an incident photon by a quadrupole polariton that ionizes the excitonic component. In fact, this mechanism can mimic Auger-type collisional loss of quadrupole polaritons, and therefore, measuring and controlling this process could be an important issue for achieving a high-density polariton system.

Another interesting direction is to use “quadrupole-induced” second harmonic generation (SHG) to efficiently generate high-density quadrupole polaritons using a *non-collinear orthogonal polarization geometry* [Figliozzi *et al.* (2005)]. Interestingly, the corresponding SHG polarization is largest when the incident electric fields are mutually orthogonal and is proportional to  $\sin \psi$ , where  $\psi$  is the angle between two wavevectors inside the crystal. This condition is quite different from that for two-beam two-photon absorption as explained above. The technique was developed to investigate the surface structure of Si nanocrystals embedded in  $\text{SiO}_2$  matrix using SHG signals, which is enhanced by several orders of magnitude [Figliozzi *et al.* (2005)]. Since  $\text{Cu}_2\text{O}$  has a centrosymmetric crystal structure, SHG is not viable in the dipole approximation. However, one can turn on SHG in this semiconductor by exploiting this technique. Clearly, it is an interesting question whether quadrupole polariton generation can be further improved via enhanced quadrupole SHG.

### 7. Third-order nonlinearity and nonlinear processes at quadrupole resonance

Although  $\text{Cu}_2\text{O}$  has a rich history as a prototype material for studying fundamental exciton physics, its nonlinear optical properties have received little attention presumably because of its vanishing second-order susceptibility  $\chi^{(2)}$  stemming from its centrosymmetric crystal structure. Consequently, the lowest-order optical nonlinearity in  $\text{Cu}_2\text{O}$  arises from the third-order susceptibility  $\chi^{(3)}$ . Precise characterization of the nonlinear optical parameters such as  $\chi^{(3)}$  and the two-photon absorption coefficient  $\beta$  is crucial in evaluating its potential for nonlinear optical applications and estimating the densities of excitonic matter under two-photon excitation. Recently, we have reported the first measurement of the nonlinear refractive index  $n_2 \propto \text{Re}[\chi^{(3)}/n]$  ( $n = 2.65$ ) and  $\beta$  based on the Z-scan technique [Mani *et al.* (2009b)].

The single-beam Z-scan technique relies on the phenomenon of self-focusing of an intense Gaussian laser beam in the presence of a nonlinear medium [Sheik-Bahae *et al.* (1990; 1991)].

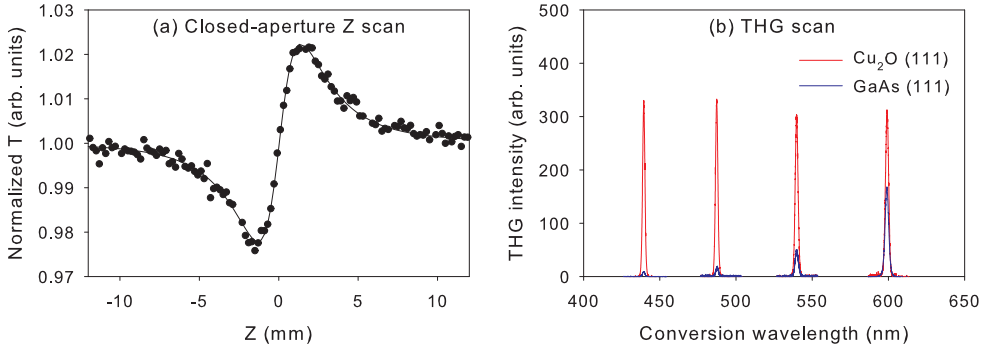


Fig. 10. (a) Normalized closed-aperture Z-scan data (dots) obtained from a (110)-oriented natural-growth Cu<sub>2</sub>O sample with 20% aperture transmittance, superimposed by a theoretical fit (solid trace). (b) Wavelength-dependent THG from Cu<sub>2</sub>O (red) and GaAs (blue).

One can characterize both  $n_2$  and  $\beta$  using the closed- and open-aperture Z-scan configurations, respectively. The dots in Fig. 10(a) correspond to the normalized closed-aperture Z-scan trace showing a valley-peak configuration, indicating positive nonlinearity of Cu<sub>2</sub>O, when the on-axis irradiance at the focus is set to  $I(Z = 0) = 0.86 \text{ GW/cm}^2$  at  $\lambda = 1064 \text{ nm}$ . At this relatively low irradiance level, with negligible  $e$ - $h$  pair generation by two-photon transition, the closed-aperture Z-scan accounts for purely refractive nonlinearity due to the bound electronic Kerr effect;  $\Delta n = n_2 I$ , where  $\Delta n$  is the on-axis index change at focus. Transmittance change at the detector ( $\Delta T$ ) is related to  $\Delta n$  by

$$\Delta T \simeq 0.406(1 - S)^{0.25} \frac{2\pi}{\lambda} d_{eff} \Delta n, \quad (9)$$

where  $S = 20\%$  is the aperture transmittance and  $d_{eff} = (1 - e^{-\alpha d})/\alpha$ , with the linear absorption coefficient  $\alpha = 47 \text{ cm}^{-1}$  at  $\lambda = 1064 \text{ nm}$  for the sample thickness  $d = 100 \mu\text{m}$ . The solid curve is a least-square fit to the data, yielding  $n_2 = 1.32 \times 10^{-10} \text{ esu}$ . We have found that similar values of  $n_2$  are obtained from our synthetic samples [Mani *et al.* (2009b)]. This measured  $n_2$  value of Cu<sub>2</sub>O seems comparable with those of other conventional nonlinear semiconductors with large  $n_2$  values. However, it is important to note that  $n_2 \propto 1/E_g^4$ , where  $E_g$  is the bandgap, and that the best  $\chi^{(3)}$  materials have bandgap energies far below that for Cu<sub>2</sub>O [see for example Table III of Sheik-Bahae *et al.* (1991)]. This implies that the matrix elements entering  $\chi^{(3)}$  are very large in Cu<sub>2</sub>O but the overall response is scaled down by its relatively large bandgap energy. Considering this factor, we believe that Cu<sub>2</sub>O is a potential  $\chi^{(3)}$  material with a bandgap energy lying in the visible region.

This is further confirmed by Fig. 10(b), showing the measured THG signals from Cu<sub>2</sub>O and GaAs, both oriented along a (111) direction and 0.5 mm thick, when the input OPA wavelength is varied from 1300 nm to 1800 nm. Considering that  $n_2$  of GaAs is about two times that of Cu<sub>2</sub>O, it is initially surprising that THG from Cu<sub>2</sub>O is more intense. This basically arises from two reasons: (i) since  $\chi^{(2)}$  of GaAs is very large, the incident laser most strongly contributes to the lower-order SHG process and (ii) GaAs is a dipole-allowed semiconductor in which

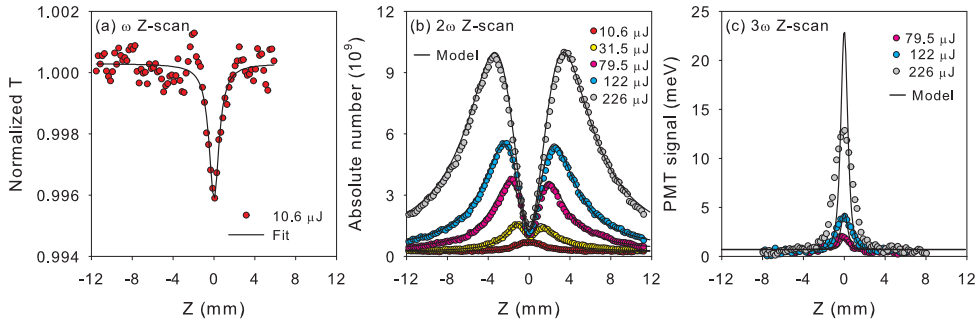


Fig. 11. (a) Normalized  $\omega$  Z-scan (red dots) for  $10 \mu\text{J}/\text{pulse}$ , superimposed by a theoretical fit (solid trace) with  $\beta = 0.217 \text{ cm}/\text{GW}$ . (b)  $2\omega$  Z-scan traces (colored dots) for various excitation levels in the range of  $10.4 - 226 \mu\text{J}/\text{pulse}$ , fit by the theoretical model (solid traces). (c)  $3\omega$  Z-scan traces (colored dots) for  $79.5, 122,$  and  $226 \mu\text{J}/\text{pulse}$ . The solid curves correspond to a model assuming no fundamental depletion.

the THG light being above the bandgap is strongly absorbed compared with the case for a dipole-forbidden semiconductor of  $\text{Cu}_2\text{O}$ . In support of the latter, Fig. 10(b) shows that the THG intensity from GaAs sharply depends on the OPA input wavelength, whereas for  $\text{Cu}_2\text{O}$  it does not. Most importantly, it is noteworthy that measurable THG signals can be transmitted through a  $0.5 \text{ mm}$ -thick  $\text{Cu}_2\text{O}$  sample used in the measurements since the absorption lengths for the converted THG wavelengths shown in Fig. 10(b) are known to be less than a few microns [O'Hara *et al.* (1999b)]. This implies that  $\text{Cu}_2\text{O}$  could be utilized for an active THG medium working at  $\omega_{\text{IR}}$  in the mid-IR range such that  $3\omega_{\text{IR}}$  is still below the bandgap of  $\text{Cu}_2\text{O}$  without any complication from  $\chi^{(2)}$  contributions.

Recently, it has been suggested that three-photon excitation [Ideguchi *et al.* (2008)] and THG [Mani *et al.* (2009b)] can affect population dynamics of quadrupole polaritons in  $\text{Cu}_2\text{O}$  under strong two-photon excitation. Considering possible complications caused by these high-order processes, the feasibility of quadrupole polariton BEC remains an open question. In pursuit of this question we systematically investigate various nonlinear optical processes such as two-photon absorption, Auger-type recombination, and THG under resonant two-photon excitation at  $2 \text{ K}$ . By extending the standard *open-aperture* Z-scan method (that only monitors the intensity at  $\omega$ ), we also keep track of the frequency-doubled ( $2\omega$ ) and tripled ( $3\omega$ ) Z-scan outputs to probe the quadrupole polariton PL and THG responses using appropriate band-pass filters [Mani *et al.* (2010)].

In order to estimate the *absolute* number of quadrupole polaritons generated under two-photon excitation, it is essential to precisely determine  $\beta$ , basically arising from  $\text{Im}[\chi^{(3)}]$  at the quadrupole resonance. The red dots in Fig. 11(a) correspond to the normalized  $\omega$  Z-scan trace, showing two-photon absorption for  $10.4 \mu\text{J}/\text{pulse}$ . Note that only  $0.4\%$  of the incident beam is absorbed at the focus ( $Z = 0$ ). The solid trace is a theoretical fit [Sheik-Bahae *et al.* (1990)] with  $\beta = 0.217 \text{ cm}/\text{GW}$  and the beam waist of  $\omega_0 = 15.1 \mu\text{m}$  at  $Z = 0$ . This  $\omega_0$  is consistent with the standard Gaussian width  $\sigma_s = 0.19 \text{ cm}$  of the incident beam through  $\sigma_s/f = \lambda/\pi\omega_0$ , where  $f = 7.5 \text{ cm}$  and  $\lambda = 1219.4 \text{ nm}$ . Unlike conventional band-to-band two-photon absorption, the effect at the narrow quadrupole resonance depends on the spectral width  $\delta\omega$  of the incident laser. In our case of  $\delta\omega \simeq 8 \text{ meV}$ , we have confirmed

that  $\beta = 0.217 \text{ cm/GW}$  within a 50% uncertainty based on the series of  $\omega$  Z-scan experiments. We also find that the measured  $\beta$  value persists up to  $226 \mu\text{J/pulse}$  without any evidence for higher-order multiphoton absorption. This implies that one-photon transition induced by subsequent absorption of the THG light apparently mimics three-photon excitation. With  $\beta$  determined, depletion of the fundamental intensity  $I$  along the beam path  $z$  due to two-photon absorption can be calculated and is given by

$$\frac{dI}{dz} = -\beta I^2 \rightarrow I(z; Z, t) = \frac{I_0(Z, t)}{I_0(Z, t)\beta z + 1}, \quad (10)$$

where  $I_0(Z, t)$  is the photon flux at the incident sample surface, which is a function of the focusing lens position  $Z$  and given by

$$I_0(Z, t) = \frac{2P(t)}{\pi\omega^2(Z)} \rightarrow \frac{2P}{\pi\omega^2(Z)} = \frac{2P}{\pi\omega_0^2(1 + Z^2/Z_0^2)}, \quad (11)$$

where  $P(t)$  is the input pulse power with a 30 ps temporal profile and  $Z_0 = \pi\omega_0^2/\lambda \simeq 0.06 \text{ cm}$  is the confocal parameter. Since Z-scan yields the time-averaged data, we use the *time-integrated* pulse power  $P$  to evaluate  $I_0(Z)$ . In Eq. (11), a factor of 2 is correctly introduced for the averaged power of the TEM<sub>00</sub> mode Gaussian beam.

Figure 11(b) plots the  $2\omega$  Z-scan traces (colored dots) under several excitation levels from  $10.4 \mu\text{J/pulse}$  to  $226 \mu\text{J/pulse}$ , showing quadrupole polaritons generated by resonant two-photon excitation. Note that we plot the time-averaged *absolute* number of quadrupole polaritons using the measured  $\beta$  as explained below. As predicted for two-photon absorption in a finite-thickness sample, for a given excitation level, the measured quadrupole polariton number increases quadratically with the corresponding  $I_0(Z)$  as we sweep  $Z$ .<sup>9</sup> However, a striking dip-like feature develops in the vicinity of  $Z = 0$  as we increase the pulse energy and quadrupole polariton generation severely saturates at the focus. In order to check whether any signal was lost due to the finite aperture of the PMT collector, we have probed the quadrupole polariton spatial profile in the far field as a function of  $Z$  using a gated intensified CCD camera and verified that this mechanism is negligible [Mani *et al.* (2010)]. Together with  $\omega$  Z-scan indicating negligible higher-order contributions, this implies that quadrupole polaritons undergo an Auger-type two-body decay process at high densities.

In order to explain  $2\omega$  Z-scan, we now model the population and relaxation dynamics of quadrupole polaritons. The quadrupole polariton generation rate  $G$  should match the laser absorption profile;  $G(\mathbf{r}; Z) = -(dI/dz)/2 = \beta I^2/2$ , where a factor of 1/2 accounts for energy conservation during two-photon absorption. The temporal behavior of the local quadrupole polariton density  $n(\mathbf{r}; Z, t)$  is described by

$$\frac{dn}{dt} = G(\mathbf{r}; Z) - \frac{n}{\tau} - An^2, \quad (12)$$

where  $\tau$  is the quadrupole polariton lifetime and  $A$  is an Auger coefficient [Jang & Wolfe (2005; 2006a;c); Jang & Ketterson (2008)]. The analytical solution to Eq. (12) exists and the

<sup>9</sup> If the sample is infinitely thick, the incident IR photons  $N$  should be all absorbed and the number of quadrupole polaritons created is simply  $N/2$ , independent of  $I_0(Z)$ .

time-averaged density  $n(\mathbf{r}; Z)$  is given by

$$n(\mathbf{r}; Z) = \frac{\int n(\mathbf{r}; Z, t) dt}{\int dt} = \frac{\ln[1 + An_0(\mathbf{r}; Z)\tau]}{A\tau}, \quad (13)$$

where the initial density is well approximated by  $n_0(\mathbf{r}; Z) = \{[1 + 4G(\mathbf{r}; Z)A\tau_p^2]^{1/2} - 1\} / 2A\tau_p$  with the pulse width  $\tau_p = 30$  ps. While  $n_0$  is essentially  $G\tau_p$  at low excitation, it approaches to  $(G/A)^{1/2}$  and is limited by fast Auger-type decay during the 30 ps buildup time when  $GA\tau_p^2 \gg 1$ . To obtain the time-averaged quadrupole polariton number  $N(Z)$  for a given  $Z$ , we numerically integrate  $n(\mathbf{r}; Z)$  over the sample dimension ( $d = 100 \mu\text{m}$ ):

$$N(Z) = \int n(\mathbf{r}; Z) d^3r = \pi\omega^2(Z) \int_0^d n(z; Z) dz. \quad (14)$$

Note that  $N(Z)$  contains only two independent fit parameters of  $\tau$  and  $A$ , since  $G$  is accurately determined with  $\beta = 0.217 \text{ cm/GW}$ . The solid traces in Fig. 11(b) show  $N(Z)$  using a single fit-parameter set of  $\tau = 2 \text{ ns}$  and  $A = 0.55 \times 10^{-16} \text{ cm}^3/\text{ns}$ , showing excellent fits to the series of  $2\omega$   $Z$ -scan data. A value  $\tau = 2 \text{ ns}$  is consistent with that obtained from coherent quantum beat spectroscopy [Frohlich *et al.* (1991)] and  $A$  is about 2 times smaller than that reported based on Lyman absorption spectroscopy [Jang & Ketterson (2008); Tayagaki *et al.* (2006)].

Most of all, it is remarkable that the measured  $A$  value for quadrupole polaritons is more than 10 times *smaller* than that for thermalized excitons [Jang & Wolfe (2005; 2006a;c)]. This significantly reduced  $A$  seems puzzling but we can qualitatively explain it based on the unique property a quadrupole polariton possesses but an exciton does not. This two-body decay process for excitons is exclusively caused by “matter-matter collision” via Coulomb interaction between two  $e$ - $h$  pairs consisting of two excitons. Since this process arises from random collision of excitons, it depends on the exciton *gas* temperature [Jang & Wolfe (2005; 2006a;c)]. However, as a quantum superposition of a photon (light) and a bright orthoexciton (matter), a quadrupole polariton also carries the *light* character that is not relevant to this collisional process. Unlike diffusive excitons, quadrupole polaritons all move in the same direction with a definite nonzero wavevector primarily determined by the incident laser beam. Therefore, they should have a greatly reduced probability for random collision. In this view, it is not surprising that quadrupole polaritons have a much suppressed Auger coefficient.

Figure 11(c) displays  $3\omega$   $Z$ -scan traces (colored dots) for 79.5, 122, and 226  $\mu\text{J}/\text{pulse}$ , resulting from THG of the input laser. We confirmed that  $3\omega$   $Z$ -scan responses were very small for lower excitation. Again, considering a submicron absorption length at 406.5 nm in  $\text{Cu}_2\text{O}$ , it is remarkable that measurable THG signals are transmitted through the sample. Since fundamental depletion due to two-photon absorption is negligible, the THG field intensity  $E_{3\omega}$  as a function of  $Z$  is given by [Boyd (2008)]

$$E_{3\omega}(Z) = \frac{i3\omega}{2nc} \chi^{(3)} E^3(Z) J_{3\omega}(\Delta kd), \quad (15)$$

where  $n$  is the index of refraction for  $\text{Cu}_2\text{O}$ ,  $c$  is the speed of light in vacuum,  $E(Z) = [I_0(Z)/2nc]^{1/2}$ , and  $J_{3\omega}(\Delta kd)$  is the phase-matching factor. The solid traces in Fig. 11(c) are the predicted THG photon counting  $[\propto \pi\omega^2(Z)|E_{3\omega}(Z)|^2]$  properly scaled to match the overall data, simply assuming phase matching ( $J_{3\omega} = d$ ) and using  $I_0(Z)$  in Eq. (11). While this



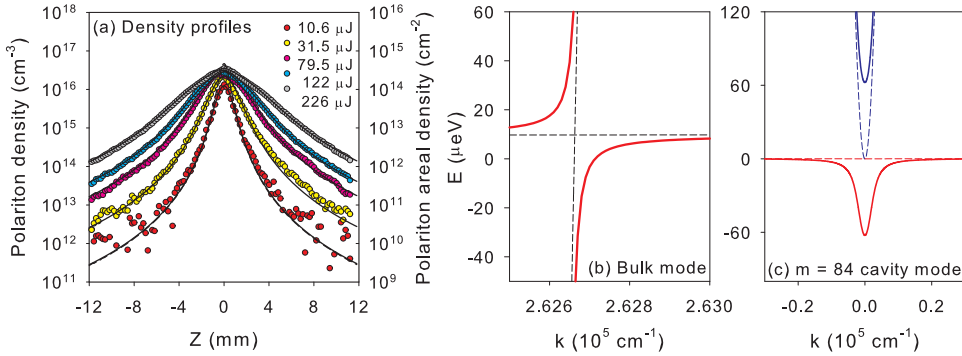


Fig. 12. (a) Time-averaged quadrupole polariton densities (colored dots) as a function of  $Z$ , superimposed by our Auger model (solid traces). Calculated quadrupole polariton dispersion for (b) 3D bulk and (c)  $10\ \mu\text{m}$ -thick cavity ( $m = 84$ ) modes in Cu<sub>2</sub>O for a (110) direction.

simple model basically corresponds to a  $I^3$  fit, the observed  $3\omega$  Z-scan data reveal a different power dependence of  $I^{1.8}$ . We believe that this rather unusual power dependence stems from complicated processes involving (i) strong absorption of THG beam that crucially affects phase coherence between the fundamental and THG lights inside Cu<sub>2</sub>O and/or (ii) possible contribution due to the generation of higher harmonics. Although a full understanding of detailed THG mechanism in Cu<sub>2</sub>O awaits more experimental and theoretical studies, it is clear that high-density quadrupole polariton generation is more affected by an Auger-type process rather than THG, as indicated by our Auger model explaining  $2\omega$  Z-scan data without a  $\chi^{(3)}$  parameter [see Fig. 11(b)].

Unlike typical dipole coupling encountered in other semiconductors, quadrupole coupling near the crossover is much smaller in bulk Cu<sub>2</sub>O, causing relatively large curvature of the dispersion near the quadrupole polariton bottleneck; the associated group velocity is relatively fast and the effective mass is very small, several orders of magnitude smaller than the exciton mass [see Fig. 12(b)]. This should result in a significant reduction in the BEC transition density. Furthermore, the Auger-type cross section is significantly reduced for quadrupole polaritons owing to their half-matter/half-light characters. This implies that the experimentally achievable quadrupole polariton densities can be well above the critical density for BEC.

In order to estimate experimental quadrupole polariton densities attainable, we plot the time-averaged density  $n(Z) = N(Z)/\pi\omega^2(Z)d$  (colored dots) in Fig. 12(a) using  $N(Z)$  in Fig. 11(b). The solid traces correspond to our Auger model with  $A = 0.55 \times 10^{-16}\ \text{cm}^3/\text{ns}$ . In our excitation range, the spatial extent of quadrupole polaritons along the propagation direction is limited by the sample thickness of  $d = 100\ \mu\text{m}$ , which is smaller than the two-photon absorption length  $(\beta I)^{-1}$ . The corresponding areal densities  $N(Z)/\pi\omega^2(Z)$  are also plotted in Fig. 12(a). Despite considerable decrease in  $N(Z)$  around  $Z = 0$  in Fig. 11(b), it is important to note that the maximum density still locates at the focus in which it saturates around  $3 \times 10^{16}\ \text{cm}^{-3}$  under high excitation levels. This is more than 10 times higher than the maximum thermal exciton density ( $\simeq 10^{15}\ \text{cm}^{-3}$ ) [O'Hara & Wolfe (2000)], basically due to the suppression of  $A$  by the same amount.

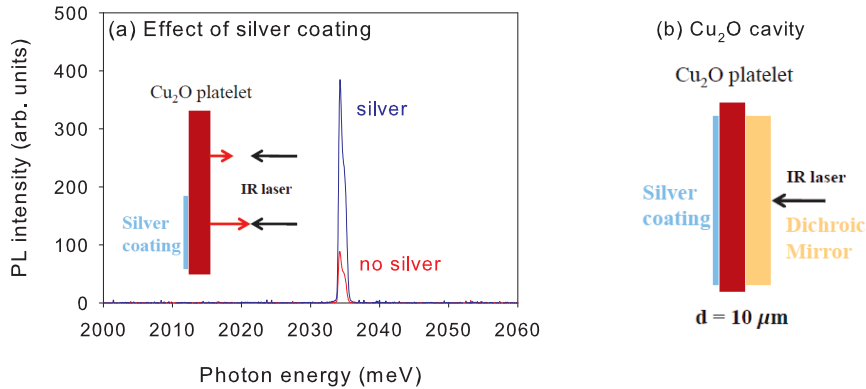


Fig. 13. (a) Time-integrated PL recorded using a reflection geometry, showing effective confinement of quadrupole polaritons from a silvered region. Inset depicts the sample and collection geometry. (b) Schematic diagram for a Cu<sub>2</sub>O Fabry-Perot cavity.

Although the areal densities for quadrupole polaritons we observe in Cu<sub>2</sub>O are much higher than the critical BEC density ( $\approx 10^9 \text{ cm}^{-2}$ ) in the 2D cavity-polariton structures [Balili *et al.* (2007); Deng *et al.* (2003); Kasprzak *et al.* (2006)], BEC is not expected to arise in practice, since the *absence of a local minimum* precludes condensation as shown in Fig. 12(b); of course such minima have been engineered into the polariton dispersion curves of the 2D microcavities. This limitation might be circumvented by depositing partially transmitting mirrors on opposing sides of a flat platelet of Cu<sub>2</sub>O, thereby forming a Fabry-Perot cavity [see Fig.13(b)]. In Fig. 12(c), we plot our simulation result for the  $m = 84$  cavity-photon mode assuming a  $10 \mu\text{m}$ -thick Cu<sub>2</sub>O platelet that forms a Fabry-Perot cavity (blue dashed curve) sitting just above the exciton mode (red dashed curve).<sup>10</sup> Then, the lower-polariton branch (red solid curve) would develop a local minimum via quadrupole coupling associated with a very small effective mass ( $\approx 10^{-5} m_e$ ) in which long-lived quadrupole polaritons can condense.

Recently, we have experimentally confirmed that depositing a silver film on Cu<sub>2</sub>O significantly enhances the quadrupole polariton confinement without altering underlying excitonic structures, as demonstrated by Fig. 13(a). The quadrupole polariton PL from a silvered region (blue trace) is about 4 times stronger than that from an unsilvered region (red trace). This behavior persists when we move the excitation position around the silvered portion. Figure 13(b) illustrates a detailed schematic of the proposed cavity system for quadrupole polariton BEC. The excitation surface of a Cu<sub>2</sub>O platelet is attached to a commercial dichroic mirror that transmits the incident excitation beam in the IR (1219.4 nm), but strongly reflects the quadrupole polariton PL in the visible range (609.7 nm), thereby forming a *high-Q cavity with efficient quadrupole polariton generation*. Optimally coupling the OPA output to the cavity poses a more challenging problem, as it requires a way to continuously vary this coupling. We have two strategies for matching of mode frequency

<sup>10</sup> Smaller node numbers and large mode spacings would require a thinner sample. A promising technology to make thin Cu<sub>2</sub>O films showing sharp exciton lines was reported by Markworth *et al.* (2001).

either by (i) adjusting the propagation direction of quadrupole polaritons relative to the plane normal or (ii) placing a silver mirror on the far side of the sample with a variable thickness. Unlike our previous experiments based on time-integrated methods, we plan to directly time-resolve the population and relaxation dynamics of two-photon generated quadrupole polaritons as a function of the input IR power and the angle of incidence. This will clearly reveal not only the impact of two-body decay on high-density quadrupole polaritons but also the coherent temporal evolution of long-lived quadrupole polariton condensate once achieved.

## 8. Concluding remarks

The goal of this chapter is to study both fundamental and technological aspects of natural-growth/synthetic cuprous oxide ( $\text{Cu}_2\text{O}$ ) crystals that host long-lived excitonic matter and exhibit large third-order nonlinear optical responses. All these remarkable physical properties primarily originate from the centrosymmetric crystal structure and the dipole-forbidden bandgap of  $\text{Cu}_2\text{O}$ . Bright orthoexcitons intersecting the light cone quadrupole couple to the electromagnetic field and split into two polariton branches. A quadrupole polariton in  $\text{Cu}_2\text{O}$  is special in that it propagates over a macroscopic distance with a very long coherence time, compared with polaritons in conventional dipole-allowed semiconductors.

Based on the series of experiments under resonant two-photon excitation, we have demonstrated various interesting phenomena essentially arising from unique half-matter/half-light characteristics of quadrupole polaritons. However, our current understanding of the properties of a quadrupole polariton is rather empirical and accessible only experimentally, calling for a more rigorous microscopic description of this quasiparticle. More importantly, our findings imply that high-density quadrupole polaritons can be effectively confined inside  $\text{Cu}_2\text{O}$  and we have proposed a promising direction for long-lived polariton Bose-Einstein condensation (BEC). Clearly, BEC in a forbidden-gap semiconductor would be a valuable addition to the current BEC class from the perspective of fundamental physics. Also, polariton BEC on the order of several nanoseconds at nominal cryogenic temperatures will be a revolutionary step toward quantum computers and information sciences.

Various nonlinear optical parameters have been quantitatively characterized using Z-scan and third harmonic generation (THG) techniques. Distinctive and interesting properties of this semiconductor allow us to consider possible optoelectronic applications involving polariton-based waveguides and whispering gallery resonators, polariton lasers, and active third-order nonlinear optical devices. We have also discussed a set of particularly interesting and timely issues. This includes detailed research directions such as (i) high-density quadrupole polariton dynamics near BEC regime, (ii) impact of external stress on quadrupole polaritons, (iii) nonlinear optics at the quadrupole resonance using both two-beam two-photon absorption and quadrupole-induced second harmonic generation, and (iv) clarification of underlying THG mechanism.

## 9. Acknowledgments

The author acknowledges the essential collaboration of J. B. Ketterson at Northwestern University, S. Mani at Intel Corporation, and J. P. Wolfe at the University of Illinois. This work is supported by the National Science Foundation under (i) the Northwestern Materials Research Center; Grant DMR-0520513, (ii) the U.S./Ireland cooperation; Grant 0306731, and (iii) the Integrative Graduate Education and Research Training program; Grant 0801685.

## 10. References

- Amsel, G.; Battistig, G. & L'Hoir, A. (2003). Small angle multiple scattering of fast ions, physics, stochastic theory and numerical calculations, *Nucl. Instrum. Methods Phys. Res. B* 201, 325.
- Balili, R.; Hartwell, V.; Snoke, D.; Pfeiffer, L. & West, K. (2007). Bose-Einstein condensation of microcavity polaritons in a trap, *Science* 316, 1007.
- Beg, M. M. & Shapiro, S. M. (1976). Study of phonon dispersion relations in cuprous oxide by inelastic neutron scattering, *Phys. Rev. B* 13, 1728.
- Boyd, R. W. (2008). *Nonlinear Optics*, 3rd ed. Academic Press, San Diego. pp. 119.
- Christopoulos, S.; von Hagersthal, G. B. H.; Grundy, A. J. D.; Lagoudakis, P. G.; Kavokin, A. V.; Baumgerg, J. J.; Christmann, G.; Butte, R.; Feltin, E.; Carlin, J. -F. & Grandjean, N. (2007). Room-temperature polariton lasing in semiconductor microcavities, *Phys. Rev. Lett.* 98, 126405.
- Dahl, J. P. & Switendick, A. C. (1966). Energy bands in cuprous oxide, *J. Phys. Chem. Solids* 27, 931.
- Dasbach, G.; Frohlich, D.; Klieber, R.; Suter, D.; Bayer, M. & Stolz, H. (2004). Wave-vector-dependent exchange interaction and its relevance for the effective exciton mass in Cu<sub>2</sub>O, *Phys. Rev. B* 70, 045206.
- Deng, H.; Weihs, G.; Snoke, D.; Bloch, J. & Yamamoto, Y. (2003). Polariton lasing vs. photon lasing in a semiconductor microcavity, *Proc. Natl. Acad. Sci. U.S.A.* 100, 15318.
- Deng, H.; Haug, H. & Yamamoto, Y. (2010). Exciton-polariton Bose-Einstein condensation, *Rev. Mod. Phys.* 82, 1489.
- Elliot, R. J. (1961). Symmetry of excitons in cuprous oxide, *Phys. Rev.* 124, 340.
- Figliozzi, P.; Sun, L.; Jiang, Y.; Matlis, N.; Mattern, B.; Downer, M. C.; Withrow, S. P.; White, C. W. & Mendoza, B. S. (2005). Single-beam and enhanced two-beam second-harmonic generation from silicon nanocrystals by use of spatially inhomogeneous femtosecond pulses, *Phys. Rev. Lett.* 94, 047401.
- Fishman, D.; Faugeras, C.; Potemski, M.; Revcolevschi, A. & van Loosdrecht, P. H. M. (2009). Magneto-optical readout of dark exciton distribution in cuprous oxide, *Phys. Rev. B* 80, 045208.
- Fortin, E.; Farfard, S. & Mysyrowicz, A. (1993). Exciton transport in Cu<sub>2</sub>O: Evidence for excitonic superfluidity?, *Phys. Rev. Lett.* 70, 3951 and references therein.
- Frohlich, D.; Kulik, A.; Uebbing, B.; Mysyrowicz, A.; Langer, V.; Stolz, H. & von der Osten, W. (1991). Coherent propagation and quantum beats of quadrupole polaritons in Cu<sub>2</sub>O, *Phys. Rev. Lett.* 67, 2343.
- Goto, T.; Shen, M. Y.; Koyama, S. & Yokouchi, T. (1997). Bose-Einstein statistics of orthoexcitons generated by two-photon resonant absorption in cuprous oxide, *Phys. Rev. B* 55, 7609.

- Grun, J. B.; Seiskind, M. & Nikitine, S. (1961). Etude spectrophotometrique des spectres continus de Cu<sub>2</sub>O a diverses temperatures, *J. Phys. Chem. Solids* 19, 189.
- Hayashi M. & Katsuki, K. (1952). Hydrogen-like absorption spectrum of cuprous oxide, *J. Phys. Soc. Jpn.* 7, 599.
- Hopfield, J. J. (1958). Theory of the contribution of excitons to the complex dielectric constant of crystals, *Phys. Rev.* 112, 1555.
- Hopfield, J. J. & Thomas, D. G. (1963). Theoretical and experimental effect of spatial dispersion on the optical properties of crystals, *Phys. Rev.* 132, 563.
- Hulin, D.; Mysyrowicz, A. & Benoit a la Guillaume, C. (1980). Evidence for Bose-Einstein statistics in an exciton gas, *Phys. Rev. Lett.* 45, 1970.
- Ideguchi, T.; Yoshioka, K.; Mysyrowicz, A. & Kuwata-Gonokami, M. (2008). Coherent quantum control of excitons at ultracold and high density in Cu<sub>2</sub>O with phase manipulated pulses, *Phys. Rev. Lett.* 100, 233001.
- Inoue, M. & Toyozawa, Y. (1965). Two-photon absorption and energy band structure, *J. Phys. Soc. Jpn.* 20, 363.
- Jang, J. I.; O'Hara, K. E. & Wolfe, J. P. (2004). Spin-exchange kinetics of excitons in Cu<sub>2</sub>O: Transverse acoustic phonon mechanism, *Phys. Rev. B* 70, 195205.
- Jang, J. I. & Wolfe, J. P. (2005). Biexcitons in the semiconductor Cu<sub>2</sub>O: An explanation of the rapid decay of excitons, *Phys. Rev. B* 72, 241201(R).
- Jang, J. I. (2005). Lifetimes of excitons in cuprous oxide, *Ph.D. thesis*, University of Illinois.
- Jang, J. I. & Wolfe, J. P. (2006). Exciton decay in Cu<sub>2</sub>O at high density and low temperature: Auger recombination, spin-flip scattering, and molecule formation, *Solid State Commun.* 137, 91.
- Jang, J. I. & Wolfe, J. P. (2006). Relaxation of stress-split orthoexcitons in Cu<sub>2</sub>O, *Phys. Rev. B* 73, 075207.
- Jang, J. I. & Wolfe, J. P. (2006). Auger recombination and biexcitons in Cu<sub>2</sub>O: A case for dark excitonic matter, *Phys. Rev. B* 74, 045211.
- Jang, J. I.; Sun, Y.; Watkins, B. & Ketterson, J. B. (2006). Bound excitons in Cu<sub>2</sub>O: Efficient internal free exciton detector, *Phys. Rev. B* 74, 235204.
- Jang, J. I. & Ketterson, J. B. (2007). Impact of impurities on orthoexciton-polariton propagation in Cu<sub>2</sub>O, *Phys. Rev. B* 76, 155210.
- Jang, J. I. & Ketterson, J. B. (2008). Suppression of molecule formation for orthoexciton-polaritons in Cu<sub>2</sub>O, *Solid State Commun.* 146, 128.
- Jang, J. I.; Sun, Y. & Ketterson, J. B. (2008). Indirect generation of quadrupole polaritons from dark excitons in Cu<sub>2</sub>O, *Phys. Rev. B* 77, 075201.
- Jang, J. I.; Sun, Y.; Mani, S. & Ketterson, J. B. (2008). Resonantly enhanced reflection of quadrupole polaritons in Cu<sub>2</sub>O, *Appl. Phys. Lett.* 93, 121111.
- Kasprzak, J.; Richard, M.; Kundermann, S.; Baas, A.; Jeambrun, P.; Keeling, J. M. J.; Marchetti, F. M.; Szymanska, M. H.; Andre, R.; Staehli, J. L.; Savona, V.; Littlewood, P. B.; Deveaud, B. & Dang, L. S. (2006). Bose-Einstein condensation of exciton polaritons, *Nature* 443, 409.
- Kavoulakis, G. M.; Chang, Y. -C. & Baym, G. (1997). Fine structure of excitons in Cu<sub>2</sub>O, *Phys. Rev. B* 55, 7593.
- Kuwabara, G.; Tanaka, M. & Fukutani, H. (1977). Optical absorption due to paraexciton of Cu<sub>2</sub>O, *Solid State Commun.* 21, 599.

- Kuwata-Gonokami, M.; Shimano, R. & Mysyrowicz, A. (2002). Phase-coherent manipulation of cold biexcitonic waves, *J. Phys. Soc. Jpn.* 71, 1257.
- Lagoudakis, K. G.; Wouters, M.; Richard, M.; Baas, A.; Carusotto, I.; Andre, R.; Dang, L. S. & Deveaud-Pledran, B. (2008). Quantized vortices in an exciton-polariton condensate, *Nat. Phys.* 4, 706.
- Lai, C. W.; Kim, N. Y.; Utsunomiya, S.; Roumpos, G.; Deng, H.; Fraser, M. D.; Byrnes, T.; Recher, P.; Kumada, N.; Fujisawa, T. & Yamamoto, Y. (2007). Coherent zero-state and  $\pi$ -state in an exciton-polariton condensate array, *Nature* 450, 529.
- Landau, L. D. & Lifshitz, E. M. (1977). *Quantum Mechanics*, 3rd ed. Pergamon, New York. pp. 339.
- Langer, V.; Stolz, H. & von der Osten, W. (1995). Picosecond quantum-beat spectroscopy of quadrupole polaritons in  $\text{Cu}_2\text{O}$ , *Phys. Rev. B* 51, 2103.
- Lin, J. L. & Wolfe, J. P. (1993). Bose-Einstein condensation of paraexcitons in stressed  $\text{Cu}_2\text{O}$ , *Phys. Rev. Lett.* 71, 1222.
- Liu, Y. & Snoke, D. (2005). Resonant two-photon excitation of 1s paraexcitons in cuprous oxide, *Solid State Commun.* 134, 159.
- Mani, S.; Jang, J. I.; Ketteron, J. B. & Park, H. Y. (2009). High-quality  $\text{Cu}_2\text{O}$  crystals with various morphologies grown by thermal oxidation, *J. Cryst. Growth* 311, 3549.
- Mani, S.; Jang, J. I. & Ketterson, J. B. (2009). Large third-order susceptibility and third-harmonic generation in centrosymmetric  $\text{Cu}_2\text{O}$  crystal, *Opt. Lett.* 34, 2817.
- Mani, S.; Jang, J. I. & Ketterson, J. B. (2010). Nonlinear optical processes at quadrupole polariton resonance in  $\text{Cu}_2\text{O}$  as probed by a Z-scan technique, *Phys. Rev. B* 82, 113203.
- Markworth, P. R.; Chang, R. P. H.; Sun, Y.; Wong, G. K. L. & Ketterson, J. B. (2001). Epitaxial stabilization of orthorhombic cuprous oxide films on  $\text{MgO}$  (110), *J. Mater. Res.* 16, 914.
- Mysyrowicz, A.; Trauernicht, D. P.; Wolfe, J. P. & Trebin, H. -R. (1983). Stress dependence of the paraexciton in  $\text{Cu}_2\text{O}$ , *Phys. Rev. B* 27, 2562.
- Naka, N. & Nagasawa, N. (2002). Nonlinear paraexciton kinetics in a potential trap in  $\text{Cu}_2\text{O}$  under two-photon resonance excitation, *Phys. Rev. B* 65, 245203.
- O'Hara, K. E.; Suilleabhain, L. O. & Wolfe, J. P. (1999). Strong nonradiative recombination of excitons in  $\text{Cu}_2\text{O}$  and its impact on Bose-Einstein statistics, *Phys. Rev. B* 60, 10565.
- O'Hara, K. E.; Gullingsrud, J. R. & Wolfe, J. P. (1999). Auger decay of excitons in  $\text{Cu}_2\text{O}$ , *Phys. Rev. B* 60, 10872.
- O'Hara, K. E. & Wolfe, J. P. (2000). Relaxation kinetics of excitons in  $\text{Cu}_2\text{O}$ , *Phys. Rev. B* 62, 12909.
- Olsen, L. C.; Addis, F. W. & Miller, W. (1982). Experimental and theoretical studies of  $\text{Cu}_2\text{O}$  solar cells, *Solar Cells* 7, 247.
- Pekar, S. I.; Piskovoi, V. N. & Tsekvava, B. E. (1981). Transmission and reflection of light at the vacuum-crystal interface in the region of a quadrupole exciton transition, *Sov. Phys. Solid State* 23, 1113.
- Pestov, D.; Wang, X.; Ariunbold, G. O.; Murawski, R. K.; Sautenkov, V. A.; Dogariu, A.; Sokolov, A. V. & Scully, M. O. (2008). Single-shot detection of bacterial endospores via coherent Raman spectroscopy, *Proc. Natl. Acad. Sci. U.S.A.* 105, 422.
- Petroff, Y. P.; Yu, P. Y. & Shen, Y. R. (1975). Study of photoluminescence in  $\text{Cu}_2\text{O}$ , *Phys. Rev. B* 12, 2488.

- Pushkarsky, M. B.; Webber, M. E.; Macdonald, T. & Patel, C. K. N. (2006). Sub-parts-per-billion level detection of NO<sub>2</sub> using room-temperature quantum cascade lasers, *Proc. Natl. Acad. Sci. U.S.A.* 103, 10846.
- Schmidt-Whitley, R. D.; Martinez-Clemente, M. & Revcolevschi, A. (1974). Growth and microstructural control of single crystal cuprous oxide Cu<sub>2</sub>O, *J. Cryst. Growth* 23, 113.
- Serebryakov, V. A.; Boiko, E. V.; Petrishchev, N. N. & Yan, A. V. (2010). Medical applications of mid-IR lasers. Problems and prospects, *J. Opt. Technol.* 77, 6.
- Sheik-Bahae, M.; Said, A. A.; Wei, T.; Hagan, D. J. & Van Stryland, E. W. (1990). Sensitive measurement of optical nonlinearities using a single beam, *IEEE J. Quantum Electron.* 26, 760.
- Sheik-Bahae, M.; Hutchings, D. C. ; Hagan, D. J. & Van. Stryland, E. W. (1991). Dispersion of bound electronic nonlinear refraction in solids, *IEEE J. Quantum Electron.* 27, 1296.
- Snoke, D. W.; Wolfe, J. P. & Mysyrowicz, A. (1987). Quantum saturation of a bose gas; excitons in Cu<sub>2</sub>O, *Phys. Rev. Lett.* 59, 827.
- Snoke, D. W.; Wolfe, J. P. & Mysyrowicz, A. (1990). Evidence for Bose-Einstein condensation of excitons in Cu<sub>2</sub>O, *Phys. Rev. B* 41, 11171.
- Snoke, D. W. & Negroita, V. (2000). Pushing the Auger limit: Kinetics of excitons in traps in Cu<sub>2</sub>O, *Phys. Rev. B* 61, 2904.
- Sun, Y.; Wong, G. K. L. & Ketterson, J. B. (2001). Production of 1s quadrupole-orthoexciton polaritons in Cu<sub>2</sub>O by two-photon pumping, *Phys. Rev. B* 63, 125323.
- Takagahara, T. (1985). Theory of dephasing relaxation of excitonic polaritons, *Phys. Rev. B* 31, 8171.
- Tayagaki, T.; Mysyrowicz, A. & Kuwata-Gonokami, M. (2006). Collision between supercooled excitons in Cu<sub>2</sub>O studied by time-resolved Lyman spectroscopy, *Phys. Rev. B* 74, 245127.
- Toth, R. S.; Kilson, R. & Trivich, D. (1960). Preparation of large area single-crystal cuprous oxide, *J. Appl. Phys.* 31, 1117.
- Trauernicht, D. P. & Wolfe, J. P. (1986). Drift and diffusion of paraexcitons in Cu<sub>2</sub>O: Deformation-potential scattering in the low-temperature regime, *Phys. Rev. B* 33, 8506.
- Trebin, H. -R.; Cummins, H. Z. & Birman, J. L. (1981). Excitons in cuprous oxide under uniaxial stress, *Phys. Rev. B* 23, 597.
- Utsunomiya, S.; Tian, L.; Roumpos, G.; Lai, C. W.; Kumada, N.; Fujisawa, T.; Kuwata-Gonokami, M.; Loffler, A.; Hofling, S.; Forchel, A. & Yamamoto, Y. (2008). Observation of Bogoliubov excitations in exciton-polariton condensates, *Nat. Phys.* 4, 700.
- Vollmer, F. & Arnold, S. (2008). Whispering-gallery-mode biosensing: label-free detection down to single molecules, *Nature* 5, 591.
- Waters, R. G.; Pollak, F. H.; Bruce, R. H. & Cummins, H. Z. (1980). Effects of uniaxial stress on excitons in Cu<sub>2</sub>O, *Phys. Rev. B* 21, 1665.
- Wolfe, J. P.; Lin, J. L. & Snoke, D. W. (1995). Bose-Einstein condensation of a nearly ideal gas: Excitons in Cu<sub>2</sub>O, In: *Bose-Einstein Condensation*, Griffin, A.; Snoke, D. W. & Stringari, S. (Ed.), Cambridge University Press, Cambridge, England. pp. 281-329.
- Wolfe, J. P. & Jang, J. I. (2005). New perspectives on kinetics of excitons in Cu<sub>2</sub>O, *Solid State Commun.* 134, 143.

- Yoshioka, K. & Kuwata-Gonokami, M. (2006). Dark excitons in  $\text{Cu}_2\text{O}$  crystals for two-photon coherence storage in semiconductors, *Phys. Rev. B* 73, 081202(R).
- Yu, P. Y. & Shen, Y. R. (1975). Resonance Raman studies in  $\text{Cu}_2\text{O}$ . I. The phonon-assisted 1s yellow excitonic absorption edge, *Phys. Rev. B* 12, 1377.
- Zipfel, W. R.; Williams, R. M. & Webb, W. W. (2003). Nonlinear magic: Multiphoton microscopy in the biosciences, *Nat. Biotechnol.* 21, 1369.



# Optoelectronic Properties of ZnSe, ITO, TiO<sub>2</sub> and ZnO Thin Films

S. Venkatachalam<sup>1</sup>, H. Nanjo<sup>1</sup>, K. Kawasaki<sup>1</sup>, H. Hayashi<sup>1</sup>,  
T. Ebina<sup>1</sup> and D. Mangalaraj<sup>2</sup>

<sup>1</sup>*National Institute of Advanced Industrial Science and Technology,*

<sup>2</sup>*Department of Nanoscience and Technology, Bharathiar University,*

<sup>1</sup>*Japan*

<sup>2</sup>*India*

## 1. Introduction

Zinc selenide (ZnSe) a II-VI compound semiconductor with cubic zinc blende structure and a direct bandgap of 2.7 eV is found to be a very promising material for optoelectronic devices (Venkatachalam et al., 2007a). Semiconductor heterostructures employing zinc selenide and related alloys are an option for the production of optoelectronic devices emitting in the blue - green spectral range (Haase et al., 1991; Jeon et al., 1991). Nowadays there is a concentrated effort to produce high quality p-type zinc selenide based blue laser diodes (Drechsler et al., 1997; Fung et al., 1997). Particularly, Schottky photodiodes with fast response in the ultraviolet-visible range is more focused. Because Schottky barriers result in both very fast switching times and low forward voltage drop. The silicon photodiodes give more response in the infrared range; the main reason for this is the band gap value. The reported band gap value of Si is 1.1 eV. By providing an overlayer on the silicon surface, the silicon Schottky diodes give more response in the ultraviolet-visible range. Due to their direct energy gap in the visible range, zinc selenide would be perfectly suitable for this. The lattice mismatch, the difference in the thermal expansion coefficients, as well as the different chemical properties of zinc selenide and silicon (Si) are some of the sources of crystal defects generated at the interface between zinc selenide and silicon heterostructures. Zinc selenide has either a sphalerite structure with lattice parameter  $a = 5.668 \text{ \AA}$  or wurtzite structure with lattice parameters  $a = 3.820 \text{ \AA}$  and  $c = 6.626 \text{ \AA}$ . The lattice constant value of cubic silicon is reported as 5.6576 (JCPDS, 1990, card number 37). Usually, zinc selenide films were deposited onto gallium arsenide substrate, because of the high lattice match between zinc selenide and gallium arsenide (0.27 %). However, the production cost of gallium arsenide-based device is much higher than that of silicon. The lattice mismatch between zinc selenide and silicon is quite large (4.4 %) compared with gallium arsenide (0.27 %). However, in practice, the substrate strongly influences the nucleation and the mobility of the elements deposited on the substrate. In fact, the higher the substrate temperature, the higher the mobility of the deposited elements; therefore, the stoichiometric composition of zinc (Zn) and selenium (Se) in the zinc selenide film occurs at a sufficiently high substrate temperature (Chrisey & Hübner, 1994). A new PIN - like (Si (p)/ZnSe (n-)/ZnSe (n+)) visible photodiode was fabricated in 1996 using vapor phase epitaxy (Lour & Chang, 1996). They

used a two-step growth method in order to overcome the problem of lattice mismatch existing at the interface between zinc selenide and silicon. Zinc selenide-based silicon photodiode was recently fabricated (Ullrich, 1998). In order to bypass the lattice mismatch, the indium selenide (25Å) layer was used as a buffer layer between zinc selenide and silicon. These two techniques are very expensive. However, vacuum evaporation is very simple and inexpensive; it can be used for the deposition of film with large surface area. In this chapter, we investigate the effect of substrate temperature on the composition, structural, optical and electrical properties of vacuum evaporated zinc selenide thin films on silicon (100) and glass substrates at different substrate temperatures.

Indium-doped tin oxide (ITO) thin film is a wide band gap semiconductor with good conductivity and high optical transmission in the visible spectral range of 400 – 700 nm. Indium-doped tin oxide thin films are often used in a wide variety of applications, including solar cells and other optoelectronic devices. In recent years, metal oxide materials such as titanium dioxide and zinc oxide thin films have been extensively studied for various applications such as solar cells, gas sensors and protective coating (Feng et al., 2008). Among them, titanium dioxide is a very suitable oxide material for dye-sensitized solar cell (DSC) applications. Glass substrate can be used for solar cell applications, but glass is very brittle, and is too heavy, especially for large-area solar cell devices. These disadvantages can be overcome by using flexible substrates, which are lightweight and inexpensive. Optically transparent substrates with high glass transition temperature are desired for the above-mentioned applications. In addition, they need to withstand the growth conditions of metal oxides while maintaining their mechanical and optical properties. Particularly, the thermal resistant stability of flexible substrates should be maximal (~450°C). Because the anodized amorphous titanium dioxide can be changed into anatase titanium dioxide after the heat treatment in the range of 350-400°C (Lee et al., 2006). The deformation temperatures of polyethylene terephthalate and polycarbonate substrates were reported as 220 and 140°C, respectively (Wu & Chiou, 1997; Kim et al., 2001). Therefore, the polyethylene terephthalate and polycarbonate substrates could not be applied for the crystallization of amorphous titanium dioxide in the temperature range of 350-400°C. Recently, a very transparent flexible clay substrate was fabricated and it has more flexibility and high thermal resistance (Kawasaki et al., 2010). In the present work, titanium dioxide nanowires, nanorods and nanotubes are fabricated using hydrothermal and anodization method, respectively. In this chapter, we also report the surface morphology, photovoltaic and structural properties of titanium dioxide nanorods and nanotubes, which are prepared by hydrothermal method and electrochemical anodization method, respectively. The fabrication procedure of flexible dye-sensitized solar cells and the factors that affect the device performance will be discussed. Finally, the photovoltaic parameters of dye-sensitized solar cell based on titanium dioxide are compared with the dye-sensitized solar cell based on zinc oxide decorated titanium dioxide.

## 2. Experimental details

The appropriate weight zinc, selenium and iodine compounds were taken in an evacuated sealed quartz ampoule under a vacuum of  $4 \times 10^{-3}$  Pa. High purity zinc (99.999 %), selenium (99.999 %) and iodine (99.99 %) were used to prepare this zinc selenide compound. The zinc selenide compounds were prepared at 1148 K with iodine as a reactive agent. The prepared compound was yellow in colour. In the present work, the substrates are silicon (100) and

glass, which are used for the deposition of zinc selenide thin films. The silicon wafers were thoroughly rinsed with double distilled water and then treated with methanol for removing the organic impurities. The silicon substrates were then cleaned with trichloroethylene to break the organic molecules. Once again, the cleaned silicon substrates were treated with methanol. Finally, 48% hydrofluoric acid was used to remove the thin silicon dioxide layer on the silicon surface. The silicon wafers were inserted into the deposition chamber immediately after chemical cleaning. Pure aluminum (99.999 % Balzers, Switzerland) layer was deposited onto the back surface of silicon wafers by vacuum evaporation technique. Zinc selenide alloy was thermally evaporated from a molybdenum boat onto well-cleaned silicon (100) and glass substrates at different substrate temperatures (483 - 589 K) under a vacuum of  $4 \times 10^{-3}$  Pa, and gold was used as the top electrode. The completed device had an active area of about  $2 \times 10^{-6}$  m<sup>2</sup>. In order to stabilize the deposited film, all the deposited films were annealed at 373 K for 30 minutes under a vacuum of  $4 \times 10^{-3}$  Pa. The composition of the film deposited onto glass substrate was studied using the Rutherford Backscattering spectrometry (RBS). In this case, 2 MeV He<sup>+</sup> ion beam was used for the experiment. The details of the experimental set-up could be found elsewhere (Jamieson, 1998). The structural analyses of the films were made by X-ray diffractometer in the  $2\theta$  range from 20° to 80°. Optical transmission of zinc selenide films deposited onto micro glass slide was recorded using a ultraviolet-visible-near infrared spectrophotometer (CARY 2390). Electrical measurements were done in a rotary vacuum of 1.33 Pa at different temperatures (305 - 365 K) by using a cryostat equipped with a PT100 thermocouple. The capacitance values were measured using multifrequency LCR meter (4275HP). In the spectral response analysis, an Oriel 150 W Xenon Lamp was used as a light source, along with a monochromator from Acton Research Corporation. At each wavelength, the power  $P$  of the light incident on the gold mesa was carefully measured using a Newport 835 optical power meter that uses a UV-enhanced silicon photodiode (818UV) as the detector.

### 3. Results and discussion

#### 3.1 Optoelectronic properties of zinc selenide (ZnSe) thin films

A typical Rutherford backscattering spectrum for a film deposited at a substrate temperature of 553 K is shown in Fig. 1. The edge of the overlapping bands corresponding to the elements zinc and selenium are seen as well as those corresponding to silicon in the silicon substrate. The collected Rutherford backscattering spectra (Red Line) were then fitted by code Rump (Doolittle, 1985) to find the relative concentrations of various elements in the film. Spectra similar to this are obtained for other deposited films. The average ratio of the deposited films is found to be (ZnSe) I<sub>0.001</sub>. The composition is found to be nearly stoichiometric and the percentage of iodine is minimal. Figure 2 shows the X-ray diffraction patterns of zinc selenide thin films grown on silicon (100) substrates at different substrate temperatures. Only one peak of zinc selenide and two peaks of silicon are observed. It is observed that the X-ray diffraction patterns of all the films show a most preferred orientation along (111) plane. The (111) direction is the close-packing direction of the zinc blende structure and all the deposited films are polycrystalline having cubic zinc blende structure. The (111) peak for the films deposited at  $T_s = 483$  K is broad and very weak. It may be due to the mixed phase of amorphous and crystalline in Zn - Se bonding in zinc selenide thin films. The X-ray diffraction intensity of (111) peak increases and the peak becomes narrower as the substrate temperature is increased from 483 to 589 K.

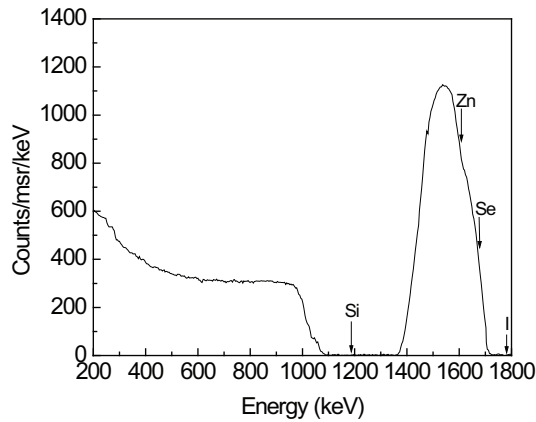


Fig. 1. Rutherford backscattering spectrum of vacuum evaporated zinc selenide thin film deposited at a substrate temperature of 553 K. [Reprinted with permission from (Venkatachalam et al., 2006). Copyright @ IOP Publishing Ltd (2006)].

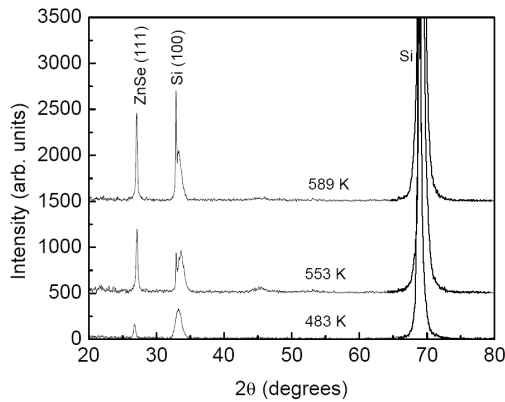


Fig. 2. X-ray diffraction patterns of zinc selenide thin films deposited on silicon substrate at different substrate temperatures. [Reprinted with permission from (Venkatachalam et al., 2006). Copyright @ IOP Publishing Ltd (2006)]

The particle size ( $D$ ) is calculated using Debye - Scherrer's formula from the full width at half maximum ( $\beta$ ) (Warren, 1990). The particle size values are calculated as 22, 36 and 41 nm at 483, 553 and 589 K, respectively. The best films (characterized by lower value of full width at half maximum and higher value of particle size) are obtained with the growth temperature between 553 and 589 K. The lattice constant values are calculated as 5.72, 5.678 and 5.6785 Å at 483, 553 and 589 K, respectively. If we compare these values with the reported value of bulk  $a_{\text{ZnSe}}$  (5.6684 Å) (JCPDS #37-1463), the calculated lattice constant value for the film deposited at 483 K is larger than that of reported value. However, the lattice constant values are very close to the reported value for the films deposited at 553 and 589 K. This result suggests that the deposited zinc selenide thin film at 483 K is strongly

affected by the two dimensional compressive stress at the ZnSe/Si interface in the growth plane, in order to accommodate the lattice misfit. But the compressive stress shows a decreasing trend at the higher substrate temperature (553 and 589 K).

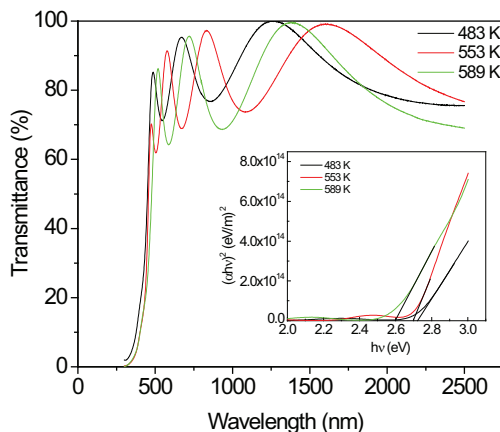


Fig. 3. Transmittance spectra of zinc selenide thin films deposited at different substrate temperatures. [Reprinted with permission from (Venkatachalam et al., 2006). Copyright @ IOP Publishing Ltd (2006)].

The transmittance spectra of the zinc selenide thin films deposited at different substrate temperatures are shown in Fig. 3. This sharp fall of transmittance occurs in the lower wavelength region corresponding to the band gap of the film. The optical band gap ( $E_g$ ) values are calculated as 2.72, 2.69 and 2.60 eV for 483, 553 and 589 K, respectively. The energy band gap value decreases from 2.72 to 2.6 eV as the substrate temperature is increased from 483 to 589 K and all the films are found to have direct allowed transition. The calculated optical band gap values are in good agreement with the bulk reported value (2.7 eV) (Venkatachalam et al., 2007b).

The ZnSe/p-Si heterojunction prepared at 553 K is studied using current - voltage and capacitance - voltage characteristics. Figure 4 shows a typical plot of  $I - V$  characteristics of ZnSe /p-Si Schottky diodes in forward and reverse biases measured at different temperatures. This  $I - V$  characteristics follow the standard diode equation (Rakhshani et al., 1998) for forward bias below  $\approx 0.4$  V as given by

$$[I = I_0[\exp(qV / nkT) - 1]] \quad (1)$$

where  $n$  is called the ideality factor,  $q$  is the electronic charge,  $k$  is the Boltzmann constant and  $T$  is the temperature.

The ideality factor is evaluated from the plot between  $\ln I$  vs.  $V$  [inset of Fig. 4] and is found to be in the range from 2.01 to 3.51. Compared with previous reports (Montes & Herino, 2000), the calculated value of ideality factor is low. In general when the ideal diffusion current is the dominating factor, then the value of the ideality factor  $n$  will be equal to 1, whereas this value equal to 2 when the recombination current is the dominating factor (Sze, 1985). However, in the present case the value of ideality factor is greater than 2. The departure of the ideality factor from unity may be due to the fact that the Schottky barrier

contains an interfacial layer on the silicon surface. However, in the present work, we could not observe any interfacial layer on the silicon surface (Fig.5). Figure 5 shows the high-resolution transmission electron microscopy (HRTEM) image of a ZnSe/Si heterostructures, which reveals a clear interface between substrate (silicon) and overlayer (zinc selenide layer). The main reason is the existence of a laterally varying potential barrier height, caused by a non-uniform interface.

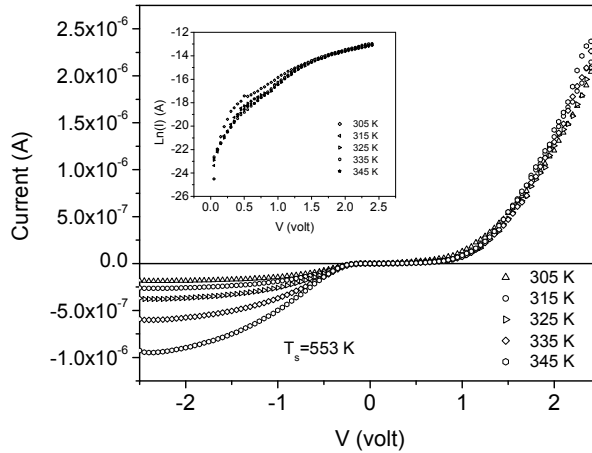


Fig. 4. Forward and reverse current versus voltage characteristics of ZnSe/Au Schottky diode. The inset of Fig.4 shows the plot of voltage versus  $\text{Ln}I$ . [Reprinted with permission from (Venkatachalam et al., 2006). Copyright @ IOP Publishing Ltd (2006)].

The reverse bias characteristics would be controlled by the generation-recombination and band-to-band tunneling mechanisms at small (up to -0.4 V) and large bias, respectively, which might be the reason for a small kink at -0.4 V (Chiang & Bedair, 1985). The plot between the measured values of capacitance and voltage for ZnSe/p-Si diodes is shown in Fig. 6a. We obtained a straight line by plotting a curve between  $1/C^2$  versus  $V$ , which implies a similar behaviour for an abrupt heterojunction (Khlyap & Andrukhiv, 1999). The intercept of this plot at  $1/C^2 = 0$  corresponds to the built-in potential  $V_{bi}$ , and is found to be 1.51 V. The value of barrier height (Singh et al., 1993; Pfister et al., 1977) can be calculated from the measured value of  $V_{bi}$ .

$$\phi_{Bn} = V_{bi} + V_n + \frac{kT}{q} \quad (2)$$

where  $V_n = kT/q$ .  $\text{Ln}(N_v/N_A)$ ,  $k$  is the Boltzmann constant,  $T$  is the temperature,  $q$  is the charge of the electron,  $N_v$  is the density of states in the valence band and  $N_A$  is the effective carrier concentration. From the slope of the  $1/C^2$  versus voltage plot, the value of effective carrier concentration is calculated as  $3.55 \times 10^{19} (\text{m}^2/\text{F})^2 / \text{V}$ . The calculated values of barrier height and acceptor concentration ( $N_A$ ) are calculated as 1.95 eV and  $4.37 \times 10^{11} \text{ cm}^{-3}$ , respectively. The spectral photoresponse of the device prepared at 589 K is shown in Fig. 6b. It shows a very good photoresponse in the UV-Visible range. The quantum efficiency for the device prepared at 553 and 589 K is calculated as 0.25 and 0.1 %, respectively.

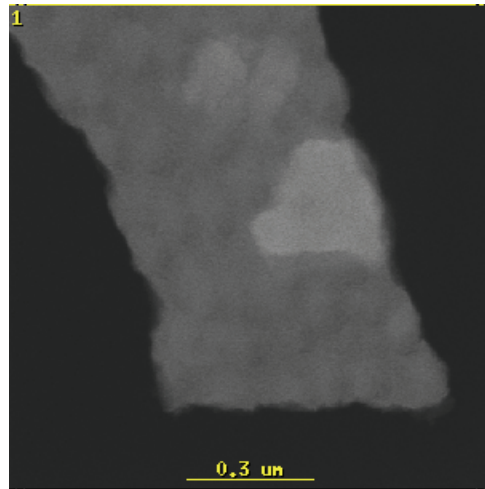


Fig. 5. High-resolution transmission electron microscopy image of the prepared ZnSe/p-Si Schottky diodes. [Reprinted with permission from (Venkatachalam et al., 2006). Copyright @ IOP Publishing Ltd (2006)].

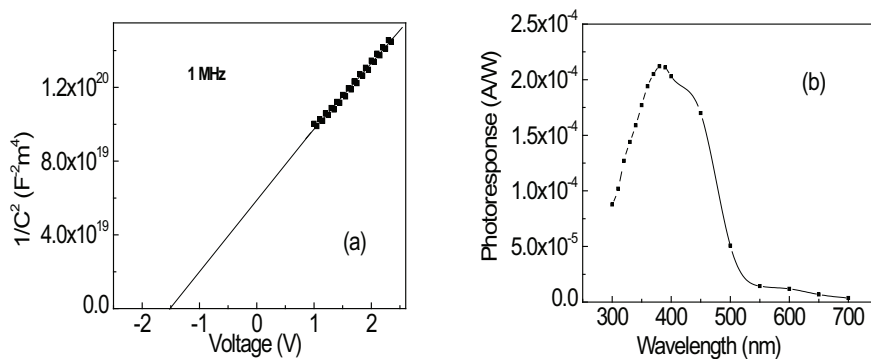


Fig. 6. Dependence of  $1/C^2$  value on applied voltage (a) and spectral photoresponse (b) of ZnSe/p-Si Schottky diode. [Reprinted with permission from (Venkatachalam et al., 2006). Copyright @ IOP Publishing Ltd (2006)].

### 3.2 Preparation and characterization of indium-doped tin oxide thin films

Nanocrystalline indium-doped tin oxide (ITO) thin films were prepared on glass and clay substrates by ion beam sputter deposition method. Preparation and deposition parameters of nanocrystalline indium-doped tin oxide thin films were found elsewhere (Venkatachalam et al., 2010). The scanning electron microscope (SEM) images show that the surface morphology of indium-doped tin oxide thin film on glass substrate is smooth (Fig. 7a); in contrast, the surface morphology of indium-doped tin oxide thin film on clay substrate is rough (Fig. 7b). The inset of Figure 7b shows the flexibility of indium-doped tin oxide thin film coated clay substrate. Flexibility of indium-doped tin oxide thin film coated clay substrate is estimated as 17 mm, from a diameter of curvature. X-ray diffraction patterns of annealed indium-doped tin oxide thin film are

shown in Fig. 8; the X-ray diffraction patterns showed two different orientations, i.e., (400) and (222) on different substrates, i.e., glass and clay, respectively. The sheet resistances of indium-doped tin oxide thin film on glass ( $32 \Omega/\square$ ) is lower than that on clay ( $41 \Omega/\square$ ); it is due to the difference in substrate surface roughness between ITO/glass and ITO/clay.

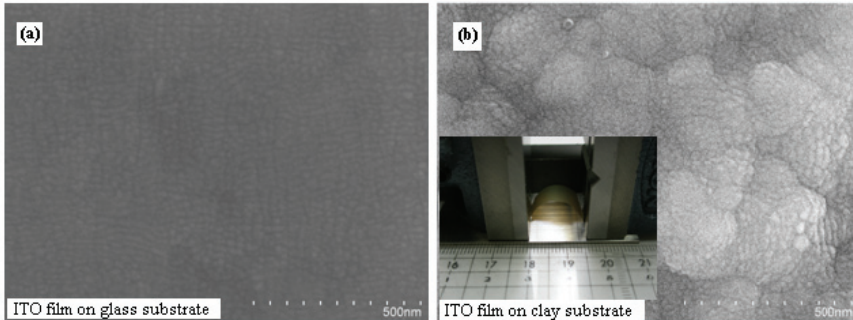


Fig. 7. Scanning electron microscope images of indium tin oxide thin films (inset Fig. 7b shows photograph of flexible ITO/Clay substrate). [Reprinted with permission from (Venkatachalam et al., 2011) Copyright @ The Japan Society of Applied Physics (2011)].

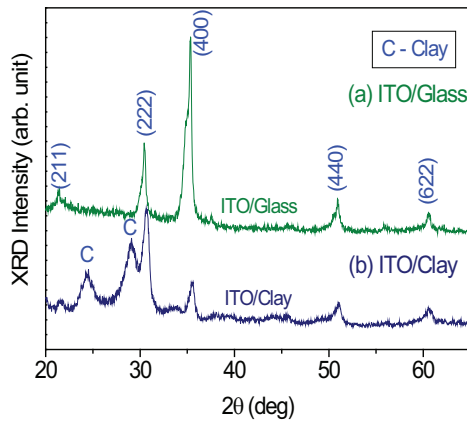


Fig. 8. X-ray diffraction patterns of annealed indium tin oxide thin films. [Reprinted with permission from (Venkatachalam et al., 2011) Copyright @ The Japan Society of Applied Physics (2011)].

### 3.3 Preparation and characterization of nanostructured titanium dioxide films

The hydrothermal synthesis of titanium dioxide ( $\text{TiO}_2$ ) film was carried out in a Teflon-lined stainless steel autoclave. In a typical synthesis process, titanium n-butoxide (1.0 ml) was used with hydrochloric acid (20 ml) and deionized water (40 ml). The reaction time and temperature were fixed at 17 h and  $160^\circ\text{C}$ , respectively. Scanning electron microscope images of as-prepared titanium dioxide films on indium-doped tin oxide and fluorine-doped tin oxide (FTO) films coated glass substrates are shown in Fig. 9. It shows that the surface morphology of titanium dioxide films on indium-doped tin oxide substrate indicates



the existence of many uniform, dandelion-like structures with diameter in the range of 6-7  $\mu\text{m}$  (Fig. 9a). A selected area of high magnification image (inset of Fig.9a) shows that each dandelion-like structure is composed of nanorods with an average diameter of 150 nm. It is attributed that if there is no lattice match between titanium dioxide and indium-doped tin oxide substrate, the titanium dioxide initially nucleates as islands and then the nanorods grow from these islands to form dandelion-like morphology. In contrast, the surface morphology of titanium dioxide films on fluorine-doped tin oxide substrate (Fig. 9c) shows that the whole surface is composed of ordered titanium dioxide nanorods with square top facets. The cross-sectional view (inset of Fig.9c) confirms that the growth of the titanium dioxide nanorods is along the direction perpendicular to the fluorine-doped tin oxide substrate. This shows that titanium dioxide thin film grows epitaxially on fluorine-doped tin oxide substrate; it is due to the small lattice mismatch ( $\sim 2\%$ ) between titanium dioxide and fluorine-doped tin oxide films, because fluorine-doped tin oxide films and titanium dioxide films have similar crystal structure. The length and size of the nanorods are evaluated as 3.9  $\mu\text{m}$  and 150 nm, respectively.

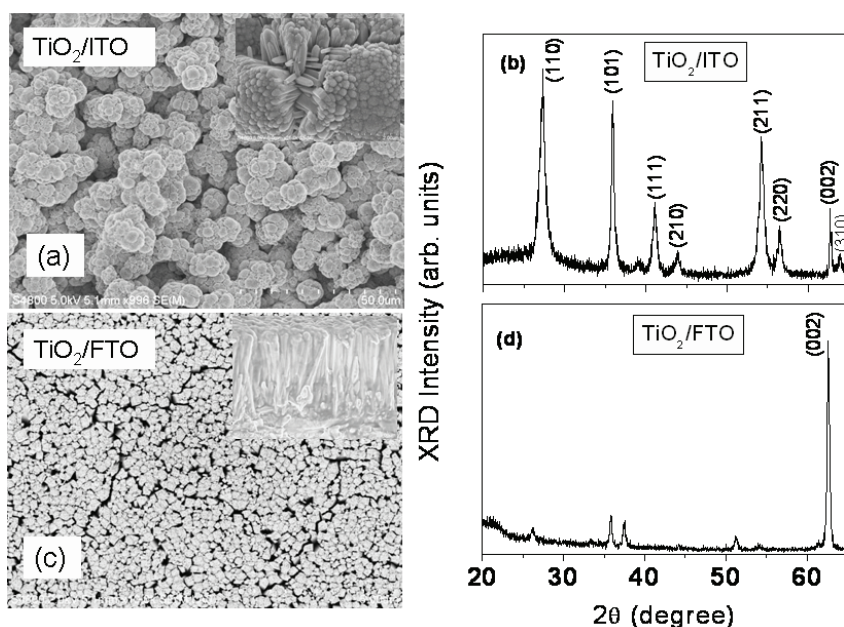


Fig. 9. Scanning electron microscope images and X-ray diffraction patterns of titanium dioxide films on different substrates; (a and b) TiO<sub>2</sub> film on ITO/glass, (c and d) TiO<sub>2</sub> film on FTO/glass.

Figure 9b shows the X-ray diffraction pattern of titanium dioxide films prepared on indium-doped tin oxide substrate. A very strong rutile peak is observed at  $2\theta$  of  $27.37^\circ$ , assigned to (110) plane. Other rutile peaks are observed at  $2\theta$  of  $36.10^\circ$  (101),  $41.26^\circ$  (111),  $44.01^\circ$  (210),  $54.36^\circ$  (211),  $56.59^\circ$  (220),  $62.92^\circ$  (002) and  $64.10^\circ$  (310). In contrast, titanium dioxide film on fluorine-doped tin oxide shows a preferred orientation in the (002) direction (Fig. 9d), as indicated by strong characteristic peak at  $2\theta$  of  $62.92^\circ$ . Here, the absence of (110), (111) and

(211) peaks indicate that the nanostructured titanium dioxide film is highly oriented with respect to the substrate surface and the titanium dioxide nanorods grow in the (002) direction with the growth axis parallel to the substrate surface normal (Bang & Kamat, 2010).

After preparing the freestanding nanostructured titanium dioxide films, it is transferred from a glass substrate onto an indium-doped tin oxide film coated transparent flexible clay substrate. The photograph of freestanding layer of titanium dioxide prepared by hydrothermal method is shown in Fig. 10a; it can be easily handled with tweezers. Figure 10b shows the scanning electron microscope images of freestanding titanium dioxide layer. The size of the nanorod is calculated as 150 nm. A very thin layer of titanium dioxide paste is used between the freestanding titanium dioxide and indium-doped tin oxide film coated flexible clay (LiSA-TPP) substrate in order to improve the adhesion. The freestanding titanium dioxide layer deposited on flexible ITO/clay substrate is used as an anode. The platinum sputtered indium-doped tin oxide film coated flexible clay/mica substrate is used as a counter electrode. Surlyn spacer film with a thickness of 60  $\mu\text{m}$  is used as a spacer. The completed device had an active area of 0.5  $\text{cm}^2$ . From the photocurrent density-voltage characteristic, the open circuit voltage, short circuit current and fill factor are calculated as 0.51 V, 1.14 mA and 56 %, respectively. However, the efficiency of the prepared device is less than 1 %. It is considered that the adhesion layer restricts the flow of electrons from titanium dioxide photoelectrode into the collector (ITO) (Park et al., 2011).

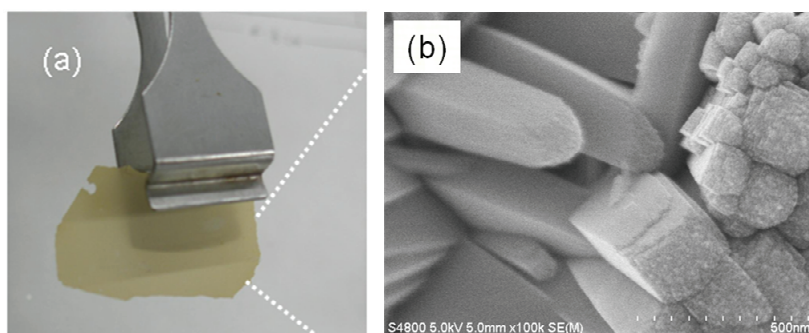


Fig. 10. SEM images and photograph of freestanding  $\text{TiO}_2$  layer.

### 3.4 Preparation of titanium dioxide nanotube arrays and titanium dioxide nanowire covered titanium dioxide nanotube arrays on titanium foil and plate

Nanostructured titanium dioxide films were prepared by anodization of titanium foil and plate at room temperature. The anodization was performed in ethylene glycol containing 2 vol.%  $\text{H}_2\text{O}$ + 0.3 wt.% ammonium fluoride ( $\text{NH}_4\text{F}$ ) for different anodization time. The anodized titanium sample was then annealed in air at 400°C for an hour. Figure 11(a-d) shows top and bottom-side view scanning electron microscope images of anodized titanium plate and foil. It clearly shows the formation of well-ordered titanium dioxide nanotube arrays on both titanium plate and foil. The bottom side-views of the tube layer (Figs. 11c and d) reflects an uneven morphology. At the bottom, the tubes are closely packed together. The diameter and length of titanium dioxide nanotube arrays on Ti plate are calculated as 100 nm and 5.6  $\mu\text{m}$ , respectively.

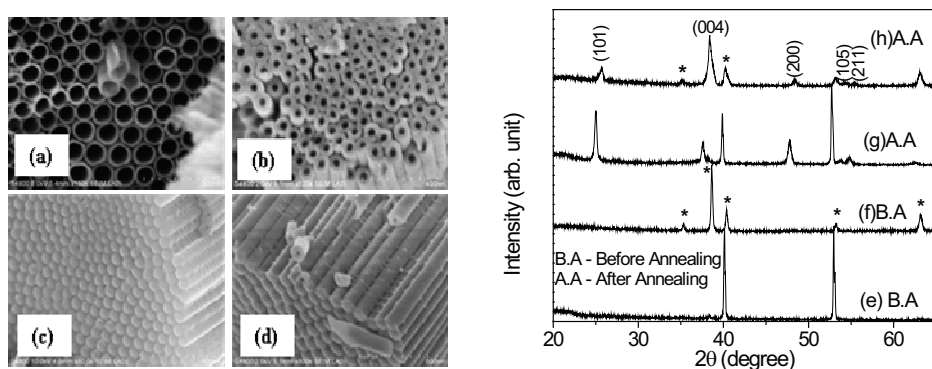


Fig. 11. Scanning electron microscope images [Top views (Ti plate (a); foil (b)) and bottom side views (Ti plate (c); foil (d))] and XRD patterns [Ti plate (e and g) and Ti foil (f and h)] of anodized Ti plate and Ti foil.

Figure 11(e-h) shows the X-ray diffraction patterns of anodized titanium plate and Ti foil before and after annealing. In Fig. 11e and f, the X-ray diffraction peaks at 35.3, 38.64, 40.4, 53.2 and 63.18 correspond to titanium. This is attributed that the as-prepared titanium dioxide is amorphous before annealing; only titanium peaks are seen (Fig.11e and f). In order to change the amorphous titanium dioxide into anatase titanium dioxide, anodized titanium sample was annealed in air at 400°C for an hour. After annealing, the amorphous titanium dioxide has been changed into crystalline with a more preferred orientation along (101) direction. The particle size values of titanium dioxide on titanium plate and titanium foil are calculated as 41 and 24 nm, respectively. The calculated lattice parameters of TiO<sub>2</sub>/Ti plate and TiO<sub>2</sub>/foil coincide well with the reported value of bulk titanium dioxide ( $a=3.7822\text{\AA}$ ) (JCPDS #21-1272). The stress in the TiO<sub>2</sub>/Ti plate is tensile. On the other hand, the TiO<sub>2</sub>/Ti foil is under compressive stress (see Table 1).

Sample code	Anodization Time	2θ	FWHM (degree)	Lattice parameter (a) (Å)	Stress (%)
TiO <sub>2</sub> /Ti plate	240 min	25.00	0.209	3.804	0.57
TiO <sub>2</sub> /Ti foil	180 min	25.63	0.360	3.761	-0.56

Table 1. Structural parameters of anodized Ti plate and foil.

Figure 12A and D shows the scanning electron microscope images of titanium dioxide nanowires covered titanium dioxide nanotube arrays prepared by anodization method. The nanotubes divided into several parts are observed near the mouth (Fig.12C). The electrochemical etching causes the divided nanotubes to further split into several parts that lead to the formation of nanowires. Figure 12B shows that titanium dioxide nanotube arrays with diameter of 100 nm exist underneath the nanowires.

Figure 13 shows the photocurrent density-voltage characteristics of dye-sensitized solar cells based on titanium dioxide nanotube arrays and nanoparticles. Under backside illumination, the short-circuit current density and power conversion efficiency of dye-sensitized solar cells based on titanium dioxide nanotube arrays are much higher than that of P25 (see Table

2). Similar results have been observed by (Tao et al., 2010). This result shows that the main factor responsible for the enhancement of the short circuit current is the improvement of electron transport and electron lifetime in titanium dioxide nanotube arrays. This increased light-harvesting efficiency in titanium dioxide nanotube-based dye-sensitized solar cell could be a result of stronger light scattering effects that leads to significantly higher charge collection efficiencies of nanotube-based dye-sensitized solar cells relative to those of nanoparticles-based dye-sensitized solar cells (Jennings et al., 2008). The dye-sensitized solar cells device performance under backside illumination is very low. This is attributed that the backside illumination affects the light absorption capacity of the dyes, because the  $I_3^-$  electrolyte cuts the incident light in the wavelength range of 400 – 650 nm.

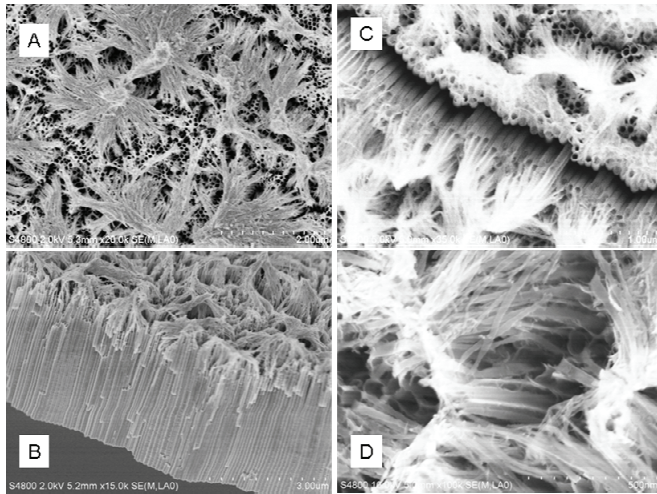


Fig. 12. Scanning electron microscope images of anodized Ti foil and Ti plate. Top views of Ti foil (A) and plate at low (C) and high magnification (D)]; cross-sectional view of Ti foil (B).

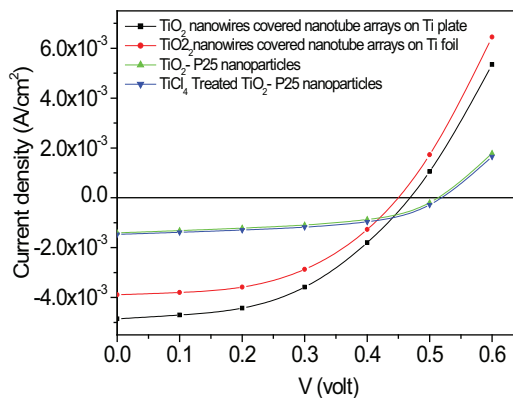


Fig. 13. Photocurrent density-voltage characteristics of dye-sensitized solar cells based on TiO<sub>2</sub> nanotube arrays and nanoparticles.

Sample code	Anodization Time (min)	V <sub>oc</sub> (V)	J <sub>sc</sub> (mA/cm <sup>2</sup> )	FF	Efficiency (%)
Sample 1 (Ti Plate)	240	0.470	4.85	0.463	1.06
Sample 2 (Ti Foil) (Film thickness=3μm)	180	0.450	3.85	0.493	0.854
Sample 3 [TiO <sub>2</sub> (P25)] (Film thickness=2μm)		0.518	1.4	0.522	0.23
Sample 4 [TiO <sub>2</sub> (P25)+TiCl <sub>4</sub> ] (Film thickness=2μm)		0.523	1.5	0.499	0.391

Table 2. Photovoltaic parameters of dye-sensitized solar cells based on titanium dioxide nanotube arrays and P25 films.

### 3.5 Preparation of titanium dioxide nanotube arrays on indium-doped tin oxide and silicon substrates

From the previous results, we observed that the use of foil and plate limits their potential applications, particularly in the fabrication of solar cells. An alternative approach is the preparation of nanostructured titanium dioxide films on transparent conducting glass substrate by anodization method. In the electrochemical anodization process, the substrate temperature, lattice mismatch between the substrate and film, and film thickness affect the properties of the films; because of which the anodization process is affected (Sadek et al., 2009). (Wang & Lin, 2009) reported that the formation of titanium dioxide nanotube arrays were not only affected by electrolytes and applied potential, but also affected by electrolyte temperature. Recently, titanium dioxide nanotube array films were successfully prepared by anodization of as-prepared ion-beam sputtered titanium thin films at low electrolyte temperature (5°C) and the key parameter to achieve the titanium dioxide nanotube arrays is the electrolyte temperature (Macak et al., 2006). In the present work, the titanium dioxide nanotube arrays are successfully prepared by anodization of as-prepared ion-beam sputtered titanium films at room temperature. Titanium thin films were deposited on indium-doped tin oxide and silicon substrates by ion beam sputter deposition method at room temperature. The acceleration voltage supplied to main gun was fixed at 2500 V. Pure Ar was employed as the sputtering gas. Nanostructured titanium dioxide thin films were prepared by electrochemical anodization method. The Ti/ITO/glass was anodized in glycerol containing 2.5 vol. % H<sub>2</sub>O+0.5 wt.% NH<sub>4</sub>F at an applied potential of 30 V for the anodization time of 240 min. On the other hand Ti/Si sample was anodized in ethylene glycol containing 2.0 vol. % H<sub>2</sub>O + 0.3wt. % NH<sub>4</sub>F at an applied potential of 20 V for 180 min. Nanostructured titanium dioxide thin films are formed by anodization using a two electrode configuration with Ti film as an anode and platinum as a cathode.

Generally, the formation mechanism of the titanium dioxide nanotube array films is proposed as two competitive processes, electrochemical oxidation and chemical dissolution. From these results, we observed that no titanium dioxide nanotubes, but titanium dioxide nanoholes were formed for anodization time of 60 min (Figure not shown). It shows that the titanium dioxide nanohole array films are easily formed during the short-time of anodization. Titanium dioxide nanotube arrays can also be prepared on the titanium film surface, but this can be accomplished by increasing the anodization time; this is due to the

high chemical dissolution at the inter-pore region. These results clearly show that high dissolution rate at the inter-pore region is very important in order to get the ordered nanotube arrays. Figure 14 shows the top-view scanning electron microscope images of titanium film anodized in different electrolytes at 30 and 20 V for anodization time of 240 and 180 min, respectively. It can be found that the pore growth and formation of titanium dioxide nanotube arrays on the titanium film surface are uniformly distributed. Scanning electron microscope images confirm the formation of titanium dioxide nanotubes on indium-doped tin oxide coated glass and silicon substrates. The growth rate and diameter of the titanium dioxide nanotube arrays prepared in ethylene glycol containing electrolyte is larger than that in glycerol containing electrolyte. The film thickness is calculated as 400 nm. In order to change the amorphous titanium dioxide into anatase titanium dioxide, the as-prepared titanium dioxide nanotube array film was annealed in air at 350°C for an hour. The annealed titanium dioxide electrode is used for preparing the dye-sensitized solar cell device. The platinum-coated indium-doped tin oxide substrate is used as a counter electrode. The photovoltaic parameters such as open circuit voltage ( $V_{oc}$ ), short-circuit current density ( $J_{sc}$ ) and fill factor (FF) are calculated as 0.432 V, 1.58 mA/cm<sup>2</sup> and 0.36, respectively. The low value of fill factor is attributed to the large value of series resistance at the interface between titanium dioxide and indium-doped tin oxide films. The efficiency of the prepared device is less than 1 %. In this method, the film thickness is one of the disadvantages for DSC applications. Because the amount of dye adsorption can be increased by increasing the internal surface area as well as the thickness of the films.

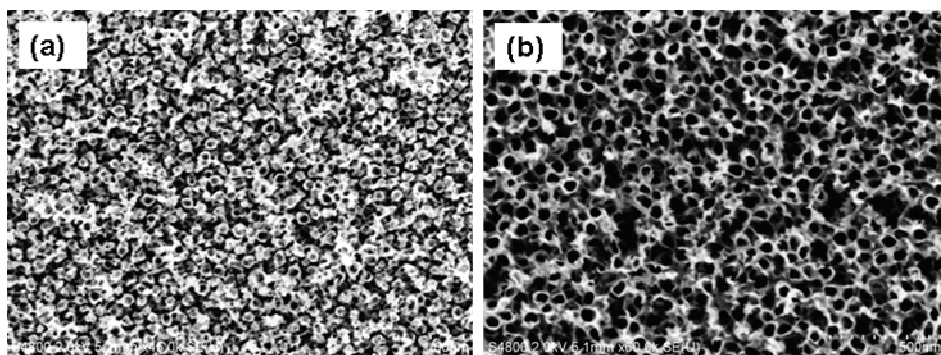


Fig. 14. SEM images of Ti/ITO/glass and Ti/Si after anodization in glycerol containing 2.5 vol. % H<sub>2</sub>O + 0.5wt. % NH<sub>4</sub>F at 30 V and ethylene glycol containing 2.0 vol. % H<sub>2</sub>O + 0.3wt. % NH<sub>4</sub>F at 20 V for 240 min (a) and 180 min (b), respectively.

### 3.6 Preparation and characterization of zinc oxide nanorods on different substrates

There are many reports about fabrication and characterization of dye-sensitized solar cells. However, the review results suggest that the recombination rate of the injected photoelectrons in dye-sensitized solar cell based on titanium dioxide electrode is very high compared to zinc oxide decorated titanium dioxide electrode, it is due to the absence of an energy barrier at the electrode to electrolyte interface. In the present work, we study the effect of growth conditions on the surface morphological and structural properties of zinc oxide films. We also investigate the photovoltaic performance of dye-sensitized solar cells based on titanium dioxide and titanium dioxide decorated with zinc oxide nanoparticles.

Finally, discussion on possible factors that improve the dye-sensitized solar cell device performance, because two different kinds of photoelectrodes have been used in this study. Nanostructured zinc oxide paste was prepared by using hydrothermal method. In order to study the effect of substrates surface condition on the surface morphological properties of zinc oxide, zinc oxide films were also prepared on different substrates such as indium-doped tin oxide film coated flexible clay, glass, zinc plate and copper wire substrates. Nanocrystalline indium-doped tin oxide films were prepared on clay and glass substrates by ion beam sputter deposition method (Venkatachalam et al., 2011). The hydrothermal synthesis of zinc oxide paste and films were carried out in a Teflon-lined stainless steel autoclave. In a typical synthesis process, zinc chloride (40 ml) was used with 2 ml of ammonia solution.

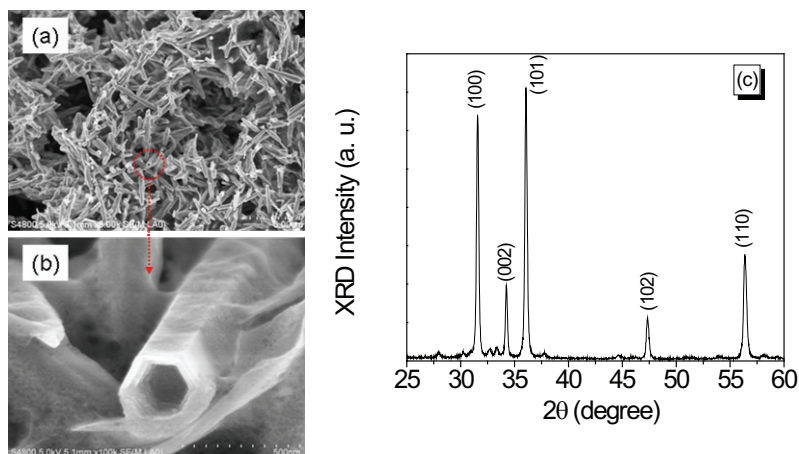


Fig. 15. Scanning electron microscope images of ZnO paste at low magnification (a) and high magnification (b); XRD pattern of ZnO paste prepared by hydrothermal method (c).

Figure 15 shows the scanning electron microscope images and X-ray diffraction pattern of zinc oxide paste prepared by hydrothermal method. The surface morphology (Fig. 15a) of as-prepared zinc oxide paste clearly shows the formation of zinc oxide nanorod like structure which are uniformly distributed throughout the surface of the sample. The formation of hexagonal shaped zinc oxide nanotube is clearly shown in Fig. 15b. The formation mechanism of the porous zinc oxide nanotube is mainly due to the preferential etching along the c-axis and slow etching along the radial directions. The X-ray diffraction peaks at  $2\theta$  of 31.9°, 34.76°, 36.3°, 47.6° and 56.68° arise from the (100), (002), (101), (102) and (110) hexagonal planes. All the X-ray diffraction peaks match well with the wurtzite zinc oxide structure with lattice constants of  $a = 3.25 \text{ \AA}$  and  $c = 5.16 \text{ \AA}$  (Wang et al., 2008). It shows that the zinc oxide nanotubes have good crystallinity, exhibiting a hexagonal structure. The presence of very weak intensity of the (002) in the X-ray diffraction pattern (Fig. 15c) supports the formation of zinc oxide tubular structure. Similar results have been observed by (Wang et al., 2008).

Figure 16A and B shows the scanning electron microscope images of zinc oxide films prepared on indium-doped tin oxide film coated glass and clay substrates. The diameters of zinc oxide nanorods on both clay and glass substrates are not uniform; they are in the range

from hundred to several hundred nanometers. The size of the zinc oxide nanorod on clay substrate is larger than that on glass substrate. The growth parameters of zinc oxide films on both glass and clay were same. The substrate surface roughnesses of indium-doped tin oxide film deposited on glass and clay were calculated by AFM. The substrate surface roughnesses of ITO/glass and ITO/clay are calculated as 4.3 and 83 nm, respectively. The substrate surface of ITO/clay is much larger than that of ITO/glass. This is attributed that the substrate surface roughness strongly influences the growth rate of zinc oxide films. X-ray diffraction pattern for zinc oxide film grown on glass shows a main peak at  $2\theta=34.76^\circ$ , it corresponds to (002) orientation of hexagonal zinc oxide. In contrast, the zinc oxide film deposited on clay shows a main peak at  $2\theta=32.08^\circ$ , it corresponds to (100) plane. X-ray diffraction patterns show two different orientations i.e., (002) and (100) on different substrates (glass and clay) (figure not shown). The exact reason, which determines the crystal growth and orientation, is the difference in substrate surface roughness between the glass and clay. Figure 16C and D shows the scanning electron microscope images of zinc oxide nanorods synthesized by hydrothermal method on copper and zinc substrates. The zinc oxide nanorods on both copper and zinc substrates are vertically oriented and well aligned (Fig. 16C and D). It also reveals that the nanorods are grown in a very high density. Scanning electron microscope images clearly show that the morphology of the final product is strongly dependent on the substrate surface condition.

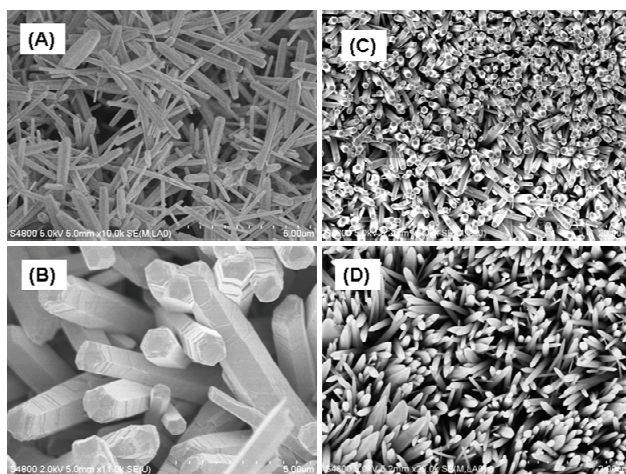


Fig. 16. Scanning electron microscope images of zinc oxide nanorods prepared on different substrates; (A) ITO/glass, (B) ITO/clay, (C) copper wire and (D) zinc plate.

The titanium dioxide paste was coated on indium-doped tin oxide coated glass substrate by doctor blade method. At first, the titanium dioxide coated ITO sample was annealed in air at  $150^\circ\text{C}$  for 30 min. Then the annealed  $\text{TiO}_2/\text{ITO}$  samples were placed into the zinc oxide solution for 30 sec. Finally, all the samples were annealed in air at  $400^\circ\text{C}$  for 2 h. The titanium dioxide film thicknesses are calculated as 1.5 and 3  $\mu\text{m}$ . In the present work, we employed a very thin layer of titanium dioxide film (1.5 or 3  $\mu\text{m}$ ) in order to check the effect of zinc oxide on the performance of the dye-sensitized solar cells. Finally, all the titanium dioxide electrodes were immersed into the ethanol solution containing ruthenium (N-719) dye. Then the dye-anchored titanium dioxide electrodes were rinsed with ethanol solution and then dried in air.



Figure 17 shows the photocurrent density-voltage characteristics of dye-sensitized solar cells based on titanium dioxide nanoparticulate film and zinc oxide decorated titanium dioxide films. The short circuit density of titanium dioxide based dye-sensitized solar cell is lower than that of dye-sensitized solar cell based on zinc oxide decorated titanium dioxide (see Table 3). This is attributed that the titanium dioxide electrode introduces charge recombination that mainly occurs at the electrode/electrolyte, so that the open circuit voltage and fill factor values are low compared to zinc oxide decorated titanium dioxide, this is due to the absence of energy barrier layer (Wang et al., 2009). The performance of the dye-sensitized solar cell based on zinc oxide decorated titanium dioxide has been improved; because the photogenerated electrons are more effectively extracted and, thereby, open circuit voltage ( $V_{oc}$ ), short-current density ( $J_{sc}$ ) and fill factor (FF) increase together. This is attributed that the protection of titanium dioxide surface with additional zinc oxide layer is considered to be another possible reason for the improved efficiency in zinc oxide decorated titanium dioxide photoanode. This result indicates that the power conversion efficiency of dye-sensitized solar cell based on zinc oxide decorated titanium dioxide can be increased by increasing the titanium dioxide film thickness.

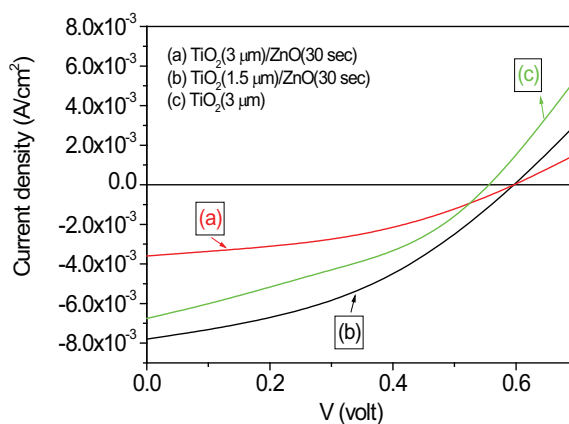


Fig. 17. Photocurrent density-voltage characteristics of dye-sensitized solar cell based on TiO<sub>2</sub> and ZnO/TiO<sub>2</sub> films.

Photoelectrode	TiO <sub>2</sub> (P25) Thickness	$V_{oc}$ (V)	$J_{sc}$ (mA/cm <sup>2</sup> )	FF	$\eta$ (%)
ZnO(30sec)/TiO <sub>2</sub>	1.5 $\mu$ m	0.606	3.60	0.41	0.9
ZnO(30sec)/TiO <sub>2</sub>	3.0 $\mu$ m	0.606	7.80	0.42	2.0
TiO <sub>2</sub>	3.0 $\mu$ m	0.560	6.75	0.35	1.32

Table 3. Photovoltaic parameters of dye-sensitized solar cell based on ZnO/TiO<sub>2</sub> and TiO<sub>2</sub> photoelectrodes.

#### 4. Conclusions

The zinc selenide thin films were deposited on Si and glass substrates by vacuum evaporation method at different substrate temperatures (483, 553 and 589K). All the films were polycrystalline and showed the cubic zinc blende structure with a preferred orientation along

the (111) direction. In the optical studies, the band gap value decreased from 2.72 to 2.60 eV as the substrate temperature was increased from 483 to 589 K. In the current-voltage studies, the departure of the ideality factor from unity was due to the existence of a laterally varying potential barrier height, caused by a non-uniform interface. From the capacitance-voltage study, the examined heterostructures are abrupt heterojunctions. Indium-tin oxide thin films were deposited on clay and glass substrates by ion beam sputter deposition method at room temperature. The flexibility of indium doped tin oxide coated clay substrate was measured as 17 mm. The as-deposited indium doped tin oxide coated films on flexible clay substrate showed low sheet resistance ( $41 \Omega/\square$ ) and high optical transmittance (~80%). Titanium dioxide nanorods were prepared on indium doped tin oxide coated glass and fluorine doped tin oxide coated glass substrates by hydrothermal method. The titanium dioxide nanorods were grown perpendicular to the fluorine doped tin oxide substrate; it was attributed to epitaxial growth of titanium dioxide films. Finally, flexible dye-sensitized solar cell was successfully fabricated. The titanium dioxide nanotube arrays and nanowires covered titanium dioxide nanotube arrays were successfully prepared by electrochemical anodization method. In this case, the dye adsorption capacity and power conversion efficiency of dye-sensitized solar cells based on nanowire covered titanium dioxide nanotube arrays were much higher than that of dye-sensitized solar cells based on titanium dioxide nanotube arrays. The titanium films were deposited on indium doped tin oxide coated glass substrate. The titanium dioxide nanotube arrays were successfully prepared on titanium films at room temperature. Nanostructured zinc oxide films were successfully deposited on different substrates by hydrothermal method. X-ray diffraction study clearly showed that the crystal quality and orientation of the final products were strongly dependent on the experimental parameter. Scanning electron microscope images showed that the shape and size of the nanorods could be perfectly generated by controlling the substrate surface roughness. The efficiency of ZnO/TiO<sub>2</sub> based DSC significantly improved from 0.9 to 2 % as the titanium dioxide film thickness was increased from 1.5 to 3  $\mu\text{m}$ . It showed the positive role of zinc oxide coating that leads to the improvement of the efficiency. This result indicated that the zinc oxide coating on the titanium dioxide surface suppresses the recombination at the TiO<sub>2</sub>/dye/electrolyte interface. The power conversion efficiency could be increased by increasing the TiO<sub>2</sub> film thickness.

## 5. References

- Bang, J.H.; Kamat, P.V. (2010). Solar Cell by Design. Photoelectrochemistry of TiO<sub>2</sub> Nanorod Arrays Decorated with CdSe. *Adv. Funct. Mater.* Vol.20, (June 2010), pp.1970-1976, ISSN 1616-3028
- Chiang, P. K.; Bedair, S. M. (1985). P-n junction formation in InSb and InAs<sub>1-x</sub>Sb<sub>x</sub> by Metalorganic chemical vapor deposition. *Appl. Phys. Lett.* Vol. 46, (February 1985), pp. 383-385, ISSN 1077-3118
- Chrisey, D.B.; Hubler, G.K. (1994). *Pulsed Laser Ablation and Deposition of Thin Films*, John Wiley, ISBN: 978-0-471-59218-1, New York
- Doolittle, L. R. (1985). Algorithms for the rapid simulation of Rutherford backscattering spectra. *Nucl. Instrum. Meth. B*, Vol. 9, (June 1985), pp. 344-351, ISSN 0969-8051
- Drechsler, M.; Meyer, B.K.; Hofmann, D. M.; Ruppert, P.; Hommel, D. (1997). Optically detected cyclotron resonance properties of high purity ZnSe epitaxial layers grown on GaAs. *Appl. Phys. Lett.* Vol. 71, (August 1997), pp. 1116-1117, ISSN 1077-3118
- Fung, K.K.; Wang, N.; Sou, I.K. (1997). Direct observation of stacking fault tetrahedra in ZnSe/GaAs(001) pseudomorphic epilayers by weak beam dark-field transmission

- electron microscopy. *Appl. Phys. Lett.* Vol. 71, (September 1997), pp. 1225-1228, ISSN 1077-3118
- Feng, X.; Shankar, K.; Varghese, O.K.; Paulose, M.; Latempa, T.J. (2008). Single crystal TiO<sub>2</sub> nanowire arrays grown directly on transparent conducting oxide coated glass: synthesis details and applications. *Nano Lett.* Vol. 8, No. 11, (October 2008), pp. 3781-3786, ISSN 1530-6984
- Haase, M.A.; Qiu, J.; DePuydt, J. M.; Cheng, H. (1991). Blue-green laser diodes. *Appl. Phys. Lett.* Vol. 59, (September 1991), pp. 1272-1274, ISSN 1077-3118
- Jennings, J.R.; Ghicov, A.; Peter, L.M.; Schmuki, P.; Walker, A.B. (2008). Dye-Sensitized Solar Cells Based on Oriented TiO<sub>2</sub> Nanotube Arrays: Transport, Trapping, and Transfer of Electrons. *J. Am. Chem. Soc.* Vol. 130, No. 40, (September 2008), pp. 13364-13372, ISSN 0002-7863
- Jeon, H.; Ding, J.; Patterson, W.; Nurmikko, A.V.; Xie, W.; Grillo, D.C.; Kobayashi, M.; Gunshor, R.L. (1991). Blue-green injection laser diodes in (Zn,Cd)Se/ZnSe quantum wells. *Appl. Phys. Lett.* Vol. 59, (December 1991), pp. 3619-3621, ISSN 1077-3118
- Jamieson, D. N. (1998). Structural and electrical characterisation of semiconductor materials using a nuclear microprobe. *Nucl. Instrum.Meth. B*, Vol. 136, (March 1998), pp. 1-13, ISSN 0969-8051
- Khlyap, G.; Andrukhiv, M. (1999). New Heterostructures n-PbS/n-ZnSe: Long-Term Stability of Electrical Characteristics. *Cryst. Res. Technol.* Vol. 34, No. 5-6, (June 1999), pp. 751-756, ISSN 1521-4079
- Kim, H.; Horwitz, J. S.; Kushto, G.P.; Kafafi, Z.H.; Chrisey, D.B. (2001). Indium tin oxide thin films grown on flexible plastic substrates by pulsed-laser deposition for organic light-emitting diodes. *Appl. Phys. Lett.* Vol. 79, No.3, (July 2001), pp. 284-286, ISSN 1077-3118
- Kawasaki, K.; Ebina, T.; Tsuda, H.; Motegi, K. (2010). Development of flexible organo saponite films and their transparency at high temperature. *Appl. Clay Sci.* Vol. 48, (March 2010), pp. 111-116, ISSN 0169-1317
- Lour, W-S.; Chang, C.-C. (1996). VPE grown ZnSe/Si PIN-like visible photodiodes. *Solid State Electron.* Vol. 39, (September 1996), pp. 1295-1298, ISSN 0038-1101
- Lee, W. J.; Alhoshan, M.; Smyrl, W.H. (2006). Titanium dioxide nanotube arrays fabricated By anodizing processes. *J. Electrochem. Soc.* Vol. 153, (September 2006), pp. B499-505, ISSN 00134651
- Montes, L.; Herino, R. (2000). Luminescence and structural properties of porous silicon with ZnSe intimate contact. *Mater. Sci. Eng. B*, Vol. 69-70, (January 2000), pp. 136-141, ISSN 0921-5107
- Macak, J.M.; Tsuchiya, H.; Berger, S.; Bauer, S.; Fujimoto, S.; Schmuki, P. (2006). On wafer TiO<sub>2</sub> nanotube-layer formation by anodization of Ti-films on Si. *Chem. Phys. Lett.* Vol.428, (September 2006), pp. 421-425, ISSN 0009-2614
- Pfister, G.; Melnyk, A. R.; Scharfe, M. E. (1977). Enhancement of hole drift velocity in amorphous As<sub>2</sub>Se<sub>3</sub> by iodine doping. Original Research Article. *Solid State Commun.* Vol. 21, No. 9, (March 1977), pp. 907-910, ISSN 0038-1098
- Park, H.; Kim, W.-R.; Jeong, H.-T.; Lee, J.-J.; Kim, H.-G.; Choi, W.-Y. (2011). Fabrication of dye sensitized solar cells by transplanting highly ordered TiO<sub>2</sub> nanotube arrays. *Sol. Energy Mater. Sol. Cells*, Vol. 95, No. 1, (January 2011), pp. 184-189, ISSN 0927-0248
- Rakhshani, A. E.; Makdisi, Y.; Mathew, X.; Mathews, N. R. (1998). Charge Transport Mechanisms in Au-CdTe Space-Charge-Limited Schottky Diodes. *Phys. Status Solidi a*, Vol. 168, (July 1998), pp. 177-187, ISSN 1862-6319

- Sze, S. M. (2<sup>nd</sup> Eds.). (1985). *Semiconductor Devices, Physics and Technology*, John Wiley, ISBN 0-471-33372-7, New York
- Singh, A.; Cova, P.; Masut, R. A. (1993). Energy density distribution of interface states in Au Schottky contacts to epitaxial  $\text{In}_{0.21}\text{Ga}_{0.79}\text{As}:\text{Zn}$  layers grown on GaAs by metalorganic vapor phase epitaxy. *J. Appl. Phys.* Vol. 74, (December 1993), pp. 6714-6719, ISSN 0021-8979
- Sadek, A.A.; Zheng, H.; Latha, K.; Wlodarski, W.; Kalantar-zadeh, K. (2009). Anodization of Ti thin film deposited on ITO. *Langmuir*, Vol.25, (November 2009), pp. 509-514, ISSN 0743-7463
- Tao, R-H.; Wu, J-M.; Xue, H-X.; Song, X-M.; Pan, X.; Fang, X-Q.; Fang, X-D.; Dai, S-Y. (2010). A novel approach to titania nanowire arrays as photoanodes of back-illuminated dye sensitized solar cells. *J. Power Sources*, Vol. 195, (May 2010), pp. 2989-2995, ISSN 0378-7753
- Ullrich, B. (1998). Comparison of the photocurrent of ZnSe/InSe/Si and ZnSe/Si heterojunctions. *Mater. Sci. Eng. B*, Vol. 56, (October 1998), pp. 69-71, ISSN 0921-5107
- Venkatachalam, S.; Mangalaraj, D.; Narayandass, Sa. K. (2006). Influence of substrate temperature on the structural, optical and electrical properties of zinc selenide (ZnSe) thin films. *J. Phys. D: Appl. Phys.* Vol. 39, (November 2006), pp. 4777-4782, ISSN 1361-6463
- Venkatachalam, S.; Agilan, S.; Mangalaraj, D.; Narayandass, Sa.K. (2007a). Optoelectronic properties of ZnSe thin films. *Mat. Sci. Semicon. Proc.* Vol. 10, (July 2007), pp. 128-132, ISSN 1369-8001
- Venkatachalam, S.; Mangalaraj, D.; Narayandass, Sa.K.; Velumani, S.; Schabes-Retchkiman, P.; Ascencio, J.A. (2007b). Structural studies on vacuum evaporated ZnSe/p-Si Schottky diodes. *Mater. Chem. Phys.* Vol. 103, (June 2007), pp. 305-311, ISSN 0254-0584
- Venkatachalam, S.; Iida, Y.; Kanno, Y. (2008). Preparation and characterization of Al doped ZnO thin films by PLD. *Superlattices and Microstructures*, Vol. 44, No.1, (July 2008), pp. 127-135, ISSN 0749-6036
- Venkatachalam, S.; Nanjo, H.; Hassan, F.M.B.; Kawasaki, K.; Kanakubo, M.; Aizawa, T.; Aida, T.; Ebina, T. (2010). Characterization of nanocrystalline Indium Tin Oxide thin films prepared by ion-beam sputter deposition method. *Thin Solid Films*, Vol. 518, (September 2010), pp. 6891-6896, ISSN 0040-6090
- Venkatachalam, S.; Nanjo, H.; Hassan, F.M.B.; Kawasaki, K.; Wakui, Y.; Hayashi, H.; Ebina, T. (2011). Properties of Indium Tin Oxide Thin Films Deposited on Glass and Clay Substrates by Ion-Beam Sputter Deposition Method. *Jpn. J. Appl. Phys.* Vol. 50, (January 2011), pp. 01AK03-1-01AK03-4, ISSN 1347-4065
- Wu, W.F.; Chiou, B.S. (1997). Deposition of indium tin oxide films on polycarbonate substrates by radio-frequency magnetron sputtering. *Thin Solid Films*, Vol. 298, No. 1-2, (April 1997), pp. 221-227, ISSN 0040-6090
- Warren, B. E.; X-ray Diffraction; Dover: New York; 1990, p 253.
- Wang, H.; Li, G.; Jia, L.; Wang, G.; Tang, C. (2008). Controllable Preferential-Etching Synthesis and Photocatalytic Activity of Porous ZnO Nanotubes. *J. Phys. Chem. C*, Vol. 112, No. 31, (July 2008), pp. 11738-11743, ISSN 1932-7455
- Wang, J.; Lin, Z. (2009). Anodic Formation of Ordered TiO Nanotube Arrays: Effects of Electrolyte Temperature and Anodization Potential. *J. Phys. Chem. C*, Vol.113, (February 2009), pp.4026-4030, ISSN 1932-7455
- Wang, M.; Huang, C.; Cao, Y.; Yu, Q.; Deng, Z.; Liu, Y.; Huang, Z.; Huang, J.; Huang, Q.; Guo, W.; Liang, J. (2009). Dye-sensitized solar cells based on nanoparticle-decorated ZnO/TiO<sub>2</sub> core/shell nanorod arrays. *J. Phys. D: Appl. Phys.* Vol. 42, (2009), pp. 155104, ISSN 1361-6463

## **Part 2**

# **Polymer Optoelectronic Materials**



# Side-Chain Multifunctional Photoresponsive Polymeric Materials

Luigi Angiolini<sup>1</sup>, Tiziana Benelli<sup>1</sup>, Loris Giorgini<sup>1</sup>,  
Attilio Golemme<sup>2</sup>, Elisabetta Salatelli<sup>1</sup> and Roberto Termine<sup>2</sup>  
<sup>1</sup>*Dipartimento di Chimica Industriale e dei Materiali, Università di Bologna,*  
<sup>2</sup>*CNR-IPCF UOS di Cosenza-LiCryL, INSTM UdR Calabria,*  
*Centro di Eccellenza CEMIF CAL, Dipartimento di Chimica,*  
*Università di Calabria,*  
*Italy*

## 1. Introduction

Several potential advantages are connected to the availability of functional organic polymeric materials for advanced applications with respect to inorganic materials. They include structural flexibility (i.e. the possibility to achieve by synthetic methods different composition features, as well as molecular and physical properties), lighter weight, thermoplastic behaviour (allowing to prepare stable thin films), possibility of being processed by different procedures, potential low cost etc. Further advantages are also given by the chemical anchorage of the photoactive moieties to the macromolecular structure, thus avoiding several drawbacks deriving from crystallization, inhomogeneity in the bulk, phase segregation etc. which are present when small active molecules are dispersed into a plastic matrix.

Indeed, since several decades a very wide academic and industrial interest has arisen around this topic, as demonstrated by the huge amount of publications appeared in the literature. We shall limit here to review the recent literature concerning the state-of-the-art of the research on amorphous polymeric derivatives bearing side-chain photoactive moieties such as the azo-aromatic and the carbazole chromophore as functional groups, in addition to the presence of structural or chemical features suitable to also provide the macromolecules of chiral properties.

## 2. Functional polymers containing side-chain azoaromatic moieties

Azobenzene derivatives represent a most widely investigated chromophoric system, due in particular to their photochromic properties. When submitted to irradiation with appropriate light, the more stable azo-*trans* form isomerizes reversibly to the azo-*cis* form, possessing higher dipole moment and free volume requirement (Fig. 1), with several relevant consequences if the moiety is incorporated into polymers or other materials. The azo-*cis* form gives again the *trans* isomer thermally or by light irradiation.

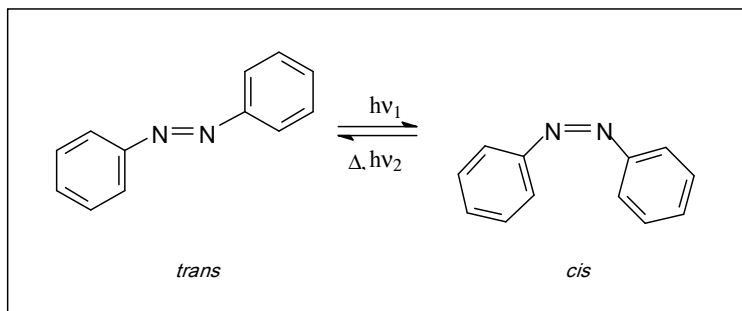


Fig. 1. Photoisomerization of azobenzene

Thus, the light-induced geometric change allows these systems to be used as photoswitches, with important effects on various chemical, mechanical, electronic and optical properties of the material. An exhaustive review paper focused on the photoinduced motions in azo-containing polymers covering the literature up to 2001, has been published by Natansohn and Rochon (Natansohn & Rochon, 2002). Recently, a book devoted to azobenzene-containing polymers and liquid crystals as light-responsive materials has appeared (Zhao & Ikeda, 2009).

Three levels of induced motions, at molecular, domain and mass (macroscopic) level, in order of increasing size scale, are considered in connection with polarization and power of incident light, although the motion at any scale invariably affects the other scales (Fig. 2).

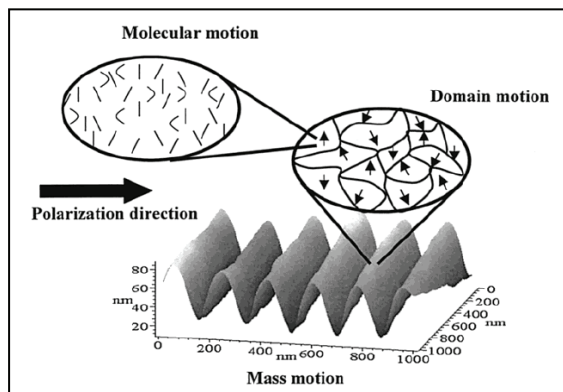


Fig. 2. Illustration of the three levels of polymer motion produced with light (Reprinted with permission from ref. Natansohn & Rochon 2002. Copyright 2002 American Chemical Society)

At the first scale level, this behaviour can be exploited in the optical storage of information, as optical birefringence in the material can be induced in consequence of a statistical process based on the absorption of linearly polarized (LP) light, *trans-cis-trans* isomerisation and reorientation of the azo groups. As the groups which reorient with their electronic transition dipole moments along a direction perpendicular to the light electric field, are unable to absorb again the radiation, a net excess of chromophores oriented in that direction, and consequently birefringence, is produced in the material (Fig. 3a).



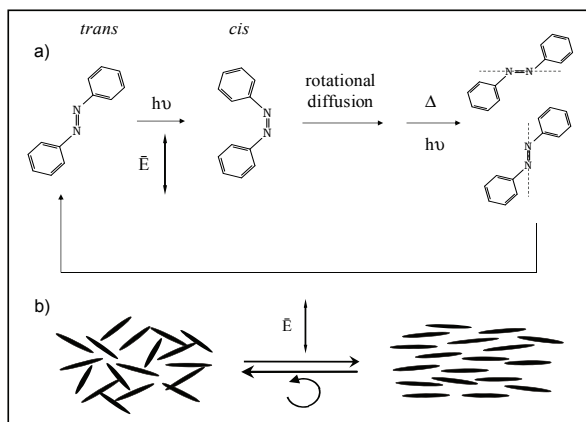


Fig. 3. Statistical photoorientation of azomolecules

The photoinduced birefringence can then be erased by irradiation with depolarized or circularly polarized (CP) light (Fig. 3b), thus recreating the original isotropic arrangement of the dipoles in the material. This reversible process can be repeated many times (up to hundred thousands of times). The application has been reported for poly(meth)acrylates functionalized in the side chain with the Disperse Red 1 (**DR1**) dye (Fig.4) (Natansohn et al., 1992; Ho et al., 1995) and demonstrated for rewritable optical disk systems (Sabi et al., 2001 as cited in Natansohn & Rochon, 2002).

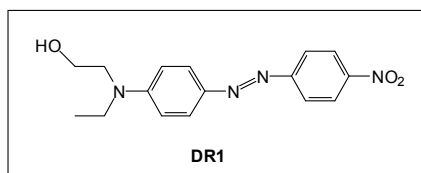


Fig. 4. Chemical structure of **DR1** molecule

More recently, enhanced photoinduced linear birefringence, lower relaxation after pump removal and long-term storage stability, although with lower stability to repeated cycles of irradiation with respect to **DR1** functionalized polymers, has been reported for side-chain azoaromatic polymethacrylates characterized by the presence of a chiral moiety with one prevailing absolute configuration interposed between the main chain and the chromophore (poly[(S)-**MAP-N**] Fig. 5).

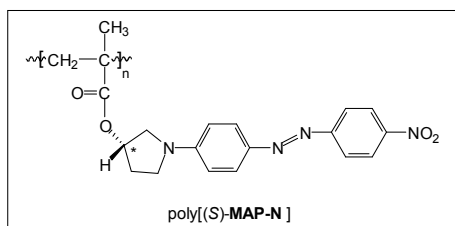


Fig. 5. Chemical structure of poly[(S)-**MAP-N**]

The presence of a chiral moiety in the material allows also the photomodulation of the chiroptical properties of the film at the domain level, upon irradiation with CP light of one single, L or R, rotation sense, with the possibility to reversibly invert the original supramolecular helical handedness of the native material without any need of preorientation with linearly polarized (LP) light for the circular dichroism to be photoinduced (Angiolini et al., 2002, 2003a, 2003b).

A similar intriguing phenomenon was previously observed in achiral smectic liquid crystalline side-chain azopolymers already possessing a supramolecular conformational order (Naydenova et al., 1999) and also in an achiral amorphous MMA azo-copolymer (**1**, Fig. 6) upon irradiation with L- or R-CP light, after preorientation by LP light (Ivanov et al., 2000). This was interpreted on the basis of circular momentum transfer from the CP light to the azobenzene chromophores (Nikolova et al., 2000).

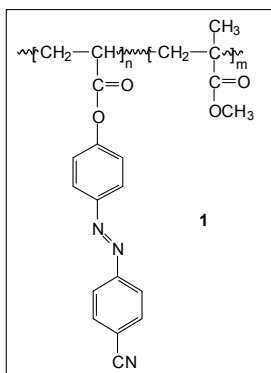


Fig. 6. Chemical structure of an achiral amorphous MMA azo-copolymer

The methacrylic copolymers bearing in the side chain both the above mentioned chiral moiety [(*S*)-MAP-N] and the DR1 methacrylate (DR1M) moiety (Fig. 7) display intermediate birefringence properties and increased stability at low content of chiral co-units (Angiolini et al., 2006).

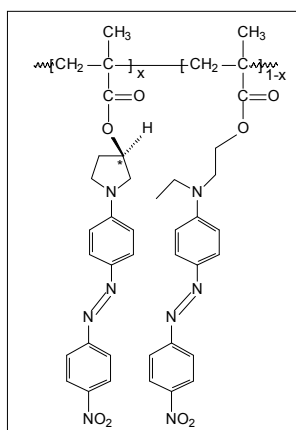


Fig. 7. Chemical structure of the copolymeric system poly[(*S*)-MAP-N-co-DR1M]

Side-chain bis-azo chromophores (Fig. 8) afford higher birefringence with respect to mono-azo ones, but limited solubility (Meng et al. 1997; J. Wang et al., 2003) and their isomerization mechanism was investigated (Jin et al., 2004). The application of these polymeric materials as rewritable digital data carriers and for optical recording has been patented (Hagen et al., 2003; Berneth et al., 2003).

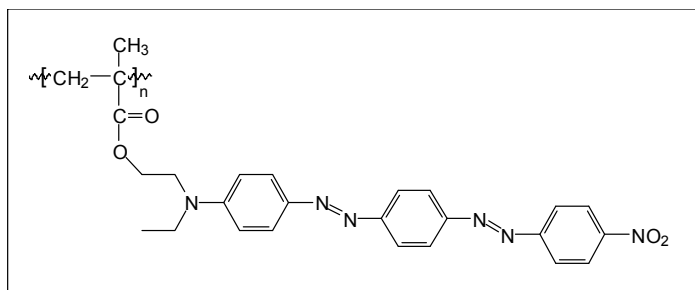


Fig. 8. Chemical structure of side-chain bis-azo chromophore

Experiments of photoinduced birefringence on chiral, optically active bis-azo homo- and copolymers with MMA (**2**, Fig. 9) (Angiolini et al., 2007a) show that, although these copolymers display slower optical response rates in comparison to similar derivatives containing only one azo bond (Angiolini et al., 2002), large and relatively stable birefringence and all-optical switching effects can be achieved with polymer films having a low content of photochromic co-units, along with better solubility and processability.

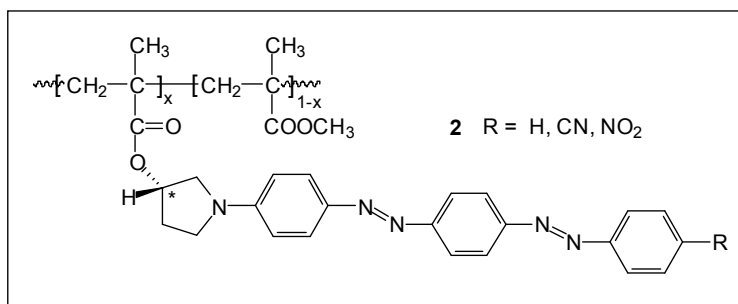


Fig. 9. Chemical structure of optically active bis-azo homo- and co-polymers with MMA

Non linear optical (NLO) properties, requiring an asymmetric response by the electronic system, can be achieved with push-pull substituents giving strongly differentiated electron distribution, and overall noncentrosymmetry in the bulk. They are based on electric field poling of dipoles in the material spin coated over a conducting substrate and then heated at a temperature above the glass transition temperature ( $T_g$ ) (corona-poling), or submitted to photoassisted alignment in order to improve the electric field poling (Sekkat & Dumont, 1992). Azoaromatic derivatives are natural candidates to this application due to their large second-order NLO properties, ease of processing and architectural versatility with respect to inorganic counterparts such as  $\text{LiNbO}_3$ . Of course, for achieving temporal stability of the system, the polar alignment has to be maintained at the working temperature of the material and a high value of  $T_g$ , well above the room temperature, is required. The NLO response is

usually assessed by measuring the second harmonic generation (SHG), i.e. the emission of light at a double frequency of the incident beam, the electrooptic (EO) effect (change of refractive index under an electric field), or through wave-mixing experiments (generation of various frequencies of light), all of these being also related to the main applications of NLO materials (Zhao & Ikeda, 2009).

A significant number of polymers functionalized, in particular, with **DR1** dye in the side chain are reported (Blanchard et al. 1993a, 1993b as cited in Natansohn & Rochon, 2002; Loucif-Saibi et al., 1993 as cited in Natansohn & Rochon, 2002; Hill et al., 1995 as cited in Natansohn & Rochon, 2002) to have been submitted to photoassisted alignment, thus achieving improved NLO properties. An all-optical poling, in which the aligning electric field is actually generated by the laser light has also been envisaged since 1993 on **DR1M-MMA** copolymer (Charra et al., 1993; Chalupczak et al., 1996) and subsequently applied to a new phosphine oxide azo-dye-MMA copolymer (Fiorini et al., 1997) achieving increased transparency with respect to the **DR1** functionalized material, together with large second-order properties. Differently from the polymeric **DR1M-MMA** material, efficient optical poling of thin films of norbornene functionalized with azo-dye have also been achieved, but without appreciable enhancement of second-order susceptibility, however, in the related polymeric poly-norbornene derivative, due probably to the increased rigidity of the poly-norbornene backbone with respect to the poly-MMA backbone (Churikov et al., 2000). Accordingly, copolymers based on side-chain push-pull azobenzene grafted to poly(N-methacryloyl-N'-phenylpiperazine) (**3**, Fig. 10) displayed much lower orientability and stability of the polar order with respect to the related guest-host systems having the chromophore physically dispersed into the unfunctionalized polymer. In addition, flexible structures gave better results than the rigid ones (Tirelli et al., 2000).

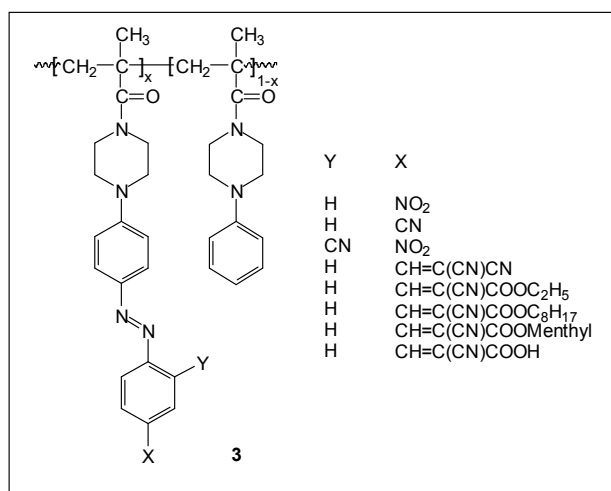


Fig. 10. Chemical structure of copolymers based on side-chain push-pull azobenzene grafted to poly(N-methacryloyl-N'-phenylpiperazine)

The influence of main-chain mobility on the effectiveness of optical or thermal poling is witnessed by many literature examples. For instance, the all-optical poling of a side-chain poly(urethane-imide) film containing the azobenzene chromophore displayed less surface

defects with respect to traditional corona poling (Sui et al., 2001), however in the case of crosslinkable polymeric thick films of isocyanate prepolymer functionalized with push-pull azobenzene moieties, corona-poling appears to be more efficient with respect to optical poling (Xu et al., 1999).

An interesting review paper on the state of the art in the field of second-order NLO polymers is reported by Samyn (Samyn et al., 2000), where a comparison is made among several side-chain azopolymers differing in the main chain structure. It turns out that poly(methacrylate) appears as the most favourable backbone in terms of second-harmonic coefficient values and temporal stability with respect to the related poly(alkyl vinyl ether)s and poly(styrene)s.

Chiral polymers, being inherently non-centrosymmetric on the molecular and macroscopic scale, could in principle not require poling in order to display NLO properties, but their symmetry in the bulk is high enough to prevent the production of frequency doubling. However it is sufficient for obtaining EO effect and frequency mixing (Beljonne et al., 1998). Recently, corona-poled chiral side-chain azobenzene polymethacrylates of various composition (**4**, Fig. 11) have been reported (Angiolini et al., 2008a) to afford higher values of their second-order coefficients with respect to similar achiral materials (S'Heeren et al., 1993) and confirmed that the best compromise between content and orientational mobility of the push-pull chromophore is obtained in the copolymers containing the 20-40% molar concentration of azo-chromophore.

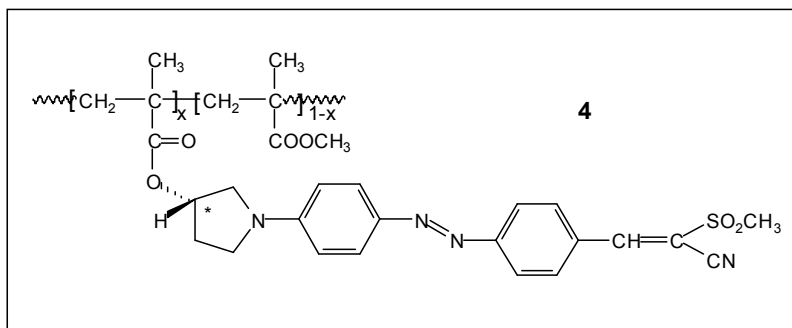


Fig. 11. Chemical structure of corona-poled chiral side-chain azobenzene polymethacrylates

When two interfering coherent laser beams are used as irradiation source on azobenzene polymeric films for a period of time longer than that required for photoinduced orientation, a motion at macroscopic level may be produced with formation of stable surface relief gratings (SRG) spatially modulated of the order of hundreds of nanometers (Fig. 12).

The first reports on this behaviour of azobenzene polymers appeared in 1995 (Rochon et al., 1995; Kim et al., 1995) and the phenomenon was accurately investigated (Viswanathan et al., 1999). These structures behave as holographic diffraction gratings, thus allowing to record polarization holograms in polymeric films (Nikolova et al., 1996 as cited in Natansohn & Rochon, 2002). Accordingly, holographic phase grating can be rapidly produced, erased and switched in polymeric azobenzene liquid crystals (Yamamoto et al., 2001) by irradiation with CP light or heating the material above its glass transition temperature. Interestingly, when the **DR1** polymethacrylate, which is known to not display, under normal conditions,

the presence of mesophases, is submitted, subsequently to the photoinduced grating, to annealing above its glass transition temperature accompanied by irradiation with He-Ne laser light, a "buried density grating" is observed immediately below the film surface (Pietsch & Rochon, 2003). This finding has been interpreted by the authors as the first case of photoinduction of liquid-crystalline properties in a material lacking of thermotropic properties.

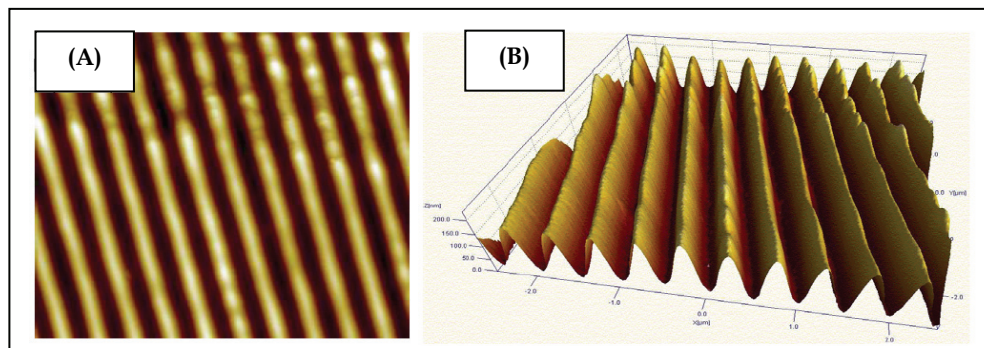


Fig. 12. Bidimensional (A) and tridimensional (B) AFM 5x5  $\mu\text{m}$  surface profile of an optically inscribed grating on a film of azobenzene polymer

Applications of SRG on azobenzene polymers have been investigated for rewritable optical recording (Fukuda, 2004; Ramos et al., 2004; Raschellà et al., 2004) and optical devices (Viswanathan et al. 1999; Ramanujam et al., 1999; Dantsker et al., 2001; Matsui et al., 2002; Ubukata et al., 2005).

### 3. Functional polymers containing side-chain carbazole moieties

Since the discovery of photoconductivity in poly(N-vinylcarbazole) (Fig. 13) sensitized with suitable electron acceptors (Hoegl, 1965), an intense interest has grown around this topic, which has been subsequently dedicated to the development of polymeric light emitting diodes, organic photorefractive materials and photovoltaic devices (Grazulevicius et al., 2003).

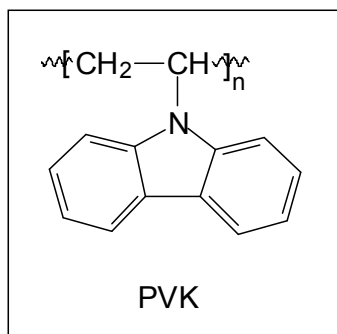


Fig. 13. Chemical structure of poly(N-vinylcarbazole) (PVK)

Photoconduction is promoted by initial light absorption producing charge photogeneration followed by charge transport upon action of an electrical field, in which the carbazole behaves as electron donor moiety (hole or radical cation) moving through a hopping process from one localized site to another in the general direction of the electric field (Naarmann & Strohhriegl, 1992). To improve photoconductivity, **PVK** can be chemically modified in order to increase the absorption in the visible region by linkage to moieties such as phthalimide (Biswas & Das., 1982), Cu phthalocyanine (H.Z. Chen et al., 1993; M. Wang et al., 1995), fullerene C60 (Y. Chen et al., 1996a, 1996b).

However **PVK**, formerly used as charge transporting host in pristine photorefractive polymer composites in combination with a push-pull azoaromatic molecule as EO chromophore, 2,4,7-trinitro-9-fluorenone (**TNF**) as photosensitizer and N-ethylcarbazole added to lower the T<sub>g</sub> of the material (Meerholz, 1994), displays a severely restricted conformational mobility of the macromolecules, due to the steric hindrance between neighbouring carbazole groups, originating the presence of undesired excimer-forming sites which give radiative decay as a loss process in charge photogeneration and mobility. Lowering the T<sub>g</sub> by addition of a plasticizer or introducing a spacer between the main chain and the chromophore may improve the photorefractive performance, although the relative content of chromophore is diminished. Indeed, poly(2-(N-carbazolyl)ethyl methacrylate) exhibits charge carrier mobility comparable to that of **PVK**, despite the lower chromophore concentration (Keyanpour-Rad et al., 1978) and the photophysical properties of similar carbazolyl polymethacrylates indicate the absence of excimer-forming sites when the carbazole unit is not directly bound to the polymer main chain (Ledwith et al., 1981). Accordingly, the photoconductive properties of poly(N-epoxypropyl-carbazole) (**PEPK**) are comparable or even better than those of **PVK** (Gaidelis et al., 1976).

A significant number of other polymers containing side-chain carbazole moieties are reported and discussed with reference to the influence of the macromolecular rigid main chain and the side-chain mobility on their photoresponsive properties: polystyrenes (Kanbara et al. 2000; C. Chang et al. 2010), poly(*p*-phenylenevinylene) (Vellis et al., 2008; Ravindranath et al., 2007), polyisocyanides (Schwartz et al., 2010) and poly((amino)amide)s (Thomas et al., 2001; Liou et al., 2006), polythiophenes (W. Li et al., 2010) and polyimides (Ghaemy et al., 2009).

In connection with studies concerning the amplification of chirality in polymeric materials, helical polyacetylenes (Fujii et al., 2007; Qu et al., 2007a, 2007b) and vinyl polymers bearing in the side chain the carbazole group functionalized with chiral moieties (Chiellini et al., 1977, 1978, 1980, 1984) have been investigated and characterized in terms of optical activity of the macromolecules originated by ordered chiral arrangements. In this context, a new class of functional polymers possessing an optically active chiral functionality interposed between the polymethacrylic backbone and the carbazole moiety have also been tested for photoconductivity (Fig. 14).

These materials do not require the presence of a dopant in order to exhibit photoconductivity, but poly[(S)-**MECP**], bearing the electron donor pyrrolidine ring, favours the formation of a charge transfer complex with carbazole more effectively than poly[(S)-**MECSI**], where the electron acceptor succinimide ring is linked to carbazole (Angiolini et al., 2008b).

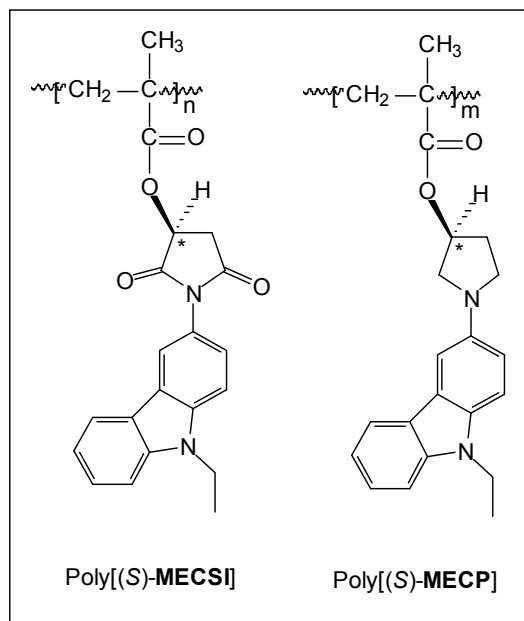


Fig. 14. Chemical structures of poly[(S)-MECSI] and poly[(S)-MECP]

Accordingly, poly[(S)-MCPP] (Fig. 15) exhibits higher photoconductivity than poly[(S)-MCPS], whereas the achiral sample poly[MCPE] displays even higher photoconductivity, attributed to the flexible spacer favouring a more convenient mutual arrangement of the chromophores (Angiolini et al., 2010).

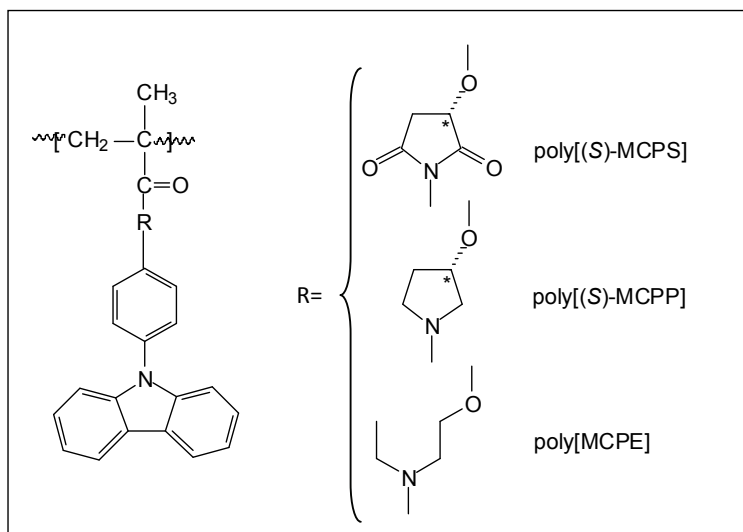


Fig. 15. Chemical structure of poly[(S)-MCPS], poly[(S)-MCPP] and poly[MCPE]



#### 4. Multifunctional polymers containing side-chain azoaromatic and carbazole moieties

When azoaromatic chromophores and carbazole moieties are combined together in a photoresponsive system, further properties may be generated, among which photorefractivity, in addition to those mentioned above. Photorefractive materials are those in which charges photogenerated by a non-uniform light pattern redistribute in space, setting up an internal electric field that, in turn, changes the refractive index: the resulting hologram is a replica of the original light distribution. To be photorefractive, a material must display photoinduced charge generation, charge transporting, charge trapping and an EO response (electric field dependent refractive index, or Pockels effect) (Y. Zhang et al., 1998). The last three conditions may be satisfied by second order NLO chromophores, such as, e.g., push-pull conjugated azoaromatic derivatives, which can be submitted to orientation by suitable light irradiation, while the first condition requires the presence of a photosensitive component capable of charge generation. Photoconduction is also an important requirement in order to observe photorefractivity, a phenomenon widely studied for its applications in different areas, such as image treatment, optical limiting and amplification, dynamic holography.

Consequently, organic materials require the presence of different functionalities in order to achieve photorefractivity, including photosensitivity, photoconductivity and EO response.

In this context, bifunctional photorefractive polymers, possessing both photoconductivity and EO response, have been largely investigated, in particular polymers functionalized with pendant azoaromatic and carbazole moieties respectively located on different repeating units or linked to each other by a covalent bond. An additional functionality, constituted by the presence of asymmetric centers providing chirality to the macromolecule, may also participate to the system.

##### 4.1 Copolymers containing side-chain azoaromatic and carbazole moieties

The presence of both the conductive and the EO moiety linked to the same backbone appears to give better results in comparison to the physical dispersion of chromophoric molecules into a carbazole-functionalized polymeric matrix. For instance, low  $T_g$  multifunctional copolymers constituted by polymethacrylates bearing in the side chain the carbazole moiety and a push-pull azoaromatic dye spaced from the main chain by methylene groups have been reported (Maertens et al., 2000) to display photoinduced orientation more than three orders of magnitude higher in the grafted material as compared to the dispersion of the azo dye in **PVK** and *N*-ethylcarbazole. However, the  $T_g$  of the functional copolymer appears to play a predominant role in the optical properties of the material.

A new class of high- $T_g$  multifunctional photorefractive polymers obtained from a rigid maleimide monomer bearing differently spaced hole transporting carbazole moieties, by alternating copolymerization with methyl vinyl isocyanate, followed by functionalization of the isocyanate groups with different amounts of methanol and hydroxyalkyl NLO chromophores ( $D\pi A$ ), including **DR1** dye, (**5**, Fig. 16), has been reported (Hattemer et al., 2000). The sample with  $T_g$  ca. 80°C, containing the **DR1** dye, added with **TNF** and *N*-ethylcarbazole as plasticizer, investigated by two-beam coupling (2BC) and degenerate four-wave mixing experiments, displayed response times in the order of 100 ms, a value very low for high  $T_g$  systems, comparable to those of low- $T_g$  photorefractive materials.

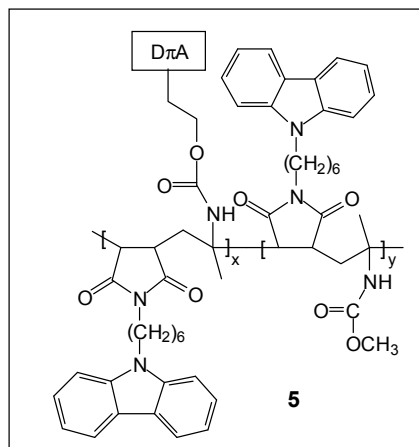


Fig. 16. Chemical structure of multifunctional photorefractive polymers

Copolymers of N-hydroxyethyl carbazole acrylate with azoaromatic push-pull acrylate (**6**, Fig. 17) of various compositions, possessing  $T_g$  values much over  $200^\circ\text{C}$ , mixed with N-ethylcarbazole as plasticizer and doped with **TNF**, have been prepared and investigated for EO properties and photorefractivity by 2BC experiments (Y. Chen et al., 2001).

Interesting alternating copolymers obtained by radical copolymerization between N-vinyl carbazole and azoaromatic acrylate having elevated  $T_g$  values have also been synthesized and characterized (Altomare et al., 2004).

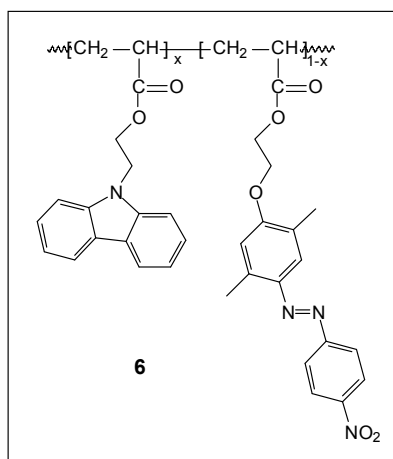


Fig. 17. Chemical structure of copolymers of N-hydroxyethyl carbazole acrylate with azoaromatic push-pull acrylate

A further functionality, chirality, is present in methacrylic copolymers bearing a side-chain chiral rigid group with one prevailing absolute configuration interposed between the backbone and the photoactive moiety (carbazole and azoaromatic), possessing  $T_g$  values above  $200^\circ\text{C}$  (Angiolini et al., 2007b; H. Li et al., 2009) (Fig. 18).

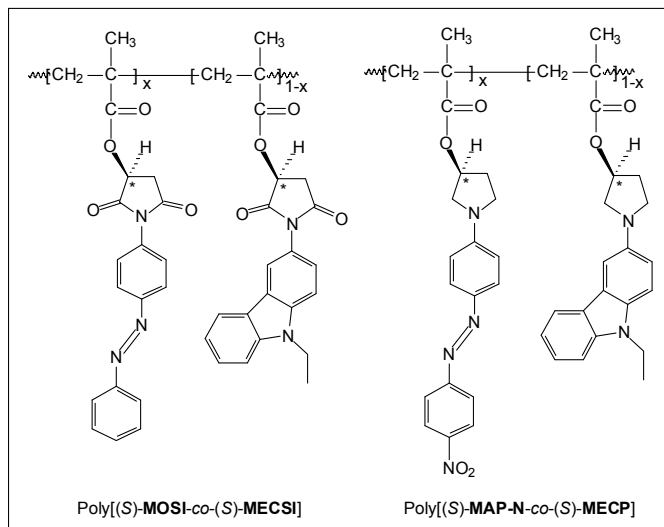


Fig. 18. Chemical structures of copolymers poly[(S)-MOSI-co-(S)-MECSI] and poly[(S)-MAP-N-co-(S)-MECP]

The additional functionality allows to obtain informations by Circular Dichroism (CD) spectroscopy about the presence of ordered helix-type structures of the macromolecules and of cooperative interactions between chromophores (Angiolini et al., 2009b), opening the possibility to use these polymeric derivatives as chiroptical switches, too (Angiolini et al., 2002, 2003a, 2003b). Differently from literature reports concerning amorphous systems containing azo-compounds, where electrically prepoled materials or an operating temperature close to  $T_g$  was required, the photorefractivity of these materials was achieved at room temperature without prepoling. This behaviour is attributed to a chromophore reorientation process induced by the electric field applied during the measurements, which is assisted by photoisomerization of the azo-chromophore.

The first photorefractive sol-gel material, constituted by the NLO chromophore **DR1** and carbazole grafted to the polysiloxane backbone in variable ratios, has also been reported (Chaput et al., 1996). In the presence of a small amount of **TNF**, the material displays photorefractivity, upon 2BC measurements, and NLO properties, as deduced from SHG measurements.

Macromolecular architectures other than linear polymers such as hyperbranched polyisophthalate containing pendant carbazolyl and azobenzene groups as terminal moieties, having very low  $T_g$  (21°C), in the presence of C<sub>60</sub> as photosensitizer, displayed photorefractive and electrooptical properties, with fast response time (Kou & Shi, 2004).

#### 4.2 Polymers containing side-chain carbazole moieties covalently linked to azoaromatic groups

The required components for photorefractivity (EO chromophore, charge traps and possibility of photopoling) may also be satisfied when both azo-chromophore and carbazole moiety are directly bonded together into a single multifunctional (monolithic) unit located in the polymeric side chain (Fig. 19).

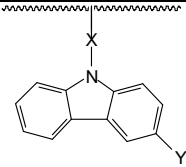
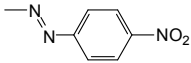
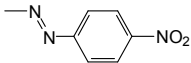
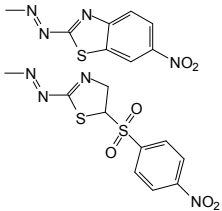
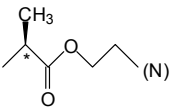
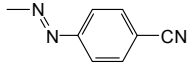
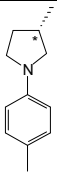
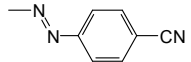
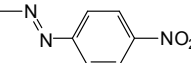
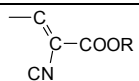
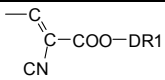
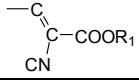
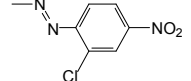
			
Derivative	Main chain	X	Y
C1	polymethacrylate	$-(CH_2)_n-$	
C2	polyacrylate	$-(CH_2)_6-$	
C3	polymethacrylate	$-(CH_2)_2-$	
C4	polymethacrylate		
C5	polymethacrylate		
C6	polyphosphazene	$-(CH_2)_3-$	
C7	polymethylsiloxane	$-(CH_2)_3-$	
C8	polyvinyl	$-(CH_2)_0-$	
C9	polyvinyl	$-(CH_2)_0-$	
C10	epoxy resin	$-CH_2-$	

Fig. 19. Chemical structure of side-chain carbazole-azoaromatic polymers

The first report concerning this class of materials appeared in 1996 (Ho et al., 1996), dedicated to the synthesis and optical properties of the methacrylic polymer obtained by

polymerization of N-hydroxyethyl carbazole methacrylate bearing the p-nitro phenylazo moiety linked to the position 3 of carbazole ring (**C1**,  $n=2$ , Fig.19). This material proved to be suitable to produce optically induced birefringence, surface gratings and photorefractivity. Subsequently, polymethacrylates prepared similarly with various spacer length ( $n = 3-6, 8-10$ ) and  $T_g$  values ranging gradually from 127 to 65°C, were investigated (Barrett et al., 1998) (**C1**,  $n=3-6, 8-10$ , Fig. 19) confirming the previous findings and that the orientational order photoinduced in the material is higher with the derivatives possessing lower spacer length.

Relevant thermal stability of the photoinduced surface gratings and high stability of the birefringence was also observed in polyimides bearing the carbazole group in the main chain linked to pendant azo chromophore (J.P. Chen et al., 1999).

An investigation on a series of copolymeric polyacrylates constituted by butyl acrylate and various monolithic chromophores, including azocarbazole (**C2**, Fig. 19) with molar composition photorefractive monomer/butyl acrylate 1:2.2, suggested that the photorefractivity was strongly dependent on the NLO property of the chromophore rather than photoconductivity, and, additionally, that the charge transporting species in these materials could be altered (hole or electron) according to the chromophore structure (Hwang et al., 2003).

Monolithic photorefractive polymethacrylates bearing side-chain azo-carbazole (**C3**, Fig. 19) were shown to display a much more significant photoconductivity with respect to the related copolymers with butyl methacrylate in the ratio 1:1 and a considerable increase of photoconductivity (one order of magnitude) in the presence of **TNF** as photosensitizer, due to efficient charge transfer between carbazole and **TNF** (Diduch et al., 2003).

An optically active methacrylic side-chain azocarbazole homopolymer containing a chiral moiety interposed between the main chain and the azocarbazole moiety, characterized by high  $T_g$  value (147°C) (**C4**, Fig. 19) displayed photorefractive and photoconductive properties at room temperature without pre-poling, with high optical gain, as noticed for the above mentioned copolymeric samples (poly[(*S*)-**MAP-N-co-(S)**-**MECP**]) (Fig. 18), which were similarly interpreted on the basis of a field-induced chromophore reorientation mechanism (Angiolini et al., 2007c; H. Li et al., 2009). In addition, **C4** was also apt to produce photoinduced SRG as well as birefringence, thus demonstrating several features typical of a multifunctional photoresponsive material. Besides the assessment of chiroptical properties investigated by CD, optically induced linear dichroism and birefringence, as well as SRG, were also produced without pre-poling on thin films of side-chain azocarbazole polymers containing the chiral pyrrolidine moiety (**C5**, Fig. 19), although the  $T_g$  values of these materials were very high (between 160 and 200°C), demonstrating the possibility to obtain temporally stable photoinduced anisotropy, particularly with the more conformationally rigid system containing the pyrrolidine ring (Angiolini et al., 2009a).

An alternative synthetic access to side-chain azo-carbazole moieties involves the functionalization of side-chain carbazole groups by coupling with a p-nitrophenyl diazonium salt to give the corresponding azo-derivative located at the position 3 of carbazole. In this case, being the functionalization reaction incomplete, a copolymeric product is obtained containing actually a molar amount of 20% of azocarbazole moiety (**C1**,  $n=3$ , Fig. 19) (Y. Chen et al. 2000). To achieve filmability, it is needed to add N-ethyl carbazole as a plasticizer, in addition to a small amount of **TNF** as a photosensitizer. However, both photorefractivity and EO response are observed in the material. Improved functionalization extent up to 67% was instead obtained by azo-coupling on carbazole

polymethacrylates with shorter spacer length (**C1**,  $n=2$ , Fig. 19), thus allowing the availability of polymeric derivatives with higher molecular mass with respect to those obtained by direct polymerization of the monolithic functional monomer (Shi et al., 2004a). The material with 32% of functionalization and longer spacer length (**C1**,  $n=10$ , Fig. 19) (Shi et al., 2004b) displayed appreciable optical gain coefficient, comparable to that obtained previously by Barrett (Barret et al., 1998) for the same material with homopolymeric structure, but lower molecular mass.

The post-polymerization azo-coupling procedure has also been applied to polyphosphazenes bearing side-chain carbazole moieties (L. Zhang et al. 2006) with formation of a copolymeric product possessing 29% of functionalization degree of the two carbazole moieties present in each repeating unit (**C6**, Fig. 19). The material displays a low  $T_g$  value (50°C) and photorefractivity without any added plasticizer or sensitizer. Polymethylsiloxane bearing side-chain carbazole groups was also submitted to functionalization with EO chromophores (Hua et al., 2007). In this case, a different approach to the synthesis of multifunctional polymeric derivatives has been followed, the EO chromophore resulting electronically isolated from the side-chain carbazole moiety. Thus, the carbazole was firstly formylated at the position 3, then treated with the cyanoacetyl derivative of push-pull azobenzenes (**C7**, Fig. 19) to afford up to a 32% molar functionalization with the EO chromophore. Although possessing a rather low molecular mass, these materials displayed, upon doping with TNF, SHG comparable to those of polymers containing **DR1** chromophores.

Similarly, partially formylated (50%) **PVK** was functionalized with the cyanoacetyl derivative of **DR1** (**C8**, Fig. 19) (Zhuang et al., 2010) or of push-pull azobenzene bearing additional N-alkyl carbazole linked to the aromatic ring (**C9**, Fig. 19) (Z. Li et al., 2010). The former derivative displayed capability to produce inter- or intra-chain donor (carbazole)-acceptor (**DR1**) nanoaggregated assemblies with good memory performance, the latter displayed relatively large SHG in the NLO field.

The advantages of azo-carbazole moieties chemically bound to polymer matrix for NLO applications by Maker-fringe technique were also demonstrated with regard to the third harmonic generation (THG) by bisphenolic epoxy resins containing 3-(2'-chloro-4'-nitrophenylazo-)N-(2,3-epoxypropyl)-carbazole (**C10**, Fig. 19) (Niziol et al., 2009).

## 5. Conclusion

In the recent years photoresponsive polymeric materials based on azoaromatic and carbazole moieties have generated a quite remarkable research interest, which has led to envisage a wide range of potential applications in advanced technologies achievable by using the same multifunctional material. As most of the properties are originated by the arrangement assumed by the chromophores at the "domain" level, roughly at the nanoscale level, through cooperative motions, the presence in the material of sufficiently organized macromolecular structures plays a major role. To this regard, the control of architecture, molecular mass and polydispersity of the macromolecular material, in addition to the presence of suitable functionalities, is predicted to assume increasing relevance. In particular, several synthetic procedures, allowing a "living"/controlled free-radical polymerization (LFRP), such as atom transfer radical polymerization (ATRP), reversible addition-fragmentation chain transfer (RAFT) polymerization and nitroxide-mediated free-

radical polymerization (NMP), could be conveniently adopted in order to obtain derivatives (block copolymers, multiarms architectures of appropriate size etc.) conveniently tailored to the use. In this context, the presence of helical structures of one prevailing sense of the macromolecules could play an important role in photoinduced phase transitions, amplification phenomena and photoswitched chirality.

To positively conclude the present note, photoresponsive polymeric materials are finding new opportunities in applications that in the past seemed only idealistic. This has arisen along with recent developments in nanosciences and nanotechnologies, opening new ways to make engineered polymers as novel macromolecular structures. Improvements in the design of multifunctional photoresponsive systems in which the relevant functionalities (photochromic and photoconductive) can be located within specialized nanoenvironments are presently worth of investigation.

Above all, collaborative efforts among different scientific disciplines will be the major factor that will develop the full potential of any photoresponsive system.

## 6. Acknowledgment

The financial support by MIUR (PRIN 2007) and INSTM Consortium is gratefully acknowledged.

## 7. References

- Altomare, A., Ciardelli, F., Mellini, L., & Solaro, R. (2004). Photoactive Azobenzene Polymers Containing Carbazole Chromophores (pages 1611–1619). *Macromol. Chem. Phys.*, Vol.205, No. 12, (August 2004), pp.1611-1619, ISSN 1521-3935
- Angiolini, L., Bozio, R., Giorgini, L., Pedron, D., Turco, G., & Daurù, A. (2002). Photomodulation of the chiroptical properties of new chiral methacrylic polymers with side chain azobenzene moieties. *Chem. Europ. J.*, Vol.8, No.18, (September 2002), pp. 4241-4247, ISSN 1521-3765
- Angiolini, L., Giorgini, L., Bozio, R., & Pedron, D. (2003a). Reversible chirality inversion of photochromic methacrylic polymers upon irradiation with one-handed circularly polarized light. *Synth. Met.*, Vol.138, No.1-2, (June 2003), pp. 375-379, ISSN 0379-6779
- Angiolini, L., Benelli, T., Bozio, R., Daurù, A., Giorgini, L., & Pedron, D. (2003b) Photoinduced chiroptical bistability in new chiral methacrylic azobenzene-containing polymers. *Synth. Met.*, Vol.139, No.3, (October 2003), pp. 743-746, ISSN 0379-6779
- Angiolini, L., Benelli, T., Giorgini, L., Salatelli, E., Bozio, R., Daurù, A., & Pedron, D. (2006). Improvement of photoinduced birefringence properties of optically active methacrylic polymers through copolymerization of monomers bearing azoaromatic moieties. *Macromolecules*, Vol.39, No.2, (January 2006), pp. 489-497, ISSN 0024-9929
- Angiolini, L., Benelli, T., Giorgini, L., Mauriello, F., Salatelli, E., Bozio, R., Daurù, A., & Pedron D. (2007a). Synthesis, chiroptical properties and photoinduced birefringence of optically active methacrylic copolymers bearing side-chain bisazoaromatic moieties. *Europ. Polym. J.* Vol.43, No.8, (August 2007), pp. 3550-3561, ISSN 0014-3057

- Angiolini, L., Benelli, T., Giorgini, L., Mauriello, F., & Salatelli E. (2007b). Synthesis and chiroptical properties of copolymers containing in side-chain optically active carbazole and azochromophores. *Proc. of SPIE*, Vol.6653, (September 2007), pp. 66531C-1-6653C-8, ISSN 1996-756X
- Angiolini, L., Bozio, R., Dainese, T., Giorgini, L., Golemme, A., Mauriello, F., Pedron, D., & Termine, R. (2007c). Photoresponsive polymers containing side-chain chiral azocarbazole chromophores as multifunctional materials. *Proc. of SPIE*, Vol. 6653, (September 2007), pp. 665305-1, ISSN 1996-756X
- Angiolini, L., Benelli, T., Bozio, R., Cozzuol, M., Giorgini, L., Pedron, D., & Salatelli, E. (2008a). Second order nonlinear optical properties of multifunctional chiral azobenzene polymers. *e-Polymers*, No.13, ISSN 1618-7229
- Angiolini, L., Benelli, T., Giorgini, L., Golemme, A., Mauriello, F., Salatelli, E., & Termine, R. (2008b). Methacrylic Polymers Containing Optically Active Side-Chain Carbazole: Synthesis, Characterization and Photoconductive Properties *Macromol. Chem. Phys.*, Vol.209, No.9, (May 2008), pp. 944-956, ISSN 1521-3935
- Angiolini, L., Giorgini, L., Mauriello, F., & Rochon, P. (2009a). Synthesis and photoresponsive properties of optically active methacrylic polymers bearing side-chain azocarbazole moieties. *Macromol. Chem. Phys.*, Vol.210, No.1, (January 2009), pp. 77-89, ISSN 1521-3935
- Angiolini, L., Benelli, T., Giorgini, L., Mauriello, F., & Salatelli, E. (2009b). Relevant chiroptical and thermal properties in optically active methacrylic copolymers containing carbazole and azoaromatic chromophores in the side-chain. *React. Funct. Polym.*, Vol.69, No.12, (December 2009), pp. 898-904, ISSN 1381-5148
- Angiolini, L., Giorgini, L., Li, H., Golemme, A., Mauriello, F., & Termine, R. (2010). Synthesis, characterization and photoconductive properties of optically active methacrylic polymers bearing side-chain 9-phenylcarbazole moieties *Polymer*, Vol.51, No.2, (January 2010), pp. 368-377, ISSN 0032-3861
- Barrett, C., Choudhury, B., Natansohn, A., & Rochon, P. (1998). Azocarbazole polymethacrylates as single-component electrooptic materials. *Macromolecules*, Vol.31, No.15, (July 1998), pp. 4845-4851, 1520-5835
- Beljonne, D., Shuai, Z., Brédas, J.L., Kauranen, M., Verbiest, T., & Persoons A. (1998). Electro-optic response of chiral helicenes in isotropic media. *J. Chem. Phys.*, Vol.108, No.4, (January 1998), pp. 1301-1304, ISSN 1089-7690
- Berneth, H., Bieringer, T., Hagen, R., & Kostromine, S. (Bayer AG, Germany) (2003). United States Patent no. 2003113664 A1. Re-inscribable optical recording materials with good solubility, 2003
- Biswas, M., & Das, S.K. (1982). Chemical modification of poly(N-vinylcarbazole). II. Some properties of poly(N-vinylcarbazole-3,6-diphthalimide). *J. Polym. Sci., Polym. Lett. Ed.*, Vol.20, No.6, (June 1982), pp.333-339, ISSN 1543-0472
- Blanchard, P.M., & Mitchell, G.R. (1993a). Localized room temperature photo-induced poling of azo-dye-doped polymer films for second-order nonlinear optical phenomena. *J. Phys. D: Appl. Phys.*, Vol.26, No.3, (March 1993), pp. 500-503, ISSN 1361-6463 6463
- Blanchard, P.M., & Mitchell, G.R. (1993b). A comparison of photoinduced poling and thermal poling of azo-dye-doped polymer films for second order nonlinear optical



- applications. *Appl. Phys. Lett.*, Vol.63, No.15, (October 1993), pp. 2038-2040, ISSN 1077-3118 6463
- Chalupczak, W., Fiorini, C., Charra, F., Nunzi, J.M., & Raimond, P. (1996). Efficient all-optical poling of an azo-dye copolymer using a low power laser. *Opt. Commun.*, Vol.126, No.1-3, (May 1996), pp. 103-107, ISSN 1873-0310
- Chang, C., Zhu, J., Zhang, Z., Zhou, N., Cheng, Z., & Zhu, X. (2010). Synthesizing and characterization of comb-shaped carbazole containing copolymer via combination of ring opening polymerization and nitroxide-mediated polymerization. *Polymer*, Vol.51, No.9, (April 2010), pp. 1947-1953, ISSN 0032-3861
- Chaput, F., Riehl, D., Boilot, J.P., Cargnelli, K., Canva, M., Le'vy, Y., & Brun, A. (1996). New nonlinear sol-gel films exhibiting photorefractivity. *Chem. Mater.*, Vol.8, No.2, (February 1996), pp. 312-314, ISSN 1520-5002.
- Charra, F., Kajzar, F., Nunzi, J.M., Raimond, P., & Idiart, E. (1993). Light-induced second-harmonic generation in azo-dye polymers. *Opt. Lett.*, Vol.18, No.12, (June 1993), pp. 941- 943, ISSN 1539-4794
- Chen, H.Z., Wang, M., Feng, L.X., & Yang, S. (1993). Synthesis and photoconductivity study of phthalocyanine polymers. II. PVK-co-CuPc (COOH)<sub>3</sub>. *J. Polym. Sci., Part A: Polym. Chem.*, Vol.31, No.5, (April 1993), pp. 1165-1170, ISSN 1099-0518
- Chen, J.P., Labarthe, F.L., Natansohn, A., & Rochon, P. (1999). Highly stable optically induced birefringence and holographic surface gratings on a new azocarbazole-based polyimide. *Macromolecules*, Vol.32, No.25, (December 1999), pp. 8572-8579, ISSN 1520-5835
- Chen, Y., Cai, R.F., Huang, Z.E., Bai, X., Yu, B.C., Jin, W., Pan, D.C., & Wang, S. (1996a). Researches on the photoconductivity and UV-visible absorption spectra of the first C<sub>60</sub>-chemically modified poly(N-vinylcarbazole). *Polym. Bull.*, Vol.36, No.2, (February 1996), pp. 203-208, ISSN 1436-2449
- Chen, Y., Huang, Z.E., Cai, R., Fan, D., Hou, X., Yan, X., Chen, S., Jin, W., Pan, D., & Wang, S. (1996b). Photoconductivity and paramagnetism of fullerene chemically modified polymers. *J. Appl. Polym. Sci.*, Vol.61, No.12, (September 1996), pp. 2185-2190, ISSN 1097-4628
- Chen, Y., He, Y., Chen, H., Wang, F., Chen, Z., & Gong, Q. (2000). Photorefractive effect in a new composite based on bifunctional host polymer. *J. Appl. Polym. Sci.*, Vol.77, No.1, (July 2000), pp. 189-194, ISSN 1097-4628
- Chen, Y., He, Y., Wang, F., Chen, H., & Gong, Q. (2001). Synthesis and characterization of bifunctional photorefractive polymers. *Polymer*, Vol.42, No.3, (February 2001), pp. 1101-1107, ISSN 0032-3861
- Chiellini, E., Solaro, R., & Ledwith, A. (1977). Optically active vinyl polymers containing fluorescent groups. 2. Synthesis of optically active vinylcarbazole derivatives. *Makromol. Chem.*, Vol.178, pp. 701-713, ISSN 0025-116X
- Chiellini, E., Solaro, R., & Ledwith, A. (1978). Optically active vinyl polymers containing fluorescent groups. 3. Synthesis and characterization of optically active polymers containing carbazolyl groups. *Makromol. Chem.*, Vol.179, pp. 1929-1937, ISSN 0025-116X
- Chiellini, E., Galli, G., Solaro, R., & Ledwith, A. (1980). Optically active vinyl polymers containing fluorescent groups. 8. Synthesis and properties of copolymers of N-

- vinylcarbazole and (-)-menthyl acrylate and (-)-menthyl methacrylate. *Macromolecules*, Vol.13, No.6, (November 1980), pp. 1654-1660, ISSN 1520-5835
- Chiellini, E., Galli, G., Solaro, R., & Ledwith, A. (1984). Optically active synthetic polymers containing pendant carbazolyl groups. *Adv. Polym. Sci.*, Vol.62, pp. 143-169, ISSN 0065-3195
- Churikov, V.M., Hung, M.F., Hsu, C.C., Shiau, C.W., & Luh, T.Y. (2000). Encoding of macroscopic second-order non-linearity via all-optical polar alignment in substituted norbornene polymer thin films. *Chem. Phys. Lett.*, Vol.332, No.1-2, (December 2000), pp. 19-25, ISSN 1873-4448
- Dantsker, D., Kumar, J., Tripathy, S.K. (2001). Optical alignment of liquid crystals. *J. Appl. Phys.*, Vol.89, No.8, (April 2001), pp. 4318-4325, ISSN 1089-7550
- Diduch, K., Wubbenhorst, M., & Kucharski, S. (2003). Photocurrent generation of bi-functional carbazole containing polymers. *Synth. Met.*, Vol.139, No.2, (September 2003), pp. 515-520, ISSN 1879-3290
- Fiorini, C., Nunzi, J.M., Charra, F., Kajzar, F., Lequan, M., Lequan, R.M., & Chane-Ching, K. (1997). Light-induced orientation of a low absorbing phosphine oxide azo-dye/PMMA copolymer: towards a trade-off between transparency and photoinduced non-linearity. *Chem. Phys. Lett.*, Vol.271, No.4-6, (June 1997), pp. 335-340, ISSN 1873-4448
- Fukuda T. (2004). Re-writable high-density optical recording on azobenzene thin film. *Optics in Information System*, Vol.15, No.1, (February 2004)
- Fujii, T., Shiotsuki, M., Inai, Y., Sanda, F., & Masuda, T. (2007). Synthesis of helical poly(N-propargylamides) carrying azobenzene moieties in side chains. Reversible arrangement-disarrangement of helical side chain arrays upon photoirradiation keeping helical main chain intact. *Macromolecules*, Vol.40, No.20, (October 2007), pp. 7079-7088, ISSN 1520-5835
- Gaidelis, V., Krisciunas, V., & Montrimas, E. (1976). Optical and photoelectric properties of thin layers of poly-n-epoxypropylcarbazole. *Thin Solid Films*, Vol.38, No.1, (October 1976), pp. 9-14, ISSN 1879-2731
- Ghaemy, M., Alizadeh, R., & Behmadi, H. (2009). Synthesis of soluble and thermally stable polyimide from new diamine bearing N-[4-(9H-carbazol-9-yl)phenyl] formamide pendent group. *European Polymer Journal*, Vol.45, No.11, (November 2009), pp. 3108-3115, ISSN 0014-3057
- Grazulevicius J. V., Strohriegl P., Pielichowski J., Pielichowski K. (2003). Carbazole-containing polymers: synthesis, properties and applications. *Progress Polym. Sci.*, Vol.28, No.9, (September 2003), pp. 1297-1353, ISSN 1873-1619
- Hagen, R., Bieringer, T., Kostromine, S., & Berneth, H. (Bayer AG, Germany) (2003). United States Patent no. 2003049549 A1. Optical storage method for rewritable digital data carriers, 2003
- Hattemer, E., Zentel, R., Mecher, E., & Meerholz K. (2000). Synthesis and Characterization of Novel Multifunctional High- $T_g$  Photorefractive Materials Obtained via Reactive Precursor Polymers. *Macromolecules*, Vol.33, No.6, (March 2000), pp. 1972-1977, ISSN 1520-5835
- Hill, R.A., Dreher, S., Knoesen, A., & Yankelevich, D.R. (1995). Reversible optical storage utilizing pulsed, photoinduced, electric - field - assisted reorientation of

- azobenzenes. *Appl. Phys. Lett.*, Vol.66, No.17, (April 1995), pp. 2156-2158, ISSN 1077-3118
- Ho, M.S., Natansohn, A., & Rochon, P. (1995). Azo polymers for reversible optical storage. 7. The effect of the size of the photochromic groups. *Macromolecules*, Vol.28, No.18, (August 1995), pp. 6124-6127, ISSN 0024-9929
- Ho, M.S., Barrett, C., Paterson, J., Esteghamatian, M., Natansohn, A., & Rochon P. (1996). Synthesis and optical properties of poly{(4-nitrophenyl)-[3-[N-[2-(methacryloyloxy)ethyl]-carbazolyl]]diazene}. *Macromolecules*, Vol.29, No.13, (June 1996), pp. 4613-4618, ISSN 1520-5835
- Hoegl, H. (1965). On photoelectric effects in polymers and their sensitization by dopants. *J. Phys. Chem.*, Vol.69, No.3, (March 1965), pp. 755-766, ISSN 1541-5740
- Hua, J., Li, Z., Qin, J., Li, S., Ye, C., & Lu, Z. (2007). Synthesis and characterization, second-order nonlinear optical and photorefractive properties of new multifunctional polysiloxane with broad optical transparent pentafluorophenyl azo chromophore. *React. Funct. Polym.*, Vol.67, No.1, (January 2007), pp. 25-32, ISSN 1873-166X
- Hwang, J., Sohn, J., & Park, S.Y. (2003). Synthesis and structural effect of multifunctional photorefractive polymers containing monolithic chromophores. *Macromolecules*, Vol.36, No.21, (October 2003), pp. 7970-7976, ISSN 1520-5835
- Ivanov, M., Naydenova, I., Todorov, T., Nikolova, L., Petrova, T., Tomova, N., & Dragostinova, V. (2000). Light-induced optical activity in optically ordered amorphous side-chain azobenzene containing polymer. *J. Mod. Opt.*, Vol.47, No.5, (April 2000), pp. 861-867, ISSN 1362-3044
- Jin, M., Yang, Q.X., Lu, R., Xu, T.H., & Zhao, Y.Y. (2004). Syntheses of bisazo-containing polymethacrylates using atom transfer radical polymerization and the photoalignment behavior. *Journ. Polym. Sci., Part A: Polym. Chem.*, Vol.42, No.17, (September 2004), pp. 4237-4247, ISSN 1099-0518
- Kanbara, T., Yokokawa, Y., & Hasegawa, K. (2000). *J. Polym. Sci. Part A: Polym. Chem.*, Vol.38, No.1, (January 2000), pp. 28-34, ISSN 1099-0518.
- Keyanpour-Rad, M., Ledwith, A., Hallam, A., North, A. M., Breton, M., Hoyle, C., & Guillet J.E. (1978). Some photophysical properties of five new carbazole-containing methacrylate polymers. *Macromolecules*, Vol.11, No.6, (November 1978), pp. 1114-1118, ISSN 1520-5835
- Kim, D.Y., Tripathy, S.K., Li, L., & Kumar, J. (1995). Laser - induced holographic surface relief gratings on nonlinear optical polymer films. *Appl. Phys. Lett.*, Vol.66, No.10, (March 1995), pp. 1166-1168, ISSN 1077-3118
- Kou, H., & Shi W. (2004). Photorefractivity of hyperbranched polyisophthalate endcapped with pendant carbazolyl and azobenzene groups. *Eur. Polym. J.*, Vol.40, No.7, (July 2004), pp. 1337-1342, ISSN 0014-3057
- Ledwith, A., Rawley, N.J., & Walker, S.M. (1981). Fluorescence emission from poly[2-(9-ethyl)carbazolyl-methylmethacrylate]. *Polymer*, Vol.22, No.4, (April 1981), pp. 435-436, ISSN 0032-3861
- Li, H., Termine, R., Angiolini, L., Giorgini, L., Mauriello, F., & Golemme, A. (2009). High Tg, nonpoled photorefractive polymers. *Chem. Mat.*, Vol.21, No.12, (June 2009), pp. 2403-2409, ISSN 1520-5002

- Li, W., Han, Y., Chen, Y., Li, C., Li, B., & Bo, Z. (2010). Polythiophenes with carbazole side chains: design, synthesis and their application in organic solar cells. *Macromol. Chem. Phys.*, Vol.211, No.8, (April 2010), pp. 948-955, ISSN 1521-3935
- Li, Z., Wang, L., Xiong, B., Ye, C., Qin, J., & Li, Z. (2010). Novel, side-on, PVK-based nonlinear optical polymers: Synthesis and NLO properties. *Dyes and Pigments*, Vol.84, No.1, (January 2010), pp. 134-139, ISSN 1873-3743
- Liou, G.S., Hsiao, S.H., Huang, N.K., & Yang, Y.L. (2006). *Macromolecules*, Vol.39, No.16, (August 2006), pp. 5337-5346, ISSN 0024-9297
- Loucif-Saibi, R., Nakatani, K., Delaire, J.A., Dumont, M., & Sekkat, Z. (1993). Photoisomerization and second harmonic generation in disperse red one-doped and -functionalized poly(methyl methacrylate) films. *Chem. Mater.*, Vol.5, No.2, (February 1993), pp. 229-236, ISSN 1520-5002 6463
- Maertens, C., Dubois, P., Jérôme, R., Blanche, P.-A., & Lemaire Ph.C. (2000). Synthesis and polarized light-induced birefringence of new polymethacrylates containing carbazolyl and azobenzene pendant groups. *J. Polym. Sci.: Part B: Polym. Phys.*, Vol.38, No.1, (January 2000), pp. 205-213, ISSN 1099-0488
- Matsui, T., Ozaki, M., Yoshino, K., & Kajzar, F. (2002). Fabrication of flexible distributed feedback laser using photoinduced SRG on azo-polymer film as a template. *Jpn. J. Appl. Phys.*, Vol.41, part 2, No. 12A, (2002), pp. L1386-L1388, ISSN 0021-4922
- Meerholz, K., Volodin, B.L., Kippelen, B., & Peyghambarian, N. (1994). A photorefractive polymer with high optical gain and diffraction efficiency near 100%. *Nature*, Vol.371, (October 1994), pp. 497-500, ISSN 1476-4687
- Meng, X., Natansohn, A., & Rochon, P. (1997). Azo polymers for reversible optical storage: 13. Photoorientation of rigid side groups containing two azo bonds. *Polymer*, Vol.38, No.11, (May 1997), pp. 2677-2682, ISSN 0032-3861
- Naarmann, H., & Stroehriegel, P. (1992). *Handbook of Polymer Synthesis, Part B* (Kricheldorf H. R., ed.), New York: Marcel Dekker; p. 1353, ISBN 0824754735
- Natansohn, A., Rochon, P., Gosselin, J., & Xie, S. (1992). Azo polymers for reversible optical storage. 1. Poly[4'-[[2-(acryloyloxy)ethyl]ethylamino]-4-nitroazobenzene]. *Macromolecules*, Vol.25, No.8, (April 1992), pp. 2268-2273, ISSN 0024-9297
- Natansohn, A., & Rochon, P. (2002). Photoinduced Motions in Azo-Containing Polymers. *Chem. Rev.*, Vol.102, No.11, (October 2002), pp. 4139-4175, ISSN 0009-2665
- Naydenova, I., Nikolova, L., Ramanujam, P.S., & Hvilsted, S. (1999). Light-induced circular birefringence in cyanoazobenzene side-chain liquid-crystalline polyester films. *J. Opt. A: Pure Appl. Opt.*, Vol.1, No.4, (July 1999), pp. 438-441, ISSN 1741-3567
- Nikolova L., Todorov T., Ivanov M., Andruzzi F., Hvilsted S., Ramanujam P. (1996). Polarization holographic gratings in side-chain azobenzene polyesters with linear and circular photoanisotropy. *Appl. Opt.* 1996, Vol.35, No.20, (July 1996), pp. 3835-3840, ISSN 1539-4522
- Nikolova, L., Nedelchev, L., Todorov, T., Petrova, Tz., Tomova, N., Dragostinova, V., Ramanujam, P.S., & Hvilsted, S. (2000). Self-induced light polarization rotation in azobenzene-containing polymers. *Appl. Phys. Lett.*, Vol.77, No.5, (July 2000), pp. 657-659, ISSN 1077-3118 6463
- Nizioł, J., Essaïdi, Z., Bednarz, M., & Sahraoui, B. (2009). Thermal stability of blends containing azo-carbazole derivatives and epoxy resin, designed for nonlinear

- optical applications. *Opt. Mat.*, Vol.31, No.3, (January 2009), pp. 501-504, ISSN 1873-1252
- Pietsch, U., & Rochon, P. (2003). Evidence of a density grating under light induced formation of SRG at polymers containing azobenzene moieties. *J. Appl. Phys.*, Vol.94, No.2, (July 2003), pp. 963-967, ISSN 1089-7550
- Qu, J., Kawasaki, R., Shiotsuki, M., Sanda, F., & Masuda, T. (2007a). Synthesis and properties of helical polyacetylenes containing carbazole. *Polymer*, Vol.48, No.2, (January 2007), pp. 467-476, ISSN 0032-3861
- Qu, J., Suzuki, Y., Shiotsuki, M., Sanda, F., & Masuda, T. (2007b). Synthesis and electro-optical properties of helical polyacetylenes carrying carbazole and triphenylamine moieties. *Polymer*, Vol.48, No.16, (July 2007), pp. 4628-4636, ISSN 0032-3861
- Ramanujam, P.S., Pedersen, & M., Hvilsted, S. (1999). Instant holography. *Appl. Phys. Lett.*, Vol.74, No.21, (May 1999), pp. 3227-3230, ISSN 1077-3118
- Ramos, G., Herrero, A.A., Belenguer, T., Nùñez, A., del Monte, F., & Levy, D. (2004). Photopolymerizable hybrid sol-gel materials for holographic recording. *Optics in Information System*, Vol.15, No.8
- Raschellà, R., Marino, I., Lottici, P., Bersani, D., Lorenzi, A., & Montenero, A. (2004). Photorefractive gratings in DR1-doped hybrid sol-gel. *Opt. Mater.*, Vol.25, No.4, (May 2004), pp. 419-423, ISSN 0925-3467
- Ravindranath, R., Ajikumar, P.K., Bahulayan, S., Hanafiah, N.B.M., Baba, A., Advincula, R.C., Knoll, W., & Valiyaveetil, S.J. (2007). *J. Phys. Chem. B*, Vol.111, No.23, (June 2007), pp. 6336-6343, ISSN 1520-5207
- Rochon, P., Batalla, E., & Natansohn, A. (1995). Optically induced surface gratings on azoaromatic polymer films. *Appl. Phys. Lett.*, Vol.66, No.2, (January 1995), pp. 136-138, ISSN 1077-3118
- Sabi, Y., Yamamoto, Y., Watanabe, H., Bieringer, T., Haarer, D., Hagen, R., Kostromine, S.G., & Berneth, H. (2001). Photoaddressable polymers for rewritable optical disc systems. *Jpn. J. Appl. Phys.*, Vol.40, No.3B, (2001), pp. 1613-1618, ISSN 0021-4922 6463
- Samyn, C., Verbiest, T., & Persoons, A. (2000). Second-order non-linear optical polymers. *Macrom. Rapid Commun.* Vol.21, No.1, (January 2000), pp. 1-15, ISSN 1521-3927
- Schwartz, E., Lim, E., Gowda, C.M., Liscio, A., Fenwick, O., Tu, G., Palermo, V., de Gelder, R., Cornelissen, J.J.L.M., Van Eck, E.R.H., Kentgens, A.P.M., Cacialli, F., Nolte, R.J.M., Samori, P., Huck, W.T.S., & Rowan, A.E. (2010). *Chem. Mat.*, Vol.22, No.8, (April 2010), pp. 2597-2607, ISSN 1520-5002
- Sekkat, Z., & Dumont, M. (1992). Photoassisted poling of azo dye doped polymeric films at room temperature. *Appl. Phys. B*, Vol.54, No.6, (May 1992), pp. 486-489, ISSN 1432-0649
- S'Heeren, G., Persoons, A., Rondou, P., Wiersman, J., Van Beylen, M., & Samyn, C. (1993). Synthesis of nonlinear optical polymers functionalized with 4-amino-4'-cyanostilbene and -azobenzene dyes. Second harmonic generation in corona-poled thin films. *Makromol. Chem.* Vol.194, No.6, (March 2003), pp. 1733-1744, ISSN 0025-116X
- Shi, J., Jiang, Z., & Cao, S. Synthesis of carbazole-based photorefractive polymers via post-azo-coupling reaction. *React. Funct. Polym.*, Vol.59, No.1, (May 2004a), pp. 87-91, ISSN 1873-166X

- Shi, J., Huang, M., Chen, Z., Gong, Q., & Cao, S. (2004b). Carbazole-based azo group-containing single component polymer exhibiting photorefractive performance. *J. Mat. Sci.*, Vol.39, No.11, (June 2004), pp. 3783-3785, ISSN 1573-4803
- Sui, Y., Yu, X., Yin, J., Zhong, X., Li, Q., Chen, Y., Zhu, Z., & Wang, Z. (2001). All-optical poling of a side-chain poly(urethane-imide) film and surface morphology studies. *Opt. Commun.*, Vol.191, No.3-6, (May 2001), pp. 439-444, ISSN 1873-0310
- Thomas, K.R.J., Lin, J.T., Tao, Y.T., & Ko, C.W. (2001). *J. Am. Chem. Soc.*, Vol.123, No.38, (September 2001), pp. 9404-9411, ISSN 1520-5126
- Tirelli, N., Altomare, A., Solaro, R., Ciardelli, F., Follonier, S., Bosshard, C., & Günter, P. (2000). Structure-activity relationship of new NLO organic materials based on push-pull azodyes: 4. Side chain polymers. *Polymer*, Vol.41, No.2, (January 2000), pp. 415-421, ISSN 0032-3861
- Ubukata, T., Isoshima, T., & Hara, M. (2005). Wavelength-programmable organic DFB laser based on a photoassisted polymer-migration system. *Adv. Mater.*, Vol.17, No.13, (July 2005), pp. 1630-1633, ISSN 1521-4095
- Vellis, P.D., Mikroyannidis, J.A., Cho, M.J., & Choi, D.H.J. (2008). *Polym. Sci., Part A: Polym. Chem.*, Vol.46, No.16, (August 2008), pp. 5592-5603, ISSN 1099-0518
- Viswanathan, N.K., Kim, D.Y., Bian, S., Williams, J., Liu, W., Li, L., Samuelson, L., Kumar, J., Tripathy, S.K. (1999). Surface relief structures on azo polymer films. *J. Mater. Chem.*, Vol.9, pp. 1941-1955, ISSN 1364-5501
- Wang, M., Chen, H.Z., & Yang, S.L. (1995). Synthesis and photoconductivity study of VK-AA copolymer containing CuPc. *J. Photochem. Photobiol., Part A: Chem.*, Vol.88, No.2-3, pp. 183-186, ISSN 1873-2666
- Wang, J., Zhang, L., Niu, Y., Liang, Z., Chen, Y., Huang, Y., Wang, H., & Lin, W. (2003). Photo-induced birefringence phenomenon of a double azo polymer. *Polym. Intern.*, Vol.52, No.7, (July 2003) pp. 1165-1168, ISSN 1097-0126
- Xu, G., Liu, X., Si, J., Ye, P., Li, Z., & Shen, Y. (1999). Optical poling in a crosslinkable polymer system. *Appl. Phys. B.*, Vol.68, No.4, (April 1999), pp. 693-696, ISSN 1432-0649
- Yamamoto, T., Ohashi, A., Yoneyama, S., Hasegawa, M., Tsutsumi, O., Kanazawa, A., Shiono, T., & Ikeda, T. (2001). Phase-type gratings formed by photochemical phase transition of polymer azobenzene liquid crystal. 2. Rapid switching of diffraction beams in thin films. *J. Phys. Chem. B*, Vol.105, No.12, (March 2001), pp. 2308-2313, ISSN 1520-5207
- Zhang, Y., Wada, T., & Sasabe, H. (1998). Carbazole photorefractive materials. *J. Mater. Chem.*, Vol.8, No.4, pp. 809-828, ISSN 1364-5501
- Zhang, L., Huang, M., Jiang, Z., Yang, Z., Chen, Z., Gong, Q., & Cao, S. (2006). A carbazole-based photorefractive polyphosphazene prepared via post-azo-coupling reaction. *React. Funct. Polym.*, Vol.66, No.12, (December 2006), pp. 1404-1410, ISSN 1873-166X
- Zhao, Y., & Ikeda, T. (2009). *Smart Light-Responsive Materials*, Wiley & Sons, ISBN 978-0-470-17578-1, Hoboken, New Jersey
- Zhuang, X.-D., Chen, Y., Liu, G., Zhang, B., Neoh, K.-G., Kang, E.-T., Zhu, C.-X., Li, Y.-X., & Niu, L.-J. (2010). Preparation and memory performance of a nanoaggregated dispersed red 1-functionalized poly (*N*-vinylcarbazole) film via solution-phase self-assembly. *Adv. Funct. Mat.*, Vol.20, No.17, (July 2010), pp. 2916-2922, ISSN 1616-3028

# Ladder Polysiloxanes for Optoelectronic Applications

Zhongjie Ren, Shouke Yan and Rongben Zhang  
*Beijing University of Chemical Technology & Institute of Chemistry, CAS,  
China*

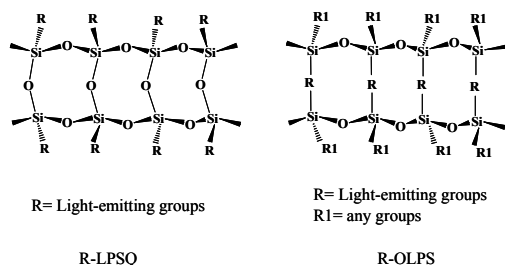
## 1. Introduction

Electroluminescence (EL) of conjugated polymers was first reported in 1990 with poly(*p*-phenylenevinylene) by Burroughes et al. (Burroughes et al., 1990) Since then polymer light-emitting diodes (PLED) have attracted the attention of many researchers and many efforts have been made to develop PLED in recent years (Kido et al., 1995; Service, 2005; Holder et al., 2005; D'Andrade & Forrest, 2004) because of the significant advantages that PLED present for displays, especially for flat panel displays. Those advantages include highly luminous efficiency, wide viewing angle, low operating voltage, high brightness, vivid color, low cost, light weight, and particular flexibility. Many approaches have been used in attempts to improve the performance of PLED device, for instance, improving deposition technologies (de Gans & Schubert, 2003; Singhet et al., 2010) and controlling the interfacial microstructure of multilayer-structured devices (Segalman et al., 2009) in the process of preparing the devices; improving the electrical and optical properties of the light-emitting material layer (Grimsdale et al., 2009) and so on. Especially, the light-emitting material layer is crucial to get a high performance PLED device.

Considerable efforts have been devoted to developing conjugated materials as the active layers in PLED. (Gather et al., 2010; Wang et al., 2009; Xiao et al., 2010) The ongoing preparation of new light-emitting materials has produced in higher efficiencies, enhanced brightness, and longer lifetimes of optoelectronic devices. (Martin & Diederich, 1999; van Hutten & Hadziioannou, 2000; Müllen & Wegner, 1999) However, the stability of these materials under operating conditions needs further improvement if they are to be widely used in real products, some common causes resulting in degradation of PLED still remain to be unsolved. For instance, molecular aggregation induced by the  $\pi$ - $\pi$  stacking of polymer chain results in quenching of fluorescence; (Wu, et al., 2002; Amrutha & Jayakannan, 2007) poor film-forming property and poor morphological stability; low thermal stability (Weinfurtner et al., 2000) and so on.

For the first case, controlling the  $\pi$ - $\pi$  stacking induced molecular aggregation of the polymer chains is one of important tasks in the development of ideal PLED devices. To solve this problem, one method is that units of structural asymmetry are introduced in order to limit the ability of chains to pack effectively in the solid state. For example, Son et al. (Son, et al., 1995) controlled the distribution of *cis*-linkages in poly(phenylenevinylene) chains, the *cis*-linkages interrupt conjugation and interfere with the packing order of the polymer chains. Liao et al

(Liao et al., 2001) introduced a *meta*-linkage in the conjugated polymer chain, which reduced the conjugation length and allowed the polymer to blend and twisted more effectively than that of *para*-linkage. Another approach is to end-cap conjugation polymer, such as polyfluorenes, with a bulky group, (Klaerner et al., 1998, 1999; Setayesh et al., 2001) a crosslinkable moiety (Chen et al., 1999) or a charge-transporting moiety. (Yu et al., 1999) The third method is to prepare the dendronized polymer as the EL layer materials. It has been demonstrated that adding dendritic bulky moieties can effectively suppress the formation of aggregation (Ego et al., 2002; Marsitzky et al., 2001) and reduce self-quenching of luminescence duo to intermolecular interactions. (Pogantsch et al., 2002) In addition, a good film-forming ability, a good morphological stability and a high thermal stability also are crucial to the practical application of PLED. (Smith et al., 1998; Fenter et al., 1997) They can be improved by increasing the molecular weight of the EL polymer materials or introducing, compounding the thermostable groups or molecules into the EL polymer materials. It is reported that semiconducting polymers containing polyhedral oligosilsesquioxanes (POSS) segments, when used in PLED devices, exhibit the better thermal stability, higher brightness, and higher external quantum efficiency as compared to the corresponding parent polymers. (Imae et al., 2005; Froehlich et al., 2007; Xiao et al., 2003; Yang et al., 2009, 2010; Singh et al., 2009) However, a light-emitting material with outstanding comprehensive performance still is few. Thus, to synthesize a new kind of materials, which features both preventing the intermolecular aggregation and possessing the excellent thermal stability, is especially important. In addition, polymer solar cells active materials have the similar requirements with that of PLED.



Scheme 1. Schematic structure of R-LPSQ and R-OLPS.

Toward this goal, we incorporate light-emitting units into polymer backbone forming well-defined ladder or double-stranded structure. Ladder structure with limited conformational freedom is expected to reduce the electron delocalization of conjugated polymer and thus suppress the formation of aggregation. Fortunately, among the ladder polymers, both the ladder organo-bridged polysiloxanes (R-LPSQ) and ladder polysilsesquioxanes (R-LPSQ) possess incomparable comprehensive merits, which can be readily used to prepare thin film devices. These merits are the good solubility in common organic solvents, good film-forming ability, fair adhesion to various substrates and the excellent resistances to thermal, chemical and irradiation degradation of the thin film. (Unno et al., 2002; Shea & Loy, 1995, 2001) Therefore, we introduce the light-emitting groups into the side chains of R-LPSQ or into the bridge of R-OLPS to prepare novel light-emitting materials as shown in Scheme 1.

During the last three decades, our research group proposed a supramolecular template strategy named "supramolecular architecture-directed stepwise coupling and polymerization", (Zhou et al., 2008; R. B. Zhang et al., 1999) by which a series of well-



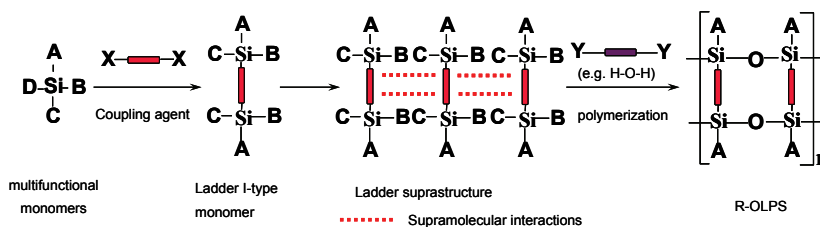
defined organo-bridged ladder polysiloxanes R-OLPS and ladder polysilsesquioxanes R-LPSQ have been prepared. (Wan et al., 2006; Sun et al., 2003a, 2003b; Guo et al., 2002; Li et al., 2002; Liu et al., 2000) The synthesis, properties and applications of ladder polysiloxanes materials would be discussed in detail in the following sections.

## 2. General synthetic method and characterization of ladder polysiloxanes

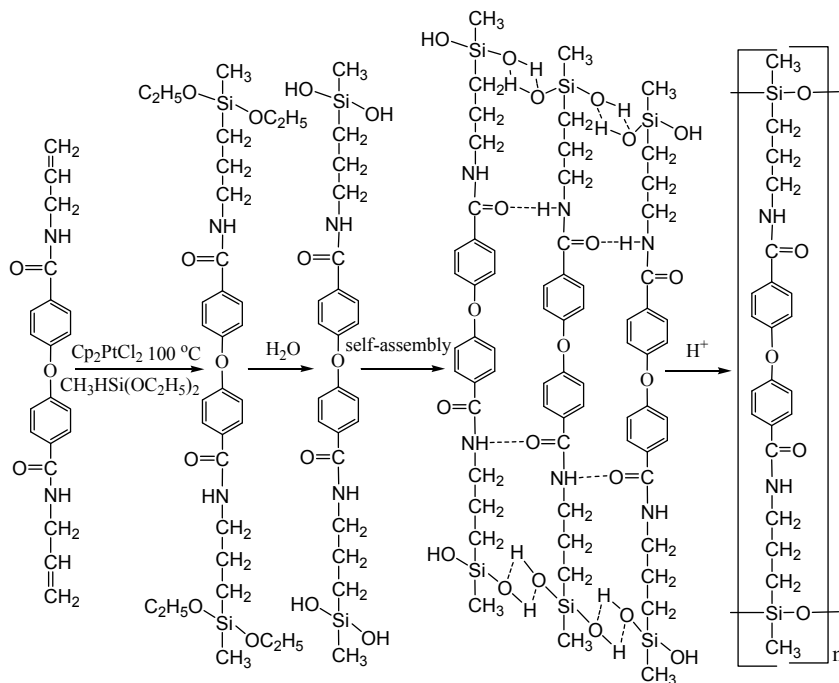
For carbon based ladder polymer, two general routes have been used to prepare ladder type materials: (Scherf et al., 1995, 1998, 1999) (1) the polymerization of multifunctional monomers, in which both the strands of ladder structure are generated in a single reaction; and (2) the cyclization of suitably functionalized open-chain (single-stranded) precursor polymers in a polymer-analogous process. Both strategies pre-suppose certain essentials to arrive at structurally defined ladder polymers, especially the exclusion of side-reactions and an almost quantitative conversion of the starting materials. For ladder polysiloxanes, these routes also are feasible and we adopt the method one to synthesize them, i.e. polymerization from the multifunctional monomers. As mentioned in the introduction section, the ladder polysiloxanes contains the R-LPSQ and R-OLPS, so we will introduce the synthesis and characterization of them respectively.

### 2.1 Synthesis and characterization of R-OLPS

The preparation of R-OLPS generally starts from the multifunctional monomer containing Si-X ( $x = F, Cl, Br$ ) or Si-OH groups. Because of the silicon atom has bigger atomic radius and smaller electro-negativity than carbon atom, Si-X or Si-OH bonds have the bigger polarity and higher reactivity than that of carbon. Thus to obtain the high molecular weight R-OLPS with any single uniform structure would be extremely difficult because of branches and crosslinking are often unavoidable. The traditional polymer synthetic methods usually emphasized chemical reactivity of monomers and ignored other strategies such as lately developed supramolecular concept, i.e., confining reactive monomer within a supramolecular assembly, which can be used as template to direct polymerization. As Bailey (Bailey, 1990) pointed out, the most desirable type of reaction for the formation of a real ladder is one in which both sides of the ladder should be formed simultaneously. Therefore, the problem may only be solved if the precursors' configuration can be effectively controlled during the whole polymerization process like the formation of biopolymers. Towards this goal, we developed a supramolecular template strategy named "supramolecular architecture-directed stepwise coupling and polymerization", which emphasized directive role of the weak supramolecular assembly and thus the polymerization could proceed in the confined environment.



Scheme 2. Illustration of synthesizing R-OLPS by supramolecular architecture-directed stepwise coupling and polymerization



Scheme 3. Synthetic route to ladder polymer A-LPMS.

Synthesizing R-OLPS by supramolecular architecture-directed stepwise coupling and polymerization are illustrated as shown in Scheme 2. Firstly, a silicon monomer, trifunctional silane (e.g.,  $\text{MeSiCl}_3$ ) or potentially tetrafunctional silane (e.g.,  $\text{HSiCl}_3$  or  $\text{CH}_2=\text{CHSiCl}_3$ ), reacts with a coupling agent X-X (e.g., phenylenediamine) to form a separable coupled ladder monomer. Then ladder monomer is self-assembled to form the ladder suprastructure by means of the concerted noncovalent interactions, including hydrogen bonding,  $\pi$ - $\pi$  stacking, and donor-acceptor effects. Next, the ladder suprastructure reacts with the second coupler Y-Y (e.g. H-O-H) to form a covalent ladder polymer R-OLPS. The method has been confirmed by the following practical reactions.

Tang et al. (Tang et al., 2002) reported the preparation of a template, N, N'-diallyl-[4,4'-oxybis(benzyl amide)] as shown in Scheme 3, which possesses strong intermolecular amide hydrogen bonding. Firstly, ladder monomer was synthesized via a hydrosilylation reaction of the template with methyl-diethoxysilane. And then ladder monomer was hydrolyzed and further formed the ladder suprastructure by the hydrogen bonding of  $\text{C}=\text{O}\cdots\text{H}-\text{N}$  and  $\text{Si}-\text{OH}$  themselves. Lastly, the ladder suprastructure was condensed with concentrated  $\text{H}_2\text{SO}_4$  as catalyst to form a highly ordered aryl amide-bridged ladder polymethylsiloxane (A-LPMS). X-ray diffraction (XRD) analysis is an effective method to characterize ordered structures and it was successfully applied to characterize ladder structure. Brown (Brown et al., 1960) pointed out that the diffraction peak in the small-angle region represented the intermolecular chain-to-chain distance of the ladder polymer (*i.e.* the ladder width) and the diffusion peak in the wide-angle region was the thickness of the macromolecular chain (*i.e.* the ladder thickness). There are two distinct peaks representing ladder width (2.40 nm) and

ladder thickness (0.48 nm) in the XRD spectrum of polymer A-LPMS, indicating the ladder structure formed as shown in Fig. 1. Moreover, the regularity of ladder can be inferred from  $^{29}\text{Si}$ -NMR. It was known that the smaller peak width at half-height for  $^{29}\text{Si}$ -NMR peak in solution, the higher the ladder regularity of the polysiloxane. As shown in Fig. 2, except for the peak at 6.9 ppm for the external standard hexamethyldisiloxane and peak at 12.4 ppm for the trimethylsilyloxy end-capping group, a peak with the narrower half-peak width (less than 1ppm) at -18.8 ppm emerge, indicating A-LPMS has high ladder regularity and excluding the presence of the branch structure. In addition, the radius of gyration ( $R_g$ )/the radius of hydrodynamic ( $R_h$ ) = 1.6-1.8 of A-LMPS determined by static light scattering, indicating it is not like a flexible coil but like a semi-rigid soft ladder.

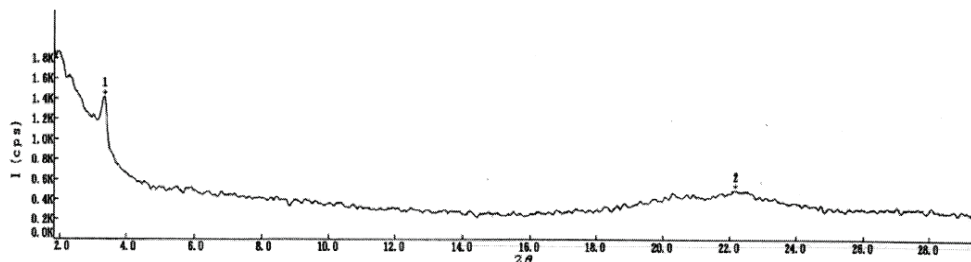


Fig. 1. XRD spectrum of polymer A-LPMS.

Usually, the Mark-Houwink-Sakurada equation is used to express the intrinsic viscosity as a function of the molar mass.

$$[\eta] = K M^\alpha \quad (1)$$

$K$  and  $\alpha$  are constants for a given polymer-solvent system at a given temperature. The exponent  $\alpha$  is characteristic for the polymer topology and reaches from  $\alpha = 0$  (solid spheres) over  $\alpha = 0.5$  (random coil under  $\theta$  conditions) to  $\alpha = 2$  (rigid rod). (Vanhee et al., 1996; Okoshi et al., 2005) The viscosity index ( $\alpha$ ) of A-LPMS can be roughly estimated by the slope of the plots ( $\log [\eta] / \log M_w$ ) and was 1.15, indicating the greater stiffness of the ladder chain. The glass transition temperature of A-LPMS is as high as 125.2°C, revealing its relative stiff backbone.

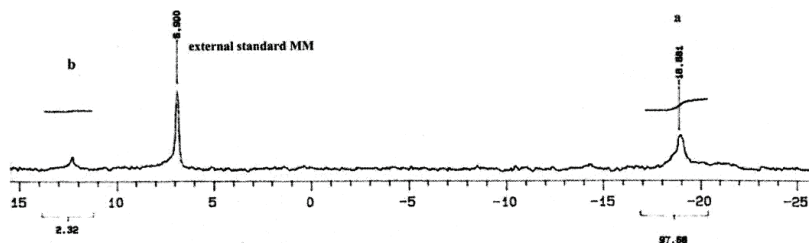
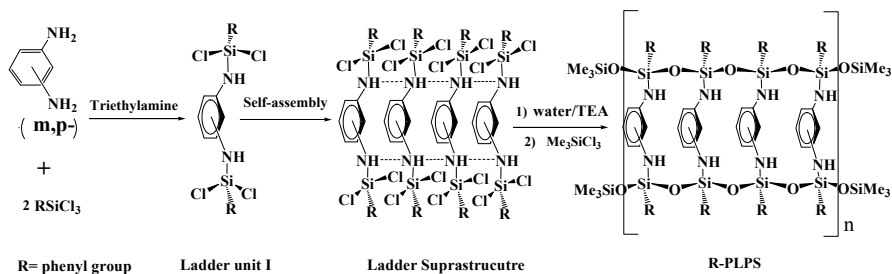


Fig. 2.  $^{29}\text{Si}$ -NMR spectrum of polymer A-LPMS.

Zhang et al. (T. Zhang et al., 2006) synthesized a perfect *p*-phenylenediimino-bridged ladder polyphenylsiloxane as shown in Scheme 4. The first step involves a reaction of phenyltrichlorosilane with the coupler *m* or *p*-phenylenediamine to form a separable

coupled ladder unit, which is self-assembled by a concerted interaction of N-H and Si-OH hydrogen bonding to ladder suprastructure. Then the ladder suprastructure underwent a novel stoichiometric hydrolysis/dehydrochlorination-condensation reaction leading to the desired Ph-PLPS.



Scheme 4. Synthetic route to ladder polymer Ph-PLPS.

Ladder structure also has been confirmed as follows: 1) there are two reflection peaks in XRD spectrum representing the ladder width and thickness, which were consistent with that calculated by molecular simulation. 2) as shown in Fig. 3, Ph-PLPS displays a extremely sharp absorption peak with small half-peak width (less than 0.3ppm) in  $^{29}\text{Si}$ -NMR spectrum, suggesting the presence of the perfect ladder structure. 3) the results of FI-IR, Fluorescence spectroscopy and the glass transition temperature also indicate successful preparation of ladder Ph-PLPS.

It should be noted that the tacticity of R-OLPS mainly depends on the intensity of the supramolecular interaction; in general, a stronger interaction leads to a more regular ladder structure. As shown in Fig. 3, when a hydrogen-bonding blocking reagent urea is added into the ladder suprastructure system, half-peak width of the final polymer becomes as large as 4 ppm in  $^{29}\text{Si}$ -NMR spectrum, indicating the resultant polymer Ph-PLPS became more irregular.

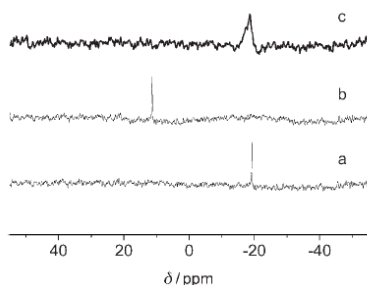
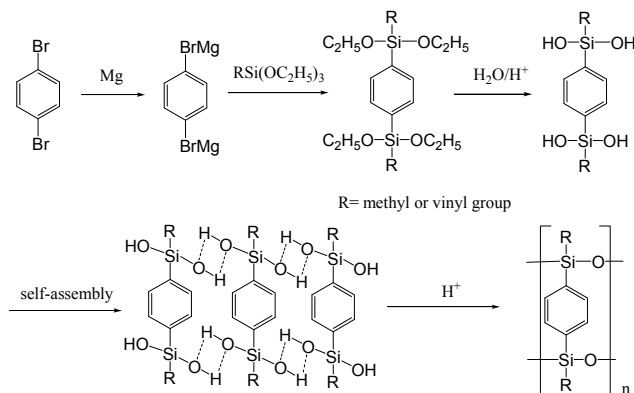


Fig. 3.  $^{29}\text{Si}$ -NMR spectra of a) polymer Ph-PLPS, b) ladder suprastructure, and c) the polymer Ph-PLPS derived from the ladder suprastructure adding urea.

Liu et al. (Liu et al, 2000) adopted another method to prepare ladder phenylene-bridged polymethylsiloxane and polyvinylsiloxane as shown in Scheme 5. Firstly, 1, 4-dibromobenzene reacts with magnesium give the Grignard reagent, which then reacts with methyltriethoxysilane or vinyltriethoxysilane to produce the ladder unit. The ladder unit is hydrolyzed and then condensed subsequently to get the target ladder polymer Me-PLPS or Vi-PLPS.



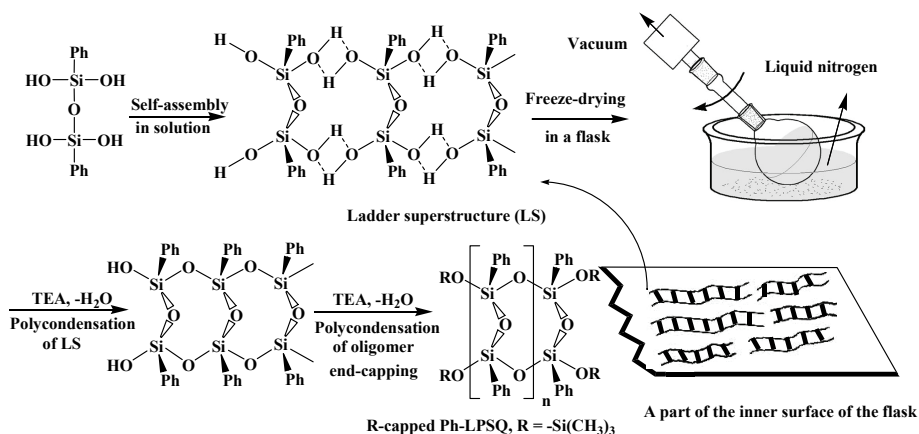
Scheme 5. Synthetic route to ladder polymer Me-PLPS or Vi-PLPS.

In summary, the preparation of ladder R-OLPS by supramolecular architecture-directed stepwise coupling and polymerization was confirmed to be feasible. And more ladder R-OLPS also have been synthesized by this method.

## 2.2 Synthesis and characterization of R-LPSQ

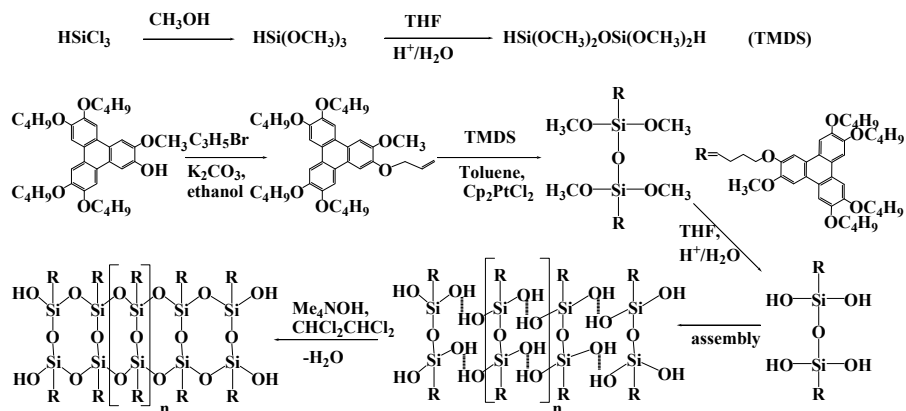
In 1960, Brown *et al.* (Brown *et al.*, 1960) first reported a high molecular weight ( $M_w$ ) ladder polyphenylsilsesquioxane (Ph-LPSQ) via “equilibration polycondensation”. Nevertheless, its structure was refuted later by Frye *et al.* (Frye & Klosowski, 1971) who indicated that the so-called Ph-LPSQ actually was “partially opened polycyclic cages and short-range order but random on large scale”. In 2004, Yamamoto *et al.* (Yamamoto *et al.*, 2004) reported an oligomeric polyphenylsilsesquioxane ladder with low ladder regularity. Lately, Brook (Brook, 2000) mentioned that the high  $M_w$  ladder polysilsesquioxanes reported are generally random networks, but the ladder structure may be obtained under certain controlled conditions. Similar to the preparation of R-OLPS, R-LPSQ also could be synthesized by supramolecular architecture-directed stepwise coupling and polymerization. The typical example will be introduced in the following section.

Zhang *et al.* (Z. X. Zhang *et al.*, 2008) synthesized a well-defined ladder polyphenylsilsesquioxane (Ph-LPSQ) via a three-step approach: pre-organizing in solution, freeze drying, surface confined polycondensation as shown in Scheme 6. In the first step, ladder superstructure was formed by self-assembly of 1, 3-diphenyl-tetrahydroxy-disiloxane monomer in an acetonitrile solution. In the second step, lyophilization was realized by rotating a flask containing monomer/acetonitrile solution, while the flask was immersed in liquid nitrogen. This results in the formation of a continuous thin layer on the inner surface of the rotating flask (Scheme 6). In the third step, the self-assembled ladder superstructure immobilized in the solid thin layer was further converted into covalent ladder polymer by dehydrating polycondensation under TEA atmosphere. The rotation of the flask induced the orientation of ladder superstructures. Lyophilization fixed their orientation and structure. These factors promoted the confined polycondensation and prevented the cyclization and gelation side reactions, resulting in the formation of a soluble, high molecular-weight, and highly regular Ph-LPSQ.



Scheme 6. Systematic representation of the preparation of Ph-LPSQ via monomer self-organization-lyophilization-surface-confined polycondensation.

$^{29}\text{Si}$ -NMR analysis showed a very narrow peak (peak width at half-height of 2.5 ppm) at  $-78.5$  ppm assigned to a  $\text{Ph-SiO}_{3/2}$  unit, indicating a high degree of regularity of the Ph-LPSQ structure. The XRD profile of Ph-LPSQ also demonstrated two distinct peaks at  $2\theta$  around  $7.0^\circ$  (ladder width,  $12.1 \text{ \AA}$ ) and  $20.0^\circ$  (ladder thickness,  $4.5 \text{ \AA}$ ), respectively. Ren et al. (Ren et al., 2010) synthesized a well-defined triple-chain ladder polyphenylsiloxane by the similar strategy.



Scheme 7. Synthetic route to the ladder triphenylene-containing polysilsesquioxane.

Zhang et al. (X. J. Zhang et al, 2006) reported a soluble, high  $M_w$  and perfect ladder triphenylene-containing polysilsesquioxane (LP) by a confined synthesis method as shown in Scheme 7. The self-organization of  $\alpha,\omega$ -ditriphenylene tetrahydroxy-disiloxane (M) by concerted  $\pi$ - $\pi$  stacking and H-bonding yield a high regular ladder superstructure (LS), and then LS converted into LP by dehydration condensation. In this case, introduction of electro-rich triphenylene groups intensified the supramolecular interactions and resulted in a supramolecular channel for a confined synthesis.

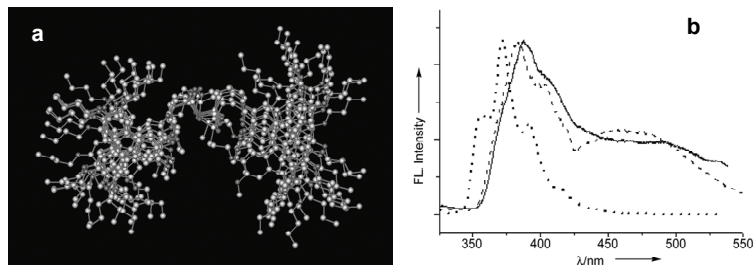


Fig. 4. (a) Top view of the molecular simulated ladder chain of LP with six repeat units (Hyper Chem 7.0 geometry optimization with RMS gradient of 0.1 kcal.mol<sup>-1</sup>). (b) Fluorescence emission spectra of M (dotted line), LS (dashed line), and LP (solid line) in n-hexane solution (10<sup>-6</sup> M).

<sup>29</sup>Si-NMR and XRD measurements indicated the LP is prepared successfully. The top view of the molecular simulation of the chain (Fig. 4a) shows that all the triphenylene units are arranged on the same side of the ladder backbone and LP has a cis-isotactic structure. The regular stereoconfiguration of LP is also supported by fluorescence emission spectra as shown in Fig. 4b. In comparison to M, a new emission band at 493 nm appears in the spectrum of LS and LP, which is attributed to the excimer formed by the face to face  $\pi$ - $\pi$  stacking of the triphenylene side groups. It is also found that the ratio of the fluorescence emission intensities ( $I_m/I_e$ ) at 390 nm ( $I_m$ ) and at 493 nm ( $I_e$ ) is independent of the concentration of LP, and no red-shift of the emission spectra occurs as the concentration is changed. The existence of the intramolecular excimer further confirms the cis-isotactic structure.

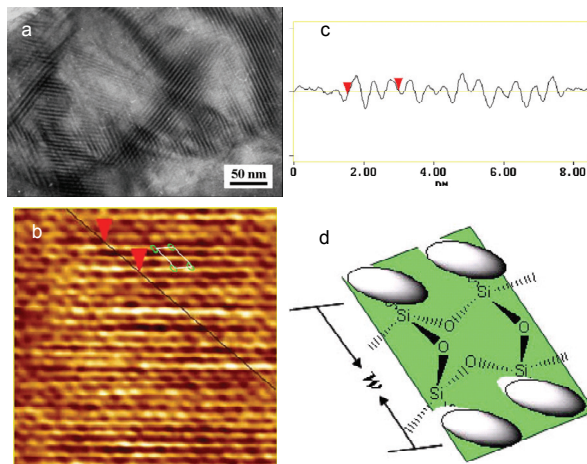
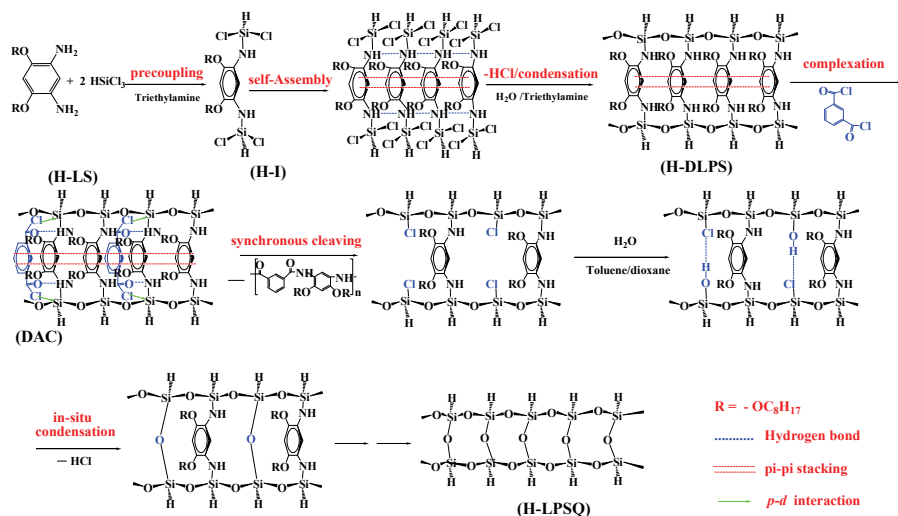


Fig. 5. TEM and AFM images of LP: (a) A bright-field TEM image obtained by freeze-drying a benzene solution; (b) high-resolution AFM image of a spin-coated film obtained from benzene solution; (c) AFM section analysis; (d) schematic representation of the ladder structure observed by AFM and the average value of  $w$  is 1.30 nm.

The transmission electronic microscopy (TEM) image (Fig. 5a) shows domains with dark lamellas with widths of about 2.5 nm, which are in agreement with the XRD results of LP.

However, high-resolution atomic force microscopy (AFM) images of a spin-coated film of LP on mica (Fig. 5b,c) show clear features (three parallel bright lines) of extended ladder chains (shown schematically in Fig. 5d): double chains align on the surface with the triphenylene side groups at the edge—the bright lines of two sides correspond to stacked triphenylene cores, and the middle one corresponds to the main chain of the ladder silsesquioxane. Careful observation shows the disc plane is aligned tilted to the chain axis. Section analysis gives the width of the repeat ladder unit  $w=1.30$  nm, which is reasonable for the distance between the centers of the triphenylene cores at the two sides.

Ren et al. (Ren et al., 2009) prepared a reactive and purely inorganic high Mw perfect ladder polyhydrosilanesquioxane (H-LPSQ) under direction of the two imperative supramolecular architectures: ladder superstructure (H-LS) and donor-acceptor complex (DAC) as shown in Scheme 8. It includes two steps: 1) precoupling and H-LS based synthesis of sacrificial 1,5-diimino-2,4-bis(octyloxy)-phenylene-bridged ladder polyhydrosiloxanes (H-DLPS) and 2) DAC based synchronous cleavage of the bridge and in-situ condensation. It is necessary to emphasize that H-LS and DAC are two imperative supramolecular architectures determining ladder regularity of H-LPSQ.



Scheme 8. Synthetic route to H-LPSQ

For the first step, the preparation of H-DLPS is similar to R-OLPS. The key for successfully conversion of H-DLPS to H-LPSQ is DAC based synchronous cleavage of the bridge and in-situ condensation. To achieve “synchronous cleavage”, isophthaloyl dichloride (IPC) was selected as the cleaving agent. It is proposed that when IPC is added into H-DLPS, it can form DAC with the diaminophenylene-bridge by a synergy of hydrogen bonding between carbonyl and amino groups, benzene ring's  $\pi$ - $\pi$  stacking and  $d\pi$ - $p\pi$  interaction of p-electrons of Cl-atom and d-orbital of Si-atom. The Cl-atom of IPC then links to Si-atom, and breaks the Si-N bonds of the bridge and further transfer them into two Si-Cl bonds. The formation of DAC ensures the synchronous break of the two Si-N bonds on the same bridge, so that Si-O-Si can be formed in situ by hydrolysis and dehydrochlorination condensation of the two new-born Si-Cl bonds. The formation of a stable donor-accept complex (DAC) of



IPC with H-DLPS also was confirmed. As shown in Fig. 6, when IPC and H-DLPS were mixed with equal mole of IPC/the bridge, a low-energy absorbance at 386 nm emerged, which is different from the characteristic peaks of IPC and H-DLPS. That suggests the formation of DAC adducts apparently.

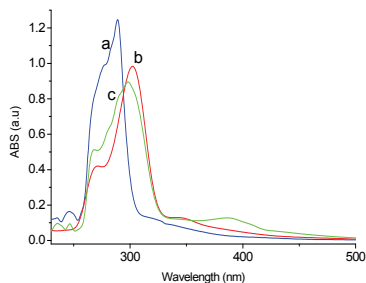


Fig. 6. UV spectra of (a) IPC; (b) H-DLPS; (c) H-DLPS and IPC (IPC and the bridge of H-DLPS is in equal mole)

The perfect ladder structure of H-LPSQ was also confirmed by elemental analysis, IR spectrum, XRD,  $^{29}\text{Si}$ -NMR and so on. Moreover, ladder H-LPSQ was functionalized by the hydrosilylation of cyclohexylene catalyzed by  $\text{Cp}_2\text{PtCl}_2$  to get ladder polycyclohexylsilsequioxane (Ch-LPSQ). The perfection of Ch-LPSQ further demonstrates the perfection of the precursor H-LPSQ. The successful preparation of Ch-LPSQ also verifies the high reactivity of Si-H groups on H-LPSQ.

Using the similar method, the Ladder Polyphenylsilsequioxanes (Ph-LPSQ) with a high regularity was prepared. MALDI-TOF-MS spectrum of Ph-LPSQ confirmed its ladder structure. As shown in Fig. 7, due to measuring mechanism, there was only the information of polymers with  $M_w < 6500$  Daltons. It bears the characteristic shape of a condensation polymer and make up of clusters of isotopic peaks. The nominal separation between these alternate major clusters, 258 Daltons, is exactly equal to the Ph-Si(O) $_{2/2}$ -O-Si(O) $_{2/2}$ -Ph repeat unit, indicating that the synthesis proceeded as expected to give double chain ladder structure without other side reactions. The displacement of the major clusters is attributed to the  $\text{Me}_3\text{SiO}$ - and  $\text{HOSiO}$ -capped Ph-LPSQ respectively, because the precursor was capped by trimethylchlorosilane in the end of polycondensation.

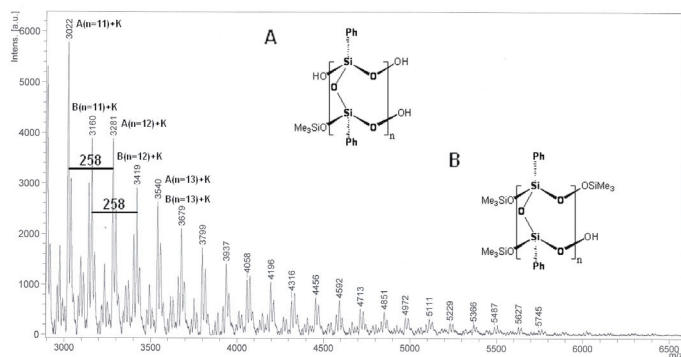


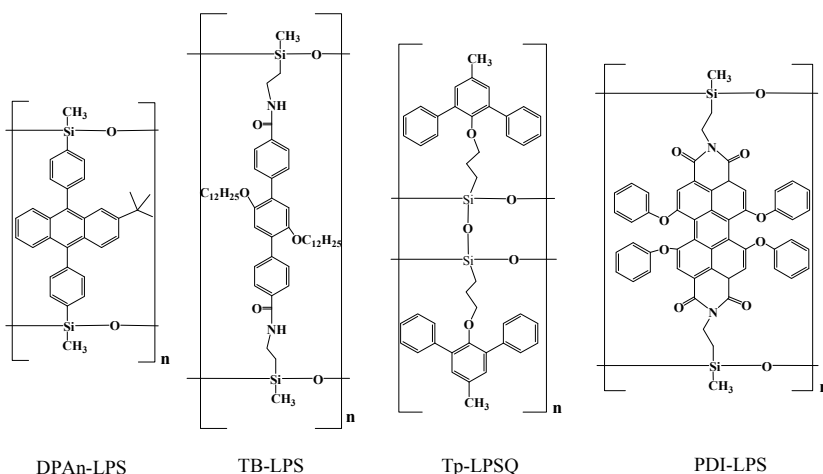
Fig. 7. MALDI-TOF MS of Ph-LPSQ.

### 3. Application of ladder polysiloxanes in polymer light-emitting diodes (PLED)

#### 3.1 Fluorescent materials

As mentioned in the introduction section, ladder polysiloxane is expected to reduce the electron delocalization of conjugated polymer and thus suppress the formation of aggregation. In fact, it was found that it could effectively prevent the aggregation of conjugated light-emitting groups so as to obtain stable, high efficiency and good film-forming materials.

It is well known that anthracene is typical for self-quenching of luminescence due to intermolecular aggregation. Zhang et al. (J. T. Zhang et al., 2010) introduced 9,10-Diphenylanthryl groups into the polysiloxanes skeleton to synthesize a 9,10-diphenylanthryl-bridged ladder polysiloxane (DPAn-LPS) as shown in Scheme 9.



Scheme 9. Chemical structure of DPAn-LPS, TB-LPS, Tp-LPSQ and PDI-LPS.

DPAn-LPS exhibits an emission band around 430 nm and absorption peaks in the range of 260–420 nm as shown in Fig. 8a. Note that there is only less than 2 nm red shift for UV-vis and photoluminescence spectra (PL) when the sample was varied from solution to film states, suggesting no aggregation of chromophore during film preparation. We suppose that the negligible variation of spectra between solution and film was due to confinement of 9,10-diphenylanthryl moieties within individual double-stranded ladder structure. Post-solution processing did not induce substantial change of local rearrangement of 9,10-diphenylanthryl units, which as return offered good film-forming property. PL spectra of DPAn-LPS show little variation after heating the film at 200 °C in air for 2 h as shown in Fig. 8b. This result demonstrates that DPAn-LPS is free of low energy defects (e.g., caused by crystallization) and has great thermal and color stability.

The fluorescence quantum efficient yield ( $\Phi_F$ ) of DPAn-LPS in THF is found to be 0.89 using 9,10-diphenylanthracene as a reference standard (cyclohexane solution,  $\Phi_F=0.9$ ). This value is notably higher than the reported values for some anthracene-containing compounds, such as 0.47 of 2-tert-butyl-9,10-bis[4-(iminostilbenyl)phenyl]anthracene (Danel et al., 2002) and 0.44 of 9-phenyl-10-(4-triphenylamine)anthracene. (Hamai & Hirayama, 1983)

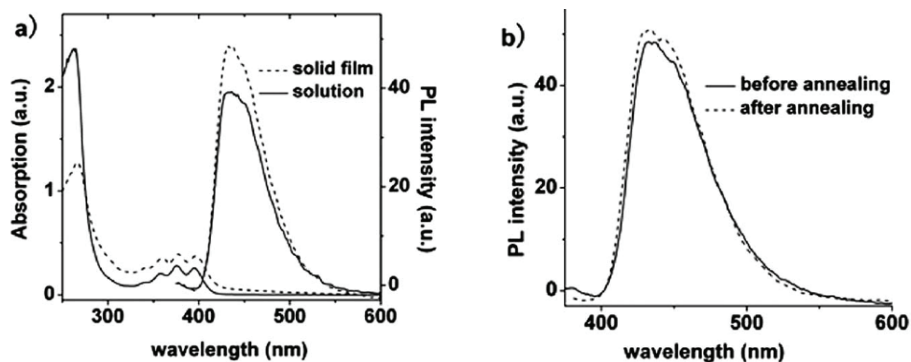


Fig. 8. (a) Absorption and photoluminescence emission spectra of DPAn-LPS in THF solution and thin film; (b) emission intensity of the spin-coated DPAn-LPS film before and after annealing at 200 °C for 2 h.

As expected, DPAn-LPS has the good emission stability at high temperature with high fluorescence quantum efficient yield because intramolecular aggregation of chromophores is effectively prevented by the rigid ladder structure.

Zhou et al. (Zhou et al., 2008) prepared a novel blue-light emitting terphenyl-bridged ladder polysiloxane (TB-LPS) as shown in Scheme 9. TB-LPS emits narrow blue light (420 nm) as shown in Fig. 9a with high quantum yields (0.96) in diluted solution. Comparing the solution state, TB-LPS shows no evident fluorophore aggregation in the solid state, indicating that the terphenyls are well isolated due to confinement of the ladder rungs. In addition, TB-LPS exhibits 5% weight loss at ca. 350 °C, and Tg of 143 °C revealing by thermogravimetric analysis and differential scanning calorimetry, indicating a good thermal stability. TB-LPS has the excellent color emission stability at high temperature based on annealing in air at 200 °C for 2 h as shown in Fig. 9b. Overall, TB-LPS can be considered as a potential material for fabricating stable and high-efficiency blue-light emitting optoelectronic devices.

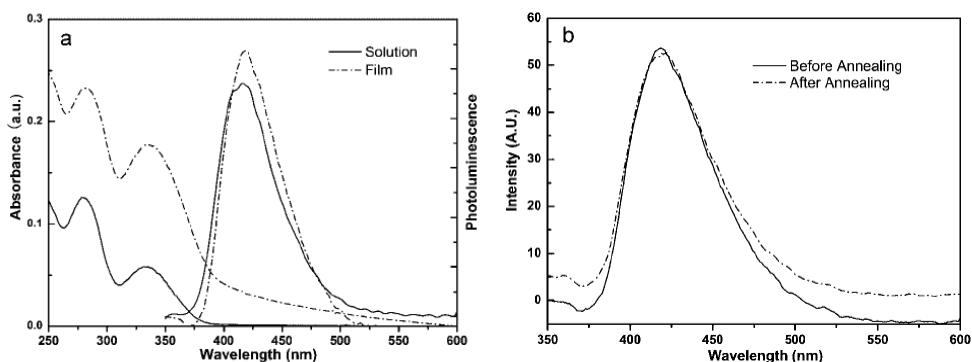


Fig. 9. (a) Absorption and photoluminescence emission spectra of TB-LPS in THF solution and in film. (b) Emission intensity of the spin-coated TB-LPS film before and after annealing at 200 °C for 2 h.

### 3.2 Phosphorescent host materials

In the development of high efficiency PLED, employing phosphorescent dyes in the electroluminescent light-emitting layer is an important method to realize high efficiency PLED because of the phosphorescent dyes, such as iridium bis(4,6-difluorophenyl)pyridinato-*N,C*picolinate (FIrpic), can enable the internal quantum efficiency as high as 100% converting of both singlet and triplet excitons into photons. (Kawamura et al, 2005; Lamansky et al., 2001) In general, dopant/host systems are used for electrophosphorescent PLED to resolve the annihilation of both triplet-triplet and triplet-polaron. (Baldo et al., 2000) High efficiency host materials for green and red phosphorescence have been realized, but the research for blue phosphorescence emitting and host materials still are demanding. An ideal host for blue-light electrophosphorescence should essentially meet the follows: high enough singlet and triplet energy levels ( $E_T$ ) to confine singlet and triplet excitons, high charge mobility, and wide energy gap ( $E_g$ ). Of course, good chemical and thermal stabilities of the host materials are also of great importance. Ladder polysiloxane shows high thermal stability, good film-forming property. In addition, silicon-containing low conjugation structure may give a high  $E_T$ . Thus it may be a potential host material for blue-light emitting triplet emitter.

Ren et al. synthesized 3-methyl-1,5-diphenylbenzene containing ladder polysilsesquioxane (Tp-LPSQ) with a wide bandgap of ca. 4.0 eV as shown in Scheme 9. The absorption spectrum of Tp-LPSQ in dichloromethane solution and thin film features two peaks at 241 nm and 296 nm as shown in Fig. 10A. The PL spectrum of Tp-LPSQ shows an emission peak at 364 nm in dichloromethane solution and thin film (Fig. 10B). The absorption and PL spectra of Tp-LPSQ thin film are almost identical to that in solution without any bathochromic shift, indicating negligible intermolecular interactions between Tp-LPSQ molecules in the solid packing state. The PL emission of Tp-LPSQ at low temperature was also measured to calculate  $E_T$ , which reaches to 2.82 eV. It is much higher than that of FIrpic ( $E_T = 2.62$  eV). So the generated triplet excitons could be confined in the emissive layer for Tp-LPSQ/FIrpic doped system.

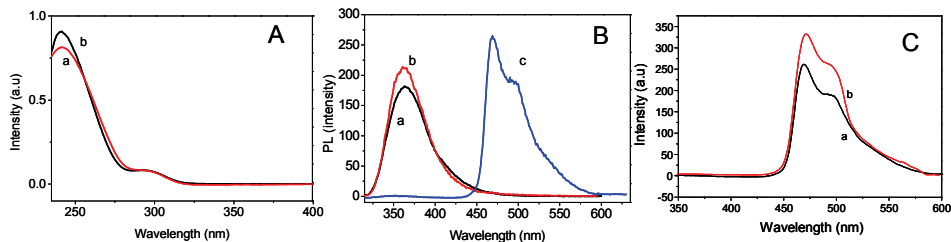


Fig. 10. (A) UV-vis spectra of Tp-LPSQ a) film; b) solution; (B) PL spectra of a) Tp-LPSQ solution; b) Tp-LPSQ film. c) Tp-LPSQ film doped with 8 wt % FIrpic. (C) PL spectra of Tp-LPSQ a) doped 8 wt% FIrpic and b) doped 8 wt% FIrpic aging 120 °C for 4h.

PL spectrum of Tp-LPSQ film blended with 8 wt% FIrpic shows a maximum emission peak at 469 nm and a shoulder peak at 496 nm, typical for FIrpic, with no trace of host Tp-LPSQ left at ca. 364 nm, (Fig. 10C) which indicate an efficient energy transfer from Tp-LPSQ to FIrpic and back transfer from the FIrpic to Tp-LPSQ does not occur at all. The PL spectrum shows the little variation after annealing at 120 °C in air for 4h, as shown in the Fig. 10B, suggesting Tp-LPSQ is free of low energy defects (e.g., caused by crystallization) and has great thermal and color stability.

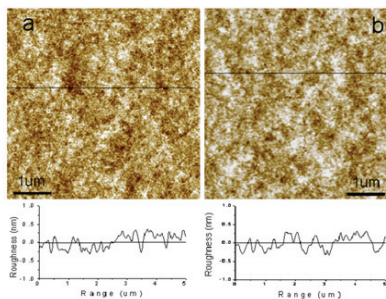


Fig. 11. AFM images and surface roughness of (a) Tp-LPSQ film doped with 8 wt% Flrpic and (b) Tp-LPSQ film doped with 8 wt% Flrpic after heating at 120 °C for 4h.

The film-forming ability, morphological stability of Tp-LPSQ and miscibility to the dopant Flrpic also were investigated by the atomic force microscopy (AFM) as shown in Fig. 11. The topographical image of Tp-LPSQ with 8 wt % doped Flrpic reveals that surface is smooth and uniform with 0.6 nm surface roughness, free of pinholes, particle aggregation, or phase separation as shown in Fig. 11a. Moreover, it is thermally stable as confirmed by annealing the film at 120 °C in air for 4h and the surface roughness is nearly unchanged.

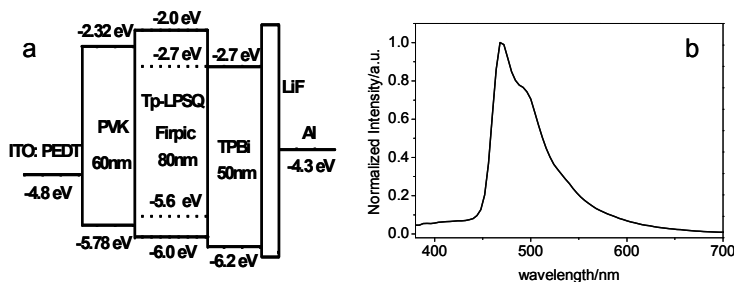


Fig. 12. (a) Energy level diagram for the device and (b) EL spectra of Tp-LPSQ doped with 8 wt% Flrpic at 10V

The PLED of Tp-LPSQ doping blue light Flrpic as active emitting layer was fabricated. As shown in Fig. 12a, the device configuration is [polyethylenedioxythiophene(PEDT) fabricated indium tin oxide (ITO)/poly(N-vinylcarbazole) (PVK) /8 wt % Flrpic doped Tp-LPSQ /1,3,5-tris(N-phenylbenzimidazol-2-yl)benzene (TPBI) /LiF/Al]. The EL spectra of the device displays bluer emission with an emission peak at 468 nm and a shoulder peak at 491 nm with a narrow full-width at half maximum of 53nm as shown in Fig. 12b. Commission International de L'Eclairage (CIE) coordinates is (0.17, 0.30).

As shown in Fig. 13, the turn-on voltage of device is 5.8 V, which is lower than that of reported polymer host materials. The device reaches the maximum brightness of 883 cd/m<sup>2</sup> at 13 V and shows a maximum luminous efficiency of 8.7 cd/A or the maximum power efficiency of 3.1 lm/W, which is superior to that of the reported polymer host (9,9'-bis(2-ethylhexyl)-3,6-fuorene) (Wu et al., 2008) and PVK, (Kido et al., 1993) even comparable to the small molecule host 4,4'-bis(9-carbazolyl)biphenyl (CBP). (Hu et al., 2009) The external quantum of the device is 4.6% ph/el, which is best blue light polymer host for Flrpic reported so far.

In summary, ladder polysilsesquioxanes shows good film-forming property, high thermal and morphological stability, and good miscibility to the dopant FIrpic, in addition it has high triplet energy and wide band-gap. Therefore it may be potential host for phosphorescence emitter. We believe high efficiency materials may be obtained by tuning chromophore groups of ladder polysilsesquioxanes.

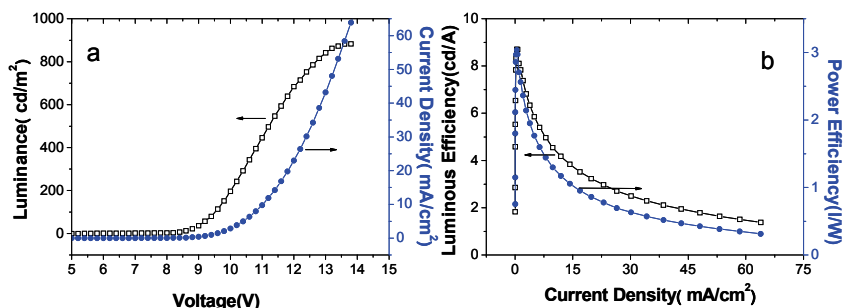


Fig. 13. (a) current density-voltage-luminance curve and (b) luminous efficiency and power efficiency as a function of current density of device.

#### 4. Application of ladder polysiloxane in polymer solar cells materials

Polymer solar cells (PSCs) are being extensively studied because of their great potential application. Compared with inorganic materials based solar cells, PSCs can be easily fabricated via spincoating, enabling the manufacture of large area, flexible, lightweight, inexpensive, and renewable devices. Generally, all of the solar cell devices require both hole-transporting (p-type) and electron-transporting (n-type) materials. From the view of improving performance the PSCs, controlling the metal/polymer semiconductor interfaces may lower the open circuit potential, and engineering the nanoscale morphology of the polymer semiconductor thin film may improve the mobility of the charge carriers. Apart from the necessity for efficiency improvement, stability is another problem for PSCs. Especially under light illumination and by simultaneous exposure to oxygen or water vapor, a rapid photooxidation/degradation occurs. Protection from air and humidity is necessary to achieve long device lifetimes (Günes et al., 2007).

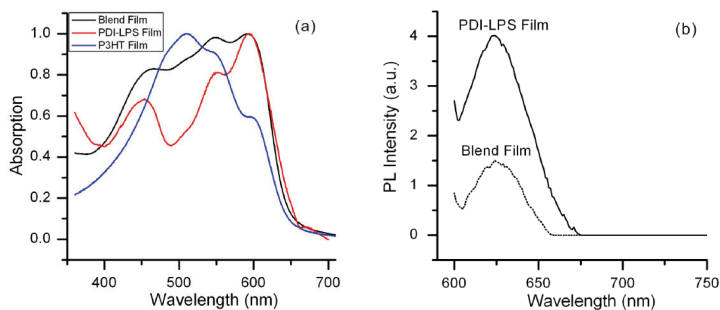


Fig. 14. (a) UV-vis spectra of blend film, PDI-LPS and P3HT films. (b) Fluorescence emission spectra.

The better film-forming ability, thermal stability, fair adhesion to various substrates and the excellent resistances to thermal, chemical and irradiation degradation of ladder polysiloxanes thin film may benefit the PSCs.

Perylene and its derivatives show an n-type, electron conducting behaviour and commonly serve as electron-acceptor materials of PSCs. Fu et al. (Fu et al., 2011) introduced a perylenediimide derivative into the central bridge of ladder polysiloxane to form PDI-LPS as shown in Scheme 9. Through chemically incorporating perylenediimide derivative (PDI) into ladder polymer backbone, it is expected to minimize the conglomeration of PDI and improve materials' thermostability and solubility while retaining its optoelectronic properties.

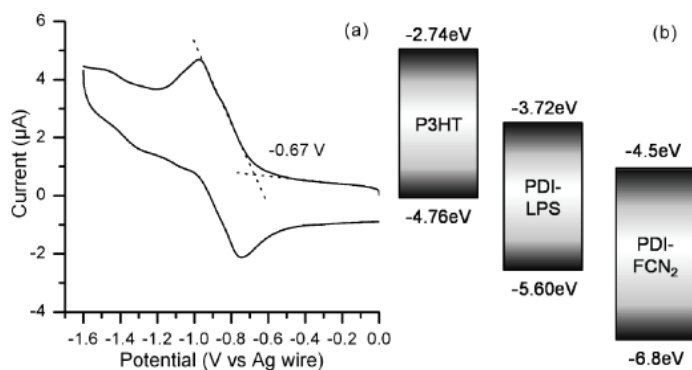


Fig. 15. (a) Cyclic voltammogram of PDI-LPS. (b) Energy levels diagram of ITO/PEDOT:PSS/P3HT:PDI-LPS:PDI-FCN<sub>2</sub>.

The PDI-LPS began to decompose at 442 °C and lost ca. 5 wt % at ca. 430 °C by TGA. The DSC curve shows that the PDI-LPS does not have any melting peaks, and its T<sub>g</sub> locates at ca. 310 °C, which is much higher than that of the low molar mass PDI derivatives. (Shin et al., 2006) The higher T<sub>g</sub> is due to the excellent regular ladder structure of the PDI-LPS and the double-strained structure could provide PDI-LPS with excellent thermal property and dimensional stability due to the minimized movements of chain segments.

It is well known that P3HT is as good p-type, hole conducting materials that works as electron donor. As a potential electron acceptor of PSCs, PDI-LPS was blended with P3HT and their optoelectronic properties were determined. As shown in Fig. 14a, UV-vis absorption edge of PDI-LPS extends to 660 nm and its corresponding optical energy gap is 1.88eV. Moreover, it is found the blends of PDI-LPS and P3HT (1:1) showed enhanced absorption areas spectrum compared to their precursors. Photoluminescence showed the blended thin film had strong fluorescence quenching indicating efficient energy transfer from P3HT to PDI-LPS as shown in Fig. 14b. The HOMO and LUMO energy levels of PDI-LPS were determined using cyclic voltammetry. As shown in Fig. 15, PDI-LPS has the proper HOMO and LUMO level with P3HT. Compared with the low molar mass PDI derivatives (e.g., PDI-FCN<sub>2</sub>), PDI-LPS has higher LUMO level, which could help the solar cell device to own higher open circuit voltage.

Especially the ladder polysiloxanes film is hydrophobic and it could resist photooxidation/degradation by simultaneous exposure to oxygen or water vapor. Thus the PSCs devices may achieve long device lifetimes.

## 5. Conclusion and perspectives

In summary, the ladder polysiloxanes have been successfully prepared by a supramolecular template strategy named "supramolecular architecture-directed stepwise coupling and polymerization". The ladder polysiloxanes displays good solubility in common organic solvents, good film-forming ability, fair adhesion to various substrates and the excellent resistances to thermal, chemical and irradiation degradation. Thus they offer great potentials in engineering the PLED and the PSCs. Except improving the thermal stability of the PLED and PSCs, the ladder polysiloxanes also could control the  $\pi$ - $\pi$  stacking induced molecular aggregation of the polymer chains. Therefore, high performance PLED and PSCs would be obtained by tuning the chemical structure of the ladder polysiloxanes and controlling the interface micro-structure of devices and it may be a kind of promising optoelectronic materials.

## 6. Acknowledgment

The financial supports of NSFC and China Postdoctoral Science Fund (No. 20100480182) are gratefully acknowledged. Also we sincerely thank Prof. Ping Xie, Dr. Qilong Zhou, Jingtao Zhang, Wenxin Fu and Zhize Chen.

## 7. References

- Amrutha, S. R. & Jayakannan, M. (2007). Structure Control of  $\pi$ -Conjugated Polymers for Enhanced Solid-State Luminescence: Synthesis and Liquid Crystalline and Photophysical Properties of New Bulky Poly(p-phenylenevinylene)s and Oligo(phenylenevinylene)s Bearing Tricyclodecane Pendants. *Macromolecules*, Vol.40, No.7, (March 2007), pp.2380-2391, ISSN 0024-9297.
- Bailey, W. J. (1990). *Concise Encyclopedia of Polymer Science and Engineering*, pp.516-528, John Wiley & Sons, ISBN 0-471-51253-2, New York.
- Baldo, M.; Adachi, C. & Forrest, S. (2000). Transient analysis of organic electrophosphorescence. II. Transient analysis of triplet-triplet annihilation. *Phys. Rev. B.*, Vol.62, No.16, (October 2000) pp.10967-10977, ISSN 1098-0121.
- Brook, M. A. (2000). *Silicon in Organic, Organometallic, and Polymer Chemistry*, John Willey & Sons, ISBN 0-471-19658-4, New York.
- Brown, J. F.; Vogt, L.; Katchman, H. A.; Eustance, J. W.; Kiser, K. M. & Krantz, K. W. (1960). Double Chain Polymers of Phenylsilsesquioxanes. *J. Am. Chem. Soc.*, Vol.82, No.23, (December 1960) pp.6194-6195, ISSN 0002-7863.
- Burroughes, J. H.; Bradley, D. D. C.; Brown, A. R.; Marks, R. N.; Mackay, K.; Friend, R. H.; Burns, P. L. & Holmes, A. B. (1990). Light-emitting diodes based on conjugated polymers. *Nature*, vol.347, (October 1990), pp. 539-541, ISSN 0028-0836.
- Chen, J. P.; Klärner, G.; Lee, J. I.; Maarkiewicz, D.; Lee, V. Y.; Miller, R. D. & Scott, J. C. (1999). Efficient, blue light-emitting diodes using cross-linked layers of polymeric arylamine and fluorine. *Synth. Met.*, Vol.107, No.2, (November 1999) pp.129-135, ISSN 0379-6779.



- D'Andrade, B. W. & Forrest, S. R. (2004). White organic light-emitting devices for solid-state lighting. *Adv. Mater.*, Vol.16, No.18, (September 2004) pp.1585-1595, ISSN 0935-9648.
- Danel, K.; Huang, T. H.; Lin, J. T.; Tao, Y. T. & Chuen, C. H. (2002). Blue-Emitting Anthracenes with End-Capping Diarylamines. *Chem Mater.*, Vol.14, No.9, (September 2002) pp.3860-3865, ISSN 0897-4756.
- de Gans, B. J. & Schubert, U. S. (2003). Inkjet printing of polymer micro-arrays and libraries: Instrumentation, requirements, and perspectives. *Macromol. Rapid Commun.*, Vol.24, No.11, (September 2003) pp.659-666, ISSN 1022-1336.
- Ego, C.; Grimsdal, A. C.; Uckert, F.; Yu, G.; Srdanov, G. & Müllen, K. (2002). Triphenylamine-Substituted Polyfluorene—A Stable Blue-Emitter with Improved Charge Injection for Light-Emitting Diodes. *Adv. Mater.*, Vol.14, No.11, (June 2002) pp.809-811, ISSN 0935-9648.
- Fenter, P.; Schreiber, F.; Bulovis, V. & Forrest, S. R. (1997). Thermally induced failure mechanisms of organic light emitting device structures probed by x-ray specular reflectivity. *Chem. Phys. Lett.*, Vol.277, No.5-6, (June 1997) pp.521-526, ISSN 0009-2614.
- Froehlich, J. D.; Young, R.; Nakamura, T.; Ohmori, Y.; Li, S. & Mochizuki, A. (2007). Synthesis of Multi-Functional POSS Emitters for OLED Applications. *Chem. Mater.*, Vol.19, No.20, (October 2007) pp.4991-4997, ISSN 0897-4756.
- Frye, C. L. & Klosowski, J. M. (1971). So-called "ladder structure" of equilibrated phenylsilsesquioxane. *J. Am. Chem. Soc.*, Vol.93, No.18, (September 1971) pp.4599-4601, ISSN 0002-7863.
- Fu, W.; He, C.; Jiang, S.; Chen, Z.; Zhang, J.; Li, Z.; Yan, S. & Zhang, R. (2011). Synthesis of a Polymeric Electron Acceptor Based on Perylene-dimide-Bridged Ladder Polysiloxane. *Macromolecules*, Vol.44, No.2, (November 2010) pp. 203-207, ISSN 0024-9297.
- Gather, M. C.; Kohnen, A. & Meerholz, K. (2011). White Organic Light-Emitting Diodes. *Adv. Mater.*, Vol.23, No.2, (January 2011) pp.233-248, ISSN 0935-9648.
- Grimsdale, A. C.; Chan, K. L.; Martin, R. E.; Jokisz, P. G. & Holmes, A. B. (2009). Synthesis of Light-Emitting Conjugated Polymers for Applications in Electroluminescent Devices. *Chem. Rev.*, Vol.109, No.3, (March 2009) pp.897-1091, ISSN 0009-2665.
- Gunes, S.; Neugebauer, H. & Sariciftci, N. S. (2007). Conjugated Polymer-Based Organic Solar Cells. *Chem. Rev.*, Vol.107, No.4, (April 2007) pp.1324-1338, ISSN 0009-2665.
- Guo, G.; Zhang, Y.; Li, H.; Xie, P. & Zhang, R. (2002). Synthesis of a novel 2,5-dipropylhydroquinone-bridged ladder-like polymethylsiloxane using a hydroquinone H-bonding self-assembling template. *Macromol. Rapid Commun.*, Vol.23, No.5-6, (April 2002) pp.366-369, ISSN 1022-1336.
- Hamai, S. & Hirayama, F. (1983). Actinometric determination of absolute fluorescence quantum yields. *J. Phys. Chem.*, Vol.87, No.1, (January 1983) pp.83-89, ISSN 0022-3654.
- Holder, E.; Langeveld, B. M. W. & Schubert, U. S. (2005). New Trends in the Use of Transition Metal-Ligand Complexes for Applications in Electroluminescent Devices. *Adv. Mater.*, Vol.17, No.9, (May 2005) pp.1109-1121, ISSN 0935-9648.

- Hu, D.; Lu, P.; Wang, C.; Liu, H.; Wang, H.; Wang, Z.; Fei, T.; Gu, X. & Ma, Y. (2009). Silane coupling di-carbazoles with high triplet energy as host materials for highly efficient blue phosphorescent devices. *J. Mater. Chem.*, Vol.19, No.34, (August 2009) pp.6143-6148, ISSN 0959-9428.
- Imae, I. & Kawakami, Y. (2005). Unique photoluminescence property of a novel perfectly carbazole-substituted POSS. *J. Mater. Chem.*, Vol.15, No.43, (November 2005) pp.4581-4583, ISSN 0959-9428.
- Kawamura, Y.; Goushi, K.; Brooks, J.; Brown, J.; Sasabe, H. & Adachi, C. (2005). 100% phosphorescence quantum efficiency of Ir(III) complexes in organic semiconductor films. *Appl. Phys. Lett.*, Vol.86, No.7, (February 2005) pp.071104 1-3, ISSN 0003-6951.
- Kido, J.; Hongawa, K.; Okuyama, K. & Nagai, K. (1993). Bright blue electroluminescence from poly(N-vinylcarbazole). *Appl. Phys. Lett.*, Vol.63, No.19, (November 1993) pp.2627-2629, ISSN 0003-6951.
- Kido, J.; Kimura, M. & Nagai, K. (May 1995). Multilayer white light-emitting organic electroluminescent device. *Science*, Vol.267, No.5202, (1995) pp.1332-1334, ISSN 0036-8075.
- Kläerner, G.; Davy, M. H. ; Chen, W. D.; Scott, J. C. & Miller, R. D. (1998). Colorfast Blue-Light-Emitting Random Copolymers Derived from Di-*n*-hexylfluorene and Anthracene. *Adv. Mater.*, Vol.10, No.13, (September 1998) pp.993-997, ISSN 0935-9648.
- Kläerner, G.; Lee, J. I.; Davey, M. H. & Miller, R. D. (1999). Exciton Migration and Trapping in Copolymers Based on Dialkylfluorenes. *Adv. Mater.*, Vol.11, No.2, (February 1999) pp.115-119, ISSN 0935-9648.
- Lamansky, S.; Djurovich, P.; Murphy, D.; Abdel-Razzaq, F.; Lee, H.; Adachi, C.; Burrows, P.; Forrest, S. & Thompson, M. (2001). Highly Phosphorescent Bis-Cyclometalated Iridium Complexes: Synthesis, Photophysical Characterization, and Use in Organic Light Emitting Diodes. *J. Am. Chem. Soc.*, Vol.123, No.18, (May 2001) pp.4304-4312, ISSN 0002-7863.
- Li, H.; Liu, C.; Guo, G.; Zhou, X.; Xie, P.; Yu, S. & Zhang, R. (2002). Self-assembling directed synthesis of a novel terephthalamide-bridged ladderlike polysiloxane. *J. Polym. Sci. A: Polym. Chem.*, Vol.40, No.18, (September 2002) pp.3161-3170, ISSN 0887-624X.
- Liao, L.; Pang, Y.; Ding, L. & Karasz, F. E. (2001). Blue-Emitting Soluble Poly(m-phenylene-vinylene) Derivatives. *Macromolecules*, Vol.34, No.21, (September 2001) pp.7300-7305, ISSN 0024-9297.
- Liu, C.; Zhao, H.; Zhang, Y.; Xie, P. & Zhang, R. (2000). Synthesis and characterization of a novel reactive ladderlike 4,4'-phenylene ether-bridged polyvinylsiloxane. *J. Polym. Sci. A: Polym. Chem.*, Vol.38, No.15, (August 2000) pp.2702-2710, ISSN 0887-624X.
- Loy, D. A. & Shea, K. J. (1995). Bridged Polysilsesquioxanes. Highly Porous Hybrid Organic-Inorganic Materials. *Chem. Rev.*, Vol.95, No.5, (July 1995) pp.1431-1442, ISSN 0009-2665.
- Marsitzky, D.; Vestberg, R.; Blainey, P.; Tang, B. T.; Hawker, C. J. & Carter, K. R. (2001). Self-Encapsulation of Poly-2,7-fluorenes in a Dendrimer Matrix. *J. Am. Chem. Soc.*, Vol.123, No. 29, (July 2001) pp.6965-6972, ISSN 0002-7863.

- Martin, R. E. & Diederich, F. (1999). Linear monodisperse  $\pi$ -conjugated oligomers: model compounds for polymers and more. *Angew. Chem., Int. Ed.*, Vol.38, No.10, (May 1999) pp.1351-1377, ISSN 1433-7851.
- Müllen, K. & Wegner, G. (1999). *Electronical Materials: The Oligomer Approach*, Müllen, & Wegner, K. G. Eds., Wiley-VCH, ISBN 3527294384, Weinheim, Germany.
- Okoshi, K.; Sakajiri, K.; Kumaki, J. & Yashima, E. (2005). Well-Defined Lyotropic Liquid Crystalline Properties of Rigid-Rod Helical Polyacetylenes. *Macromolecules*, Vol.38, No.10, (May 2005) pp.4061-4064, ISSN 0024-9297.
- Pogantsch, A.; Wenzl, F. P.; List, E. J. W.; Leising, G.; Grimsdale, A. C. & Müllen, K. K. (2002). Polyfluorenes with Dendron Side Chains as the Active Materials for Polymer Light-Emitting Devices. *Adv. Mater.*, Vol.14, No.15, (August 2002) pp.1061-1064, ISSN 0935-9648.
- Ren, Z.; Cao, X.; Xie, P.; Zhang, R.; Yan, S. & Ma, Y. (2009). Supramolecular architecture-directed synthesis of a reactive and purely inorganic ladder polyhydrosilsesquioxane. *Chem. Commun.*, Vol.45, No.27, (July 2009) pp.4079-4081, ISSN 1359-7345.
- Ren, Z.; Xie, P.; Jiang, S.; Yan, S. & Zhang, R. (2010). Study of the Supramolecular Architecture-directed Synthesis of a Well-defined Triple-chain Ladder Polyphenylsiloxane. *Macromolecules*, Vol.43, No.5, pp.2130-2136, ISSN 0024-9297.
- Scherf, U. & Müllen, K. (1995). The Synthesis of Ladder Polymers, In: *Adv. Polym. Sci.*, Abe, A. et al., Vol. 123, pp.1-40, Springer Berlin, ISBN 978-3-540-58908-2, Heidelberg, Germany.
- Scherf, U. (1998). Conjugated Ladder-Type Structures, In: *Handbook of Conducting Polymers*, Second Edition, Skotheim, T.; Elsenbaumer, R. L. & Reynolds, J. R., Chapter 14, p.363, Marcel Dekker, ISBN 0824700503, New York, Basel, Hong Kong.
- Scherf, U. (1999). Ladder-type materials. *J. Mater. Chem.*, Vol.9, No.9, (September 1999) pp.1853-1864, ISSN 0959-9428.
- Segalman, R. A.; McCulloch, B.; Kirmayer, S. & Urban, J. J. (2009). Block Copolymers for Organic Optoelectronics. *Macromolecule*, Vol.42, No.23, (December 2009) pp.9205-9208, ISSN 0024-9297.
- Service, R. F. (2005). Organic LEDs Look Forward to a Bright, White Future. *Science*, Vol.310, No.5755, (December 2005) pp.1762-1763, ISSN 0036-8075.
- Setayesh, S.; Grimsdale, A. C.; Weil, T.; Enkelmann, V.; Müllen, K.; Meghdadi, F.; List, E. J. W. & Leising, G. (2001). Polyfluorenes with Polyphenylene Dendron Side Chains: Toward Non-Aggregating, Light-Emitting Polymers. *J. Am. Chem. Soc.*, Vol.123, No.5, (February 2001) pp.946-953, ISSN 0002-7863.
- Shea, K. J. & Loy, D. A. (2001). Bridged Polysilsesquioxanes. Molecular-Engineered Hybrid Organic-Inorganic Materials. *Chem. Mater.*, Vol.13, No.10, (October 2001) pp.3306-3319, ISSN 0897-4756.
- Shin, W. S.; Jeong, H. H.; Kim, M. K.; Jin, S. H.; Kim, M. R.; Lee, J. K.; Lee, J. W. & Gal, Y. S. (2006). Effects of functional groups at perylene diimide derivatives on organic photovoltaic device application. *J. Mater. Chem.*, Vol.16, No.4, (January 2006) pp.384-390, ISSN 0959-9428.

- Singh, M.; Chae, H. S.; Froehlich, J. D.; Kondou, T.; Li, S.; Mochizuki, A. & Jaabbour, G. E. (2009). Electroluminescence from printed stellate polyhedral oligomeric silsesquioxanes. *Soft. Mater.*, Vol.5, No.16, (August 2009) pp.3002-3005, ISSN 1744-683X.
- Singh, M.; Haverinen, H. M.; Dhagat, P. & Jabbour, G. E. (2010). Inkjet Printing—Process and Its Applications. *Adv. Mater.*, Vol.22, No.6, (February 2010) pp.673-685, ISSN 0935-9648.
- Smith, P. F.; Gerrior, P.; Xie, S.; Hor, A. M. & Popovic, Z. (1998). Degradation of Organic Electroluminescent Devices. Evidence for the Occurrence of Spherulitic Crystallization in the Hole Transport Layer. *Langmuir*, Vol.14, No.20, (September 1998) pp.5946-5950. ISSN 0743-7463.
- Son, S.; Dodabalapur, A.; Lovinger, A. J. & Galvin, M. E. (1995). Luminescence enhancement by the introduction of disorder into poly(p-phenylene vinylene). *Science*, Vol.269, No.5222, (March 1995) pp.376-378, ISSN 0036-8075.
- Sun, J.; Jiang, J.; Zhang, Y.; Xie, P.; Tang, H. & Zhang, R. (2003). H-bonding assisted template synthesis of a novel ladder-like organo-bridged polymethylsiloxane. *Polymer*, Vol.44, No.10, (May 2003) pp.2867-2874, ISSN 0032-3861.
- Sun, J.; Jiang, J.; Gao, X.; Tang, H.; Xie, P. & Zhang, R. (2003). Hydrogen-bonding-aided synthesis of novel ladderlike organobridged polysiloxane containing side-chain naphthyl groups. *J. Polym. Sci. A: Polym. Chem.*, Vol.41, No.5, (March 2003) pp.636-644, ISSN 0887-624X.
- Tang, H.; Sun, J.; Jiang, J.; Zhou, X.; Hu, T.; Xie, P. & Zhang, R. B. (2002). A Novel Aryl Amide-Bridged Ladderlike Polymethylsiloxane Synthesized by an Amido H-Bonding Self-Assembled Template. *J. Am. Chem. Soc.*, Vol.124, No.35, (September 2002) pp.10482-10488, ISSN 0002-7863.
- Unno, M.; Suto, A.; Matsumoto, H. (2002). Pentacyclic Laddersiloxane. *J. Am. Chem. Soc.*, Vol.124, No.8, (February 2004) pp.1574-1575, ISSN 0002-7863.
- Vanhee, S.; Rulkens, R.; Lehmann, U.; Rosenauer, C.; Schulze, M.; Kohlher, W. & Wegner, G. (1996). Synthesis and Characterization of Rigid Rod Poly(p-phenylenes). *Macromolecules*, Vol.29, No.15, (July 1996) pp.5136-5142, ISSN 0024-9297.
- van Hutten, P. F. & Hadziioannou, G. (2000). *Semiconducting polymers*, van Hutten, P. F. & Hadziioannou, G. Eds., pp. 561-613. Wiley-VCH, ISBN 9783527295074, Weinheim, Germany.
- Wan, Y.; Yang, L.; Zhang, J.; Zhang, P.; Fu, P.; Zhang, T.; Xie, P. & Zhang, R. (2006). Template of Concerted CT and H-Bonding Interactions-Directed Synthesis of a Highly Soluble and Perfect Organo-Bridged Ladder Polymethylsiloxane. *Macromolecules*, Vol.39, No. 2, (January 2006) pp.541-549, ISSN 0024-9297.
- Wang, Q.; Ding, J.; Zhang, B.; Mei, C.; Cheng, Y.; Xie, Z.; Wang, L.; Jing, X. & Wang, F. (2009). Harvesting Excitons Via Two Parallel Channels for Efficient White Organic LEDs with Nearly 100% Internal Quantum Efficiency: Fabrication and Emission-Mechanism Analysis. *Adv. Funct. Mater.*, Vol.19, No.1, (January 2009) pp.84-95, ISSN 1616-301X.
- Weinfurtnner, K. H.; Fujikawa, H.; Tokito, S. & Taga, Y. (2000). Highly efficient pure blue electroluminescence from polyfluorene: Influence of the molecular weight

- distribution on the aggregation tendency. *Appl. Phys. Lett.*, Vol.76, No.18, (May 2000) pp.2502-2504, ISSN 0003-6951.
- Wu, W. C.; Yeh, H. C.; Chan, L. H. C. & Chen, T. (2002). Red Organic Light-Emitting Diodes with a Non-doping Amorphous Red Emitter. *Adv. Mater.*, Vol.14, No.15, (August 2002) pp.1072-1075, ISSN 0935-9648.
- Wu, Z.; Xiong, Y.; Zou, J.; Wang, L.; Liu, J.; Chen, Q.; Yang, W.; Peng, J. & Cao, Y. (2008). High-Triplet-Energy Poly(9,9'-bis(2-ethylhexyl)-3,6-fluorene) as Host for Blue and Green Phosphorescent Complexes. *Adv. Mater.*, Vol.20, No.12, (June 2008) pp.2359-2364, ISSN 0935-9648.
- Xiao, L.; Chen, Z., Qu, B.; Luo, J.; Kong, S.; Gong, Q. & Kido, J. (2010). Recent Progresses on Materials for Electrophosphorescent Organic Light-Emitting Devices. *Adv. Mater.*, Vol.23, No.8, (February 2011) pp.926-952, ISSN 0935-9648.
- Xiao, S.; Nguyen, M.; Gong, X.; Cao, Y.; Wu, H.; Moses, D. & Heeger, A. J. (2003). Stabilization of Semiconducting Polymers with Silsesquioxane. *Adv. Funct. Mater.*, Vol.13, No.1, (January 2003) pp.25-29, ISSN 1616-301X.
- Yamamoto, S.; Yasuda, N.; Ueyama, A.; Adachi, H. & Ishikawa, M. (2004). Mechanism for the Formation of Poly(phenylsilsesquioxane). *Macromolecules*, Vol.37, No.8, (April 2004) pp.2775 -2778, ISSN 0024-9297.
- Yang, X.; Froehlich, J. D.; Chae, H. S.; Li, S.; Mochizuki, A. & Jaabour, G. E. (2009). Efficient Light-Emitting Devices Based on Phosphorescent Polyhedral Oligomeric Silsesquioxane Materials. *Adv. Funct. Mater.*, Vol.19, No.16, (August 2009) pp.2623-2629, ISSN 1616-301X.
- Yang, X.; Froehlich, J. D.; Chae, H. S.; Harding, B. T.; Li, S.; Mochizuki, A. & Jabbour, G. E. (2010). Efficient Light-Emitting Devices Based on Platinum-Complexes-Anchored Polyhedral Oligomeric Silsesquioxane Materials. *Chem. Mater.*, Vol.22, No.16, (August 2010) pp.4776-4782, ISSN 0897-4756.
- Yu, W. L.; Cao, Y.; Pei, J.; Huang, W. & Heeger, A. J. (1999). Blue polymer light-emitting diodes from poly(9,9-dihexylfluorene-alt-co-2, 5-didicyloxy-para-phenylene). *Appl. Phys. Lett.*, Vol.75, No.21, (November 1999) pp.3270-3272, ISSN 0003-6951.
- Zhang, J.; Chen, Z.; Fu, W.; Xie, P.; Li, Z.; Yan, S. & Zhang, R. (2010). Supramolecular Template-Directed Synthesis of Stable and High-Efficiency Photoluminescence 9, 10-Diphenylanthryl-Bridged Ladder Polysiloxane. *J. Polym. Sci., A: Polym. Chem.*, Vol.48, No.11, (May 2010) pp.2491-2497, ISSN 0887-624X.
- Zhang, R. B.; Dai, D. R.; Cui, L.; Xu, H.; Liu, C. Q. & Xie, P. (1999). A glance at the relation of stepwise coupling polymerization to supramolecular chemistry. *Mater. Sci. Eng. Vol.C10*, No.1-2, (December 1999) pp.13-18, ISSN 0928-4931.
- Zhang, T.; Deng, K.; Zhang, P.; Xie, P. & Zhang, R. B. (2006). Supramolecular Template-Directed Synthesis of Perfect Phenelenediimino-Bridged Ladderlike Polyphenylsiloxanes. *Chem. Eur. J.*, Vol.12, No.13, (April 2006) pp.3630-3635, ISSN 0947-6539.
- Zhang, X.; Xie, P.; Shen, Z.; Jiang, J.; Zhu, C.; Li, H.; Zhang, T.; Han, C. C.; Wan, L.; Yan, S. K. & Zhang, R. B. (2006). Confined Synthesis of a cis-Isotactic Ladder Polysilsesquioxane by Using a p-Stacking and H-Bonding Superstructure. *Angew. Chem., Int. Ed.*, Vol.45, No.19, (May 2006) pp.3112-3116, ISSN 1433-7851.

- Zhang, Z. X.; Hao, J.; Xie, P.; Zhang, X.; Han, C. C. & Zhang, R. B. (2008). A Well-Defined Ladder Polyphenylsilsesquioxane (Ph-LPSQ) Synthesized via a New Three-Step Approach: Monomer Self-Organization-Lyophilization–Surface-Confined Polycondensation. *Chem. Mater.*, Vol.20, No.4, (February 2008) pp.1322-1330, ISSN 0897-4756.
- Zhou, Q.; Yan, S.; Han, C. C.; Xie, P. & Zhang, R. (2008). Promising Functional Materials Based on Ladder Polysiloxanes. *Adv. Mater.*, Vol.20, No.15, (August 2008) pp.2970-2976, ISSN 0935-9648.
- Zhou, Q.; Zhang, J.; Ren, Z.; Yan, S.; Xie, P. & Zhang, R. (2008). A Stable and High-Efficiency Blue-Light Emitting Terphenyl-Bridged Ladder Polysiloxane. *Macromol. Rapid. Commun.*, Vol.29, No.14, (July 2008) pp.1259-1263, ISSN 1022-1336.

# Synthesis of Aromatic-Ring-Layered Polymers

Yasuhiro Morisaki and Yoshiki Chujo  
*Kyoto University,  
Japan*

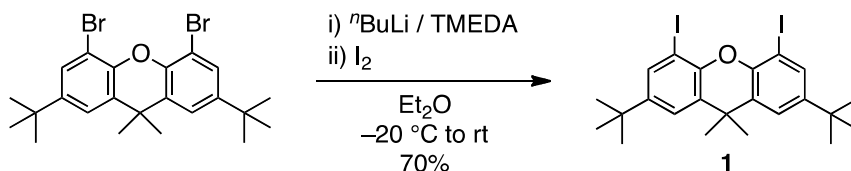
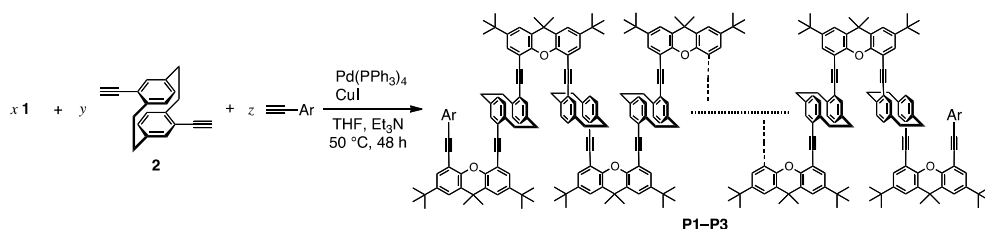
## 1. Introduction

In the fields of polymer and material chemistry, conjugated polymers (Skotheim et al., 2006) are an important class of polymers for next-generation optoelectronic materials due to their intriguing conductivity, photoluminescence, electroluminescence, and liquid crystallinity. Numerous conjugated polymers have been synthesized thus far, and a variety of unique conjugation systems have been incorporated into conjugated polymer backbones. One of the current research topics in this field focuses on the construction of layered and/or  $\pi$ -stacked structures. Layered  $\pi$ -electron systems are commonly found in both nature and artificial materials; for example, light-harvesting antenna complexes in photosynthetic systems, such as chlorophylls and bacteriochlorophylls, consist of layered  $\pi$ -electron systems. In optoelectronic materials, charges are delocalized in some layers and transferred from one electrode to the opposite one through the layered  $\pi$ -electron systems. Despite the importance of the layered structures of the  $\pi$ -electron systems, the synthesis of polymers comprising layered-aromatic rings and  $\pi$ -electron systems in a single polymer chain has rarely been studied (Morisaki & Chujo, 2006; Morisaki & Chujo, 2008a; Morisaki & Chujo, 2009d; Nakano, 2010).

To achieve the construction of the desired layered structure, xanthene, anthracene, and naphthalene compounds can be employed as scaffolds. The rotary motion of two aromatic units substituted at the 4,5-positions of xanthene, 1,8-positions of anthracene, and 1,8-positions of naphthalene is restricted due to steric hindrance, leading to a face-to-face structure. Thus, this review presents a summary of the syntheses and properties of a new class of aromatic ring-layered polymers, as well as oligomers containing xanthene, anthracene, and naphthalene scaffolds. Due to the vast number of studies on xanthene-, anthracene-, and naphthalene-based face-to-face dimeric systems, the polymers and oligomers (i.e., three or more face-to-face aromatic rings) are drawn.

## 2. Xanthene-based polymers

The 4,5-positions of xanthene can be readily functionalized by the treatment of xanthene compounds with alkyllithium reagents to yield the corresponding 4,5-dilithiated xanthenes due to the lithium-oxygen interaction, as shown in Scheme 1 (Morisaki & Chujo, 2005). The reaction of the 4,5-dilithiated xanthenes with halogens such as iodine results in the formation of diiodoxanthene derivative **1**, which is used in the palladium-catalyzed coupling reactions.

Scheme 1. Synthesis of monomer **1**Scheme 2. Synthesis of polymers **P1-P3**

entry	Mono-ethynylarene	Feed ratio $x : y : z$	Polymer	Yield (%)	$M_n$ (calcd.)	$M_n$ (found by $^1\text{H NMR}$ )
1		10 : 9 : 2	<b>P1a</b>	79	5956	4100
2		5 : 4 : 2	<b>P1b</b>	65	3082	3100
3		3 : 2 : 1	<b>P1c</b>	50	1933	2100
4		10 : 9 : 2	<b>P2a</b>	70	5896	7500
5		5 : 4 : 2	<b>P2b</b>	50	3022	4200
6		3 : 2 : 1	<b>P2c</b>	65	1872	2600
7		10 : 9 : 2	<b>P3a</b>	76	5786	5750
8		5 : 4 : 2	<b>P3b</b>	59	2912	3000
9		3 : 2 : 1	<b>P3c</b>	56	1762	1700

Table 1. Polymerization results

As shown in Scheme 2, the Sonogashira-Hagihara coupling (Tohda et al., 1975; Sonogashira, 2002) of diiodoxanthene **1** with either a diethynylarene, such as pseudo-*p*-diethynyl[2.2]paracyclophane **2**, or mono-ethynylarenes **3-5** proceeded smoothly to produce [2.2]paracyclophane-layered polymers (Morisaki et al., 2008b; Morisaki et al., 2009b). The results are summarized in Table 1. In the presence of mono-ethynylarenes **3-5**, aromatic groups were introduced as end-capping units. Polymers **P1**, **P2**, and **P3** possess [2.2]paracyclophane, anthracene, and nitrobenzene as the end-capping units, respectively. Their molecular weights were controlled by the molar ratios of the monomers, as shown in Table 1. For example, in the case of a molar ratio ( $x:y:z$ ) of 9:10:2, the number average molecular weights ( $M_n$ ) of **P1a**, **P2a**, and **P3a** were 4100, 7500, and 5750 (entries 1, 4, and 7), respectively, which were calculated from their respective  $^1\text{H NMR}$  spectra.



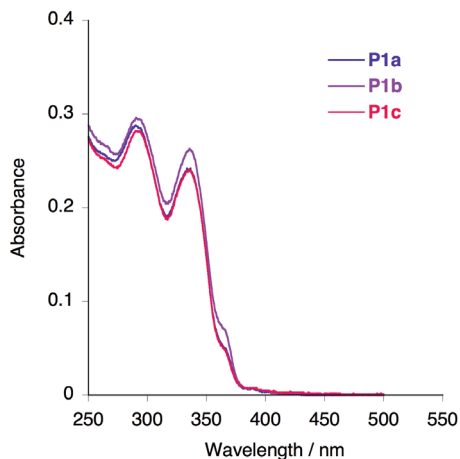


Fig. 1. UV-vis absorption (UV) spectra of polymers **P1a-c** in  $\text{CHCl}_3$  ( $1.0 \times 10^{-5}$  M).

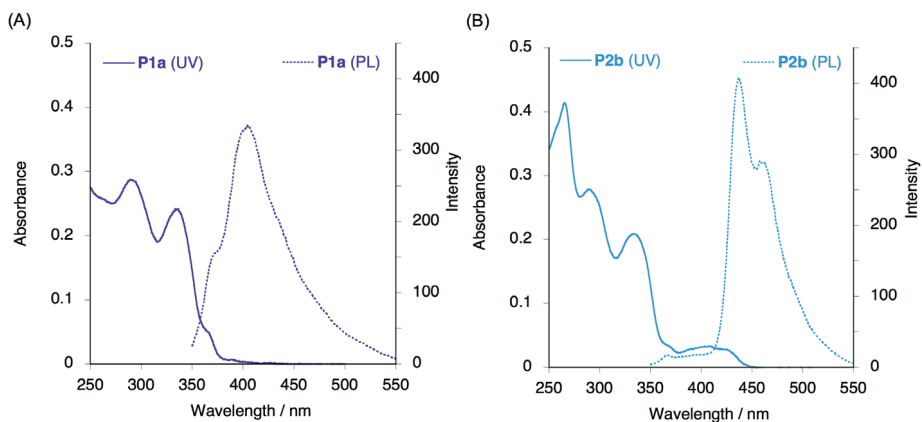


Fig. 2. (A) UV-vis absorption spectra in  $\text{CHCl}_3$  ( $1.0 \times 10^{-5}$  M) and photoluminescence (PL) spectra in  $\text{CHCl}_3$  ( $5.0 \times 10^{-7}$  M) of **P1a**. (B) UV-vis absorption spectra in  $\text{CHCl}_3$  ( $1.0 \times 10^{-5}$  M) and PL spectra in  $\text{CHCl}_3$  ( $5.0 \times 10^{-7}$  M) of **P2b**.

As shown in the UV-vis absorption spectra (in  $\text{CHCl}_3$ ,  $1.0 \times 10^{-5}$  M) of polymers **P1a-c** (Figure 1), there were  $\pi\text{-}\pi^*$  absorption bands at around 290 and 330 nm. The absorption spectra of **P1a-c** were independent of the number of the layered [2.2]paracyclophanes. It is reported that neighboring [2.2]paracyclophane units in the polymer backbone have sufficient free space according to X-ray crystallographic analysis of the model compound (Morisaki et al., 2009a). Therefore,  $\pi\text{-}\pi$  interactions among [2.2]paracyclophane units in a single polymer chain are considered to be weak in the ground state.

The optical properties of polymers **P1a** ( $M_n = 4100$ ) and **P2b** ( $M_n = 4200$ ) were compared. Figures 2A and 2B show the UV-vis absorption and emission spectra of polymers **P1a** and **P2**, respectively. As shown in Figure 2A (see also Figure 1), the  $\pi\text{-}\pi^*$  band of the layered [2.2]paracyclophane units was observed in the spectrum of **P1a**, whereas a sharp absorption peak at around 270 nm and a broad absorption peak at around 400 nm appeared in the

spectrum of **P2b** (Figure 2B). These new absorption bands were derived from the anthracene units at the polymer **P2b** chain ends.

Polymer **P1a** emitted blue light with a peak at around 400 nm after excitation at 334 nm (Figure 2A), which was attributed to emission from the layered [2.2]paracyclophane moieties. **P2b** exhibited a quite different photoluminescence spectrum with a peak at around 450 nm with a vibrational structure on the excitation wavelength of 334 nm (Figure 2B). This excitation wavelength excited only the layered [2.2]paracyclophane moieties because the end-capping anthracene units do not have an absorption band around 334 nm. Thus, **P2b** emitted from the terminal anthracenes instead of emitting from the layered [2.2]paracyclophanes. As shown in Figures 2A and 2B, the emission peak of the layered cyclophane units (at 400 nm in Figure 2A) efficiently overlapped with the absorption band of the anthracene moieties (at around 400 nm in Figure 2B). Time-resolved photoluminescence spectra of **P2b** are shown in Figure 3; these spectra indicate that emission from the cyclophane units decreased while that from the anthracene units increased. These results suggest that fluorescence resonance energy transfer (FRET) (Förster, 1946) from the cyclophane units to the end-capping anthracenes occurs.

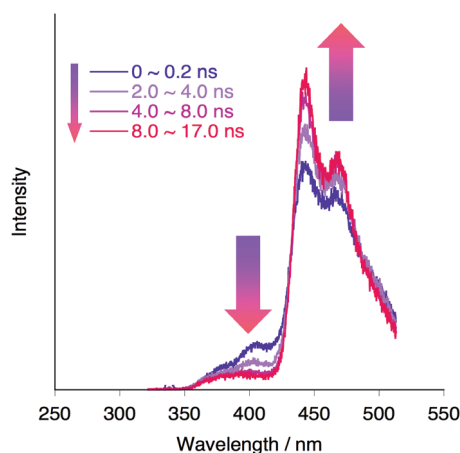


Fig. 3. Time-resolved PL spectra of polymer **P2b** in  $\text{CHCl}_3$ .

The UV-vis absorption spectra of the nitrobenzene-end-capped polymers **P3a-c** (in  $\text{CHCl}_3$ ,  $1.0 \times 10^{-5}$  M) are shown in Figure 4A. These spectra exhibited broad absorption bands around 400 nm in addition to the  $\pi-\pi^*$  transition band of the layered [2.2]paracyclophanes; the absorbance around 400 nm increased as the  $M_n$  value decreased. This absorption band arises from the polymer chain ends that contain nitrophenyl groups as the concentration of the end-capping nitrophenyl groups increased with a decreasing  $M_n$  value. As can be expected, the emission from the [2.2]paracyclophane moieties was quenched by the introduction of the nitrophenyl units at the polymer chain ends due to the good overlap between the emission peak of the [2.2]paracyclophane moieties and the absorption band of the nitrophenyl moieties. As shown in Figure 4B, the photoluminescence peak intensities and the photoluminescence quantum efficiencies of **P3a-c** decreased relative to those of **P1a**. The end-capping nitrophenyl groups of **P3a-c** effectively quenched the photoluminescence from the layered [2.2]paracyclophane moieties by FRET. It is reported that the end-capping nitrophenyl group quenched photoluminescence  $1.0 \times 10^4$  times more effectively than the addition of nitrobenzene to a **P1a** solution.

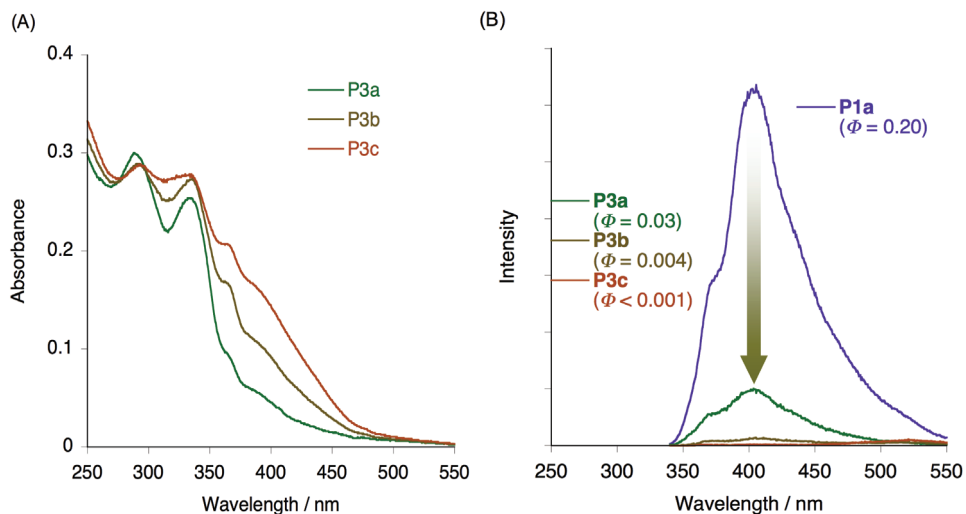
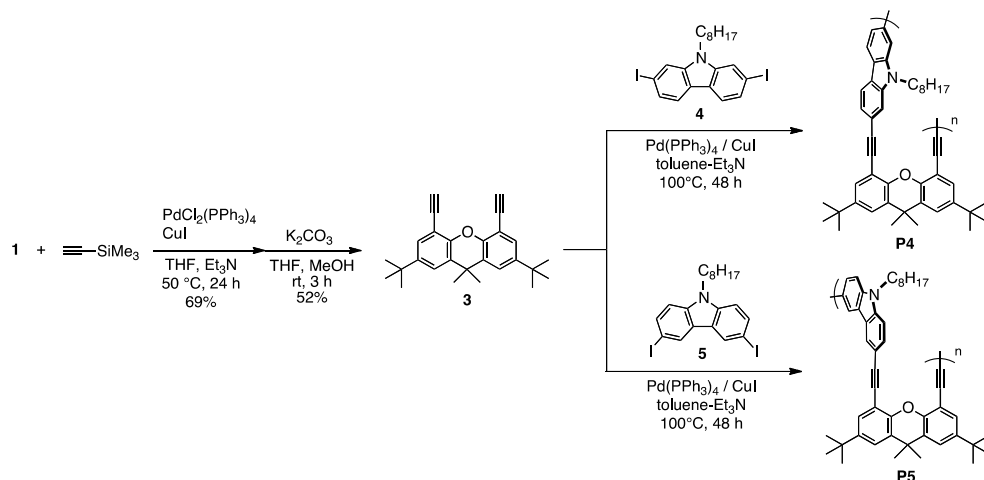


Fig. 4. (A) UV spectra in CHCl<sub>3</sub> (1.0 × 10<sup>-5</sup> M) and photoluminescence (PL) spectra in CHCl<sub>3</sub> (5.0 × 10<sup>-7</sup> M) of polymers **P3a-c**. (B) UV spectra in CHCl<sub>3</sub> (1.0 × 10<sup>-5</sup> M) and PL spectra in CHCl<sub>3</sub> (5.0 × 10<sup>-7</sup> M) of polymers **P1a** and **P3a-c**.

This synthetic approach using xanthene as the scaffold makes it possible to incorporate various aromatic compounds as the layered ring units in a single polymer chain. Scheme 3 shows the synthesis of 4,5-diethynylxanthene **3** as well as its polymerization with diiodocarbazoles **4** and **5**. The results of polymerization are summarized in Table 2. Polymers **P4** (Fernandes et al., 2010) and **P5** (Morisaki et al., 2009e) comprise 2,7-substituted and 3,6-substituted carbazoles, and their  $M_n$  values were calculated to be 2500 and 2300 (Table 2), respectively.



Scheme 3. Synthesis of monomer **3** and polymers **P4** and **P5**.

entry	Polymer	Yield (%)	$M_n$	$M_w/M_n$
1	<b>P4</b>	63	2500	1.3
2	<b>P5</b>	62	2300	1.1

Table 2. Synthesis of polymers **P4** and **P5**

$M_n$  and  $M_w/M_n$  were calculated by MALDI-TOF mass spectra and GPC ( $\text{CHCl}_3$ , polystyrene standards), respectively.

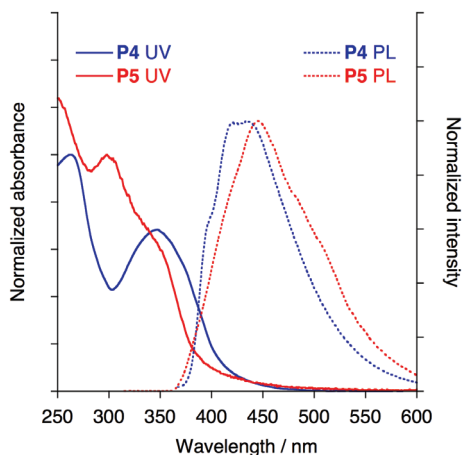


Fig. 5. UV spectra in  $\text{CHCl}_3$  ( $1.0 \times 10^{-5}$  M) and PL spectra in  $\text{CHCl}_3$  ( $1.0 \times 10^{-7}$  M) of polymers **P4** and **P5**.

The UV-vis absorption and photoluminescence spectra of **P4** and **P5** in diluted  $\text{CHCl}_3$  solution are shown in Figure 5. The conjugation length of **P4**, which consists of 2,7-linked carbazole units, was longer than that of **P5**, which has 3,6-linked carbazole units.  $\pi$ -Conjugation of the 3,6-linked carbazole unit is not effective because the 3,6-linked carbazole unit on xanthene is twisted due to steric hindrance, which results in the shorter wavelength of the absorption peak in **P5** as compared to that of **P4**. In Figure 5, **P4** and **P5** are shown to exhibit emission peak maxima at 431 and 425 nm, respectively. The Stokes shift of **P5** was greater than that of **P4** suggesting that the conformation change from the ground state to the excited state of the 3,6-linked carbazole is larger than that of 2,7-linked carbazole due to the boomerang shape of the 3,6-linked carbazole unit (Morin et al., 2005; Grazulevicius et al., 2003).

The fluorescence emission spectrum of *N*-(*p*-tolyl)carbazole-layered polymer **P6** with nitrophenyl groups at the polymer chain ends was investigated to show its potential as a single molecular wire in comparison with **P7**. Figure 6A shows the photoluminescence spectra of polymers **P6** and **P7** in  $\text{CHCl}_3$ . The peak intensity of **P6** clearly decreased and the photoluminescence quantum yield ( $\Phi_{\text{PL}}$ ) of **P6** was estimated to be 1% indicating that the terminal nitrophenyl moieties in **P6** quenched the emission from the layered carbazole units. To compare, 1, 10, and 100 equivalents of nitrobenzene molecules per carbazole unit were added as a fluorescence quencher to a solution of **P7**, as shown in Figure 6B. However, ineffective quenching of the emission from the layered carbazole in **P7** was observed. The carbazole-layered polymer can also act as a molecular wire that transfers energy and/or electrons to the polymer termini in the same manner as the cyclophane-layered polymers discussed above.

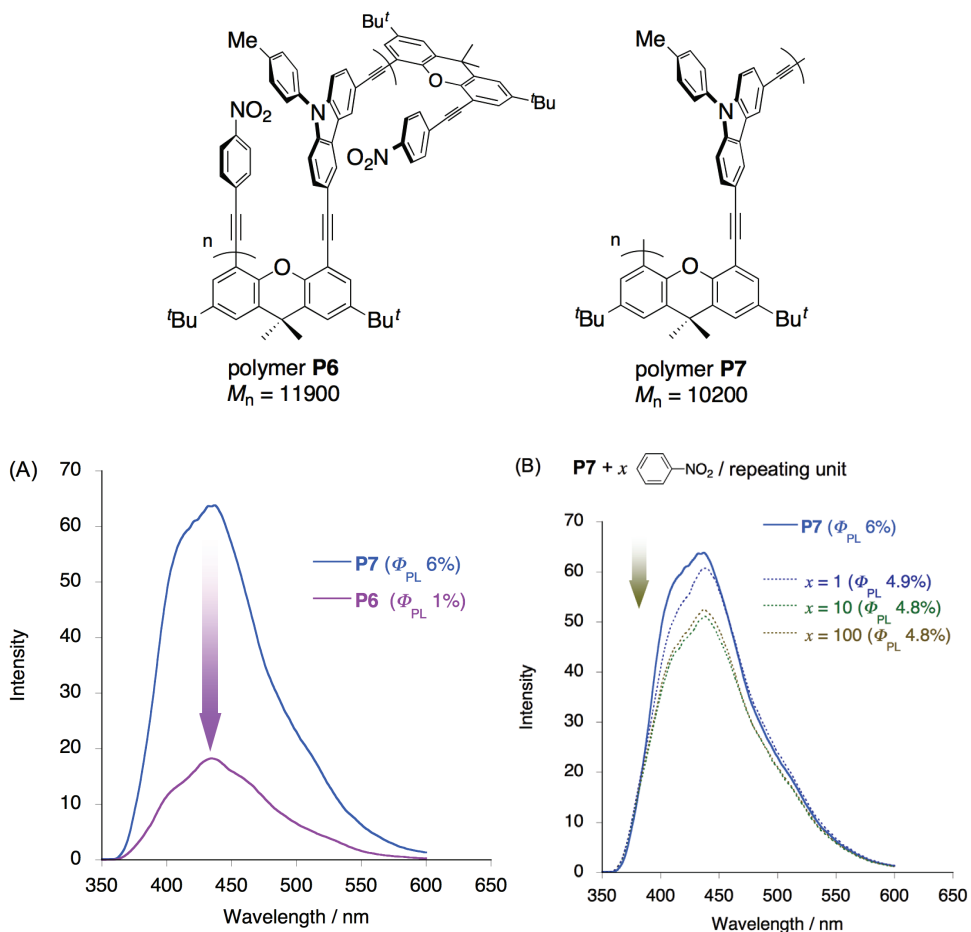
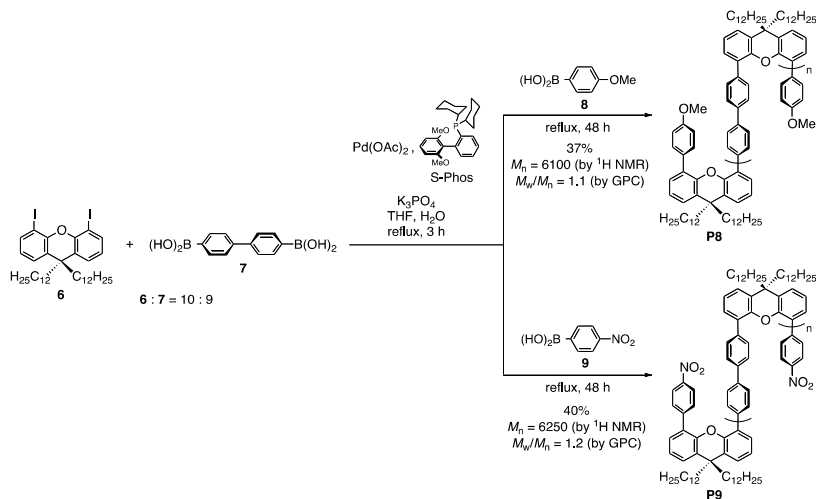


Fig. 6. (A) UV spectra of polymers **P6** and **P7** in  $\text{CHCl}_3$  ( $1.0 \times 10^{-5}$  M). (B) PL spectra of polymer **P7** with nitrobenzene in  $\text{CHCl}_3$  ( $1.0 \times 10^{-7}$  M).

By using xanthene as the scaffold, not only aromatic compounds but also  $\pi$ -conjugated oligomers can be one-dimensionally layered in a single polymer chain. Scheme 4 outlines the synthetic procedure of the oligo(*p*-phenylene)-layered polymers (Morisaki et al., 2009c) by modified Suzuki-Miyaura coupling (Miyaura et al., 1979; Miyaura & Suzuki, 1995). In this case, *tert*-butyl groups were not introduced into the xanthene skeleton because of their steric bulk and dodecyl groups were substituted at the 9-position of xanthene in order to improve the solubility of the polymers. The reaction of monomers **6** and **7** (10:9) was carried out in the presence of  $\text{Pd}(\text{OAc})_2$  with 2-dicyclohexylphosphino-2',6'-dimethoxybiphenyl (S-Phos) as the ligand (Scheme 4) (Barder et al., 2005), and the successive addition of *p*-methoxyphenyl boronic acid **8** and *p*-nitrophenyl boronic acid **9** afforded the corresponding polymers **P8** and **P9** in 37% and 40% isolated yields with  $M_n$  values of 6100 and 6250, respectively.



Scheme 4. Synthesis of polymers **P8** and **P9**.

Figure 7A shows the photoluminescence spectra of **P8** and **P9** in diluted  $CHCl_3$  solutions; the spectra are almost identical and feature peak maxima at around 410 nm. As can be expected, the peak intensity of **P9** ( $\Phi_{PL} = 55\%$ ) was lower than that of **P8** ( $\Phi_{PL} = 25\%$ ), indicating that the end-capping nitrobenzene units of **P9** quench the emission from the layered biphenylenes. The photoluminescence spectra of **P8**, which possesses *p*-methoxyphenyl chain ends, with an excess amount of nitrobenzene are shown in Figure 7B. However, the quenching effect of the additional nitrobenzene was quite low despite the addition of 100 equivalents of nitrobenzene per biphenylene unit. According to the Stern–Volmer plots, the Stern–Volmer coefficient ( $K_{sv}$ ) of **P9** was  $10^4$  times larger than that of **P8** upon the addition of nitrobenzene. The two end-capping nitrophenyl moieties in **P9** effectively quenched the photoluminescence from the layered biphenylenes via through-space interactions of the single polymer chain.

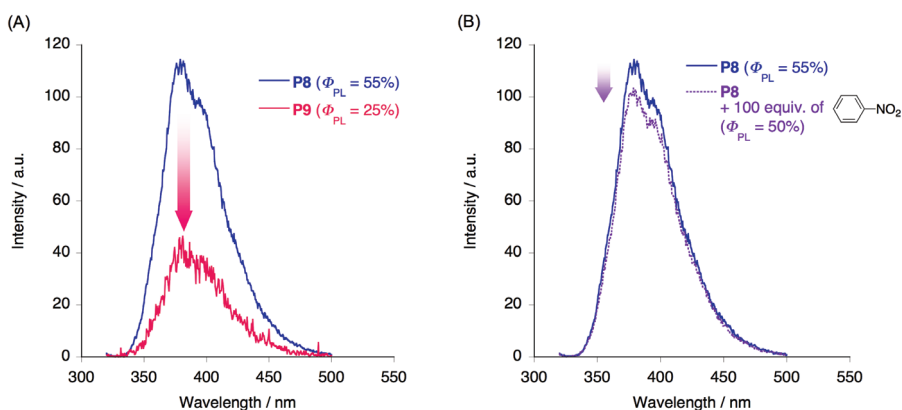
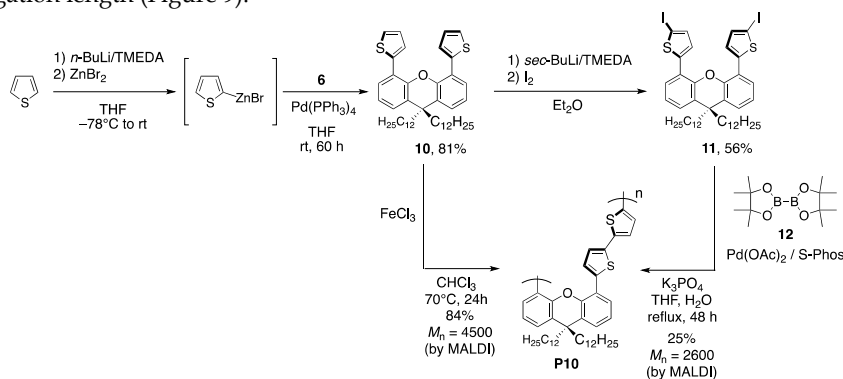


Fig. 7. (A) UV spectra of polymers **P8** and **P9** in  $CHCl_3$  ( $1.0 \times 10^{-5}$  M). (B) PL spectra of polymer **P8** with 100 equiv of nitrobenzene in  $CHCl_3$  ( $1.0 \times 10^{-7}$  M).

Oligothiophenes were also layered on xanthenes (Morisaki et al., 2009f; Morisaki et al., 2010b); the synthetic routes for the bithiophene-layered polymer **P10** by iron-mediated oxidative coupling and modified Suzuki-Miyaura coupling are shown in Scheme 5. Bis(thienyl)xanthene monomer **10** was prepared in 81% yield by Negishi coupling (Negishi et al., 1977; Negishi, 1982) of 2-thienylzinc bromide and **6** and then treated with  $\text{FeCl}_3$  to obtain the corresponding polymer **P10** in 84% isolated yield with an  $M_n$  of 4500. However, **P10** was contaminated with a small amount of iron species. Therefore, an alternate synthesis was pursued; compound **10** was readily iodinated to afford monomer **11** in 56% yield, which was reacted with bis(pinacolato)diboron **12** in the presence of a catalytic amount of  $\text{Pd}(\text{OAc})_2/\text{S-Phos}$  to give **P10** in 25% isolated yield with an  $M_n$  of 2600.

The UV-vis absorption spectra of **P10** and model compound **13** in  $\text{CHCl}_3$  solutions are shown in Figure 8. The absorption maximum of **P10** was observed at around 360 nm, while that of **13** appeared at 379 nm due to the contribution of the coplanarity of the bithiophene and the methoxyphenyl groups of **11** in the ground state (Figure 9). This was supported by the  $^1\text{H}$  NMR spectrum of **13**. The bithiophene units in **P10** rotate freely to avoid steric hindrance, while the bithiophene units in **13** adopt a relatively planar structure to extend its conjugation length (Figure 9).



Scheme 5. Synthesis of polymer **P10**.

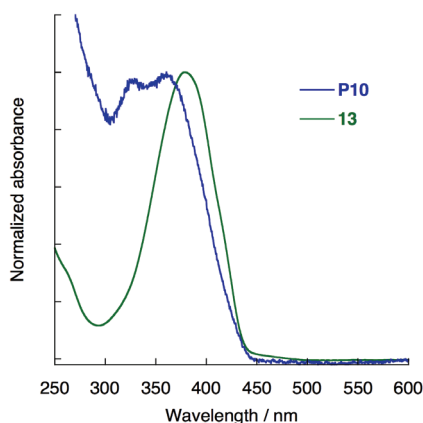


Fig. 8. UV spectra of polymer **P10** and compound **13** in  $\text{CHCl}_3$  ( $1.0 \times 10^{-5}$  M).

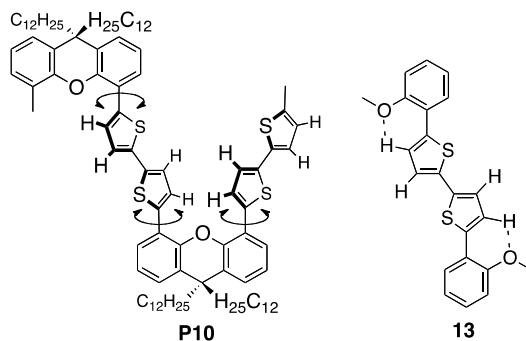
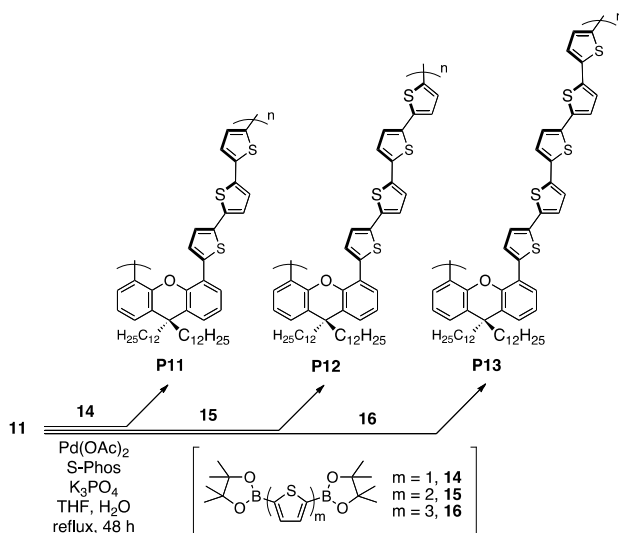


Fig. 9. Structures of polymer **P10** and compound **13**.

Terthiophene-, quarterthiophene- and quinquethiophene-layered polymers were synthesized by the coupling reaction of **11** with monomers **14–16**, as shown in Scheme 6; the polymerization results are listed in Table 3. The isolated yields of **P10–13** were relatively low (19%–40%) due to repeated reprecipitation and purification using recyclable liquid chromatography. The polymers obtained were soluble in common organic solvents such as THF,  $\text{CH}_2\text{Cl}_2$ ,  $\text{CHCl}_3$ , and toluene. The polymer thin films were readily formed by spin-coating from their toluene solution. The thermal stabilities of the polymers were examined by thermogravimetric analysis (TGA) and all polymers were sufficiently stable with a 10% weight loss at temperatures around 400 °C under  $\text{N}_2$  (Figure 10).



Scheme 6. Synthesis of polymers **P11–P13**.

The UV-vis absorption spectra and PL spectra of **P10–P13** in  $\text{CHCl}_3$  are shown in Figure 11; the data are listed in Table 3. In Figure 11A, absorption bands assigned to the  $\pi\text{--}\pi^*$  transition of oligothiophenes were observed, and the absorption maxima bathochromically shifted as the number of thiophene rings increased.



entry	Polymer	Yield (%)	$M_n$	$M_w/M_n$	$\lambda_{\text{abs,max}}$ (nm)	$\lambda_{\text{PL,max}}$ (nm)	$\Phi_{\text{PL}}$
1	<b>P10</b>	25	2600	1.1	360	440, 470	0.12
2	<b>P11</b>	40	3200	1.0	358, 380(sh)	480, 504	0.20
3	<b>P12</b>	30	2800	1.1	412	520(sh), 541	0.29
4	<b>P13</b>	19	3800	1.1	420	534, 562	0.27

Table 3. Polymerization results and optical properties

$M_n$  and  $M_w/M_n$  were calculated by MALDI-TOF mass spectra and GPC ( $\text{CHCl}_3$ , polystyrene standards), respectively.  $\lambda_{\text{abs,max}}$  was measured in  $\text{CHCl}_3$  ( $1.0 \times 10^{-5}$  M).  $\lambda_{\text{PL,max}}$  was measured in  $\text{CHCl}_3$  ( $1.0 \times 10^{-7}$  M) excited at each absorption maximum.  $\Phi_{\text{PL}}$  was absolute quantum efficiency in solution.

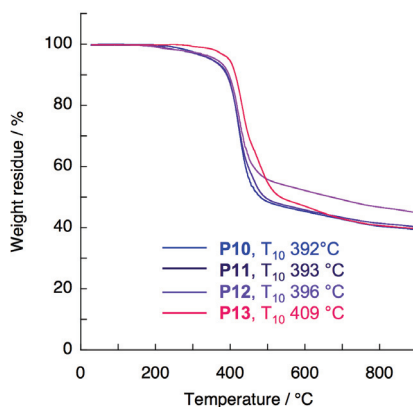
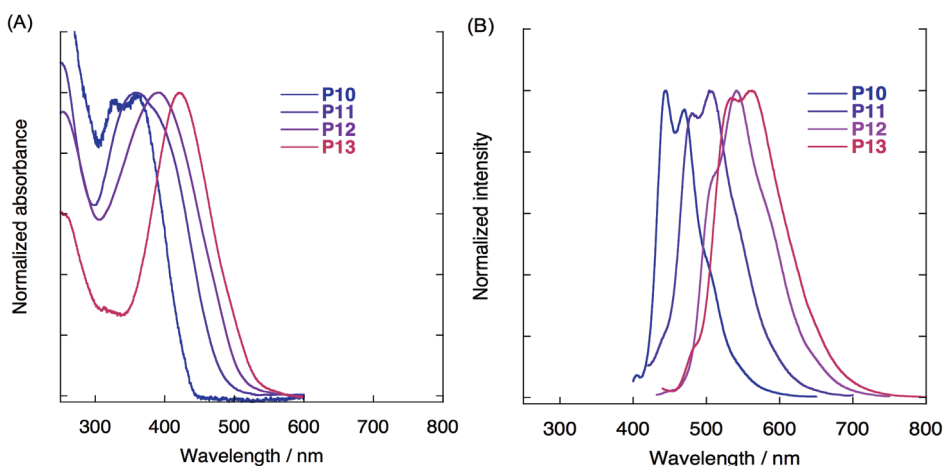
Fig. 10. TGA thermograms of polymers **P10-13**.Fig. 11. (A) UV spectra of polymers **P10-13** in  $\text{CHCl}_3$  ( $1.0 \times 10^{-5}$  M). (B) PL spectra of polymers **P10-13** in  $\text{CHCl}_3$  ( $1.0 \times 10^{-7}$  M).

Figure 11B exhibits the photoluminescence spectra of **P10–P13** by excitation at each absorption maximum. The red-shift of the spectra was observed with an increase in the number of the thiophene rings in the same manner as in common conjugated systems. The photoluminescence absolute quantum efficiencies ( $\Phi_{\text{PL}}$ ) in  $\text{CHCl}_3$  solutions were estimated to be 0.12–0.29, as listed in Table 3. Generally, the  $\Phi_{\text{PL}}$  values of the  $\pi$ -stacked bithiophenes were low (0.001–0.054) because of the intermolecular aggregation of bithiophenes due to strong  $\pi$ - $\pi$  interactions. The layered oligothiophenes are considered to be isolated in a single polymer chain due to the relatively long distance between the 4- and 5-positions of the xanthene skeleton despite the layered structure of **P10–P13**.

Cyclic voltammetric (CV) analyses of **P10–P13** were carried out in  $\text{CH}_2\text{Cl}_2$ , and the resultant cyclic voltammograms are shown in Figure 12. Broad oxidation peaks were observed ranging from 0.4 to 0.5 V with a ferrocene/ferrocenium ( $\text{Fc}/\text{Fc}^+$ ) external reference, as shown in Figure 12. The onset potentials of **P10–P13** were found to be approximately 0.15 V (vs.  $\text{Fc}/\text{Fc}^+$ ); they decreased slightly as the number of thiophene rings increased. The HOMO energy levels of the polymers were calculated to be approximately  $-5.0$  eV, suggesting that the oligothiophene-layered polymers have potential for applications in optoelectronic devices as hole-transporting materials.

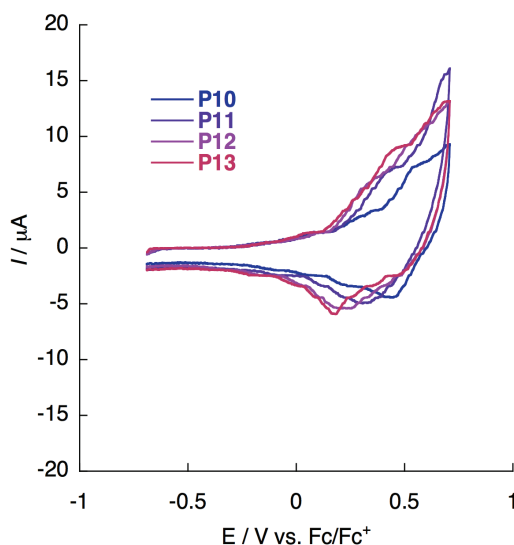
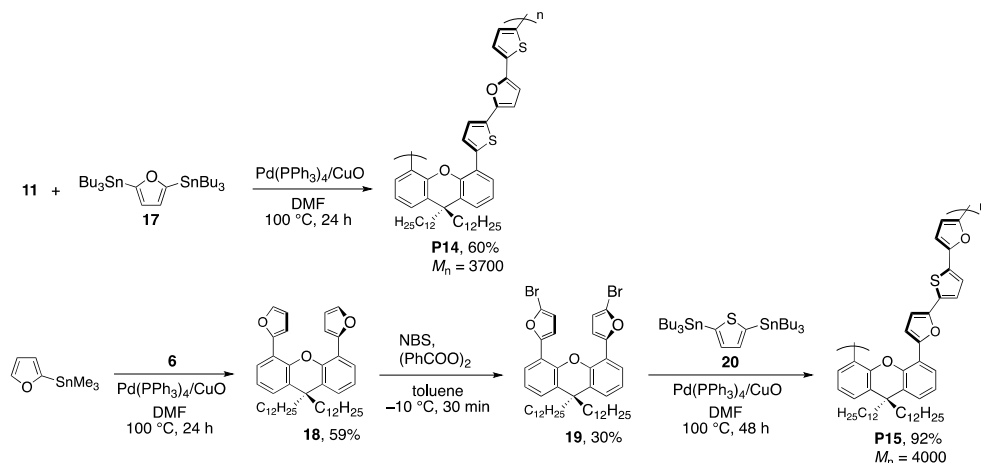
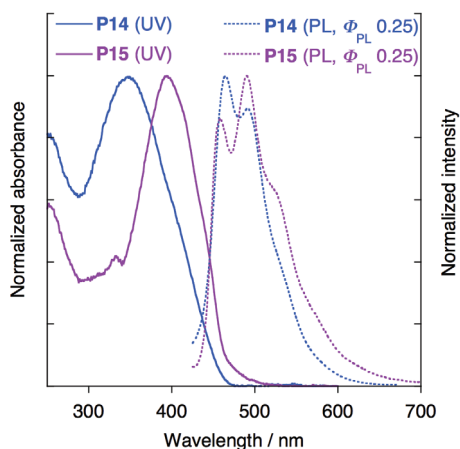


Fig. 12. Cyclic voltammograms of polymers **P10–13** in  $\text{CH}_2\text{Cl}_2$  (vs. ferrocene/ferrocenium).

Furan can also be incorporated as the layered-aromatic unit into the oligothiophene-layered polymers (Fernandes et al., 2011). As shown in Scheme 7, the treatment of **11** with 2,5-bis(tributylstannyl)furan **17** in the presence of  $\text{Pd}(\text{PPh}_3)_4/\text{CuO}$  afforded the corresponding polymer **P14**, which contains a thiophene/furan/thiophene oligomer as the layered unit. Migita-Kosugi-Stille coupling (Kosugi et al., 1977; Milstein & Stille, 1978) of 4,5-bis(bromofuryl)xanthene **19** and 2,5-bis(tributylstannyl)thiophene **20** yielded polymer **P15**, which contains a furan/thiophene/furan oligomer as the layered unit (Scheme 7). The  $M_n$  values of **P14** and **P15** were 3700 and 4000, respectively.

Scheme 7. Synthesis of polymers **P14** and **P15**.

In the UV-vis absorption spectra ( $1.0 \times 10^{-5}$  M in THF) of **P14** and **P15** (Figure 13), the absorption maximum of **P14**, which was ascribed to the  $\pi$ - $\pi^*$  transition band of the thiophene/furan/thiophene moieties, was observed at 344 nm, while the absorption maximum of **P15**, consisting of furan/thiophene/furan units, appeared at 396 nm. It is reported that the absorption spectra were almost identical regardless of the thiophene/furan sequence. In addition, in the case of furan- and thiophene-substituted porphyrin systems, a longer  $\pi$ -conjugation length between the porphyrin ring and *meso*-substituted-furan was observed than between the porphyrin ring and *meso*-substituted-thiophene due to steric repulsion. Therefore, it is implied that the thiophene/furan/thiophene moiety in **P14** is more twisted against the xantheno scaffold than the furan/thiophene/furan moiety in **P15** in the ground state.

Fig. 13. UV spectra in  $\text{CHCl}_3$  ( $1.0 \times 10^{-5}$  M) and PL spectra in  $\text{CHCl}_3$  ( $1.0 \times 10^{-7}$  M) of polymers **P14** and **P15**.

The photoluminescence spectra of **P14** and **P15** ( $1.0 \times 10^{-7}$  M in THF) are shown in Figure 13. Both polymers exhibited similar photoluminescence spectra with the peak around 480 nm and photoluminescence quantum efficiencies of 0.25. The conformational change of **P14** from the twisted structure to the coplanar structure by photo-excitation resulted in a larger Stokes shift for **P14** than for **P15**. It is possible that the interactions among the layered  $\pi$ -electron systems in a single polymer chain are weak because of the relatively long distance between the 4- and 5-positions of the xanthene skeleton as well as because of the coplanarity of the layered  $\pi$ -electron system with xanthene in the excited state.

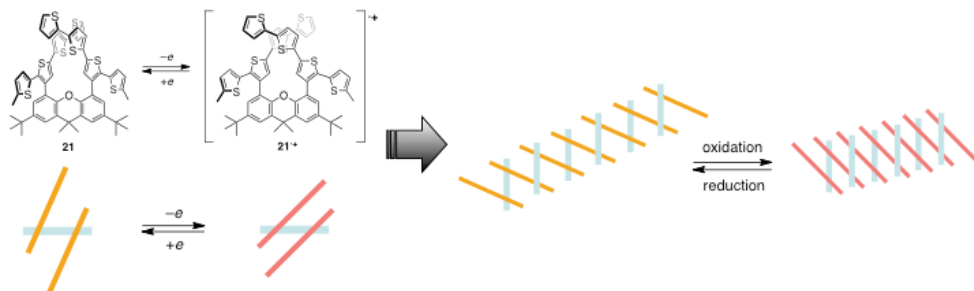


Fig. 14. Redox behavior of compound **21**.

Although it is not a polymer, xanthene-based compound **21**, which consists of layered quaterthiophenes, was synthesized (Takita et al., 2008), as shown in Figure 14. By chemical oxidation with  $\text{Et}_3\text{O SbCl}_6$  or electrical oxidation, one quaterthiophene was oxidized to form a  $\pi$ -dimer (mixed-valence compound). This class of polymer can potentially be applied to molecular actuation responding to the redox of quaterthiophenes (Figure 14). Oligothiophene-layered polymers based on calix[4]arene also exhibit similar redox behaviors (Yu et al., 2003; Yu et al., 2004; Casanovas et al., 2006; Alemán et al., 2006; Scherlis & Marzari, 2005; Song & Swager, 2008), suggesting that they are candidates for sensing and actuating materials as well.

### 3. Xanthene-based oligomers

Perilenediimide and its derivatives have been focused on as the active materials for light-harvesting system photovoltaics and charge/electron transfer processes. In order to obtain insight into the nature of the photophysical properties of perilenediimide aggregates, they were layered onto the xanthene scaffold. As shown in Figure 15, reference compound **22** as well as oligomers **23a-b**, and **24**, which contain two and three cofacial perilenediimides, respectively, were prepared (Giaino et al., 2008; Yoo et al., 2010). Their photophysical data are listed in Table 4. The absorption maxima of **23a-b** and **24** were shifted hypsochromically in comparison with that of **22** due to the formation of *H*-like aggregates. The photoluminescence spectrum of **22** exhibited a sharp spectrum with an emission maximum at 534 nm and vibronic structures at 576 nm and 624 nm. In contrast, the photoluminescence spectra of **23a-b** and **24** were broad and featureless; the spectrum of **23a** was highly broad with a peak at around 700 nm, and that of **23b** had a shoulder peak at around 550 nm and a broad peak at 650 nm. Time-resolved absorption and photoluminescence spectroscopy indicated that **23b** having 12-tricosanyl substituents exhibited slower formation of the

excimer-like excited state and had a higher energy than **23a**, which has n-octyl substituents, because of its more bulky substituents. These results imply that perilenediimide chromophores in **23a** adopt nearly optimal  $\pi$ -stacking. Their photophysical properties in the polymer matrix were also studied (Yoo et al, 2010). It was observed that the photoluminescence intensity and lifetime depended on the molecular conformations in the polymer matrix. Intramolecular overlap of the  $\pi$ -electron systems in perilenediimides would favor the use of n-type semiconductors.

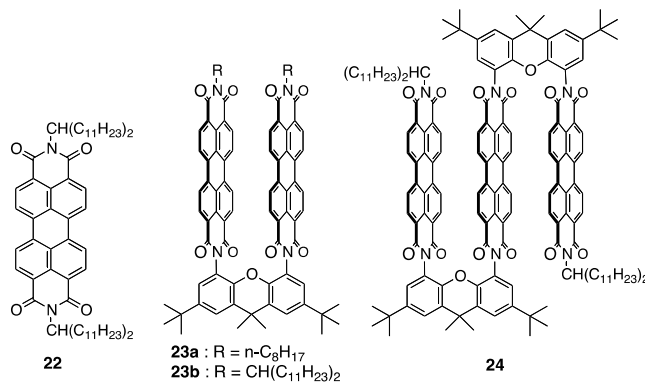


Fig. 15. Structures of compounds **22-24**.

entry	Compound	$\lambda_{\text{abs,max}} / \text{nm}$	$\lambda_{\text{em,max}} / \text{nm}$	$\Phi_{\text{PL}}$	$\tau_{\text{PL}} / \text{ns} (\lambda_{\text{em}})$
1	<b>22</b>	527	533	0.98	3.8±0.1 (550)
2	<b>23a</b>	490	735	0.02	9.2±0.1 (700)
3	<b>23b</b>	491	647	0.19	0.05±0.01 (550) 28.6±0.1 (700)
4	<b>24</b>	488	647	0.13	0.05±0.01 (550) 22.5±0.1 (700)

Table 4. Photophysical Data of Compounds **22-24**

Photoluminescence spectra, quantum efficiencies ( $\Phi_{\text{PL}}$ ), and lifetimes ( $\tau_{\text{PL}}$ ) were determined with an excitation wavelength of 400 nm.

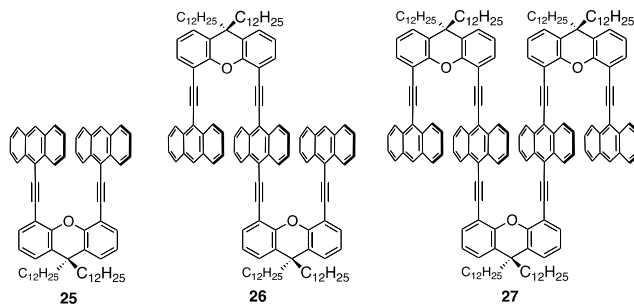
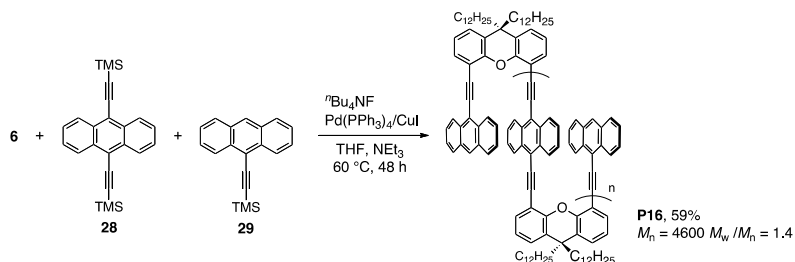


Fig. 16. Structures of oligomers **25-27**.

$\pi$ -Stacked oligomers **25–27** comprising anthracene as the layered unit and xanthene as the scaffold were synthesized (Morisaki et al., 2010a) by repeated Sonogashira-Hagihara couplings (Figure 16). An anthracene-stacked polymer, **P16**, was also prepared by the reaction of **6** with **28** and **29** in 59% yield with an  $M_n$  of 4600, as shown in Scheme 8. According to the  $^1\text{H}$  NMR spectra of oligomers **25–27** and polymer **P16**, the chemical shifts of the anthracene protons moved to a higher magnetic field than those of the common anthracene derivatives. Their signals gradually shifted as the number of stacked anthracene moieties increased because of the effect of the ring current of the neighboring anthracene rings.



Scheme 8. Synthesis of polymer **P16**.

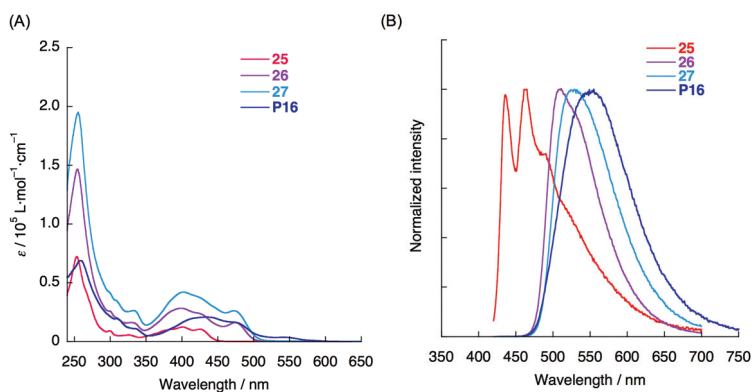
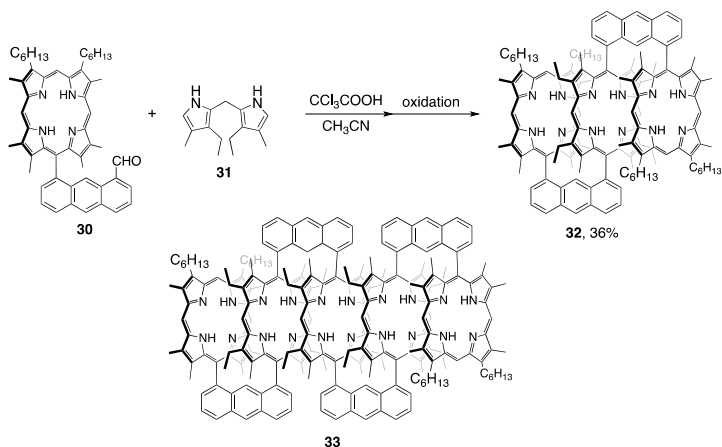


Fig. 17. (A) UV spectra of oligomers **25–27** and polymer **P16** in  $\text{CHCl}_3$  ( $1.0 \times 10^{-5}$  M). (B) PL spectra of oligomers **25–27** and polymer **P16** in  $\text{CHCl}_3$  ( $1.0 \times 10^{-7}$  M).

As shown in Figure 17A, the molar extinction coefficient ( $\epsilon$ ) of an absorption and a broad band at around 250 nm and 400 nm, respectively, increased in accordance with the number of anthracene rings. The photoluminescence spectrum of **25** in  $\text{CHCl}_3$  revealed an emission peak at around 450 nm with a clear vibrational structure (Figure 17B); excimer-like emission did not appear despite the face-to-face orientation of the two anthracenes in **25**. In contrast, the photoluminescence spectra of **26**, **27**, and **P16** were broad without any vibrational structure. A fluorescence life time measurement of **P16** indicated emission from the excimer-like structures of the anthracene moieties, whereas oligomers **26**, **27**, and polymer **P16** exhibited emission mainly from aggregates because of the buttressing effect of the anthracene rings. These phenomena are attributed to the intramolecular  $\pi$ -stacked structure of the anthracene rings in both the excited and ground states.

#### 4. Anthracene-based oligomers and polymers

Anthracene can be employed as the scaffold to layer aromatic rings one-dimensionally. Aromatic rings at the 1- and 8-positions of anthracene readily face each other due to the presence of hydrogen at the 9-position. Face-to-face porphyrin arrays, **32**, were constructed by condensation of formyl- and porphyrin-substituted anthracene, **30**, with dipyrromethane **31** followed by oxidation (Scheme 9) (Nagata et al., 1990). In addition, oligomer **33** comprising five-layered porphyrin was prepared from dimeric porphyrin (Scheme 9).



Scheme 9. Synthesis of oligomer **32** and structure of oligomer **33**.

According to the absorption spectra of **32–35** in 1,2-dichlorobenzene solutions, the Soret bands of the zinc complexes of **32** and **33** (face-to-face systems) were hypsochromically shifted, without being split, as the number of layered porphyrins increased. In contrast, those of **34** and **35** (linear systems, Figure 18) bathochromically shifted with a split that became larger with an increasing number of porphyrins. These results can be explained by the exciton coupling theory.

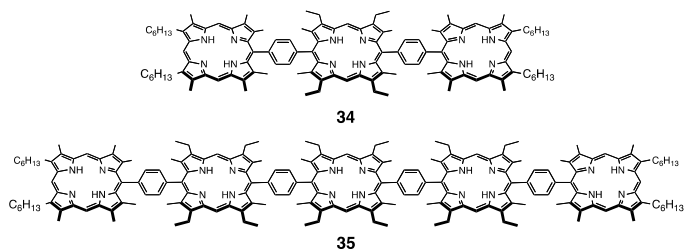


Fig. 18. Structures of linear oligomers **34** and **35**.

A 1,8-anthracene-linked Fe(III)-porphyrin trimer, **36**, (Figure 19) was synthesized (Naruta et al., 1994); the Fe(III) ions were connected by imidazoles. According to electron paramagnetic resonance (ESR) and magnetic susceptibility measurements, the anti-ferromagnetic exchange coupling ( $-J$ ) was calculated to be  $15.3 \text{ cm}^{-1}$ . Without the imidazole moieties, no magnetic interaction among the Fe(III) ions was observed. The appropriate

distance and the face-to-face arrangement of the Fe(III) ions resulted in a short distance of  $\sim 2.0$  Å between the Fe(III) ion and nitrogen atom of imidazolate leading to the anti-ferromagnetic exchange coupling among the Fe(III) ions.

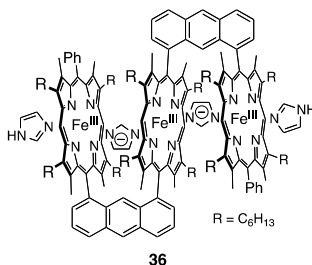
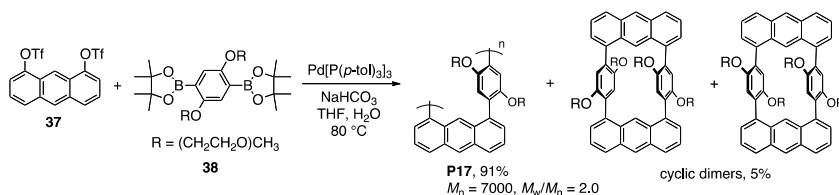


Fig. 19. Structure of oligomer **36**.

A benzene ring-layered polymer, **P17**, was synthesized via Suzuki-Miyaura polycondensation between 1,8-bis(trifluoromethyl)anthracene **37** and *p*-phenylene diboronate **38**, as shown in Scheme 10 (Sangvikar et al., 2009). Additionally, cyclic dimers were also isolated in 5% yield. The  $M_n$  of **P17** was relatively high ( $M_n = 7000$ ,  $M_w/M_n = 2.0$ ), which suggests the possibility of obtaining this class of polymers with a longer chain length.



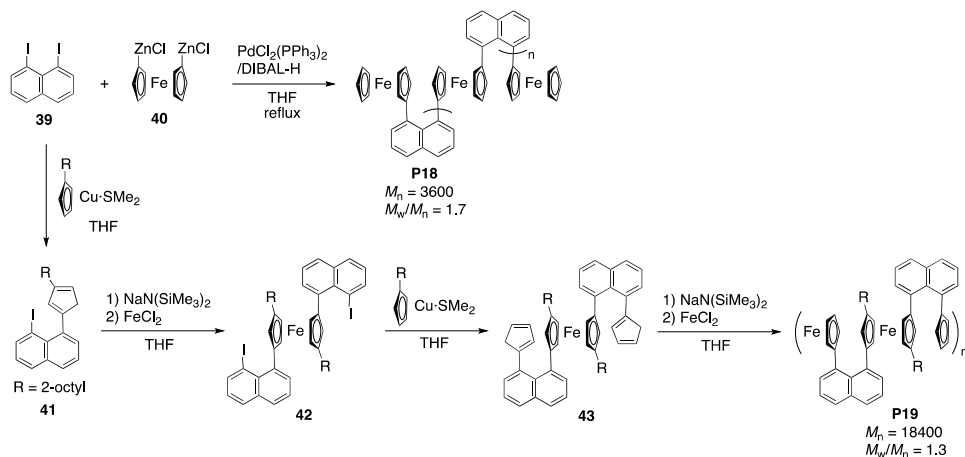
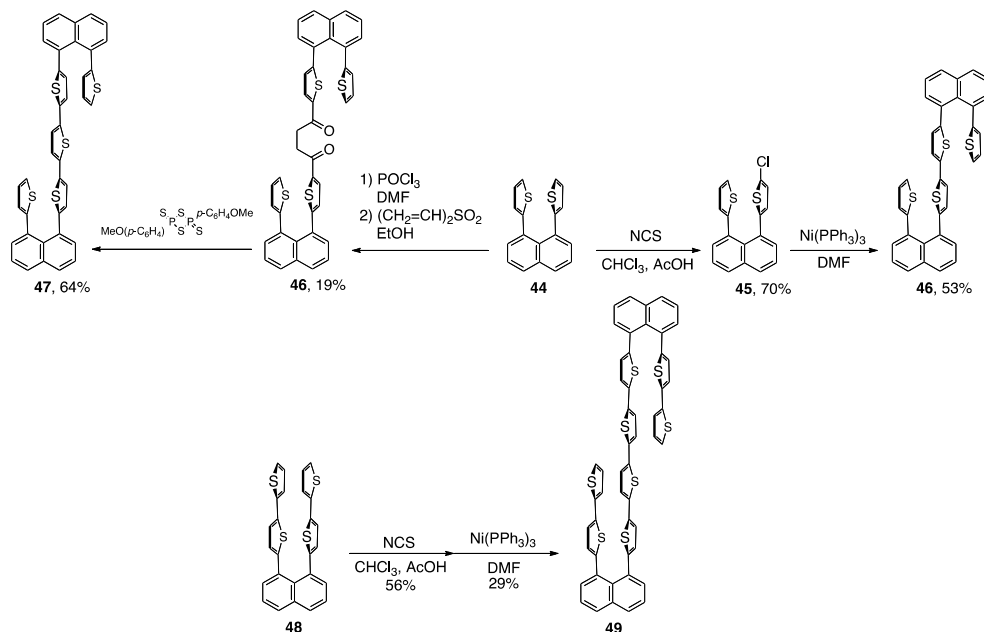
Scheme 10. Synthesis of polymer **P17**

## 5. Naphthalene-based oligomers and polymers

The distance between the 1- and 8-carbon atoms of naphthalene compounds is approximately 2.5–2.6 Å; therefore, aromatic groups substituted at the 1,8-positions of naphthalene derivatives are constrained in a face-to-face arrangement. Various 1,8-diarylnaphthalenes have been synthesized, and their  $\pi$ -stacked structures and  $\pi$ - $\pi$  interactions have been studied. However, oligomers and polymers composed of multi-stacked aromatic rings have rarely been developed.

$\pi$ -Stacked metallocene polymers were obtained, as shown in Scheme 11. The treatment of 1,8-diiodonaphthalene **39** with 1,1'-ferrocenyldizinc chloride **40** by Negishi coupling afforded polymer **P18** with a relatively low  $M_n$  of 3600 (Arnold et al., 1988). The synthetic procedure was modified as follows: the treatment of bis(2-octyl)ferrocene **43** with  $\text{NaN}(\text{SiMe}_3)_2$  and  $\text{FeCl}_2$  provided the ferrocene-stacked polymer **P19** with an  $M_n$  of 18400 (Nugent & Rosenblum, 1993; Rosenblum et al., 1995; Hudson et al., 1999). The addition of  $\text{CoCl}_2$  and  $\text{NiBr}_2$  instead of  $\text{FeCl}_2$  yielded the corresponding ferrocene/cobaltocene-stacked and ferrocene/nickelocene-stacked polymers, respectively. The stacked ferrocenes in **P19** adopted a weakly interacting mixed-valence system by chemical doping with  $\text{I}_2$ , after which the electrical conductivity increased from  $10^{-12}$  to  $6.7 \times 10^{-3} \text{ Scm}^{-1}$ .

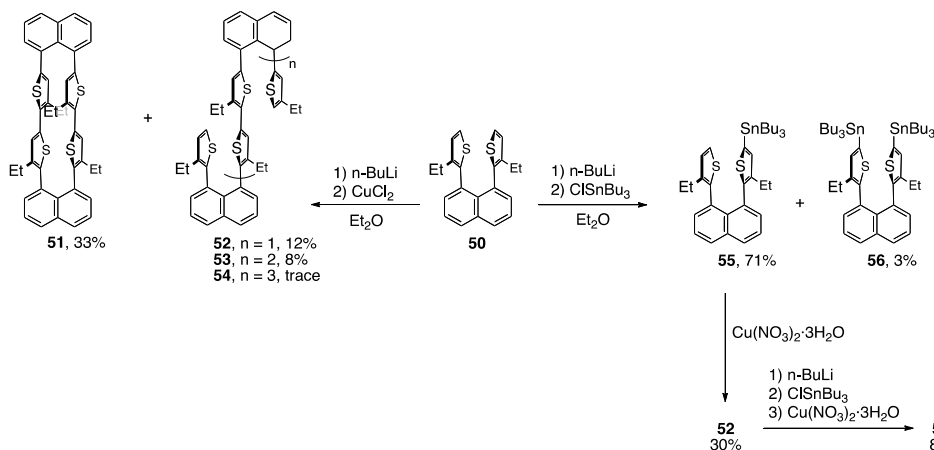


Scheme 11. Synthesis of polymers **P18** and **P19**.Scheme 12. Synthesis of oligomers **46**, **47**, and **49**.

Oligothiophenes were stacked by a step-wise reaction. Scheme 12 illustrates the construction of three oligothiophene-layered systems (Kuroda et al., 1994). The chlorination of the thiophene ring by *N*-chlorosuccinimide (NCS) and a successive Ni-catalyzed coupling reaction afforded compounds **46** and **49**. Compound **47** was synthesized by cyclization with Lawesson's reagent. X-ray crystallographic analysis of **46** revealed that the outer thiophene rings and the inner bithiophene moiety are almost parallel and that the dihedral angle

between the thiophene planes and naphthalenes is approximately 53°. The CV oxidation potentials of **46**, **47**, and **49** decreased with the increasing number of thiophenes and were lower than the CV oxidation potentials of the monomeric compounds due to the stabilization of radical cations among the three-layered oligothiophenes.

Stepwise coupling reactions of the naphthalene-based stannylthiophenes yielded the corresponding oligothiophene-stacked oligomers (Scheme 13) (Iyoda et al., 2001; Nakao et al., 2008). Cyclic dimer **51** was primarily obtained along with oligomers **52–54** by the oxidative coupling reaction of **50** with BuLi and CuCl<sub>2</sub>. The treatment of **55** with Cu(NO<sub>3</sub>)<sub>2</sub>·3H<sub>2</sub>O afforded the coupling product **52** in 30% yield. Compound **52** was reacted with BuLi and ClSnBu<sub>3</sub> followed by treatment with Cu(NO<sub>3</sub>)<sub>2</sub>·3H<sub>2</sub>O to obtain the corresponding thiophene-layered oligomer **54** in 8% yield.



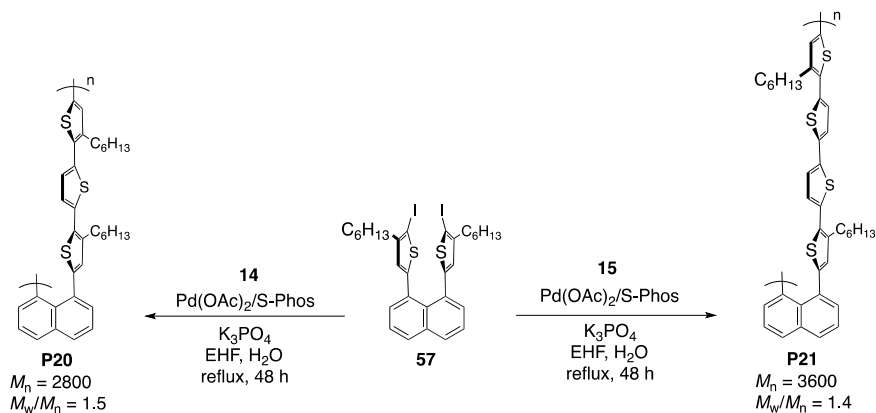
Scheme 13. Synthesis of oligomers **52–54**.

entry	Oligomer	$\lambda_{\text{abs,max}} / \text{nm}$	$\lambda_{\text{em,max}} / \text{nm}$	$\Phi_{\text{PL}}$	$E_{\text{ox}}^1, E_{\text{ox}}^2 / \text{V}$
1	<b>52</b>	325	471	0.033	0.67
2	<b>53</b>	330	481	0.021	0.40, 0.60
3	<b>54</b>	333	485	0.007	0.40, 0.64

Table 5. Optical Data and Oxidation Potentials

Optical data were collected in their benzene solutions. Oxidation potentials were determined in *o*-dichlorobenzene using a ferrocene/ferrocenium external reference.

The optical and electrochemical behaviors of the compounds were studied and the results are summarized in Table 5. The absorption maxima of the oligomers were slightly red-shifted as the number of layered thiophenes increased. The long-wavelength absorption was assigned to the S<sub>0</sub> to S<sub>1</sub> transition of the bithiophene moieties. Their photoluminescence spectra were broad and featureless, and the photoluminescence quantum efficiencies, which were estimated to range from 0.007–0.033, were low. Oligomers **52–54** exhibited the redox properties of the  $\pi$ -donor. Oligomer **52** showed the one-electron oxidation wave ( $E_{\text{ox}} = 0.67$  V) of a bithiophene unit, while two-step one-electron oxidation waves were observed for **53** and **54**.



Scheme 14. Synthesis of polymers **P20** and **P21**.

Scheme 14 shows the synthetic pathway for oligothiophene-stacked polymers. Polymers **P20** and **P21** were synthesized by the polymerization of **57** and co-monomers **14** and **15** via modified Suzuki-Miyaura coupling using a catalytic amount of  $\text{Pd(OAc)}_2$  and a bulky phosphine ligand (S-Phos) (Morisaki et al., 2010c). The  $M_n$  values of **P20** and **P21** were estimated to be 2800 and 3600, from which the number-average degrees of polymerization were estimated to be 5 and 6, respectively.

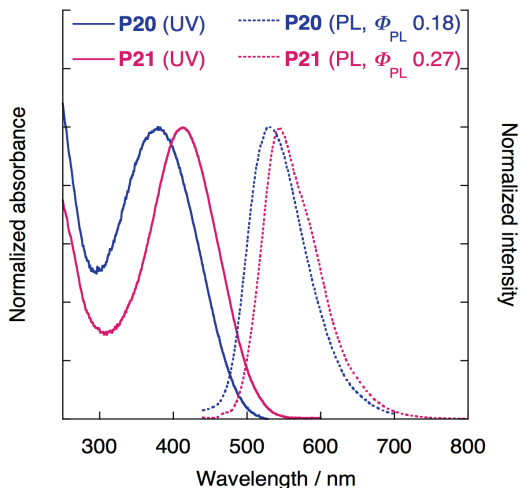


Fig. 20. UV spectra in  $\text{CHCl}_3$  ( $1.0 \times 10^{-5}$  M) and PL spectra in  $\text{CHCl}_3$  ( $1.0 \times 10^{-7}$  M) of polymers **P20** and **P21**.

The UV-vis absorption spectra in  $\text{CHCl}_3$  ( $1.0 \times 10^{-5}$  M) and photoluminescence spectra in  $\text{CHCl}_3$  ( $1.0 \times 10^{-7}$  M) of **P20** and **P21** are shown in Figure 20. An increase in the absorption maxima was observed with an increasing number of thiophene rings. The absorption maxima of **P20** and **P21** appeared at 379 and 410 nm, respectively. It is suggested that this absorption band should also be assigned to the  $S_0 \rightarrow S_1$  transition of the bithiophene-

naphthalene moieties. It is expected that the  $S_1$  state forms a quinoidal-like structure of thiophene with naphthalene (Seixas de Melo et al., 2001; Pina et al., 2009). Bathochromic shifts of the photoluminescence spectra and an increase in the absolute  $\Phi_{PL}$  were observed with an increasing number of thiophene rings. The  $\Phi_{PL}$  values of **P20** and **P21** were similar to the values found for naphthalene-based bithiophene and quaterthiophene oligomers, respectively. Concentration-quenching was not observed among the layered oligothiophenes indicating that the main quenching pathway is radiationless intersystem crossing from  $S_1$  to  $T_1$ . The HOMO energy levels of **P20** and **P21** were approximately -5.30 and -5.25 eV, respectively, as calculated from the  $E_{onset}$  values of their cyclic voltammograms. The oligothiophene-stacked polymers can potentially be applied in electronic devices such as hole-transporting materials.

## 6. Conclusion

In this chapter, the synthesis and properties of aromatic-ring- and  $\pi$ -electron-systems-layered polymers using xanthene, anthracene, and naphthalene as scaffolds were depicted. The oligomers introduced here were limited to three or more face-to-face aromatic systems, although dimeric compounds prevail. From a synthetic point of view, the method of using xanthene, anthracene, and naphthalene scaffolds is ideal for constructing face-to-face arrangements of a variety of aromatic rings and  $\pi$ -electron systems. The application of this class of polymers and oligomers to optoelectronic devices such as field emission transistors, photovoltaic devices, and charge-transporting materials has not yet been extensively investigated. It is worth noting that the presence of the  $\pi$ -stacked structure and the orientation of the  $\pi$ -electron systems play an important role in the effective charge transfer, energy transfer, and delocalization of excitons in the devices, leading to great potential of these systems in optoelectronic devices. The challenge for the near future is the development of controlled polymerization instead of stepwise oligomer synthesis to obtain aromatic-ring-layered polymers with narrow polydispersity, which would lead to high-performance next-generation organic optoelectronic devices.

## 7. References

- Alemán, C.; Zanuy, D. & Casanovas, J. (2006) Conformational isomerism of electroactive calyx[4]arenes: influence of the electronic state in the flexibility of thiophene-containing calyx[4]arene. *J. Org. Chem.*, Vol. 71, No. 18, (September 2006) 6952-6957, ISSN 0022-3263
- Arnold, R.; Matchett, S. A. & Rosenblum, M. (1988) Preparation and properties of stacked oligomeric and polymeric metallocenes. *Organometallics*, Vol. 7, No. 11, (November 1988) 2261-2266, ISSN 0276-7333
- Barder, T. E.; Walker, S. D.; Martinelli, J. R. & Buchwald, S. L. (2005) New catalysts for Suzuki-Miyaura coupling processes: scope and studies of the effect of ligand structure. *J. Am. Chem. Soc.*, Vol. 127, No. 13, (March 2005) 4685-4696, ISSN 0002-7863
- Casanovas, J.; Zanuy, D. & Alemán, C. (2006) Conducting polymer actuator mechanism based on the conformational flexibility of calyx[4]arene. *Angew. Chem. Int. Ed.*, Vol. 45, No. 6, (February 2006) 1103-1105, ISSN 1521-3773

- Fernandes, J. A.; Morisaki, Y. & Chujo, Y. (2010) Aromatic ring-Layered polymer containing 2,7-linked-carbazole on xanthene. *Polym. Bull.*, Vol. 65, No. 5, (September 2010) 465-476, ISSN 0170-0839.
- Fernandes, J. A.; Morisaki, Y. & Chujo, Y. (2011)  $\pi$ -Electron-system-layered polymers comprising thiophene/furan oligomers. *J. Polym. Sci. Part A: Polym. Chem.*, Vol. 49, No. 16, (August 2011) 3664-3670, ISSN 0887-624X
- Förster, T. (1946) Energiewanderung und fluoreszenz. *Naturwissenschaften*, Vol. 33, No. 6, (June 1946) 166-175, ISSN 0028-1042.
- Gaiimo, J. M.; Lockard, J. V.; Sinks, L. E.; Scott, A. M.; Wilson, T. M. & Wasielewski, M. R. (2008) Excited singlet states of covalently bound, cofacial dimers and trimers of perylene-3,4:9,10-bis(dicarboximide)s. *J. Phys. Chem. A*, Vol. 112, No. 11, (March 2008) 2322-2330, ISSN 1089-5639
- Grazulevicius, J. V.; Strohriegel, P.; Pielichowski, J. & Pielichowski, K. (2003) Carbazole-containing polymers: synthesis, properties, and applications. *Prog. Polym. Sci.*, Vol. 28, No. 9, (September 2003) 1297-1353, ISSN 0079-6700
- Hudson, R. D. A.; Foxman, B. M. & Rosenblum, M. (1999) *Organometallics*, Vol. 18, No. 20, (September 1999) 4098-4106, ISSN 0276-7333
- Iyoda, M.; Nakao, K.; Kondo, T.; Kuwatani, Y.; Yoshida, M.; Matsuyama, H.; Fukami, K. & Nagase, S. (2001) [6.6](1,8)Naphthalenophane containing 2,2'-bithienyl-5,5'-ylene bridges. *Tetrahedron Lett.*, Vol. 42 No. 39, (September 2001) 6869-6872, ISSN 0040-4039
- Kosugi, M.; Sasazawa, K.; Shimizu, Y. & Migita, T. (1977) Reactions of allyltin compounds. III. Allylation of aromatic halides with allyltributyltin in the presence of tetrakis(triphenylphosphine)palladium(0). *Chem. Lett.*, Vol. 6, No. 3, (March 1977) 301-302, ISSN 0366-7022
- Kuroda, M.; Nakayama, J.; Hoshino, M.; Furusho, N. & Ohba, S. (1994) Synthesis and properties of a-oligothiophenes carrying three cofacially oriented thiophene rings through peri positions of naphthalene. *Tetrahedron Lett.*, Vol. 35, No. 23, (June 1994) 3957-3960, ISSN 0040-4039
- Milstein, D. & Stille, J. K. (1978) A general, selective, and facile method for ketone synthesis from acid chlorides and organotin compounds catalyzed by palladium. *J. Am. Chem. Soc.*, Vol. 100, No. 11, (May 1978) 3636-3638
- Miyaura, N.; Yamada, K. & Suzuki, A. (1979) A new stereospecific cross-coupling by the palladium-catalyzed reaction of 1-alkenylboranes with 1-alkenyl or 1-alkynyl halides. *Tetrahedron Lett.*, Vol. 20, No. 36, (September 1979) 3437-3440, ISSN 0040-4039
- Miyaura, N. & Suzuki, A. (1995) Palladium-catalyzed cross-coupling reactions of organoboron compounds. *Chem. Rev.*, Vol. 95, No. 7 (July 1995) 2457-2483, ISSN 0009-2665
- Morin, J. F.; Leclerc, M.; Ades, D. & Siove, A. (2005) Polycarbazoles: 25 years of progress. *Macromol. Rapid Commun.*, Vol 26, No. 11, (May 2005) 761-778, ISSN 1022-1336
- Morisaki, Y. & Chujo, Y. (2005). Construction of benzene ring-layered polymers, *Tetrahedron Lett.* Vol. 46, No. 15, (April 2005) 2533-2537, ISSN 0040-4039

- Morisaki, Y. & Chujo, Y. (2006). Through-space conjugated polymers based on cyclophanes. *Angew. Chem. Int. Ed.*, Vol. 45, No. 39, (October 2006) 6430-6437, ISSN 1521-3773
- Morisaki, Y. & Chujo, Y. (2008a). Cyclophane-containing polymers. *Prog. Polym. Sci.*, Vol. 33, No. 3, (March 2008) 346-364, ISSN 0079-6700
- Morisaki, Y.; Murakami, T. & Chujo, Y. (2008b). Synthesis and properties of [2.2]paracyclophane-layered polymers. *Macromolecules*, Vol. 41, No. 16, (August 2008) 5960-5963, ISSN 0024-9297
- Morisaki, Y.; Murakami, T. & Chujo, Y. (2009a). Synthesis, structure, and properties of aromatic ring-layered polymers containing ferrocene as a terminal unit. *J. Inorg. Organomet. Polym. Mater.* Vol. 19, No. 1, (March 2009) 104-112, ISSN 1574-1443.
- Morisaki, Y.; Murakami, T.; Sawamura, T. & Chujo, Y. (2009b). [2.2]Paracyclophane-layered polymers end-capped with fluorescence quenchers. *Macromolecules*, Vol. 42, No. 10, (May 2009) 3656-3660, ISSN 0024-9297
- Morisaki, Y.; Imoto, H.; Miyake, J. & Chujo, Y. (2009c) Synthesis and properties of oligophenylene-layered polymers. *Macromol. Rapid Commun.*, Vol 30, No. 13, (July 2009) 1094-1100, ISSN 1022-1336
- Morisaki, Y. & Chujo, Y. (2009d). Synthesis of  $\pi$ -stacked polymers on the basis of [2.2]paracyclophane. *Bull. Chem. Soc. Jpn.*, Vol. 82, No. 9, (September 2009) 1070-1082, ISSN 0009-2673
- Morisaki, Y.; Fernandes, J. A.; Wada, N. & Chujo, Y. (2009e) Synthesis and properties of carbazole-layered polymers. *J. Polym. Sci. Part A: Polym. Chem.*, Vol. 47, No. 17, (September 2009) 4279-4288, ISSN 0887-624X.
- Morisaki, Y.; Fernandes, J. A. & Chujo, Y. (2009f) Synthesis of oligothiophene-layered polymers. *Macromol. Rapid Commun.*, Vol 30, No. 24, (December 2009) 2107-2111, ISSN 1022-1336
- Morisaki, Y.; Sawamura, T.; Murakami, T. & Chujo, Y. (2010a) Synthesis of anthracene-stacked oligomers and polymer. *Org. Lett.*, Vol. 12, No. 14, (July 2010) 3188-3191, ISSN 1523-7060
- Morisaki, Y.; Fernandes, J. A. & Chujo, Y. (2010b) Xanthene-Based Oligothiophene-Layered Polymers. *Macromol. Chem. Phys.*, Vol. 211, No. 22, (November 2010) 2407-2415, ISSN 0003-3146
- Morisaki, Y.; Fernandes, J. A. & Chujo, Y. (2010c) Naphthalene-based oligothiophene-stacked polymers. *Polym. J.*, Vol. 42, No. 12, (December 2010) 928-934, ISSN 0032-3896
- Nagata, T.; Osuka, A. & Maruyama, K. (1990) Synthesis and optical properties of conformationally constrained trimeric and pentameric porphyrin arrays. *J. Am. Chem. Soc.*, Vol. 112, No.8, (April 1990) 3054-3059, ISSN 0002-7863
- Nakano, T. (2010). Synthesis, structure and function of  $\pi$ -stacked polymers. *Polym. J.*, Vol. 42, No. 2, (February 2010) 103-123, ISSN 0032-3896
- Nakao, K.; Nishiuchi, T. & Iyoda, M. (2008) Syntheses, structures, and properties of bithiophenophanes bridged at 1,8-positions of naphthalenes. *Heterocycles*, Vol. 76, No. 1, (September 2008) 727-745, ISSN 0385-5414

- Naruta, Y.; Sawada, N.; Tadokoro, M. (1994) Imidazolate-mediated antiferromagnetic coupling between Fe(III) ions in rigidly-linked porphyrin dimers and trimers. *Chem. Lett.*, Vol. 23, No. 9, (September 1994) 1713-1716, ISSN 0366-7022
- Negishi, E.; King, A. O. & Okukado, N. (1977) Selective carbon-carbon bond formation via transition metal catalysis. 3. A highly selective synthesis of unsymmetrical biaryls and diarylmethanes by the nickel- or palladium-catalyzed reaction of aryl- and benzylzinc derivatives with aryl halides. *J. Org. Chem.*, Vol. 42, No. 10, (May 1977) 1821-1823, ISSN 0022-3263
- Negishi, E. (1982) Palladium- or nickel-catalyzed cross coupling. A new selective method for carbon-carbon bond formation. *Acc. Chem. Res.*, Vol. 15, No. 11, (November 1982) 340-348, ISSN 0001-4842
- Nugent, H. M. & Rosenblum, M. (1993) *J. Am. Chem. Soc.*, Vol. 115, No. 10, (May 1993) 3848-3849, ISSN 0002-7863
- Pina, J. & Seixas de Melo, J. A. (2009) Comprehensive investigation of the electronic spectral and photophysical properties of conjugated naphthalene-thiophene oligomers. *Phys. Chem. Chem. Phys.*, Vol. 11, No. 39, (October 2009) 8706-8713, ISSN 1463-9076
- Rosenblum, M.; Nugent, H. M.; Jang, K.-S.; Labes, M. M.; Cahalane, W.; Klemarczyk, P. & Reiff, W. M. (1995) *Macromolecules*, Vol. 28, No. 18, (August 1995) 6330-6342, ISSN 0024-9297
- Sangvikar, Y.; Fischer, K.; Schmidt, M.; Schlüter, A. D. & Sakamoto, J. (2009) Suzuki polycondensation with a hairpin monomer. *Org. Lett.*, Vol. 11, No. 18, (September 2009), 4112-4115, ISSN 1523-7060
- Scherlis, D. A. & Marzari, N. (2005)  $\pi$ -Stacking in thiophene oligomers as the driving force for electroactive materials and devices. *J. Am. Chem. Soc.*, Vol. 127, No. 9, (March 2005) 3207-3212, ISSN 0002-7863
- Seixas de Melo, J., Silva, L. M., & Kuroda, M. (2001) Photophysical and theoretical studies of naphthalene-substituted oligothiophenes. *J. Chem. Phys.*, Vol. 115, No. 12, (September 2001) 5625-5636, ISSN 0021-9606
- Skotheim, T. A.; Elsenbaumer, R. L. & Reynolds, J. R. (Eds.). (2006). Handbook of organic conducting polymers, 3rd ed., Marcel Dekker, ISBN 0824700503, New York
- Song, C. & Swager, T. M. (2008)  $\pi$ -Dimer formation as the driving force for calyx[4]arene-based molecular actuators. *Org. Lett.*, Vol. 10, No. 16 (August 2008), 3575-3578, ISSN 1523-7060
- Sonogashira, K. (2002). In: *Handbook of Organopalladium Chemistry for Organic Synthesis*, Negishi, E., pp. 493-529, Wiley-Interscience, ISBN 047131506,0 New York
- Takita, R.; Song, C. & Swager, T. M. (2008)  $\pi$ -Dimer formation in an oligothiophene tweezer molecule. *Org. Lett.*, Vol. 10, No. 21 (November 2008), 5003-5005, ISSN 1523-7060
- Tohda, Y.; Sonogashira, K. & Hagihara, N. (1975). A convenient synthesis of acetylenes: catalytic substitutions of acetylenic hydrogen with bromoalkenes, iodoarenes and bromopyridines. *Tetrahedron Lett.*, Vol 16, No. 50, (December 1975), 4467-4470, ISSN 0040-4039
- Yoo, H.; Yang, J.; Yousef, A.; Wasielewski, M. R. & Kim D. (2010) Excimer formation dynamics of intramolecular  $\pi$ -stacked perylene diimides probed by single-molecule

- fluorescence spectroscopy. *J. Am. Chem. Soc.*, Vol. 132, No. 11, (March 2010) 3939-3944, ISSN 0002-7863
- Yu, H.-h.; Xu, B. & Swager, T. M. (2003) A proton-doped calyx[4]arene-based conducting polymer. *J. Am. Chem. Soc.*, Vol. 125, No. 5, (February 2003) 1142-1143, ISSN 0002-7863
- Yu, H.-h.; Pullen, A. E.; Büschel, M. G. & Swager, T. M. (2004) Charge-specific interactions in segmented conducting polymers: an approach to selective ionoresistive responses. *Angew. Chem. Int. Ed.*, Vol. 43, No. 28, (July 2004) 3700-3703, ISSN 1521-3773



# Nanomorphologies in Conjugated Polymer Solutions and Films for Application in Optoelectronics, Resolved by Multiscale Computation

Cheng K. Lee<sup>1</sup> and Chi C. Hua<sup>2</sup>

<sup>1</sup>*Research Center for Applied Sciences, Academia Sinica,*

<sup>2</sup>*Department of Chemical Engineering, National Chung Cheng University, Taiwan*

## 1. Introduction

Conducting conjugated polymers, which provide flexibility as polymers as well as conductivity as metals, have nowadays become an essential solution-processable material for fabricating polymer light-emitting diodes (PLEDs) and plastic solar cells. In addition to the possibility of producing large-area thin films at room temperature, an appealing feature of exploiting long-chain organic semiconductors lies in the capability to fine-tune the optoelectronic behavior of solution-cast films by exploiting a broad variety of solvents or hybrid solvents in preparing the precursor solutions, later fabricated into dry thin films via spin coating or ink-jet printing. To improve the solubility in usual organic solvents, the polymers are often modified by grafting flexible alkyl or alkoxy side chains to the phenyl backbone, rendering the polymer chemical amphiphilicity. The semiflexible backbone and chemical amphiphilicity, in turn, give rise to a vast swath of single-chain and aggregation morphologies as different types of solvents are used to cast the polymer thin films, through mechanisms—generally referred to as the memory effect (Nguyen et al. 1999)—as schematically illustrated in Figure 1. Clearly, understanding how the above-mentioned material properties evolve during a practical processing is of paramount importance, yet this central goal remains challenging to conventional experimental protocols. Computation simulations, therefore, provide an important alternative by which in-depth information may be readily extracted that complement our knowledge from experimental characterizations, and thereby facilitates the pursuit of gaining practical controls over the molecular states of solution-cast thin films.

This monograph aims to provide a comprehensive review of recently developed multiscale computation schemes that have been dedicated to resolving fundamental material properties in conjugated polymer solutions and films; prospects on emerging opportunities as well as challenges for upcoming applications in the area of organic optoelectronics are also remarked. Utilizing a standard, widely studied, conjugated polymer—poly(2-methoxy-5-(2'-ethylhexyloxy)-1,4-phenylenevinylene) (MEH-PPV; see sketches in Figure 3)—as a representative example, we introduce the fundamentals and protocols of constructing self-

consistent, parameter-free, coarse-grained (CG) polymer models and simulation schemes capable of capturing single-chain and aggregation properties at various length/time scales pertinent to a wide range of experimental measurements, as depicted in Figure 2. Meanwhile, predictions on specific material properties are discussed in view of the central implications for understanding known, yet-unresolved, experimental features, as well as for unveiling molecular properties for innovatory purposes. The main text is so organized: Sec. 2 describes the details of four different molecular dynamics schemes that virtually constitute a versatile multiscale computation “network,” which can be utilized in an economic way to gain practical access to fundamental single-chain and aggregation properties from solution to the quenching state for, in principle, any specific conjugated polymers and solvent systems. The major computational results are summarized and discussed in Sec. 3. Finally, Sec. 4 concludes this review by outlining some future perspectives and challenges that become evident based on the current achievements.

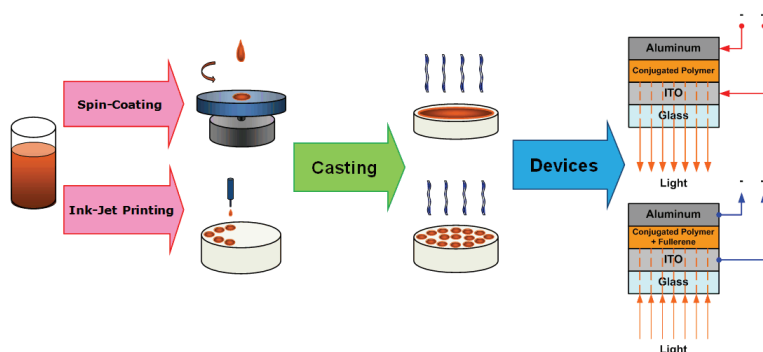


Fig. 1. Typical procedures for fabricating PLED devices or polymer-based solar cells.

## 2. Simulation protocols

Contemporary multiscale computations that concern polymer species typically begin with full-atom or united-atom molecular dynamics schemes—both are referred to as AMD scheme for simplicity—with incorporated interatomic force fields often built in a semi-empirical manner for atoms or molecular units that share similar chemical structures and environments. Of course, these default force fields and associated parameter values should always be selected carefully and, if necessary, checked against the results of first-principles computation. The basic principle of constructing a CG polymer model is, once the polymer has been redefined by lumping certain molecular groups into single CG particles, self-consistent force fields that govern these CG particles may be built using AMD simulation data on the original, atomistic polymer model. For the case of intramolecular (bonded) CG potentials, the statistical trajectories of the redefined bond lengths and angles are first collected from the AMD simulation, and then Boltzmann inversions of their distribution functions are performed to evaluate the new potential functions which, in turn, are utilized in the corresponding CG simulation and the results checked against the AMD predictions for self-consistency; if necessary, repeat the above procedure until the imposed tolerance criteria are met. The situation is similar in constructing the intermolecular (non-bonded) CG potentials, except that one utilizes the so-called radial distribution functions (RDFs) and that

a greater number of iterations are usually required because of a more pronounced effect of many-body interactions. Some of the details are provided in the following text, and abundant literature addressing these issues may be consulted (Carbone et al. 2010; Faller 2004; Müller-Plathe 2002; Noid et al. 2008; Padding & Briels 2011; Tschöp et al. 1998).

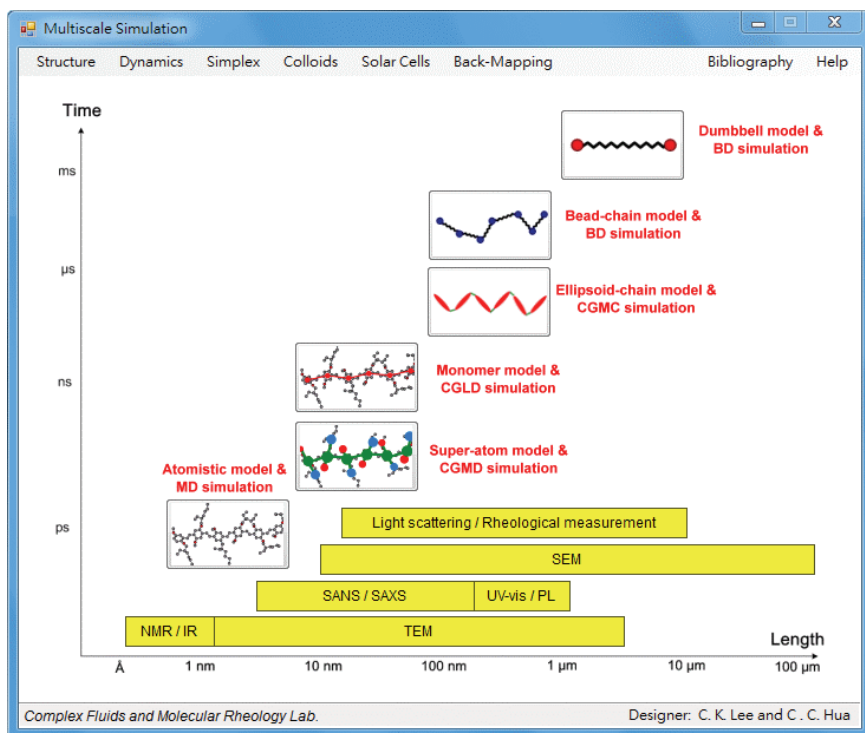


Fig. 2. Multiscale simulation schemes that provide molecular information at various length/time scales pertinent to a wide range of experimental measurements.

### 2.1 Coarse-Grained Molecular Dynamics (CGMD) simulation

The most primitive CG scheme for simulating a polymer solution is to explicitly retain the solvent molecules and treat them as usual CG particles as for the polymer molecule. In this way, the simulation of the CG system may be carried out by the same software package as for previous AMD simulations, provided the newly constructed bonded and non-bonded potentials for all CG particles. Figure 3 depicts how a MEH-PPV chain may be coarse-grained by introducing suitable "super-atoms" to represent essential molecular units—in this case, the repeating phenyl backbone unit and two asymmetric alkoxy side-chain groups. Likewise, solvent molecules are cast into single CG "beads" of similar size. All CG particles are mapped at the mass centers and conserve the full masses of the molecular units they represent. As has been noted earlier, the next step involves rebuilding self-consistent, parameter-free, intramolecular potentials governing the CG particles by using the Boltzmann inversions of essential statistical trajectories gathered from AMD simulations of the original, full-atom or united-atom, representation of the model system:

$$U(z) = -k_B T \ln P(z), \quad (1)$$

where  $k_B T$  is the Boltzmann constant times the absolute temperature, and  $P(z)$  is the probability distribution function of the independent variable  $z$  (i.e., bond lengths or angles) redefined in the CG polymer model. Similarly, the RDFs retrieved from specially designed AMD simulations are adopted in the construction of intermolecular CG potentials. Subsequent iterations to ensure self-consistencies between AMD and CGMD simulations may be enforced by simplex optimizations:

$$f = \int_0^{\text{cutoff}} \left( U^{\text{AMD}}(z) - U_i^{\text{CGMD}}(z, \{p_n\}) \right)^2 dz \rightarrow \min, \quad (2)$$

$$f = \int_0^{\text{cutoff}} \left( \text{RDF}^{\text{AMD}}(r) - \text{RDF}_i^{\text{CGMD}}(r, U_i^{\text{CGMD}}\{p_n\}) \right)^2 dr \rightarrow \min. \quad (3)$$

If the usual 12-6 Lennard-Jones (LJ) type of intermolecular potentials are assumed for the CG particles, as in the present case, the initial guess may be obtained via the following relation:  $U_{i=1}^{\text{CGMD}}(r) = 4\epsilon[(\sigma/r)^{12} - (\sigma/r)^6] \approx -k_B T \ln(\text{RDF}^{\text{AMD}}(r))$ . The full set of parameters  $\{p_n\}$  in this case denote the well depth  $\epsilon$  and the van der Waals diameter  $\sigma$ , and  $i$  stands for the number of iterations attempted. An important advantage of the above choice is, in fact, that a simple mixing rule may be adopted to describe the pair potentials for unlike CG particles, thus saving a lot of computational effort. Justifications of such simplified treatment for the simulation systems under investigation have been discussed in earlier work (Lee et al. 2009; Lee et al. 2011).

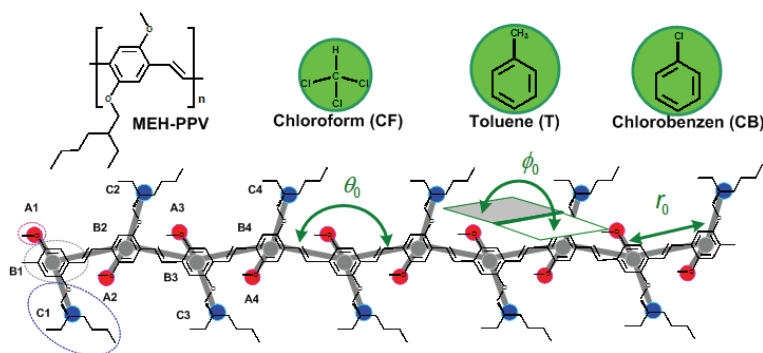


Fig. 3. Specifications of representative bond lengths and angles for the super-atom model of MEH-PPV, where B, A and C denote the aromatic backbone, short- and long-alkoxy side chains, respectively.

For the polymer model depicted in Figure 3, which represents the “finest” CG polymer model in this review article, the two side-chain groups are treated as independent CG particles so as to discriminate the chemical affinities of various types of solvent molecules with respect to different parts of the polymer chain. Moreover, tetrahedral defects (which represent a localized breakage of single/double-bond conjugation) are incorporated and

assigned uniformly to every 10 repeating units on the polymer backbone, in order to realistically capture the collapsed morphologies of real synthesized chains during the quenching process. Simulation results based on this CG solution system have been obtained for a 300-mer MEH-PPV, close to the chain length of a commercial sample commonly used in experiment. Both AMD and CGMD simulations utilized the *NPT* ensemble at  $T = 298$  K and  $P = 1$  atm, with the same software package (Forester & Smith 2006) where the incorporated force fields (Mayo et al. 1990) were noted to lead to generally good agreement with known experimental features of MEH-PPV solution (Lee et al. 2008), as well as with force fields (particularly for torsional angles) suggested by first-principles computations (De Leener et al. 2009).

## 2.2 Coarse-Grained Langevin Dynamics (CGLD) simulation

As our primary interest turns to large-scale material properties, such as the morphologies of long single chains or interchain aggregates, the CGMD scheme described above becomes inefficient because most of the computational times must be devoted to the uninterested, generally overwhelming in number, solvent molecules. A classical solution to this problem is treating the solvent as a continuum thermal bath and, accordingly, modifying the Newton's equations of motion to be the Langevin ones—the solution schemes of which are often referred to as Brownian dynamics—by adding self-consistent frictional drag and thermal Brownian forces. Conventional Brownian dynamics simulations, however, differ distinctively from the one introduced below in both the degree of coarse-graining and the retrieval of parameter values for drag coefficient. More specifically, the drag coefficient used in conventional Brownian dynamics is typically derived from the Einstein-Stokes relation for large, Brownian particles, and usually bears no direct link with the molecular attributes of the specific polymer-solvent pair under investigation. In fact, at the previous level of coarse-graining, the frictional drags have been treated as dissipative forces, independent of the solvent quality which might be accounted by the “excess” non-bonded bead interactions. Recently, considering a CG polymer model of MEH-PPV as depicted in Figure 4, we have proposed strategies that help reconcile the dilemma noted above for usual Brownian dynamics schemes for dilute solution (Lee et al. 2008). The central idea is that, instead of assuming the Einstein-Stokes relation—which strictly applies only to Brownian particles that are sufficiently larger than the solvent molecules—the diffusivity of a CG particle representing a monomer unit,  $D$ , was “measured” directly from an AMD simulation, and the frictional drag coefficient,  $\zeta$ , was later evaluated from the more fundamental Einstein equation,  $\zeta = k_B T / D$ . As usual, this allows the Brownian forces to be constructed self-consistently from fluctuation-dissipation theorem. The resulting Langevin equation bears the form

$$m_i \frac{d^2 \mathbf{r}_i}{dt^2} = -\zeta_i \frac{d\mathbf{r}_i}{dt} + \sum_j \mathbf{F}_{ij} + \boldsymbol{\xi}_i, \quad (4)$$

where  $m_i$  and  $\mathbf{r}_i$  denote the mass and positional vector of the  $i$ th bead on a certain polymer chain, respectively,  $\sum_j \mathbf{F}_{ij}$  and  $\boldsymbol{\xi}_i$  represent the sum of the conservative forces (i.e., the intra- and intermolecular forces) and the random force, respectively, acting on the same bead, and  $\zeta_i$  is the frictional drag coefficient. The following expression of Brownian forces

with a Gaussian statistics can be constructed:  $\langle \xi_i \rangle = \mathbf{0}$  and  $\langle \xi_i(t) \xi_j(t) \rangle = 2\zeta_i k_B T \delta_{ij} \mathbf{I}$ , where the broken brackets denote taking the ensemble average of the quantity within them,  $\mathbf{I}$  is a unit tensor, and  $\delta_{ij}$  is the Kronecker delta function.

Significantly, the results shown in Table 1 suggest that the CGLD scheme so constructed is able to capture both the dynamic and structural properties of single MEH-PPV chains, and the computational efforts so saved are enormous. To gain a better feeling, we mention that for the results shown in Table 1, it takes ca. 36 hrs of the CGMD simulation with 4 CPUs running in parallel, while it requires only about 10 minutes for the CGLD simulation executed in a single-CPU personal computer. As an important consequence, longer MEH-PPV chains (i.e., above 300-mers), their supramolecular aggregates, and longer real times (up to several hundred nanoseconds) may be simulated in a single-CPU personal computer.

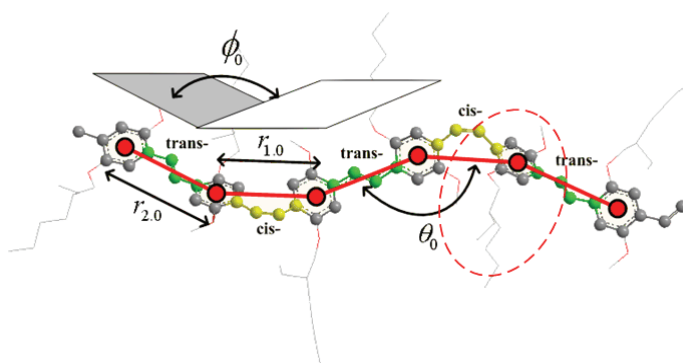


Fig. 4. Specifications of a few representative bond lengths and angles for the monomer model of MEH-PPV (circles).

100-mer MEH-PPV	Radius gyration ( $\text{\AA}$ )	Diffusivity ( $\text{m}^2/\text{s}$ )
CGMD	$R_{g,MT} = 26.77 \pm 1.42$	$D_{MT} = 2.97 \times 10^{-10}$
CGLD	$R_{g,MT} = 26.48 \pm 1.02$	$D_{MT} = 2.62 \times 10^{-10}$
CGMD	$R_{g,MC} = 33.40 \pm 1.19$	$D_{MC} = 5.90 \times 10^{-10}$
CGLD	$R_{g,MC} = 34.03 \pm 0.97$	$D_{MC} = 4.66 \times 10^{-10}$

Table 1. Comparisons between CGLD and CGMD simulations for the predicted radius of gyration and center-of-mass diffusivity in MEH-PPV/toluene (MT) or MEH-PPV/chloroform (MC) solution.

### 2.3 Coarse-Grained Monte Carlo (CGMC) simulation

Considering the planar or ellipsoidal backbone segments of typical conjugated polymers, the classical Gay-Berne (GB) potential (Gay & Berne 1981) seems ideal for describing the segmental interactions of large oligomer units. The GB potential and the associated ellipsoid-chain model, as sketched in Figure 5, is appealing also in that synthesized defects, tetrahedral

ones in particular, may be naturally embodied in the form of connecting springs between any two adjacent ellipsoid segments. If ten percent of such defects were assumed, for example, each ellipsoid effectively represents a 10-mer MEH-PPV segment, thus greatly enlarging the degree of coarse-graining. Given that the GB potential is able to treat the effects of molecular anisotropy in both attractive and repulsive interactions in an explicit and computationally efficient manner, it has nowadays become a standard model for studying the phase behavior and microstructures of liquid crystals, anisotropic colloids and liquid crystalline polymers, albeit most of the early applications were restricted to small molecules with aspect ratios generally below five. As addressed in an early work (Lee et al. 2010), applying the GB potential for a *semiflexible, large* oligomer species like a 10-mer MEH-PPV requires special cares in establishing the potential of mean forces (PMFs) between two ellipsoids, as well as in fixing simultaneously a large set of floating parameters. The functional form, the principal set of parameters and their determinations can be found elsewhere (Lee et al. 2010).

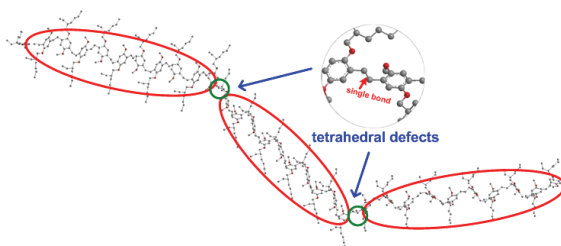


Fig. 5. Atomistic model representation and the ellipsoid-chain model (line contour) for a MEH-PPV oligomer with uniformly distributed tetrahedral defects.

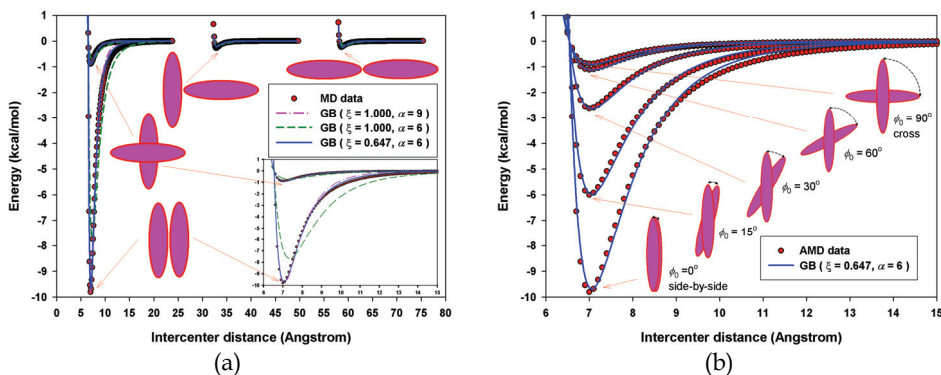


Fig. 6. Comparison of the predicted potential curves between AMD computations (symbols) and the parameterized GB model (lines) for (a) four representative arrangements and (b) various other arrangements of two like MEH-PPV oligomers.

Figure 6(a) shows how the parameter values in the GB potential may be determined based on the PMFs found in the AMD simulations for four representative mutual alignments of two like ellipsoids; the significances of the symbols appearing in the inset and the comparisons made can be found in early discussion (Lee et al. 2010). Figure 6(b) confirms

that the GB potential so parameterized can also capture quite well the PMFs of other mutual alignments that are deemed the most important to capture for a dense or condensed system. Unlike the CG polymer models described earlier, however, the segmental interactions described by the GB potential cannot be easily cast into usual equations of motion, and hence, only results from Monte Carlo simulations have been reported. Moreover, since the potential functions were previously parameterized for vacuum environment, the effects of solvent quality must be further accounted for. For the latter aspect, we have recently devised a similar procedure in building the PMFs for a pair of ellipsoids suspended in specific solvent media, and the ellipsoid-chain model so constructed leads to good agreement for the predicted solvent qualities as compared with the CGLD simulation results; more details will be published in a future work.

## **2.4 Brownian dynamics (BD) simulations of bead-spring chain and dumbbell models**

### **2.4.1 Bead-spring chain models**

As mentioned above, a notable drawback of the GB potential and the associated ellipsoid-chain model is that it is inherently more compatible with MC schemes and, hence, is not convenient for investigating dynamic properties. In addition, polymer segments with an aspect ratio as high as 10, for example, can easily be trapped in local minima in dense or condensed systems in a MC simulation. An alternative way to attain a similar level of coarse-graining, while compatible with usual dynamics schemes, is to resort to conventional bead-spring models, such as freely rotating (FR) chain and freely joined (FJ) chain. These kinetic models have a long history of being deployed to investigate a wide range of polymeric and biological systems. Figure 7 shows how a MEH-PPV chain may be coarse-grained into consecutive bead-spring segments, each essentially modeling the end-to-end orientation and separation of a certain group of monomer units. Depending on the number of monomers included in such a segment with respect to that constituting a Kuhn segment, a FR chain or FJ chain can be selected as the CG polymer model, and the implementation of Brownian dynamics schemes is straightforward. For instance, if the simulation aims to capture the local rodlike structure as well as the global coil-like feature of a sufficiently long MEH-PPV chain, the FR chain model may be adopted for this purpose. On the other hand, the FJ chain model will be more efficient as the morphologies of large aggregate clusters are of major concern. In practice, both models can be utilized interchangeably in the forward/backward mappings to compromise efficiency and efficacy, as we discuss later.

A serious problem arises, however, while constructing non-bonded bead potentials, and this foreseen difficulty is reminiscent of the inherent inadequateness of mapping ellipsoidal or rodlike segments of a semiflexible chain onto spherical beads. Thus, with increasing degree of coarse-graining, determinations of the effective bead diameter inevitably become ambiguous. This situation clearly reflects the tradeoff as one picks the bead-spring models as an expedience in lieu of the much more complicated, yet realistic, ellipsoid-chain models for semiflexible chains. In a recent work, we proposed strategies that utilize material properties of intermediate length scales—e.g., the Kuhn length and polymer coil density—that can readily be known from finer-grained simulations, along with a single set of small angle neutron scattering (SANS) data, to parameterize the bonded and non-bonded potentials of a FR chain, with the latter assuming a LJ form (Shie et al. 2010). In the next section, we examine the performance of Brownian dynamics simulations based on the FR chain model in describing large-scale aggregation properties, which also manifest themselves in the same set of SANS data previously used to determine the parameters for single chains.



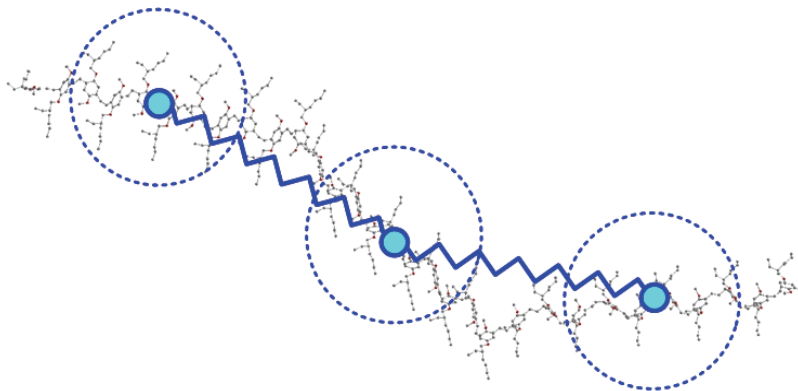


Fig. 7. Atomistic model versus bead-chain model representation for a MEH-PPV oligomer.

#### 2.4.2 The dumbbell model

The dumbbell model, as depicted in Figure 8, in conventional polymer kinetic theories has been to mimic the end-to-end orientation and separation of a polymer chain without account of any intermediate details as may be captured by a bead-spring chain model introduced above. In both cases of the FJ and dumbbell models, there exist standard classical theories relating the spring potential with the number of Kuhn segments belonging to a chain segment or the dumbbell. In simulating an aggregated polymer system, the non-bonded bead potential plays an important role, too, and must be constructed on a sound basis. The protocols proposed in an early work (Shie et al. 2007) resemble the one described in Sec. 2.3 for two ellipsoid segments, except that the PMFs of two previously parameterized FJ chains were used for this purpose. The dumbbell model so constructed is especially useful for simulating large-scale aggregation properties, as the detailed chain conformation is of less concern, or when the simulation results are meant to be back-mapped to the FJ or FR models to expedite the subsequent equilibration.

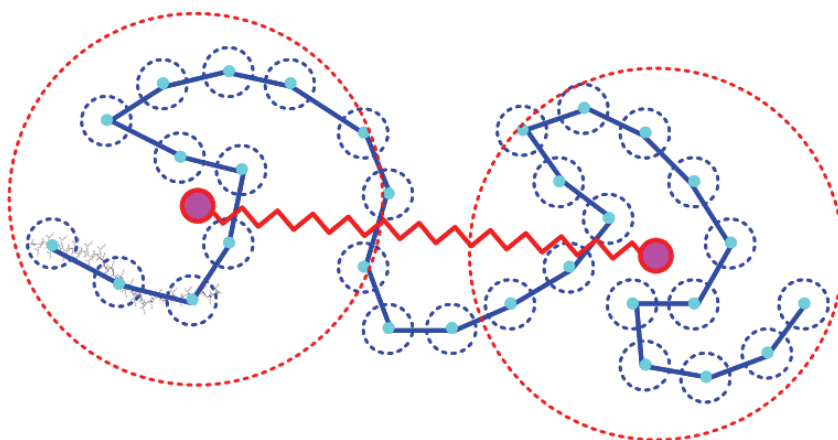


Fig. 8. Bead-chain and dumbbell model representations for a single MEH-PPV chain.

Before closing this introductory section for various CG polymer models and simulation schemes for MEH-PPV, it is very important to keep in mind that their conventional counterparts have mostly been used for more qualitative purposes, often without specifications of the particular polymer-solvent considered. In contrast, the cases of our current interest are meant to be predictive in the first place. It also appears that no early studies have covered such a wide range of CG models and simulation schemes for a single polymer system as have been demonstrated for MEH-PPV. The last perspective, intriguingly, points to the open opportunity of utilizing multiscale schemes to capture real large-scale material properties of specific macromolecular systems.

### 3. Results and discussion

In this section, the simulation results are presented according to increasing degree of coarse-graining, similar to the way the models have been introduced above. It can be seen that large-scale material properties become progressively accessible as some molecular details become irrelevant and, hence, more coarse-grained views may be adopted. To delve into how material properties evolve during a practical processing, it is also instructive to understand first elementary solution properties before their impacts on the eventual quenching state are scrutinized.

#### 3.1 Single-chain properties in binary solvent media

The polymer model depicted in Figure 3 and the corresponding CGMD simulation are especially relevant to resolving the detailed polymer-solvent interactions in various solvent or hybrid-solvent systems; more details can be found in an early work (Lee et al., 2011). In the literature, some confusion prevailed regarding the “solvent quality” for an amphiphilic conjugated polymer like MEH-PPV, and further clarification on this fundamental issue for polymer solution would be possible if a better understanding into such interactions can be gained in an unequivocal way. For instance, an aromatic solvent, such as toluene, is expected to be attractive to the phenyl backbone of MEH-PPV and, intuitively, might be conjectured to serve as a better solvent than an aliphatic solvent, such as chloroform, which may be attractive to the alkoxy side chains at best. The interesting question is: which of the two helps bolster a relatively expanded chain conformation or, in a statistical sense, larger mean coil size? The situation is even complicated, more intriguing as well, as two distinct solvents are concurrently present in a hybrid-solvent system. In both cases, it should be evident that treating the side-chain and backbone molecules as different CG particles are essential to address these issues.

Figure 9 shows the predicted mean radii of gyration as functions of the solvent composition for two representative sets of binary solvents, chloroform (CF)/toluene (T) and chloroform/chlorobenzene (CB). As far as single-solvent systems are concerned, the apparent solvent quality clearly follows the ordering  $CF > CB > T$ . Interestingly, the previous prediction is at odd with the naïve, prevailing notion that aromatic solvents—which bear better chemical affinity with the backbone molecules—would result in a better solvent quality. As we turn our attention to the more complicated, binary-solvent systems, Figure 9 reveals another significant feature that cannot be foreseen on the basis of the results just revealed for single-solvent systems. It can be seen that the mean coil size, and thus the apparent solvent quality, is not a monotonic function of the solvent composition, and there appears to be an optimum mixing ratio in each case, i.e.,  $CF/T=1:1$  or  $CF/CB=2:1$  in number density, that renders the best solvent quality. Some representative snapshots given in Figure 10 are instructive in light of what the overall chain conformation might look like in each of

these systems. It is of interest to note the highly extended chain conformations corresponding to the two optimum solvent qualities. Noticing that the detailed chain conformation in dilute solution is dictated by localized polymer-solvent interactions, we next scrutinize the simulation results that offer the relevant details—features that cannot be assessed by experimental protocols.

Because the two hybrid-solvent systems exhibit essentially the same trends, the following discussion is focused on the CF/CB solvent system of MEH-PPV. Figure 11(a) plots the local ratio of the two solvent species, normalized by the bulk one, as a function of the normal distance away from the polymer backbone, as schematically illustrated in the same figure.

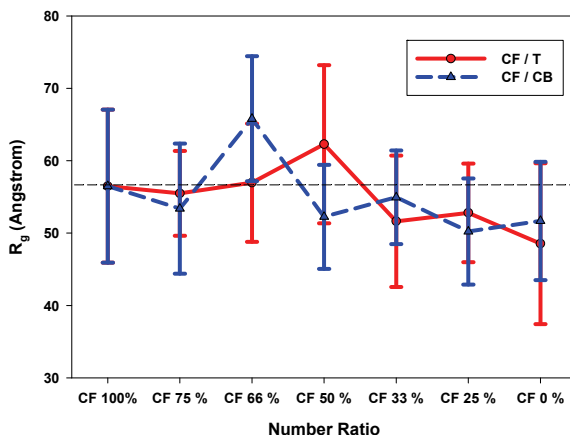


Fig. 9. The predicted mean radius of gyration for single 300-mer MEH-PPV chains in single- or binary-solvent system at 298 K and 1atm. The lines are used to guide the overall trend.

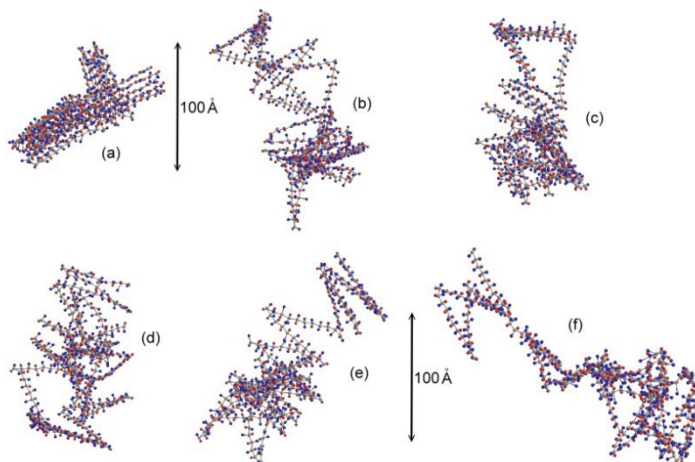


Fig. 10. Snapshots of MEH-PPV chain conformations in (a) quenching system, (b) chloroform, (c) toluene, (d) chlorobenzene, (e) chloroform/toluene=1:1 and (f) chloroform/chlorobenzene=2:1.

It can be seen that, within a thin shell of thickness ca. 3 nm, local solvent compositions differ noticeably from the bulk one. In particular, at a mixing ratio of CF/CB=2:1, which corresponds to an optimum solvent quality in Figure 9, the (positive) deviation seems to be the most prominent. The observation that local CF population could substantially outnumber that in the bulk phase is clearly suggestive of certain coupling effects that, in turn, are sensibly affected by the blending ratio of the two solvent species.

Figure 11(b) shows the corresponding RDFs, and the results for single-solvent CF system are also included for comparison. Several interesting features can be noted immediately. Firstly, the first (dominant) peaks in the RDFs clearly indicate that while CF molecules are considerably more attractive to the alkoxy side-chain units (C) of MEH-PPV, CB molecules are slightly more attractive to the backbone (B), as might be expected using chemical affinity arguments. Comparing the results with those for pure CF solvent system, however, reveals that CB molecules have a drastic impact on the peak height of the C-CF pair distribution. That is, without the presence of CB molecules, CF is normally depleted from the polymer territory, possibly to avoid the backbone molecules. Further, an intriguing feature is that both curves of C-CF and B-CB display conspicuous oscillations beyond the first peak, a phenomenon rarely observed with single-solvent systems. The sketch given in the same figure suggests that this peculiar feature could be indicative of a somewhat ordered, lattice-like or layered structure of solvent molecules encompassing the polymer units that are attractive to them.

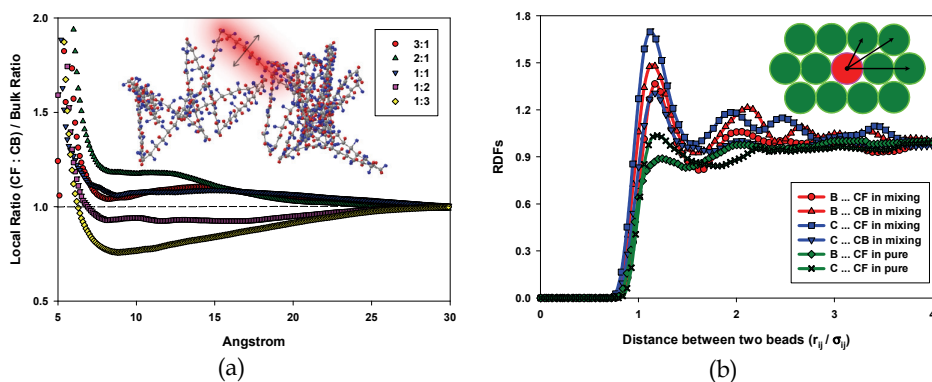


Fig. 11. (a) Solvent particle distributions measured at a normal distance away from the polymer backbone in the CF/CB binary-solvent medium of MEH-PPV. (b) The RDFs (for CF/CB=2:1) reflecting the distributions of solvent molecules with respect to the backbone (B) or the long-alkoxy side chain (C) of the polymer; the results for single-solvent CF system are also shown for comparison. The distance in (b) has been normalized using the mean van der Waals diameters of the two CG particles involved.

We suggest the following interpretations of the phenomena noted above. The role played by CB molecules in the CF/CB hybrid solvent system of MEH-PPV is twofold: They attract, and thus “stabilize,” the MEH-PPV backbone preventing too collapsed a chain conformation, especially with the presence of the “disliked” CF molecules that are to be avoided by the phenyl backbone. On the other hand, they help shield the “repulsions” directly between CF and MEH-PPV backbone, thus encouraging immigration of CF

molecules into the shell regime to better attract the side-chain groups. *Altogether, this sophisticatedly compromised, local molecular environment warrants the sustainability of exceptional, highly extended MEH-PPV chains – which obviously require a free exposure of both the side-chain and backbone units that can only be fulfilled in a hybrid-solvent medium for an amphiphilic polymer like MEH-PPV.* Moreover, compared with toluene (T) molecules, the somewhat amphiphilic attribute of CB is expected to be a superior “mediator” to play the essential roles as suggested above, besides its better affinity to the CF molecule as well. Note, however, that as CF molecules progressively migrate into the boundary layer regime, they must do so against the bulk osmotic pressure, until an eventual balance between the two “phases” has been established. Thus, the peculiar features manifested by Figures 9-11 may be perceived as arising from a subtle balance between local-phase chemical affinities and bulk-phase osmotic pressure – the latter being basically entropic in nature.

### 3.2 Structural and dynamic properties of single chains and interchain aggregates

The central difference between the polymer models depicted in Figures 3 and 4, respectively, lies in that each repeating unit, including the bulky side-chain groups, is treated as a single CG particle in the latter representation, so that the corresponding CGMD or CGLD simulations become more efficient, especially for studying long single chains or interchain aggregates. Of course, the model becomes inadequate, though, for hybrid solvents as discussed above. As an example that demonstrates the robustness of CGLD simulations, Figure 12 shows the mean end-to-end distance of MEH-PPV for chain lengths up to 500 repeating units, which seems sufficient to determine the solvent quality exponents for the two solvents examined, i.e., chloroform and toluene.

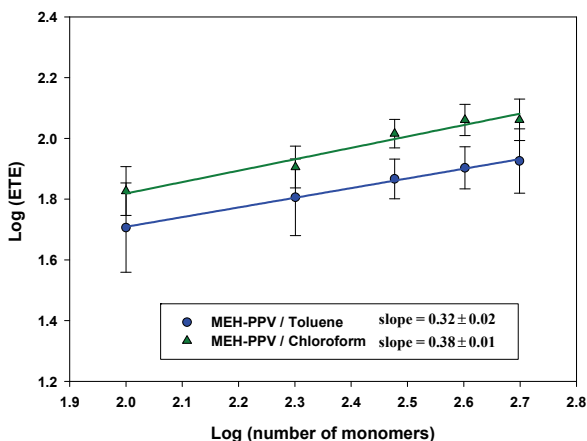


Fig. 12. The scaling law of the mean end-to-end distance (ETE) as functions of molecular weight (number of monomers per chain) for single MEH-PPV chain in two different solvent systems.

For long, the solvent quality of MEH-PPV solutions remained somewhat mysterious, due to the fact that experimental protocols, such as viscometric measurements and light scatterings, commonly purporting to assess this fundamental quantity for dilute solution become ineffective because of a great tendency for the polymer chains to associate and form interchain aggregates even at large dilution. Under this circumstance, computer simulations

become indispensable to extract information for such analysis. The results shown in Figure 12 yield a solvent quality exponent of 0.38 for chloroform and 0.30 for toluene, suggesting that both are rather poor solvents for MEH-PPV. Given that chloroform is arguably the best solvent known so far for MEH-PPV, the interesting implication appears to be that no solvents can actually be “good” for this amphiphilic conjugated polymer, which requires a scaling exponent above 0.5—the theta solvent condition. This central implication explains why intra- and interchain aggregates prevails even at large dilution.

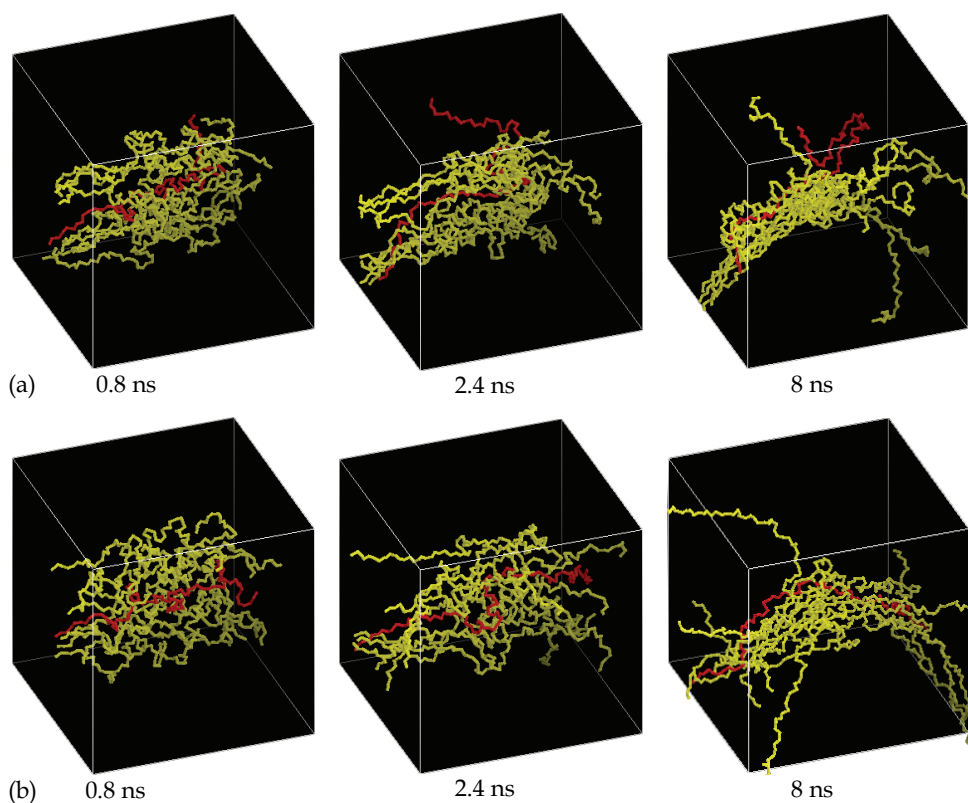


Fig. 13. Snapshots of ten MEH-PPV chains collapsing into an aggregate cluster in (a) toluene or (b) chloroform at various times at  $T = 298$  K and 1 atm, where all chains were initially placed in parallel and assumed a fully extended chain configuration. The simulation time has been re-scaled to coincide with the real, AMD time.

Recently, SANS has been utilized to assess the Kuhn length of MEH-PPV in solution, by assuming that this localized chain property is unaffected by segmental or interchain aggregation (Ou-Yang et al. 2005). Thus, it is of interest to compare the simulation results with the experimental estimate. The persistence length of MEH-PPV is estimated in the CGLD simulation to be  $65.1 \pm 11.8$  (Å) in toluene and  $73.3 \pm 12.5$  (Å) in chloroform, which correspond to the mean end-to-end distance of about 25 MEH-PPV monomers, or 50 monomers in a Kuhn segment—if a ratio of two is assumed for these quantities. For

comparison, we note that light scattering data have suggested a value of ca. 60 Å in p-xylene (Gettinger et al. 1994), while SANS data yielded 87.5 Å in chloroform (Ou-Yang et al. 2005). The agreement between simulation and experiments may be deemed fairly good, considering the large uncertainties involved in these methods.

As stressed in earlier introductions, developing CG models and simulation schemes for conjugated polymers has been motivated in a large part by the imperative need of resolving supramolecular aggregation properties in solution, and later in quenching thin film. This essential goal, however, poses notable challenges to usual AMD and CGMD simulations for realistic chain lengths. At present, only some preliminary results from CGLD simulation are available, leaving the major discussion and analysis to later subsections, where more efficient simulation schemes are employed to investigate larger-scale aggregation properties. Figures 13 show the snapshots of ten MEH-PPV chains collapsing into a single aggregate cluster in two different solvents. The results provide basic insights into how fast individual chains may coalesce into an aggregate cluster, as well as how the eventual morphologies are dependent on the solvent used. To further characterize the structural compactness of an aggregate cluster, which may be assessed by combined dynamic and static light scatterings, we use the following definition of monomer density:

$$\rho_N = \frac{N_b}{\frac{4}{3}\pi R_g^3}, \quad (5)$$

where  $N_b$  and  $R_g$  denote the number of monomers and radius of gyration of the cluster, respectively. The monomer density (number of monomers/nm<sup>3</sup>) is thus estimated to be  $\rho_N = 0.4$  in chloroform and  $\rho_N = 0.7$  in toluene. If similar structural features apply for the bulk majority of aggregate species in dilute MEH-PPV solution, the monomer densities so obtained may also be utilized to estimate the mean aggregation number in experiment, which would be difficult, if not impossible, to evaluate from usual light scattering analysis as the commonly practiced Zimm plots cease to be reliable for a highly aggregated system. More details about the simulation protocols, data analysis and discussion can be found elsewhere (Lee et al. 2008)

### 3.3 Aggregation properties predicted by ellipsoid-chain models

The CGLD scheme discussed above, though much more efficient than usual AMD and CGMD simulations, still suffers serious constraints in investigating real large-scale aggregation properties of practical interest. For instance, an ongoing light-scattering study suggests the prevalence of aggregate clusters each consisting of a few tens or even hundreds of chains in dilute MEH-PPV solution. Therefore, more efficient CG models and simulation schemes must be developed in order to facilitate experimental analyses or interpretations. To fulfill this requirement, the CG model considered in Figure 5 or 7 may be exploited. The merits and drawbacks of each of the two CG models have been highlighted in the preceding section, and it is tantalizing to make some comparisons of the predicted aggregation properties. Since a major part of the CGMC simulation based on the ellipsoid-chain model belongs to an ongoing work, only preliminary results are presented in Figure 14, which shows representative single-chain conformations and aggregate morphologies of MEH-PPV in toluene (top left and right) or chloroform (bottom left and right). The monomer densities

for the aggregates were found to be 0.62 and 0.17, respectively. Comparing the results with those from the CGLD simulation for 10-chain MEH-PPV systems, there seems to be reasonable agreement between the two, while the monomer densities systematically fall below the values predicted by the CGLD simulation. It could be that the structural compactness decreases with increasing number of polymer chains forming an aggregate cluster, until a critical aggregation number has been reached. Of course, this conjecture awaits further evaluation as simulation results for even larger aggregate clusters become available.

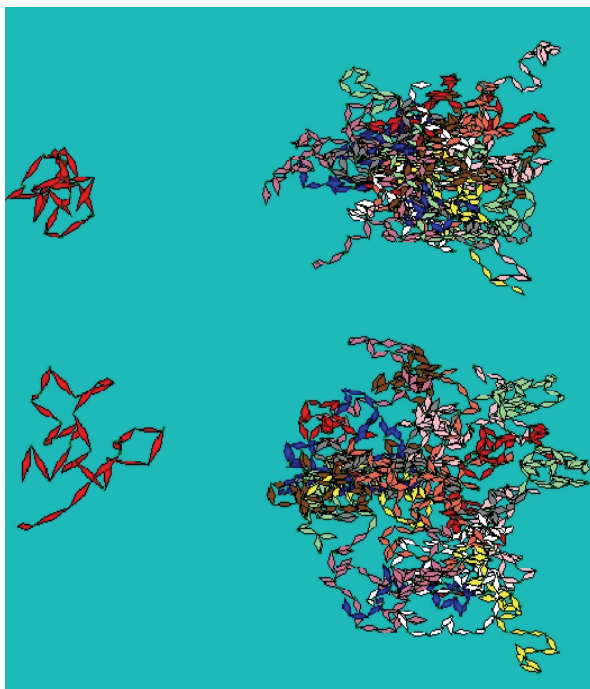


Fig. 14. Realizations of a single, 300-mer MEH-PPV chain (consisting of 30 ellipsoids) based on ellipsoid-chain model in toluene (top-left) or chloroform (bottom-left); realizations of an aggregate cluster made of 20 MEH-PPV chains in toluene (top-right) or chloroform (bottom-right).

### 3.4 Comparison with SANS data on single-chain and interchain aggregate structures

In the literature, the FR chain model and the associated Brownian dynamics schemes have a long history of being employed in studying semiflexible biopolymers such as DNA. To our knowledge, the model has not been employed earlier to study conjugated polymers. Despite a similar level of coarse-graining as with the ellipsoid-chain model considered above, it is possible to carry out usual Brownian dynamics simulations with the FR chain model. The main interest here is twofold: the first is to compare the predicted interchain aggregation properties with what we have briefly reviewed based on the MC simulation of the ellipsoid-chain model, and the second is to make direct comparisons with a set of recently reported



SANS data on MEH-PPV solutions. To simultaneously capture the local rodlike feature and the global coil-like conformation of MEH-PPV, as probed by SANS experiments (Ou-Yang et al. 2005), we have assigned five FR segments to representing a Kuhn segment of MEH-PPV, which is equivalent to treating 10 repeating units of MEH-PPV as one FR segment (Shie et al. 2010) – a CG level identical with the ellipsoid-chain model discussed above. For the sake of simplicity, however, synthesized defects are not considered in the simulation making use of FR chains.

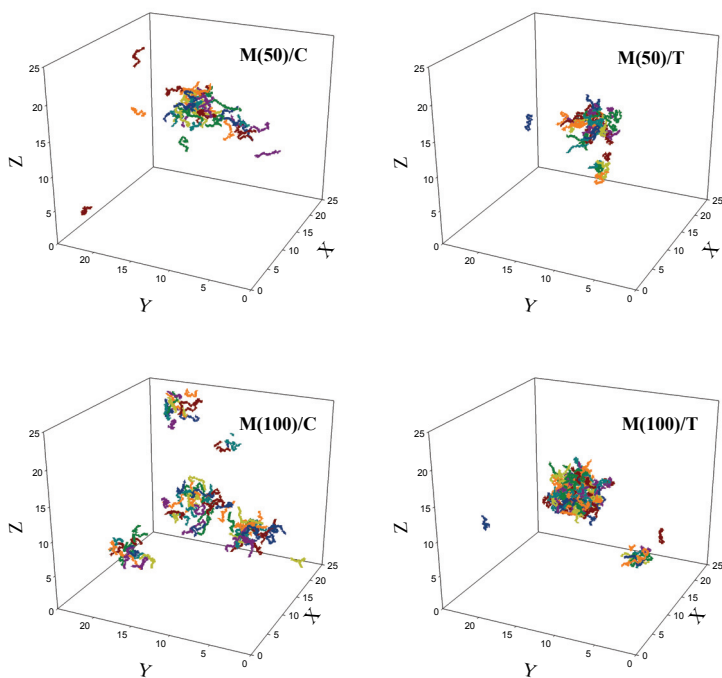


Fig. 15. Snapshots of the aggregation morphologies of MEH-PPV (M) in chloroform (C) or toluene (T) for 50-chain (top) or 100-chain (bottom) system.

Figure 15 shows the results for two many-chain systems consisting of 50 and 100 MEH-PPV chains, respectively. The simulation starts with randomly distributed isolated chains in a periodic cubic box, and equilibration was judged by eyes to maintain stable aggregation morphologies in both solvent systems. To expedite the simulation, the FJ chains were used to commence the process of aggregation and foster stable aggregate clusters, before a systematic back-mapping was performed to return the system to their children FR chains. Despite the difference in the total number of chains used, remarkable similarity can be noted in the overall aggregation features. While mainly a few compact aggregate clusters are seen for MEH-PPV/toluene system, a larger number of loose aggregate clusters and sporadic isolated chains survive in MEH-PPV/chloroform system. These features, as a whole, are in agreement with the predictions based on the finer-grained models discussed earlier. Thus, the simulation results should allow for a meaningful comparison with the SANS data and, accordingly, render insights not readily perceivable in the SANS data, as we discuss below.

As has been noted earlier, the FR chain model requires a priori single-chain properties as an input to determine the bonded and non-bonded potentials in general, along with preliminary experimental data to help fix the effective bead diameter in particular. The bead diameter so determined, presumably, should stay insensitive to the solvent considered, and hence, there will remain only one floating parameter readily determinable from a finer-grained simulation if a different solvent is to be considered. From this perspective, the model may be regarded as possessing predictive capability for all solvent systems of the same polymer. Figure 16 shows direct theory/data comparisons for a wide range of scattering vectors,  $q$ . Firstly, one sees a good agreement at large and intermediate values of  $q$ , where contribution to the total scattering intensity is dominated by the solvent-induced single-chain conformations. The results suggest that interchain aggregates have insignificant influence on single-chain conformations, inasmuch as the structural compactness does not change appreciably after aggregate formation. On the other hand, there exist notable discrepancies in the low  $q$  range, where the contribution from interchain aggregates becomes increasingly important.

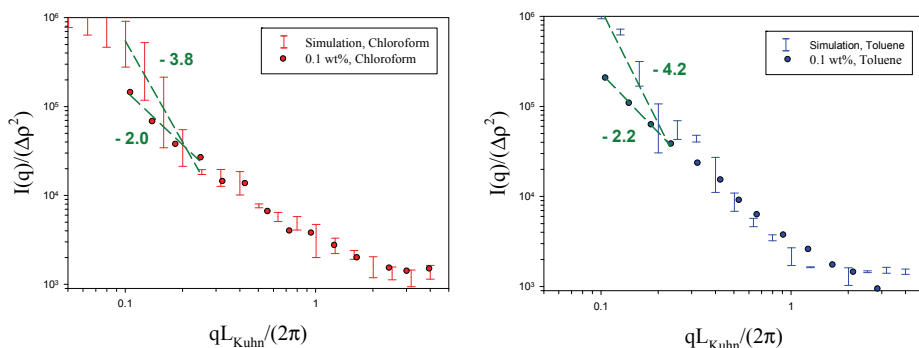


Fig. 16. Comparison between the simulation (using two model aggregate clusters for each solvent system as chosen from the realizations shown in Fig. 15) and SANS data for the total scattering intensity as functions of the scattering vector  $q$ .

In early experimental interpretations (Ou-Yang et al. 2005), the apparent scaling exponents, ca. 2, in this low- $q$  regime have been assigned to 2D fractal structures of the aggregation network. The simulation, on the other hand, implies that the nominal scaling exponents could be a consequence of cooperative contributions from a broad variety of aggregate clusters, whose structure remains spherical colloid-like (with a scaling exponent ca. 4), and single, isolated chains, whose contribution was noted to level off *but not vanish* in this regime. Thus, until even smaller  $q$  may be probed, say, by light scattering, the effects of isolated chains and small aggregate clusters—both bear 2D fractal structures—cannot be fully ignored, and the significance of the apparent scaling exponents remains elusive in these cases. Overall, this is an interesting example demonstrating how computer simulations might help resolve issues that otherwise remain ambiguous at an experimental level. To evaluate an earlier proposal concerning structural compactness of the aggregate clusters, we have also examined the monomer density of the largest aggregate cluster in each solvent system, and the results (0.02 for MEH-PPV/chloroform and 0.05 for MEH-PPV/toluene) seem to confirm the expected trends with increasing aggregation number. It should be noted, however, that self-consistency between different CG models awaits to be established before definitive conclusions may be drawn.

### 3.5 Aggregation morphologies predicted by the dumbbell model

As the main interest in a polymer solution is concerned with the average chain alignment, but not the detailed chain conformation, the dumbbell model depicted in Figure 8—which grasps only polymer end-to-end orientation and represents the most coarse-grained polymer model of all—suffices for this purpose. Figures 17-18 depict the snapshots showing the aggregate formation for 100 such dumbbells that mimic MEH-PPV chains in two different solvents, where the dumbbells at first are randomly placed in the simulation box. The simulation time has been made dimensionless by the estimated Rouse time of the parent FJ chains.

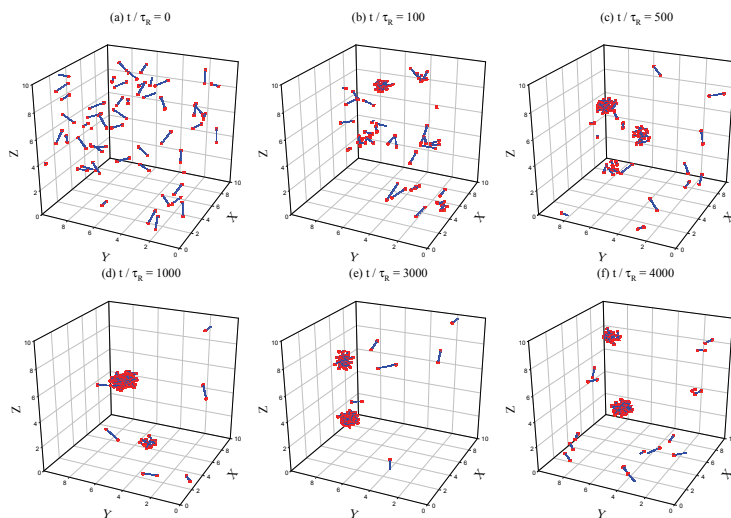


Fig. 17. Snapshots of dynamic aggregation morphologies in MEH-PPV/chloroform solution.

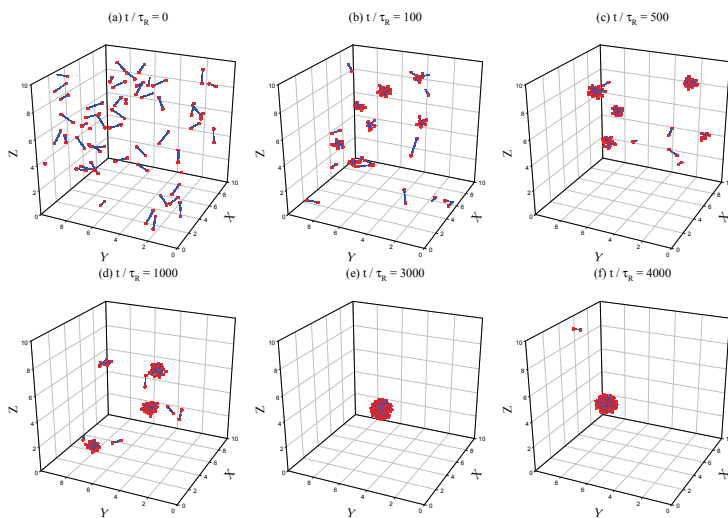


Fig. 18. Snapshots of dynamic aggregation morphologies in MEH-PPV/toluene solution.

Despite the crudeness of the model used, it is significant to notice a striking similarity with the results shown in Figure 15 based on the more sophisticated FR chain model, in view of the effects of solvent quality on the overall aggregation morphologies. The close agreement seems to suggest the dominance of interchain attractions over the effects of polymer entanglement. More results and discussion can be found elsewhere (Shie et al. 2007), including the influences of a steady shearing that grossly mimics flow processing.

### 3.6 Quenched MEH-PPV chain morphologies investigated by reverse mapping

To shed light on the effects of solvent on the quenched-chain morphologies, the simulation results introduced in Sec. 3.1 for single- and hybrid-solvent systems are systematically back-mapped to full-atom coordinates. For simplicity, and to gain general insights, we assume an instant evacuation of solvent molecules, although real film casting involves a more gradual solvent evaporation. The back-mapped, atomistic chains were first allowed to equilibrate for their local structures in the AMD simulation, before the quenching process formally commences. The simulation of chain quenching was carried out in a vacuum, NVT environment at the same system temperature (i.e., 298 K), and the time required for a complete chain collapsing has been estimated to be about 2.0 ns based on the re-scaled, real AMD time. In fact, such an extremely short period compared with the time scales associated with typical film casting might, at least in part, be utilized to justify omitting the effects of solvent evaporation rate.

Figure 19(a)-(b) shows the snapshots of single MEH-PPV chains being quenched from two different solvent media, which have been selected for their stark contrast in the corresponding solvent qualities. It is evident that a previously extended and loose chain conformation, such as that formed in the CF/CB=2:1 medium, permits a relatively regular chain folding along the pivotal tetrahedral defects and, in turn, results in a notably higher degree of ordered  $\pi-\pi$  stacking, which promotes the electronic delocalization quintessential for local charge transports. Note, in particular, that the eventual quenching structure shown in Figure 19(a) has been arrested by localized, anisotropic  $\pi-\pi$  interactions. In contrast, for a previously compact chain conformation, like that formed in toluene and shown in Figure 19(b), the quenched chain ubiquitously becomes much collapsed and featureless, due to the predominant, isotropic van der Waals segmental interactions. Quantitatively, Figure 19(c) (which has been created using time plus ensemble averaging) shows the RDFs revealing the fingerprint of ordered  $\pi-\pi$  stacking, which bears a characteristic center-to-center distance about 4.1 Å—or about 3.5 Å for the vertical distance between the two phenyl planes, which is more often referred to—for MEH-PPV chains quenched from various solvent media. Clearly, the chain quenched from the CF/CB=2:1 solvent medium accommodates the greatest amount of  $\pi-\pi$  stacking, about 60 percent higher than the second place for CF/T=1:1 medium and substantially surpassing the rest single-solvent systems. Moreover, a close correspondence between the mean coil-size (or effective solvent quality) in solution, as previously revealed in Figure 9, and the degree of  $\pi-\pi$  stacking in the quenching state can be observed. An interesting exception should be noted, however, with the case of single-solvent CB medium, which apparently results in a higher mean degree of  $\pi-\pi$  stacking despite a smaller mean coil size than in the single-solvent CF medium. The disparity may be explicated by noting that the CB-induced backbone exposure—as contrasted with the CF-induced side-chain exposure—of MEH-PPV evidently serves as an advantageous precursor for the subsequent formation of  $\pi-\pi$  stacking. Thus, not only does the overall chain expansion in solution matter, the detailed solvent-induced chain conformation has an important impact on quenched-chain morphologies as well. In

future perspective, the quenched chain conformations so obtained may serve as the reference state, based on which quantum chemistry computations may be carried out to further explore the optoelectronic properties of the polymer as quenched from various solvent media. In this way, it should be possible to establish an unequivocal link between the material properties in solution and in quenching thin film.

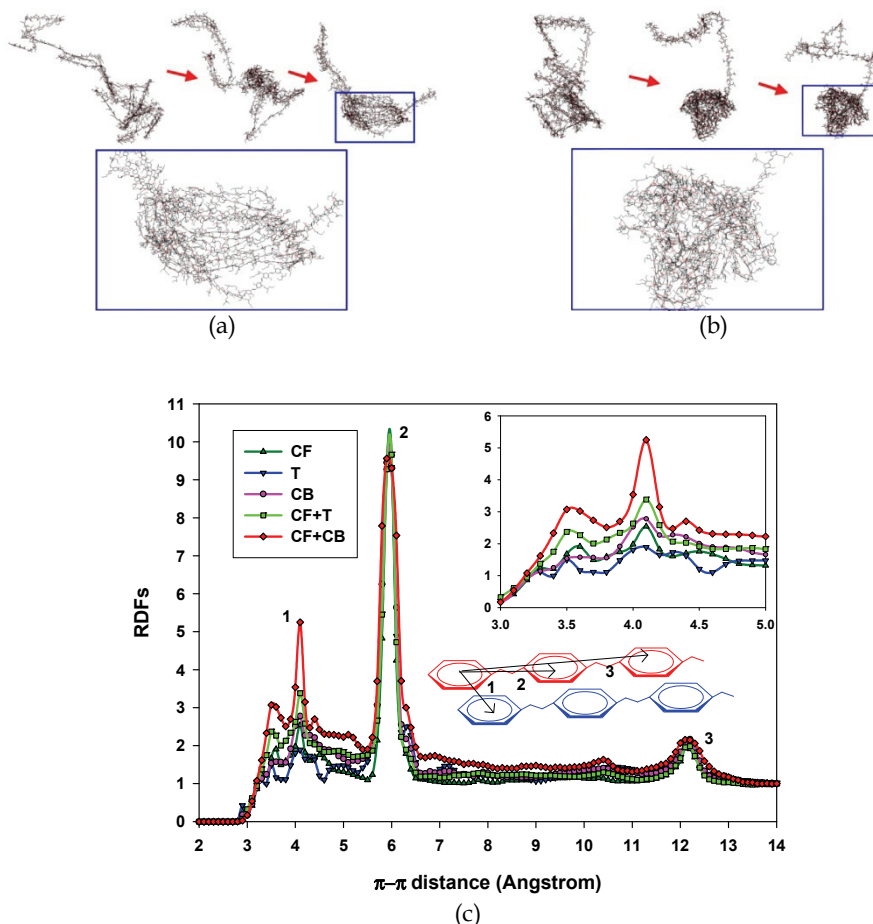


Fig. 19. Snapshots of a single 300-mer MEH-PPV chain quenched from (a) a binary-solvent medium, CF/CB=2:1, and (b) a single-solvent system, T; (c) the RDFs revealing the formation of ordered  $\pi - \pi$  stacking for a single MEH-PPV chain quenched from various solvent media, where the inset shows the zoomed plot that best illuminates the relative partition of  $\pi - \pi$  stacking (at ca. 4.1 Å).

### 3.7 Phase-separated nanomorphologies in hybrid C60/MEH-PPV system

An emerging area that shall find profound applications of CG simulations is to unravel the detailed mechanisms regulating nanoscale phase-separated morphologies of hybrid fullerene/conjugated polymer systems, which have received growing attention recently in

fabricating heterojunction thin films for application in organic solar cells. Among them, C60/MEH-PPV has since served as a primitive model system to unveil how the aforementioned nanomorphologies impact the optoelectronic properties of a solar cell device. At a preliminary stage, we have obtained results as shown in Figure 20 using the interparticle potential found in an early CGMD simulation of C60 (Izvekov et al. 2005) and recast into a LJ form. For the TiO<sub>2</sub> nanorods, for example, deployed as an electrode for conducting the electrons to the outer circuit, the potential functions established in a recent multiscale computation on silica nanoparticles (Lee & Hua 2010) were directly transplanted onto the building blocks of TiO<sub>2</sub> to model the interactions with C60 or MEH-PPV. An intriguing feature in Figure 20 is the appearance of phase-separated, yet interconnected, nano-domains that are crucial for the transports of light-triggered electrons or holes. Ongoing studies utilizing more accurate potential functions will systematically explore the impacts of several essential factors, including the blending ratio and the solvent medium, on the eventual nanomorphologies of similar fullerene/conjugated polymer mixtures.

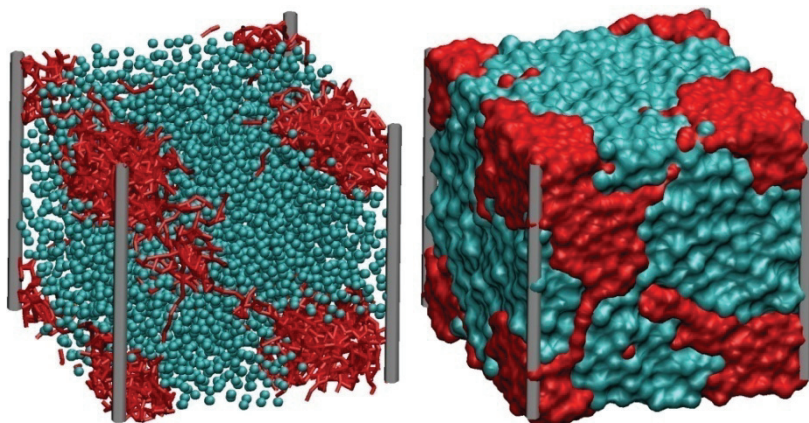


Fig. 20. Phase-separated nanomorphologies, sketched in two different perspectives, of a hybrid C60(dots)/MEH-PPV(fuzzy lines in the left picture) system with the presence of four vertical nanorods made of TiO<sub>2</sub>.

#### 4. Conclusion

This chapter reviews recent progresses in developing self-consistent, parameter-free CG models and simulation schemes aimed to capture fundamental single-chain and aggregation properties of standard conducting conjugated polymers from solution to the quenching state. Molecular insights so gained are essential to complement our current knowledge from conventional experimental characterizations, which become ineffective, if not impossible, in resolving nanoscale material properties of single chains and aggregate clusters in various solvent media and quenching processes. We demonstrated through these simulations how an unequivocal link between the material properties in solution and in the quenching state may be established, and remarked on the promising prospects of making direct predictions on the optoelectronic behavior of a particular polymer quenched from specific solvents or hybrid solvents. Progress along this line should help guide future molecular designs and process controls that best meet the quest of maneuvering the device performances at nanoscale levels. It should be reemphasized, however, that the strategies proposed and the applications

discussed should not be restricted to the particular polymer or solvent species considered, and the hierarchy of CG models and simulation schemes introduced in this monograph—presumably, starting from quantum-level computations to the construction of predictive dumbbell models—may be dexterously exploited in conjunction with the forward/backward mapping schemes to resolve material properties of practical interest. In future perspectives, these multiscale schemes may be automated in such a way that, given a specific polymer-solvent pair, interested material properties can be assessed in advance, subject only to the limits of contemporary computing resources. The prime challenges, however, seem to so far lie in the difficulties of treating anisotropic, highly localized intermolecular potentials, such as hydrogen-bond forces and  $\pi-\pi$  interactions, in any CG models beyond the atomistic level. This situation would imply that such interaction forces, quintessential in dense or condensed states, may be realistically accounted for at the current stage only through a series of back mappings to the atomistic level. A recent study, nonetheless, suggested that these localized interaction forces might play only minor roles in solution state (Lee et al. 2009), for which the demand of CG simulations is among the most stringent. Another appealing outlook for exploiting multiscale computation schemes is the emerging possibility to treat the interactions between fullerene/polymer and a solid substrate (Lee & Hua 2010), as hinted by the last example discussed with Fig. 20. Fulfilling this objective should make the current applications on thin-film devices more complete and powerful. Of course, it remains an essential task to ensure self-consistencies between various CG models and simulation schemes, and there still remains plenty room for future refinements. In conclusion, the seemingly concurrent advances in contemporary multiscale computations and organic optoelectronics have brought in not only strong motivations but also new opportunities for researchers who find themselves enthralled by, and to practically benefit from, an increasing interplay of the two.

## 5. Acknowledgment

The authors thank the supports from the National Science Council of ROC as well as the resources provided by the National Center for High-Performance Computing.

## 6. References

- Carbone, P.; Karimi-Varzaneh, H. A., & Müller-Plathe, F. (2010). Fine-Graining without Coarse-Graining: An Easy and Fast Way to Equilibrate Dense Polymer Melts. *Faraday Discussions*, Vol. 144, No. pp. 25-42, ISSN 1364-5498.
- De Leener, C.; Hennebicq, E.; Sancho-Garcia, J. C., & Beljonne, D. (2009). Modeling the Dynamics of Chromophores in Conjugated Polymers: The Case of Poly (2-methoxy-5-(2'-ethylhexyloxy)-1,4-phenylenevinylene) (MEH-PPV). *Journal of Physical Chemistry B*, Vol. 113, No. 5, pp. 1311-1322, ISSN 1520-6106.
- Faller, R. (2004). Automatic Coarse Graining of Polymers. *Polymer*, Vol. 45, No. 11, pp. 3869-3876, ISSN 0032-3861.
- Forester, T. R., & Smith, W. (2006). *The DL\_POLY\_2 Reference Manual*, Laboratory Daresbury, Daresbury.
- Gay, J. G., & Berne, B. J. (1981). Modification of the Overlap Potential to Mimic a Linear Site-Site Potential. *Journal of Chemical Physics*, Vol. 74, No. 6, pp. 3316-3319, ISSN 0021-9606.
- Gettinger, C. L.; Heeger, A. J.; Drake, J. M., & Pine, D. J. (1994). A Photoluminescence Study of Poly(phenylene vinylene) Derivatives: the Effect of Intrinsic Persistence Length. *Journal of Chemical Physics*, Vol. 101, No. 2, pp. 1673-1678, ISSN 0021-9606.

- Izvekov, S.; Violi, A., & Voth, G. A. (2005). Systematic Coarse-Graining of Nanoparticle Interactions in Molecular Dynamics Simulation. *Journal of Physical Chemistry B*, Vol. 109, No. 36, pp. 17019-17024, ISSN 1520-6106.
- Lee, C. K., & Hua, C. C. (2010). Nanoparticle Interaction Potentials Constructed by Multiscale Computation. *Journal of Chemical Physics*, Vol. 132, No. 22, pp. 224904, ISSN 0021-9606.
- Lee, C. K.; Hua, C. C., & Chen, S. A. (2008). Single-Chain and Aggregation Properties of Semiconducting Polymer Solutions Investigated by Coarse-Grained Langevin Dynamics Simulation. *Journal of Physical Chemistry B*, Vol. 112, No. 37, pp. 11479-11489, ISSN 1520-6106.
- Lee, C. K.; Hua, C. C., & Chen, S. A. (2009). Multiscale Simulation for Conducting Conjugated Polymers from Solution to the Quenching State. *Journal of Physical Chemistry B*, Vol. 113, No. 49, pp. 15937-15948, ISSN 1520-6106.
- Lee, C. K.; Hua, C. C., & Chen, S. A. (2010). Parametrization of the Gay-Berne Potential for Conjugated Oligomer with a High Aspect Ratio. *Journal of Chemical Physics*, Vol. 133, No. 6, pp. 064902, ISSN 0021-9606.
- Lee, C. K.; Hua, C. C., & Chen, S. A. (2011). Hybrid Solvents Incubated  $\pi$ - $\pi$  Stacking in Quenched Conjugated Polymer Resolved by Multiscale Computation. *Macromolecules*, Vol. 44, No. 2, pp. 320-324, ISSN 0024-9297.
- Mayo, S. L.; Olafson, B. D., & Goddard, W. A. (1990). Dreiding-A Generic Force-Field for Molecular Simulations. *Journal of Chemical Physics*, Vol. 94, No. 26, pp. 8897-8909, ISSN 0022-3654.
- Müller-Plathe, F. (2002). Coarse-Graining in Polymer Simulation: from the Atomistic to the Mesoscopic Scale and Back. *Chemphyschem*, Vol. 3, No. 9, pp. 754-769, ISSN 1439-4235.
- Nguyen, T. Q.; Doan, V., & Schwartz, B. J. (1999). Conjugated Polymer Aggregates in Solution: Control of Interchain Interactions. *Journal of Chemical Physics*, Vol. 110, No. 8, pp. 4068-4078, ISSN 0021-9606.
- Noid, W. G.; Chu, J. W.; Ayton, G. S.; Krishna, V.; Izvekov, S.; Voth, G. A.; Das, A., & Andersen, H. C. (2008). The Multiscale Coarse-Graining Method. I. A Rigorous Bridge between Atomistic and Coarse-Grained Models. *Journal of Chemical Physics*, Vol. 128, No. 24, pp. 244114, ISSN 0021-9606.
- Ou-Yang, W. C.; Chang, C. S.; Chen, H. L.; Tsao, C. S.; Peng, K. Y.; Chen, S. A., & Han, C. C. (2005). Micellelike Aggregates in Solutions of Semirigid Hairy-Rod Polymers. *Physical Review E*, Vol. 72, No. 3, pp. 031802, ISSN 1550-2376.
- Padding, J. T., & Briels, W. J. (2011). Systematic Coarse-Graining of the Dynamics of Entangled Polymer Melts: the Road from Chemistry to Rheology. In: *Soft Condensed Matter*, Available from: [arxiv.org/pdf/1102.0732](http://arxiv.org/pdf/1102.0732).
- Shie, S. C.; Hua, C. C., & Chen, S. A. (2007). Brownian Dynamics Simulation of Self-Consistently Coarse-Grained Dilute Aggregated Polymer Suspensions. *Macromolecular Theory and Simulations*, Vol. 16, No. 1, pp. 111-122, ISSN 1022-1344
- Shie, S. C.; Lee, C. K.; Hua, C. C., & Chen, S. A. (2010). A Predictive Coarse-Grained Model for Semiflexible Polymers in Specific Solvents. *Macromolecular Theory and Simulations*, Vol. 19, No. 4, pp. 179-189, ISSN 1022-1344
- Tschöp, W.; Kremer, K.; Batoulis, J.; Bürger, T., & Hahn, O. (1998). Simulation of Polymer Melts. I. Coarse-Graining Procedure for Polycarbonates. *Acta Polymerica*, Vol. 49, No. 2-3, pp. 61-74, ISSN 1521-4044.



## **Part 3**

### **Techniques and Characterization**



# Optoelectronic Techniques for Surface Characterization of Fabrics

Michel Tournalonias<sup>1</sup>, Marie-Ange Bueno<sup>1</sup> and Laurent Bigué<sup>2</sup>  
*University of Haute Alsace, Ecole Nationale Supérieure d'Ingénieurs Sud-Alsace,*  
*<sup>1</sup>Laboratoire de Physique et Mécanique Textiles (EAC 7189 CNRS/UHA),*  
*<sup>2</sup>Laboratoire Modélisation Intelligence Processus Systèmes (EA 2332),*  
*France*

## 1. Introduction

In the textile field, fabric surface properties influence the tactile feel, the visual aspect and some mechanical properties. They are strongly linked to manufacturing process, particularly to surface processes. Therefore the study of these fabric surface properties proves of importance. More precisely, the tactile feel is one of the most important garment selling points since one of the first consumer actions is to touch the fabric. Thanks to objective tactile parameters, the manufacturer can design and produce fabrics which please the consumers while respecting functionality of cloth. Moreover, for standard woven or knitted structures or low grammage nonwovens, the surface state can give some information about tensile properties or strain during tensile stress.

In order to characterize surface contact devices, such as tribometers<sup>1</sup>, are often used. They provide some information about friction behaviour, roughness of the surface or some other criteria more or less complex. This type of devices is often designed and used for hard materials. Concerning textile surfaces, because of their softness, these methods can have an influence on measurements in so far as superficial hairiness and even intrinsic structure may be modified. Both of these structural characteristics, hairiness and texture, are predominant in the tactile feel of textile surfaces.

Complementary to tribological methods widely used but whose precision may be insufficient, non-contact methods have been developed in order to characterise fabric surface state. These methods are mainly based on optical principles and have been getting a growing interest.

In this chapter we will present our contributions to the non-contact characterization of textile surfaces, firstly through the characterization of the state of surface (intrinsic structure and hairiness) and then through the evaluation of some mechanical properties of textile fabrics (strain and tensile properties). Implementations resulting in various apparatuses and some results are given in order to illustrate our purpose.

## 2. Basics of textile materials and description of our test samples

Fibrous materials must be considered at three different scales. First, fibres are the basic elements of textile materials; they correspond to the microscopic scale of the textiles. Second,

---

<sup>1</sup> Device for measuring friction and wear properties.

a yarn is an assembly of fibres and corresponds to the mesoscopic scale. And third, yarns are interlaced to make knitted fabrics or intercrossed to make woven fabrics. There is another type of textile surfaces which is directly made of fibres (or filaments if their length is infinite), without intermediate yarn step: the nonwovens. Fibres or filaments are randomly tangled as a web whose cohesion is given thanks to different processes which can be mechanical, thermal or chemical.

During manufacturing process, the end of some fibres can emerge from the yarn and the fabric: it produces a superficial hairiness. This hairiness can be also the consequence of an abrasive wear, for instance with emery paper or as a consequence of use. Length, size orientation relative to the surface and density are the main parameters characterising this hairiness.

As a summary the surface is then composed of elements at two different scales: a structure, i.e. the fabric itself, and a superficial hairiness. The surface state of fabrics is therefore linked to phenomena at microscopic scale (fibres and their mechanical properties) and at macroscopic scale through textile structure due to yarn and/or knitted, woven or nonwoven structures.

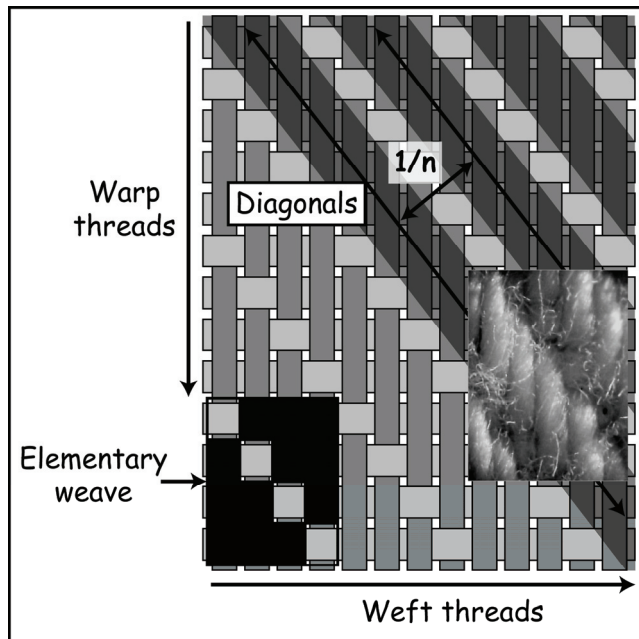


Fig. 1. Structure of a twill woven fabric.

In the following, various textile surfaces (woven fabrics and thermobonded nonwovens) have been tested.

Table 1 summarizes the characteristics of the plain woven fabric as well as those of three twill fabrics. The structure of twill woven is detailed in Figure 1. The kind of weave of each textile surface and the surface process are also indicated in Table 1. NE means the sample is not emerized contrary to E. SEM Pictures are presented for S2-NE and S2-E in Figure 2. For S1, samples emerized at two intensity levels are tested according to the size and the density

of abrasive particles of the emery paper. P80 corresponds to a density of 80 particles per mm<sup>2</sup> with an average 201 μm in diameter and P800 correspond to a density of 800 particles per mm<sup>2</sup> with an average 21.8 μm in diameter.

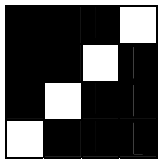
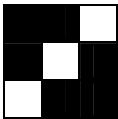
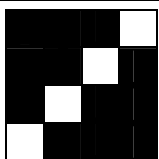
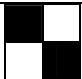
Notation	Elementary weave	Surface state	Material	Number of elements /cm
S1		NE E-P80 E-P800	100 % cotton	28 warp yarns/cm 17 weft yarns/cm 8.5 diagonals/cm
S2		NE E	96 % polyester 4 % elasthanne	44 warp yarns/cm 37 weft yarns/cm 21 diagonals/cm
S3		NE E	100 % cotton	29 warp yarns/cm 19 weft yarns/cm 11 diagonals/cm
plain woven fabric		NE	100 % cotton	26.5 warp yarns/cm 11.5 weft yarns/cm

Table 1. Characteristics of the woven fabrics used in our tests.

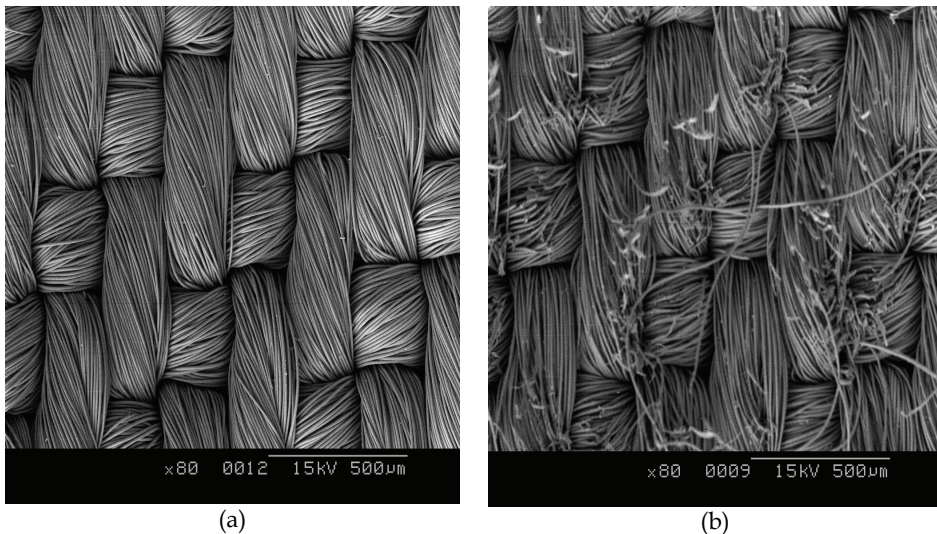


Fig. 2. SEM images of twill woven fabric (a) non-emerized S2, and (b) emerized S2.

Spunbonded nonwovens for medical use are also studied. Two samples are available; one was defined by the manufacturer as not compliant (noted NT4-NC) in terms of softness in comparison with the second one (NT4-C) (Figure 3). The cohesion of this filament web was obtained by thermobonding.

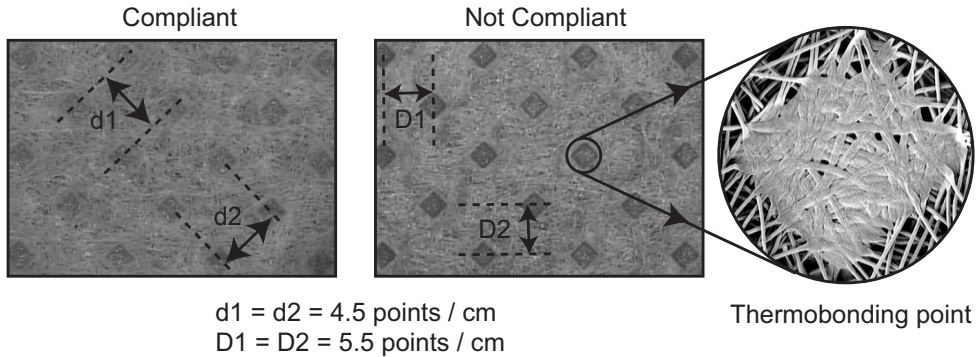


Fig. 3. Our test samples of spunbonded nonwovens.

### 3. Profilometry

#### 3.1 State of the art

Two elements have to be considered for characterizing textile surfaces: the structure and the hairiness.

In order to scan surfaces for constructing a profile of the sample, several methods have to be cited. Based on a point by point scanning of a surface different technologies of optical profilometers exist. The laser triangulation technique is used by Ramgulam et al. (1993). Seifert et al. (1995) compare this method with a classical contact method using a stylus probe. At each scanned point of the surface, the laser beam is reflected on an optical sensor. Hence the vertical coordinate of the point is recorded. From several points it is possible to reconstruct the surface profile. A confocal microscope can also be used (Becker et al., 2001 and Calvimontes et al., 2010). The principle consists in moving the lens in order to focus a laser beam on a sample with the maximum light intensity.

Other devices are based on the basic study of the reflected light energy by a sample highlighted by a light beam. The bigger the distance between the photodiode and the surface, the lower the reflected light intensity is (Ringens et al., 2002). Ishizawa et al. (2002) note the high correlation between such a measurement and "brightness", "roughness" and "luster" parameters defined for human visual characterization.

Xu et al. (1998) use a principle consisting in projecting a laser line on the surface of the sample. This line is deviated because of the surface roughness. Surface state criteria can be evaluated through deviations compared to the average line. This study is performed several times in different orientations in order to characterize the surface and to determine the main orientation of the structure.

Finally, a 3D scanning system based on laser triangulation technique can be used in order to obtain a profile of the sample. Interferometric methods and more particularly interferometric profilometer allow the user to determine the profile of the surface. A laser

beam is splitted into a part which goes on the fabric and the other which goes on a fixed mirror. The difference in the optical path between the two beams generates interferential fringes. The number of fringes is proportional to the optical path difference. As the position of the mirror is known the altitude of the surface point can be obtained.

Methods based on the projection of fringes (Conte et al.,1990) or speckle (Wang et al., 1998) on the surface are also used to obtain information about the roughness of the surface in so far as fringe patterns are obtained and analysed by image processing.

The measurement of textile hairiness was historically performed on yarns. The methods used are optical with signal or image processing techniques. The most famous devices are marketed and are the Uster Hairiness Tester (Durand and Schutz, 1983; Felix and Wampfler, 1990), the Zweigle hairiness meter or the Shirley hairiness monitor (Barella and Manich, 1993). Some other published techniques are based on different methods: light depolarization due to yarn hairiness (Anand et al., 2005), image processing after image capture (Cybulska, 1999; Kuratle, 1999; Nevel et al., 1999), optical coding of yarn shadow with an optical matrix (Stusak, 2004) or different shapes of optical digital sensors (Hensel et al., 2001). Fabric hairiness study was recently reported in the literature. Actually fabric hairiness is not commonly measured, essentially for on-line process control, as singeing, raising and so on. Like for yarn hairiness control, the method can be optical with a signal or an image processing (Osthoff-Senge; Governi and Furferi, 2005; Militky and Blesa, 2008).

### 3.2 Hairinessmeter

By lighting a textile surface with an oblique light, the structure and the surface hairiness can be detected. Then structure and hairiness have to be separated.

The optical assembly (Figure 4 and 5) proposed by Bueno et al. (2000) includes a laser diode for the sake of compactness. In front of the fabric, the beam goes through a beam expander and then illuminates the fabric. An image with structure and fibres appearing in dark on a bright background is then obtained (Figure 6a). The use of a DC-stop in the back focal plane of a lens allows the user to remove the direct component of the image (it now appears with external fibres in bright on a dark background) and to strongly attenuate the low-frequency component of the image (Figure 6b). The hairiness information is focused with a lens and directed onto a CCD camera.

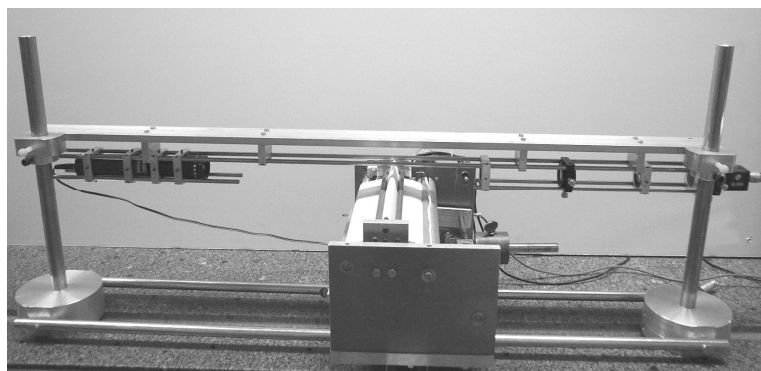


Fig. 4. Photograph of the hairiness meter optical part and of the sample carrier.

The fabric moves during the measurement with the help of a motorized sample carrier. In order to present a great curvature, the fabric goes on a blade (Figure 5).

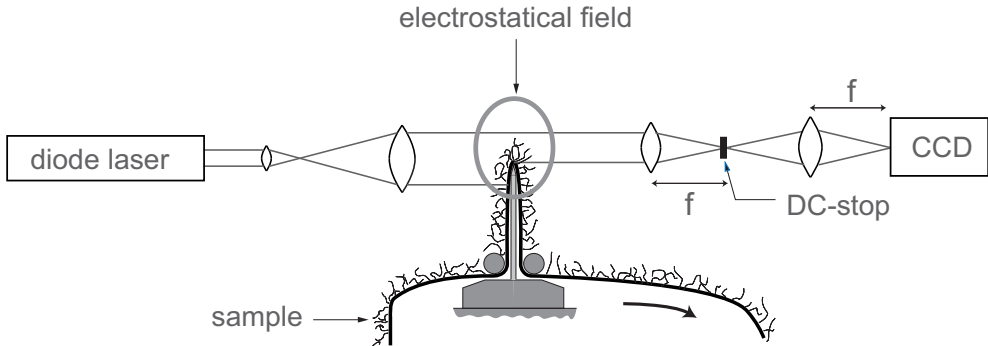


Fig. 5. Hairiness meter optical assembly.

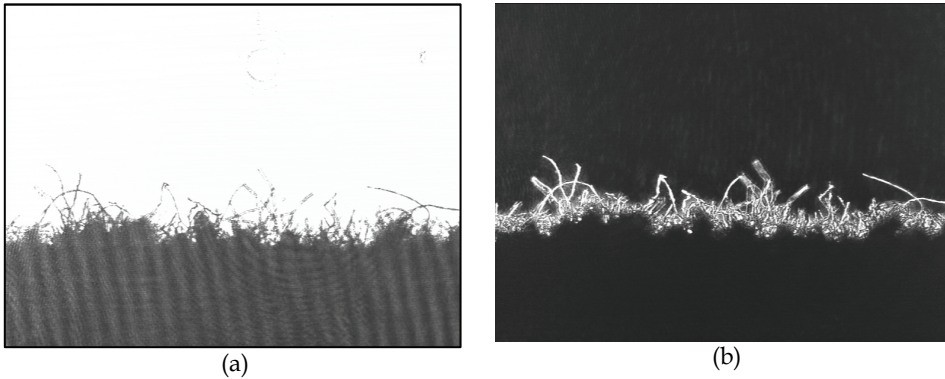


Fig. 6. Images of fabric hairiness without DC-stop (a), and with DC-stop (b).

The processing consists in computing the average grey level for each line, image by image. The average value of grey level for each line can be determined for the whole movie:

$$e(j) = \frac{1}{n} \sum_{k=1}^{k=n} \left( \frac{1}{w} \sum_{i=1}^{i=h} g_k(i, j) \right) \quad (1)$$

where

$j$  is the row number,

$i$  is the column number,

$k$  is the image number,

$n$  is the total number of images in the movie (in this paper  $n=200$ ),

$g_{i,j,k}$ : grey level of the  $i,j$  pixel for the  $k^{\text{th}}$  image,

$w$ : width of an image,

$h$ : height of an image.



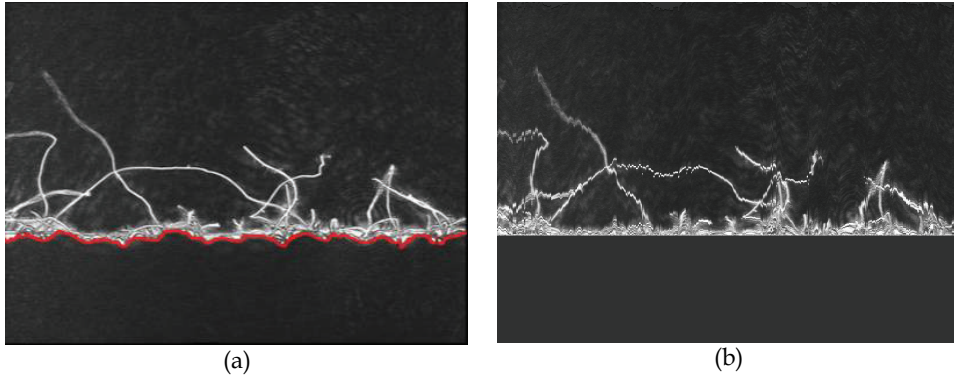


Fig. 7. Image before (a) and after (b) the image processing which eliminates the structure roughness.

The length distribution of hairiness can be plotted. Excepting for a totally smooth surface where the lower limit corresponds to a horizontal line, the obtained figures take into account the texture and the hairiness. In order to obtain the length probability function, the influence of the fabric structure roughness has to be eliminated, therefore another image processing has to be applied to these images. This processing eliminates profile and the obtained figures concern only the emergent hairiness (Figure 7).

Tests have been realized on S1-NE, S1-EP800. In Figure 8 we present length distribution obtained for these samples and the associated probability function. Emerising increases length of emergent fibres.

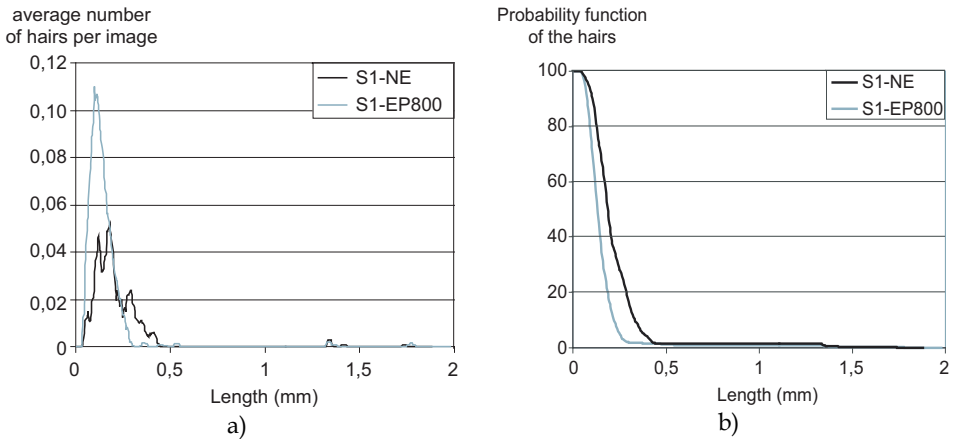


Fig. 8. Length distribution (a) and probability function (b) of the hairs before and after emerising.

### 3.3 Profilometer

The same device can be used as a profilometer the implementation of a further image processing. During the processing described above the fabric structure profile is estimated

(red line in Figure 7a) for each image. The 3D profile of the sample can be reconstructed. In Figure 9 the profile obtained with the S2 twill fabric is presented. Classical roughness parameters can be computed from this type of profile picture in order to characterize tested samples.

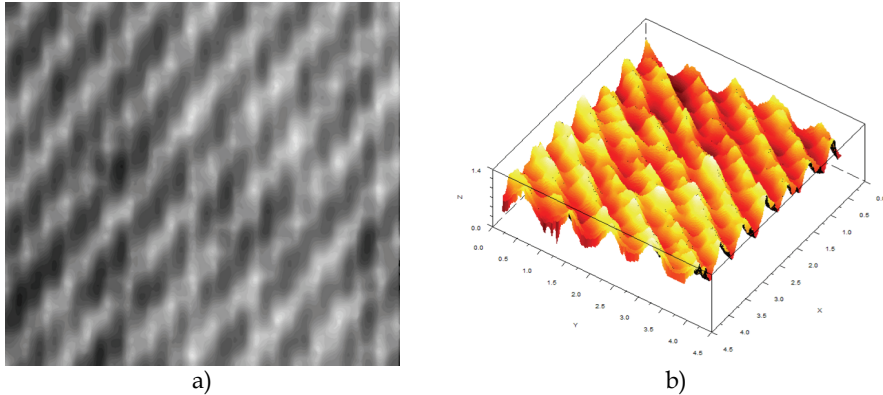


Fig. 9. Profile of S2-E obtained with the profilometer in 2D-representation (a) and 3D-representation (b).

### 3.4 Conclusion

In the measurement of textile structures, profile and hairiness have to be considered in order to obtain global information. We presented a method which allows us, through two different signal processings, to obtain the structure profile of the tested sample (profilometer) and its hairiness (hairinessmeter).

The structure profile can be characterised by standard statistical parameters: total and mean roughness, mean standard deviation, Root Mean Square, skewness, Kurtosis ... Hairinessmeter allows the user to have information about the density and the length of the emerging fibres.

## 4. Texture characterisation

### 4.1 State of the art

Textile texture is a set of surface state properties, mechanical and optical, which are often linked to tactile and visual aspects. The characteristics of the texture have to be related to the application and the product. In fact, texture information is complex and is different than criteria given by a profilometer. Several devices exist in order to bring this information. They are based on two principles: surface scanning and image processing.

An original method using a scan of the surface is presented by Xu et al. (1998) which also determine information about the texture through its device described above.

Nevertheless most methods used to characterize textile textures are based on surface pictures. After the acquisition, images are processed with Fourier Transform (Haggerty and Young, 1989; Wood, 1990; Wood, 1996; Millan and Escofet, 1996; Tsai and Hsieh, 1999), wavelet Transform (Kreißl et al., 1997; Tsai and Hsiao, 2001; Shakher et al., 2002; Tsai and Chiang, 2003; Shakher et al., 2004), other filters (Ciamberlini et al., 1996; Escofet et al., 1998),

or with statistical methods as those presented by Herlidou (1999). These techniques also allow the user to determine defects in textile samples which can be periodic or not. They use basic pictures of the sample but the image processing is often complex.

We have developed two methods. The first one is based on a kind of particular surface scanning useful for periodical textile surfaces. The second method is an image processing whose interest is to take into account the polarimetric properties of the textile surface.

#### 4.2 Texturometer dedicated to fibrous material

We implemented a texturometric device using active lighting (Bueno et al., 1999). The sample is clamped on a rotating sample carrier as in a record player. A laser beam projected by a laser diode onto the sample is focused as a line at the surface by passing through a cylindrical lens. The laser line is radial to the rotating sample carrier. A beamsplitter plate send the reflected beam to a photodetector and a spectral analysis is processed. The laser line is focused and aligned with the centre of rotation of the sample carrier in order to be radial, so during the rotation of the sample carrier, it scans the textile surface following a ring (Figure 10).

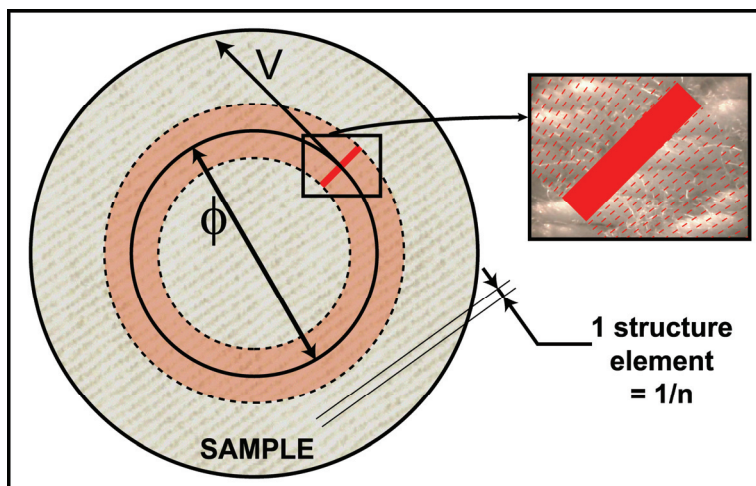


Fig. 10. Surface scanning principle of the texturometer, where  $n$  is the number of periodical elements per length unit,  $\Phi$  the ring diameter and  $V$  the linear speed.

The Fourier Transform of the temporal signal exhibits some peaks which correspond to the structural periodicities of the sample (Figure 11). The central frequencies of the peaks correspond to the distances between the elements and their amplitudes are linked to the surface state of these elements. The analysis of the spectral figures consists in determining these peaks and computing the energy of each peak. For sure two different fabrics (different in raw material, yarn, kind of weave or knit) present peaks whose frequencies can be very different (Figure 12), but much simpler devices would have made such a differentiation. The major point in using such a device is when it comes to differentiate fabrics whose only surface state is different. These differences can come from wear or mechanical abrasive process (for instance, emerizing). In this case, peaks have the same frequency and differences are evaluated through the energy of each peak. Results are obtained within a few seconds.

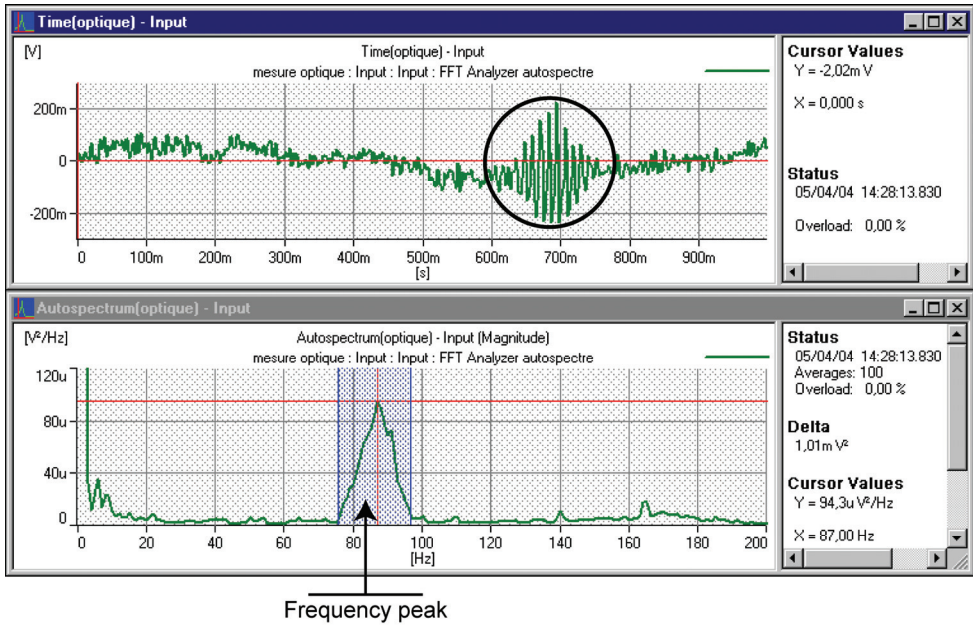


Fig. 11. Example of temporal signal and Fourier spectrum obtained with the texturometer.

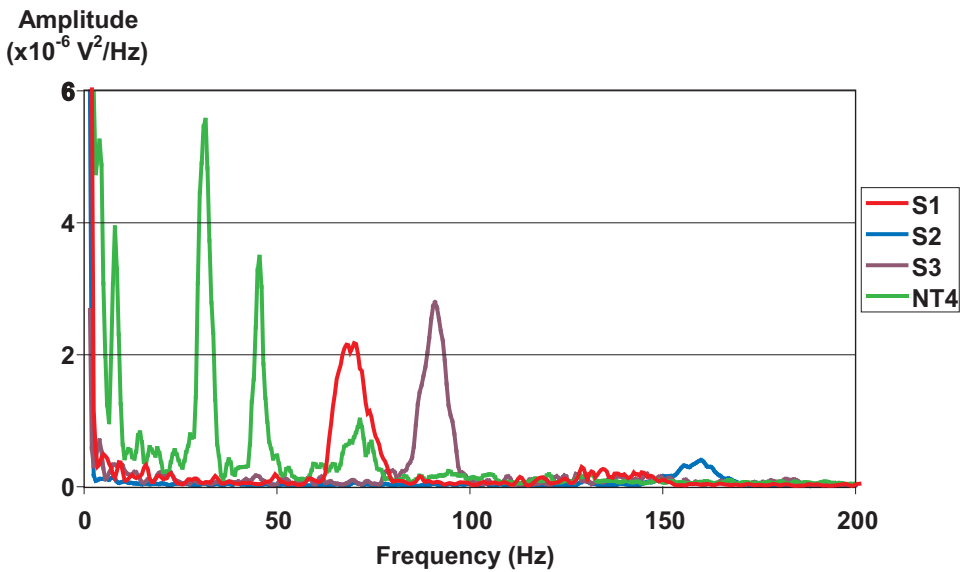


Fig. 12. Example of Fourier spectra obtained for different textile surfaces.

However, although it allows a good differentiation between samples, its results are not always easily tractable. For instance the same finishing process applied to two different fabrics can produce opposite peak evolutions: Sometimes the energy of the peak increases with the hairiness density and other times it decreases. According to the fibres extraction phenomena with abrasive process, the relief of the texture elements can be amplified or reduced.

We therefore implemented an enhanced version of this device taking polarimetric properties of the surface into account, in order to better characterize hairiness and periodical structure of the sample.

Let us briefly remind the reader the basics of polarimetry.

A light wave is an electromagnetic wave whose polarization characteristics can be completely represented by its Stokes vector (Goldstein, 2003):

$$\vec{S} = \begin{bmatrix} S_0 \\ S_1 \\ S_2 \\ S_3 \end{bmatrix} = \begin{bmatrix} I_0 + I_{90} \\ I_0 - I_{90} \\ I_{+45} - I_{-45} \\ I_r - I_l \end{bmatrix} \quad (2)$$

where

$I_0$ : the linearly polarized component along the horizontal axis,

$I_{90}$ : the linearly polarized component along the vertical axis,

$I_{+45}$ : the linearly polarized component at  $45^\circ$ ,

$I_{-45}$ : the linearly polarized component at  $-45^\circ$ ,

$I_r$ : the right circularly polarized component,

$I_l$ : the left circularly polarized component.

The degree of polarization (DOP) of such a light beam is defined as:

$$P = \frac{I_{\text{pol}}}{I_{\text{tot}}} = \frac{\sqrt{S_1^2 + S_2^2 + S_3^2}}{S_0} \quad (3)$$

$S_0$  corresponds to the total light intensity of the light wave and the other components to the polarized parts.

As  $P = 1$ , the wave is totally polarized.

As  $P = 0$ , the wave is totally non-polarized.

If  $0 < P < 1$ ,  $P$  represents the amount of beam polarization.

A preliminary study with an incident linearly polarized beam allowed us a common optical simplification. It showed that under normal incidence only a phenomenon of depolarization occurs, i.e. only the  $S_0$  and  $S_1$  components are non-zero, which means that neither rotation nor circularization of the polarization occur. So it is possible to simplify equation 3 which could be calculated only from  $I_0$  and  $I_{90}$  components. We rename  $I_0$   $I_{\parallel}$  (component whose polarization is parallel to the polarization of the incident beam) and  $I_{90}$  becomes  $I_{\perp}$ .

So the Stokes vector becomes:

$$\vec{S} = \begin{bmatrix} S_0 \\ S_1 \\ S_2 \\ S_3 \end{bmatrix} = \begin{bmatrix} I_0 + I_{90} \\ I_0 - I_{90} \\ I_{+45} - I_{-45} \\ I_d - I_g \end{bmatrix} = \begin{bmatrix} I_{//} + I_{\perp} \\ I_{//} - I_{\perp} \\ 0 \\ 0 \end{bmatrix} \quad (4)$$

And the degree of polarization is:

$$P = \frac{I_{\text{pol}}}{I_{\text{tot}}} = \frac{\sqrt{S_1^2}}{S_0} = \frac{|S_1|}{S_0} = \frac{|I_{//} - I_{\perp}|}{I_{//} + I_{\perp}} \quad (5)$$

The DOP being totally defined with  $I_{//}$  and  $I_{\perp}$ , it is only necessary to acquire these two crossed components in order to estimate it. The incident laser beam is polarized as it was already in the previous device. We have just added a polarizer in the first measurement arm and a second arm similar to the first one but equipped with a polarizer which is crossed to the other is used (Figure 13). The reflected beam is separated into two acquisition arms thanks to a beamsplitter cube. In real time, the DOP of the laser beam is computed from a spectrum analyzer and the Fourier processing is the same than for the previous device (Tourolonias et al., 2007).

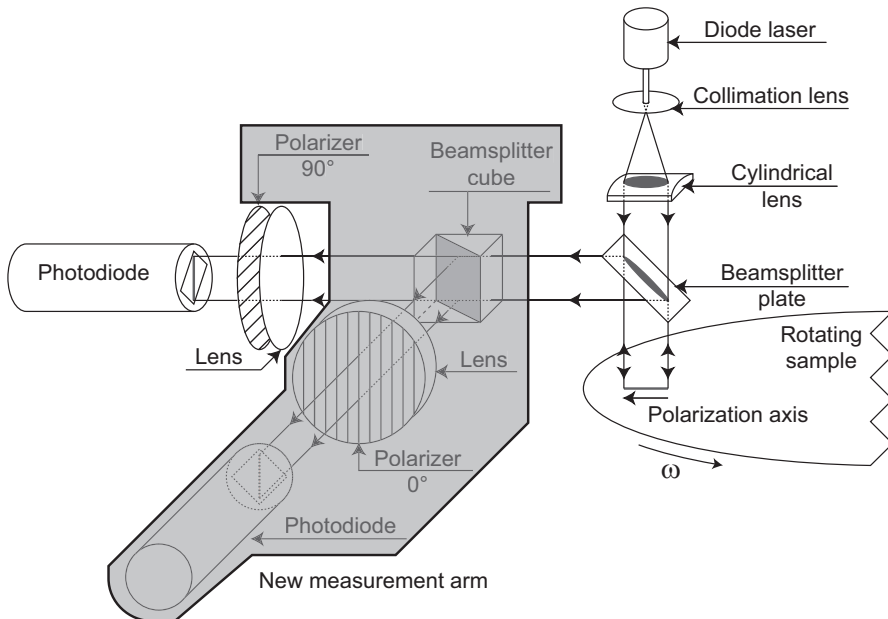


Fig. 13. Optical principle of the polarimetric texturometer.

Studies conducted with this device consists in calculating energy of structural peaks of the textile surfaces described in Table 1. In Figure 14 only diagonal peaks of twill fabric are studied and we present results obtained with the polarimetric texturometer compared to initial texturometer. Other peaks prove too noisy.

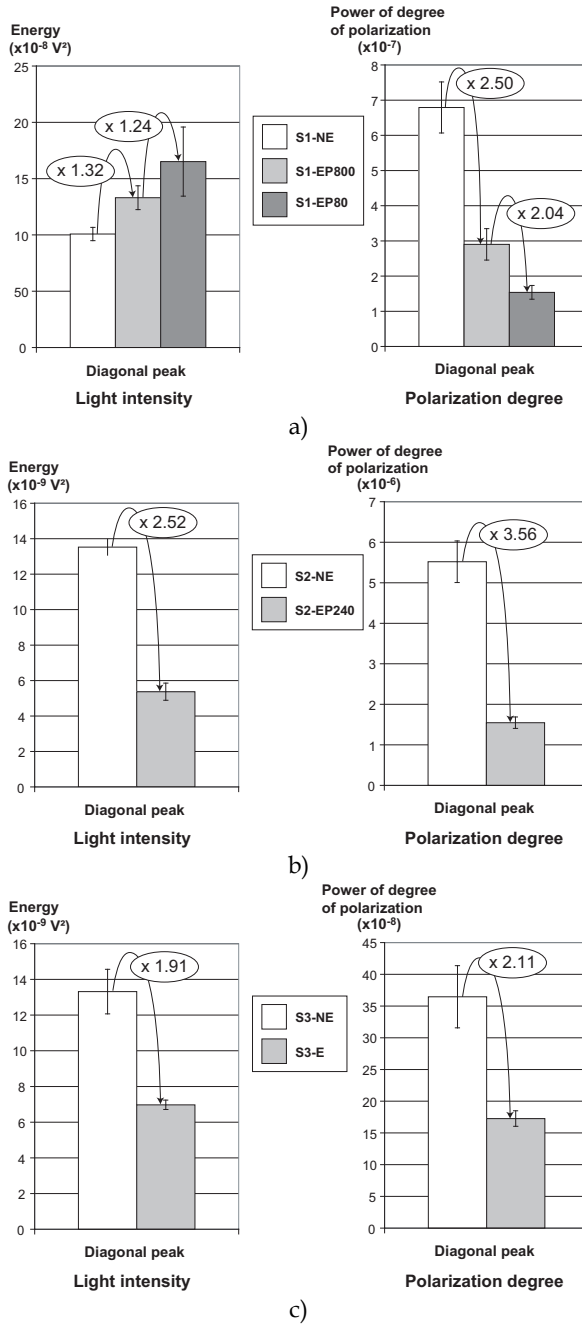


Fig. 14. Differentiation of S1 (a), S2 (b) and S3 (c) samples with polarimetric and non-polarimetric texturometer.

We can first note that with the non-polarimetric device, emerizing process not always has the same influence on the results. It depends on the initial fabric. S1 energy increases with emerizing, whereas energy decreases for the two other samples.

For all three fabrics, the differentiation between samples is reinforced with polarimetric measurement. For the S1 case, classification is inverted because measurement with the polarimetric device also takes into account the fibrous disorder due to the emerizing process.

### 4.3 Image processing techniques applied to images in degree of polarization

The principle used in the previous analysis proved well adapted to woven or knitted fabrics. But it cannot be used in the case of non-periodic structures (needled nonwovens for instance) and gives non relevant results when the surface presents zones with very different characteristics (thermobonded nonwovens in this study). In this case direct imaging is considered. A polarimetric setup was implemented from the beginning, since it can also provide classical intensity results (Tourlonias et al., 2010).

The sample is enlightened by a linearly polarized beam. A rotating quarterwave plate and a fixed polarizer (as analyser) are placed between the textile surface and the camera (Figure 15). As suggested by Terrier and Devlaminck (2000), four orientations of the quarterwave plate are sufficient to determine the whole Stokes vector. For the sake of simplicity we chose a configuration scheme with five symmetric angles. Since we chose a quarterwave plate which is not achromatic, a monochromatic light source should be used.

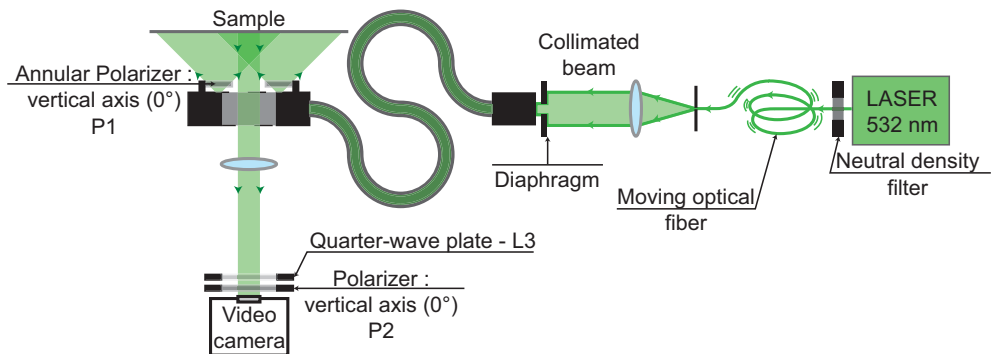


Fig. 15. Optical assembly for polarimetric imaging.

An annular device allows us to have a normal incidence to the surface of the sample and to get the reflected beam through the ring. In order not to be disturbed by the coherent properties of the laser light (speckle phenomenon), a vibration is given to the optical fibre which guides the laser beam to the annular device.

We computed images in DOP and compared them to classical images in intensity.

The study considered nonwoven samples described in Table 1 (NT4-C and NT4-NC). Two main parts can be distinguished in these textile surfaces: thermobonded points and fibrous background as it is described in Figure 16. For the structure basic stripes, DOP and classical intensity are evaluated. Data are averaged column by column.



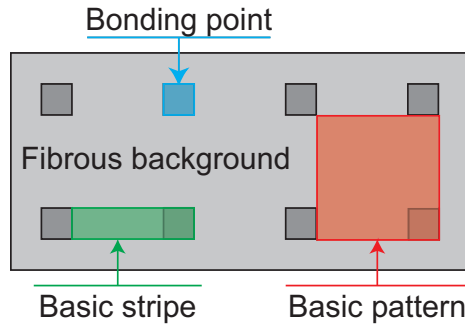


Fig. 16. Elementary areas of thermobonded nonwovens (NT4).

For the “compliant” nonwoven as for the “not compliant” one, the degree of polarization of the bonding points is smaller than that of the fibrous background. That is due to the calendaring process. During this process, fibres are molten at the contact of the calendaring cylinders and these points become more uniform. The depolarization of the light at the calendaring points is lesser than the one at the fibrous background. Compared to images in intensity, images in degree of polarization allow us a better discrimination between bonding points and fibrous background as it is illustrated in Figure 17a and 17b.

The study of these graphs also shows that we obtain a better discrimination between the two types of nonwovens when DOP is used instead of intensity. Clearly studying the DOP of the bonding points can help us in characterizing the calendaring process.

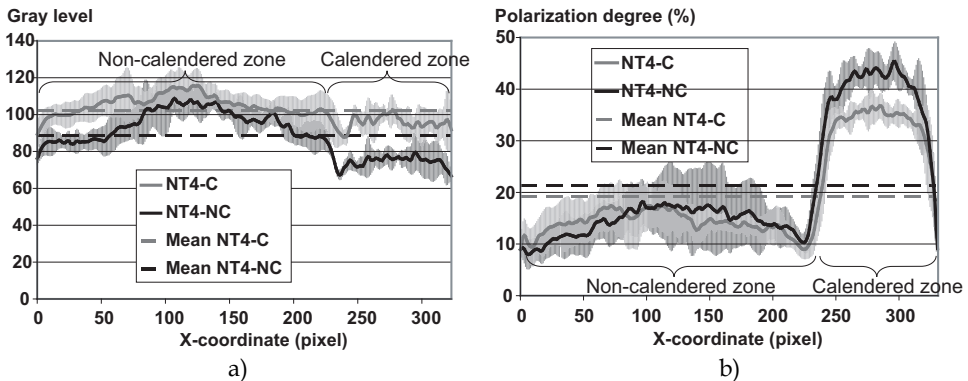


Fig. 17. Average data in basic stripes of NT4 in intensity images (a) and in DOP (b).

**4.4 Conclusion**

We implemented a texturometric technique dedicated to periodic surfaces. It consists of an opto-electronic active setup and a Fourier analysis performed in real-time. It allows us to differentiate surfaces with different finishing processes. Considering polarimetric information instead of classical intensity figures allows us a better discrimination.

In order to study non periodic surfaces we implemented a direct imaging process considering polarimetry. The method proved its interest for the characterization of spunbonded nonwovens.

## 5. Applications to characterize mechanical properties of textile surfaces

### 5.1 State of the art

Above mentioned optical methods allow the user to obtain information about surface state of textile materials but we also would like to get some information about mechanical properties of such materials. Tensile properties would be of particular interest.

Several non-contact extensometers have been developed when it is not the better solution to use strain gauges, especially for great deformations. Hiver et al. (2002) and François et al. (1994), present methods where marks (lines or dots) are added at the surface of the sample. Their displacement during a tensile test is studied thanks to a video camera. Fiedler Company, Grellmann et al. (1997), Casarotto et al. (2003) and Chmelik et al. (2002) also use such methods. Marks which are normal to the tensile direction have reflective properties and are scanned by a laser beam. The reflective beam is acquired by a photodiode and the distance between marks, i.e. strain of the surface, is obtained relative to tensile load. Grellmann and Bierögel present a more complete device based on the same principle, but through several laser sources it is possible to study the strain at different locations.

Other methods without any added mark have also been developed. Lighting rough surfaces with coherent light induce speckle pattern whose properties are modified with strain. Image processing have been used by Anwander et al. (2000), Zhang et al. (2002), Laraba-Abbes et al. (2003) and Amodio et al. (2003) using these optical properties. Image correlation techniques allow following strains of the sample. Stereoscopic correlation is also used in order to determine the 3D coordinates of points of the tested material and the displacements of these points correspond to strain as it is proposed by Luo and Chen (2000) and Mistou et al. (2003). Dumont et al. (2003) also characterize woven fabrics with this method.

Tension properties of thermobonded nonwovens depend on mechanical properties of the bonding points and on the fibre orientation in the fibrous background. In bonding points material is molten and can be considered as a film. The difficulty consists in evaluating fibre orientation in the fibrous background. Hearle and Stevenson (1963) list and explain different methods in order to determine fibre orientation in their study of nonwoven fabrics. A manual and tedious method, corresponding to means available in 1963, consists in counting fibres in 101 angular parts. Histogram gathers obtained results. Methods based on the study of transmitted light and phenomena of dichroism and birefringence does not seem to give good results.

More recently Pourdeyhimi et al. (1993, 1996a, 1996b, 1997a, 1997b, 1999) have conducted a whole study on nonwoven fabrics. A model of nonwoven image is proposed and several image processing techniques are tested in order to determine fibre orientation of this virtual sample. First a tracking algorithm is applied and the end-to-end chord of each fibre gives its orientation, leading to the orientation distribution function. Alternatively a digital Fourier Transform can be used and gives similar information. The third proposed method is a flow field analysis. It is the most accurate method but only gives the mean orientation angle. In the last part of the series of papers Pourdeyhimi et al. explain how to process real nonwoven images in order to apply these techniques. They perform a thresholding process after a contrast enhancement procedure. The tracking method is presented as the best in order to determine the orientation distribution functions whereas Fourier transform proves better for quality control. A device is presented in order to realize an optical Fourier transform. Results obtained with both Fourier studies are similar and the main advantage of the optical method is speed. Pourdeyhimi and Kim (2002) also presented a method based on Hough transform but this method seems to be complex and slow.

**5.2 Use of the optical texturometer as an extensometer**

We were interested in using the texturometer as an extensometer. The principle of the measurement consists in following the evolution of the distance between warp and weft yarns (or other periodic structure elements). These elements that belong to the specific structure of the textile fabrics play the role of the marks of the classical non contact extensometers (Tourlonias et al., 2005).

The initial version of the texturometer (Bueno et al., 1999) allows the user to determine the frequency of each periodic structure element of the tested surface. The goal is to follow that periodicity during a tensile test. As in the previous device, the sample has to be in rotation and the laser probe is motionless, a new device has been designed (Figure 18) whose rotating movement is given to the laser probe.

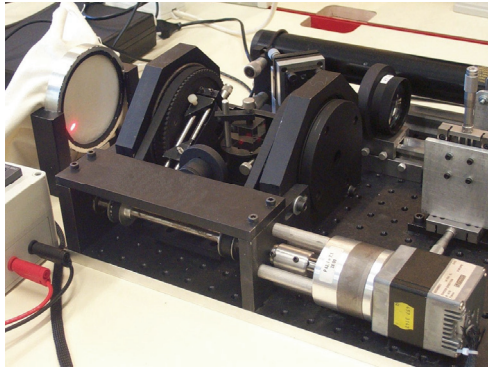


Fig. 18. Photograph of the mechanical device of the rotating texturometer used in the extensometry application.

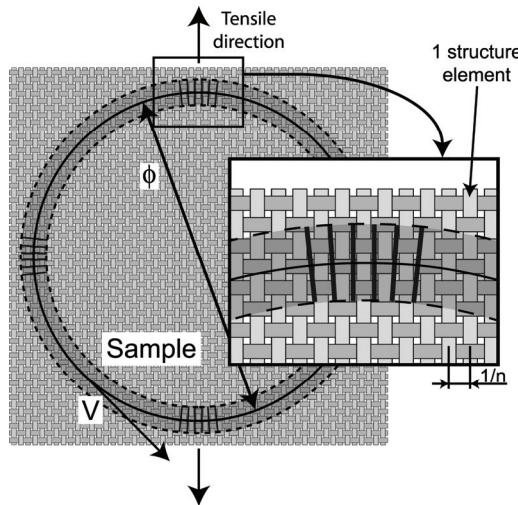


Fig. 19. Studied areas for strain characterization of a plain woven fabric during a tensile test, where  $n$  is the number of periodical elements per length unit,  $\Phi$  the ring diameter and  $V$  the linear speed.

The experience has been realized with a tensile tester adapted to textile materials. The optical device is located in front of the sample and centred with the sample. In order to follow the sample and always analyse the same part of the sample, its displacement velocity is half the velocity of the tensile test.

Measurements have been realized on the plain woven sample (Table 1). Because of the yarn intercrossing of such a fabric, two structure periodicities exist. The first one comes from warp yarns and the second one from weft yarns, i.e. in two crossed directions. In consequence, as the laser probe describes a ring at the surface of the sample two zones are studied concerning each structural element (Figure 19). Conventionally tensile tests are realized parallel to warp or weft yarns. That is why the study can also give information in tensile and crossed directions (i.e. lateral direction).

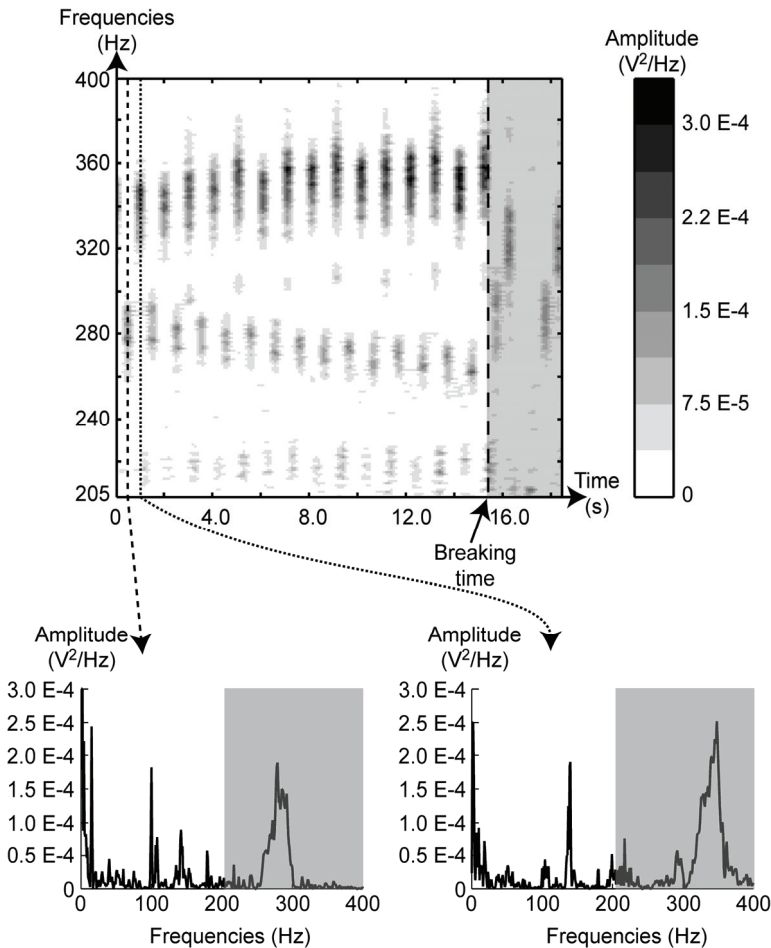


Fig. 20. Time-frequency diagram obtained during tensile test and two single Fourier spectra. The left spectrum corresponds to the laser probe in the lateral direction and the right spectrum, computed 0.5 s later, to the laser probe in the tensile direction.

So it is possible to study a time–frequency diagram constituted of successive frequential spectra. The distance variations between periodic elements of the sample correspond to the evolution of the local strain in each direction.

Figure 20 presents a time–frequency diagram that we obtain with a representation of two examples of elementary Fourier spectra due to two crossed periodic structure elements. The central frequency corresponding to their periodicity is quite different. On the time–frequency diagram we can easily follow the frequency variations of each structure element.

In the lateral direction, the length variation of a structure element orthogonal to the tensile direction is:

$$\delta l = \left( \frac{V}{F_1} - \frac{V}{F_0} \right) \Rightarrow dl = \left( \frac{V}{F_1} - \frac{V}{F_0} \right) nl \quad (6)$$

where

$\delta l$ : length variation of a structure element orthogonal to the tensile direction ( $10^{-3}$  m),

$dl$ : width variation of the sample ( $10^{-3}$  m),

$l$ : width of the sample ( $10^{-3}$  m),

$V$ : linear speed of the laser beam ( $10^{-3}$  m.s $^{-1}$ ),

$n$ : number of studied structure elements per length unit ( $10^{-3}$  m $^{-1}$ ),

$F_0$ : frequency of the studied element before deformation (Hz),

$F_1$ : frequency of the studied element at time  $t_1$  (Hz).

Using the same principle, the strain in the longitudinal direction can be calculated:

$$\delta L = \left( \frac{V}{F_1} - \frac{V}{F_0} \right) \Rightarrow dL = \left( \frac{V}{F_1} - \frac{V}{F_0} \right) nL \quad (7)$$

where

$\delta L$ : length variation of one structure element in the tensile direction ( $10^{-3}$  m),

$dL$ : length variation of the sample ( $10^{-3}$  m),

$L$ : length of the sample ( $10^{-3}$  m).

Actually, from the study of the structural peaks of these graphs it is possible to determine the local strain in each direction during the tensile test. By averaging five tests we can obtain results presented in Figure 21. These tests are performed in the weft direction. Local strains are evaluated in directions parallel and crossed to the tensile test. We finally reported local strain vs. mean strain. As expected when the sample stretches in the tensile direction, it shrinks in width.

Comparative tests have been realized on the same samples with a classic commercial laser extensometer whose principle consists in sticking marks perpendicular to the tensile direction (Fiedler). Results graphs are reported in Figure 22. This graph shows that the two series of results are very close. Nevertheless the commercial device only gives information in one direction at a time. Furthermore, during the tensile test, because of the contraction of the sample, marks made wrinkles that disturb measurement. Finally the drawback of our implementation would be its reduced speed because of the rotation speed of the laser line.

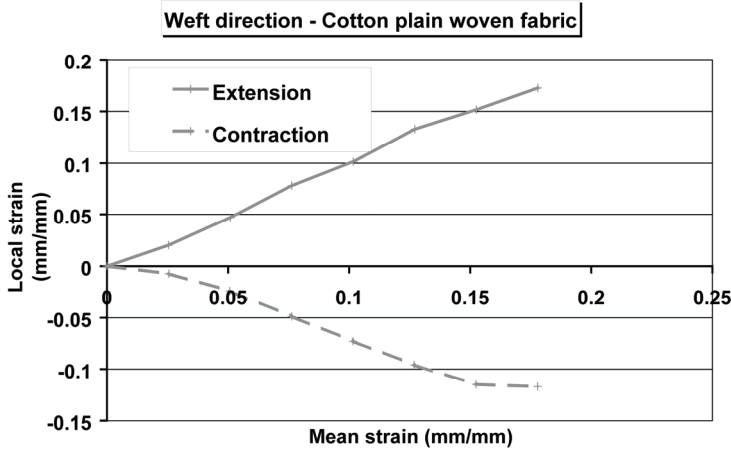


Fig. 21. Longitudinal and lateral strains obtained in weft directions for the plain woven fabric.

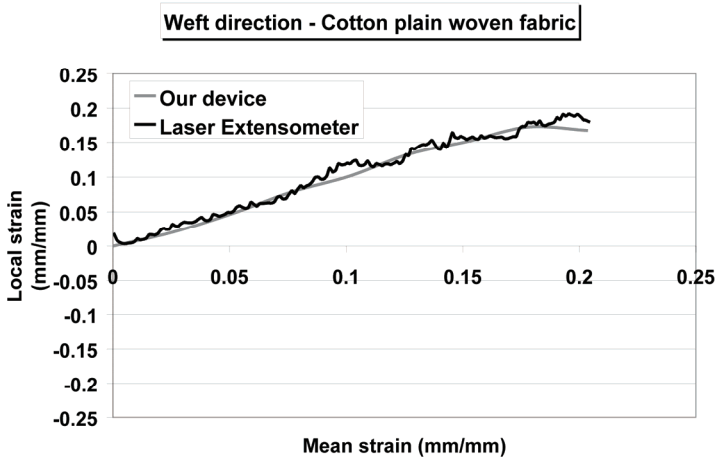


Fig. 22. Longitudinal strain obtained in weft directions for the plain woven fabric with commercial laser extensometer in comparison with our optical extensometer.

### 5.3 Estimation of fibre orientation in a nonwoven using polarimetric imaging

We proved in §4.4 that considering thermobonded nonwovens, polarimetric imaging allowed differentiating the bonding points from the fibrous background through a basic image processing.

In this part we will only consider the fibrous background. We propose to apply another image processing to the same images in degree of polarization in order to determine the fibre orientation. By visual analysis of images in degree of polarization it is obvious that fibres are emphasized compared to images in intensity (Figure 23).

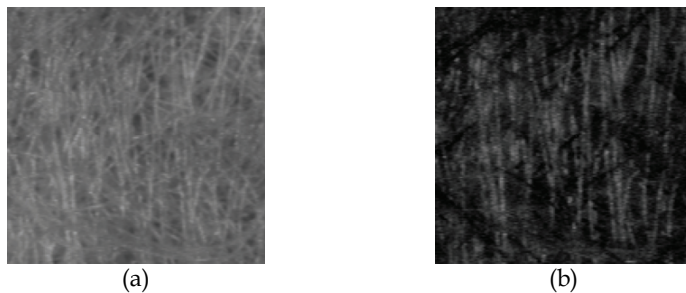


Fig. 23. Examples of images of the fibrous background of thermobonded nonwoven in intensity (a) and in DOP (b).

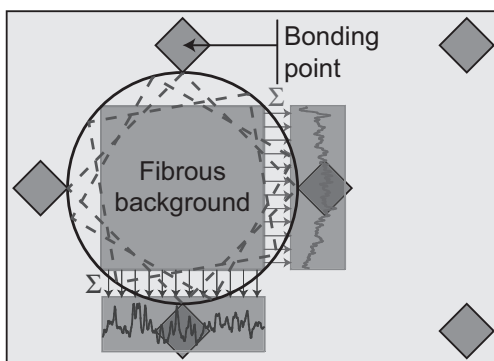


Fig. 24. Image processing technique for characterizing fibrous background.

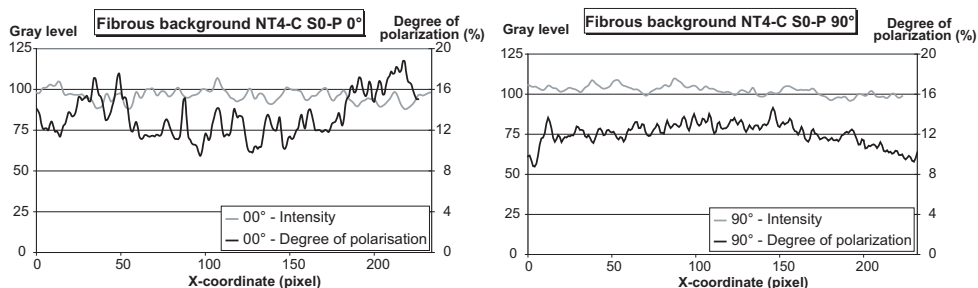


Fig. 25. Examples of results obtained by averaging data values along the vertical direction of the images taken at two different angles (0° and 90°).

The principle of the technique is to rotate the sample, to grab the image, to crop it to a square and then to average data along the columns (Figure 24).

From the same processing a comparison is done between the results obtained from basic images in intensity and images in degree of polarization. Contrary to profiles drawn along the fibres, profiles drawn crossed to the main fibre orientation present many peaks (Figure 25) corresponding to each fibre. That is why we have characterized each profile with a unique and basic parameter we call the average slope:

$$\overline{\text{slope}} = \frac{1}{\bar{n}(L-4)} \sum_{i=4}^L |n_i - n_{i-4}| \quad (8)$$

where

$\bar{n}$  : average value of the image (in order to normalize values),

L: width of the square (in number of pixels),

$n_i$ : average value of the  $i^{\text{th}}$  column of the image.

It is then possible to draw a graph reporting the evolution of this parameter vs. the analysis angle.

In Figure 26 we present results obtained for images in DOP and images in intensity, both for “compliant” and for “not compliant” thermobonded nonwovens. The results are averaged over five DOP or intensity images.

The asymmetry of the graphs comes from a shift during the rotation procedure which means that the studied zone may vary.

The main fibre orientation corresponds to the direction  $0^\circ$ - $180^\circ$ , i.e. the machine direction in our case. Whether considering NT4-C or NT4-NC, the trend is the same. DOP images provide a better discrimination between the  $0^\circ$ - $180^\circ$  direction (main orientation) and the crossed direction (direction where fibres are the least oriented). The ratio is 2 with DOP images and only 1.5 with intensity images.

By comparing results obtained with NT4-C and NT4-NC, we can notice that values are higher for “not compliant” samples than for “compliant” samples. It may be explained by the cohesion process. Although fibres in the fibrous background are not melted, heat can modify their own structure and more particularly their birefringence (Hamza et al., 2007; Chand et al., 2001). That is why study has to be conducted by comparing a ratio of different directions.

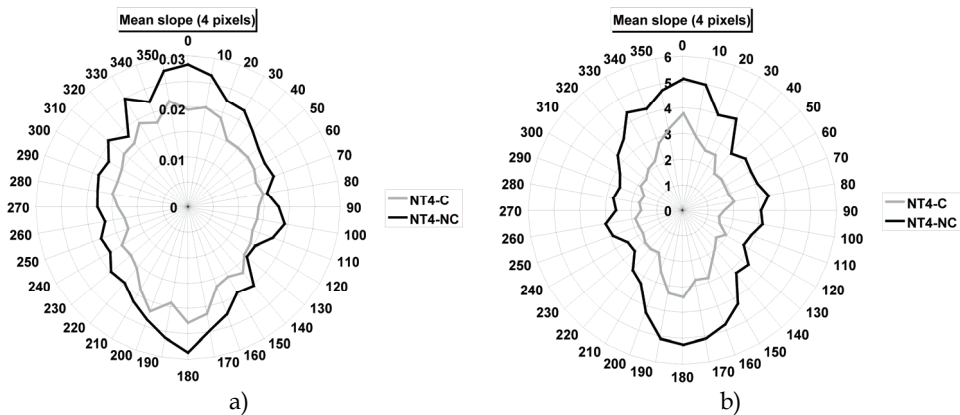


Fig. 26. Graphs showing the main orientation of the fibres in the NT4 nonwovens from intensity images (a) and image in DOP (b).

## 6. Conclusion

We have presented several methods to characterize textile surfaces in terms of structure and hairiness which are important in their tactile feel, but also in terms of mechanical properties.



In order to avoid artifacts likely to occur with mechanical techniques when studying this tiny hairiness, we only considered optical techniques, therefore contactless. These techniques combine active imaging, enhanced detection (esp. polarimetric detection) and post-processing and were implemented into three setups. One is a hairinessmeter also able to work as a profilometer for any soft material, the second is a texturometer for periodically structured materials whose a modified version allows to study samples in situ and the third one consists of a polarimetric imager. Through detailed examples, these methods have proved their interest in particular applications considering industrial issues (differentiation of very close samples, characterization or control during manufacturing process) as well as their speed of operation compared to methods often based on tedious data acquisition or long processings. It was also shown that obtaining several parameters or metrics with a unique measurement (for instance, periodical structure and state of surface with the polarimetric texturometer) is possible.

## 7. Acknowledgements

The authors wish to thank the Région Alsace for partial funding of this research.

## 8. References

- Amodio, D., Broggiato, G. B., Campana, F. & Newaz, G.-M., Digital Speckle Correlation for Strain Measurement by Image Analysis, *Experimental Mechanics* 43(4) (2003) 396-402.
- Anand, Arun, Chhaniwal, Vani K. & Narayanamurthy, C. S., Hairiness measurement of textile yarns using crossed polarizers, *Review of Scientific Instruments* 76(7) (2005) 076104-3.
- Anwander, M., Zagar, B. G., Weiss, B. & Weiss, H., Noncontacting Strain Measurements at High Temperatures by the Digital Laser Speckle Technique, *Experimental Mechanics* 40(1) (2000) 98-105.
- Barella, A. & Manich, A.M., The hairiness of yarns, *Textile Progress* 24(3) (1993) 1-49.
- Becker, Jean-Marie, Grousson, Stephane & Jourlin, Michel, Surface state analysis by means of confocal microscopy, *Cement and Concrete Composites* 23(2-3) (2001) 255-259.
- Bueno, Marie-Ange, Durand, Bernard & Renner, Marc, Noncontact Measurements of Sanding and Raising Effects, *Textile Research Journal* 69(8) (1999) 570-575.
- Bueno, Marie-Ange, Durand, Bernard & Renner, Marc, Optical characterization of the state of fabric surfaces, *Optical Engineering* 39(6) (2000) 1697-1703.
- Calvimontes, Alfredo, Dutschk, Victoria & Stamm, Manfred, Advances in Topographic Characterization of Textile Materials., *Textile Research Journal* 80(11) (2010) 1004-1015.
- Casarotto, L., Tutsch, R., Ritter, R., Weidenmuller, J., Ziegenbein, A., Klose, F. & Neuhauser, H., Propagation of deformation bands investigated by laser scanning extensometry, *Computational Materials Science* 26 (2003) 210-218.
- Chand, Subhash, Bhat, Gajanan S., Spruiell, Joseph E. & Malkan, Sanjiv, Structure and properties of polypropylene fibers during thermal bonding, *Thermochimica Acta* 367-368(2001) 155-160.
- Chmelik, Frantisek, Ziegenbein, Alf, Neuhauser, Hartmut & Lukac, Pavel, Investigating the Portevin-Le Chatelier effect by the acoustic emission and laser extensometry techniques, *Materials Science and Engineering A* 324(1-2) (2002) 200-207.

- Ciamberlini, Claudio, Francini, Franco, Longobardi, Giuseppe, Sansoni, Paola & Tiribilli, Bruno, Defect detection in textured materials by optical filtering with structured detectors and self-adaptable masks, *Society of Photo-Optical Instrumentation Engineers* 35(3) (1996) 838-844.
- Conte, M., Jamet, Y., Duhamel, J., Jarrigeon, M. & Calonnier, M., Roughness Measurement by Laser, *Industrie Textile* 1212) (1990) 105-107.
- Cybulska, Maria, Assessing Yarn Structure with Image Analysis Methods, *Textile Research Journal* 69(5) (1999) 369-374.
- Dumont, Francois, Hivet, Gilles, Rotinat, Rene, Launay, Jean, Boisse, Philippe & Vacher, Pierre, Mesures de champs pour des essais de cisaillement sur des renforts tissés: Field measurements for shear tests on woven reinforcements, *Mecanique & Industries* 4(6) (2003) 627-635.
- Durand, B. & Schutz, R. A., *Procédé et dispositif pour analyser les éléments émergeant de la surface d'un produit*. 1983: French Patent 3 556 837.
- Escofet, Jaume, Navarro, Rafael, Millan, Maria S. & Pladellorens, Josep, Detection of local defects in textile webs using Gabor filters, *Optical Engineering* 37(8) (1998) 2297-2307.
- Felix, Ernst & Wampfler, Hans, *Method and apparatus for examining hairiness of yarn*. 1990, Zellweger Uster: US.
- Fiedler, Laser Extensometer/Laser Doppler Extensometer, <http://www.foe.de/>.
- François, P., Gloaguen, J.-M., Hue, B. & Lefebvre, J.-M., Volume strain measurements by optical extensometry: application to the tensile behaviour of RT-PMMA, *Journal de Physique III* 4(2) (1994) 321-329.
- Goldstein, Dennis, *Polarized Light - Second Edition, revised and expanded*, Marcel Dekker, New-York, Basel, 2003.
- Governì, Lapo & Furferi, Rocco. An Image Processing based Method for Monitoring the Raising Process. in *Abstracts of the Fiber Society Symposium*. 2005. Sankt Gallen (Switzerland).
- Grellmann, Wolfgang & Bierögel, Christian, Laserextensometrie anwenden: Einsatzmöglichkeiten und Beispiele aus der Kunststoffprüfung = Equipment for laser extensometry. Potential of employment and examples for the application in testing of polymers, *Materialprüfung* 40 (11-12) (1998) 452-459.
- Grellmann, Wolfgang, Bierögel, Christian & König, S., Evaluation of deformation behaviour in polyamide using laser extensometry, *Polymer Testing* 16(3) (1997) 225-240.
- Haggerty, Joe & Young, Matt, Spatial light modulator for texture classification, *Applied Optics* 28(23) (1989) 4992-4995.
- Hamza, A.A., Belal, A.E., Sokkar, T.Z.N., El-Bakary, M.A. & Yassien, K.M., Measurement of the spectral dispersion curves of low birefringence polymer fibres, *Optics and Lasers in Engineering* 45(9) (2007) 922-928.
- Hearle, J.W.S. & Stevenson, P.J., Nonwoven Fabric Studies - Part III: The Anisotropy of Nonwoven Fabrics, *Textile Research Journal* 33(11) (1963) 877-888.
- Hensel, Rolf, Wampfler, Hans, Raynor, Jeffrey Mitchell & Seitz, Peter Markus, *Device for optically recording, digitally, a parameter on a longitudinally moved thread-type material*. 2001, Zellweger Luwa AG: US.
- Herlidou, Sandra, Ph.D thesis: *Caractérisation tissulaire en IRM par l'analyse de texture : Etude du tissu musculaire et de tumeurs intracrâniennes*. 1999, Université de Rennes 1: Rennes.

- Hiver, Jean-Marie, Dahoun, Abdesslam & Christian, G'Sell. Endommagement plastique dans les mélanges de polymères : mesure in-situ en temps réel dans la striction. in *Matériaux : de la conception à la mise en oeuvre*. 2002. Tours.
- Ishizawa, H., Nishimatsu, T., Kamijyo, M. & Toba, E., Measurement of Surface Properties of Woven Fabrics Using an Optical Bundle, *Journal of Textile Engineering* 48(1) (2002) 5-10.
- Kreißl, Mario, Heiko, Schwarzer & Teiwes, Stephan, Optical processor for real-time detection of defects in textile webs, *Proc. SPIE 3073 : Optical Pattern Recognition VIII* (1997) 307-311.
- Kuratle, Christoph, *Method and device for determining the optical features of treads*. 1999, Maschinenfabrik Rieter AG: World.
- Laraba-Abbes, Fazilay, Ienny, Patrick & Piques, Roland, A new 'tailor-made' methodology for the mechanical behaviour analysis of rubber-like materials: I. Kinematics measurements using a digital speckle extensometry, *Polymer* 44(3) (2003) 807-820.
- Luo, P. F. & Chen, J. N., Measurement of Curved-surface Deformation in Cylindrical Coordinates, *Experimental Mechanics* 40(4) (2000) 345-350.
- Militky, Jiri & Blesa, Martin, Evaluation of patterned fabric surface roughness., *Indian Journal of Fibre & Textile Research* 33(3) (2008) 246-252.
- Millan, Maria S. & Escofet, Jaume, Fourier-domain-based angular correlation for quasiperiodic pattern recognition. Applications to web inspection, *Applied Optics* 35(31) (1996) 6253-6260.
- Mistou, Sebastien, Karama, Moussa, Dalverny, Olivier, Siguier, Jean-Michel & Guigue-Joguet, Pascale, Mesure 3D sans contact des déplacements et déformations sur des films plastiques transparents par stereo-correlation: 3D non-contact measurement of strain and displacement on transparent plastic films by stereo correlation, *Mecanique & Industries* 4(6) (2003) 637-643.
- Nevel, Avishai, Gordon, Kendall W. & Leary, Steven, *System and method for determining yarn hairiness*. 1999, Lawson Hamphill Inc.: US.
- OSTHOFF-SENGE. - Hairiness Measuring Device Hamsat,  
<http://www.osthoff-senge.com/en/produkte.html>.
- Pourdeyhimi, B., Assessing Fiber Orientation In Nonwoven Fabrics, *INDA J. Nonwoven Res* 5(4) (1993) 29-36.
- Pourdeyhimi, B. & Dent, R., Measuring Fiber Orientation in Nonwovens - Part IV: Flow Field Analysis, *Textile Research Journal* 67(3) (1997) 181-187.
- Pourdeyhimi, B., Dent, R. & Davis, H., Measuring Fiber Orientation in Nonwovens - Part III: Fourier Transform, *Textile Research Journal* 67(2) (1997) 143-151.
- Pourdeyhimi, B., Dent, R., Jerbi, A., Tanaka, S. & Deshpande, A., Measuring Fiber Orientation in Nonwovens - Part V: Real Webs, *Textile Research Journal* 63(3) (1999) 185-192.
- Pourdeyhimi, B. & Kim, H. S., Measuring Fiber Orientation in Nonwovens: The Hough Transform., *Textile Research Journal* 72(9) (2002) 803.
- Pourdeyhimi, B., Ramanathan, R. & Dent, R., Measuring Fiber Orientation in Nonwovens - Part I: Simulation, *Textile Research Journal* 66(11) (1996a) 713-722.
- Pourdeyhimi, B., Ramanathan, R. & Dent, R., Measuring Fiber Orientation in Nonwovens - Part II: Direct Tracking, *Textile Research Journal* 66(12) (1996b) 747-753.
- Ramgulam, R.-B., Amirbayat, J. & Porat, I., Measurement of fabric roughness by a non-contact method, *Journal of the Textile Institute* 84(1) (1993) 99-106.

- Ringens, Werner, Bahners, Thomas & Schollmeyer, Eckhard, Characterisation and control of thread data in textil processes using optical profilometry, *Melliand Textilberichte/International Textile Reports* 83(20) (2002) 715-716/E140.
- Seifert, Ralph, Raue, Peter, Offermann, Peter, Bahners, Thomas, Schollmeyer, Eckhard, Mägel, Matthias & Fuchs, Hilmar, Surface Characterisation of Textile Fabrics.: Part 3: Profilometric Measuring Systems, *Melliand Textilberichte/International Textile Reports* 76(9) (1995) 636-639/E164-E166.
- Shakher, C., Ishtiaque, S.M. , Singh, S.K. & Zaidi, H.N., Application of Wavelet Transform in Characterization of Fabric Texture, *Journal of the Textile Institute* 95(1) (2004) 107 - 120.
- Shakher, Chandra, Istiaque, S.-M. & Singh, Shashi-Kumar, Application of wavelet transform in characterization of fabric texture, *Proc. SPIE* 4929 : Optical Information Processing Technology (2002) 158-164.
- Stusak, Miroslav, *Method and device for contactless measurement of a linear tactile formation such as yarn etc.* 2004: US - 10/405,581.
- Terrier, Patrick & Devlaminck, Vincent, Système polarimétrique pour l'analyse d'images, *Traitement du Signal* 17(5-6) (2000) 479-490.
- Tourlonias, Michel, Bigué, Laurent & Bueno, Marie-Ange, Contribution of polarimetric imaging for the characterization of fibrous surface properties at different scales, *Optics and Lasers in Engineering* 48(1) (2010) 75-82.
- Tourlonias, Michel, Bigué, Laurent & Bueno, Marie-Ange, Polarimetric measurements of fabric surfaces, *Optical Engineering* 46(8) (2007) 083602.
- Tourlonias, Michel, Bueno, Marie-Ange, Bigué, Laurent, Durand, Bernard & Renner, Marc, Contactless Optical Extensometer for Textile Materials, *Experimental Mechanics* 45(5) (2005) 420-426.
- Tsai, Du-Ming & Chiang, Cheng-Huei, Automatic band selection for wavelet reconstruction in the application of defect detection, *Image and Vision Computing* 21(5) (2003) 413-431.
- Tsai, Du-Ming & Hsiao, Bo, Automatic surface inspection using wavelet reconstruction, *Pattern Recognition* 34(6) (2001) 1285-1305.
- Tsai, Du-Ming & Hsieh, C. -Y., Automated surface inspection for directional textures, *Image and Vision Computing* 18(1) (1999) 49-62.
- Wang, W., L. Wong, P., B. Luo, J. & Zhang, Z., A new optical technique for roughness measurement on moving surface, *Tribology International* 31(5) (1998) 281-287.
- Wood, Errol-J., Applying Fourier and Associated Transforms to Pattern Characterization in Textiles, *Textile Research Journal* 60(4) (1990) 212-220.
- Wood, Errol-J., Objective measurement of carpet appearance by image analysis - Part 1 : Principles and methodology, *Melliand Textilberichte/International Textile Reports* 77(7-8) (1996) 452-459/E99-E102.
- Xu, Bugao, Cuminato, D.-F. & Keyes, N.-M., Evaluating Fabric Smoothness Appearance with a Laser Profilometer, *Textile Research Journal* 68(12) (1998) 900-906.
- Zhang, Dongsheng, Eggleton, Charles D. & Arola, Dwayne D., Evaluating the Mechanical Behavior of Arterial Tissue using Digital Image Correlation, *Experimental Mechanics* 42(4) (2002) 409-416.

# Optoelectronic Circuits for Control of Lightwaves and Microwaves

Takahide Sakamoto

*National Institute of Information and Communications Technology (currently, also with University of California, Davis)  
Japan*

## 1. Introduction

Interaction of lightwaves are very important, especially in the area of optical fiber communication and microwave photonic systems. Optical modulation and demodulation based on lasers, modulators, photodiodes, etc., have been intensively investigated, so far. As a result, so many optoelectronic devices have been matured enough to be practically used in real optical communication systems. Now, we are ready to explore novel functional optoelectronic circuits combining these devices as primary elements. In this chapter, we describe recent progress of the optoelectronic circuits, which enhances functionalities of optical fiber communication/ microwave photonic systems, introducing our latest results.

The first key word in this chapter is "data modulation/demodulation". Here, we describe novel optoelectronic circuits for advanced data modulation/demodulation. Our two approaches, multilevel signaling and spectral shaping, by the optoelectronic circuits are introduced. These technologies will be essentially useful to ultimately enhance spectral efficiency of the optical transmission systems, which is also applicable to microwave photonic systems.

Another keyword is "photonic oscillators." If we consider communication systems, in general, oscillators are very important as much as the data modulation/demodulation. In the transmitter side, optical carrier should be provided; in the receiver side, local oscillators should be prepared for the demodulation. Stable and precise, and flexible in some cases, oscillators are always required both for the optical fiber communication and microwave photonic systems. Here, we describe novel photonic oscillator technologies based on optoelectronic circuits, featuring our two key technologies: One is an optoelectronic oscillator circuits and the other is an optical comb generation circuits. By the circuits, multi-frequency carrier can be easily and stably generated, which would greatly simplify the parts of photonic oscillators in the optical communication/ microwave photonic systems.

## 2. Photonic oscillators, mixers

When we discuss nowadays photonic devices and components, it is a good idea to compare them with microwave components. Here, in this section, we briefly describe key photonic devices like photonic oscillators and mixers, which are really analogous to microwave ones; we clarify the photonic circuits we discuss throughout in this chapter.

Laser sources are essential elements for optical communication, measurement and other technology, which plays important roles as an oscillator source at an optical frequency. Lasers have very high oscillation frequencies like 100 THz or higher, whereas microwave oscillators oscillates at Hz - 100 GHz. Such high frequency oscillation characteristics of lasers offers several attractive applications. It allows synthesis or generation of ultrafast and wideband signals, like optical pulses and combs, which are applicable to test and measurements for investigating ultrafast phenomena. In addition, lightwaves generated from laser sources can be used as a carrier for data transmission in telecommunications, which is advantageous for large-capacity or ultra high-speed data transmissions because of its high-frequency oscillation characteristics. Huge capacity data transmission much beyond the capacity of radio-wave telecommunications have been reported, so far.

Laser as a photonic oscillator also offer another important features: they have good coherence as microwave oscillators do. This feature enables several useful applications in the area of measurements, signal synthesis, coherent communications and so on, which rely on interference of lightwaves. In general, it is not so easy to stabilize optical frequency and phases of lasers comparing with microwave oscillators. Recently, linewidth of semiconductor or fiber lasers are getting narrower in the order of kHz MHz, which accelerates progress of research and development in this area.

To educe these great potential of photonic oscillators, we need to consider and devlope methods for interaction and control of lightwaves. For the purposes, mixers are commonly used in microwave technologies for mixing two signals to generate product of them. In photonic technologies, mixers should deal with interaction between lightwaves and between lightwaves and electrical signals (microwaves). Modulators and detectors are key elements as the photonic mixers. Modulators accepts input of lightwaves and electrical (microwave) signals, outputting their products at an optical frequency. Detectors, represented by photodetectors, are another important mixer, where an electrical signal is output as a mixing result of lightwaves.

Modulators are essential for shaping the sinusoidal optical carrier into a signal with a specific waveform and pulse shape. Intensity modulation technique has been investigated for long time to enable high-speed intensity modulation on lightwaves. Including direct modulation technique, several approaches have been investigated. Among them, currently, waveguide type modulators based on EO effects show promise owing to its capability of pure and ideal phase modulation. Modulation methods on amplitude, frequency and phase of lightwaves have been developed, which triggered, especially in telecom area, several types of modulation formats other than OOK. Vector modulation by IQ modulator is a powerful way to perform any modulation; thus the modulator is commonly used for advanced modulation in optical communications.

Demodulators (or detectors) are also important components for the interactions between light and microwaves. Photodiodes with PIN structure and avalanche-photodiodes at 10Gb/s or higher are now matured well, and balanced detection with the photodiodes are useful for coherent detection, with great sensitivity. Especially, a phase diversity is a powerful detection scheme to orthogonally demodulate phase and amplitude modulated lightwaves.

The modulators as a transmitter and photodiodes as a receiver are typical ways for the use in optical communication systems. However, we can explore more additional functions using the photonic mixers. Electrical or optical frequency conversion techniques allow the oscillators to generate sinusoidal signals at other frequencies. Linearly driven EOM upconverts baseband electrical signal to optical carrier frequency band, whereas, OE converter downconverts the signal over optical carrier to baseband by direct detection. IQ modulator enable vector modulation, orthogonal detection can vectorially downconverts signals.

Functions as harmonic mixing are also available by photonic mixers. Any nonlinearities in EO modulator or OE mixers cause nonlinear distortion to input signals. Electro-optic absorption in the EAMs and photocurrent in the PDs can be saturated for relatively large amplitude signals. The electro-optic effects in EO crystals easily generates higher order harmonics because of the nature of phase modulation characteristics. Nonlinearities in optical fiber or semiconductor materials are also useful for photonic mixing. Second-harmonic generation (SHG), four-wave-mixing (FWM) have been intensively investigated, eventually progressed and shows a promise for ultrafast or ultrawideband mixing process.

We know that there are many other important optical components and elements; optical fibers and fiber amplifiers are great technologies and other components such as optical filters, isolators, polarization controllers, AWG and so on are also important; however, they are not discussed in detail, here. Instead, we would like to state that the main subject of this chapter is to explore functional photonic circuits. To smoothly prompt the story of this chapter, we focus on the modified photonic oscillator structure consisting of EO and OE converters in its loop. This is a general form to deal with photonic oscillation and interaction with lightwaves and microwaves, and in some sense extension of photonic oscillators. In the loop, EO and OE converters (mixers) are involved. This configuration is a pair of OE/EO conversions if the electrical feedback is open. If the photocurrent detected in the PD is positively fed back to the EO mixer, this loop-structured circuit starts oscillation at a microwave frequency. This oscillator is called optoelectronic oscillator (OEO) and it has electrical and optical parts in its loop, thus good for dealing with interaction between lights and microwaves. The OEOs have been investigated in the context of ultra-stable microwave sources stabilization of mode-locked lasers, and so on. In this chapter, we discuss to modify the OEO to add functionality.

If the signal is down-converted to a baseband with a photo-mixer, the phase difference between the signal and local oscillator (LO) is detected and it can be used as a feedback signal. In this case, phase tracking operation is achieved with appropriate negative feedback. This loop is called a phase-locked loop (PLL). The PLL dealing with optical signal is called OPLL; there are basically two types of OPLL: one is for phase locking with optical carrier and the other is with optical clock. In general, the former one has a difficulty in phase tracking because laser stability is not good enough. On the other hand, challenges in the latter one is that we need to deal with high frequency or high clock-rated signals.

Although all of the topics related to the loop structure cannot be covered, this chapter picks up some. We know that advantage of the optical components and circuits are their wideband characteristics, while electronic circuits are advantageous for precise control and several functionalities for signal processing. Thus, the topics introduced here is, I believe, good examples to suitably use each of the merits. In the next sections, functional OEOs in special structures are described. In section 4, we discuss PLL structure, where ultrafast signal and its phase is controlled with low speed electronics. The topics in section 5 are regarding photonic harmonic mixers, which can extend the functionality of the photonic oscillators. In section 5, we describe ultraflat comb and ultrashort pulse generation from CW light and microwave signal.

### 3. Photoelectronic oscillator

Optoelectronic oscillators (OEOs) Yao & Maleki (1994) are very attractive devices for optical clock or subcarrier signal generation. OEO consists of an EO converter, and OE converter and feedback lines that connects the converters. In the circuit, EO- modulated lightwave by the EO converter is photodetected by the OE-converter; the photocurrent is fed back to the

EO converter again. If positive feedback gain is given enough, the circuits oscillates at the microwave frequency, in which electrical and optical signals are converted with each other, exchanging their energy. If this gain is large enough to compensated for the loss in the OEO cavity, the OEO can be oscillated by using the energy of the pump light without supplying energy to the active components the OEO cavity.

The OEO has optical and electrical parts, which offers some interesting features different from optical or electrical oscillators. It has unique oscillation characteristics. For characterization of oscillators, in general, it is a useful way to analyze transfer function, i.e. output power from the oscillator measured against input power for pumping it. By this analysis, information of threshold, injection efficiency and other important basic characteristics can be obtained. Since the OEO has electrical and optical parts, it can output both electrical and optical signals for electrical or optical pumping; therefore, there are totally four input-output combinations for transfer functions.

Since the dimension of electrical and optical is different, the transfer function could be nonlinear. For example, the trace would have a shape of  $y = \sqrt{x}$ , if electrical output power is measured against optical pump power. If the transfer function has nonlinearity or wavelength (frequency) dependent characteristics, behavior of oscillation would be more complex, as discussed later. If we appropriately configure the OEO taking the nonlinear transfer functions into account, the OEO can oscillates even if feedback lines are passive without gain blocks because, EO or OE converters can equivalently give positive gain. This feature is attractive in some systems, ex. microwave photonic systems for remotely distributing microwave or millimeter signals without power supply at the remote places.

One of the important merits of the OEO is that such signals can be generated without any external microwave sources. Clock recovery or other functions useful for optical signal processing are easily obtained by this technology. Especially, in microwave or millimeter-wave photonic technologies, OEOs can play significant roles as photonic local oscillators. In addition, this configuration is advantageous for achieving ultra stable, low-phase-noise microwave sources because the optical fiber deployed in the optical part enables long cavity configuration which is known to be effective for decreasing intrinsic phase noise of the oscillator.

In this section, after brief description of principle of OEO, we describe OEO configurations for (1) single-mode oscillation, (2) wideband signal generation. In this section, we discuss to modify the OEO to add some useful functions, especially focusing on wideband signal generation. Once again, the oscillator has a distinctive hybrid structure consisting of electrical and optical parts. The optical part is suitable to deal with wideband signals. In electrical part, electrical functional components can be applied. If sufficient positive feedback gain is given to the components at a specific oscillation frequency  $f$  after one round trip, any functional components can be involved in the electrical and/or optical parts of the loop. For example, nonlinear components like frequency converter, harmonic generator, and other analog or digital circuits can be involved into the oscillator. Here, in this section, two cases are picked up as examples of modified OEOs: (1) bias-shift OEO and (2) harmonic OEO. The former one is effective to shift optical bias of the EO modulator deployed in the oscillator, which can generate optical two-tone signal. In the latter case, the oscillator consists of harmonic signal generator in its optical part, by which wideband optical signal like optical comb is generated by self oscillation.

### 3.1 Single-mode oscillation

In general, oscillators can oscillates at the multiple frequencies of cavity principle mode. This phenomena is called multi-mode oscillation. Multi-mode oscillation is an easy way to obtain



a wideband comb-like signal, because generated signal has multiple frequency components with equal frequency spacing. However, mode competition observed in the multi-mode oscillators causes intensity fluctuation of the generated frequency components. The mode competition is originated by the use of one common gain medium in its cavity. In addition, phase relationship is not fixed and almost randomly varying because the oscillation of each frequency component is independent but slightly coupled with each other.

For a stable operation, single-mode oscillators are preferable, where the oscillators are allowed to oscillate at a single frequency. To achieve single-mode operation, positive feedback gain is selectively given to a particular oscillation mode of the cavity and to suppress undesired oscillation modes, as shown in Fig. \*\* (a). Narrow-band filters or gain media can be utilized in the cavity for this purpose. In some gain media, the gain concentrates on the oscillated component after starting oscillation, which sometimes helps suppressing undesired components to be oscillated especially if the bandwidth of gain media or filter is not narrower enough comparing with FSR of the cavity.

OEO could be also operated either single or multi mode; the former is advantageous for stable operation. In the OEO, "single-mode" means the microwave cavity mode since the OEO is basically equivalent with a microwave oscillator. For the single-mode operation of the OEOs, there are two approaches to be taken. One is the approach, in which an microwave bandpass filter is applied in the electrical domain. High-Q narrowband filters at microwave frequency are available; for example, passband = 10 MHz, center frequency = 10 GHz,  $Q = 1000$ , etc.. The other approach is to adopt optical filtering in the optical domain. In this case, filtering should be applied the modulated lightwave. Thus, passband should be repeated Etalon resonator an suitable for the filters with periodical passband. The etalons cover the large FSR region, typically  $FSR = 10\text{-}1000$  GHz, because of the difficulty in assembling long cavity structure. Optical disk cavities are also promising for the mode selection, which have a high Q characteristics. FSR of the disk filters is determined by its radius and reflective index of the material; typically  $FSR = 10\text{GHz}$ ,  $Q = 1000$ . A loop filter consisting of an optical fiber is another candidate. Taking advantage of low-loss characteristics of optical fiber, the loop filter can exhibit ultra-high Q characteristics.  $Q = 100000$ , for example. On the other hand, FSR of the fiber-based loop filter is smaller, typically 10 100 MHz, since it cannot help having longer cavity length. This loop filter is sometimes called sub loop coupled with the main cavity. Challenging is to stabilize optical fiber isolating thermal effects to prevent frequency drift of the cavity.

Narrowband amplification in optical domain is also applicable to the mode selection in the OEO. Typical optical amplifiers based on stimulated emission, such as EDFA and SOA, have broad band width, which are not suitable for mode filtering in the OEO. Recently, it has been demonstrated to use a SBS based fiber amplifier for the mode selection. SBS is a nonlinear effects induced in optical fiber. The SBS gain bandwidth is very narrow, MHz. If the pump light is modulated at  $f_{pump}$ , the passband becomes multiple with the frequency separation of  $f_{pump}$ . Although it requires bulky setup, this method has some good points in terms of functionalities: (1) ultra narrow-passband effective for clear mode selection, (2) stable mode stability, (3) flexible tunability in oscillation frequency.

In the rest part of this section, another approach is discussed Sakamoto, Kawanishi, Shinada & Izutsu (2005). This filtering function can be commonized with resonant enhancement of optoelectronic effects. Filtering effects are mostly based on resonance, where the optical/electrical field can be enhanced at the resonant frequency. Efficiency of OE/EO conversions can be enhanced The SBS based OEO, mentioned above, is an example of such resonant enhancement obtained together with narrow filtering in the optical domain.

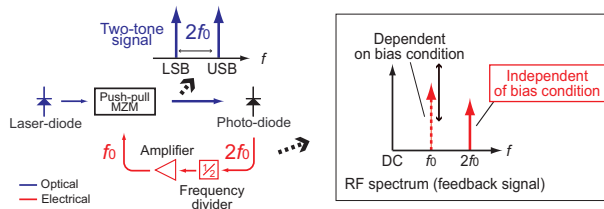


Fig. 1. Concept of two-tone signal generation using the proposed OEO.

Another example is shown in Fig. \*, which called resonant-electrode-type OEO (RE-OEPO). In this case, EO- modulator for the EO conversion in the OEO is resonantly enhanced. Usually, electro-optic devices are designed for wideband operation, which covers from around DC to 10 GHz frequency range, aiming for high-speed baseband data modulation. On the other hand the EO components in the OEO could be operated only at/around the oscillation frequency, which allows alternative design approach. The modulator, elements of the OEO, has a resonant structure in the modulation electrode, so that its modulation bandwidth is limited but the modulation efficiency is improved. A standing wave arises if a sinusoidal signal is fed to the electrode. Note that the OEO can oscillate only at the frequency of the resonance without using any optical or RF filters, because the modulation efficiency out of the resonant frequency is suppressed. Therefore, single-mode operation is easily obtained. In addition, it is expected that the OEO made of such modulators oscillate with lower threshold power. This scheme can greatly reduce complexity and cost of OEOs.

Recently, several types of resonant enhancement is discussed in terms of high-efficient optical modulation. Disk type modulator constructed on silicon substrate is a good candidate, where modulator is fabricated over an optical ring resonator. Similar to the scheme, this resonant enhancement in the OE conversion would effectively increase the OEO feedback gain.

### 3.2 Two-tone signal generation

For electro-optic (EO) modulation implemented in such an OEO setup, a Mach-Zehnder modulator (MZM) is often used. Conventionally, the OEO usually generates a sinusoidal clock signal, *i.e.* an intensity-modulated double-sideband signal with a carrier in the frequency domain, where the MZM should be biased at or around the quadrature point. The MZM in the OEO has so far never been operated at or around the top/null bias conditions, which are  $\frac{\pi}{2}$ -shifted from the quadrature point, because feed back gain is intrinsically dismissed around these conditions. If the MZM can be biased at the null point, for instance, it is possible to generate an optical two-tone signal, *i.e.*, a carrier-suppressed dual-sideband signal, in the mode of self-oscillating operation. Such a two-tone signal is useful for distributing optical clocks to remote places because it exhibits good tolerance to the fading effect in dispersive fibers.

To overcome the limitation in the bias condition, a modified OEO configuration has been demonstrated, where the MZM can be operated at the bias conditions  $\frac{\pi}{2}$ -shifted from the quadrature point, Sakamoto, Kawanishi & Izutsu (2005). In the modified OEO, a feedback signal is extracted from optical beat between the upper-sideband (USB) and the lower-sideband (LSB) components of EO-modulated lightwave to achieve oscillation even if the MZM is biased at the top/null point. Figure 1 shows the basic concept of the proposed OEO. It consists of an MZM, a photodetector, a frequency divider, and an radio-frequency (RF) amplifier. The photodetector connected at the output of the modulator converts the modulation components into an RF signal. The frequency of the detected signal is divided

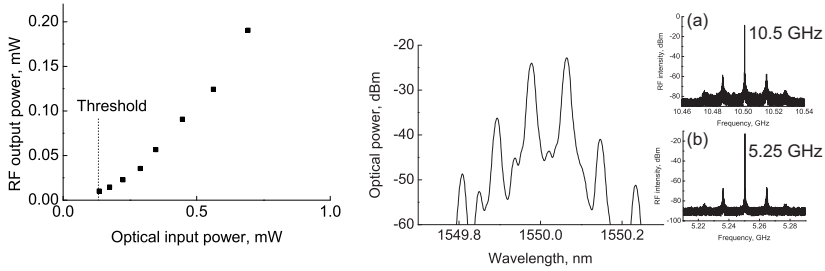


Fig. 2. (a) RF output power vs. optical input power. (b) Optical spectrum and RF spectra : (c) around 10.5 GHz, (d) around 5.25 GHz

in half by the frequency divider. The signal is amplified with the RF amplifier and positively fed back to the electrode of the modulator. If a lightwave with enough intensity is launched into the modulator, the loop gain of the oscillator becomes greater than one, and then the OEO starts oscillating. In this OEO, the oscillation frequency,  $f_0$ , is half the frequency of the optical beat between the USB and LSB components generated by the modulator. At the output of the photodetector, the photocurrent contains  $2f_0$  frequency components, while the frequency of the driving signal at the MZM is  $f_0$ .

We explain here why the use of a frequency divider is essential in the  $\frac{\pi}{2}$ -shift bias operation. When the MZM is driven with a sinusoidal signal at repetition frequency  $f_0$ , the optical field of the EO-modulated lightwave is given as

$$E_{\text{out}} = \frac{1}{2} E_{\text{in}} \sum_{k=-\infty}^{\infty} \left[ J_k(A_1) e^{jk\omega t + \theta_2} + J_k(A_2) e^{jk\omega t + \theta_2} \right],$$

where  $E_{\text{in}}$  is the input field, and  $J_k(\cdot)$  denotes the  $k$ -th order Bessel functions. The photocurrent of the direct-detected signal can be written as

$$i_{\text{ph}} = \frac{\eta |E_{\text{in}}|^2}{2} \left[ 1 + \cos \Delta\theta \left\{ J_0(\Delta A) + 2 \sum_{k=1}^{\infty} (-1)^k J_{2k}(\Delta A) \cos 2k\omega t \right\} \right. \\ \left. - \sin \Delta\theta \left\{ 2 \sum_{k=1}^{\infty} (-1)^k J_{2k-1}(\Delta A) \cos(2k-1)\omega t \right\} \right],$$

where  $\eta$  is the conversion efficiency of the photodiode. The amplitude of each mode at  $kf_0$  is a sinusoidal function of bias  $V$ . It should be noted that the odd-order harmonic modes of the detected photo current are governed by sine functions, whereas the even-order modes are governed by cosine functions. In conventional OEOs, the fundamental mode at  $f_0$  is fed back to the modulation electrode, where  $i_{\text{ph}}$  is maximized at the quadrature bias point ( $\Delta\theta = \pm\frac{\pi}{2}$ ) but minimized at the zero/top-biased conditions. Therefore, less feedback gain is obtained in an OEO if the MZM is biased around the zero or top point. In the proposed OEO, on the other hand, the frequency divider divides the frequency in half so that the second-order mode is fed back to the modulation electrode. In this case, the feedback gain is minimized at the quadrature bias condition,  $\Delta\theta = \frac{\pi}{2}$ , and maximized at the zero/top bias conditions,  $\Delta\theta = 0, \pm\pi$ . An optical two-tone signal is generated by using the OEO employing an push-pull operated MZM biased at the null point.

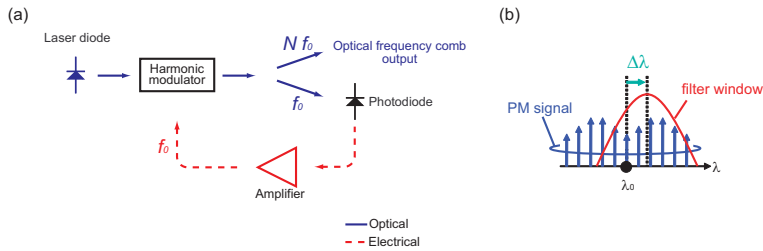


Fig. 3. (a) Concept of the OEO made of a harmonic modulator for optical frequency comb generation. (b) Offset filtering to convert phase-modulated lightwave to intensity-modulated feed-back signal.

Figure 2(a) shows threshold characteristics of the OEO, where RF output power is plotted against optical input power. Increasing the optical input power to the OEO, it started oscillating and the oscillation was stably maintained. The input power at the threshold for oscillation was 0.1 mW. The trace of the oscillation characteristics of the OEO is largely different from that of a conventional OEO. In our OEO output RF power is proportional to the square of the optical input power, whereas conventional OEOs have square-root input-to-output transfer function. This is because the RF signal introduced back to the modulation electrode is clipped to a constant level by the frequency divider comprised of a logical counter. The optical input power does not change the feedback signal level; therefore, the output RF power is proportional to the square of the input power.

The optical output spectrum is shown in Fig. 2(b). An optical two-tone signal was successfully generated. The RF spectra before and frequency division are also shown in the inset of Fig. 2 (c)(d). The upper trace (c) indicates the spectrum of the signal at the input of the frequency divider. A 10.5-GHz single-tone spectrum was obtained there. The RF spectrum of the frequency-divided signal, which drives the modulator, is shown in the lower trace (d). In both spectra, side-mode suppression ratios were more than 50 dB, which can be improved by using a more appropriate BPF with a narrower frequency passband.

In this subsection, an optoelectronic oscillator employing a Mach-Zehnder modulator biased at the null/top conditions has been described, which is suitable for generating optical two-tone signals. Under the bias conditions, a frequency divider implemented in the OEO was crucial for extracting a feedback signal from the upper- and lower-sideband components of an electro-optic modulated lightwave.

### 3.3 Comb generation

Optical frequency comb generators can provide many attractive applications in micro-wave or millimeter-wave photonic technologies [Jemison (2001)]: such as, optical frequency standard for absolute frequency measurement systems, local-oscillator remoting in radio-on-fiber systems, control of phased array antenna in radio astronomy systems, and so on.

Conventionally, a mode-locked laser is a popular candidate for such an optical frequency comb generation [Arahira et al. (1994)]. Viewed from a practical perspective, however, the technology has difficulties in control of starting and keeping the state of mode-locking. This is because typical mode-locked lasers, consisting of multi-mode optical cavities, have multi stabilities in their operations. In this subsection, an OEO modified for comb generation is described: optoelectronic oscillator (OEO) made of a harmonic modulator is described. [Sakamoto et al. (2006b) Sakamoto et al. (2007b) Sakamoto et al. (2006a)]

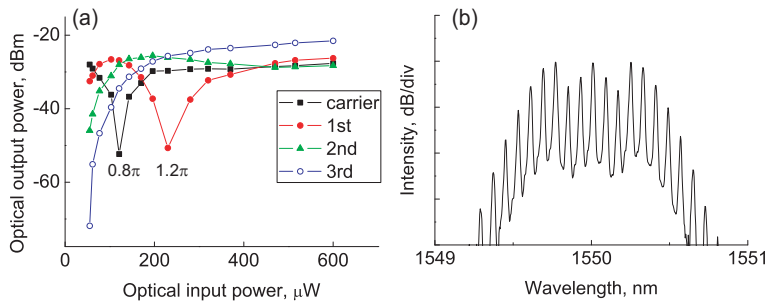


Fig. 4. (a) Optical intensity of each harmonic components against optical input power. Squares: at the carrier, dots: at the 1st-order, triangles: 2nd-order, circles: 3rd-order components. (b) Optical spectrum generated from the OEO (wavelength resolution = 0.01 nm).

It is known that EO modulation with larger amplitude signal promotes generating higher-order harmonics of the driving signal, obeying Bessel functions as discussed in the next section in detail. The OEO described in this subsection aims at the generation of frequency components higher than the oscillation frequency. In the OEO, an optical phase modulator is implemented in its oscillator cavity and driven by large-amplitude single-tone feed-back signal. Even this simple setup can generate multi-frequency components, i.e. optical frequency comb, with self oscillation as well as the conventional mode-locked lasers do. The most important difference from the mode-locking technologies is that the proposed comb generator is intrinsically a single-mode oscillator at a microwave frequency. Therefore, it is much more easy to start and maintain the oscillation comparing to the mode locking. A regenerative mode-locked laser is one of the successful examples of the wideband signal generation based on OEO structure, where a laser cavity is constructed in the optical part. However, it still relies on complex laser structure, while harmonic-OEO has a single one-direction optical path structure without laser cavity.

Figure 3(a) shows the schematic diagram of the proposed OEO. The OEO consists of an optical harmonic modulator, a photodetector, and an RF amplifier. The harmonic modulator generates optical harmonic components of a modulation signal. The photodetector, connected at the output of the modulator, converts the fundamental modulation component ( $f_0$ ) into an RF signal. The signal is amplified with the RF amplifier and led to the electrode of the modulator. If a lightwave with enough intensity is launched on the input of the harmonic modulator, the OEO starts oscillation because the fundamental modulation component at the frequency of  $f_0$  is positively fed back to the modulator. Note that harmonic components ( $Nf_0$ ) are generated at the output of the harmonic modulator, while the OEO is oscillating at  $f_0$ . Contrast to the conventional mode-locked lasers, the generated harmonics does not contribute to the oscillation, so that the OEO yields much more stable operation without complex control circuitry.

In this paper, an optical phase modulator is applied to the harmonic modulation in the OEO, where the modulator is driven by an RF signal with large amplitude. The modulator easily generates higher-order frequency components over the bandwidth of its modulation electrode. In order to achieve optoelectronic oscillation, it is required to detect feed back signal from the phase-modulated (PM) lightwave. For this purpose, we apply optical asymmetric filtering on the PM components, as shown in Fig. 3(b). By giving some frequency offset between the lightwave and the optical filter, the PM signal is converted into

intensity-modulated (IM) signal. This scheme is effective especially when the bandwidth of the filter is narrower than that of the PM signal. A fiber Bragg grating (FBG) is suitable for such an asymmetric filtering on deeply phase modulated signal since its stop band is typically narrower than the target bandwidth of frequency comb to be generated (100 GHz).

The OEO was made of an LiNbO<sub>3</sub> optical phase modulator, an optical coupler, an FBG, a photodiode (PD), an RF amplifier, a band-pass filter (BPF) and an RF delay line. The FBG had a 0.2-nm stop band and its Bragg wavelength was 1550.2 nm. The BPF determined the oscillation frequency of the OEO, and its center frequency and bandwidth of the BPF were 9.95 GHz and 10 MHz, respectively. The delay line aligned the loop length of the OEO to control the oscillation frequency, precisely. A CW light launched on the OEO was generated from a tunable laser diode (TLD). The center wavelength was aligned at 1550 nm, which was just near by the FBG stop band. The output lightwave from the FBG was photo-detected with the PD and introduced into the electrode of the phase modulator followed by the BPF and the amplifier. The harmonic modulated signal was tapped off with the optical coupler connected at the output of the modulator.

Increasing the optical power launched on the phase modulator, the OEO started oscillating. Fig. 4(a) shows optical output power of the phase-modulated components as a function of input power of the launched CW light. The squares, dots, triangles and circles indicate the 0th, 1st, 2nd and 3rd-order harmonic modulation components, respectively. As shown in Fig. 4(a), the input power at the threshold for oscillation was around 50  $\mu$ W. Then, at the optical input power of 140  $\mu$ W, we measured the optical spectrum of the generated signal. The output spectrum of the generated frequency obtained at (C) is shown in Fig.4 (b). Optical frequency comb with 120-GHz bandwidth and 9.95-GHz frequency spacing was successfully generated. The single-tone spectrum indicates that the OEO single-mode oscillated at the frequency of 9.95 GHz. The frequency spacing of the generated optical frequency comb was accurately controlled with a resolution of 30 kHz. By controlling the delay in the oscillator cavity, the oscillation frequency was continuously tuned within the passband of the BPF; the tuning range was about 10 MHz. The maximum phase-shift available in our experimental setup was restricted to about  $1.7\pi$  [rad]. It is expected that more deep modulation using a high-power RF amplifier and/or a low-driving-voltage modulator would generate more wideband frequency comb.

In conclusion, in this subsection, an optoelectronic oscillator made of a LiNbO<sub>3</sub> phase modulator for self-oscillating frequency comb generation has been described. Deeply phase-modulated light was converted to intensity-modulated signal through asymmetric filtering by an FBG, and fed back to the modulator. Frequency comb generation with 120-GHz bandwidth and 9.95-GHz accurate frequency spacing was achieved. The frequency spacing of the comb signal was tunable in the range of 10 MHz with the resolution higher than 30 kHz. The comb generator was selfstarting single-mode oscillator and stable operation was easily achieved without complex control technique required for conventional mode-locked lasers.

#### 4. Spectral enhancement and short pulse generation by photonic harmonic mixer

Generation of broadband comb and ultra short pulse train have been investigated for long time Margalit et al. (1998); Yokoyama et al. (2000); Yoshida & Nakazawa (1998); ?; ?; ?; ?; ?; ?. Especially in the last decade, compact and practical comb/pulse sources have been rapidly improved in the areas of test and measurements, optical telecommunications, and so on, accelerated by progress in semiconductor and fiber optics. For test and measurements, optical fiber mode-locked lasers based on passive mode-locking have been developed into compact packages, which can simply generate pulse train in femto-second region with a high

peak power of  $k$  - MWatt and a repetition rate of MHz or so Arahira et al. (1994). The technology is also useful for generation of ultra broadband optical comb that covers octave bandwidth. For telecomm use, active mode locked lasers and regenerative mode-locked lasers based on semiconductor or fiber laser structures have been intensively investigated, so far ????. Optical combs generated from the sources have large frequency spacing and they can be utilized as multi-wavelength carriers for huge capacity transmission. They are also useful for ultra high-speed communications because the pulse train generated is in high repetition. For practical use, however, stabilization technique is inevitable for keeping mode-locked lasing operation. Flexible controllability and synchronization with external sources are also important issues.

Recently, approaches based on electro-optic (EO) synthesizing techniques are becoming increasingly attractive Kourogi et al. (1994). Behind this new trend, we know rapid progress in EO modulators like  $\text{LiNbO}_3$ - and semiconductor-based waveguide modulators with improved modulation bandwidth and decreased driving voltage Kondo et al. (2005); Sugiyama et al. (2002); Tsuzuki et al. (n.d.). In the approaches, wideband optical comb with a bandwidth of several 100 GHz-THz and picosecond (or less) pulse train at a repetition of 10 100 GHz are generated from continuous-wave (CW) sources, which do not rely on any complex laser oscillation or cavity structures. This is of a great advantage for stable and flexible generation of optical comb/pulses.

In the former section, we described self-oscillating comb generation based on OEO configuration, where it is clarified that comb generation can be achieved without losing features of single-mode oscillators. The modulator used in the harmonic OEO is phase modulator in that case. As discussed in the section, EO modulators are useful way for the comb generation because it is superior in stable and low-phase-noise operation. A difficulty remained is to flatly generate optical comb; in other words, it is difficult to generate optical comb which has frequency components with the equal intensity. In fact, with a use of a phase modulator the amplitude of each frequency component obeys Bessel's function in different order, thus we can see that the spectral profile is far from flat one. Looking at applications of the comb sources, it can be clearly understood why lack or weakness of any frequency components causes problems. If we consider to use the comb source in WDM systems, for example, each channel should have almost equivalent intensity; otherwise the channels with weak intensity has poor signal-to-noise characteristics; the high-intensity channel suffers from nonlinear distortion through transmission. One of the possible ways to solve this problem is to apply an optical filter to the non-flat comb. However, this approach has some problems. To equalize and make the comb signal flat, the filter should have special transmittance profile. In addition, the efficiency of the comb generation would be worse because all components would be equalized to the intensity level of the weakest one.

In this section, we focus on this issue: flat comb generation by using electro-optic modulator, where a flat comb is generated by a combination of two phase-modulated non-flat comb signals. By this method, spectral ripples between the two phase-modulated lights are cancelled each other to form a flat spectral profile. A noticeable point of this method is that only single interferometric modulator is required for the operation. Another point is that the flat comb is generated from CW light and microwave sources, and no optical cavities are required.

First, in this section, flat comb generation and its theory is described. Four principle modes of operation are clarified, which are essential for the flat comb generation by two phase-modulated lights. Next, synthesis of optical pulse train from the flat comb is described. Spectral enhancement and/or pulse compression with an aid of nonlinear fiber is also discussed.

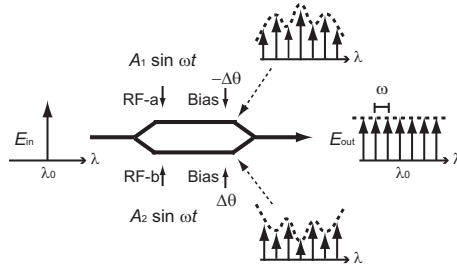


Fig. 5. Concept of ultraflat optical frequency comb generation using a conventional Mach-Zehnder modulator. A CW lightwave is EO modulated by a dual-drive Mach-Zehnder modulator driven with large sinusoidal signals with different amplitudes.

#### 4.1 Ultra-flat comb generation

Fig. 5 shows the principle of flat comb generation by the combination of two phase modulated lightwaves Sakamoto et al. (2007a). In the optical frequency comb generator, an input continuous-wave (CW) lightwave is EO modulated with a large amplitude RF signal using a conventional MZM. Higher-order sideband frequency components (with respect to the input CW light) are generated. These components can be used as a frequency comb because the signal has a spectrum with a constant frequency spacing. Conventionally, however, the intensity of each component is highly dependent on the harmonic order. We will find, in this section, that the spectral unflatness can be cancelled if the dual arms of the MZM are driven by in-phase sinusoidal signals, RF-a and RF-b in Fig. 5, with a specific amplitude difference.

##### 4.1.1 Principle operation modes for flat comb generation

Here, in this subsection, principle operation modes for flatly generating optical comb using an MZM are analytically derived. Sakamoto et al. (2007a)

Suppose that the optical phase shift induced by signals RF-a and RF-b are  $\Phi_a(t) = (\bar{A} + \Delta A) \sin(2\pi f_0 t + \Delta\phi_{ab})$ ,  $\Phi_b(t) = (\bar{A} - \Delta A) \sin(2\pi f_0 t - \Delta\phi_{ab})$ , respectively, where  $\bar{A}$  is the average amplitude of the zero-to-peak phase shift induced by RF-a and RF-b;  $2\Delta A$  is difference between them;  $f_0$  is the modulation frequency;  $2\Delta\phi_{ab}$  is the phase difference between RF-a and RF-b.

For large-amplitude driving signals, power conversion efficiency from the input CW light to each harmonic mode can be asymptotically approximated as

$$\begin{aligned}
 \eta_k &\equiv \frac{P_k}{P_{in}} \\
 &\approx \frac{1}{2\pi\bar{A}} \left| e^{\alpha(\Delta\theta + k\Delta\phi_{ab})} \cos(\alpha + \Delta A) + e^{-\alpha(\Delta\theta + k\Delta\phi_{ab})} \cos(\alpha - \Delta A) \right|^2 \\
 &= \frac{1}{2\pi\bar{A}} [1 + \cos(2\Delta A) \cos(2\Delta\theta + 2k\Delta\phi_{ab}) + \cos(2\Delta A) \cos\beta \cos(k\pi) \\
 &\quad + \cos(2\Delta\theta + 2k\Delta\phi_{ab}) \cos\beta \cos(k\pi)]
 \end{aligned} \tag{1}$$

, where  $\beta \equiv \bar{A} - \frac{\pi}{2}$  (+Higher-order term). This expression describes behavior of the generated comb well as long as  $\bar{A}$  is large enough. Generally, the conversion efficiency is highly dependent on the harmonic order of the driving signal,  $k$ , which means that the frequency comb generated from the MZM has a non-flat spectrum.



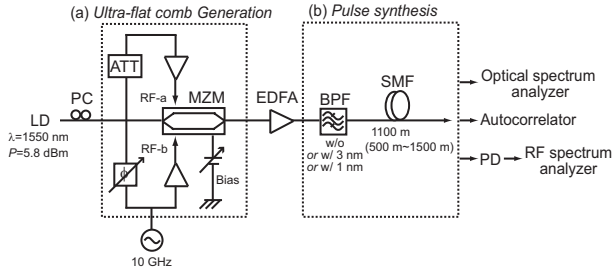


Fig. 6. Experimental setup; LD: laser diode, PC: polarization controller, MZM: Mach-Zehnder modulator, ATT: RF attenuator, EDFA: Erbium-doped fiber amplifier, BPF: optical bandpass filter, SMF: standard single-mode fiber, PD: photodiode.

To make the comb flat in the optical frequency domain, the intensity of each mode should be independent of  $k$ . From Eq. 1, the condition is

$$\cos(2\Delta A) + \cos(2\Delta\theta + 2k\Delta\phi_{ab}) = 0 \tag{2}$$

To keep this equation for any  $k$ , the second term should be independent of  $k$ .  $\Delta\phi_{ab}$  should satisfy

$$\Delta\phi_{ab} = 0 \text{ or } \pm \frac{\pi}{2}. \tag{3}$$

It should be noted that  $\Delta\phi_{ab} = 0$  and  $\Delta\phi_{ab} = \frac{\pi}{2}$  correspond to the cases of “in-phase” and “out-of-phase (push-pull)” driven conditions, respectively.

In the “in-phase” driven case ( $\Delta\phi_{ab} = 0$ ), the difference of the induced phase difference and bias difference should be related as

$$\Delta A \pm \Delta\theta = n\pi + \frac{\pi}{2}. \tag{4}$$

to make the spectral envelope flattened. Sakamoto et al. (2007a)

In the case of  $\Delta\phi_{ab} = \frac{\pi}{2}$ , the MZM is allowed to be “out-of-phase (push-pull)” driven Sakamoto et al. (2011). From Eq. 2, the flat spectrum condition yields

$$\Delta A = \pm \frac{\pi}{4}, \Delta\theta = \pm \frac{\pi}{4} \tag{5}$$

From Eq. 4 and Eq. 5, it is found that there are conditions for flat frequency comb generation both for “in-phase” and “out-of-phase” driving cases, and the former condition is more robust since we only need to keep the balance between  $\Delta A$  and  $\Delta\theta$ . If we make the efficiency of the generated comb maximum, however, the driving condition for “in-phase” driven case also results in  $\Delta A = \pm \frac{\pi}{4}, \Delta\theta = \pm \frac{\pi}{4}$ .

#### 4.1.2 Experimental proof

Next, the flat spectrum condition in the four operation modes are experimentally proved. Fig. 6 shows the experimental setup, which is commonly referred in this chapter hereafter. The optical frequency comb generator consisted of a semiconductor laser diode (LD) and a LiNbO<sub>3</sub> dual-drive MZM having half-wave voltage of 5.4 V. A CW light was generated from the LD, whose center wavelength and intensity of the LD was 1550 nm and 5.8 dBm, respectively. The

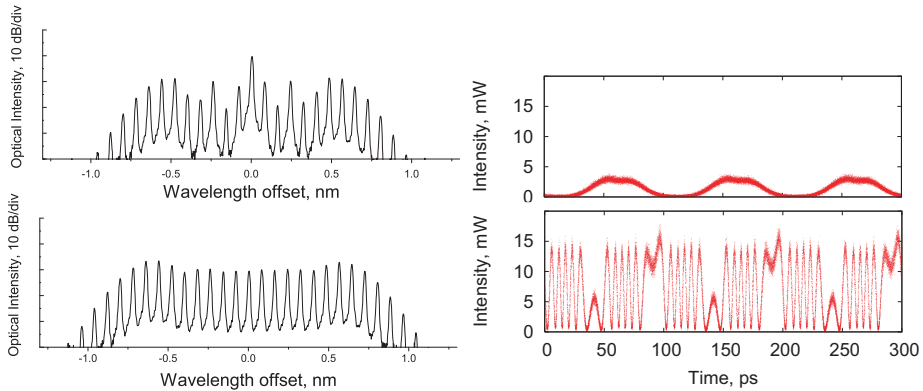


Fig. 7. Optical spectra; (a) Single-arm driven, (b)  $\Delta_{phi} = 0$  (in-phase), (c)  $\Delta_{phi} = 0.4\pi$ , (d)  $\Delta_{phi} = \pi/2$  (out-of-phase), Optical waveforms measured with an four-wave-mixing-based all-optical sampler (temporal resolution = 2 ps); (a) in-phase mode, (b) out-of-phase mode

CW light was introduced into the modulator through a polarization controller to maximize modulation efficiency. The MZM was dual-driven with sinusoidal signals with different amplitudes (RF-a, RF-b). The RF sinusoidal signal at a frequency of 10 GHz was generated from a synthesizer, divided in half with a hybrid coupler, amplified with microwave boosters, and then fed to each modulation electrode of the modulator. The intensity of RF-a injected into the electrode was attenuated a little by giving loss to the feeder line connected with the electrode. The input intensities of RF-a and RF-b were 35.9 dBm and 36.4 dBm, respectively Sakamoto et al. (2008). In order to select the operation modes, mechanically tunable delay line with tuning range over 100 ps was implemented in the feeder line for RF-a. The modulation spectra obtained from the frequency comb generator were measured with an optical spectrum analyzer. Optical waveform was measured with a four-wave-mixing-based all-optical sampler having temporal resolution of 2 ps.

Fig. 7 shows the optical spectra of the generated frequency comb. (a) is the case obtained when the MZM was driven in a single arm, where the driving condition was far from the "flat-spectrum" condition. (b) is the spectrum under the "flat-spectrum" condition in the "in-phase" operation mode. The delay between the RF-a and RF-b was set at 0 ( $\Delta\phi_{ab} = 0$ ). The RF power of the driving signals were 35.9 dBm and 36.4 dBm, respectively. Keeping the intensities of the driving signals, delay between RF-a and RF-b was detuned from  $\Delta\phi_{ab} = 0$ . The spectral profile became asymmetric as shown in (c), where  $\Delta\phi_{ab} \approx 0.2\pi$ . The spectrum became flat again when  $\Delta\phi_{ab} = \pi/2$  as shown in (d). The spectral at (b) and (d) were almost the same as expected and the 10-dB bandwidth was about 210 GHz in the experiments. Optical spectra with almost same the profile was monitored even when the optical bias condition was changed from the up-slope bias condition to the down-slope one. It has been confirmed that there are totally four different operation modes for flat comb generation using the MZM.

Characterization of the temporal waveform helps account for the behavior of the operation modes. Fig. 7 shows the optical waveforms measured with the all-optical sampler. Fig. 7(a) is the case obtained when the MZM was operated in the in-phase mode. The optical waveform was sinusoidal like since the optical amplitude is modulated within the range between 0 to  $\pi$  under the condition. On the other hand, Fig. 7(b) is measured at the push-pull operation mode. In this case, the temporal waveform was sharply folded back and forth and it is found that the optical amplitude was over swang far beyond the full-swing range of  $0-\pi$ .

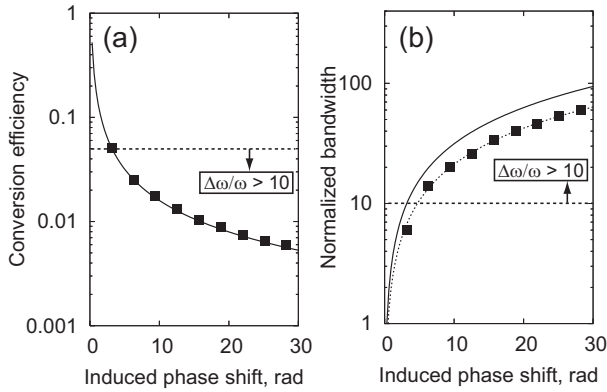


Fig. 8. (a) Maximum conversion efficiency,  $\eta_{k,max}$  vs. induced phase shift  $\bar{A}$ ; theoretically (asymptotically) [solid line] and numerically averaged conversion efficiency within  $0.5\Delta\omega$  [squares];(b) bandwidth,  $\Delta\omega$ , vs.  $\bar{A}$ ; theoretically (asymptotically)  $(\Delta\omega)$ [solid line], number of CW components within 3-dB drop of  $\eta_k$  [squares], fitted curve  $(0.67\Delta\omega)$  [dashed line]; in each graph, the region of  $\Delta\omega/\omega > 10$  is practically meaningful, where more than 10 frequency components are generated.

**4.1.3 Characteristics of optical frequency comb generated from single-stage MZM**

Here, primary characteristics of the generated comb are described providing with additional analysis. Conversion efficiency, bandwidth, noise characteristics are analyzed, in this subsection.

**Conversion Efficiency**

The output power should be maximized for higher efficient comb generation. Here, we discuss efficiency of comb generation. First, we define two parameters that stands for conversion efficiency of the comb genearation. One is a “total conversion efficiency”, which is defined as the total output power from the modulator to the intensity of input CW light. The other is simply called “conversion efficiency”, which is defined as the intensity of individual frequency component to the input power.

Under the flat spectrum condition for “in-phase” mode, Eq. 3, the intrinsic conversion efficiency, excluding insertion loss due to impairment of the modulator and other extrinsic loss, is theoretically derived from Eq. 1 and Eq. 4, resulting in

$$\eta_k = \frac{1 - \cos 4\Delta\theta}{4\pi\bar{A}}, \tag{6}$$

which means that the conversion efficiency is maximized upto

$$\eta_{k,max} = \frac{1}{2\pi\bar{A}}, \text{ when } \Delta A = \Delta\theta = \frac{\pi}{4}. \tag{7}$$

Note that this is the optimal driving condition for flatly generating an optical frequency comb with the maximum conversion efficiency. Hereafter, we call this equation the “maximum-efficiency condition” for ultraflat comb generation.

For the out-of-phase operation mode, the conversion efficiency yields,

$$\eta_{k,\text{out-of-phase}} = \frac{1}{2\pi\bar{A}}, \quad (8)$$

, which is equivalent with the maximum-efficiency condition for the inphase operation mode, Eq. 7.

Fig. 8(a) shows the maximum conversion efficiency,  $\eta_{k,\text{max}}$  plotted against the average induced phase shift of  $\bar{A}$ . The solid curve indicates the theoretically derived conversion efficiency, Eq. 7 or 8. The squares in the plot indicate the numerically calculated average conversion efficiencies within the  $0.5\Delta\omega$  bandwidth with respect to each value of  $\bar{A}$ . For the calculation, optical spectrum of the generated comb is calculated by using a First-Fourier-Transform (FFT) method, which is commonly used for spectral analysis of modulated lightwave. The range of  $\bar{A}$  for the calculation is restricted in the range of  $\frac{\Delta\omega}{\omega} > 10$ , where the generated comb has practically sufficient number of frequency components. The good agreement with numerical data proves that Eq. 7 or 8 is valid in the practical range.

#### Bandwidth

Bandwidth of the comb under the flat spectrum conditions is estimated, here. Under the flat spectrum conditions, energy is equally distributed to each frequency component of the generated comb. From the physical point of view, however, the finite number of the generated frequency comb is, obviously, allowed to have the same intensity in the spectrum; otherwise, total energy is diverged. The approximation for Eq. 1 is valid as long as  $k \ll k_0$  and  $\eta_k$  rapidly approaches zero for  $k \gg k_0$ . It is reasonable to assume that optical energy is equally distributed to each frequency mode around the center wavelength (i.e.  $k \ll k_0$ ). Since the total energy,  $\overline{P_{\text{out}}}$ , can be calculated in time domain, the bandwidth of the frequency comb becomes

$$\Delta\omega = \frac{\overline{P_{\text{out}}}\omega}{\eta_k P_{\text{in}}} \approx \pi\bar{A}\omega \quad (\text{for small } \Delta A), \quad (9)$$

which is almost independent of  $\Delta A$  (or  $\Delta\theta$ ).

As for the comb generated under the out-of-phase operation mode, the analysis also results in the same bandwidth.

In Fig.8(b), the bandwidth,  $\Delta\omega$  is plotted as a function of  $\bar{A}$ . In the graph, the solid curve indicates the theoretical bandwidth derived in Eq. 9; the squares represent the calculated 3-dB bandwidths required for keeping conversion efficiency of less than 3-dB rolling off from the center wavelength. These data almost lie on the fitted curve of  $0.67\Delta\omega$ , which is also plotted as a dashed curve in the graph. From this analysis, frequency components within 67% of the theoretical bandwidth of  $\Delta\omega$  are numerically proven to have sufficient intensity with less than a 3-dB drop in the conversion efficiency. The 33% difference from the predicted  $\Delta\omega$  is mainly because the shape of actual spectrum of the generated comb slightly differs from a rectangle assumed in the derivation of Eq. 7.

#### 4.2 Linear pulse synthesis

Generation of picosecond optical pulse train at a high repetition rate ?????? has been extensively studied to achieve highly stable and flexible operation, aiming at the use in ultra-high-speed data transmission or in ultra-fast photonic measurement systems. Conventionally, actively/passively mode-locked lasers based on semiconductor or fiber-optic

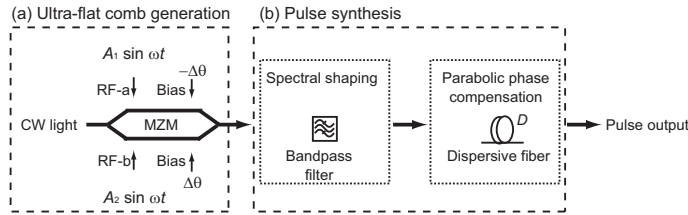


Fig. 9. Generation of ultra-short pulses by using a single-stage conventional Mach-Zehnder modulator.

technologies have been typically used to generate such pulse trains ???. In the technologies, however, the laser cavity should be strictly designed and stabilized to generate stable pulse trains, which reduces flexibility in the operation. Especially, its repetition rate of the generated pulses is almost fixed and its scarce tunability has been provided. In addition, the highly nonlinear properties involved in generating pulses also restrict its operating conditions, which leads to limited output optical power and to uncontrollable chirp characteristics.

In the previous section, ultra-flat frequency comb generation by using only an MZM has been described. In this section, we apply it to generation of ultrafast pulse train. Basically, the strategy to synthesize optical pulse train from the comb source is as follows: (1) Phase differences between frequency components are aligned to be zero to form impulsive pulse train. (2) Profile of temporal waveform is controlled by spectral shaping to the generated comb.

By this approach, pulse trains with a pulse width of picosecond order can be obtained as discussed in this section. These two operations can be achieved in a linear process by simple passive components, as discussed in this section. The first one, phase compensation, is easily achieved by using a commonly used optical dispersive fiber. The second one, spectral shaping, is also achieved with a typical optical bandpass filter. Thin-film filters can be used for this purpose.

Figure 9 shows the basic construction of the picosecond pulse generator employing single-stage MZM. The pulse source consists of two sections: one for (a) comb generation and the other for (b) pulse synthesis. Section (a), consisting of a single-stage MZM, has a role to flatly generate a frequency comb. In this section, a continuous-wave (CW) light is EO modulated with the MZM, which is dual-driven by sinusoidal in-phase or out-of-phase signals having different amplitudes. Section (b), on the other hand, is comprised of an optical filter and a fiber, and it spectrally shapes the generated comb into a pulse train having a  $\text{sync}^2$ -like or a Gaussian-like temporal waveform.

The advantages of this pulse source are 1) the pulses are generated in an optically linear process, so that the optical level of the generated pulse is easily controlled; 2) the pulse source can be started up quickly without the need for complicated control procedures; 3) the repetition rate and the center wavelength of the generated pulse can be flexibly and quickly controlled; 4) the generated pulse train is highly stable due to the simple structure of the pulse generator and to the maturity of the components employed; 5) the pulse generator guarantees ultra-low timing jitter due to the high coherence of the generated comb.

Phase characteristics of comb

To clarify the phase characteristics of the generated comb, we modify Eq. 1 to look into higher-order terms of the output field, yielding

$$\begin{aligned}
E_{\text{out}} &= \frac{1}{2} E_{\text{in}} \sum_{k=-\infty}^{\infty} \left[ J_k(A_1) e^{j(k\omega t + \theta_1)} + J_k(A_2) e^{j(k\omega t + \theta_2)} \right] \\
&\approx \frac{E_0}{2} \sqrt{\frac{2}{\pi}} \bar{A}^{-\frac{1}{2}} \sum_{k=-\infty}^{\infty} \left\{ \cos \left( \bar{A} - \frac{(2k+1)\pi}{4} + \frac{4k^2-1^2}{8} \bar{A}^{-1} + \Delta A \right) e^{ae\Delta\theta} \right. \\
&\quad \left. \cos \left( \bar{A} - \frac{(2k+1)\pi}{4} + \frac{4k^2-1^2}{8} \bar{A}^{-1} - \Delta A \right) e^{-ae\Delta\theta} \right\} e^{ae(\bar{\theta} + k\omega t)}, \quad (10)
\end{aligned}$$

Since we have already derived the flat spectrum conditions, we substitute Eq. 3 and Eq. 4 into Eq. 10, respectively. Under the flat spectrum condition for in-phase and out-of-phase modes, respectively, the amplitude and the phase of the frequency modes can be approximated as

$$A_k = \frac{E_0 \sin(2\Delta\theta)}{\sqrt{2\pi\bar{A}}}, \Phi_k = \pm \frac{4k^2 - 1}{8\bar{A}}, \quad (11)$$

where those series higher than the fourth order series of  $\Phi_k$  are neglected. It should be noted that the amplitude is independent of the harmonic order of the generated frequency components,  $k$ ; the optical phases of the modes are related through a parabolic function of  $k$ . This equation is valid as long as  $|k| \ll k_{\text{max}} = \pi\bar{A}$  is satisfied.

Linear pulse synthesis by fiber-optic circuits

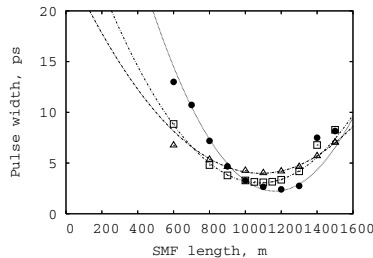


Fig. 10. Pulse width measured as a function of SMF length; solids: w/o filter, squares: w/ 3-nm filter, triangles: w/ 1-nm filter

Next, it is explained how the generated ultra-flat frequency comb is shaped into an ultra-short pulse train in section (b) of the pulse source by using Fourier spectral synthesis. In the case of in-phase operation mode, the story becomes more simple. From Eq. 11, it is found that the optical phase relationship between each mode is in a parabolic function of the mode number. Note that phase compensation with  $-\Phi_k$  makes the temporal waveform of the generated comb impulsive. Such a phase compensation can be easily achieved by using a piece of standard optical fiber that gives a parabolic phase shift, i.e., a counter group delay, to the generated comb. The optimal length for the pulse generation is simply obtained as,

$$L = \mp \frac{\partial^2 \Phi_k}{\partial k^2} (\beta_2 \omega_0^2)^{-1} = \mp (\beta_2 \bar{A} \omega_0^2)^{-1}, \quad (12)$$

where  $\beta_2$  denotes group velocity dispersion in the fiber.

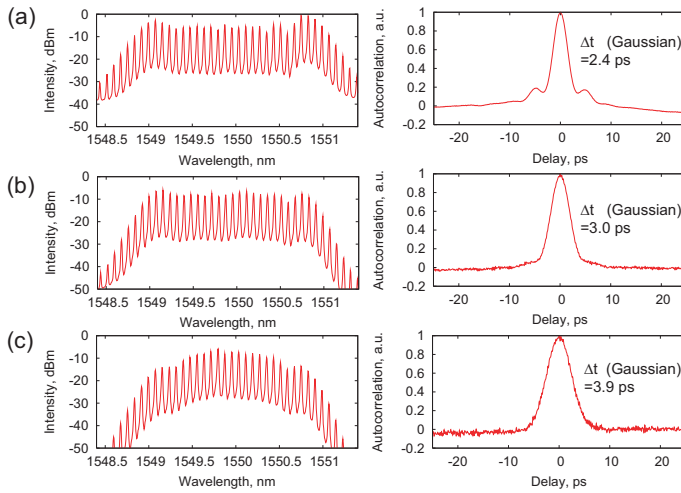


Fig. 11. Optical spectra (left side) and autocorrelation traces (right side); (a) W/o filtering, (b)  $\text{sinc}^2$ -like shape, (c) Gaussian-like shape.

The synthesized pulse train, however, has a rather temporal waveform of the  $\text{sinc}^2$  function causing a large pedestal around the main pulse, because the generated comb has a rectangular spectrum. In many cases, it is required to shape the temporal waveform of the pulse into Gaussian to suppress the undesired pedestal. If an optical bandpass filter (OBPF) is applied to the generated comb having a cut-off frequency of  $f \ll \frac{1}{2\pi}k_{\max}\omega$ , the spectral envelope is shaped into the passband profile of the OBPF; thus, the temporal waveform should be a Fourier transform of the filter passband profile. For instance, if a Gaussian filter is applied to the generated comb together with the appropriate phase compensation of  $-\Phi_k$ , it is possible to generate Fourier-transform limited Gaussian pulse train with a pulse width of  $T = 0.44/f$  and with a repetition of  $T_0 = \frac{2\pi}{\omega}$ . From this analysis, it is found that the optical pulses can be generated only using linear fiber-optic components. This has numerous practical advantages.

#### Experimental proof

Figure 6 shows the experimental setup for picosecond pulse generation using a single-stage MZM. In section (a) of the setup, an ultra-flat frequency comb was generated. A CW light was generated from a laser diode (LD), whose center wavelength and intensity were 1550 nm and 5.8 dBm, respectively. The CW light was introduced into the conventional  $\text{LiNbO}_3$  dual-drive MZM that was driven under the flat spectrum condition. The MZM, having half-wave voltage of 5.4 V, was dual-driven with 10-GHz sinusoidal signals of RF-a and RF-b. The RF signals were generated from a synthesizer, divided in half with a hybrid coupler, amplified with microwave boosters, and fed into the electrodes of the modulator. The intensity of the RF-a fed into the electrode was attenuated a little by giving loss to the feeder line connected with the electrode. The average input intensity of RF-a and of RF-b was 38.5 dBm, and the difference between them was 1.0 dB. The average zero-to-peak deviation in the phase shift induced in the modulator was estimated to be  $4.3\pi$ . The phase difference between RF-a and RF-b was aligned to be zero by using a mechanically tunable delay line placed in the feeder cable for RF-a.

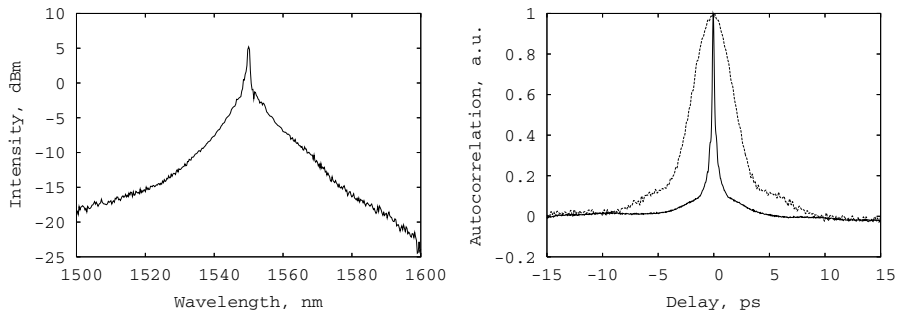


Fig. 12. Characteristics of generated pulse train; (a) optical spectrum , (b) autocorrelation traces, dotted: seed pulse, solid: compressed pulse

In section (b) of the experimental setup, the generated comb was converted into a pulse train. The comb was amplified with an Erbium-doped fiber amplifier (EDFA), and led to an optical thin-film band-pass filter (OBPF) followed by a piece of standard single-mode fiber (SMF). In addition to the function of the spectral shaping, the OBPF filtered out ASE noise generated from the EDFA. The characteristics of the generated pulse train were evaluated with an optical spectrum analyzer and an autocorrelator, and the timing jitter was analyzed with an RF spectrum analyzer.

First, in this experiment, the length of the SMF was optimized by evaluating evolution of the pulses through the fiber. Figure 10 shows pulse width dependence measured as a function of the SMF length. The pulse width was estimated from the autocorrelation traces assuming the Gaussian waveform. The circles, squares and triangles in the graph correspond to pulse widths measured (a) without a filter, (b) with a 3-nm filter ( $\Delta\lambda_{\text{bpf}} = 3 \text{ nm}$ ) and (c) with a 1-nm filter ( $\Delta\lambda_{\text{bpf}} = 1 \text{ nm}$ ). We found that  $\sim 1100 \text{ m}$  is the optimal length for the pulse synthesis, where a group delay of  $22 \text{ ps}^2/\text{nm}$  was introduced. Thus, the experimentally optimized length of the SMF is in good agreement with the theoretical value estimated from Eq. 12.

Figure 11 shows the optical spectra and the autocorrelation traces of the generated pulse trains. The narrowest pulse was obtained without using the OBPF, where the pulse width was estimated to be 2.4 ps. In this case, however, the pulse train had a large pedestal around the mainlobe of the pulse. For  $\Delta\lambda_{\text{bpf}} = 3 \text{ nm}$ , the temporal waveform was a sinc<sup>2</sup>-like function since the shape of the spectral envelope was square. The estimated pulse width was 3.0-ps. In the case of  $\Delta\lambda_{\text{bpf}} = 1 \text{ nm}$ , which is narrower than the spectral width of the generated comb, the optical spectrum had almost the same shape as the passband of the OBPF. It is confirmed that a Gaussian-like pulse train with a pulse width of 3.9 ps was generated, where time-bandwidth product was 0.45. The root-mean-square timing jitter evaluated from the single-sideband phase noise was as low as 130 fs, which almost reached the synthesizer's limit of the driving signal fed to the MZM. The generated pulse was greatly stable in long term, maintaining its waveform for at least a couple of hours.

In conclusion, we have proposed and demonstrated picosecond pulse generation using a conventional MZM. A 10-GHz, 2.4-ps pulse train was generated with  $< 130\text{-fs}$  timing jitter. The pulse source is potentially more stable and more agile than conventional mode-locked lasers, and the setup is much simpler.



**4.3 Nonlinear spectrum enhancement/ pulse compression**

Femtosecond or sub-picosecond pulse train at GHz or higher repetition is promising for ultra-high speed optical transmissions and ultrafast photonic measurements. To generate such a short pulse train at high repetition rate, it is effective to use pulse compression technique together with a picosecond seed pulse source. As previously described, MZM-FCG based pulse source can simply and stably generate a picosecond pulse train. Here, we describe generation of 500-fs pulse train at repetition of 10 GHz using a conventional LiNbO<sub>3</sub> MZM, where compression ratio from driving RF signal reached 100 Morohashi et al. (2008) Morohashi et al. (2009). The generated pulse train exhibits great stability and ultra-low phase noise almost same the level as the synthesizer limit.

Among the pulse compression technologies, adiabatic soliton compression gathers great attention because of its easiness for handling, where a pulse train adiabatically evolves into shorter one in a dispersion decreasing fiber (DDF), keeping the fundamental soliton condition. In the adiabatic soliton compression using DDF, the compression ratio is proportional to the ratio of group velocity dispersion around input and output regions of the DDF. The pulse width of the seed pulse launched into the DDF should be ps to achieve generation of femtosecond or sub-picosecond pulse train because the compression ratio available in the DDF is typically 10-100.

For the soliton compression technique, we should keep soliton parameter defined as follows, as 1

$$N = \sqrt{\frac{\gamma P_0 T_0^2}{|\beta_2|}} \tag{13}$$

Since the comb generated from the MZM-FCG has a bandwidth derived as Eq. 9, pulse width should be

$$T_{FWHM} = \frac{2c}{A\omega}, \tag{14}$$

where c is a constant in the order of 1-10.

Therefore, average power of the pulse train launched into the DDF results in

$$P_{ave} = \frac{\omega T_{FWHM} P_0}{2\pi} = \frac{\beta_2 \omega^3 A^2}{2\pi \gamma 4c^2}, \tag{15}$$

which is a practical parameter for designing the compression stage.

Experimental setup is common as Fig. 6, but it has extended stage for nonlinear compression. In this stage, the generated pulse train is converted into femtosecond pulses using the adiabatic soliton compression technique. The picosecond pulse was amplified with an EDFA upto the average power of 10 dBm; introduced into a dispersion-flattened dispersion decreasing fiber with the length of 1 km. In the fiber, wavelength dispersion was gradually decreased along the fiber from 10 ps/nm/km to 1 ps/nm/km (estimated), and that was flattened enough in the wavelength range of 1550 nm to 1560 nm. Autocorrelation traces are shown in Fig. 3. (a) is the trace measured at the output of the seed pulse generator (at point (A) in Fig. 1). The half width of the summing Sech<sup>2</sup> waveform, the pulse width of the seed pulse is estimated to be 2 ps; the pulse was compressed into 500-fs pulse train using DDF-DDF.

From this experiments, it is shown that an ultrashort pulse train in femtosecond order can be generated from a CW light. This femtosecond pulse train also inherits the features of

Conditions	RF driving signals ( $V_1 \sin \omega t, V_2 \sin \omega t$ )	(Single-arm) bias voltage ( $V_{\text{bias}}$ )	Conversion efficiency ( $\eta_k$ )	Normalized bandwidth ( $\frac{\Delta\omega}{\omega}$ )
Flat spectrum condition	$(\bar{V} \pm \frac{V_{\pi}}{2} \mp \frac{V_{\text{bias}}}{2}) \sin \omega t$	$V_{\text{bias}}$	$\frac{V_{\pi}}{4\pi^2 \bar{V}} \left[ 1 - \cos\left(\frac{2\pi V_{\text{bias}}}{V_{\pi}}\right) \right]$	$\pi^2 \frac{\bar{V}}{V_{\pi}}$
Maximum-efficiency condition	$(\bar{V} \pm \frac{V_{\pi}}{4}) \sin \omega t$	$\frac{V_{\pi}}{2}$	$\frac{V_{\pi}}{2\pi^2 \bar{V}}$	$\pi^2 \frac{\bar{V}}{V_{\pi}}$

Table 1. Formulas for ultraflat frequency comb generation using MZM;  $\bar{V} \equiv \frac{V_1 + V_2}{2}$ , where  $V_1, V_2$  are zero-to-peak voltages of RF-a and RF-b, respectively,  $V_{\text{bias}}$ : bias voltage applied to one arm,  $V_{\pi}$ : half-wave voltage of the MZM.

linearly synthesized picosecond one: great stability, low-jitter characteristics, flex tunability in wavelength, repetition and so on.

#### 4.4 Formulas for the flat comb and short pulse generation

We have reviewed techniques for generation of optical comb and pulses from CW source, focusing on the MZM-FCG based method, so far. Here, we summarize the operation modes and conditions required for obtaining the signals.

For flat comb generation, we have four operation modes. For both driving cases, the maximum conversion efficiency yields  $\eta_k = \frac{1}{2\pi A}$ , which means that “in-phase” and “out-of-phase” driving modes can be effectively used with the same conversion efficiency. It is practically reasonable to operate the comb generator under the condition of the maximum conversion efficiency. By careful look at the signs of  $\Delta A$  and  $\Delta\theta$ , it is found that the MZM can be biased at the quadrature point in the up slope or down slope of its transfer function.

By the combination of polarities of the driving signal and the bias condition, the MZM can be driven in totally four different principle operation modes, summarized as follows:

- (1) Up-slope biased in-phase driven mode:  $|\Delta\phi_{\text{ab}}| = 0, \Delta A = \pm \frac{\pi}{4}, \Delta\theta = \pm \frac{\pi}{4},$
- (2) Down-slope biased in-phase driven mode:  $|\Delta\phi_{\text{ab}}| = 0, \Delta A = \pm \frac{\pi}{4}, \Delta\theta = \mp \frac{\pi}{4},$
- (3) Up-slope biased out-of-phase (push-pull) driven mode:  $|\Delta\phi_{\text{ab}}| = \frac{\pi}{2}, \Delta A = \pm \frac{\pi}{4}, \Delta\theta = \pm \frac{\pi}{4},$
- (4) Down-slope biased out-of-phase (push-pull) driven mode:  $|\Delta\phi_{\text{ab}}| = \frac{\pi}{2}, \Delta A = \pm \frac{\pi}{4}, \Delta\theta = \mp \frac{\pi}{4}.$

In-phase mode is suitable for short pulse generation because the generated pulse has smooth temporal waveform envelope and continuous phase characteristics. For picosecond pulse generation, a dispersive fiber with a length of  $(|\beta_2| \bar{A} \omega_0^2)^{-1}$  [m] converts comb signal to pulse train with a pulse width of  $2c / (\bar{A} \omega)$  [sec].

To obtain femtosecond pulses, the comb with average input power of  $(\beta_2 \omega^3 \bar{A}^2) / (2\pi \gamma 4c^2)$  [W], should be launched into the DDF having following parameters: group velocity dispersions at input and output region,  $\beta_{2,\text{in}}, \beta_{2,\text{out}}$ , nonlinearity coefficient,  $\gamma$ . The pulse width achievable is estimated to be  $2c \sqrt{\beta_{2,\text{out}}} / (\bar{A} \omega \sqrt{\beta_{2,\text{in}}})$  [sec].

Table 1 summarizes the formulas for the operations.

## 5. Applications

In this section, we briefly introduce some interesting applications of the MZM-FCG: 1) generation of picosecond/ femtosecond pulse train, 2) generation of multi-color pulses, 3) other applications, such as arbitrary waveform generation, code/label generation for optical

CDMA. The above-mentioned auto-bias control has not yet been implemented in these experimental demonstrations since the comb generator is stable enough for the lab use; however the auto bias control will practically accelerate realization of these applications.

To simply generate ultra short pulse trains in multi wavelengths is challenging but promising [1]. In future ultra-high-speed communication systems, numbers of optical time-division multiplexed channels should be multiplexed in wavelength domain for increasing transmission capacity, where a multi-color pulse source is inevitable. In photonic measurements, two-color pulses are necessary for the measurement based on pump-probe or four-wave mixing methods, which are useful for characterizing ultrafast phenomena in optical devices or components. Here, we demonstrate two-color pulse generation modifying the former pulse source. The problem in the above-mentioned MZM+SMF method is that the pulse generation is highly wavelength dependent. To cope with this problem, a dispersion-flattened dispersion compensating fiber (DF-DCF) is applied for pulse synthesis. The pulse source exhibits wavelength tunability covering the full range of telecom C band. Two color pulses can be simultaneously generated by injecting two CW sources into the MZM based pulse generator. The optical spectrum obtained from the pulse generator is shown in Fig. 8(a). It is found that two bundles of optical comb were simultaneously generated at around 1550 nm 1560 nm. Fig. 8(b) shows the autocorrelation traces measured when the BPF was tuned at the wavelengths, respectively. From the autocorrelation traces both pulses at 1550 nm and 1560 nm had the pulse width of 4.0 ps and 4.1 ps assuming a Sech<sup>2</sup> waveform. Intensity waveform of the generated two-color pulse trains were also characterized with an all-optical sampling oscilloscope. It is found that pulse trains at two different wavelengths were simultaneously generated with a temporal delay of 7 ps. This kind of operation is hardly achieved by conventional mode-locked laser.

In addition to the pulse sources, MZM-FCG offers several attractive applications. For example, MZM-FCG is useful for optical arbitrary waveform generation. Arbitrary waveform can be synthesized by controlling optical amplitude and phase of the generated comb line by line [11][12], which is a key technology for code generation in optical code-division multiplexing systems [12]. Another possibility of the MZM-FCG is application to optical coherence tomography (OCT) [13]. The comb source will be advantageous in constructing fast-scanned OCT.

In conclusion, we have proposed ultra-flat optical frequency comb generation using a conventional dual-drive modulator. We analytically derived the optimal condition required for the comb generation with excellent spectral flatness, which yields a simple formula. The numerical calculations proved that the spectrum of the generated comb is highly flattened under the driving condition. It was also shown that the formula describes the conversion efficiency and bandwidth of the generated comb well.

## 6. References

- Arahira, S., Oshiba, S., Matsui, Y., Kanii, T. & Ogawa, Y. (1994). Terahertz-rate optical pulse generation from a passively mode-locked semiconductor laser diode, *Opt. Lett.* 19(11): 834–836.
- Jemison, W. (2001). *Microwave Photonics' 01*, pp. 169–172.
- Kondo, J., Aoki, K., Kondo, A., Ejiri, T., Iwata, Y., Hamajima, A., Mori, T., Mizuno, Y., Imaeda, M., Kozuka, Y., o. Mitomi & Minakata, M. (2005). High-Speed and Low-Driving-Voltage Thin-Sheet X-cut LiNbO<sub>3</sub> Modulator with Laminated Low-Dielectric-Constant Adhesive, *IEEE Photon. Technol. Lett.* 17(10): 2077–2079.

- Kouroggi, M., Enami, T. & Ohtsu, M. (1994). A Monolithic Optical Frequency Comb Generator, *IEEE Photon. Technol.* 6(22): 214–217.
- Margalit, M., Yu, C. & Haus, E. I. H. (1998). Harmonic Mode-Locking Using Regenerative Phase Modulation, *IEEE Photon. Technol. Lett.* 10(3): 337–339.
- Morohashi, I., Sakamoto, T., Sotobayshi, H., Hosako, I., Kawanishi, T. & Tsuchiya, M. (2008). Widely repetition-tunable 200fs pulse source using Mach-Zehnder-modulator-based comb generator and dispersion-flattened dispersion-decreasing fiber, *Opt. Lett.* 33(11): 1192–1194.
- Morohashi, I., Sakamoto, T., Sotobayshi, H., Hosako, I., Kawanishi, T. & Tsuchiya, M. (2009). Broadband wavelength-tunable ultrashort pulse source using a mach-zehnder modulator and dispersion-flattened dispersion-decreasing fiber, *Opt. Lett.* 34(15): 2297–2299.
- Sakamoto, T., Kawanishi, T. & Izutsu, M. (2005). Optoelectronic oscillator using push-pull mach-zehnder modulator biased at null point for optical two-tone signal generation, *Conference on Laser and Electro Optics (CLEO/IQEC2005)*, p. CTuN5.
- Sakamoto, T., Kawanishi, T. & Izutsu, M. (2006a). 50-nm wavelength-tunable self-oscillating electro-optic frequency comb generator, *the 2006 Optical Fiber Communication Conference (OFC2006) in Anaheim, California*.
- Sakamoto, T., Kawanishi, T. & Izutsu, M. (2006b). Optoelectronic oscillator using a  $\text{LiNbO}_3$  phase modulator for self-oscillating frequency comb generation, *Opt. Lett.* 31(6): 811–813.
- Sakamoto, T., Kawanishi, T. & Izutsu, M. (2007a). Asymptotic formalism for ultraflat optical frequency comb generation using a Mach-Zehnder modulator, *Opt. Lett.* 32(11): 1515–1517.
- Sakamoto, T., Kawanishi, T. & Izutsu, M. (2007b). Optoelectronic oscillating millimetre-wave generator employing reciprocating optical modulator, *Electron. Lett.* 43(19): 19.
- Sakamoto, T., Kawanishi, T. & Izutsu, M. (2008). Widely Wavelength-Tunable Ultra-Flat Frequency Comb Generation Using Conventional Dual-Drive Mach-Zehnder Modulator, *Electron. Lett.* 43(19): 1039–1040.
- Sakamoto, T., Kawanishi, T., Shinada, S. & Izutsu, M. (2005). Optoelectronic oscillator using  $\text{LiNbO}_3$  intensity modulator with resonant electrode, *Electron. Lett.* 41(12): 716–718.
- Sakamoto, T., Morohashi, I. & Kawanishi, T. (2011). Four different principle operation modes for ultra-flat optical comb generation using electro-optic mach-zehnder modulator, *Opt. Lett.* . submitted.
- Sugiyama, M., Doi, M., Taniguchi, S., Nakazawa, T. & Onaka, H. (2002). Driver-less 40 Gb/s  $\text{LiNbO}_3$  modulator with sub-1 V drive voltage, *Optical Fiber Communication Conference (OFC' 02)*, pp. 854–856.
- Tsuzuki, K., Kikuchi, H., Yamada, E., Yasaka, H. & Ishibashi, T. (n.d.). 1.3-V<sub>pp</sub> Push-pull Drive InP Mach-Zehnder Modulator Module for 40 Gbit/s Operation. *31th European Conference on Optical Communication (ECOC 2005)*, Th.2.6.3 , Glasgow, Scotland, Sep, 2005.
- Yao, X. & Maleki, L. (1994). High frequency optical subcarrier generator, *Electron. Lett.* 30: 1525–1526.
- Yokoyama, H., Hashimoto, Y., Kurita, H. & Ogura, I. (2000). Two-stage all-optical subharmonic clock recovery using modelocked semiconductor lasers, *Electron. Lett.* 36(18): 1577–1578.
- Yoshida, E. & Nakazawa, M. (1998). Wavelength tunable 1.0 ps pulse generation in 1.530-1.555  $\mu\text{m}$  region from PLL, regeneratively modelocked fibre laser, *Electron. Lett.* 34(18): 1753–1754.

# An Analytical Solution for Inhomogeneous Strain Fields Within Wurtzite GaN Cylinders Under Compression Test

X. X. Wei

*State Key Laboratory of Explosion Science and Technology,  
Beijing Institute of Technology,  
China*

## 1. Introduction

Compression test on solid circular cylinders of finite length is a popular method in obtaining the compressive strength, the elastic moduli and the electronic properties of semiconductors ( Goroff & Kleinman, 1963; Pollak & Cardona, 1968). It was found that, by generating a strain field, the external stress may significant change the electronic energy structures and the optoelectronic behavior of semiconductors (Suzuki & Hensel, 1974; Mathieu et al, 1979; Bir & Pickus, 1974; Singh, 1992; Pollak, 1990). Several methods have been used to investigate the effect of stress and strain on band structures (Jiang & Singh, 1997; Hasegawa, 1963). For example, the multiband effective-mass theory was employed to study the electronic and optical-absorption properties of uniaxially stressed quantum wells, the envelope-function approximation was used to describe the electronic structure of superlattices and quantum wells under arbitrary uniaxial stress, the effect of uniaxial and hydrostatic strain on the optical constants and the electronic structure of Copper was investigated, the strain dependence of effective masses in tetrahedral semiconductor under uniaxial stress was also studied. In all of these studies, the homogeneous strain distributions induced by an external uniform stress were considered. Pollak (1990) made good review on the effect of homogeneous strain on band structures and electronic properties of semiconductors.

However, friction effect on the end surfaces is ignored in all of these studies. It has long been recognized that friction inevitably exists between two end surfaces of cylinders and the loading platens under compression test. The strain and stress distributions within cylinder are very sensitive to the external load acting on the surface of cylinders (Wei et al, 1999). Although numerous efforts have been made to reduce the friction between the semiconductor cylinder and the loading platens, end friction inevitably exists. Techniques developed to reduce end friction include the insertion of Telfon sheet, lubrication, iron brush contact, and the use of a loading platen of the same Poisson's ratio as the cylinder. Nevertheless, the stress distributions within cylinders under compression are normally non-uniform, and inhomogeneous strain fields are thus induced within semiconductor cylinders. Although the analytical solution for finite cylinders under arbitrary external load was obtained (Chau & Wei, 1999), the solution is for isotropic materials with force boundary condition only. Experimental results show that wurtzite GaN is a kind of transversely

isotropic crystal. There is no analysis for the inhomogeneous strain distributions within wurtzite GaN cylinders due to end friction under compression tests.

Therefore, in the present work, the inhomogeneous strain distribution within a finite and transversely isotropic cylinder of wurtzite GaN subject to compression with non-zero end friction is studied. The friction between the end surfaces and two loading platens will be modeled as non-slip as well as partially slip. Unlike the force boundary condition for finite cylinders (Wei & Chau, 1999; Chau & Wei, 1999), displacement boundary condition will have to be involved in the present problem. The Lekhnitskii's stress function is employed in order to uncouple the equations of equilibrium for transversely isotropic solids. The Fourier and Fourier-Bessel expansion technique will be used in order to satisfy all of the boundary conditions exactly. In addition, Based on the theory of Luttinger-Kohn and Bir-Pikus (Bir & Pikus, 1974), the valence-band structure of the strained wurtzite GaN is described by a Hamiltonian in the envelope-function space, and the spin-orbit interaction is also considered, numerical discussion will focus on the effects of strain and end friction on the band structure of wurtzite GaN.

## 2. Governing equations for wurtzite GaN solid

Experimental results show that wurtzite GaN is a kind of transversely isotropic solids (Wright, 1997). Let's consider a homogeneous wurtzite GaN cylinder of radius  $R$  and half-length  $h$  with the two end surfaces parallel to a plane of isotropy.

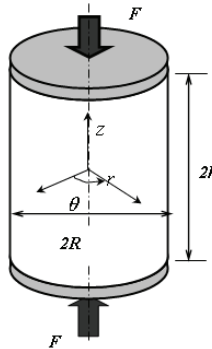


Fig. 1. A sketch of a finite cylinder under compression test

For the cylindrical coordinate system  $(r, \theta, z)$  shown in Fig.1, the generalized Hooke's law for transversely isotropic solids can be written as (Wei, 2008)

$$\begin{aligned} \varepsilon_{rr} &= a_{11}\sigma_{rr} + a_{12}\sigma_{\theta\theta} + a_{13}\sigma_{zz}, & \varepsilon_{\theta\theta} &= a_{12}\sigma_{rr} + a_{11}\sigma_{\theta\theta} + a_{13}\sigma_{zz} \\ \varepsilon_{zz} &= a_{13}\sigma_{rr} + a_{13}\sigma_{\theta\theta} + a_{33}\sigma_{zz}, & \gamma_{\theta z} &= a_{44}\sigma_{\theta z}, \gamma_{rz} = a_{44}\sigma_{rz}, \gamma_{r\theta} = a_{66}\sigma_{r\theta} \end{aligned} \quad (1)$$

where

$$\begin{aligned} a_{11} &= \frac{1}{E_T}, & a_{12} &= -\frac{\nu_T}{E_T}, & a_{13} &= -\frac{\nu_L}{E_L}, & a_{33} &= \frac{1}{E_L}, \\ a_{44} &= \frac{1}{G_L}, & a_{66} &= 2(a_{11} - a_{12}) = \frac{2(1 + \nu_T)}{E_T} = \frac{1}{G_T} \end{aligned} \quad (2)$$

The stress tensor is denoted by  $\sigma$ , and the normal and shear strains by  $\varepsilon$  and  $\gamma$  respectively. Physically,  $E_T$  and  $E_L$  are the Young's moduli governing axial deformations in the planes of isotropy (i.e. any plane parallel to two end surfaces) and along direction perpendicular to it (i.e. parallel to the z-axis) respectively. The Poisson's ratios  $\nu_T$  and  $\nu_L$  characterize transverse reductions in the plane of isotropy under tension in the same plane and under tension along the z-axis respectively. The shear moduli for the plane of isotropy and for planes parallel to the z-axis are denoted by  $G_T$  and  $G_L$ , respectively. For present axisymmetric problem, strains and displacements are related by

$$\varepsilon_{rr} = \frac{\partial u}{\partial r}, \varepsilon_{\theta\theta} = \frac{u}{r}, \varepsilon_{zz} = \frac{\partial w}{\partial z}, \varepsilon_{rz} = \frac{1}{2} \left( \frac{\partial u}{\partial z} + \frac{\partial w}{\partial r} \right) \quad (3)$$

where  $u$  and  $w$  are the displacements in the  $r$ - and  $z$ -directions, respectively. In the absence of body force, the equations of equilibrium are

$$\frac{\partial \sigma_{rr}}{\partial r} + \frac{\partial \sigma_{rz}}{\partial z} + \frac{\sigma_{rr} - \sigma_{\theta\theta}}{r} = 0 \quad (4)$$

$$\frac{\partial \sigma_{zz}}{\partial z} + \frac{\partial \sigma_{rz}}{\partial r} + \frac{\sigma_{rz}}{r} = 0 \quad (5)$$

### 3. Uniform strain in cylinders under compression without end friction

When a solid cylinder of wurtzite GaN is confined by a uniform pressure  $p_0$  on the curved surface and is compressed between two rigid smooth loading platens on the end surfaces without end friction. The stresses within the solid cylinder are uniform and can be expressed as

$$\sigma_{zz} = q_0, \quad \sigma_{rr} = \sigma_{\theta\theta} = p_0, \quad \sigma_{rz} = \sigma_{r\theta} = \sigma_{\theta z} = 0 \quad (6)$$

where  $q_0 = F / \pi R^2$  with  $F$  being the total load acting on the end surfaces as shown in Fig. 1. By adopting the usual sign convention of continuum mechanics, tension is positive, and compression is negative.

The strains within the cylinder can be obtained by substituting (6) into (1) as:

$$\varepsilon_{zz} = \left( -\frac{2\nu_L p_0}{q_0} + 1 \right) \frac{q_0}{E_L}, \quad \varepsilon_{rr} = \varepsilon_{\theta\theta} = \left[ (1 - \nu_T) \frac{E_L p_0}{E_T q_0} - \nu_L \right] \frac{q_0}{E_L}, \quad \gamma_{rz} = \gamma_{r\theta} = \gamma_{z\theta} = 0 \quad (7)$$

It is obvious that inhomogeneous strain field is induced within cylinder under compression if the end friction is ignored.

### 4. Boundary conditions for compression with end friction

Friction, however, always inevitably exists between the loading platens and the two end surfaces in usual compression tests. The end surfaces are thus somewhat constrained from free expansion of the Poisson effect. The boundary conditions for a solid cylinder under compression test with end friction and a confine pressure  $p_0$  can be written as

$$\sigma_{rr} = p_0, \quad \text{on } r = R \quad (8)$$

$$\sigma_{rz} = 0, \quad \text{on } r = R \quad (9)$$

$$u = \beta u_0 r / R, \quad \text{on } z = \pm h, \quad (10)$$

$$\frac{\partial w}{\partial r} = 0, \quad \text{on } z = \pm h, \quad (11)$$

$$\int_0^R 2\pi r \sigma_{zz} dr = F, \quad \text{on } z = \pm h \quad (12)$$

where  $F$  is the total load acting on the loading platens. Physically, these boundary conditions imply that the cylinder is subjected to an axial compression of magnitude  $F$  with confining stress of  $p_0$  and with no end rotation. Boundary condition (10) implies a uniform radial strain on the two end surfaces, and (11) ensures to loading platens to remain horizontal at all time, The factor  $\beta$  represents the degree of constraint on the radial displacement on the end surfaces. If friction is negligible, the end surface is free to expand and we have  $\beta = 1$ ; if the radial displacement on the end surfaces is completely constrained, no slip occurs between the cylinder and loading platens and we have  $\beta = 0$ ; in usual compression test, we have  $0 \leq \beta \leq 1$ , depending on the contact condition of the loading platens.

## 5. Stress function for transversely isotropic solids

As suggested by Lekhnitskii (1963), a single stress function  $\phi$  can be introduced for transversely isotropic solids as

$$\sigma_{rr} = -\frac{\partial}{\partial z} \left( \frac{\partial^2 \phi}{\partial r^2} + \frac{b}{r} \frac{\partial \phi}{\partial r} + e \frac{\partial^2 \phi}{\partial z^2} \right) \quad (13)$$

$$\sigma_{\theta\theta} = -\frac{\partial}{\partial z} \left( b \frac{\partial^2 \phi}{\partial r^2} + \frac{1}{r} \frac{\partial \phi}{\partial r} + e \frac{\partial^2 \phi}{\partial z^2} \right) \quad (14)$$

$$\sigma_{zz} = \frac{\partial}{\partial z} \left( c \frac{\partial^2 \phi}{\partial r^2} + \frac{c}{r} \frac{\partial \phi}{\partial r} + d \frac{\partial^2 \phi}{\partial z^2} \right) \quad (15)$$

$$\sigma_{rz} = \frac{\partial}{\partial r} \left( \frac{\partial^2 \phi}{\partial r^2} + \frac{1}{r} \frac{\partial \phi}{\partial r} + e \frac{\partial^2 \phi}{\partial z^2} \right) \quad (16)$$

$$u = -(1-b)(a_{11} - a_{12}) \frac{\partial^2 \phi}{\partial r \partial z} \quad (17)$$

$$w = a_{44} \left( \frac{\partial^2 \phi}{\partial r^2} + \frac{1}{r} \frac{\partial \phi}{\partial r} \right) + (a_{33}d - 2a_{13}e) \frac{\partial^2 \phi}{\partial z^2} \quad (18)$$



where

$$\begin{aligned}
 b &= \frac{a_{13}(a_{13} + a_{44}) - a_{12}a_{33}}{a_{11}a_{33} - a_{13}^2}, & c &= \frac{a_{13}(a_{11} - a_{12}) + a_{11}a_{44}}{a_{11}a_{33} - a_{13}^2} \\
 d &= \frac{a_{11}^2 - a_{12}^2}{a_{11}a_{33} - a_{13}^2}, & e &= \frac{a_{13}(a_{11} - a_{12})}{a_{11}a_{33} - a_{13}^2}
 \end{aligned}
 \tag{19}$$

To ensure force equilibrium, the stress function  $\phi$  should satisfy the following partial differential equation

$$\left( \frac{\partial^2}{\partial r^2} + \frac{1}{r} \frac{\partial}{\partial r} \right) \left( \frac{\partial^2 \phi}{\partial r^2} + \frac{1}{r} \frac{\partial \phi}{\partial r} + e \frac{\partial^2 \phi}{\partial z^2} \right) + \frac{\partial^2}{\partial z^2} \left( c \frac{\partial^2 \phi}{\partial r^2} + \frac{c}{r} \frac{\partial \phi}{\partial r} + d \frac{\partial^2 \phi}{\partial z^2} \right) = 0
 \tag{20}$$

### 6. Series expressions for the stress function

We seek for the following series solution forms for (20) as

$$\phi = \sum_{n=1}^{\infty} A'_n I_0(p \zeta_n \rho) \sin(n\pi\eta) \quad \text{and} \quad \phi = \sum_{s=1}^{\infty} C'_s \sinh(q \gamma_s \eta) J_0(\lambda_s \rho)
 \tag{21}$$

where  $\rho = r / R$ ,  $\eta = z / h$ ,  $\lambda_s$  is the  $s$ -th root of  $J_1(\lambda_s) = 0$ ;  $\gamma_s = \lambda_s \kappa$  and  $\zeta_n = n\pi / \kappa$ ;  $\kappa$  is a geometric ratio defined as  $\kappa = h / R$ ;  $p$  and  $q$  are constants to be determined.  $A'_n$  and  $C'_s$  are constants.  $J_0(x)$  and  $J_1(x)$  are the Bessel functions of the first kind of zero and first order respectively, and  $I_0(x)$  is the modified Bessel function of the first kind of zero order. Substitution of (21) into (20) yields

$$q_{1,2} = \left[ \frac{(c + e) \pm \sqrt{(c + e)^2 - 4}}{2} \right]^{1/2}, \quad q_{3,4} = -q_{1,2}, \quad \text{and} \quad p_{1,2} = q_{1,2}, \quad p_{3,4} = -p_{1,2}
 \tag{22}$$

By noting the fact that  $I_0(-x) = I_0(x)$  and  $\sinh(-x) = -\sinh(x)$ , it is clear from (21) that the solutions corresponding to  $p_{3,4}$  and  $q_{3,4}$  can be combined with those for  $p_{1,2}$  and  $q_{1,2}$ . It has been found that  $q_{1,2}$  are complex for wurtzite GaN solid. That is,  $q_{1,2}$  can be expressed in form of  $q_{1,2} = q_R \pm q_I i$ , so we can rewrite the expression for stress function  $\phi$  as

$$\begin{aligned}
 \phi &= -R^3 q_0 \left\{ A_0 \frac{\kappa^3 \eta^3}{6} + C_0 \frac{\kappa \eta \rho^2}{2} + \sum_{n=1}^{\infty} \frac{\sin(n\pi\eta)}{\zeta_n^3} \{ A_n \operatorname{Re}[I_0(p_1 \zeta_n \rho)] + B_n \operatorname{Im}[I_0(p_1 \zeta_n \rho)] \} \right. \\
 &\quad \left. + \sum_{s=1}^{\infty} \frac{J_0(\lambda_s \rho)}{\lambda_s^3} [C_s \sinh(q_R \gamma_s \eta) \cos(q_I \gamma_s \eta) + D_s \cosh h(q_R \gamma_s \eta) \sin(q_I \gamma_s \eta)] \right\}
 \end{aligned}
 \tag{23}$$

where  $q_0$  is the mean normal stress on the end surfaces defined as  $q_0 = P / \pi R^2$ , and  $A_0, C_0, A_n, B_n, C_s$ , and  $D_s$  are real unknown constants to be determined. Note that additional terms corresponding to  $A_0$  and  $C_0$  have been added and they will lead to uniform normal stresses and strains for cylinders.

Before we consider the boundary conditions (8-12), stresses and displacements will first be expressed in terms of the unknown constants in the next section.

## 7. Expressions for stress and displacement components

Substitution of (23) into (13-18) yields the following expressions for the stress and displacement as

$$\begin{aligned} \sigma_{rr} / q_0 &= A_0 e + (a+b)C_0 + \sum_{n=1}^{\infty} \cos(n\pi\eta) \{A_n \operatorname{Re}[\Pi_1(p_1, \rho)] + B_n \operatorname{Im}[\Pi_1(p_1, \rho)]\} \\ &+ \sum_{s=1}^{\infty} \{ [C_s \Lambda_1(q_R, q_I, \rho) + D_s \Lambda_2(q_R, q_I, \rho)] \cosh(q_R \gamma_s \eta) \cos(q_I \gamma_s \eta) \\ &+ [-C_s \Lambda_2(q_R, q_I, \rho) + D_s \Lambda_1(q_R, q_I, \rho)] \sinh(q_R \gamma_s \eta) \sin(q_I \gamma_s \eta) \} \end{aligned} \quad (24)$$

$$\begin{aligned} \sigma_{rz} / q_0 &= \sum_{n=1}^{\infty} \sin(n\pi\eta) \{A_n \operatorname{Re}[\Pi_2(p_1, \rho)] + B_n \operatorname{Im}[\Pi_2(p_1, \rho)]\} \\ &+ \sum_{s=1}^{\infty} J_1(\lambda_s \rho) \{ [C_s (e(q_R^2 - q_I^2) - 1) + 2D_s e q_R q_I] \sinh(q_R \gamma_s \eta) \cos(q_I \gamma_s \eta) \\ &+ [-2C_s e q_R q_I + D_s (e(q_R^2 - q_I^2) - 1)] \cosh(q_R \gamma_s \eta) \sin(q_I \gamma_s \eta) \} \end{aligned} \quad (25)$$

$$\begin{aligned} \frac{u}{q_0 R} &= (1-b)(a_{11} - a_{12}) \{C_0 \rho + \sum_{n=1}^{\infty} \frac{\cos(n\pi\eta)}{\zeta_n} \{A_n \operatorname{Re}[p_1 I_1(p_1 \zeta_n \rho)] + B_n \operatorname{Im}[p_1 I_1(p_1 \zeta_n \rho)]\} \\ &- \sum_{s=1}^{\infty} \frac{J_1(\lambda_s \rho)}{\lambda_s} \{ [C_s q_R + D_s q_I] \cosh(q_R \gamma_s \eta) \cos(q_I \gamma_s \eta) + (-C_s q_I + D_s q_R) \sinh(q_R \gamma_s \eta) \sin(q_I \gamma_s \eta) \} \} \end{aligned} \quad (26)$$

$$\begin{aligned} \frac{w}{q_0 R} &= -[2a_{44}C_0 + A_0(a_{33} - 2a_{13}e)]\kappa\eta + \sum_{n=1}^{\infty} \frac{\sin(n\pi\eta)}{\zeta_n} \{A_n \operatorname{Re}[\Pi_3(p_1, \rho)] + B_n \operatorname{Im}[\Pi_3(p_1, \rho)]\} \\ &+ \sum_{s=1}^{\infty} \frac{J_0(\lambda_s \rho)}{\lambda_s} \{ [C_s (a_{44} - (a_{33} - 2a_{13}e)(q_R^2 - q_I^2)) - 2D_s q_R q_I (a_{33} - 2a_{13}e)] \sinh(q_R \gamma_s \eta) \cos(q_I \gamma_s \eta) \\ &+ [2C_s q_R q_I (a_{33} - 2a_{13}e) + D_s (a_{44} - (a_{33} - 2a_{13}e)(q_R^2 - q_I^2))] \cosh(q_R \gamma_s \eta) \sin(q_I \gamma_s \eta) \} \end{aligned} \quad (27)$$

where

$$\Pi_1(x, \rho) = (ax^2 - e)I_0(x\zeta_n \rho) + (b-a)x \frac{I_1(x\zeta_n \rho)}{\zeta_n \rho} \quad (28)$$

$$\Pi_2(x, \rho) = (ex - x^3)I_1(x\zeta_n \rho) \quad (29)$$

$$\Pi_3(x, \rho) = [-a_{44}x^2 + (a_{33} - 2a_{13}e)]I_0(x\zeta_n \rho) \quad (30)$$

$$\Gamma(\rho) = -aJ_0(\lambda_s \rho) + (a-b) \frac{J_1(\lambda_s \rho)}{\lambda_s \rho} \quad (31)$$

$$\Lambda_1(x, y, \rho) = x\Gamma(\rho) + e(x^3 - 3xy^2)J_0(\lambda_s\rho) \tag{32}$$

$$\Lambda_2(x, y, \rho) = y\Gamma(\rho) - e(y^3 - 3x^2y)J_0(\lambda_s\rho) \tag{33}$$

with  $a=1$ . The expression for  $\sigma_{\theta\theta}$  can be obtained from (24) by replacing “ $a$ ” and “ $b$ ” by “ $b$ ” and “ $1$ ” respectively. While the expressions for  $\sigma_{zz}$  can be obtained from (24) by replacing both “ $a$ ” and “ $b$ ” by “ $-c$ ”, and “ $e$ ” by “ $-d$ ” respectively. The next step is to use the boundary conditions (8-12) to determine the unknown coefficients.

### 8. Determination of unknown coefficients

The boundary condition  $\sigma_{rz} = 0$  on the curved surface  $\rho = 1$  (or  $r = R$ ) leads to

$$A_n = E_n \operatorname{Im}[\Pi_2(p_1, 1)], \quad B_n = -E_n \operatorname{Re}[\Pi_2(p_1, 1)] \tag{34}$$

where  $E_n$  is a constant introduced to simplify the later presentation and it will be fixed later such that the subsequent formulas can be expressed in a more efficient manner.

The boundary condition  $\partial w / \partial r = 0$  on the two end surfaces  $\eta = \pm 1$  (i. e.  $z = \pm h$ ) leads to

$$C_s = F_s \psi_1(q_R, q_I) \quad , \quad D_s = -F_s \psi_2(q_R, q_I) \tag{35}$$

where  $F_s$  is another constant introduced to simplify the subsequent presentation , and

$$\begin{aligned} \psi_1(q_R, q_I) = & -2q_R q_I (a_{33} - 2a_{13}e) \sinh q_R \gamma_s \cos q_I \gamma_s \\ & + [a_{44} - (a_{33} - 2a_{13}e)(q_R^2 - q_I^2)] \cosh q_R \gamma_s \sin q_I \gamma_s \end{aligned} \tag{36}$$

$$\begin{aligned} \psi_2(q_R, q_I) = & 2q_R q_I (a_{33} - 2a_{13}e) \cosh q_R \gamma_s \sin q_I \gamma_s \\ & + [a_{44} - (a_{33} - 2a_{13}e)(q_R^2 - q_I^2)] \sinh q_R \gamma_s \cos q_I \gamma_s \end{aligned} \tag{37}$$

The radial stress  $\sigma_{rr}$  on the curved surface  $\rho = 1$  (i. e.  $r = R$ ) can be obtained by setting  $\rho = 1$  in (24) as

$$\begin{aligned} \sigma_{rr} / q_0 = & A_0 e + (a + b)C_0 + \sum_{n=1}^{\infty} \cos(n\pi\eta) \{A_n \operatorname{Re}[\Pi_1(p_1, 1)] + B_n \operatorname{Im}[\Pi_1(p_1, 1)]\} \\ & + \sum_{s=1}^{\infty} \{ [C_s \Lambda_1(q_R, q_I, 1) + D_s \Lambda_2(q_R, q_I, 1)] \cosh(q_R \gamma_s \eta) \cos(q_I \gamma_s \eta) \\ & + [-C_s \Lambda_2(q_R, q_I, 1) + D_s \Lambda_1(q_R, q_I, 1)] \sinh(q_R \gamma_s \eta) \sin(q_I \gamma_s \eta) \} \end{aligned} \tag{38}$$

By applying a Fourier expansion for the hyperbolic cosine in (38) and then expressing the result in terms of the constants  $E_n$  and  $F_s$ , we have

$$\sigma_{rr} / q_0 = A_0 e + (b + 1)C_0 + \sum_{s=1}^{\infty} F_s Q_{s0} / 2 + \sum_{n=1}^{\infty} [E_n \Delta_n + \sum_{s=1}^{\infty} F_s Q_{sn}] \cos(n\pi\eta) \tag{39}$$

where

$$\Delta_n = \text{Im}[\Pi_2(p_1, 1)]\text{Re}[\Pi_1(p_1, 1)] - \text{Re}[\Pi_2(p_1, 1)]\text{Im}[\Pi_1(p_1, 1)] \quad (40)$$

$$Q_{sn} = J_0(\lambda_s)\{[T_1 \sinh q_R \gamma_s \cos q_I \gamma_s + T_2 \cosh q_R \gamma_s \sin q_I \gamma_s]L_{sn} + [T_3 \sinh q_R \gamma_s \cos q_I \gamma_s + T_1 \cosh q_R \gamma_s \sin q_I \gamma_s]G_{sn}\} \quad (41)$$

$$G_{sn} = 2(-1)^n \times \frac{[\gamma_s^2 q_R^2 + q_I^2 \gamma_s^2 + n^2 \pi^2]q_R \gamma_s \cosh q_R \gamma_s \sin q_I \gamma_s - [\gamma_s^2 q_R^2 + q_I^2 \gamma_s^2 - n^2 \pi^2]q_I \gamma_s \sinh q_R \gamma_s \cos q_I \gamma_s}{[\gamma_s^2 q_R^2 + (q_I \gamma_s - n\pi)^2][\gamma_s^2 q_R^2 + (q_I \gamma_s + n\pi)^2]} \quad (42)$$

$$T_1 = q_I \{[a_{44} - (a_{33}d - 2a_{13}e)(q_R^2 - q_I^2)][e(q_I^2 - 3q_R^2) + 1] - 2(a_{33}d - 2a_{13}e)q_R^2[e(q_R^2 - 3q_I^2) - 1]\} \quad (43)$$

$$T_2 = q_R \{[a_{44} - (a_{33}d - 2a_{13}e)(q_R^2 - q_I^2)][e(q_R^2 - 3q_I^2) - 1] + 2(a_{33}d - 2a_{13}e)q_I^2[e(q_I^2 - 3q_R^2) + 1]\} \quad (44)$$

$$T_3 = -q_R \{[a_{44} - (a_{33}d - 2a_{13}e)(q_R^2 - q_I^2)][e(q_R^2 - 3q_I^2) - 1] + 2(a_{33}d - 2a_{13}e)q_I^2[e(q_I^2 - 3q_R^2) + 1]\} \quad (45)$$

The boundary condition  $\sigma_{rr} = 0$  on  $\rho = 1$  can now be applied and the following relations between  $A_0$  and  $C_0$  and between  $E_n$  and  $F_s$  are obtained as

$$A_0 e + (b+1)C_0 + \sum F_s Q_{s0} / 2 = 0 \quad (46)$$

$$E_n \Delta_n + \sum_{s=1}^{\infty} F_s Q_{sn} = 0 \quad (47)$$

Substitution of (34) and (35) into (26) and set  $\eta = \pm 1$  yield the following expression for the radial displacement on the two end surfaces (i.e.  $z = \pm h$ )

$$\frac{u}{q_0 R} = (1-b)(a_{11} - a_{12})\{C_0 \rho + \sum_{n=1}^{\infty} \frac{(-1)^n E_n}{\zeta_n} [\text{Im}[\Pi_2(p_1, 1)]\text{Re}[p_1 I_1(p_1 \zeta_n \rho)] - \text{Re}[\Pi_2(p_1, 1)]\text{Im}[p_1 I_1(p_1 \zeta_n \rho)]\} + \sum_{s=1}^{\infty} \frac{J_1(\lambda_s \rho) F_s}{\lambda_s} \Omega_s \} \quad (48)$$

where

$$\Omega_s = -\{[\psi_1(q_R, q_I)q_R - \psi_2(q_R, q_I)q_I] \cosh q_R \gamma_s \cos q_I \gamma_s - [\psi_1(q_R, q_I)q_I + \psi_2(q_R, q_I)q_R] \sinh q_R \gamma_s \sin q_I \gamma_s\} \quad (49)$$

To apply the end boundary condition (11), we first expand (48) into a Fourier-Bessel series as

$$\frac{u}{q_0 R} = (1-b)(a_{11} - a_{12}) \sum_{s=1}^{\infty} \frac{J_1(\lambda_s \rho)}{\lambda_s} \left[ -\frac{2C_0}{J_0(\lambda_s)} + F_s \Omega_s + \sum_{n=1}^{\infty} E_n R_{sn} \right] \quad (50)$$

where

$$R_{sn} = \frac{(-1)^n}{\zeta_n} \{ \text{Im}[\Pi_2(p_1, 1)] \text{Re}[H_{sn}(p_1)] - \text{Re}[\Pi_2(p_1, 1)] \text{Im}[H_{sn}(p_1)] \} \quad (51)$$

$$H_{sn}(x) = \frac{-2x\lambda_s^2 I_1(x\zeta_n)}{[\lambda_s^2 + \zeta_n^2 x^2] J_0(\lambda_s)} \quad (52)$$

To match the boundary condition (11) with the radial displacement given in (50), (11) is also expanded into a Fourier-Bessel series as

$$u(\rho) = \beta u_0 \sum_{s=1}^{\infty} a_s J_1(\lambda_s \rho) \quad \text{for } (0 \leq \rho \leq 1) \quad (53)$$

where

$$a_s = \frac{-2}{\lambda_s J_0(\lambda_s)} \quad (54)$$

Finally, by comparing the coefficients of (50) and (53), we have

$$-\frac{2C_0}{J_0(\lambda_s)} + F_s \Omega_s + \sum_{n=1}^{\infty} E_n R_{sn} = \frac{-\nu u_0}{(1-b)(a_{11} - a_{12})} \frac{\beta \lambda_s a_s}{E} \quad (55)$$

As remarked earlier, the expressions for  $\sigma_{zz}$  can be obtained by replacing both "a" and "b" by "-c", and "e" by "-d" in (24) as

$$\begin{aligned} \sigma_{zz} / q_0 = & -A_0 - 2cC_0 + \sum_{n=1}^{\infty} \cos(n\pi\eta) \{ A_n \text{Re}[\Pi_1(p_1, \rho)] + B_n \text{Im}[\Pi_1(p_1, \rho)] \} \\ & + \sum_{s=1}^{\infty} \{ [C_s \Lambda_1(q_R, q_I, \rho) + D_s \Lambda_2(q_R, q_I, \rho)] \cosh(q_R \gamma_s \eta) \cos(q_I \gamma_s \eta) \\ & + [-C_s \Lambda_2(q_R, q_I, \rho) + D_s \Lambda_1(q_R, q_I, \rho)] \sinh(q_R \gamma_s \eta) \sin(q_I \gamma_s \eta) \} \end{aligned} \quad (56)$$

Substitution of (56) into (12) with  $\eta = \pm 1$  leads to

$$-2cC_0 - dA_0 + \sum_{n=1}^{\infty} E_n \mathfrak{R}_n = 1 \quad (57)$$

where

$$\mathfrak{R}_n = \frac{2(-1)^n}{\zeta_n} \left[ (1 - cp_1^2)(ep_2 - p_2^3) I_1(p_2 \zeta_n) \frac{I_1(p_1 \zeta_n)}{p_1} - (1 - cp_2^2)(ep_1 - p_1^3) I_1(p_1 \zeta_n) \frac{I_1(p_2 \zeta_n)}{p_2} \right] \quad (58)$$

In summary, for the unknown coefficients  $A_0, C_0, E_n$  and  $F_s$ , the coupled system of equations, (46), (47), (55) and (57), has to be solved simultaneously. In our numerical implementation, we can truncate the infinite series in these equations and retain only the first  $n$  and  $s$  terms. Then, there will be  $(s+n+2)$  equations for the  $(s+n+2)$  unknown

coefficients of  $A_0, C_0, E_n$  and  $F_s$ . Finally,  $A_n, B_n, C_s$  and  $D_s$  can be obtained by substitution of  $F_s$  and  $E_n$  into (34) and (35). Once these coefficients are determined, the stress and displacement fields inside the cylinder can be evaluated according to (24-27), and by substituting (24-25) into (1), the strain distribution can be exactly obtained.

## 9. Numerical results and discussions

The exact analytical solution for the inhomogeneous stress and strain distribution within a finite and transversely isotropic cylinder of wurtzite GaN under compression test with end friction given in the previous section involves the calculation of systems of coupled equations for the coefficients of the infinite series. We choose wurtzite GaN as an example to get the numerical results, and five independent elastic constants were  $C_{11} = 293GPa$ ,  $C_{12} = 159GPa$ ,  $C_{13} = 106GPa$ ,  $C_{33} = 398GPa$ ,  $C_{44} = 105GPa$  (wright, 1997). Another group of independent constants can be easily obtained as  $E_T = 322Gpa$ ,  $E_L = 357Gpa$ ,  $\nu_T = 0.32$ ,  $\nu_L = 0.21$ ,  $G_L = 52.5Gpa$ . In actual computation, the infinite series have to be truncated and only finite number of terms can be retained. It was found that 50 terms in both the summations of  $n$  and  $s$  are sufficient to yield a steady solution for the solutions for displacements expressed in (26-27), while about 80 terms are need to get a converge values for the series solutions for stresses and strain given in (24-25) and (1). This is not totally unexpected since our end boundary is displacement-controlled, and the computed stresses are proportional to the derivative of the displacement. In general, more terms in  $n$  than in  $s$  are needed if  $\kappa > 1$ , while more terms in  $s$  than in  $n$  are needed to get the same error control if  $\kappa < 1$ . We found that 100 terms in both  $s$  and  $n$  are enough to get a specific error control less than 0.1%. Moreover, the inhomogeneous strain and stress distributions within the finite circular cylinder for one quarter of the meridian plane are investigated, and the rest being symmetrical.

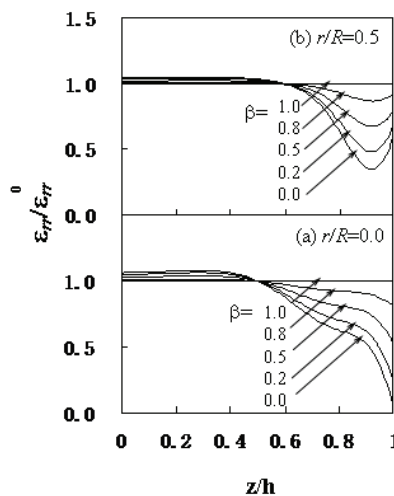


Fig. 2. The normalized strain  $\varepsilon_{rr} / \varepsilon_{rr}^0$  versus the normalized distance  $z/h$  along the axis of loading for (a)  $r/R=0.0$  and (b)  $r/R = 0.5$

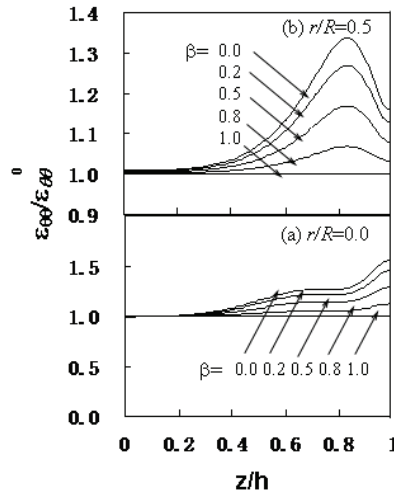


Fig. 3. The normalized strain  $\epsilon_{\theta\theta} / \epsilon_{\theta\theta}^0$  versus the normalized distance  $z/h$  along the axis of loading for (a)  $r/R=0.0$  and (b)  $r/R=0.5$

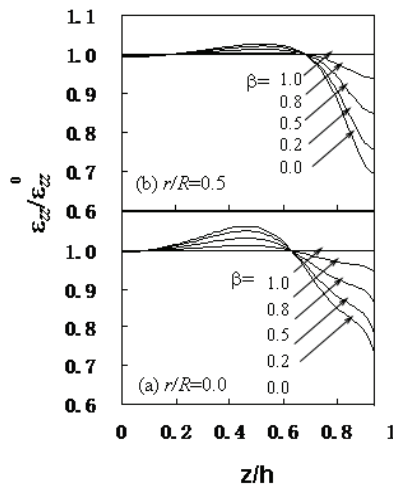


Fig. 4. The normalized strain  $\epsilon_{zz} / \epsilon_{zz}^0$  versus the normalized distance  $z/h$  along the axis of loading for (a)  $r/R=0.0$  and (b)  $r/R=0.5$

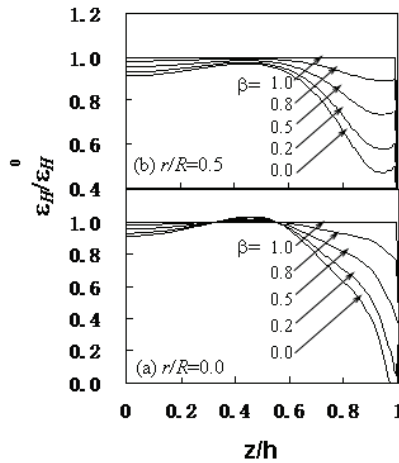


Fig. 5. The normalized strain  $\varepsilon_H / \varepsilon_H^0$  versus the normalized distance  $z/h$  along the axis of loading for (a)  $r/R=0.0$  and (b)  $r/R=0.5$

### 9.1 The strain distributions within cylinder along the loading direction

Strain distributions along the loading direction in a quarter of the meridian plane are studied in this section. In particular, Fig. 2 shows the normalized strain  $\varepsilon_{rr} / \varepsilon_{rr}^0$  versus the normalized vertical distance  $z/h$  from the center of the cylinder for various values of  $\alpha$  for  $r/R=0.0$  and  $r/R=0.5$ . The results are obtained for  $h/R=2.0$ , which are the standard shape for compression tests.  $\varepsilon_{rr}^0$  is the radial strain of the cylinder under compression without end friction and can be calculated according to (7). As mentioned earlier, the factor  $\alpha$  represents the degree of friction on the end surfaces. More specially,  $\beta=1$  is for the case without end friction, while  $\beta=0$  is for the largest end friction and no slip occurs between the cylinder and the loading platens. In usual compression test, partial slip may occur and we have  $0 \leq \beta \leq 1$ , depending on the contact condition of the loading platens. Fig. 2 indicate that the strain distribution within the cylinder along the loading direction is not uniform for  $0 \leq \beta < 1$ , a strain concentrations are usually induced in the region of  $0.5 < z/h < 1.0$ , and the maximum values can be as more than 99% and 65% for  $r/R=0.0$  and  $r/R=0.5$  respectively, comparing to that without end friction, which is the line for  $\alpha=1$  in Fig. 2. However, the strain distributions in the central region, say  $0 < z/h < 0.5$  are relatively uniform, and only 2% extra strain value of  $\varepsilon_{rr} / \varepsilon_{rr}^0$  can be induced by end friction. Fig. 3 shows the normalized circumferential strain  $\varepsilon_{\theta\theta} / \varepsilon_{\theta\theta}^0$  versus the normalized vertical distance  $z/h$  for various values of  $\beta$  for  $r/R=0.0$  and  $r/R=0.5$ , and  $\varepsilon_{\theta\theta}^0$  is the circumferential strain of the cylinder under compression without end friction and can be calculated according to (7). The other parameters used in Fig. 3 and the following Figs. 4-12 are the same as those in Fig. 2 unless specially mentioned. Fig.3 shows that strain concentrations are also induced in the region of  $0.5 < z/h < 1.0$ , and the maximum values can be as more than 57% and 34% for  $r/R=0.0$  and  $r/R=0.5$  respectively, comparing



to constant strain without end friction and  $\alpha = 1$ . Fig. 4 shows the normalized axial strain  $\varepsilon_{zz} / \varepsilon_{zz}^0$  versus the normalized vertical distance  $z/h$  for various values of  $\alpha$  for  $r/R=0.0$  and  $r/R=0.5$ , and  $\varepsilon_{zz}^0$  is the axial strain of the cylinder under compression without end friction and can be calculated according to (7). Fig.4 shows that the axial strain is also inhomogeneous, and the maximum values can be more than 40% and 30% for  $r/R=0.0$  and  $r/R=0.5$  respectively, comparing to that without end friction. Fig. 5 shows the normalized strain  $\varepsilon_H / \varepsilon_H^0$  versus the normalized vertical distance  $z/h$  for various values of  $\alpha$  for  $r/R=0.0$  and  $r/R=0.5$ , and  $\varepsilon_H^0$  is the strain of the cylinder under compression without end friction and can be calculated according to (58). Fig.5 shows that the normalized strain  $\varepsilon_H / \varepsilon_H^0$  is quite inhomogeneous, and the maximum values can be 100% and 53% more than those without end friction for  $r/R=0.0$  and  $r/R=0.5$  respectively. Overall, the inhomogeneous strain distributions are induced in the cylinder as long as friction exists between the end surface and the loading platens, and the larger the friction on the end surfaces, that is, the smaller the value of  $\beta$ , the more non-uniform inhomogeneous strain is induced within the cylinder.

**9.2 The strain distributions within cylinder for different shape of cylinder**

All of the numerical calculations given above are for  $h / R = 2.0$ . In order to investigate the shape effect on the strain distribution within cylinder under compression with end friction, Figs. 6-8 plot the normalized strains  $\varepsilon_{rr} / \varepsilon_{rr}^0$ ,  $\varepsilon_{\theta\theta} / \varepsilon_{\theta\theta}^0$  and  $\varepsilon_{zz} / \varepsilon_{zz}^0$  versus the normalized vertical distance  $z/h$  from the center of the cylinder for various values of  $h/R$  for  $r/R=0.0$  and  $\beta=0.0$ . Figs. 6-8 show that a larger deviation may be induced for shorter cylinder. For example, 35% error in  $\varepsilon_H / \varepsilon_H^0$  can be induced even at the center of the cylinder for  $h/R=0.5$ . But the strain distributions for long cylinders are more homogeneous, especially the strains are relatively uniform at the central part of the cylinder if  $h / R \geq 2$ . So a relatively long cylinder should be suggested for compression test.

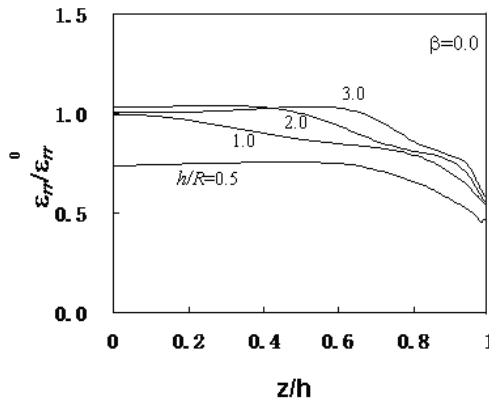


Fig. 6. The normalized strain  $\varepsilon_{rr} / \varepsilon_{rr}^0$  versus the normalized distance  $z/h$  along the axis of loading for various ratios of  $h/R$

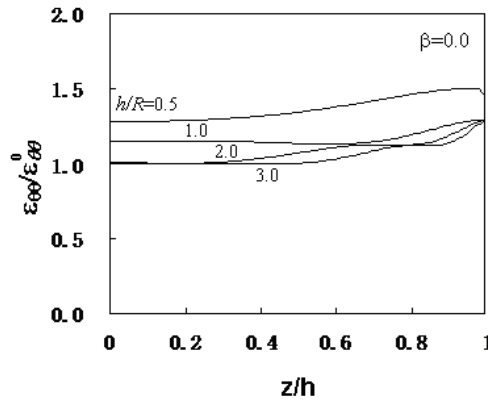


Fig. 7. The normalized strain  $\varepsilon_{\theta\theta} / \varepsilon_{\theta\theta}^0$  versus the normalized distance  $z/h$  along the axis of loading for various ratios of  $h/R$

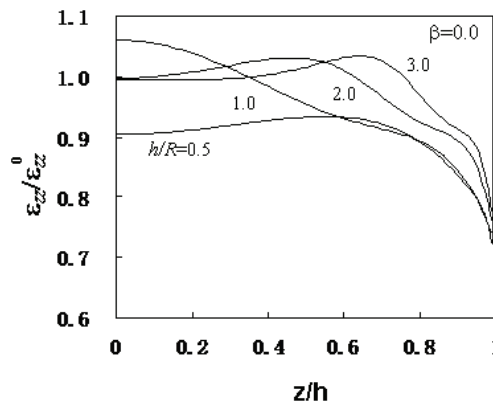


Fig. 8. The normalized strain  $\varepsilon_{zz} / \varepsilon_{zz}^0$  versus the normalized distance  $z/h$  along the axis of loading for various ratios of  $h/R$

## 10. The effect of strain on the valence-band structure of wurtzite GaN

The band structure of wurtzite GaN deserves attention since the valence bands, such as the heavy-hole, light-hole and split-off bands are close each other. The strain effects on wurtzite GaN are less understood (Chuang & Chang, 1996). Based on the deformation potential theory of Luttinger-Kohn and Bir-Pikus (Bir & Pikus, 1974), the valence-band structure of the strained wurtzite GaN can be described by a 6x6 Hamiltonian according to the envelope-function method, and the basis function for wurtzite GaN can be written as

$$\begin{aligned}
 |1\rangle &= -\frac{\alpha^*}{\sqrt{2}}|(X+iY)\uparrow\rangle + \frac{\alpha}{\sqrt{2}}|(X-iY)\downarrow\rangle \\
 |2\rangle &= -\frac{\beta}{\sqrt{2}}|(X-iY)\uparrow\rangle - \frac{\beta^*}{\sqrt{2}}|(X+iY)\downarrow\rangle \\
 |3\rangle &= \beta^*|Z\uparrow\rangle + \beta|Z\downarrow\rangle \\
 |4\rangle &= -\frac{\alpha^*}{\sqrt{2}}|(X+iY)\uparrow\rangle - \frac{\alpha}{\sqrt{2}}|(X-iY)\downarrow\rangle \\
 |5\rangle &= \frac{\beta}{\sqrt{2}}|(X-iY)\uparrow\rangle + \frac{\beta^*}{\sqrt{2}}|(X+iY)\downarrow\rangle \\
 |6\rangle &= -\beta^*|Z\uparrow\rangle + \beta|Z\downarrow\rangle
 \end{aligned} \tag{59}$$

where  $\alpha = (1/\sqrt{2})e^{i(3\pi/4+3\phi/2)}$ ,  $\beta = (1/\sqrt{2})e^{i(\pi/4+\phi/2)}$  and  $\phi = \tan^{-1}(k_y/k_x)$ .

The 6x6 Hamiltonian is obtained as

$$H(k) = \begin{bmatrix} H_{3\times 3}^U(k) & 0 \\ 0 & H_{3\times 3}^L(k) \end{bmatrix} \tag{60}$$

and

$$H_{3\times 3}^U = \begin{bmatrix} F_t & K_t & -iH_t \\ K_t & G_t & \Delta - iH_t \\ iH_t & \Delta + iH_t & \lambda_t \end{bmatrix} \tag{61}$$

$$H_{3\times 3}^L = \begin{bmatrix} F_t & K_t & iH_t \\ K_t & G_t & \Delta + iH_t \\ -iH_t & \Delta - iH_t & \lambda_t \end{bmatrix} \tag{62}$$

$$F_t = \Delta_1 + \Delta_2 + \lambda_t + \theta_t \tag{63}$$

$$G_t = \Delta_1 - \Delta_2 + \lambda_t + \theta_t \tag{64}$$

$$\lambda_t = \frac{\hbar^2}{2m_0} [A_{t1}k_z^2 + A_{t2}(k_x^2 + k_y^2)] + D_1\varepsilon_{zz} + D_2(\varepsilon_{xx} + \varepsilon_{yy}) \tag{65}$$

$$\theta_t = \frac{\hbar^2}{2m_0} [A_{t3}k_z^2 + A_{t4}(k_x^2 + k_y^2)] + D_3\varepsilon_{zz} + D_4(\varepsilon_{xx} + \varepsilon_{yy}) \tag{66}$$

$$K_t = \frac{\hbar^2}{2m_0} A_{t5}(k_x^2 + k_y^2) \tag{67}$$

$$H_t = \frac{\hbar^2}{2m_0} A_{t6} (k_x^2 + k_y^2)^{1/2} k_z \quad (68)$$

$$\Delta = \sqrt{2} \Delta_3 \quad (69)$$

where

$$A_{t3} = -2A_{t4} = A_{t2} - A_{t1} \quad (70)$$

$$A_{t3} + 4A_{t5} = \sqrt{2} A_{t6} \quad (71)$$

$$\Delta_3 = \Delta_2 \quad (72)$$

The valence-band structure can be determined by

$$\det[H(k) - EI] = 0 \quad (73)$$

which leads to

$$(E^3 + C_{t2}E^2 + C_{t1}E + C_{t0})^2 = 0 \quad (74)$$

where

$$C_{t2} = -(F_t + G_t + \lambda_t) \quad (75)$$

$$C_{t1} = F_t G_t + G_t \lambda_t + F_t \lambda_t - \Delta^2 - K_t^2 - 2H_t^2 \quad (76)$$

$$C_0 = -\det[H_{3 \times 3}^U] \quad (77)$$

so we obtained

$$E_{HH} = F_t \quad (78)$$

$$E_{LH} = \frac{G_t + \lambda_t}{2} + \sqrt{\frac{(G_t - \lambda_t)^2}{2} + \Delta^2} \quad (79)$$

$$E_{SO} = \frac{G_t + \lambda_t}{2} - \sqrt{\frac{(G_t - \lambda_t)^2}{2} + \Delta^2} \quad (80)$$

where  $E_{HH}$ ,  $E_{LH}$  and  $E_{so}$  are the energies for the heavy-hole the light-hole and split-off bands, respectively.

## 11. Conclusions

The exact analytical solution for the inhomogeneous strain field within a finite and transversely isotropic cylinder under compression test with end friction is derived. The method employed Lekhnitskii's stress function in order to uncouple the equations of

equilibrium. It was found that the end friction leads to a very inhomogeneous strain distribution within cylinder, especially in the area near the end surface. Numerical results show that all of the strain components, including the axial, radial, circumferential and shear strains, are inhomogeneous, both in distribution pattern and magnitude, the maximum value of the strain concentration near the end surfaces can be 100% higher than the constant strain in the case without end friction. However, the strain distributions are relatively uniform at the central parts of long cylinders, say in the area of  $-0.5h < z < 0.5h$ , the magnitude of the strains can be more than 2% of that without end friction. The method for analyzing the effect of the strain and end friction on the band structure of wurtzite GaN is discussed, end friction has effect on the shape of constant energy surfaces of valence bands and the band gaps between the heavy-hole, light-hole and split-off bands of wurtzite GaN.

## 12. Acknowledgment

This work was supported by the National Natural Science Foundation of China (Grant No. 11032003 and 10872033) and the State Key Laboratory of Explosion Science and Technology.

## 13. References

- Bir, G. L. & Pickus, G. E. (1974). *Symmetry and Strain Induced Effects in Semiconductors*, John Wiley, New York, USA
- Chau K. T. & Wei, X. X(1999). Finite solid circular cylinders subjected to arbitrary surface load: part I. Analytic solution. *International Journal of Solids and Structures*, Vol. 37, pp. 5707-5732
- Choi, S. W. & Shah, S. P. (1998). Fracture mechanism in cement-based materials subjected to compression. *Journal of Engineering Mechanics ASCE*, Vol. 124, pp. 94-102
- Chuang, S. L. & Chang, C. S. (1996), k-p method for strained wurtzite semiconductors. *Physical Review B*, Vol. 54, pp. 2491-2504
- Goroff, I. & Kleinman, L. (1963). Deformation potentials in silicon. III. effects of a general strain on conduction and valence levels. *Physical Review*, Vol. 132, pp. 1080-1084
- Hasegawa, H. (1963). Theory of cyclotron resonance in strained silicon crystals. *Physical Review*, Vol. 129, pp. 1029-1040
- Hussein, A & Marzouk, H(2000). Finite element evaluation of the boundary conditions for biaxial testing of high strength concrete. *Material Structure*, Vol. 33, pp. 299-308
- Jiang, H. & Singh, J. (1997). Strain distribution and electronic spectra of InAs/GaAs self-assembled dots: An eight-band study. *Physical Review B*, Vol. 56, pp. 4696-4701
- Lekhnitskii, S. G(1963). *Theory of elasticity of an anisotropic elastic body*, English translation by P. Fern , Holden-Day Inc., San Francisco, USA
- Mathieu, H. ; Mele, P. and Ameziane, E. L., et al (1979). Deformation potentials of the direct and indirect absorption edges of GaP. *Physical Review B*, Vol. 19, pp. 2209-2223
- Pollak, F. H. & Cardona, M. (1968). Piezo-Electroreflectance in Ge, GaAs, and Si. *Physical Review*, Vol. 172, pp 816-837
- Pollak, F. H. (1990). *In Strained-Layer Superlattices*, edited by T. Pearsall, Semiconductors and Semimetals, Academic, Boston, , USA
- Suzuki, K. & Hensel, J. C. (1974). Quantum resonances in the valence bands of germanium. I. Theoretical considerations. *Physical Review B*, Vol. 9, pp 4184-4218

- Singh, J. (1992). *Physics of Semiconductors and Their Heterostructures*, McGraw-Hill Higher Education, New York, USA
- Torrenti, J.M. ; Benaija, E. H. & Boulay, C. (1993). Influence of boundary conditions on strain softening in concrete compression test. *Journal of Engineering Mechanics ASCE*, Vol. 119, pp. 2369-2384
- Wei, X. X. ; Chau, K. T. & Wong, R. H. C. (1999). A new analytic solution for the axial point load strength test for solid circular cylinders. *Journal of Engineering Mechanics*, Vol. 125, pp. 1349-1357
- Wei, X. X. (2008). Non-uniform strain field in a wurtzite GaN cylinder under compression and the related end friction effect on quantum behavior of valence-bands. *Mechanics of Advanced Materials and Structures*, Vol. 15, pp. 612-622
- Wright, A. F. (1997). Elastic properties of zinc-blende and wurtzite AlN, GaN, and InN. *Journal of Applied Physics*, Vol. 82, pp. 2833-2839

# Application of Quaternary AlInGaN- Based Alloys for Light Emission Devices

Sara C. P. Rodrigues<sup>1</sup>, Guilherme M. Sipahi<sup>2</sup>, Luísa Scolfaro<sup>3</sup>  
and Eronides F. da Silva Jr.<sup>4</sup>

<sup>1</sup>*Departamento de Física - Universidade Federal Rural de Pernambuco*

<sup>2</sup>*Instituto de Física de São Carlos - Universidade de São Paulo*

<sup>3</sup>*Department of Physics - Texas State University*

<sup>4</sup>*Departamento de Física - Universidade Federal de Pernambuco*

<sup>1,2,4</sup>*Brazil*

<sup>3</sup>*USA*

## 1. Introduction

Excellent progress has been made during the past few years in the growth of III-nitride materials and devices. Today, one of the most important application of novel optoelectronic devices is the design and engineering of light-emitting diodes (LEDs) working from ultraviolet (UV) through infrared (IR), thus covering the whole visible spectrum. Since the pioneer works of Nakamura *et al.* at Nichia Corporation in 1993 (Nakamura *et al.* (1995)) when the blue LEDs and pure green LEDs were invented, an enormous progress in this field was observed which has been reviewed by several authors (Ambacher (1998); Nakamura *et al.* (2000)). The rapid advances in the hetero-epitaxy of the group-III nitrides (Fernández-Garrido *et al.* (2008); Kemper *et al.* (2011); Suihkonen *et al.* (2008)) have facilitated the production of new devices, including blue and UV LEDs and lasers, high temperature and high power electronics, visible-blind photodetectors and field-emitter structures (Hirayama (2005); Hirayama *et al.* (2010); Tschumak *et al.* (2010); Xie *et al.* (2007); Zhu *et al.* (2007)).

There has been recent interest in the  $\text{Al}_x\text{In}_{1-x-y}\text{Ga}_y\text{N}$  quaternary alloys due to potential application in UV LEDs and UV-blue laser diodes (LDs) once they present high brightness, high quantum efficiency, high flexibility, long-lifetime, and low power consumption (Fu *et al.* (2011); Hirayama (2005); Kim *et al.* (2003); Knauer *et al.* (2008); Liu *et al.* (2011); Park *et al.* (2008); Zhmakin (2011); Zhu *et al.* (2007)). The availability of the quaternary alloy offers an extra degree of freedom which allows the independent control of the band gap and lattice constant. Another interesting feature of the AlGaInN alloy is that it gives rise to higher emission intensities than the ternary AlGaIn alloy with the absence of In (Hirayama (2005); Wang *et al.* (2007)). An important issue is related to white light emission, which can be obtained by mixing emissions in different wavelengths with appropriate intensities (Roberts (1997); Rodrigues *et al.* (2007); Xiao *et al.* (2004)).

Highly conductive *p*-type III-nitride layers are of crucial importance, in particular, for the production of LEDs. Although the control of *p*-doping in these materials is still subject of discussion, remarkable progress has been achieved (Hirayama (2005); Zhang *et al.* (2011)) and

recently reported experimental results point towards acceptor doping concentration high as  $\approx 10^{19} \text{cm}^{-3}$  (Liu et al. (2011); Zado et al. (2011); Zhang et al. (2011)).

The group-III nitrides crystallize in both, the stable wurtzite (w) phase and the metastable cubic (c) phase. Unlike for the hexagonal w-structure, the growth of cubic GaN is more complicated due to the thermodynamically unstable nature of the structure. In hexagonal GaN inherent spontaneous and piezoelectric polarization fields are present along the c-axis because of the crystal symmetry. Due to these fields, non-polar and semi-polar systems have attracted interest. One method to produce real non-polar materials is the growth of the c-phase. Considerable advances in the growth of c-nitrides, with the aim of getting a complete understanding of the c-nitride-derived heterostructures have been observed (As (2009); Schörmann et al. (2007)). Successful growth of quaternary c- $\text{Al}_x\text{In}_{1-x-y}\text{Ga}_y\text{N}$  layers lattice matched to GaN has been reported (Kemper et al. (2011); Schörmann et al. (2006)). The absence of polarization fields in the c-III nitrides may be advantageous for some device applications. Besides, it has been shown that these quaternary alloys can be doped easily as p-type, and due to the wavelength localization the optical transition energies are higher in the alloys than in GaN (Wang et al. (2007)).

However, the exact nature of the optical processes involved in the alloys with In is a subject of controversy. Different mechanisms have been proposed for the origin of the carriers' localized states in the quantum well devices. One is related to the low solubility of InN in GaN, leading to the presence of nanoclusters inside the alloy, which can be suppressed by biaxial strain as predicted and measured in c-InGaN samples (Marques et al. (2003); Scolfaro et al. (2004); Tabata et al. (2002)). The second mechanism proposes that the recombination occurs through the quantum confined states (electron-hole pairs or excitons) inside the well.

In this chapter we show the results of detailed studies of the theoretical photoluminescence (PL) and absorption spectra for several systems based on nitride quaternary alloys, using the  $\vec{k} \cdot \vec{p}$  theory within the framework of effective mass approximation, in conjunction with the Poisson equation for the charge distribution. Exchange-correlation effects are also included within the local density approximation (Rodrigues et al. (2002); Sipahi et al. (1998)). All systems are assumed to be strained, so that the optical transitions are due to confinement effects. The theoretical method will be described in section 2. Through these calculations the possibility of obtaining light emission from undoped (see section 3) and p-doped (see section 4) quaternary  $\text{Al}_x\text{In}_{1-x-y}\text{Ga}_y\text{N}/\text{Al}_x\text{In}_{1-x-y}\text{Ga}_y\text{N}$  superlattices (SLs) is addressed. By properly choosing the  $x$  and  $y$  contents in the wells and the acceptor doping concentration  $N_A$  as well  $X$  and  $Y$  in the barriers, it is shown to be possible to achieve light emission which covers the visible spectrum from violet to red. The investigation is also extended to double quantum wells (DQWs), as described in section 5, confronting the results with experimental data reported on these systems (Kyono et al. (2006)). The results are compared with regard to the PL emissions for the different systems, also when an external electric field is present. Finally it is shown that by adopting appropriated combinations of SLs is possible to obtain the best conditions in order to get white-light emission. This fact is fundamental in the design of new optoelectronic devices.

## 2. Theoretical band structure and luminescence spectra calculations

During the last few years, the super-cell  $\vec{k} \cdot \vec{p}$  method has been adapted to quantum wells and superlattices (SLs) (Rodrigues et al. (2002); Sipahi et al. (1996)). Using this approach, one can self-consistently solve the  $8 \times 8$  Kane multiband effective mass equation (EME) for the charge



distribution ( Sipahi et al. (1998)). The results below are calculated assuming an infinite SL of squared wells along  $\langle 001 \rangle$  direction.

The multiband EME is represented with respect to plane waves with vectors  $\mathbf{K}=(2\pi/d)l$  ( $l$  being an integer and  $d$  the SL period) equal to the reciprocal SL vector. The rows and columns of the  $8 \times 8$  Kane Hamiltonian refer to the Bloch-type eigenfunctions  $|jm_j\vec{k}\rangle$  of  $\Gamma_8$  heavy- and light-hole bands,  $\Gamma_7$  spin-orbit-split-hole band and  $\Gamma_6$  conduction band;  $\vec{k}$  denotes a vector in the first SL Brillouin zone (BZ).

By expanding the EME with respect to plane waves ( $z|K\rangle$ ) one is able to represent this equation with respect to Bloch functions ( $\vec{r}|jm_j\vec{k} + K\vec{e}_z\rangle$ ). For a Bloch-type eigenfunction ( $z|E\vec{k}\rangle$ ) of the SL of energy  $E$  and wavevector  $\vec{k}$ , the EME takes the form:

$$\sum_{j'm'_jK'} \left( jm_j\vec{k}K | H_0 + H_{ST} + V_{HET} + V_A + V_H + V_{XC} | j'm'_j\vec{k}K' \right) \left( j'm'_j\vec{k}K' | E\vec{k} \right) = E(\vec{k}) \left( jm_j\vec{k}K | E\vec{k} \right), \quad (1)$$

where  $H_0$  is the effective kinetic energy operator, generalized for a heterostructures  $H_{ST}$  is the strain operator originated from the lattice mismatch,  $V_{HET}$  is the potential that arises from the band offset at the interfaces, which is diagonal with respect to  $jm_j$ ,  $j'm'_j$ ,  $V_{XC}$  is the exchange-correlation potential for carriers taken within Local Density Approximation (LDA),  $V_A$  is the ionized acceptor charge distribution potential, and  $V_H$  is the Hartree potential or one-particle potential felt by the carrier from the carriers charge density. So the Coulomb potential,  $V_C$  given by contribution of  $V_A$  and  $V_H$  potentials, can be obtained by means of the self-consistent procedure, where the Poisson equation stands, in the reciprocal space as,

$$(K | V_C | K') = \frac{4\pi e^2}{\epsilon} \frac{1}{|K - K'|^2} [(K | N_A(z) | K') - (K | p(z) | K')], \quad (2)$$

with  $\epsilon$  being the dielectric constant,  $e$  the electron charge,  $N_A(z)$  the ionized acceptors concentration, and  $p(z)$  being the holes charge distribution, which is given by

$$p(z) = \sum_{\substack{jm_j\vec{k} \in \\ \text{empty states}}} |(zs | jm_j\vec{k})|^2, \quad (3)$$

where  $s$  is the spin coordinate.

The next term in the Hamiltonian is the strain potential,  $V_{ST}$ . The kind of strain in these systems is biaxial, so it can be decomposed into two terms, a hydrostatic term and an uniaxial term ( Rodrigues et al. (2001)). Since the hydrostatic term changes the gap energy, thus not affecting the valence band potential depth, only the uniaxial strain component will be considered ( Rodrigues et al. (2001)). This latter may be calculated by the following expression:

$$\epsilon = -2/3D_u\epsilon_{xx}(1 + 2C_{12}/C_{11}), \quad (4)$$

where  $-2/3D_u$  is the shear deformation potential,  $C_{11}$  and  $C_{12}$  are the elastic constants, and  $\epsilon_{xx}$  is the lattice mismatch which is given by:

$$\epsilon_{xx} = (a_{\text{barrier}} - a_{\text{well}})/a_{\text{well}}, \quad (5)$$

with  $a_{barrier}$  and  $a_{well}$  being the lattice parameters of the barrier and well materials, respectively.

Through these definitions one can calculate the Fourier coefficients of the strain operator  $(K|\epsilon(z)|K')$  and express the strain term of the Hamiltonian  $V_{ST}$  as follows:

$$(jm_j\vec{k}K|H_{ST}|j'm'_j\vec{k}K') = (K|\epsilon(z)|K')M_{jm_j}^{j'm'_j}, \quad (6)$$

where  $M_{jm_j}^{j'm'_j}$  is defined as

$$M_{jm_j}^{j'm'_j} = \begin{pmatrix} 1 & 0 & 0 & 0 & 0 & 0 \\ 0 & -1 & 0 & 0 & -i\sqrt{2} & 0 \\ 0 & 0 & -1 & 0 & 0 & -i\sqrt{2} \\ 0 & 0 & 0 & 1 & 0 & 0 \\ 0 & i\sqrt{2} & 0 & 0 & 0 & 0 \\ 0 & 0 & i\sqrt{2} & 0 & 0 & 0 \end{pmatrix}. \quad (7)$$

Exchange-correlation effects can be taken into account in the local density approximation, by adopting a parameterized expression for an inhomogeneous hole gas, applying the exchange interaction only for identical particles and the correlation for all of them (Enderlein et al. (1997)). The band shift potential  $V_{HET}$  is diagonal with respect to  $jm_j, j'm'_j$ , and is defined by

$$(jm_j\vec{k}K|V_{HET}|j'm'_j\vec{k}K') = (K|V_{HET}|K')\delta_{jj'}\delta_{m_jm'_j} \quad (8)$$

where  $(K|V_{HET}|K')$  are the Fourier coefficients of  $V_{HET}$  along the growth direction.

From the calculated eigenstates, one can determine the luminescence and absorption spectra of the SL by using the following general expression (Sipahi et al. (1998))

$$I(\omega) = \frac{2\hbar\omega^3}{c} \frac{e^2}{m_0c^2} \sum_{\vec{k}} \sum_{n_e} \sum_{n_q} \sum_{q=hh, lh, so} f_{n_en_q}(\vec{k}) N_{n_e\vec{k}} [1 - N_{n_q\vec{k}}] \times \frac{\gamma}{\pi [E_{n_e}(\vec{k}) - E_{n_q}(\vec{k}) - \hbar\omega]^2 + \gamma^2}, \quad (9)$$

where  $m_0$  is the electron mass,  $\omega$  is the incident radiation frequency,  $\gamma$  is the emission broadening (assumed as constant and equal to 10 meV),  $E_{n_e}$  and  $E_{n_q}$  are the energies associated to  $n_e$  and  $n_q$ , respectively, the electron and hole states involved in the transition. The occupation functions  $N_{n_e\vec{k}}$  and  $[1 - N_{n_q\vec{k}}]$  are the Fermi-like occupation functions for states in the conduction- and valence-band, respectively.

For the calculation of luminescence (absorption) spectra, the sum in Eq. (9) is performed over the occupied states in the conduction (valence) band, and unoccupied states in the valence (conduction) band (Sipahi et al. (1998)).

The oscillator strength,  $f_{n_en_q}(\vec{k})$ , is given by

$$f_{n_en_q}(\vec{k}) = \frac{2}{m_0} \sum_{\sigma_e\sigma_q} \frac{|\langle n_e\sigma_e\vec{k}|p_x|n_q\sigma_q\vec{k}\rangle|^2}{E_{n_e}(\vec{k}) - E_{n_q}(\vec{k})}, \quad (10)$$

	GaN	InN	AlN
$\gamma_1$	2.96	3.77	1.54
$\gamma_2$	0.90	1.33	0.42
$\gamma_3$	1.20	1.60	0.64
$\Delta_{so}(\text{meV})$	17	3	19
$a(\text{\AA})$	4.552	5.030	4.380
$m_{hh}^*$	0.86	0.84	1.44
$m_{lh}^*$	0.21	0.16	0.42
$m_{so}^*$	0.30	0.24	0.63
$m_e^*$	0.15	0.10	0.067
$E_g^{\Gamma}(\text{eV})$	3.3	0.9	5.94
$a_g(\text{eV})$	-8.50	-12.98	-9.40
$2/3D_u(\text{eV})$	1.6	1.2	1.5
$C_{11}(\text{GPa})$	293	187	304
$C_{12}(\text{GPa})$	159	125	160

Table 1. Values of the parameters used in the self-consistent calculations of the  $p$ -doped cubic  $(\text{Al}_{0.20}\text{In}_{0.05}\text{Ga}_{0.75})\text{N}/(\text{Al}_x\text{In}_{1-x-y}\text{Ga}_y)\text{N}$  SLs. Data extracted from Refs. (Ramos et al. (2001); Rodrigues et al. (2000; 2002); Schörmann et al. (2006)).

where  $p_x$  is the dipole momentum in the  $x$ -direction,  $\sigma_e$  and  $\sigma_q$  denote the spin values for electron and holes, respectively.

All the parameters used in this analysis are shown in Table I. For the quaternary  $(\text{Al}_x\text{In}_{1-x-y}\text{Ga}_y)\text{N}$  band gap energy dependence on the alloy contents,  $x$  and  $y$ , was used the expression provided in Ref. (Marques et al. (2003)). For all the other quantities, linear interpolations were taken using the values for the binaries, AlN, GaN, InN. The temperature dependence of bandgap energies was evaluated through the Varshni analytical expression as applied for GaN (Kohler et al. (2002)).

### 3. Undoped cubic $\text{Al}_x\text{In}_y\text{Ga}_{1-x-y}\text{N}$ systems

In order to analyze the effects of the use of quaternary alloys in the electronic transitions, Fig. 1 presents the theoretical PL spectra at  $T = 2$  K calculated for strained undoped  $\text{In}_{0.2}\text{Ga}_{0.8}\text{N}/\text{Al}_x\text{Ga}_y\text{In}_{1-x-y}\text{N}$  SLs with  $x = 0.03, 0.10,$  and  $0.20$  and  $y = 0.40, 0.47,$  and  $0.51$ , respectively. The barriers, constituted by the ternary alloy, have width  $d_1 = 60$  nm, while the wells have width  $d_2 = 3$  nm. It is important to remark that all systems are strained, so the luminescence cannot arise from nanoclusters created during the growth. In all cases in this section the first peak seen in the PL spectra corresponds to the first electronic transition E1-HH1 (first electron level E1 and first heavy-hole level HH1) (Rodrigues et al. (2005)).

From Fig. 1 one can observe that with the appropriate choice of parameters it is possible to reach wavelengths from the red to the blue region. One can also see that, by changing the well width as depicted in Fig. 2, the peaks in the PL spectra exhibit larger variations. As the well width decreases, the transition energy gets closer to the red region. This occurs because of the changes in the energies caused by the confinement and strain effects, which become stronger as the In content increases.

As the results described above are from systems where InGaN represents the barriers and the quaternary alloy is in the wells, one can change the picture and start analyzing systems where the barriers correspond to the quaternary alloys while the InGaN alloy forms the wells.

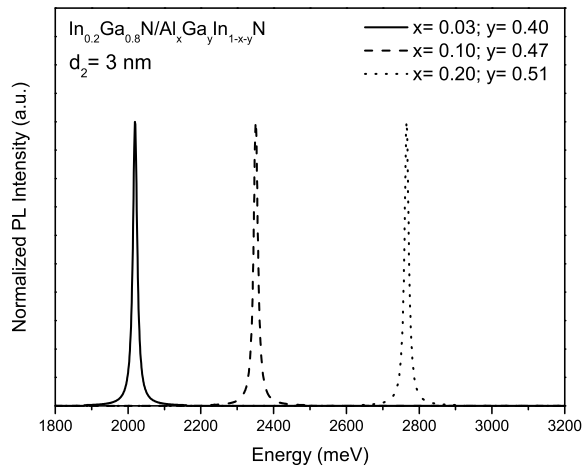


Fig. 1. Theoretical normalized PL spectra for strained undoped  $\text{In}_{0.2}\text{Ga}_{0.8}\text{N}/\text{Al}_x\text{Ga}_y\text{In}_{1-x-y}\text{N}$  SLs, with  $x=0.03$  (solid line),  $0.10$  (dashed line), and  $0.20$  (dotted line) and  $y=0.40, 0.47$ , and  $0.51$ , respectively, barrier width  $d_1 = 60$  nm, well width  $d_2 = 3$  nm.

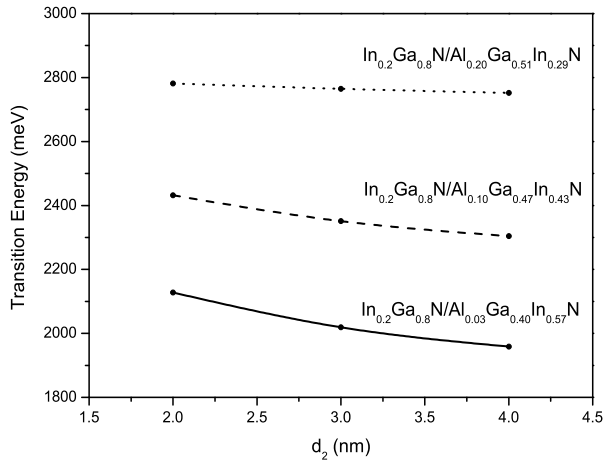


Fig. 2. PL peaks as a function of the well width  $d_2$  for the same systems of Fig. 1.

Fig. 3 presents calculated SL systems with the same configurations as Fig. 1, but using GaN as barriers instead of  $\text{Al}_x\text{Ga}_y\text{In}_{1-x-y}\text{N}$ . It presents calculated theoretical PL spectra, at  $T = 2$  K, for  $\text{Al}_{0.10}\text{Ga}_{0.47}\text{In}_{0.43}\text{N}/\text{In}_{0.55}\text{Ga}_{0.45}\text{N}$ ,  $\text{Al}_{0.17}\text{Ga}_{0.47}\text{In}_{0.36}\text{N}/\text{In}_{0.42}\text{Ga}_{0.68}\text{N}$ , and  $\text{Al}_{0.25}\text{Ga}_{0.47}\text{In}_{0.28}\text{N}/\text{In}_{0.25}\text{Ga}_{0.75}\text{N}$  SLs (solid lines). The figure presents also, for comparison, the systems of Fig. 1 (dashed lines). A similar behavior, as obtained in Fig. 1, is seen also for InGaN barriers, with the possibility of light emission covering the entire visible spectra.

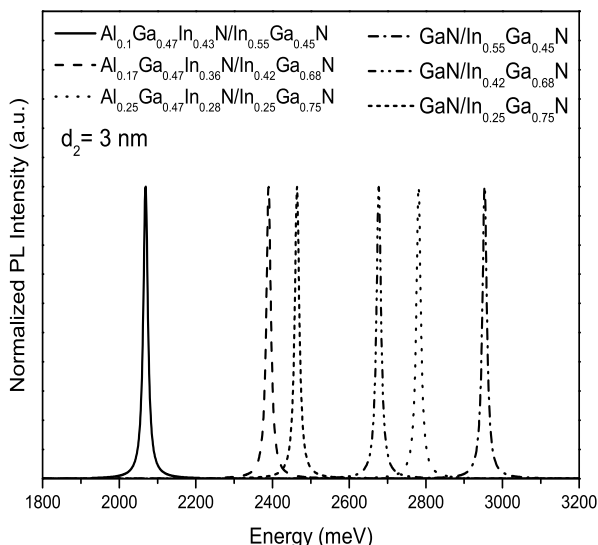


Fig. 3. Theoretical normalized PL spectra for the strained undoped SLs  $\text{Al}_{0.10}\text{Ga}_{0.47}\text{In}_{0.43}\text{N}/\text{In}_{0.55}\text{Ga}_{0.45}\text{N}$  (solid line),  $\text{Al}_{0.17}\text{Ga}_{0.47}\text{In}_{0.36}\text{N}/\text{In}_{0.42}\text{Ga}_{0.68}\text{N}$  (dashed line) and  $\text{Al}_{0.25}\text{Ga}_{0.47}\text{In}_{0.28}\text{N}/\text{In}_{0.25}\text{Ga}_{0.75}\text{N}$  (dotted line). The barrier width is  $d_1 = 60$  nm and the well width is  $d_2 = 3$  nm. For comparison, we show the results for the SLs  $\text{GaN}/\text{In}_{0.55}\text{Ga}_{0.45}\text{N}$  (dash-dotted line),  $\text{GaN}/\text{In}_{0.42}\text{Ga}_{0.68}\text{N}$  (dash-dot-dotted line), and  $\text{GaN}/\text{In}_{0.25}\text{Ga}_{0.75}\text{N}$  (short-dashed line) systems.

However, this is not possible using GaN in the barriers, since we have a limitation imposed by the fixed gap energy value for GaN. Another finding refers to the transition energies appearing higher when the quaternary alloys constitute the barriers, when compared with the case in which InGaN is in the barriers. This can be explained by the effective mass values which are higher in the  $\text{Al}_x\text{Ga}_y\text{In}_{1-x-y}\text{N}$  alloys than in InGaN.

It is also very important to investigate the influence of an external electrical field on the transition energies and how the results compare with those for the wurtzite phase structures. In Fig. 4, the theoretical PL and electroluminescence (EL) spectra were depicted at  $T = 2$  K calculated for strained undoped  $\text{In}_{0.1}\text{Ga}_{0.9}\text{N}/\text{Al}_x\text{Ga}_y\text{In}_{1-x-y}\text{N}$  SLs with  $x = 0.03, 0.10$  and  $0.20$ , and  $y = 0.50$ . For these calculations the barrier width is  $d_1 = 8$  nm and the well width is  $d_2 = 3$  nm. The magnitude of the electric field was  $1.6$  MV/cm for the EL spectra calculations. The results indicate that the electric field enhances the shift seen in the spectra towards the red region, as compared with the PL spectra. This fact can be better visualized in Fig. 5, which shows the reduction in the transition energy as the electric field increases. Such behavior is attributed to the fact that the potentials become deeper as the electrical field increases. The main consequence is the presence of more levels occupied near the bottom of the potential wells. Comparing with wurtzite structures, which have intrinsic built-in electric fields, the situation described here is very similar, however in cubic systems higher efficiencies are predicted (Rodrigues et al. (2005)).

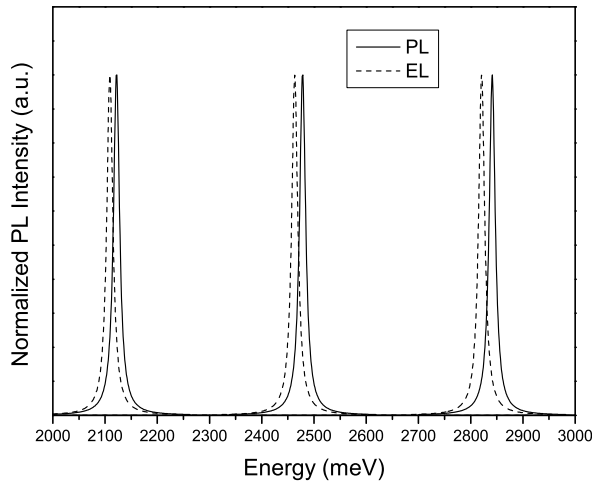


Fig. 4. Theoretical normalized PL (solid line) and electroluminescence (dashed line) spectra for strained undoped  $\text{In}_{0.1}\text{Ga}_{0.9}\text{N}/\text{Al}_x\text{Ga}_y\text{In}_{1-x-y}\text{N}$  SLs, with  $x = 0.03, 0.10,$  and  $0.20,$  and  $y = 0.50,$  respectively, barrier width  $d_1 = 8$  nm and well width  $d_2 = 3$  nm. The electric field used for EL was  $1.6$  MV/cm.

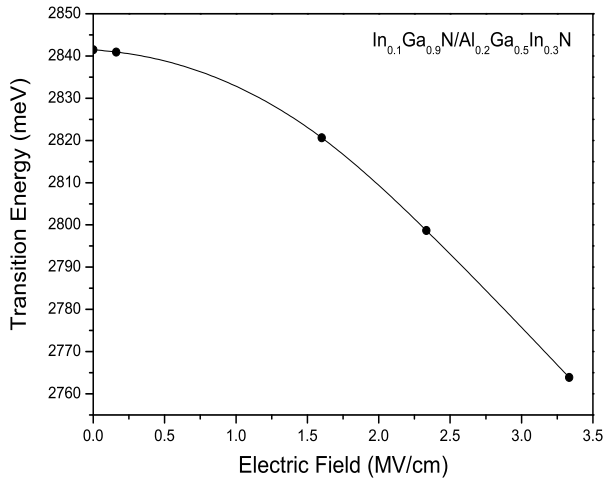


Fig. 5. PL peaks as a function of the magnitude of the electric field for systems with the same quaternary contents as the ones in Fig. 4.

#### 4. Doped cubic $\text{Al}_x\text{In}_y\text{Ga}_{1-x-y}\text{N}$ systems

An important aspect to be analyzed is the effect of the acceptor doping on the electronic transitions. Fig. 6 presents the PL spectra at  $T = 2$  K for strained p-type doped  $\text{Al}_{0.20}\text{Ga}_{0.05}\text{In}_{0.75}\text{N}/\text{Al}_x\text{In}_y\text{Ga}_{1-x-y}\text{N}$  SLs, for which  $x$  and  $y$  are varied as described in Table

2. The ionized acceptor doping concentration considered to be uniformly distributed in the barriers and fully ionized, is also varied assuming values of  $N_A = 5 \times 10^{18} \text{cm}^{-3}$  and  $N_A = 10 \times 10^{18} \text{cm}^{-3}$ . These values of  $N_A$  allow us to envisage what happens in the range from very low hole concentrations up to concentrations as high as  $\approx 10^{19} \text{cm}^{-3}$ . The undoped system is also presented for comparison. The barriers widths are 8 nm and the wells widths are 3 nm (Rodrigues et al. (2007)). The choice of values for  $x$  and  $y$ , the Al and In alloy contents was such to reach all the visible-UV wavelength region.

$c\text{-(Al}_{0.20}\text{In}_{0.05}\text{Ga}_{0.75}\text{)N}/(\text{Al}_x\text{In}_{1-x-y}\text{Ga}_y\text{)N}$	$x$	$y$	$1-x-y$
red	0.00	0.35	0.65
green	0.02	0.40	0.58
blue	0.08	0.45	0.47
blue-violet	0.10	0.50	0.40
violet	0.15	0.55	0.30

Table 2. Values used for the alloy contents  $x$  and  $y$  in the  $p$ -doped  $c\text{-(Al}_{0.20}\text{In}_{0.05}\text{Ga}_{0.75}\text{)N}/(\text{Al}_x\text{In}_{1-x-y}\text{Ga}_y\text{)N}$  SLs, properly chosen to attain light emission in the electromagnetic spectral regions indicated in the left column.

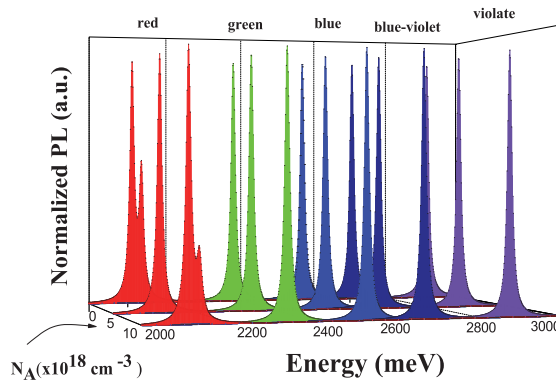


Fig. 6. Calculated normalized photoluminescence (PL) spectra, at  $T = 2 \text{ K}$ , for  $\text{Al}_{0.20}\text{In}_{0.05}\text{Ga}_{0.75}\text{N}/\text{Al}_x\text{In}_{1-x-y}\text{Ga}_y\text{N}$  SLs, for  $x$  and  $y$  values as shown in Table 2, for ionized acceptor concentrations of  $N_A = 0$ ,  $N_A = 5 \times 10^{18} \text{cm}^{-3}$ , and  $N_A = 10 \times 10^{18} \text{cm}^{-3}$ . The energy range covers the electromagnetic spectrum from red to violet.

In Fig. 7 the PL peaks are depicted as a function of the acceptor doping concentration for the first electronic transition E1-HH1. As  $N_A$  increases a red-shift in energy is observed for all regions investigated, except for the red region which presents a second electronic transition E1-HH2 (first electron level E1 and second occupied heavy-hole level HH2) for  $N_A = 0$  and  $5 \times 10^{18} \text{cm}^{-3}$ . This behavior is directly related to the transition probabilities in such systems and the potential profile due to the charges distribution. The later is determined by the balance between the Coulomb and exchange-correlation potentials contribution which defines the potential bending.

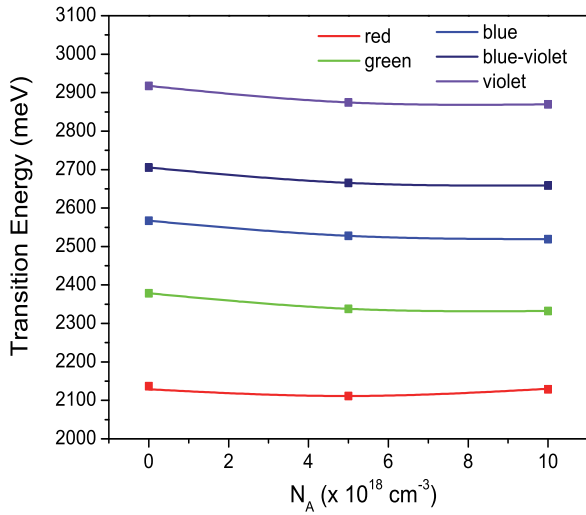


Fig. 7. Peaks of PL spectra of Fig. 6 as a function of the acceptor doping concentration,  $N_A$ .

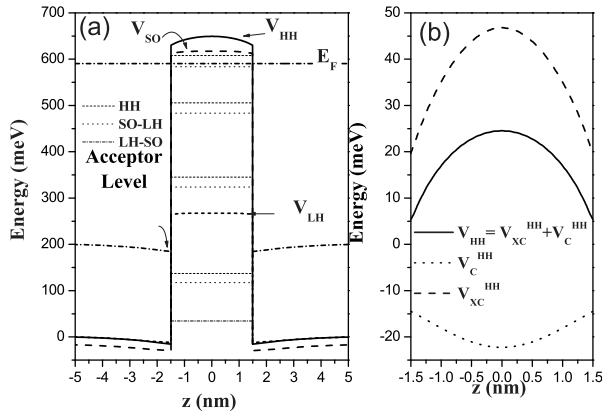


Fig. 8. p-doped  $\text{Al}_{0.20}\text{In}_{0.05}\text{Ga}_{0.75}\text{N}/\text{In}_{0.65}\text{Ga}_{0.35}\text{N}$  SL, with  $N_A = 5 \times 10^{18} \text{ cm}^{-3}$ , which emits in the red: (a) Real-space energy diagram showing the spatial dependence of the valence band edges for heavy ( $V_{hh}$ ), light ( $V_{lh}$ ), and split-off ( $V_{so}$ ) hole bands. Eight energy hole levels inside the well are depicted. Also shown, by thick dash-dotted lines, are the acceptor level in the barrier and the position of the Fermi level,  $E_F$ . The energy zero was taken at the top of the Coulomb potential at the barrier; (b) Different contributions to the self-consistent total heavy-hole potential ( $V_{hh}^{hh}$ ), due to the Coulomb ( $V_C^{hh}$ ) and due to the exchange-correlation ( $V_{XC}^{hh}$ ) potentials.

In order to enhance the visualization of this behavior, Fig. 8 shows (a) the potential profile for the  $\text{Al}_{0.20}\text{In}_{0.05}\text{Ga}_{0.75}\text{N}/(\text{In}_{0.65}\text{Ga}_{0.35}\text{N})$  SL, with  $N_A = 5 \times 10^{18} \text{ cm}^{-3}$ , corresponding to the red emission in PL depicted in Fig. 7. The potential profile for each kind of carrier:



heavy-holes,  $V_{hh}$ , light-holes  $V_{lh}$  and split-off holes,  $V_{so}$  is shown, as well as the Fermi energy,  $E_F$ . The acceptor level is also indicated; for the nitrides, the acceptor level energy is deep, around 200 meV. However, the barriers in the nitrides are high since the strain effects are strong due the large lattice mismatch. The energy zero was placed at the top of the total Coulomb potential at the barrier. Fig. 8 (b) presents the exchange-correlation ( $V_{XC}^{hh}$ ) and Coulomb potential ( $V_C^{hh}$ ) profiles inside the well for the heavy-holes. For this case, in particular, the exchange-correlation potential stands out the Coulomb potential. So the total heavy-holes potential,  $V_{hh}$  is attractive and follows the same behavior of  $V_{XC}$ .

The rapid screening of the Coulomb potential because of the higher effective masses of the nitrides is responsible for this behavior. Consequently, the electronic transition decreases and the energy shifts to the red region.

The PL spectra behavior with the increase of the temperature could also be analyzed. Fig. 9 presents the PL spectra of one of the systems shown in Fig. 6, emitting in the red wavelength, the  $\text{Al}_{0.20}\text{In}_{0.05}\text{Ga}_{0.75}\text{N}/\text{In}_{0.35}\text{Ga}_{0.65}\text{N}$  SL, with  $N_A = 10 \times 10^{18} \text{ cm}^{-3}$ . As seen above, at  $T = 2$  K one can observe two peaks, E1-HH1 and E1-HH2. As the temperature increases, a red-shift in energy is seen. Above  $T = 200$  K, other electronic transitions start to appear, showing a third peak (E1-HH3), and for  $T = 300$  K, also a fourth peak (E1-HH4). This behavior is due to the higher probability of occupation of higher valence band energy levels as the temperatures increases. The red-shift in energy is a consequence of the band gap shrinkage. One can also observe that the peaks corresponding to the higher electronic transitions seen at  $T = 200$  and 300 K are stronger due to the larger values for the oscillator strengths.

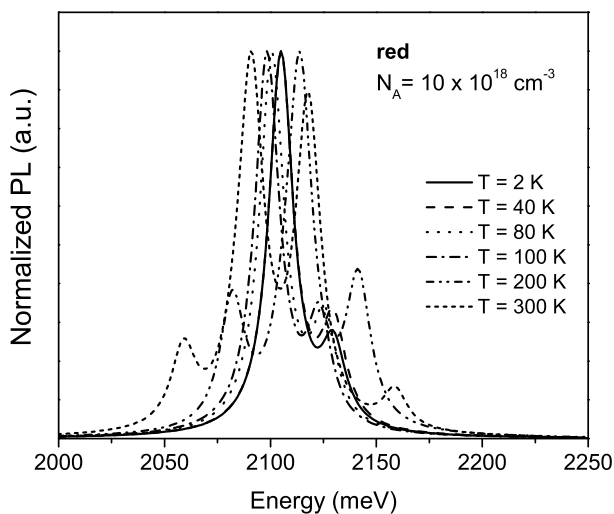


Fig. 9. Calculated PL spectra at  $T = 2$  K (solid line),  $T = 40$  K (dashed line),  $T = 80$  K (dotted line),  $T = 100$  K (dash-dotted line),  $T = 200$  K (dash-dot-dotted line) and  $T = 300$  K (short-dashed line) for the  $\text{Al}_{0.20}\text{In}_{0.05}\text{Ga}_{0.75}\text{N}/\text{In}_{0.35}\text{Ga}_{0.65}\text{N}$  SL, with  $N_A = 10 \times 10^{18} \text{ cm}^{-3}$ , which emits in the red wavelength (see table 2).

Another important element to analyze in doped systems is the PL spectra dependence on the doping concentration. Fig. 10 depicts the calculated PL and absorption spectra, at  $T = 2$  K, for a  $p$ -doped  $\text{Al}_{0.20}\text{In}_{0.05}\text{Ga}_{0.75}\text{N}/\text{Al}_x\text{In}_{1-x-y}\text{Ga}_y\text{N}$  SL, corresponding to emission in the

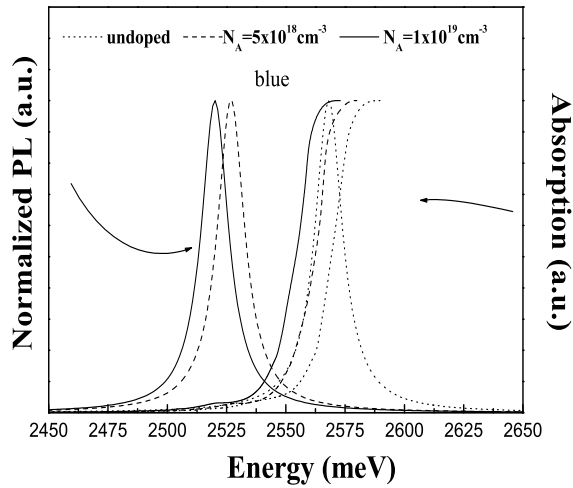


Fig. 10. Calculated PL and absorption spectra, at  $T = 2$  K, for a  $p$ -doped  $(\text{Al}_{0.20}\text{In}_{0.05}\text{Ga}_{0.75})\text{N}/(\text{Al}_x\text{In}_{1-x-y}\text{Ga}_y)\text{N}$  SL, which emits in the *blue* region (see Table II), for  $N_A = 0$  (undoped),  $N_A = 5 \times 10^{18}\text{cm}^{-3}$ , and  $N_A = 1 \times 10^{19}\text{cm}^{-3}$ .

blue region, for  $N_A = 0$  (undoped),  $N_A = 5 \times 10^{18}\text{cm}^{-3}$ , and  $N_A = 10 \times 10^{18}\text{cm}^{-3}$ . One can clearly observe a red shift in both, the PL and absorption spectra, as the acceptor doping concentration increases due to the confinement and many body effects. From these results the values obtained for the Stokes shift can be extracted, taken as the energy difference between the PL peak and the absorption edge. A significant increasing in the values of the Stokes shifts with the increase of  $N_A$  can be seen. This is due to the fact that many-body effects such as exchange and correlation within the 2DHG have shown to be relevant, particularly for high hole-density systems. The values encountered for the Stokes shifts in the systems shown in Fig. 10 are approximately 20 meV and 40 meV, respectively, for  $N_A = 5 \times 10^{18}\text{cm}^{-3}$  and  $N_A = 10 \times 10^{18}\text{cm}^{-3}$ . Similar values for the Stokes shifts have been found for  $p$ -doped ternary  $(\text{AlGa})\text{N}/\text{GaN}$  SLs (Rodrigues et al. (2007)).

### 5. Double $\text{Al}_x\text{In}_y\text{Ga}_{1-x-y}\text{N}$ quantum wells

This section is dedicated to the study of the PL spectra for undoped and  $p$ -doped  $\text{Al}_x\text{In}_{1-x-y}\text{Ga}_y\text{N}/\text{Al}_x\text{In}_{1-x-y}\text{Ga}_y\text{N}$  double quantum wells (DQWs), in which the Al and the In contents, as well as, the well and spike widths are varied. A schematic diagram of the investigated DQWs is presented in Fig. 11. The well and spike widths,  $d_w$  and  $d_s$ , respectively, are indicated. The first electronic transition is also shown and corresponds to the transition between the first electron level and the first occupied heavy-hole level (E1- HH1) (Rodrigues et al. (2008)).

Fig. 12 presents the theoretical PL spectra from undoped DQWs constituted by  $\text{Al}_{0.25}\text{In}_{0.05}\text{Ga}_{0.70}\text{N}$  in the barrier, 10 nm width, followed by a variable width well ( $d_w$ ) of  $\text{Al}_{0.08}\text{In}_{0.37}\text{Ga}_{0.55}\text{N}$ , a variable width spike ( $d_w$ ) of  $\text{Al}_{0.10}\text{In}_{0.10}\text{Ga}_{0.80}\text{N}$ , again a variable width well ( $d_w$ ) of  $\text{Al}_{0.08}\text{In}_{0.37}\text{Ga}_{0.55}\text{N}$  and a fixed barrier of 10 nm of  $\text{Al}_{0.25}\text{In}_{0.05}\text{Ga}_{0.70}\text{N}$ . This set of spectra corresponds to the cases in which the spike width is fixed in 4 nm and the well width is varied

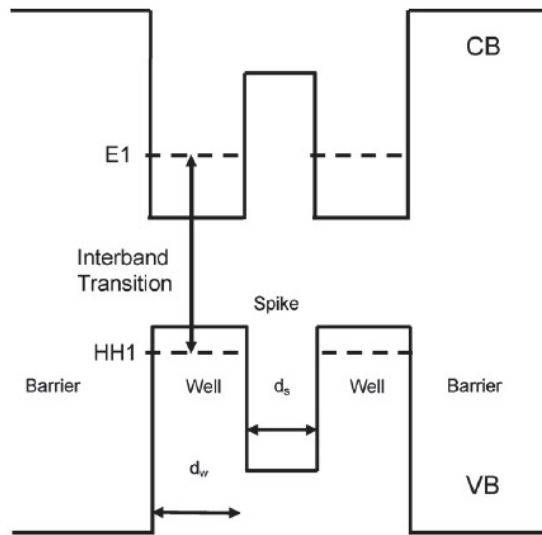


Fig. 11. Schematic diagram for the conduction and valence bands of the DQW structure investigated here.  $d_w$  and  $d_s$  are the well and the spike widths, respectively. The interband transition is also indicated, as well as the first electron (E1) and heavy-hole (HH1) occupied levels.

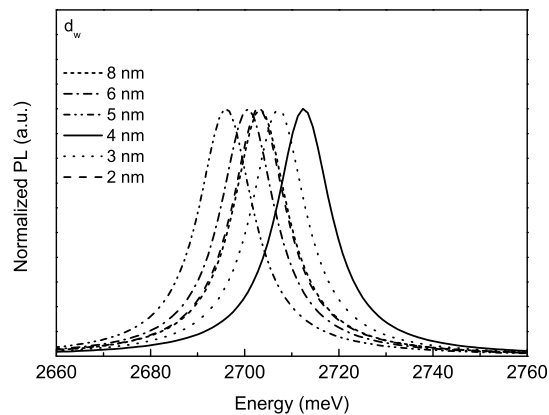


Fig. 12. Calculated PL spectra at  $T = 2$  K for undoped  $c\text{-Al}_{0.25}\text{In}_{0.05}\text{Ga}_{0.70}\text{N}/\text{Al}_{0.08}\text{In}_{0.37}\text{Ga}_{0.55}\text{N}/\text{Al}_{0.10}\text{In}_{0.10}\text{Ga}_{0.80}\text{N}$  DQWs for well width  $d_w = 4$  nm and spike widths  $d_s = 8$  nm, 6 nm, 5 nm, 4 nm, 3 nm, and 2 nm.

from 2 nm, 3 nm, 4 nm, 5 nm, 6 nm, to 8 nm. A blue-shift is present in energies up to  $d_w = 4$  nm, whereas there is a red-shift for  $d_w > 4$  nm, and beyond this value a blue-shift is observed for values of  $d_w > 5$  nm. This behavior can be explained by the fact that for  $d_w < 4$  nm the DQW is in an interacting regime and at  $d_w = 5$  nm it reaches the changing point from interacting

regime to isolated QWs. For larger wells, the spike width loses its importance and above  $d_w = 5$  nm it occurs a blue-shift in the energy due to the confinement effects for isolated wells.

Fig. 13 presents calculated PL spectra for systems with fixed well width  $d_w = 4$  nm and spike width,  $d_s$ , varying from 2 to 8 nm. One can observe a red-shift in energy as  $d_s$  increases. This leads to the conclusion that confinement levels are localized deeper, decreasing the electronic transition energies.

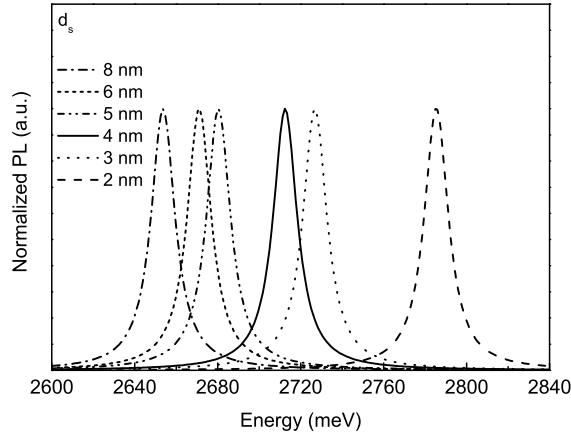


Fig. 13. Calculated PL spectra at  $T = 2$  K for undoped  $c\text{-Al}_{0.25}\text{In}_{0.05}\text{Ga}_{0.70}\text{N}/\text{Al}_{0.08}\text{In}_{0.37}\text{Ga}_{0.55}\text{N}/\text{Al}_{0.10}\text{In}_{0.10}\text{Ga}_{0.80}\text{N}$  DQWs for the spike width  $d_s = 4$  nm and well width  $d_w = 8$  nm, 6 nm, 5 nm, 4 nm, 3 nm, and 2 nm.

To analyze the properties of doped systems, Fig. 14 presents the PL spectra at 2 K for the same system depicted in Fig. 12, and for spike and well widths fixed at 4 nm. The two-dimensional (2D) acceptor doping concentration is varied assuming values of  $N_{2D} = 2 \times 10^{12}\text{cm}^{-2}$ ,  $4 \times 10^{12}\text{cm}^{-2}$ , and  $8 \times 10^{12}\text{cm}^{-2}$ . The undoped system is also presented for comparison. One can observe a red-shift in energy up to  $N_{2D} = 4 \times 10^{12}\text{cm}^{-2}$ , and for  $N_{2D} = 8 \times 10^{12}\text{cm}^{-2}$  a blue-shift is seen. This behavior is due to the potential profile, which shows a bending that curves up for low concentrations, and curves down for high concentrations, no matter whether the total potential is attractive or repulsive. An attractive potential is observed up to  $4 \times 10^{12}\text{cm}^{-2}$ , so the levels are localized near the bottom of the wells, beyond that, the potential is repulsive, and one can expect larger transition energies.

The last issue to be addressed in DQWs is the strain. Fig. 15 presents the PL spectra at  $T = 2$  K for strained p-type doping  $\text{Al}_{0.60}\text{In}_{0.05}\text{Ga}_{0.35}\text{N}/\text{Al}_{0.10}\text{In}_{0.40}\text{Ga}_{0.50}\text{N}/\text{In}_{0.10}\text{Ga}_{0.90}\text{N}$  DQWs, in order to analyze the spike effects. The two-dimensional acceptor donor concentration was fixed in  $N_{2D} = 2 \times 10^{12}\text{cm}^{-2}$ . Fig. 15(a) presents the spectra for a fixed spike width  $d_s = 4$  nm and (b) for fixed well widths  $d_w = 4$  nm. One can observe in Fig. 15 (a) a red-shift in energy due to confinement effects as  $d_s$  increases. This behavior is opposite to the one seen in Fig. 15 (b), where a blue-shift in energy exists until  $d_w = 3$  nm, followed by a red shift, where a change from an interacting to an isolated well regime occurs. After  $d_s = 5$  nm, again a blue-shift in energy is observed, due to many body effects, which become more important than the spike width contribution to these systems. It is important to note that a different behavior is observed if compared with undoped systems. This is related to the charge distribution

inside the wells, with the Fermi level lying near the bottom of wells for thicker wells, contrary to what is observed for thin ones. Note that in this case the transition from interacting to isolated regime occurs in  $d_s = 4$  nm.

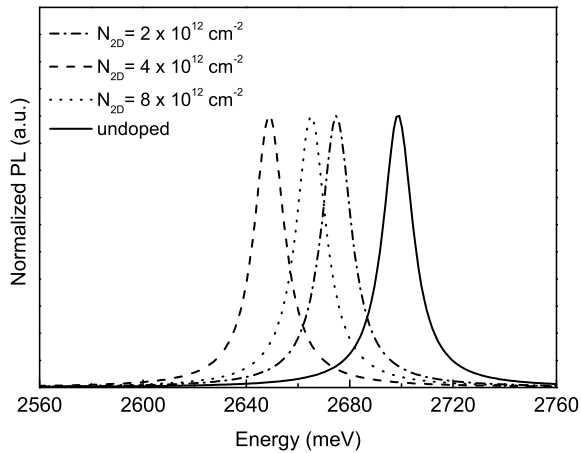
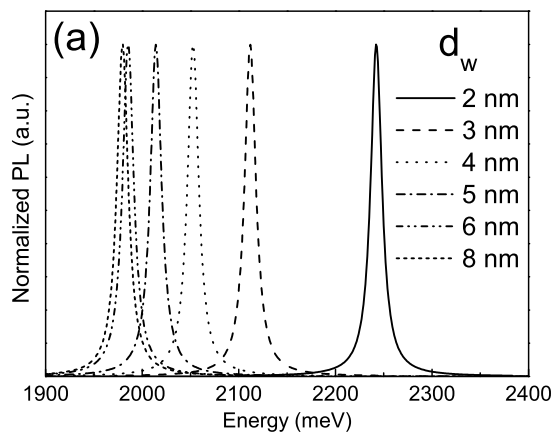


Fig. 14. Calculated PL spectra at  $T = 2$  K for  $p$ -doped  $c\text{-Al}_{0.25}\text{In}_{0.05}\text{Ga}_{0.70}\text{N}/\text{Al}_{0.08}\text{In}_{0.37}\text{Ga}_{0.55}\text{N}/\text{Al}_{0.10}\text{In}_{0.10}\text{Ga}_{0.80}\text{N}$  DQWs, for well and spike widths equal to 4 nm and doping  $N_{2D} = 2 \times 10^{12} \text{ cm}^{-2}$  (dashed-dot line),  $4 \times 10^{12} \text{ cm}^{-2}$  (dashed line),  $8 \times 10^{12} \text{ cm}^{-2}$  (dotted line), and undoped (solid line) for comparison.



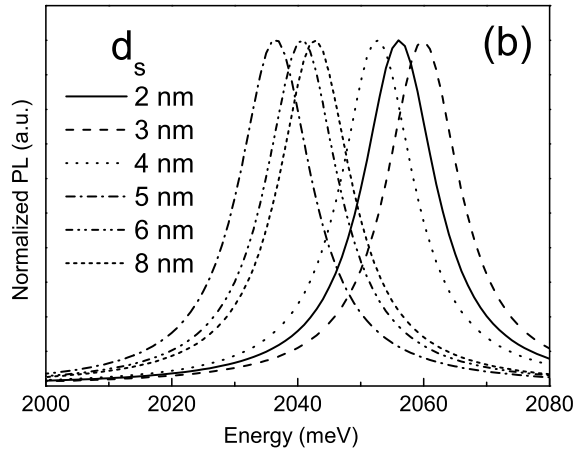


Fig. 15. Theoretical normalized PL spectra at 2 K for strained  $c\text{-Al}_{0.60}\text{In}_{0.05}\text{Ga}_{0.35}\text{N}/\text{Al}_{0.10}\text{In}_{0.40}\text{Ga}_{0.50}\text{N}/\text{In}_{0.10}\text{Ga}_{0.90}\text{N}$  DQWs, fully p-doped barrier with  $N_{2D} = 2 \times 10^{12} \text{ cm}^{-2}$ . The systems have (a) fixed  $d_s = 4 \text{ nm}$  and varying from  $d_w = 2 \text{ nm}$  to  $8 \text{ nm}$ , and (b) fixed  $d_w = 4 \text{ nm}$  and varying from  $d_s = 2 \text{ nm}$  to  $8 \text{ nm}$ .

## 6. Conclusions

In this chapter it was performed a detailed investigation of the theoretical luminescence and absorption spectra of strained undoped and doped  $c\text{-Al}_x\text{In}_{1-x-y}\text{Ga}_y\text{N}/\text{Al}_x\text{In}_{1-x-y}\text{Ga}_y\text{N}$  SLs and DQWs using a self-consistent resolution of the  $8 \times 8$  Kane Hamiltonian within the effective mass theory.

At first it was shown the feasibility of reaching emissions from red light to blue light regions by the correct combination of different quaternary alloys either in the well or in the barrier in undoped systems. When an external field is taken into account, the theoretical spectra present red shifts. A similar result could be obtained for the wurtzite phase of the structures, caused by the presence of the intrinsic piezoelectric fields. In such systems, these effects lead to a spatial segregation of the electron and hole charge distributions, causing a reduction in the light emission efficiency. For the cubic phase structures, as the piezoelectric fields are absent, the spatial segregation is smaller and therefore higher efficiency would be expected.

Analyzing the doped systems, it is pointed out that light emission arising from the recombination involving confined states in the wells has not a monotonic behavior when the doping concentration increases, even if it is always red shifted when compared to the undoped SLs. The main reason for this is the shape of the potential bending induced by the presence of a holes charge distribution inside the wells. The competition between the exchange-correlation potential and the Coulomb potential was shown to be the main reason for this behavior, since they define the total bending potential, attractive or repulsive, which affects directly the optical transitions. Again, for single QWs, it was shown that by choosing an appropriate set of alloy molar fractions and acceptor concentrations it is possible to achieve white light emission by combining the emission in three different regions of the spectra.

Regarding to different spatial arrangements, DQWs were analyzed. It was shown for p-doped  $c\text{-Al}_x\text{In}_{1-x-y}\text{Ga}_y\text{N}/\text{Al}_x\text{In}_{1-x-y}\text{Ga}_y\text{N}$  DQWs that the related PL spectra depict a different behavior depending on the spike and/or adjacent well layer widths. A change in the kind of regime from interacting wells to isolated non-interacting wells was demonstrated. Although not shown here, it is also possible to reach all wavelengths using the DQWs structures, as it was demonstrated for single QWs.

Another important conclusion that must be pointed out from the set of systems analyzed in the chapter is that the red region of electromagnetic spectrum can be reached through the quaternary alloys using less In content, as compared to the ternary InGaN alloy. From the experimental point of view this finding is fundamental, since the growth with higher In content is more difficult.

Finally, supported by the recent advances in the growth techniques, the analysis presented here intends to elucidate and guide the study of optical properties in semiconductor nitride systems, bringing new possibilities for experiments and, hopefully, novel proposals for the next generation of advanced optical devices.

## 7. Acknowledgments

The authors thank O. F. P. dos Santos of the Universidade Federal Rural de Pernambuco for the discussions and Prof. E. L. Piner of Texas State University for his suggestions. We also express our thanks to the support received from the Brazilian research financial agencies CNPq (grants nos 564.739/2010-3/NanoSemiCon, 303.880/2008-2/PQ, 470.998/2010-5/Univ, 472.312/2009-0/Univ 304936/2009-0/ PQ, 303578/ 2007-6/ PQ, 577.219/2008-1/JP), CAPES, FACEPE (grant no. 0553-1.05/10/APQ), and FAPESP. LS also acknowledges partial support from the Materials Science, Engineering and Commercialization Program of Texas State University.

## 8. References

- Ambacher, O. (1998). Growth and applications of Group III-nitrides. *Journal of Physics D: Applied Physics*, Vol. 31, No. 20, (October 1998) pp. 2653- 2710, ISSN 1361-6463
- As, D. J. (2009). Cubic group-III nitride-based nanostructures basics and applications in optoelectronics. *Microelectronics Journal*, Vol. 40, No. 2, (September 2008) pp. 204- 209, ISSN 0022-0248
- Enderlein, R.; Sipahi, G.; Scolfaro, L. M. R. & Leite, J. R. (1997). Density functional theory for holes in semiconductors. *Physical Review Letters*, Vol. 79, No. 19, (November 1997) pp. 3712-3715, ISSN 0031-9007
- Fernández-Garrido, S.; Redondo-Cubero, A.; Gago, R.; Bertram, F.; Luna, E.; Trampert, A.; Pereiro, J.; Muñoz, E. & Calleja, E. (2008). Effect of the growth temperature and the AlN mole fraction on In incorporation and properties of quaternary III-nitride layers grown by molecular beam epitaxy. *Journal Applied Physics*, Vol. 104, No. 8, (October 2010) pp. 083510-1 -083510-7, ISSN 0021-8979
- Fu, Y-K.; Jiang, R-H.; Lu, Y-H.; Chen, B-C.; Xuan, R.; Fang, Y-H.; Lin, C-F.; Su, Y-K. & Chen, J-F. (2011). The effect of trimethylgallium flows in the AlInGaN barrier on optoelectronic characteristics of near ultraviolet light-emitting diodes grown by atmospheric pressure metalorganic vapor phase epitaxy. *Applied Physics Letters*, Vol. 98, No. 12, (March 2011) pp. 121115-1 -121115-3, ISSN 0003-6951

- Hirayama, H. (2005). Quaternary InAlGa<sub>N</sub>-based high-efficiency ultraviolet light-emitting diodes. *Journal of Applied Physics*, Vol. 97, No. 9, (April 2005) pp. 091101-1-091101-19, ISSN 0021-8979
- Hirayama, H.; Noguchi, N. & Kamata, N. (2010). 222nm Deep-Ultraviolet AlGa<sub>N</sub> Quantum Well Light-Emitting Diode with Vertical Emission Properties. *Applied Physics Express*, Vol. 3, No. 3, (March 2010) pp. 032102-1-032102-3, ISSN 1882-0778
- Kemper, R. M.; Weini, M.; Mietze, C.; Härbelen, M. H.; Schupp, T.; Tshucmak, E.; Lindner, J. K. N., Lischka, K. & As, D. J. (2011). Growth of cubic Ga<sub>N</sub> on nano-patterned 3C-SiC/Si(001)substrates. *Journal Crystal Growth*, Vol. 323, No. 1, (May 2011) pp. 84-87, ISSN 0022-0248
- Kim, K. H.; Li, S.; Jin, S. X.; Lin, J. Y. & Jianga, H. X. (2003). III-nitride ultraviolet light-emitting diodes with delta doping. *Applied Physics Letters*, Vol. 83, No. 3, (July 2003) pp. 566-568, ISSN 0003-6951
- Knauer, A.; Wenzel, H.; Kolbe, T.; Einfeldt, S.; Weyers, M.; Kneissl, M. & Tränkle, G. (2008). Effect of the barrier composition on the polarization fields in near UV InGa<sub>N</sub> light emitting diodes. *Applied Physics Letters*, Vol. 92, No. 19, (may 2008) pp. 191912-1-191912-3, ISSN 0003-6951
- Kyono, T.; Hirayama, H.; Akita, K.; Nakamura, T.; Adachi, M. & Ando, K. (2006). Influence of residual oxygen impurity in quaternary InAlGa<sub>N</sub> multiple-quantum-well active layers on emission efficiency of ultraviolet light-emitting diodes on Ga<sub>N</sub> substrates. *Journal Applied Physics*, Vol. 99, No. 11, (June 2006) pp. 114509-1 -114509-7, ISSN 0021-8979
- Kohler, U.; As, D. J.; Potthast, S.; Khartchenko, A.; Lischka, K.; Noriega, O. C.; Meneses, E. A.; Tabata, A.; Rodrigues, S. C. P.; Scolfaro, L. M. R.; Sipahi, G. M. & Leite, J. R. (2002). Optical Characterization of Cubic AlGa<sub>N</sub>/Ga<sub>N</sub> Quantum Wells. *physica statu solid (a)*, Vol. 192, No. 1, (July 2002) pp. 129-134, ISSN 1862-6319
- Liu, J.; Zhang, Y.; Lochner, Z.; Kim, S-S.; Kim, H-S.; Ryou, J-H.; Shen, S-C.; Yoder, P. D.; Dupuis, R. D.; Wei, Q. Y.; Sun, K. W.; Fisher, A. M. & Ponce, F. A. (2011). Performance characteristics of InAlGa<sub>N</sub> laser diodes depending on electron blocking layer and wave guiding layer design grownby metalorganic chemical vapor deposition. *Journal of Crystal Growth*, Vol. 315, No. 1, (October 2010) pp. 272-277, ISSN 0021-8979
- Marques, M; Teles, L. K.; Scolfaro, L. M. R.; Leite, J. R.; Furthmüller, J. & Bechstedt, F. (2003). Lattice parameter and energy band gap of cubic Al<sub>x</sub>Ga<sub>y</sub>In<sub>1-x-y</sub>N quaternary alloys. *Applied Physics Letters*, Vol. 83, No. 5, (March 2003) pp. 890-893, ISSN 0003-6951
- Nakamura, S; Senoh, M.; Iwasa, N. & Nagahama, S. (1995). High-power InGa<sub>N</sub> single-quantum-well-structure blue and violet light-emitting diodes. *Applied Physics Letters*, Vol. 67, No. 13, (July 1995) pp. 1868-1870, ISSN 0003-6951
- Nakamura, S.; Pearton, S. & Fasol, G. (2000). *The Blue Laser Diode: the complete story*, Springer, ISBN 3-540-66505-6, Berlin.
- Park, S-H; Ahn, D. & Kim, J-W. (2008). Optical gain in InGa<sub>N</sub>/InGaAlN quantum well structures with zero internal field. *Applied Physics Letters*, Vol. 92, No. 17, (May 2008) pp. 171115-1 -171115-3, ISSN 0003-6951
- Ramos, L. E.; Teles, L. K.; Scolfaro, L. M. R.; Castineira, J. L. P.; Rosa, A. L. & Leite, J.R. (2001). Structural, electronic, and effective-mass properties of silicon and zinc-blende group-III nitride semiconductor compounds. *Physical Review B*, Vol. 63, No. 16, (April 2001) pp. 165210-1 -165210-10, ISSN 1098-0121



- Roberts, J. C.; McIntosh, F. G.; Aumer, M. E.; Piner, E. L.; Joshkin, V. A.; Liu, S.; El-Masry, N. A. & Bedair, S. M. (1996). Stacked InGaN/AlGaN Double Heterostructures. *1996 MRS Proceedings*, Vol. 449, No. 1, (December 1996) pp. 1161-1165, ISSN 1946-4274
- Rodrigues, S. C. P.; Scolfaro, L. M. R.; Leite, J. R. & Sipahi, G. M. (2000). Valence band structure of cubic AlGaN/GaN superlattices. *Applied Physics Letters*, Vol. 76, No. 8, (December 1999) pp. 1015-1017, ISSN 0003-6951
- Rodrigues, S. C. P.; Sipahi, G.; Scolfaro, L. M. R. & Leite, J. R. (2001). Exchange-correlation effects on the hole miniband structure and confinement potential in zincblende AlGaN/GaN superlattices. *Journal of Physics. Condensed Matter*, Vol. 13, No. 14, (April 2001) pp. 3381-3387, ISSN 0953-8984
- Rodrigues, S. C. P.; Sipahi, G.; Scolfaro, L. M. R. & Leite, J. R. (2002). Hole charge localization and band structures of p-doped GaN/InGaN and GaAs/InGaAs semiconductor heterostructures. *Journal of Physics. Condensed Matter*, Vol. 14, No. 23, (May 2002) pp. 5813-5827, ISSN 0953-8984
- Rodrigues, S. C. P.; Sipahi, G. M. & da Silva Jr, E. F. (2005). Optical and electronic properties of AlInGaN/InGaN superlattices. *Microelectronics Journal*, Vol. 36, No. 3-6, (March 2005) pp. 434-437, ISSN 0022-0248
- Rodrigues, S. C. P.; d'Eurydice, M. N.; Sipahi, G. M. & da Silva Jr, E. F. (2005). Design of InGaN/AlInGaN superlattices for white-light device applications. *Microelectronics Journal*, Vol. 36, No. 3-6, (March 2005) pp. 1002-1005, ISSN 0022-0248
- Rodrigues, S. C. P.; d'Eurydice, M. N.; Sipahi, G. M.; Scolfaro, L. M. R. & da Silva Jr, E. F. (2007). White light emission from p-doped quaternary (InGaAl)N-based superlattices: theoretical calculations for the cubic phase. *Journal Applied Physics*, Vol. 101, No. 11, (June 2007) pp. 113706-113706-6, ISSN 0021-8979
- Rodrigues, S. C. P.; dos Santos, O. F. P.; Scolfaro, L. M. R.; Sipahi, G. M. & da Silva Jr, E. F. (2008). Luminescence Studies on Nitride Quaternary Alloys Double Quantum Wells. *Applied Surface Science*, Vol. 254, No. 23, (February 2008) pp. 7790-7793, ISSN 0169-4332
- Schörmann, J.; As, D. J.; Lischka, K.; Schley, P.; Goldhahn, R.; Li, S. F.; Lffler, W.; Hetterich, M. & Kalt, H. (2006). Molecular beam epitaxy of phase pure cubic InN. *Applied Physics Letters*, Vol. 89, No. 26, (December 2006) pp. 261903-261905, ISSN 0003-6951
- Schörmann, J.; Potthast, S.; As, D. J. & Lischka, K. (2007). Molecular beam epitaxy of phase pure cubic InN. *Applied Physics Letters*, Vol. 90, No. 4, (January 2007) pp. 041918-1-041918-3, ISSN 0003-6951
- Scolfaro, L. M. R.; Teles, L. K.; Marques, M.; Ferreira, L. G. & Leite, J. R. (2004). Phase Separation and Ordering in Cubic Ternary and Quaternary Nitride Alloys, In: *Optoelectronic Devices: III-Nitrides*, M. Razegui, M. Henini, (Ed.), pp. 455-478, Elsevier, ISBN 0-08-044426-1, Oxford
- Sipahi, G. M.; Enderlein, R.; Scolfaro, L. M. R. & Leite, J. R. (1996). Band structure of holes in p-type  $\delta$ -doping quantum wells and superlattices. *Physical Review B*, Vol. 53, No. 15, (April 1996) pp. 9930-9942, ISSN 1098-0121
- Sipahi, G. M.; Enderlein, R.; Scolfaro, L. M. R.; Leite, J. R. & Levine, A. (1998). Theory of luminescence spectra from  $\delta$ -doping structures: application to GaAs. *Physical Review B*, Vol. 57, No., (April 1998) pp. 9168-9178, ISSN 1098-0121
- Suihkonen, S.; Svensk, O.; Törmä, P. T.; Ali, M.; Sopane, M.; Lipsanen, H.; Odnoblyudo, M. A. & Bougrov, V. E. (2008). MOVPE growth and characterization of InAlGaN films and InGaN/InAlGaN MQW structures. *Journal of Crystal Growth*, Vol. 310, No. 7-9, (November 2007) pp. 1777-1780, ISSN 0022-0248

- Tabata, A.; Teles, L. K.; Scolfaro, L. M. R.; Leite, J. R.; Frey, T.; Kharchenko, A.; As, D. J.; Schikora, D.; Lischka, K.; Furthmüller, J. & Bechstedt, F. (2002). Phase separation suppression in InGaN epitaxial layers due to biaxial strain. *Applied Physics Letters*, Vol. 80, No. 5, (November 2001) pp. 769-771, ISSN 0003-6951
- Tschumak, E.; Granzner, R.; Lindner, J. K. N.; Schwierz, F.; Lischka, K.; Nagasawa, H.; Abe, M. & As, D. J. (2008). Nonpolar cubic AlGaIn/GaN heterojunction field-effect transistor on Ar<sup>+</sup> implanted 3C-SiC (001). *Applied Physics Letters*, Vol. 96, No. 25, (June 2010) pp. 253501-1 - 253501-3, ISSN 0003-6951
- Xiao D.; Kim, K. W.; Bedair, S. M. & Zavada, J. M. (2004). Design of white light-emitting diodes using InGaIn/AlInGaIn quantum-well structures. *Applied Physics Letters*, Vol. 84, No. 5, (February 2004) pp. 672-674, ISSN 0003-6951
- Xie, J.; Leach, J. H.; Ni, X.; Wu, M.; Shimada, R.; Özgür, Ü. & Morkoç, H.; (2007). Electron mobility in InGaIn channel heterostructure field effect transistor structures with different barriers. *Applied Physics Letters*, Vol. 91, No. 26, (November 2007) pp. 262102-1 -262102-3, ISSN 0003-6951
- Zado, A.; Tschumak, E.; Gerlach, J. W.; Lischka, K. & As, D. J. (2011). Carbon as an acceptor in cubic GaN/3CSiC. *Journal of Crystal Growth*, Vol. 323, No. 1, (may 2011) pp. 88 -90, ISSN 0022-0248
- Zhmakin, A. I. (2011). Enhancement of light extraction from light emitting diodes *Physics Reports*, Vol. 498, No. 4-5, (November 2010) pp. 189-241, ISSN 0370-1573
- Zhang, L.; Ding, K.; Liu, N. X.; Wei, T. B.; Ji, X. L.; Ma, P.; Yan, J. C.; Wang, J. X.; Zeng, Y. P. & Li, J. M. (2011). Theoretical study of polarization-doped GaN-based light-emitting diodes. *Applied Physics Letters*, Vol. 98, No. 10, (March 2011) pp. 101110-1 -101110-3, ISSN 0003-6951
- Zhu, D.; Kappers, M. J.; McAleese, C.; Graham, D. M.; Chabrol, G. R.; Hylton, N.P.; Dawson, P.; Thrush, C. J. & Humphreys, C. J. (2007). Optical and micro-structural properties of high photoluminescence efficiency InGaIn/AlInGaIn quantum well structures. *Journal of Crystal Growth*, Vol. 298, No. 1, (November 2007) pp. 504 -507, ISSN 0022-0248
- Wang, F.; Li, S-S.; Xia, J-B.; Jiang, H. X.; Lin, J. Y.; Li, J. & Wei, S-H.; (2007). Effects of the wave function localization in AlInGaIn quaternary alloys. *Applied Physics Letters*, Vol. 91, No. 6, (August 2007) pp. 061125-1 - 061125-3, ISSN 0003-6951

# Air Exposure Improvement of Optical Properties of Hydrogenated Nanostructured Silicon Thin Films for Optoelectronic Application

Atif Mossad Ali<sup>1,2</sup>

<sup>1</sup>*Department of Physics, Faculty of Science, King Khalid University,*

<sup>2</sup>*Department of Physics, Faculty of Science, Assiut University,*

<sup>1</sup>*Saudi Arabia*

<sup>2</sup>*Egypt*

## 1. Introduction

Silicon is the desired material, because silicon optoelectronics will open the door to faster data transfer and higher integration densities at very low cost. Silicon microphotronics has boomed these last years. In addition, silicon, the most important elemental semiconductor, crystallizes in the diamond structure. The diamond lattice consists of two interpenetrating face centered cubic Bravais lattices displaced along the body diagonal of the cubic cell by one quarter of the length of the diagonal.

Nowadays, hydrogenated nanostructured silicon with grains in nanometer size has attracted more attention in optoelectronic and microelectronic devices for its superior properties (Kanicki, 1991, 1992; Canham, 1990; Lin et al., 2006, Funde et al., 2008, Cheng et al., 2008). Moreover, great efforts have been devoted to photoluminescence of silicon-based materials for developing integrated optoelectronics with the standard silicon very-large-scale integration technology (Canham, 1990). For example, to embed the nanometer-sized silicon within an insulating host will enhance the quantum confinement effect, which spreads the band gap of silicon for photoluminescence emission (Brongersma et al., 1998). During the last few years, various methods were proposed to embed nanometersized silicon, such as implantation of silicon into silicon dioxide (Brongersma et al., 1998), Si/SiO<sub>2</sub> superlattice structure (Photopoulos et al., 2000; Benyoucef, & Kuball, 2001), thermal-oxidized nanocrystalline silicon (Jeon et al., 2005). At the same time, these techniques suffer from complicated and high temperature process, thus unsuitable for developing low cost array or flexible optoelectronic nanocrystalline silicon devices.

Nanocrystalline silicon has been synthesized by several techniques such as microwave or laser induced decomposition of silane (SiH<sub>4</sub>) like precursors (Takagi et al. 1990; Ehbrecht et al., 1995), pulsed-laser deposition of silicon (Werwa et al., 1994), low pressure chemical vapor deposition (Nakajima et al., 1996), electrochemical etching of silicon wafers (Canham, 1990; Belomoin et al., 2002), ion implantation of Si<sup>+</sup> (Iwayama et al., 1994), cosputtering of silicon and silicon dioxide (Zhang et al., 1995), and plasma-enhanced chemical vapor deposition (Inokuma et al., 1998).

On the other hand, for the visible luminescence properties of nanocrystalline silicon, control of the size distribution and surface condition of nanocrystalline silicon with reproducibility is critical to the sensitive light emitting properties. The photoluminescence is highly dependent on the discrete size of silicon nanocrystals and also changes with different surface passivation. For the decomposition, pulsed-laser deposition, and low pressure chemical vapor deposition methods, both surface passivation and deposition of nanocrystalline silicon thin films without agglomeration need further investigations. For the electrochemical etching method, preparation condition dependence and degradation of the photoluminescence are major concerns. For the ion implantation method, multiple implantation at different energies is required to create a thick layer of nanocrystalline silicon. Compared with other fabrication methods, plasma-enhanced chemical vapor deposition has been extensively utilized in the industry and is compatible with ultra-large scale integration technology. Nanocrystalline silicon thin films formed by plasma-enhanced chemical vapor deposition have shown strong and stable photoluminescence, robust structure, and good surface passivation. The characteristics of nanocrystalline silicon films deposited by plasma-enhanced chemical vapor deposition can be finely tuned through silicon concentration in the films as well as post-deposition annealing and oxidation.

Study of the influence of the different deposition parameters on the growth of the material is therefore important both for newer device applications and also for understanding the basic physics of the growth process of thin films. Several deposition parameters, such as plasma energy and density, substrate temperature, rf power, gas flow rate, deposition pressure and dilution of the source gas (silane) with other gases (argon, hydrogen, or helium) will strongly influence the structure and properties of the grown nanocrystalline silicon thin films. The effect of Argon dilution on the structure of hydrogenated amorphous and microcrystalline silicon films deposited by rf glow discharge decomposition of silane has been demonstrated (Das et al. 1996; Chaudhuri & Das, 1995; Wang et al., 2003). A detailed experimental study has been reported on the effect of the dilution of silane with hydrogen on optical properties of hydrogenated amorphous silicon prepared by plasma deposition as function of the gas-volume ratio and the substrate temperature (Yamaguchi & Moigaki, 1999). However, most features of the hydrogenated amorphous silicon network structure are defined at the time of growth and therefore the optical and electric properties depend on the details of the deposition process. In the present work, we report the growth and characterization of hydrogenated nanostructured silicon thin films deposited by plasma-enhanced chemical vapor deposition technique. The large numbers of atomic hydrogen are necessary for passivation of dangling bonds and reconstruction of Si-Si bonds to improve film quality. Also, it has been known that the deposition of nanocrystalline silicon is due to the selective etching activity of hydrogen atoms towards the amorphous phase with respect to the crystalline structure. Thus, the role of hydrogen is to promote the nucleation and the crystallization of hydrogenated amorphous silicon at low temperature with desired grain size (Solomon et al., 1993). The use of  $\text{SiF}_4$  has also been successfully employed to obtain more orderly materials since fluorine atoms, produced in  $\text{SiF}_4$  plasma decomposition, are effective etchant species (Mohri et al., 1991). These facts were considered in choosing the feed gases. In the study of Lim et al. (Lim et al., 1996), the deposition temperature was decreased until 220 °C. Thus, the grain size decreased until 20 nm. In the present contribution, the deposition temperature was further decreased up to 60 °C with high  $\text{H}_2$  dilution to further decrease the grain size. The aim of this work is to get more insight into the effect of deposition temperature, air exposure and hydrogen flow rate ( $[\text{H}_2]$ ) on the optical and structural properties of hydrogenated nanostructured silicon thin films, and also the possibility to enhance the optical properties of hydrogenated nanostructured silicon

thin film. To our knowledge, the effect of air exposure on the optical and structural properties of hydrogenated nanostructured silicon thin films is not studied before.

## 2. Experimental method

The hydrogenated nanostructured silicon films were deposited by radio frequency (rf) glow-discharge (at 13.56 MHz) decomposition of a  $\text{SiH}_4/\text{SiF}_4$  (+He)/ $\text{H}_2$  mixtures in a hot-wall type fused quartz reactor with 50 mm in diameter, employing the inductive coupling of rf power, which were inserted into an electric furnace. The substrates were loaded horizontally on a quartz boat with its surface parallel to the axis of the reactor. The remarkable feature of this deposition system is that the samples are exposed to the plasma (the growing surface is bombarded with ions). When plasma-enhanced chemical vapor deposition hydrogenated nanostructured silicon films were deposited using this deposition system, it has been reported that the resultant hydrogenated nanostructured silicon films have the following two essential effects as the rf power is increased: An enhancement in the degree of preferential orientation of grains in the films an improvement in the flatness on the film surface (Hasegawa et al. 1990). Such results should be caused by an effect of ion bombardments on the film surface during growth (Hasegawa et al. 1990), and such an effect may also act to lower deposition temperature for preparing high-quality hydrogenated nanostructured silicon films as well as an effect due to fluorine chemistry. The deposition pressure was adjusted by throttling the cross section in the inlet of the pump, and was measured using an absolute pressure meter. The details of the plasma-enhanced chemical vapor deposition system used have been described elsewhere (Hasegawa et al. 1983). Just prior to the deposition of hydrogenated nanostructured silicon films, the substrates were sequentially cleaned by rinsing them for 30 min in acetone and then in ethyl alcohol using an ultrasonic syringe. The samples were more cleaned by exposing them to the  $\text{N}_2$  and then  $\text{H}_2$  plasma at 90 W for 20 min. Then hydrogenated nanostructured silicon films were deposited at the different deposition temperature with the dynamic pressure of 0.3 Torr for every deposition. The rf power supply of 20 W was used. The gas flow rates were  $[\text{SiH}_4] = 0.6$  sccm,  $[\text{SiF}_4] = 0.38$  sccm, which was diluted with 95 % helium (He: 95 %,  $\text{SiF}_4$ : 5 %), and  $[\text{H}_2] = 20, 30$  and 46 sccm. The deposition temperature was varied from 60 °C to 300 °C.

The structural properties of the nanocrystalline silicon films were investigated by means of X-ray diffraction (SHIMADZU XD-D1) employing a diffractometer with the slit width of 0.1 mm, set at the front of the detector. The average grain size,  $\langle \delta \rangle$ , in the depth direction was estimated from the half-width value of the X-ray spectrum by means of the Scherrer formula (Cohen, 1978).

The crystallinity was also characterized by Raman scattering measurements. The Raman spectra consisted of a narrow line at 520  $\text{cm}^{-1}$  due to a crystalline phase and a broad line around 480  $\text{cm}^{-1}$  due to an amorphous phase. Since the third component between 480 and 520  $\text{cm}^{-1}$  due to very small crystallites was relatively weak. Further, the surface morphology of the films was investigated by means of atomic force microscopy (Park scientific instruments, AUTOPROBE GP/M5).

Photoluminescence was analyzed using a Jobin Yvon RAMANOR HG 2S spectrometer coupled with a cold photo-multiplier tube (Hamamatsu Photonics R649S). The 488 nm Ar-ion laser with power ranging from 30 to 50 mW was used as the photoluminescence excitation source. The infrared vibration spectra, using a Fourier-transform spectrometer (JASCO FT/IR-610), were measured at a normal light incident and under vacuum, using a bare silicon wafer as reference in the range of 400 - 4000  $\text{cm}^{-1}$ . The optical transmission spectra were measured using an UV/VIS/NIR spectrophotometer (JASCO V-570).

### 3. Film structure and morphology

In order to further improve properties of hydrogenated nanostructured silicon thin films and performances of related devices, it is necessary to understand microstructure features of the films in detail. As a powerful technique, Raman spectroscopy has been extensively adopted to investigate the low-dimension structure materials because it is convenient and inexpensive and does not damage samples (Wei et al., 2007). Fig. 1 shows a typical Raman spectra from hydrogenated nanostructured silicon thin films deposited with different deposition temperature, which can be identified as two regions corresponding to two kinds of phonon modes, i.e., a transverse optical ( $TO_1$ ) branch with a peak at  $480\text{ cm}^{-1}$  from the amorphous silicon contribution and another transverse optical ( $TO_2$ ) mode at around  $520\text{ cm}^{-1}$  from the contribution of silicon nanocrystals. As revealed in this diagram, the films with deposition temperature higher than  $60\text{ }^\circ\text{C}$  exhibit a narrow peak at around  $520\text{ cm}^{-1}$ , which is due to the crystalline phase. In addition, for the film deposited at a low deposition temperature of  $60\text{ }^\circ\text{C}$  exhibits the broad peak at  $480\text{ cm}^{-1}$  due to an amorphous phase. Thus, no crystallization was observed at deposition temperature =  $60\text{ }^\circ\text{C}$ , which may be caused by a decrease in the rate of the surface migration of the adsorbates caused by elimination of hydrogen atoms on the growing surface of the film. In addition, the peak position of  $TO_2$  increases with increasing the deposition temperature. Such Raman peak shifts would be related to a change in the stress of the films. In other words, the redshift of  $TO_2$  mode peak should be considered as the total contribution from tensile strain effect of silicon nanocrystals embedded in hydrogenated nanostructured silicon thin films. Where, a positive Raman-peak shift can be interpreted as indicating an increase in the compressive stress or a decrease in the tensile stress.

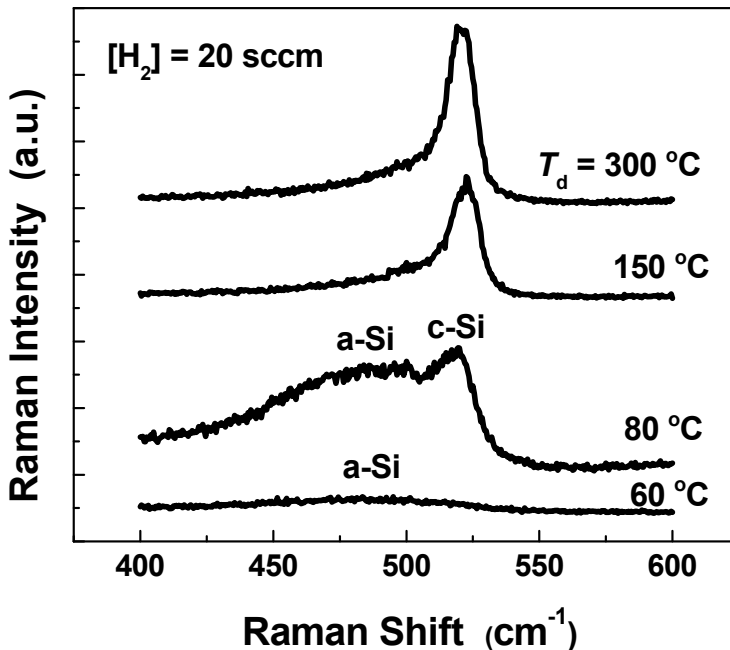


Fig. 1. Raman spectra for hydrogenated nanostructured silicon thin films deposited at different temperature,  $T_d$

Fig. 2 shows the (110) average grain size obtained from the  $\langle 110 \rangle$  x-ray diffraction spectra, for as deposited films (closed triangles) and exposed to air for two months films (closed circles), respectively, as a function of deposition temperature. As shown in Fig. 2, with decreasing deposition temperature the average grain size,  $\langle \delta \rangle$ , decreases. We can also see the effect of air exposure. When the time of air exposure increases, as shown in this diagram, it is found that the  $\langle \delta \rangle$  values decrease. It is clear that the positive shift of Raman-peak with deposition temperature is in good agreement with the increase of grain size with deposition temperature. In other words, according to a phonon confinement effect, the upshift of phonon peak is due to the increase of the hydrogenated nanostructured silicon grains size.

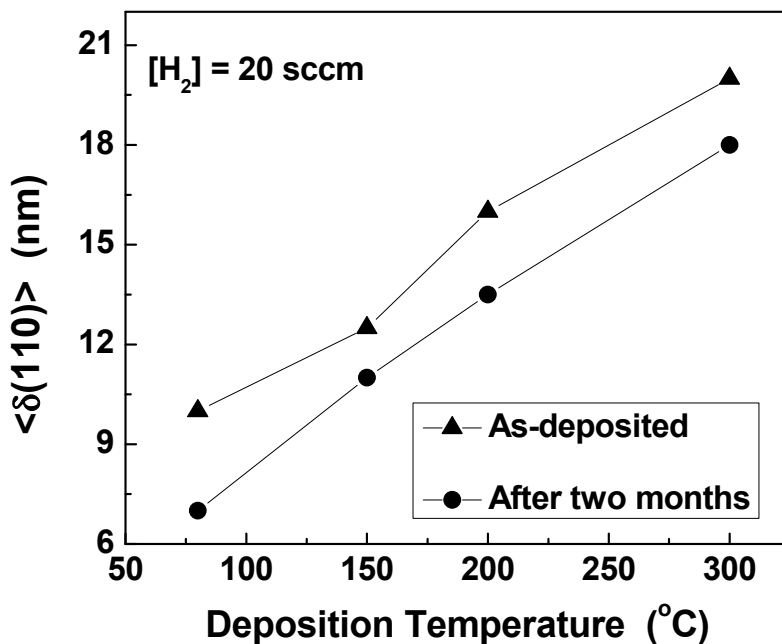


Fig. 2. Average grain size,  $\langle \delta(110) \rangle$  obtained from  $\langle 110 \rangle$  X-ray diffraction spectra as a function of deposition temperature, for as deposited films (closed triangles) and exposed films to air for two months (closed circles)

For growth of crystallites in hydrogenated nanostructured silicon thin films, SiH-related adsorbates responsible for the film growth must move on the growing surface until the adsorbates find the lattice sites for forming the crystallites with a given texture. According to the model proposed by Matsuda (Matsuda, 1983), high deposition temperature conditions should decrease the surface migration rate for eliminating the crystalline phases from films. However, as seen in Fig. 2, small grains grown in the films with deposition temperature higher than 60  $^{\circ}\text{C}$ . Furthermore, the density of SiH-related bonds monotonically decreases with deposition temperature, as shown later. These results suggest that an increase in deposition temperature causes an increase in the surface migration rate, in contrast with the model proposed by Matsuda (Matsuda, 1983). Thus,

we can obtain silicon films including nanometer-sized crystallites by decreasing deposition temperature, as seen in Fig. 2, which have attracted increased interest as optoelectronic materials. This is because the decrease in the deposition temperature will suppress the surface migration of the adsorbates as precursors for creating a crystalline phase as stated above.

The surface morphology of the thin films prepared with different deposition temperature (Figs. 3a and 3b) and the time of air exposure (Figs. 3b and 3c) has been measured by atomic force microscopy, as shown in Fig. 3. It can be seen clearly from Fig. 3a that the surface is almost flat corresponds to the amorphous tissue in good agreement with the result from Raman data (Fig. 1). On the other hand, it can be seen from Fig. 3b and 3c that the shape of the grains on the surface is spherical. In addition, the nanocrystallites of the silicon are distributed nearly uniform over the surface and hence suitable for integration in device structure. It is therefore expected that grown thin films could be used as protective coatings in device. The average grain size values estimated from atomic force microscopy data in Fig. 3b are larger than that in Fig. 3c, in good agreement with that calculated from the Scherrer's formula (Fig. 2).

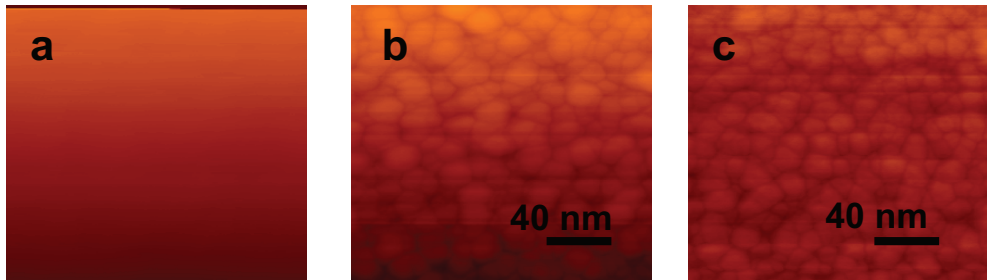


Fig. 3. The atomic force microscopy (AFM) pictures of deposited silicon thin films at  $[H_2] = 20$  sccm. (a) The AFM of sample deposited at deposition temperature ( $T_d$ ) of 60 °C. (b) The AFM of sample deposited at  $T_d$  of 150 °C before air exposure (as-deposited). (c) The AFM of sample deposited at  $T_d$  of 150 °C after two months air exposure

It is well known that when polycrystalline silicon or hydrogenated nanostructured silicon is used as a gate electrode or an interconnection material in integrated circuits, the undesirable oxidation results in a limitation of its conductivity and finally can degrade circuit performance. Furthermore, the grain boundaries in the polycrystalline silicon or hydrogenated nanostructured silicon, which has disordered structures including weak bonds, are expected to oxidize more rapidly than the inside of the grains with stable structure. By using Fourier-transform infrared spectroscopy measurement, we investigated the stability and the oxidation rates of some selected samples with different structures. To investigate the oxidation rates of these films we measured them again after two months. Fig. 4 reports the Fourier-transform infrared transmission spectra of the hydrogenated nanostructured silicon films deposited at different deposition temperature, Fig. 4a for as deposited films and Fig. 4b as the results after air exposure for two months. Firstly, considering the virgin (as deposited) samples (Fig. 4a), the spectra observed at around 650  $cm^{-1}$  and 950-980  $cm^{-1}$  are assigned to the rocking/wagging and bending vibration



modes of  $(\text{Si}_3)\text{-SiH}$  bonds, respectively (Kroll et al., 1996). The stretching mode of Si-F vibration is also located at  $800\text{-}900\text{ cm}^{-1}$ .

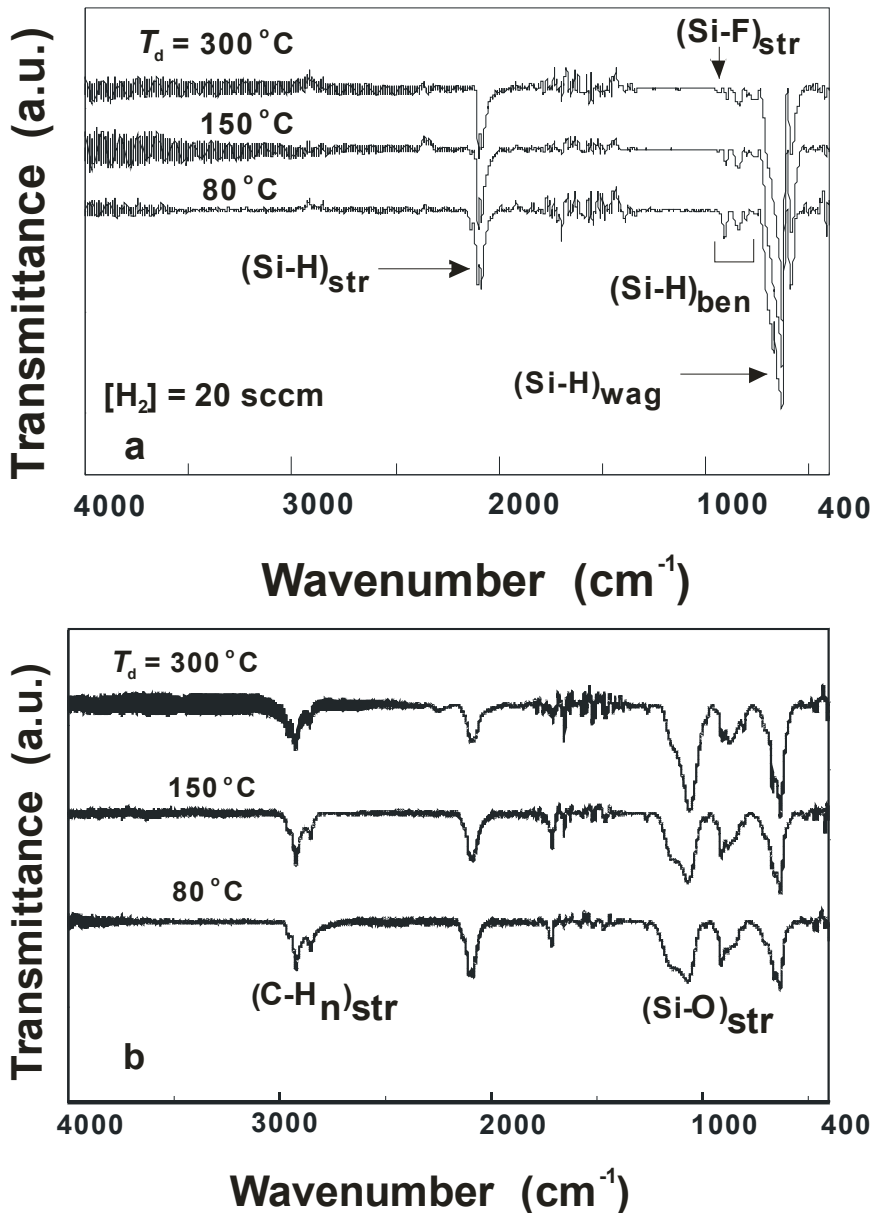


Fig. 4. Infrared transmittance spectra for hydrogenated nanostructured silicon thin films with different deposition temperature ( $T_d$ ) values. (a) As-deposited and (b) After two months air exposure

The peak at  $2100\text{ cm}^{-1}$  is assigned to the dihydride,  $((\text{Si}_2)\text{-SiH}_2)$  (Itoh et al., 2000), chain structure in the grain boundaries, or gathered  $(\text{Si}_3)\text{-SiH}$  bonds on the surface of a large void (Street, 1991), in which silicon dangling bonds are included and makes a porous structure. The intensity of the spectra at around  $2100\text{ cm}^{-1}$  is likely to decrease with increasing deposition temperature. So, the hydrogen content decreases with increasing deposition temperature. The hydrogen atoms in the hydrogenated nanostructured silicon thin films are suggested to reside mostly in the grain boundary region. On the other hand, we can see the films after two months air exposure exhibit a more oxidation (see Fig. 4b). The spectra observed at around  $1100\text{ cm}^{-1}$  and  $2700\text{-}3000\text{ cm}^{-1}$  are assigned to the stretching mode of Si-O-Si vibration and (CH) stretching, respectively (San Andre's et al., 2003). The oxygen absorption peak increases abruptly (see Fig. 4b). The presence of oxygen in the hydrogenated nanostructured silicon thin films is probably due to the oxidation at the grain boundaries, that is why  $\langle\delta\rangle$  values decrease in the films exposed to air for two months, as seen in Fig. 2 (closed circles).

A comparison between the virgin (as deposited) samples, corresponding to Fig. 4a, and those measured after two months, corresponding to 4b, shows a reduction in the  $(\text{Si}_3)\text{-SiH}$ -related peaks at  $2100$  and  $630\text{ cm}^{-1}$  and leads to an increase in the Si-O-Si vibration at  $1064\text{ cm}^{-1}$  after two months. For interpreting an increase in Si-O-Si peaks for samples measured after air exposure, we could consider the following assumption: The oxygen atoms can be replaced with hydrogen atoms on the surface of void structure in the grain boundaries or those in amorphous-like regions between the grains. Then, we assume that some of the oxygen atoms, supplied from  $\text{O}_2$  in the air, react with the SiH bonds and leaving  $\text{H}_2\text{O}$  or  $\text{H}_2$  behind.

## 4. Optical properties

### 4.1 Photoluminescence

The photoluminescence spectra are plotted in Fig. 5, 5a as deposited and 5b exposed to air for two months, respectively, as a function of photon energy for various films. They exhibit two separated photoluminescence bands: One is a relatively strong photoluminescence band with peak energy at around  $1.75\text{-}1.78\text{ eV}$  ( $708\text{-}696\text{ nm}$ ) and the other is a weak band at around  $2.1\text{-}2.3\text{ eV}$  ( $590\text{-}539\text{ nm}$ ). Both of these peaks are at energies above the band gap energy for crystalline silicon ( $1.12\text{ eV}$  at room temperature) which has an indirect band gap and is also not expected to luminescence in the visible range. In addition, Fig. 5 shows the dependence of photoluminescence spectrum on the deposition temperature and the time of air exposure. As the deposition temperature decreases and the time of air exposure increases the photoluminescence intensity and photoluminescence peak energy values increase, i.e., photoluminescence improved with air exposure. It is noted that the photoluminescence spectra from this nanocrystalline silicon were very broad, and that as the nanocrystal size was reduced, photoluminescence broadening accompanied photoluminescence blue shift. The width of the observed photoluminescence could be explained by the distributions of sizes in our hydrogenated nanostructured silicon, and therefore of energy gaps. As seen in Figs. 2, 4 and 5, the increase in the photoluminescence intensity and the peak energy with decreasing deposition temperature and increase the time of air exposure is found to correspond well with a decrease in  $\langle\delta\rangle$  (see Fig. 2 and an increase in the intensities of the  $2100\text{-cm}^{-1}$ -infrared-absorption bands (see Fig. 4a and  $1100\text{-cm}^{-1}$ -infrared-absorption bands (see Fig.4b).

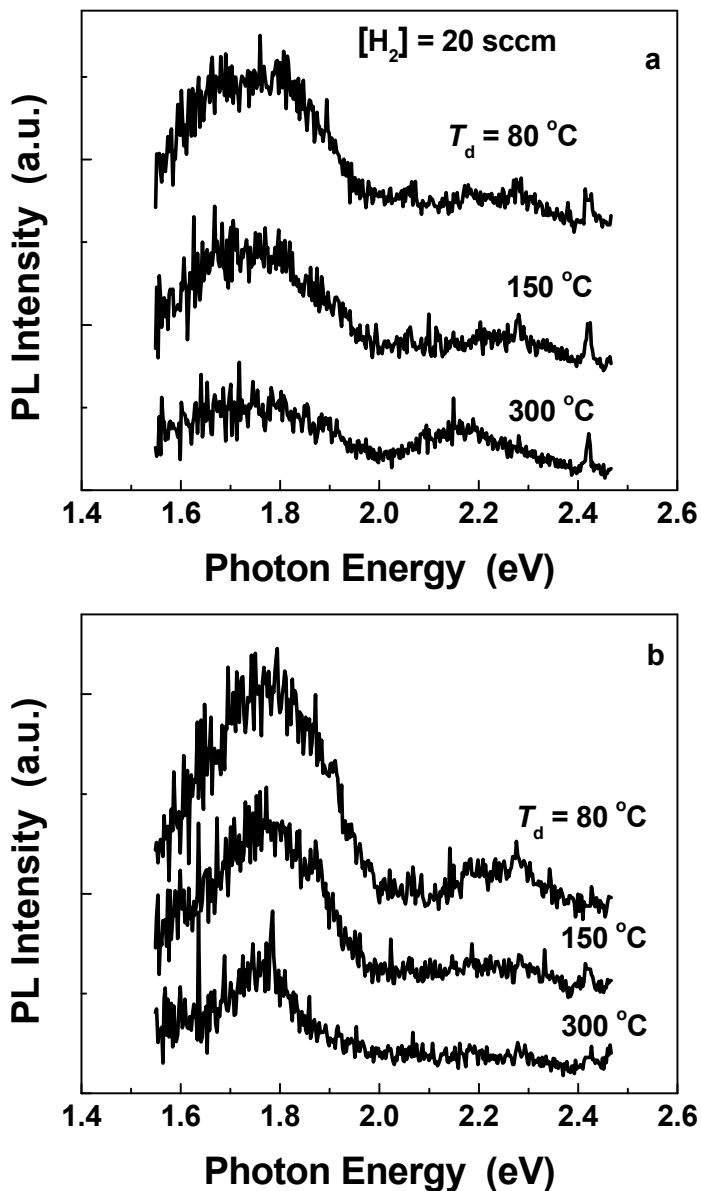


Fig. 5. Photoluminescence (PL) spectra for hydrogenated nanostructured silicon thin films with different deposition temperature values. (a) As-deposited and (b) After two months air exposure

In addition, no photoluminescence is observed for the film as deposited at 60 °C, which was amorphous as seen in Fig. 1. Therefore, it is considered that an amorphous silicon phase is not responsible for the observed luminescence in the present work. The origin of the first

peak (1.75-1.78 eV) may be ascribed to nanometersized grains, that is, the photoluminescence peak energy value for this band increases with a decrease in the  $\langle\delta\rangle$  value (Fig. 1b). And the origin of second peak (2.1-2.3 eV) may be due to defect related oxygen (Fig. 2). On the other hand, it has been suggested that the exciton localization at the Si/SiO<sub>2</sub> interface is important in determining the photoluminescence process for both 1.65 and 2.1 eV bands (Kanemitsu et al., 2000). In addition, the photoluminescence bands for H-passivated nanocrystalline silicon films show red shifts after passivation, in contrast to the cause of O-passivated films that show blue shifts after passivation (Dinh et al., 1996) in good agreement with the present work. Moreover, It has been widely established that the origins of photoluminescence from amorphous silicon dioxide are oxygen-vacancies (E' center, normally denoted by  $\text{O}=\text{Si}-\text{Si}=\text{O}$ ) (Kenyon et al., 1994; Zhu et al., 1996) and nonbridging oxygen hole (NBOH) center, denoted by  $\equiv\text{Si}-\text{O}$ ) (Munekuni et al., 1990; Nishikawa et al., 1996). Photoluminescence from E' center peaks at 2.0–2.2 eV and from nonbridging oxygen hole peaks at 1.9 eV, covering the range from 1.55-2.25 eV. Oxygen-vacancies in fact joint two  $\text{Si}^{3+}$ , and nonbridging oxygen hole,  $\text{Si}^{4+}$  with a dangling bond at one oxygen atom. So the intensity of photoluminescence from E' centers should be in proportion to the amount of  $\text{Si}^{3+}$ , and the photoluminescence intensity from nonbridging oxygen hole should be in proportion to the amount of defect  $\text{Si}^{4+}$ , which is in fact  $\text{Si}^{4+}$  containing a dangling bond, and will diminish if this dangling bond combines with other silicon atom (Fang et al., 2007).

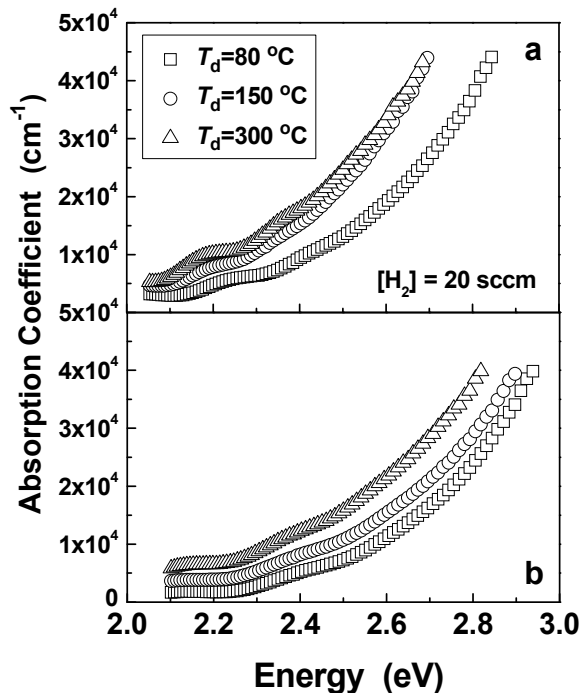


Fig. 6. Absorption coefficient as a function of photon energy for hydrogenated nanostructured silicon thin films deposited at various deposition temperature ( $T_d$ ). (a) As-deposited and (b) After two months air exposure

## 4.2 Absorption spectroscopy

Fig. 6 shows the absorption coefficient of the hydrogenated nanostructured silicon thin films deposited at various deposition temperatures, as a function of photon energy. As seen in Fig. 6, the curves are shifted to higher energy as deposition temperature decreases and after two months air exposure, which implies that for a given photon energy, the films became increasingly transparent with decreased deposition temperature and after two months air exposure. Fig. 7 illustrates the values of  $(\alpha h\nu)^{1/2}$  versus photon energy for hydrogenated nanostructured silicon thin films deposited at different deposition temperature. From these curves, the optical band gaps can be obtained from the Tauc equation. The optical band gap decreases as the deposition temperature increases. This expected behavior could be explained by the change of size and the number of the formed particles with the variation of deposition temperature. In addition, the present materials have a wide optical band gap. Thus, the increase in optical band gap (Fig. 7) corresponds with a decrease in the grain size as shown in Fig. 2. Other theoretical and experimental researches attribute this phenomenon at the quantum confinement effect, e.g. the gap energy is conditioned on the size of the nanocrystals.

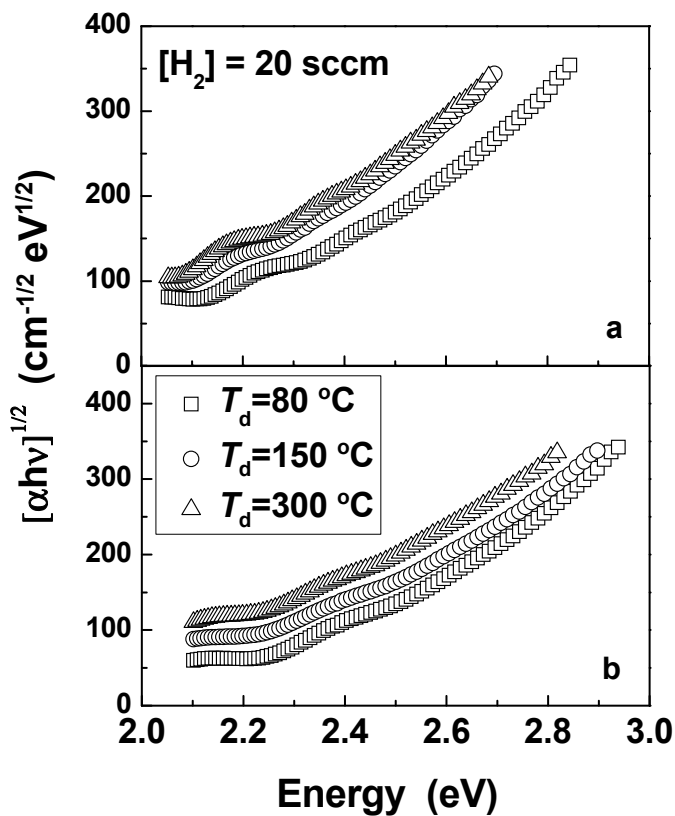


Fig. 7. Curves of  $(\alpha h\nu)^{1/2}$  vs. photon energy for hydrogenated nanostructured silicon thin films (a) As-deposited and (b) After two months air exposure

### 4.3 Band gap based on simple theory

Fig. 8 shows (a) the optical band gap,  $E_g^{opt}$ , and (b) photoluminescence peak energy,  $E_{PL}$ , of the 1.7-1.75-eV band observed for hydrogenated nanostructured silicon films deposited at different  $[H_2]$ , as a function of deposition temperature. The  $E_g^{opt}$  values were determined by drawing the Tauc plots,  $(ah\nu)^{1/2}$  versus  $(h\nu - E_g^{opt})$ , using the optical absorption coefficient,  $a$ , observed at photon energy of  $h\nu$ . As revealed in Fig. 8, an increase in  $E_{PL}$  corresponds well with an increase in  $E_g^{opt}$  with varying deposition temperature or  $[H_2]$ , though the rates in the increase of  $E_{PL}$  is considerably smaller than that of  $E_g^{opt}$ . This result suggest that the radiative recombination between excited electron and hole pair, may be caused by states other than those at both the band edges.

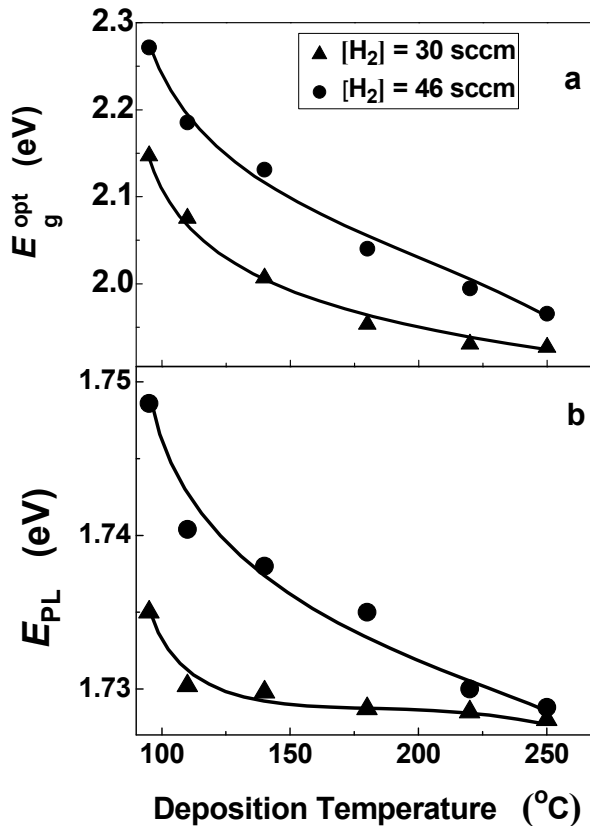


Fig. 8. (a) Optical band gap,  $E_g^{opt}$ , and (b) the peak energy,  $E_{PL}$ , of the 1.7-1.75-eV photoluminescence band observed for hydrogenated nanostructured silicon films deposited at different  $[H_2]$ , as a function of deposition temperature.

In this section, we will discuss the band gap estimated using the shifts of the Raman spectra that will reflect the characteristics of the whole grains with different size as well as the photoluminescence and the optical absorption measurements. As shown in Fig. 1, the Raman peak arising from crystalline phases shifts toward a low frequency side with

decreasing deposition temperature. Supposing that the peak shift is due only to the confinement of optical phonons in spherical nanocrystals, we can estimate the crystallite size in diameter,  $D_R$ , as (Edelberg et al., 1997):

$$D_R = 2\pi(B / \Delta\nu)^{1/2} \quad (1)$$

where  $B$  is  $2.24 \text{ cm}^{-1} \text{ nm}^2$ , and  $\Delta\nu$  the frequency shift in unit of  $\text{cm}^{-1}$ , which was defined as the difference between the observed peak-frequency value and  $522 \text{ cm}^{-1}$ . The latter value was observed for single crystal silicon. Fig. 9 shows a relationship between  $\langle\delta(111)\rangle$  and  $\langle\delta(110)\rangle$ , and  $D_R$ .

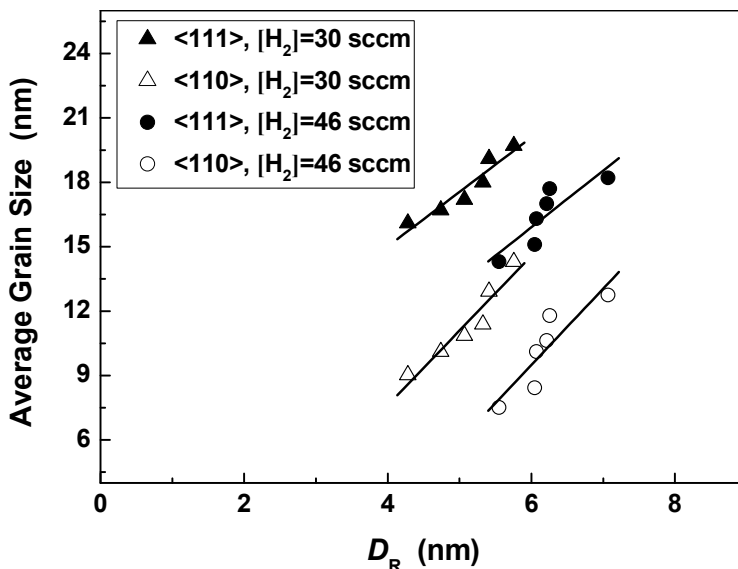


Fig. 9. Relationship between the average grain size,  $\langle\delta(111)\rangle$  and  $\langle\delta(110)\rangle$ , as a function of the diameter of grains,  $D_R$ , calculated using equation (1). The solid lines were drawn, using a method of the least square

When we compared the results obtained under a given crystal direction and a given  $[H_2]$ , we can find a close correlation between the  $\langle\delta\rangle$  and  $D_R$  values. However, it is found that the absolute values of  $\langle\delta\rangle$  observed are considerably larger than  $D_R$  values and the rate in the increase of  $\langle\delta\rangle$  are faster than that of  $D_R$ . Furthermore, based on the results shown in Fig. 9, we find a relationship of  $\langle\delta\rangle = 3.69 D_R - 7.28$  (nm) for the films with  $[H_2] = 30$  sccm and of  $\langle\delta\rangle = 3.56 D_R - 11.89$  for the films with  $[H_2] = 46$  sccm, in the measurements under a direction of the  $\langle 110 \rangle$  axis that is the dominant texture in the films. On the other hand, for the  $\langle 111 \rangle$  texture, we find a relationship of  $\langle\delta\rangle = 2.61 D_R + 4.48$  for  $[H_2] = 30$  sccm and  $\langle\delta\rangle = 2.64 D_R + 0.05$  for  $[H_2] = 46$  sccm. These formulas were obtained by fitting the values of  $\langle\delta\rangle$  vs.  $D_R$  to a linear relationship, using a method of the least square. As seen in these results, the linear relationships of  $\langle\delta\rangle$  as a function of  $D_R$  appear to be characterized by the crystal axis of grains, that is, the slope  $(3.63 \pm 0.07)$  for the  $\langle 110 \rangle$  texture is steeper than that  $(2.63 \pm 0.02)$  for the  $\langle 111 \rangle$  texture.

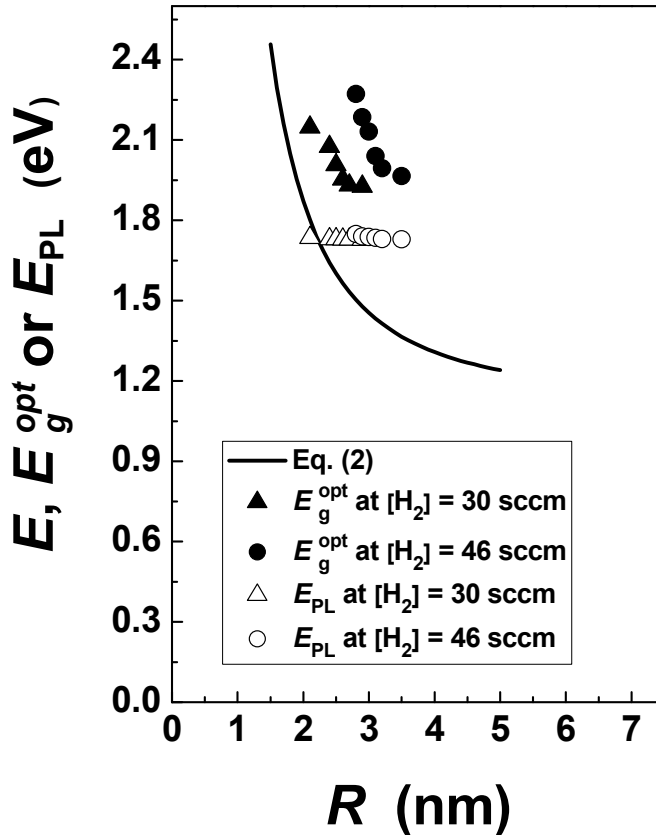


Fig. 10. Lowest excitation energy,  $E$ , as a function of  $R$  (a solid curve), obtained based on equation 2. In this diagram, the experimental values of  $E_g^{opt}$  values (closed symbols) and  $E_{PL}$  (open symbols) values, which were shown in Figs. 8a and 8b, respectively, are also shown for comparison, as a function of  $R(=D_R/2)$  through the  $D_R$  values obtained using the experimental  $\Delta\nu$  values along with equation 2

Using the values of  $D_R$  for the individual samples, we can evaluate the lowest excitation energy,  $E$ , under a simple confinement theory for electron and hole (Efros et al., 1982; Kayanuma, 1988; Edelberg et al., 1997) as follows:

$$E = E_g + 2\pi^2\hbar^2 / m_r D_R^2 - 3.572e^2 / \epsilon_r D_R + 0.284E_{Ry} \quad (2)$$

where  $E_g$  is the energy gap of crystalline silicon (1.12 eV at room temperature),  $R(=D_R/2)$  is the radius of crystals,  $m_r$  is the reduced effective mass of an electron-hole pair,  $\epsilon_r$  is the dielectric constant, and  $E_{Ry}$  is the Rydberg energy for the bulk semiconductor. The value of  $E$  correspond to the band gap of the films. In the later two terms,  $3.572e^2/\epsilon_r D_R$  corresponds to the coulomb term and  $0.284E_{Ry}$  gives the spatial correlation energy. The later two terms are minor corrections, so we neglected them in the calculation used in this work, because the contribution of these two terms to the total energy will be less than 5% (Edelberg et al., 1997).



Fig. 10 shows the  $E$  values (a solid curve) obtained based on equation 2, as a function of  $R$ . In Fig. 10, the experimental values of  $E_g^{opt}$  (closed symbols) and  $E_{PL}$  (open symbols) shown in Figs. 9a and 9b, respectively, are also shown for comparison, as a function of  $R$  through the values of  $D_R$  obtained using the experimental  $\Delta v$  values along with equation 1.

As shown in Fig. 10, we can find a qualitative agreement between the observed  $E_g^{opt}$  values (closed triangles and closed circles) and a solid curve calculated using equation 2, though the former values are considerably larger than the latter. Furukawa and Miyasato (Furukawa & Miyasato, 1988) have found also similar discrepancy between the theoretical and experimental results, and interpreted the discrepancy in terms of a difference in the surface shape of grains as boundary conditions in both the theoretical and experimental process. On the other hand, the change of  $E_{PL}$  as a function of  $R$  is considerably smaller than those of  $E$  and  $E_g^{opt}$  though the trend of the changes for  $E_{PL}$  agreed with that for  $E_g^{opt}$ . This result indicates that the photoluminescence process of the 1.7–1.75-eV band can not be connected with the transition between both the band edges, related to formation of nanocrystals.

## 5. Conclusion

Hydrogenated nanostructured silicon thin films were deposited by plasma-enhanced chemical vapor deposition. The luminescent characteristics of nc-Si and oxidized Hydrogenated nanostructured silicon thin films were studied in detail by means of the photoluminescence, optical absorption, X-ray diffraction, atomic force microscopy and Raman scattering analyses. After oxidation the size of crystallites is reduced thus enhancing the quantum confinement to increase the luminescent intensity. The presence of nanocrystals induces a widening of energy gap. The widening of the optical band gap can be explained by a quantum size effect.

## 6. Acknowledgment

Financial support by King Abdulaziz City for Science and Technology under Grant number: 08-NAN153-7 is gratefully acknowledged.

## 7. References

- Belomoin, G.; Therrien, J.; Smith, A.; Rao, S.; Twesten, R.; Chaieb, S.; Nayfeh, M.H.; Wagner, L. & Mitas, L. (2002). Observation of a Magic Discrete Family of Ultrabright Si Nanoparticles, *Applied Physics Letters*, Vol.80, No.5, (February 2002), pp. 841-843. ISSN 0003-6951
- Benyoucef, M.; Kuball, M.; Sun, J. M. ; Zhong, G. Z. & Fan, X. W. (2001). Raman Scattering and Photoluminescence Studies on Si/SiO<sub>2</sub> Superlattices, *Journal of Applied Physics*, Vol.89, No.12, (June 2001), pp. 7903-7907, ISSN 0021-8979
- Brongersma, M.L.; Polman, A.; Min, K.S.; Boer, E.; Tambo, T. & Atwater, H.A. (1998). Tuning the Emission Wavelength of Si nanocrystals in SiO<sub>2</sub> by Oxidation, *Applied Physics Letters*, Vol.72, No.20 (May 1998), pp. 2577-2579, ISSN 0003-6951
- Canham, L.T. (1990). Silicon Quantum Wire Array Fabrication by Electrochemical and Chemical Dissolution of Wafers, *Applied Physics Letters*, Vol.57, No.10, (September 1990), pp.1046-1048, ISSN 0003-6951

- Chaudhuri, P. & Das, U.K. (1995). Control of Microstructure and Optoelectronic Properties of Si:H Films by Argon Dilution in Plasma-Enhanced Chemical Vapor Deposition from Silane, *Japanese Journal of Applied Physics*, Vol.34, No.7A, (July 1995), pp. 3467-3473, ISSN 0021-4922
- Cheng, Q.; Xu, S.; Chai, J.W.; Huang, S.Y.; Ren, Y.P.; Long, J.D.; Rutkevych, P.P. & Ostrikov, K. (2008). Influence of Hydrogen Dilution on the Growth of Nanocrystalline Silicon Carbide Films by Low-frequency Inductively Coupled Plasma Chemical Vapor Deposition, *Thin Solid Films*, Vol.516, No.18, (July 2008), pp. 5991-5995, ISSN 0040-6090
- Cohen, M. (Ed.). (1978). *Elements of X-ray Diffraction*, Addison-Wesley, ISBN 0201011743, Massachusetts
- Das, U. K.; Chaudhuri, P. & Kshirsagar, S. T. (1996). Effect of Argon Dilution on the Structure of Microcrystalline Silicon Deposited from Silane, *Journal of Applied Physics*, Vol.80, No.9, (November 1996), pp. 5389-5397, ISSN 0021-8979
- Dinh, L.N.; Chase, L.L.; Baloch, M.; Siekhaus, W. J. & Wooten, F. (1996). Optical Properties of Passivated Si Nanocrystals and SiO<sub>x</sub> Nanostructures, *Physical Review B*, Vol.54, No.7, (August 1996), pp. 5029-5037, ISSN 1098-0121
- Edelberg, E.; Bergh, S.; Naone, R.; Hall, M. & Aydil, E. S. (1997). Luminescence from Plasma Deposited Silicon Films, *Journal of Applied Physics*, Vol. 81, No.5, (March 1997), pp. 2410-2417, ISSN 0021-8979
- Efros, A.L. & Efros, A.L. (1982). Interband Absorption of Light in a Semiconductor Sphere, *Soviet Physics-Semiconductors*, Vol.16, (1982), pp. 772-775
- Ehbrecht, M.; Ferkel, H.; Huisken, F.; Holz, L.; Polivanov, Y.N.; Smirnov, V.V.; Stelmakh, O.M. & Schmidt, R. (1995). Deposition and Analysis of Silicon Clusters Generated by Laser Induced Gas Phase Reaction, *Journal of Applied Physics*, Vol.78, No.9, (November 1995), pp. 5302-5306, ISSN 0021-8979
- Fang, Y.C.; Zhang, Z. J. & Lu, M. (2007). Room Temperature Photoluminescence Mechanism of SiO<sub>x</sub> Film after Annealing at Different Temperatures, *Journal of Luminescence*, Vol.126, No.1, (September 2007), pp. 145-148, ISSN 0022-2313
- Funde, A.M.; Bakr, N.A.; Kamble, D.K.; Hawaldar, R.R.; Amalnerkar, D.P. & Jadkar, S.R. (2008). Influence of Hydrogen Dilution on Structural, Electrical and Optical Properties of Hydrogenated Nanocrystalline Silicon (nc-Si:H) Thin Films Prepared by Plasma Enhanced Chemical Vapour Deposition (PE-CVD), *Solar Energy Materials and Solar Cells*, Vol.92, No.10, (October 2008), pp. 1217-1223, ISSN 0927-0248
- Furukawa, S. & Miyasato, T. (1988). Quantum Size Effects on the Optical Band Gap of Microcrystalline Si:H, *Physical Review B*, Vol.38, No.8, (September 1988), pp. 5726-5729, ISSN 1098-0121
- Hasegawa, S.; Narikawa, S. & Kurata, Y. (1983). ESR and Electrical Properties of P-doped Microcrystalline Si, *Philosophical Magazine B*, Vol. 48, No.5, (November 1983), pp. 431-447, ISSN 1364-2812
- Hasegawa, S.; Yamamoto, S. & Kurata, Y. (1990). Control of Preferential Orientation in Polycrystalline Silicon Films Prepared by Plasma-Enhanced Chemical Vapor Deposition, *Journal of The Electrochemical Society*, Vol.137, No.11, (November 1990), pp. 3666-3674, ISSN 0013-4651
- Inokuma, T.; Wakayama, Y.; Muramoto, T.; Aoki, R.; Kurata, Y. & Hasegawa, S. (1998). Optical Properties of Si Clusters and Si Nanocrystallites in High-temperature

- Annealed SiO<sub>x</sub> Films, *Journal of Applied Physics*, Vol.83, No.4, (February 1998), pp.2228-2234, ISSN 0021-8979
- Itoh, T.; Yamamoto, K.; Ushikoshi, K.; Nonomura, S. & Nitta, S. (2000). Characterization and Role of Hydrogen in nc-Si:H, *Journal of Non-Crystalline Solids*, Vol.266-269, No.1, (May 2000), pp. 201-205, ISSN 0022-3093
- Iwayama, T.S.; Nakao, S. & Saitoh, K. (1994). Visible Photoluminescence in Si<sup>+</sup> Implanted Thermal Oxide Films on Crystalline Si, *Applied Physics Letters*, Vol.65, No.14, (October 1994), pp. 1814-1816, ISSN 0003-6951
- Jeon, K.A.; Kim, J.H.; Kim, G.H.; Lee, S.Y. (2005). Oxidation Effects on the Photoluminescent Properties of Si Nanocrystalline Thin Films, *Optical Materials*, Vol.27, No.5, (February 2005), pp. 988-990, ISSN 0925-3467
- Kanemitsu, Y.; Iiboshi, M. & Kushida, T. (2000). Photoluminescence Spectrum of a-Si/SiO<sub>2</sub> and c-Si/SiO<sub>2</sub> Quantum Wells, *Journal of Luminescence*, Vol.87-89, No., (May 2000), pp. 463-465, ISSN 0022-2313
- Kanicki, J. (Ed.). (1991). *Amorphous & Microcrystalline Semiconductor Devices: Optoelectronic Devices*, Artech House, ISBN 10: 0890064903, Boston
- Kanicki, J. (Ed.). (1992). *Amorphous & Microcrystalline Semiconductor Devices: Materials and Device Physics*, Artech House, ISBN 10: 0890063796, Boston
- Kayanuma, Y. (1988). Quantum-size Effects of Interacting Electrons and Holes in Semiconductor Microcrystals with Spherical Shape, *Physical Review B*, Vol.38, No.14, (November 1988), pp. 9797-9805, ISSN 1098-0121
- Kenyon, A.J.; Trwoga, P.F.; Pitt, C.W. & Rehm, G. (1996). The Origin of Photoluminescence from Thin Films of Silicon Rich Silica, *Journal of Applied Physics*, Vol.79, No.12, (June 1996), pp. 9291-9300, ISSN 0021-8979
- Kroll, U.; Meier, J.; Shah, A.; Mikhailov, S. & Weber, J. (1996). Hydrogen in Amorphous and Microcrystalline Silicon Films Prepared by Hydrogen Dilution, *Journal of Applied Physics*, Vol.80, No.9, (November 1996), pp. 4971-7975, ISSN: 0021-8979
- Lim, H.J.; Ryu, L.B.; Ryu, J.I. & Jang, J. (1996). Structural and Electrical Properties of Low Temperature Polycrystalline Silicon Deposited Using SiF<sub>4</sub>-SiH<sub>4</sub>-H<sub>2</sub>, *Thin Solid Films*, Vol.289, No.1-2, (November 1996) 227-233, ISSN 0040-6090
- Lin, C.Y.; Fang, Y.K; Chen, S.F; Chang, S.H. & Chou, T.H. (2006). Enhancing Photoluminescence of Nanocrystalline Silicon Thin Film with Oxygen Plasma Oxidation, *Materials Science and Engineering: B*, Vol.134, No.1, (September 2006), pp. 99-102, ISSN 0921-5107
- Matsuda, A. (1983). Formation Kinetics and Control of Microcrystallite in  $\mu\text{c-Si:H}$  from Glow Discharge Plasma, *Journal of Non-Crystalline Solids*, Vol.59-60, No.2, (December 1983), pp. 767-774, ISSN0022-3093
- Mohri, M.; Kakinuma, H.; Sakamoto, M. & Sawai, H. (1991). Very-Low-Temperature Preparation of Poly-Si Films by Plasma Chemical Vapor Deposition Using SiF<sub>4</sub>/SiH<sub>4</sub>/H<sub>2</sub> Gases, *Japanese Journal of Applied Physics*, Vol.30, No.5A, (May 1991), pp. L779-L782, ISSN 0021-4922
- Munekuni, S.; Yamanaka, T.; Shimogauchi, Y.; Tohmon, R.; Ohki, Y.; Nagasawa, K. & Hama, Y. (1990). Various Types of Nonbridging Oxygen Hole Center in High Purity Silica Glass, *Journal of Applied Physics*, Vol.68, No.3, (August 1990), pp. 1212-1217, ISSN 0021-8979

- Nakajima, A.; Sugita, Y.; Kawamura, K.; Tomita, H. & Yokoyama, N. (1996). Si Quantum Dot Formation with Low-Pressure Chemical Vapor Deposition, *Japanese Journal of Applied Physics*, Vol.35, No.2B, (February 1996), pp. L189 -L191. ISSN 0021-4922
- Nishikawa, H.; Watanabe, E.; Ito, D.; Sakurai, Y.; Nagasawa, K. & Ohki, Y. (1996). Visible Photoluminescence from Si Clusters in  $\gamma$  Irradiated Amorphous SiO<sub>2</sub>, *Journal of Applied Physics*, Vol.80, No.6, (September 1996), pp. 3513-3517, ISSN 0021-8979
- Photopoulos, P.; Nassiopoulou, A.G. & Kouvatso, D.N. (2000). Photoluminescence from Nanocrystalline Silicon in Si/SiO<sub>2</sub> Superlattices, *Applied Physics Letters*, Vol.76, No.24, (June 2000), pp. 3588-3590, ISSN 0003-6951
- San Andre's, E.; del Prado, A.; Ma'rtel, I.; Gonza'lez-Di'az, G.; Bravo, D.; L'opez, F.J. & Fern'andez, M. (2003). Bonding Configuration and Density of Defects of SiO<sub>x</sub>H<sub>y</sub> Thin Films Deposited by the Electron Cyclotron Resonance Plasma Method, *Journal of Applied Physics*, Vol.94, No.12, (December 2003), pp. 7462-7469, ISSN 0021-8979
- Solomon, I.; Dr'evillon, B.; Shirai, H. & Layadi, N. (1993). Plasma Deposition of Microcrystalline Silicon: the Selective Etching Model, *Journal of Non-Crystalline Solids*, Vol.164-166, No.2, (December 1993), pp. 989-992, ISSN 0022-3093
- Street, R.A. (1991); *Hydrogenated Amorphous Silicon*, Cambridge University, ISBN 0521371562, Cambridge
- Takagi, H.; Ogawa, H.; Yamazaki, Y.; Ishizaki, Y.A. & Nakagiri, T. (1990). Quantum Size Effects on Photoluminescence in Ultrafine Si Particles, *Applied Physics Letters*, Vol.56, No.24, (June 1990), pp. 2379-2380, ISSN 0003-6951
- Wang, Y.H.; Lin, J. & Huan, C.H.A. (2003). Structural and Optical Properties of a-Si:H/nc-Si:H Thin Films Grown from Ar-H<sub>2</sub>-SiH<sub>4</sub> Mixture by Plasma-enhanced Chemical Vapor Deposition, *Materials Science and Engineering: B*, Vol.104, No.1-2, (November 2003), pp. 80-87, ISSN 0921-5107
- Wei, W.; Xu, G.; Wang, J. & Wang, T. (2007). Raman Spectra of Intrinsic and Doped Hydrogenated Nanocrystalline Silicon Films, *Vacuum*, Vol.81, No.5, (January 2007), pp. 656-662, ISSN 0042-207X
- Werwa, E.; Seraphin,A.A.; Chiu, L.A.; Zhou, C. & Kolenbrander, K.D. (1994). Synthesis and Processing of Silicon Nanocrystallites Using a Pulsed Laser Ablation Supersonic Expansion Method, *Applied Physics Letters*, Vol.64, No.14, (April 1994), pp. 1821-1823, ISSN 0003-6951
- Yamaguchi, M. & Moigaki, K. (1999). Effect of Hydrogen Dilution on the Optical Properties of Hydrogenated Amorphous Silicon Prepared by Plasma Deposition, *Philosophical Magazine B*, Vol.79, No.3, (March 1999), pp. 387-405, ISSN 1364-2812
- Zhang, Q.; Bayliss, S.C. & Hutt, D.A. (1995). Blue Photoluminescence and Local Structure of Si Nanostructures Embedded in SiO<sub>2</sub> Matrices, *Applied Physics Letters*, Vol.66, No.15, (April 1995), pp. 1977-1979, ISSN 0003-6951
- Zhu, M.; Han, Y.; Wehrspohn, R.B.; Godet, C.; Etemadi, R. & Ballutaud, D. (1996). The Origin of Visible Photoluminescence from Silicon Oxide Thin Films Prepared by Dual-plasma Chemical Vapor Deposition, *Journal of Applied Physics*, Vol.83, No.10, (May 1998), pp. 5386-5393, ISSN 0021-8979

# Fabrication and Characterization of As Doped p-Type ZnO Films Grown by Magnetron Sputtering

J.C. Fan<sup>1,2</sup>, C.C. Ling<sup>2</sup> and Z. Xie<sup>1,\*</sup>

<sup>1</sup>College of Physics and Microelectronics Science, Key Laboratory for Micro-Nano Physics and Technology of Hunan Province, Hunan University,

<sup>2</sup>Department of Physics, The University of Hong Kong, People's Republic of China

## 1. Introduction

In the past decade, there has been a great deal of interest in zinc oxide ZnO semiconductor materials lately, as seen from a surge of a relevant number of publications in Figure 1 (Wenckstern, 2008). It can be seen that the present renaissance in ZnO research started in the mid 1990s. More than 2000 papers on ZnO were published in 2005 and even higher numbers in 2006.

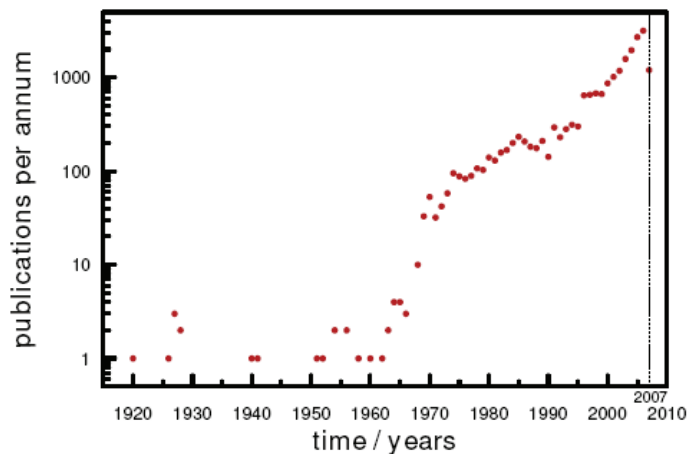


Fig. 1. Publications per annum for the search of ZnO in the abstract before 2007, For 2007, only papers published before June 6th are considered. From Ref. (Wenckstern, 2008).

With a wide band gap of 3.4eV and a large exciton binding energy of 60 meV at room temperature, ZnO has been considered as a promising material for optoelectronic devices (Klingshirn, 2007):

- ZnO as a blue/UV optoelectronics, including light emission diodes (LEDs) and laser diodes in addition to (or instead of) the GaN -based structure.

- ZnO as a radiation-hard material for electronic devices in a corresponding environment.
- ZnO as a material for electronic circuits, which is transparent in the visible.
- ZnO as a diluted or ferromagnetic material, when doped with Co, Mn, Fe, V or similar elements, for semiconductor spintronics.
- ZnO as a transparent, highly conducting oxide (TCO), when doped with Al, Ga, In or similar elements, as a cheaper alternative to indium tin oxide (ITO).

More applications about ZnO can be found in references (Janotti & Van de Walle 2009).

It is known that GaN is a III-V compound semiconductor material with in the hexagonal wurtzite-type structure and an important application in optoelectronic devices. With a similar crystallinity to GaN, ZnO has more advantages in optoelectronic application (Özgür, et al., 2005; Shur & Davis, 2004; Tsukazak, et al., 2005; Look, 2001; Janotti & Van de Walle 2009):

- a exciton binding energy of 60 meV at room temperature(RT) is higher than one of GaN (24meV), resulting in ZnO can be excited at RT and prepared the optoelectronic devices in shorter wavelength.
- the band gap of ZnO ( $E_g = 3.4$  eV) can be effectively modulated (controled) in 3- 4.5eV by doping Cd or Mg.
- ZnO film can be fabricated with large area and good uniformity on various substrates, leading to the application in a wider field, however, GaN film is prepared on some limited substrates (SiC, Sapphire, Si).
- the growth temperature for high quality ZnO film is about 500°C, which is much lower than that for GaN film ( $\geq 1000^\circ\text{C}$ ).

The properties of GaN and ZnO are summarized in Table1 (Madelung, 1996; Norton et al, 2004).

Property	GaN		ZnO
	Wurtzite	Zinc Blende	Wurtzite
Crystal Structure	Wurtzite	Zinc Blende	Wurtzite
Lattice Constant (nm)			
$a_0$ :	0.3189	0.452	0.3249
$c_0$ :	0.5185	0.45	0.5207
$a_0/c_0$ :	1.6259		1.602
Density ( $\text{g/cm}^3$ )	6.15		5.606
Thermal Conductivity ( $\text{Wcm}^{-1}\text{C}^{-1}$ )	>2.1		0.6, 1-1.2
Linear expansion coeffient ( $\text{C}^{-1}$ )			
$a_0$ :	$5.59 \times 10^{-6}$	—	$6.5 \times 10^{-6}$
$c_0$ :	$3.17 \times 10^{-6}$	—	$3.0 \times 10^{-6}$
Energy bandgap (eV)	3.51	3.3	3.4
Exciton binding energy (meV)	24	—	60
Electron effective mass	0.2	—	0.24
Electron hall Mobilty at room temperature ( $\text{cm}^2\text{V}^{-1}\text{s}^{-1}$ )	$\sim 1000$	$\sim 1000$	200
Hole effective mass	0.8		0.59
Hole hall Mobilty at room temperature ( $\text{cm}^2\text{V}^{-1}\text{s}^{-1}$ )	$\leq 200$	$\leq 350$	$\leq 50$
Electron saturation velocity ( $10^7\text{cm s}^{-1}$ )	2-2.5	2	3.2

Table 1. The properties of GaN and ZnO. From Ref. (Madelung, 1996; Norton, et al, 2004).

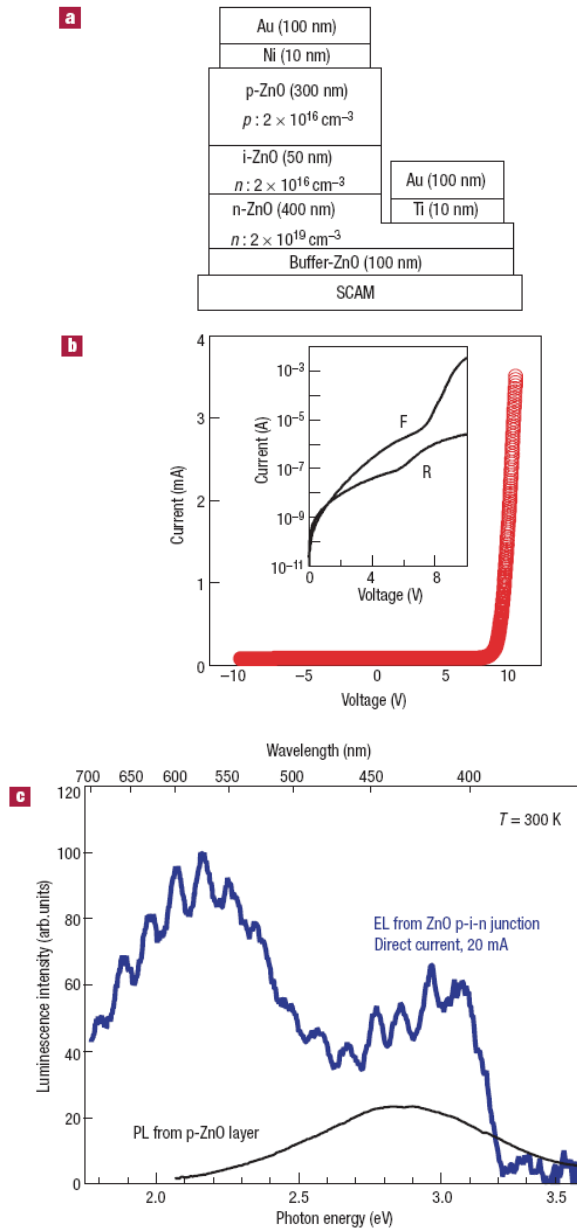


Fig. 2. (a) The structure of a typical p-i-n junction LED. (b) Current-voltage characteristics of a p-i-n junction. The inset has logarithmic scale in current with F and R denoting forward and reverse bias conditions, respectively. (c) Electroluminescence spectrum from the p-i-n junction (blue) and photoluminescence (PL) spectrum of a p-type ZnO film measured at 300K. From Ref. (Tsukazak, et al., 2005 ).

Figure 2a shows the schematic structure of a typical homostructural p-i-n junction prepared by Tsukaza et al. The I-V curve of the device displayed the good rectification with a threshold voltage of about 7V (Figure 1b). The electroluminescence spectrum from the p-i-n junction (blue) and photoluminescence (PL) spectrum of a p-type ZnO film at 300K were shown in Figure 1c, which indicated that ZnO was a potential material for making short-wavelength optoelectronic devices, such as LEDs for display, solid-state illumination and photodetector.

## 2. ZnO basic properties

ZnO is a II-V semiconductor with the ionicity at the borderline between covalent and ionic semiconductor (Özgür, et al., 2005). ZnO has three crystal structures: rocksalt, zinc blende and wurtzite, as shown in Figure 3(a), (b) and (c), respectively. Under conventional conditions, the thermodynamically stable phase is wurtzite, which has a hexagonal unit cell with space group  $C_{6v}^4$  or  $p_63mc$ , and lattice parameters  $a = 0.3296$ , and  $c = 0.52065$  nm. In this structure, the oxygen anions ( $O^{2-}$ ) and Zn cations ( $Zn^{2+}$ ) form a tetrahedral unit, composing two interpenetrating hexagonal-close-packed (hcp) sublattices and each sublattice includes four atoms per unit cell and every atom of one kind (group-II atom) is surrounded by four atoms of the other kind (groupVI), or vice versa, as shown in Figure 3(c). The wurtzite structure of ZnO lacks central symmetry and can be simply considered a number of alternating planes composed of  $O^{2-}$  and  $Zn^{2+}$ , grown alternatively along the c-axis due to the low formation energy of the direction. The zinc-blende ZnO structure can be stabilized only by growth on cubic substrates, and the rocksalt (NaCl) structure may be fabricated at relatively high pressures. The wurtzite ZnO can be transformed to the rocksalt structure at relatively modest external hydrostatic pressures.

In addition to the above crystal structures, theoretical calculation showed that a fourth phase of ZnO, cubic cesium chloride, may be possible at extremely high temperatures, however, the result has not been proved, experimentally.

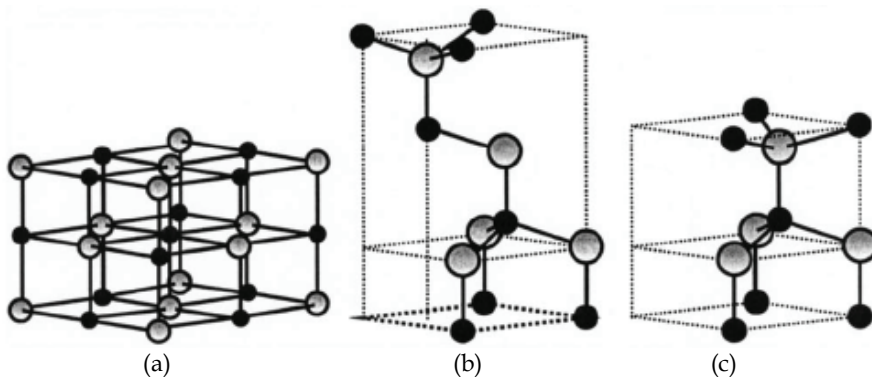


Fig. 3. ZnO crystal structures: (a) rocksalt, (b) zinc blende, (c) wurtzite. The shaded gray and black spheres denote Zn and O atoms, respectively. From Ref.(Özgür, et al., 2005).

Other basic properties of ZnO can be seen from Table 1.

Figures 4, 5 and 6 show the morphologies of ZnO single crystal, powder, film and nanomaterials.



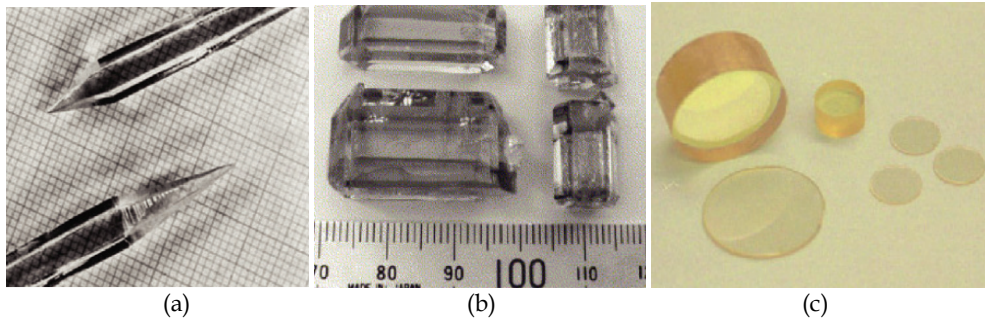


Fig. 4. Photographs of large bulk ZnO single crystals grown by different techniques: (a) gas transport, (b) hydrothermal, and (c) pressurized melt growth. From Ref.(Janotti, et al., 2009; Klingshirn, 2007).

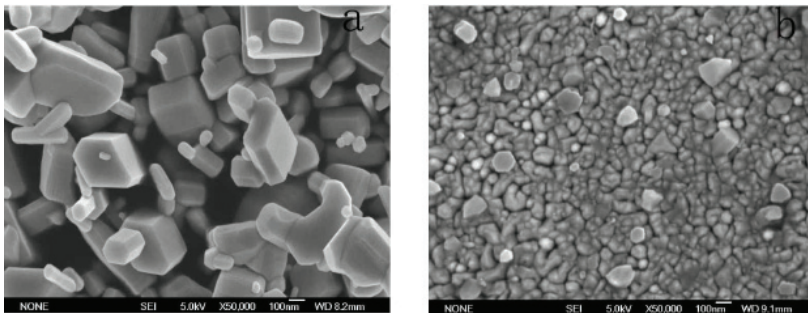


Fig. 5. SEM images of the ZnO powder (a) and ZnO film(b).

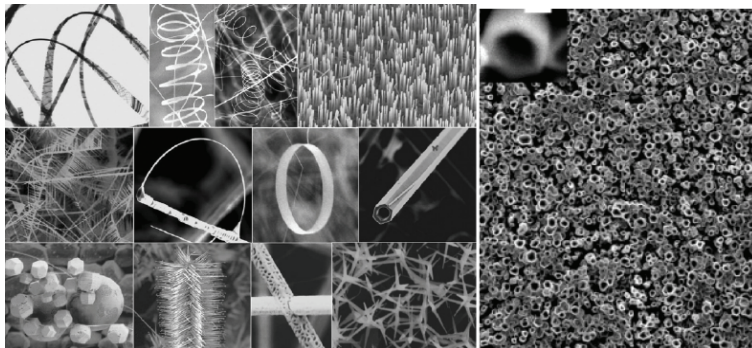


Fig. 6. A collection nanostructures of ZnO. From Ref. (Wang, 2004; Yu et al.,2005).

### 3. Challenges in ZnO

ZnO has a strong potential for various short-wavelength optoelectronic device applications. However, to realize these applications, a reliable technique for fabricating high quality p-type ZnO and p-n junction needs to be established. Compared with other II-VI semiconductor and GaN, it is a major challenge to dope ZnO to produce p-type

semiconductor due to self-compensation from native donor defects and/or hydrogen incorporation (Wang, et al., 2004; Xiu, et al., 2005). Great efforts have been made to achieve p-type ZnO by mono-doping group-I elements (Li, Na and K), group-IB elements (Ag and Cu) or group-V elements (N, P, As, and Sb) and co-doping III-V elements with various technologies, such as evaporation/sputtering process, ion implantation, pulsed laser deposition, thermal diffusion of As after depositing a ZnO film on GaAs substrate, and hybrid beam deposition (McCluskey & Jokela, 2009; Yan, et al., 2006; Kang, et al., 2006; Özgür, et al., 2005; Look, et al., 2004; Marfaing & Lusson, 2005; Yan & Zhang, 2001; Yamamoto, 2002). It is believed that the most promising dopants for p-type ZnO are the group V elements, although theory suggests some difficulty in achieving shallow acceptor level. The first p-type ZnO with a hole concentration of  $10^{16}$ – $10^{17}$  cm<sup>-3</sup> was reported in films made by vapour-phase transport in NH<sub>3</sub>, followed by molecular beam epitaxy (MBE) with an atomic nitrogen source (Minegishi, et al., 1997). The mechanism of p-type ZnO:N is considered that N substitutes for an O, forming an acceptor with a hole binding energy of 400 meV according to first-principles calculations (Park, et al., 2002), and x-ray absorption spectroscopy verified that N occupies the O substitutional site in Fons's experiment, which is consistent with the radius of N is near with that of O (Fons et al., 2006). P, As and Sb in ZnO are deep acceptor because of their large ionic radii as compared to O. However, some researchers claimed that p-type ZnO were achieved with these large-size-mismatched impurities (Heo, et al., 2003; Ryu, et al., 2000; Xiu, et al., 2005). Therefore, the microscopic structure of these impurities in ZnO has not been understood completely, which can not be contributed to these impurities occupied O site to generate holes, simply.

In this paper, we fabricated p type As doped ZnO films on glass and SiO<sub>2</sub>/Si substrates at different temperature by sputtering Zn<sub>3</sub>As<sub>2</sub>/ZnO target or cosputtering Zn<sub>3</sub>As<sub>2</sub> and ZnO targets, and investigated the optical and electrical properties of the films, systematically. Especially, the mechanism of p-type conductivity of ZnO: As film was discussed according to As<sub>Zn</sub>-2V<sub>Zn</sub> shallow acceptor model proposed by Limpijumnong *et al.*, which helped to understand the microscopic structure of As in As-doped ZnO and the microscopic origin of p-type ZnO by doping large-size- mismatched impurities.

#### 4. Experiment

Magnetron sputtering (DC sputtering, RF magnetron sputtering, and reactive sputtering) is one of the popular growth techniques for ZnO investigations because of its low cost, simplicity and low operating temperature. A schematic diagram of the magnetron sputtering system in our experiments is shown in Figure 7. Figure 8 shows a photograph of the typical glow from ZnO target when sputtering.

As-doped ZnO films were grown on glass and SiO<sub>2</sub>/Si substrates at different substrate temperatures by sputtering Zn<sub>3</sub>As<sub>2</sub>/ZnO or cosputtering ZnO and Zn<sub>3</sub>As<sub>2</sub> targets. Undoped ZnO films were deposited by sputtering ZnO target. Silicon oxide layer with a thickness of 250 nm was thermally grown in dry oxygen on Si substrate. The substrates were first cleaned by acetone and ethanol and then rinsed in de-ionized water each for 5 min at room temperature. The sputtering chamber was evacuated to a base pressure of 10<sup>-3</sup>Pa. A pure Ar (99.999%) was used as the working gas. The distance between the targets and the substrate was 14cm. The targets were presputtered for 20 min to remove contaminants. The As-doped ZnO targets were prepared by adding Zn<sub>3</sub>As<sub>2</sub> and sintering at 900°C for 3h. The Zn<sub>3</sub>As<sub>2</sub> contents in the targets were 0.5mol%, 1.0mol%, 1.5mol%, 2mol%, respectively. The pure Zn<sub>3</sub>As<sub>2</sub> target was sintered in pure Ar (purity: 99.999%; pressure: 0.1MPa) at 800°C for 2h. The film thickness was measured with ellipsometer.

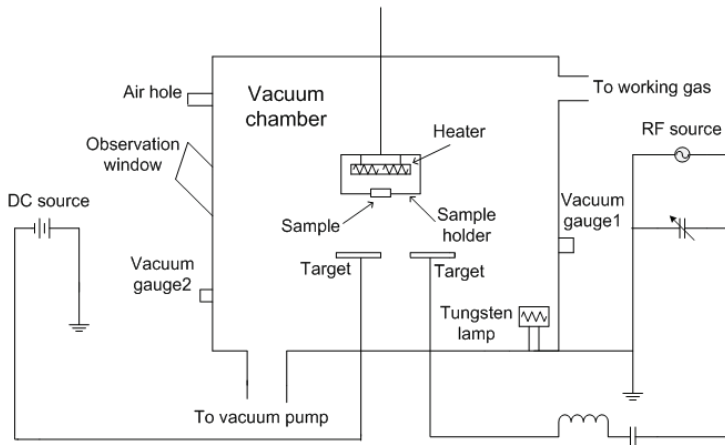


Fig. 7. Schematic diagram of the magnetron sputtering system.

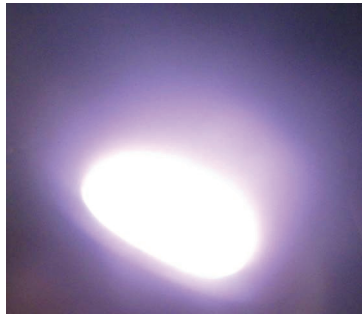


Fig. 8. Photograph of the typical glow from ZnO target when sputtering.

The structures and morphologies of the as-grown ZnO films were characterized by X-ray diffraction (XRD, Siemens D-5000, and Cu K $\alpha$ ,  $\lambda = 1.5405\text{\AA}$ ), atomic force microscopy (AFM, NTD-Pro47) and scan electron microscopy (SEM, JSM-6700F). The composition of As-doped ZnO film was analyzed by an energy dispersive X-ray (EDX) spectroscopy (INCA, Oxford) attached to the SEM. The concentration of As in ZnO film was measured with Secondary ion mass spectroscopy (SIMS, Physical Electronics model 7200). The bonding state of As in ZnO:As films were studied by x-ray photoelectron spectroscopy (XPS) using the Mg K $\alpha$  line (Physical Electronics model 5600). The x-ray source and the C 1s line were taken as the standard reference. The electrical properties of the films were investigated at room temperature in the Van der Pauw configuration using HL5500 Hall system. The measurement process was the following: ensuring Ohmic contact  $\rightarrow$  the resistivity measurement  $\rightarrow$  Hall effect measurement  $\rightarrow$  repeating Hall effect measurement. During the whole measurement, the resistivity was measured once and every sample had one value of the resistivity and several values of the mobility and carrier concentration. For one sample, if the results of several Hall effect measurements showed the same

conduction type, we consider it had stable conduction type. If the results of several Hall effect measurements were not consistent, and the conduction type of the film was not confirmed. The optical transmission spectra of the films were measured at room temperature using an UV-vis double beam spectrometer. Low temperature photoluminescence (PL) were systematically performed for ZnO films by the excitation from 325 nm He-Cd laser.

## 5. Results and discussion

### 5.1 Undoped ZnO films

First, let us investigate the properties of undoped ZnO films grown by magnetron sputtering. The undoped ZnO films were deposited on glass substrates at various temperatures from 250 to 450°C with RF power of 120W. High purity Ar (99.999%) or mixture of Ar and O<sub>2</sub> (Ar:O<sub>2</sub> = 3:1) maintained at 0.6 Pa was used as the working gas. In addition, the ZnO film measured low temperature PL was prepared on SiO<sub>2</sub>/Si substrate at 350°C with purity Ar maintained at 0.5 Pa.

Figure 9 shows the XRD patterns of ZnO powder and film deposited at 450°C.

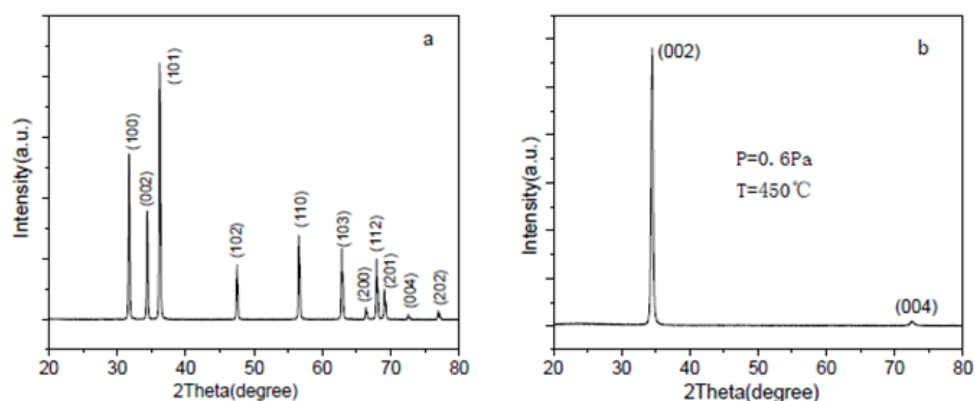


Fig. 9. XRD patterns of ZnO powder (a) and film deposited at 450°C (b).

Many diffraction peaks, such as (100), (002), (101) were seen in the pattern of ZnO powder and the (002) peak was not the strongest one. In the pattern of ZnO film deposited at 450°C, a strong peak of (002) at about 34.5° and a weak peak of (004) at 72.6° were observed. Comparison of the patterns shows that the thin film tended to be oriented on the (001) surface. SEM photograph in Figure 5 showed that the grains of ZnO film were small, around 100nm in diameter, in which exhibited hexagonal form and the powder were composed of ZnO grains with different diameters.

The optical absorption spectra of ZnO powder and film deposited at 450°C in the visible are displayed in Figure 10. The fundamental absorption for both powder and film starts from about 370 nm and the absorption of film in UV region was stronger, obviously. The inset shows a plot of  $(\alpha h\nu)^2$  against  $h\nu$  for ZnO film and the optical band gap ( $E_g$ ) value was obtained by extrapolating the linear portion to photo energy axis. It was found to be about 3.262eV.

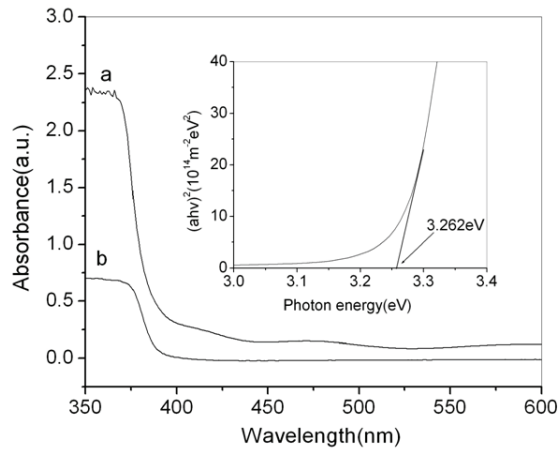


Fig. 10. Absorption spectra of ZnO powder (b) and film (a). The film thickness was about 300 nm. Inset shows plot of  $(ah\nu)^2$  against  $h\nu$  for estimation of direct allowed optical gap of the film. The estimated gap was 3.262 eV.

Figure 11 shows XRD patterns of ZnO films grown with different conditions. The growth parameters of the films were summarized in Table 2. A strong peak of ZnO (002) at about  $34.5^\circ$  was observed for each sample, indicating that the films were c-axis oriented. The full-width at half-maximum (FWHM) of (002) peaks were listed in Table 2. (103) peak in the XRD pattern of the film grown at  $250^\circ\text{C}$  (Sample<sub>S<sub>A</sub></sub>) shows that c-axis oriented grains in the film did not dominate completely due to the low growth temperature. (103) peak disappeared in the films deposited at  $350^\circ\text{C}$  (Sample<sub>S<sub>B</sub></sub>), indicating the c-axis orientation of the film became stronger and the crystallinity was improved, which was consistent with the change of (002) FWHM from  $0.40^\circ$  to  $0.38^\circ$ . Comparison of the patterns of Sample<sub>S<sub>B</sub></sub>, S<sub>C</sub> and S<sub>B</sub>+annealing shows that the induction of O<sub>2</sub> in working gas and post-annealing improved the quality of ZnO films grown with magnetron sputtering.

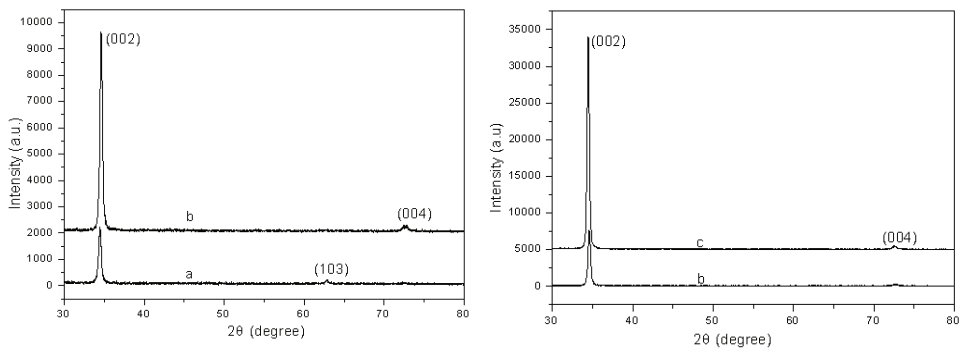


Fig. 11. XRD patterns of ZnO films grown different conditions: (a)  $P_{\text{Ar}}=0.6\text{Pa}$ ,  $250^\circ\text{C}$ ; (b)  $P_{\text{Ar}}=0.6\text{Pa}$ ,  $350^\circ\text{C}$ ; (c)  $P_{\text{Ar}}=0.45\text{Pa}$ ,  $P_{\text{O}_2}=0.15\text{Pa}$ ,  $350^\circ\text{C}$ .

Samples	P <sub>A</sub> (Pa)	P <sub>O<sub>2</sub></sub> (Pa)	Temperature (°C)	FWHM(degree)
S <sub>A</sub>	0.6	0	250	0.40
S <sub>B</sub>	0.6	0	350	0.38
S <sub>C</sub>	0.45	0.15	350	0.32
S <sub>B</sub> +annealing				0.34

Table 2. Growth parameters and (002) FWHM of ZnO films.

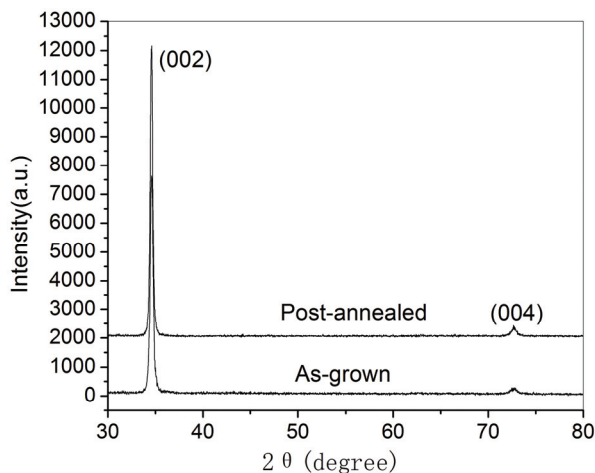


Fig. 12. XRD patterns of as-grown ZnO film at 350°C and annealed at 450 °C in air for 2h.

The surface morphologies of ZnO films were investigated by AFM. Figure 13 shows AFM images of ZnO films grown with different conditions. It can be seen that the grains of the films became larger with the temperature increased from 250 to 350°C and post-annealing improved the uniform of the film, which indicated the crystallinity of the films improved and were consisted with the results of XRD.

Figure 14 shows the optical transmittance spectra of ZnO films. The transmittances are over 70% in the visible region for all the films and the fundamental absorptions are at about 370nm. The inset of Figure 14 reveals the relationship between absorption coefficient and photo energy of ZnO film deposited at 350°C. The  $E_g$  value estimated was 3.271 eV.

Low temperature PL was performed for ZnO film grown on SiO<sub>2</sub>/Si substrate. The near band edge (NBE) part of the 10 K PL spectrum was shown in Figure 15, which had peaks at 3.355, 3.308, and 3.234eV (Fan, et al., 2009). Similar lines were also observed by Petersen et al., (3.350 and 3.303eV) in n-type ZnO grown by sol-gel process (Petersen, et al., 2008) and by Zhong et al (3.357 and 3.309eV) in ZnO tetrapod(Zhong, et al., 2008). The ~3.36 eV was ascribed to the neutral donor-bound-exciton (D<sup>0</sup>X) according to D.C.Look 's suggestion about the peak (Look & Clalin,2004). The 3.31 eV line was associated with the corresponding two-electron-satellite (TES) and/or exciton-LO phonon emission, therefore, the peaks at 3.355 and 3.308eV in Figure 15 were assigned to be the D<sup>0</sup>X and the TES/exciton-LO phonon lines, respectively. The 3.234 eV observed in Figure 15 was similar to the ~3.24eV donor-acceptor-pair (DAP) emission suggested by Peterson et al (Petersen, et al., 2008), and were thus assigned as DAP.

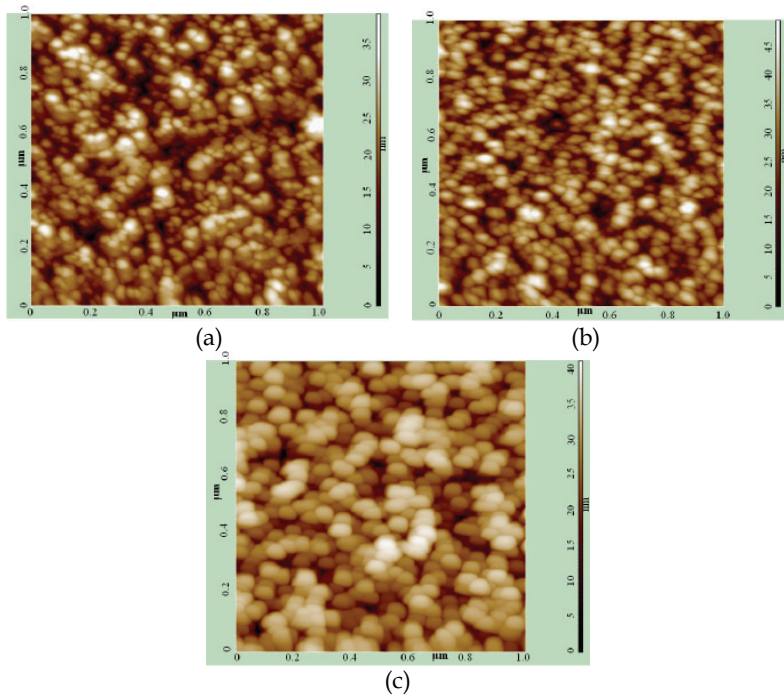


Fig. 13. AFM images of ZnO films prepared with different conditions:(a)  $P_{Ar}=0.6Pa$ ,  $250^{\circ}C$ ; (b)  $P_{Ar}=0.6Pa$ ,  $350^{\circ}C$ ; (c)  $S_B$ +annealing.

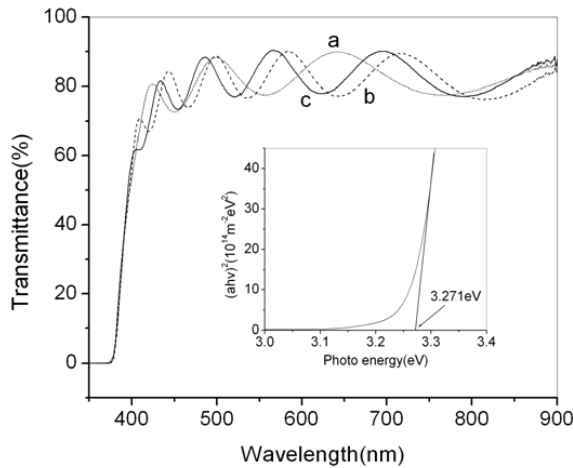


Fig. 14. Transmittance spectra of as-grown ZnO films prepared with different conditions: (a)  $P_{Ar}=0.6Pa$ , Room temperature; (b)  $P_{Ar}=0.6Pa$ ,  $250^{\circ}C$ ; (c)  $P_{Ar}=0.6Pa$ ,  $350^{\circ}C$ ; The inset is the  $(\alpha h\nu)^2$  vs  $h\nu$  curve for the optical band gap determination in the film deposited at  $350^{\circ}C$ . The  $E_g$  value estimated was  $3.271eV$ .

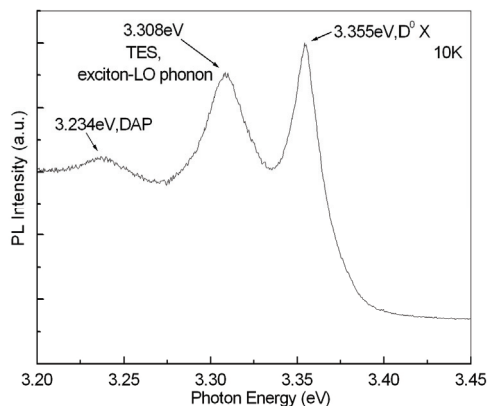


Fig. 15. NBE region of 10 K PL spectra for ZnO film grown on SiO<sub>2</sub>/Si substrate at 350°C.

### 5.2 As doped ZnO films prepared by sputtering Zn<sub>3</sub>As<sub>2</sub>/ZnO target

As doped ZnO films were prepared on glass and SiO<sub>2</sub>/Si substrates by sputtering Zn<sub>3</sub>As<sub>2</sub>/ZnO target at a substrate temperature from 50 to 450°C, respectively. The Zn<sub>3</sub>As<sub>2</sub> contents in the targets were 0.5mol%, 1.0mol%, 1.5mol%, respectively. A pure Ar (99.999%) at 0.6 Pa was used as the working gas. The films were deposited with a radio frequency (RF) power from 80 to 150W, respectively. The total thickness of the films was about 300 nm. In addition, the As-doped ZnO films performed low temperature PL were prepared on SiO<sub>2</sub>/Si substrates at 250 and 350°C with purity Ar maintained at 0.5 Pa, using the target with 1mol% Zn<sub>3</sub>As<sub>2</sub> and ZnO target.

Figure 16 shows the XRD patterns of As-doped ZnO films deposited on glass substrates at different temperatures. A strong peak of (0 0 2) at about 34.5° for all samples was observed, indicating that the films were c-axis oriented. Two peaks corresponding to (1 1 0) and (1 1 1) of Zn<sub>3</sub>As<sub>2</sub>, respectively, were detected in the patterns of the films deposited at 50 and 250°C, indicating the films were ZnO/Zn<sub>3</sub>As<sub>2</sub> or ZnO:As/Zn<sub>3</sub>As<sub>2</sub> ones (samples A and B). However, no diffraction peaks associated with Zn<sub>3</sub>As<sub>2</sub> were detected in the patterns of ZnO films deposited at 350 and 450°C, revealing the films were ZnO:As ones, corresponding to samples C and D, respectively.

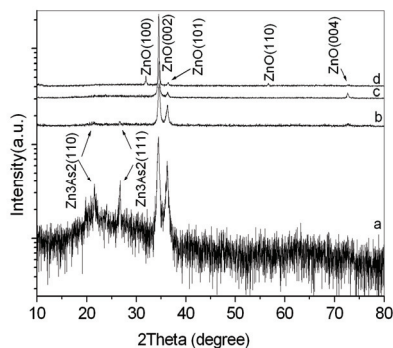


Fig. 16. XRD patterns of As-doped ZnO films deposited on glass substrates at different temperatures: 50°C (a); 250°C (b); 350°C (c); 450°C (d). From Ref.(Fan, et al., 2007a).



Similar phenomenon was observed in the XRD spectra of As-doped ZnO films deposited on  $\text{SiO}_2/\text{Si}$  substrates with different conditions, as shown in Figure 17, and the growth parameters were summarized in Table 3. The (110) and (111) peaks of  $\text{Zn}_3\text{As}_2$  were detected in the patterns of Samples S1, S2, S4 and S7, which showed that the films were ZnO/ $\text{Zn}_3\text{As}_2$  or ZnO:As/ $\text{Zn}_3\text{As}_2$  ones. Only ZnO (002) peak was observed in the patterns of Samples S3, S5 and S6, indicating the films were ZnO:As ones. Therefore, the growth parameters of ZnO:As film in our experiments were summarized in Table 4.

Samples	RF power (W)	Temperature ( $^{\circ}\text{C}$ )	$\text{Zn}_3\text{As}_2$ in target (mol%)
S1	100	350	1
S2	120	350	1
S3	150	350	1
S4	120	300	1
S5	120	400	1
S6	120	350	0.5
S7	120	350	1.5

Table 3. Growth parameters of As-doped ZnO films on  $\text{SiO}_2/\text{Si}$  substrates.

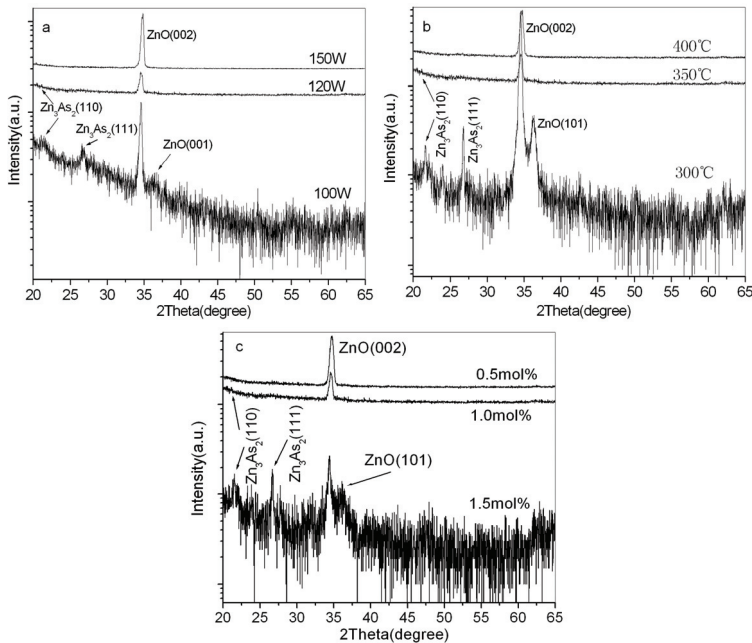


Fig. 17. (a) XRD patterns As-doped ZnO films deposited at 350 $^{\circ}\text{C}$  with various RF powers from 100 to 150W (samples S1, S2, and S3). (b) XRD patterns As-doped ZnO films deposited with RF powers of 120W at 300–400 $^{\circ}\text{C}$  (samples S2, S4, and S5). (c) XRD patterns As-doped ZnO films deposited with RF powers of 120W at 350 $^{\circ}\text{C}$  by sputtering 0.5–1.5mol%  $\text{Zn}_3\text{As}_2/\text{ZnO}$  targets (samples S5, S6, and S7).

Samples	RF power (W)	Temperature ( $^{\circ}$ C)	Zn <sub>3</sub> As <sub>2</sub> in target (mol%)	Substrate
C	100	350	1	Glass
D	120	350	1	Glass
S3	150	350	1	SiO <sub>2</sub> /Si
S5	120	400	1	SiO <sub>2</sub> /Si
S6	120	350	0.5	SiO <sub>2</sub> /Si

Table 4. Growth parameters of ZnO:As films in our experiments

The surface morphology of ZnO:As films in our experiments were investigated by AFM and SEM. Figure 18 shows AFM images of ZnO:As film deposited on glass at 350 $^{\circ}$ C (SampleC). It can be seen that the film was composed of globe-like grains and had high quality, which was consist with XRD results in Figure 16.

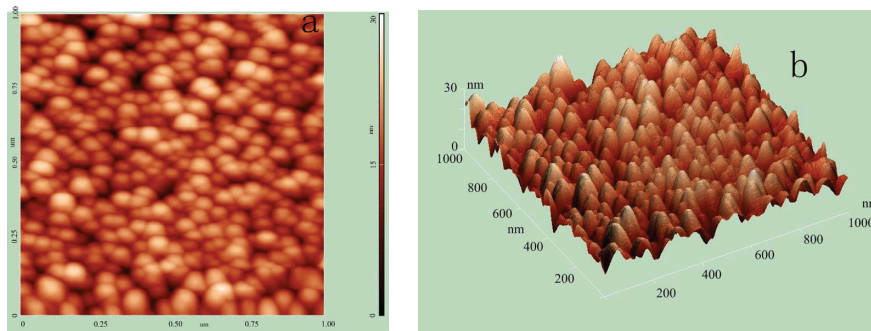


Fig. 18. AFM images of ZnO:As film deposited on glass at 350 $^{\circ}$ C (SampleC).

The microstructure of the ZnO:As films grown on SiO<sub>2</sub>/Si substrates was characterized using SEM. The SEM micrographs of the films revealed that the films had a homogeneous surface formed by globe-like grains, indicating high quality of the film microstructure. The typical SEM images obtained for samples S3 and S5 are shown in Figure 19.

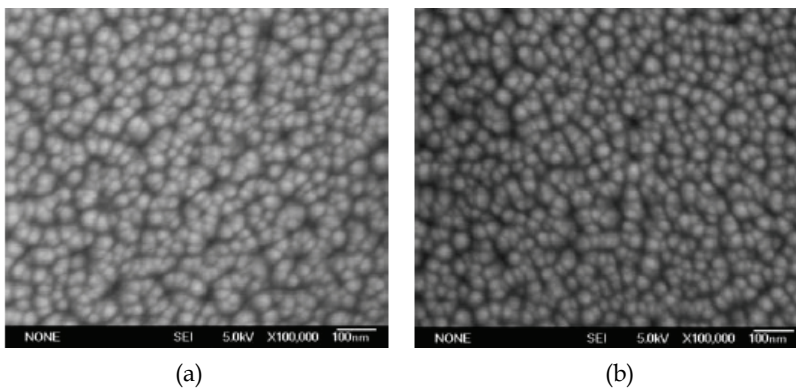


Fig. 19. SEM images of ZnO:As film deposited on SiO<sub>2</sub>/Si substrates: (a), Sample S3; (b), Sample S5.

EDS and SIMS analyses were carried out to study the As-doping content in ZnO:As films. EDS was performed in two different areas of the samples to confirm whether the films contain As or not. Figure 20 shows the typical EDS spectrum of ZnO:As film deposited at 350°C on glass, which indicated that the presence of element As besides Zn, O, Ca and Si. Obviously, the peaks of Ca and Si should be ascribed to the glass substrate. The element content in the film is illustrated in Table5 (Fan, et al., 2007a). It can be seen that the film contained almost the same As content in its different areas.

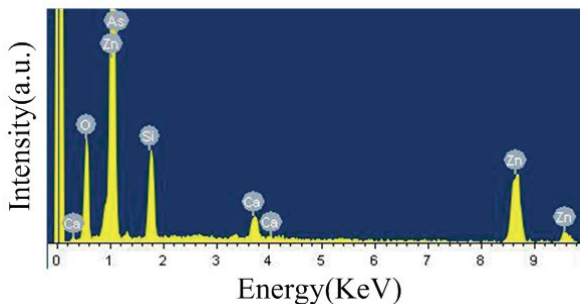


Fig. 20. EDS spectrum of ZnO:As film grown at 350°C on glass.

	Zn	O	As
Content (at%) of various elements in the first area	31.75	67.04	1.21
Content (at%) of various elements in the second area	31.83	66.94	1.23

Table 5. Content (at%) analysis of various elements in the ZnO:As film deposited at 350°C using EDS. From Ref. (Fan, et al., 2007a).

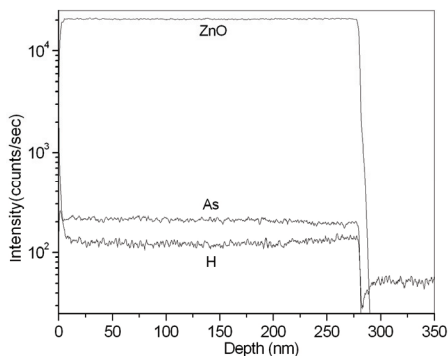


Fig. 21. SIMS spectrum showing the As depth profile of the As-doped ZnO film grown at 450°C on SiO<sub>2</sub>/Si substrate.

SIMS was characterized for ZnO:As films deposited on SiO<sub>2</sub>/Si substrate at 450°C with Ar at 0.5 Pa as working gas, as exhibited in Figure 21. The As element was found to be uniformly distributed in the film sample down to a depth of ~280nm.

XPS was employed to investigate the chemical states of As atoms in ZnO:As films. Figure 22 shows the typical XPS spectra of the As3d, Zn2p and O1s core-level spectra for ZnO:As film. The As (3d) binding energies of the As-O and As-Zn bonds were associated with the values of  $\sim 45$  eV and 41eV, respectively. The observation of the 44.8eV single peak in the As (3d) binding energy in XPS spectrum of ZnO:As film implied that the As atoms occupied the Zn site of the ZnO lattice, which was consistent with the results obtained by Wahl (Wahl, et al., 2005). Asymmetric O1s peak was detected for the sample, which had a shoulder at the higher binding energy side fitting with Gaussian distribution. The buildup of two peaks at 530.53 and 531.93eV was observed. The domination peak at 530.53 was attributed to the  $O^{2-}$  ion in the wurtzite structure surrounded by the Zn ions. The peak at 531.93eV was assigned to loosely bound oxygen, such as absorbed  $O_2$  or adsorbed  $H_2O$  on the ZnO surface or H-implanted in the fabrication of ZnO:As film, which was consistent with the result of SIMS. Two peaks at 1021.73eV and 1044.83eV with a spin-orbit splitting of 23.1eV, corresponding to Zn2p<sub>3/2</sub> and Zn2p<sub>1/2</sub>, respectively were seen in Zn2p XPS spectrum, which coincided with the findings for the Zn<sup>2+</sup> bound to oxygen in the ZnO Matrix.

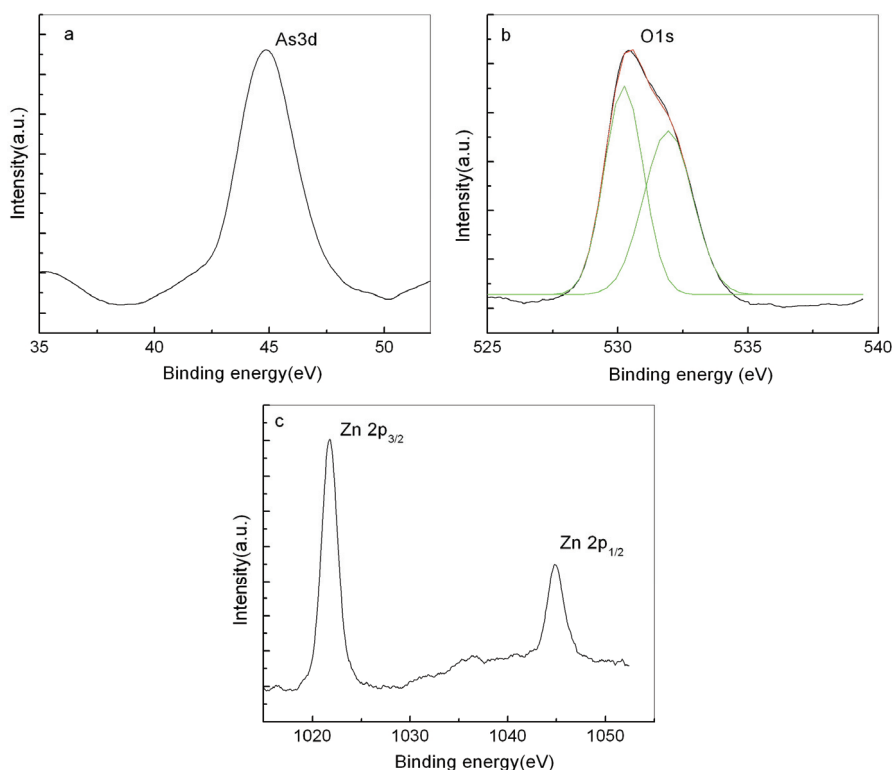


Fig. 22. (a) As3d, (b) Zn2p and (c) O1s core-level spectra for ZnO:As film.

Hall effect measurements were performed on As-doped ZnO films on glass and SiO<sub>2</sub>/Si substrates at room temperature. The electrical properties of As-doped ZnO films on glass substrates are summarized in Tables 6 (Fan, et al., 2007a) and 7.

Samples	Substrate temperature (°C)	Mobility (cm <sup>2</sup> /Vs)	Resistivity (Ω cm)	Carrier concentration (cm <sup>-3</sup> )	Type
A	50	0.979	1.84	3.46×10 <sup>18</sup>	n
B	250	0.891	7.8	8.99×10 <sup>17</sup>	p
C	350	0.3	30.3	6.88×10 <sup>17</sup>	p
D	450	1.96	90.7	3.51×10 <sup>16</sup>	n

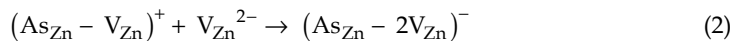
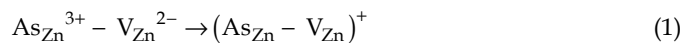
Table 6. Electrical properties of As-doped ZnO films on glass at different substrate temperatures with RF power of 120W. From Ref.(Fan, et al., 2007a).

Samples	RF power (W)	Mobility (cm <sup>2</sup> /Vs)	Resistivity (Ωcm)	Carrier concentration (cm <sup>-3</sup> )	Type
C	120	0.3	30.3	6.88×10 <sup>17</sup>	p
E	150	0.935	48.2	1.39×10 <sup>17</sup>	n

Table 7. Electrical properties of As-doped ZnO films on glass with various RF powers at 350°C.

From Tables 6 and 7, it can be seen that the As-doped ZnO films fabricated with various conditions exhibited different conduction types. The film grown at 50°C (Sample A) was n type with a carrier concentration of 3.46×10<sup>18</sup>cm<sup>-3</sup>, a mobility of 0.979cm<sup>2</sup>/Vs, a resistivity of 1.84Ωcm, however, Sample B, deposited at 250°C, became p-type ( $p = 8.99 \times 10^{17} \text{cm}^{-3}$ ,  $\mu_h = 0.891 \text{ cm}^2/\text{Vs}$ ,  $R = 7.8 \Omega \text{cm}$ ), Sample C grown at 350°C, showed p type, exhibiting a 6.88×10<sup>17</sup>cm<sup>-3</sup> carrier concentration, a 0.3 cm<sup>2</sup>/Vs mobility and 30.3Ωcm resistivity. While the substrate temperature was increased to 450°C or rf power became 150W from 120W at 350°C, corresponding to Sample D ( $n = 3.51 \times 10^{16} \text{cm}^{-3}$ ,  $\mu_e = 1.96 \text{ cm}^2/\text{Vs}$ ,  $R = 90.7 \Omega \text{cm}$ ) and sample E ( $n = 1.39 \times 10^{17} \text{cm}^{-3}$ ,  $\mu_e = 0.935 \text{ cm}^2/\text{Vs}$ ,  $R = 48.2 \Omega \text{cm}$ ), respectively, the samples exhibited n type.

For the mechanism of p-type conductivity of ZnO by doping large-size-match impurities, such as P, As and Sb, Limpijumnong et al proposed As<sub>Zn</sub>-2V<sub>Zn</sub> acceptor Model (Limpijumnong, et al., 2005; Fan, et al., 2007a). This doping mechanism differs from the substitution mechanism of As into O site (As<sub>O</sub>), in which As atom occupies Zn antisite, not O sites, forming As<sub>Zn</sub>-2V<sub>Zn</sub> acceptor with the ionization energy of 0.15eV. The process can be written as:



The formation energy of As<sub>Zn</sub>-2V<sub>Zn</sub> is lower than that of As<sub>Zn</sub> and As<sub>Zn</sub>-V<sub>Zn</sub> and its formation is easier, comparatively. Both As<sub>Zn</sub> and As<sub>Zn</sub>-V<sub>Zn</sub> are donors and As<sub>Zn</sub>-2V<sub>Zn</sub> is acceptor. Zn<sub>3</sub>As<sub>2</sub> is a p-type semiconductor materials. Obviously, the p-type conductivity of the As-doped films deposited for this study can be attributed to Zn<sub>3</sub>As<sub>2</sub> and/or As<sub>Zn</sub>-2V<sub>Zn</sub> complex, while the n-type conductivity is due to As<sub>Zn</sub>, As<sub>Zn</sub>-V<sub>Zn</sub>, intrinsic donor defects (V<sub>O</sub> and Zn<sub>i</sub>) and hydrogen as an unintentional extrinsic donor in ZnO films. For Sample A,

grown at 500°C, the electron concentration associated with donor defects ( $As_{Zn}$ ,  $As_{Zn}-V_{Zn}$ ,  $Vo$ ,  $Zni$  and  $H$ ) was higher than the hole concentration related to  $Zn_3As_2$  and  $As_{Zn}-2V_{Zn}$  complex, and for sample B, deposited at 250°C, was lower, therefore, sample A showed n-type conduction and sample B was p-type. For sample C, ZnO:As films deposited at 350°C, only  $As_{Zn}-2V_{Zn}$  complex acted as acceptor in the film, therefore, hole in the film decreased when substrate temperature increased from 250 to 350°C, however, it was majority carrier. The n-type conductivity of samples D and E was mostly due to form plentiful  $As_{Zn}$  and  $As_{Zn}-V_{Zn}$ , resulting in electron became majority carrier.

In attempting to further understand the thermal induced n-to-p-type conversion of the ZnO:As films, we have carried out Ar-atmosphere annealing study on the n-type ZnO:As film grown on the glass substrate at 450°C. After 400°C annealing for 60min, the film was converted from n type to p type having  $p = 9.10 \times 10^{15} \text{ cm}^{-3}$ , as shown in table 8.

Annealing time (min)	Mobility ( $\text{cm}^2/\text{Vs}$ )	Resistivity ( $\Omega\text{cm}$ )	Carrier concentration ( $\text{cm}^{-3}$ )	Type
20	2.91	88.7	$2.42 \times 10^{16}$	n
40	3.69	176	$9.61 \times 10^{15}$	n
60	4.07	169	$9.10 \times 10^{15}$	p

Table 8. Electrical properties of ZnO:As film (Sample D) post-annealing. From Ref. (Fan, et al., 2007a).

Similar changes of the conduction type were also found for As-doping ZnO films fabricated on  $\text{SiO}_2/\text{Si}$  substrates with various conditions, as summarized in table 9, which was agreement with the  $As_{Zn}-2V_{Zn}$  acceptor Model (Fan & Xie, 2008b).

Samples	RF power (W)	Substrate temperature ( $^\circ\text{C}$ )	Resistivity ( $\Omega \text{ cm}$ )	Mobility ( $\text{cm}^2/\text{Vs}$ )	Carrier concentration ( $\text{cm}^{-3}$ )	Type
S1	100	350	36.1	2.76	$6.26 \times 10^{16}$	P
S2	120	350	66.3	4.44	$2.12 \times 10^{16}$	P
S3	150	350	15.6	1.32	$3.03 \times 10^{17}$	P
S4	120	300	15.55	13.3	$3.02 \times 10^{16}$	n
S5	120	400	10.35	6.08	$9.92 \times 10^{16}$	P

Table 9. Growth parameters and electrical properties of As-doped ZnO films fabricated on  $\text{SiO}_2/\text{Si}$  substrates. From Ref. (Fan & Xie, 2008b).

Figure 23 shows the optical transmittance spectra of undoped ZnO and ZnO:As films deposited on glass at 350°C. The transmittances were over 70% in the visible region and the fundamental absorption edges were clearly observed the films. Compared the absorption edges of the films, the absorption edge of ZnO:As film shifted to short-wavelength, the phenomenon can be observed in the inset of Figure 23, which reveals the relationship between absorption coefficient and photo energy. The optical band gap ( $E_g$ ) value was obtained by extrapolating the linear portion to photo energy axis. As shown in the inset of Figure 23, the  $E_g$  values of the films blueshifted from 3.271 to 3.325 eV.

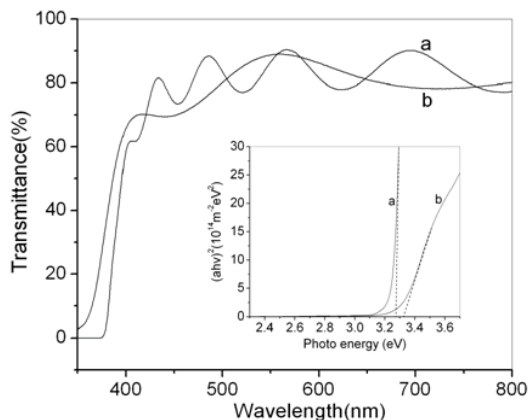


Fig. 23. Transmittance spectra of undoped ZnO (a) and ZnO:As (b) films deposited on glass at 350°C. The inset is the  $(ah\nu)^2$  vs  $h\nu$  curves for the optical band gap determination in the films.

Figure 24 shows the NBE PL spectrum at 10K of the p-type ZnO:As film deposited on SiO<sub>2</sub>/Si substrate. This film shows the dominant A<sup>0</sup>X at 3.337eV and small emission lines such as the free electron to acceptor recombination (FA) at 3.282 eV and the donor acceptor pair emissions at 3.236, 3.197 and 3.158eV (Fan, et al., 2009; Fan, et al., 2010).

The acceptor binding energy (ionization energy) can be calculated by equation (1)

$$E_A = E_{gap} - E_{FA} + k_B T / 2, \quad (1)$$

where  $E_{gap} = 3.437\text{eV}$  and  $E_{FA} = 3.282\text{eV}$  were the band gap energy and the temperature dependent transition energy, respectively. The value of  $E_A$  was calculated to be 155meV, which was nearly consistent with the ionization energy of As<sub>Zn</sub>-2V<sub>Zn</sub> as a shallow acceptor in ZnO (=0.15 eV). That is the As substitutes on the Zn site, then it induces two Zn-vacancy acceptors, forming As<sub>Zn</sub>-2V<sub>Zn</sub> acceptor, which is good agreement with the result about the A3d XPS spectrum.

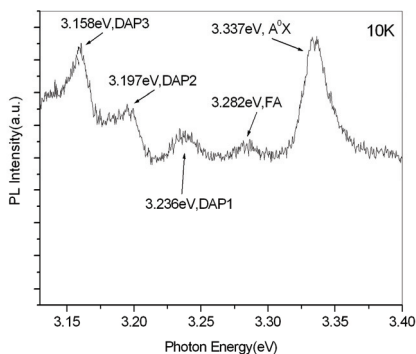


Fig. 24. NBE region of 10 K PL spectrum for p-type ZnO:As film deposited on SiO<sub>2</sub>/Si substrate.

### 5.3 As doped ZnO films prepared by co-sputtering $Zn_3As_2$ and ZnO targets

As-doped ZnO films were deposited on glass substrates by co-sputtering two targets: a pure ZnO and a pure  $Zn_3As_2$ . The working argon pressure was kept at 1.0Pa, and the substrate temperature was in the range of 250 to 500°C. The films were deposited with the RF power of 100W on ZnO target and various direct current (DC) powers (0, 2.5, 7.6 and 9.7W) on  $Zn_3As_2$  target. The grown parameters of the films were summarized in Table10. After deposition, post-annealing was carried out for SampleG at 350 and 450°C, respectively, in Ar ambient for 30min. The thickness of the films was in the range of 100 to 200nm.

Samples	DC power on $Zn_3As_2$ target (W)	Substrate temperature (°C)
F	0	350
G	7.6	350
H	9.7	350
I	2.5	250
J	2.5	300
K	2.5	350
L	2.5	400
M	2.5	450
N	2.5	500

Table 10. The grown parameters of As-doped ZnO by co-sputtering.

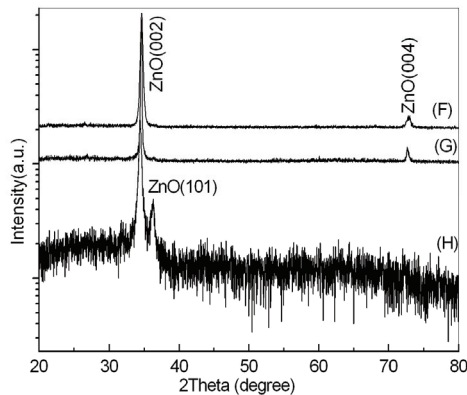


Fig. 25. XRD patterns of As-doped ZnO films with different DC powers on  $Zn_3As_2$  target: (F) 0W, (G) 7.6 W, and (H) 9.7 W. From Ref.(Fan, et al., 2007b).

XRD spectra of the As-doped ZnO films grown with various DC powers on  $Zn_3As_2$  target had a dominate peak at about  $34.4^\circ$  corresponding to the ZnO (002), and no peaks about  $Zn_3As_2$ , as shown in Figure 25, which indicated the films had single phase wurtzite structure and the c-axis preferred orientation. The appearance of ZnO(101) peak for sample H showed that the crystallinity of the film degraded due to mass As doping, observably. Figure 26 showed the XRD patterns of As-doped ZnO films deposited at different temperatures. The peak of  $Zn_3As_2$  (111) in the XRD pattern of the film deposited at 250°C indicated that the film was ZnO/ $Zn_3As_2$  or ZnO:As/ $Zn_3As_2$  one. For the samples fabricated at  $T > 250^\circ\text{C}$ , only ZnO



peaks such as (100), (002), (101), (103) and (004), were observed, indicating that the films were ZnO:As ones. Obviously, the crystallinity of the films improved when the temperature increased from 250 to 400°C, and then became poor when  $T > 400^\circ\text{C}$ . This can be interpreted from nucleation theory.

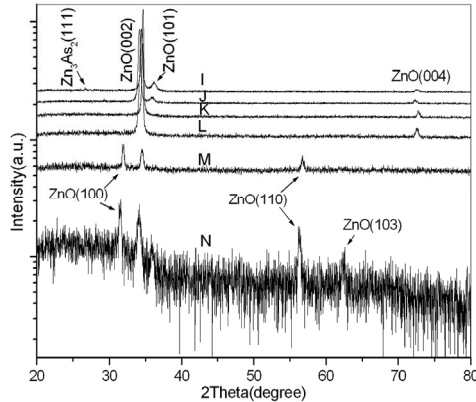


Fig. 26. XRD patterns of As-doped ZnO films grown at various temperatures: 250°C(I), 300°C (J), 350 °C(K), 400°C (L), 450 °C (M), and 500 °C(N). From Ref.(Fan&Xie, 2008a).

The typical XRD patterns of as-grown and annealed ZnO:As films were shown in Figure 27. It can be seen that the ZnO:As films remained the c-axis preferred orientation and the crystallinity did not change observably with annealing treatment in our experiment.

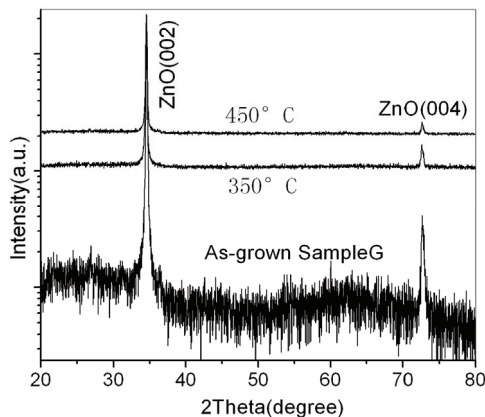


Fig. 27. XRD patterns of the as-grown SampleG and annealed ZnO:As films with different annealing temperatures.

The surface morphology of As-doped ZnO films by co-sputtering were analyzed using SEM. Figure 28 showed the SEM micrographs of ZnO:As film(SampleG: DC power of 7.6W on  $\text{Zn}_3\text{As}_2$  target) and SampleG+annealing at 450°C. The film had a homogeneous surface formed by nano-grains and post-annealing in our experiment did not change the quality of the film, observably, which was consistent with the XRD result (Figure 27).

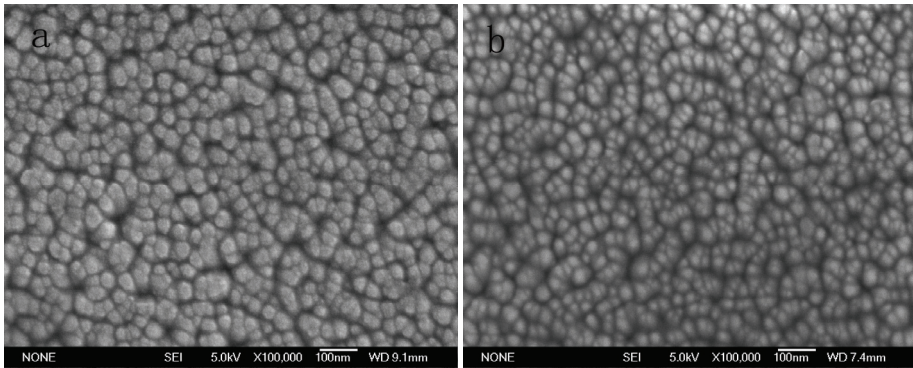


Fig. 28. The SEM micrographs of ZnO:As film(SampleG)(a) and SampleG+annealing at 450°C(b).

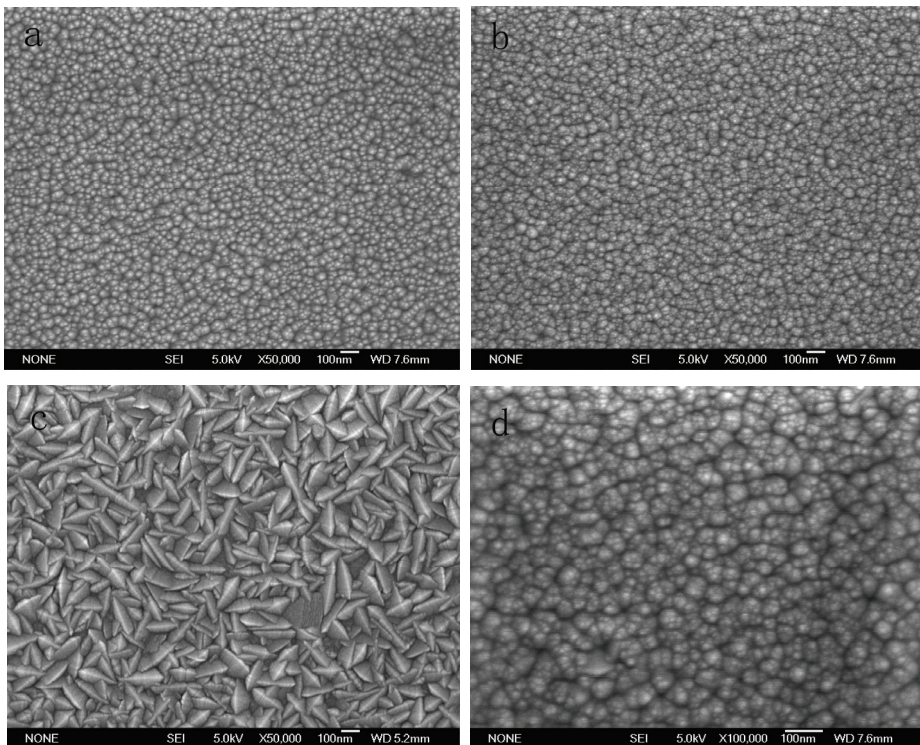


Fig. 29. The SEM micrographs of ZnO:As films deposited at various temperatures: 350°C(a), 400°C(b), (c)450°C, (d) the higher resolution of Fig.29.b .

The SEM micrographs of ZnO:As films deposited with DC power of 2.5W on Zn<sub>3</sub>As<sub>2</sub> target at substrate temperatures from 350 to 450°C, corresponding to Samples K, L and M, respectively. It can be seen that the ZnO:As films with c-axis preferred orientation had

homogeneous surface formed by globe-like grains, indicating the high quality of the films, the nonuniform surface of Sample M grown at 450°C was attributed that excessive As atoms in ZnO structure lead to poor crystallinity at higher temperature. It was noted that the grains like ones in the film deposited at 450°C (Figure 29c) was detected in the film deposited at 400°C, as shown in Figure 29d.

XPS analysis was performed for ZnO:As films deposited by co-sputtering to investigate bonding state of As in the films. The typical XPS patterns were shown in Figure 30. Only a peak at 44.8eV was detected in As3d XPS spectrum, corresponding to As-O, indicating that As was in its oxidization state and it replaced Zn site in the ZnO:As film. A dominated symmetric O 1s peak at 531.2eV was observed, as shown in Figure 30b, indicating the O<sup>2-</sup> ion in the wurtzite structure surrounded by the Zn ions. Figure 30c shows two peaks at 1021.7 and 1044.9eV, corresponding to Zn2p<sub>3/2</sub> and Zn2p<sub>1/2</sub>, respectively. The results about As and Zn chemical bonding were similar to the ones obtained for p-type ZnO:As film grown by sputtering Zn<sub>3</sub>As<sub>2</sub>/ZnO target.

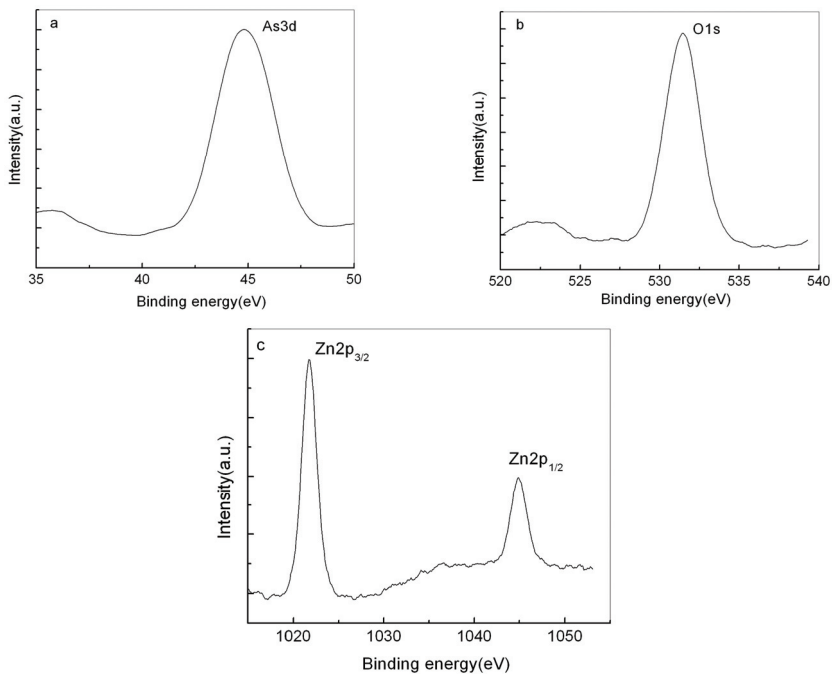


Fig. 30. The typical (a) As3d, (b) Zn2p and (c) O1s core-level spectra for ZnO:As film grown by co-sputtering (SampleH).

The electrical properties of As-doped ZnO films grown with different conditions were characterized by Hall effect measurements at room temperature. The results were summarized in Tables 11 and 12. It noted that the as-grown ZnO:As films deposited with various conditions exhibited different conduction types. For Sample G, deposited at 350°C with DC power of 7.6W on Zn<sub>3</sub>As<sub>2</sub> target showed n type conductivity:  $n = 1.33 \times 10^{18} \text{cm}^{-3}$ ,  $\mu_e = 0.215 \text{cm}^2/\text{Vs}$ ,  $R = 21.8 \Omega \text{cm}$ , however, Sample H, grown at 350°C with DC power of 9.7W on Zn<sub>3</sub>As<sub>2</sub> target, exhibited p type behavior with a carrier concentration of  $8.42 \times 10^{16} \text{cm}^{-3}$ , a

mobility of  $0.717\text{cm}^2/\text{Vs}$ , a resistivity of  $103.5\ \Omega\text{cm}$ . The change of the conduction type of the films was attributed that plentiful  $\text{As}_{\text{Zn}}-2\text{V}_{\text{Zn}}$  acceptor in the film when DC power increased from  $7.6\text{W}$  to  $9.7\text{W}$ , resulting in hole became majority carrier. In Table 11, Also noted that the conduction type of Sample G changed from n type to p type after annealing, which was owed that annealing made reactions (1) and (2) continue, forming more  $\text{As}_{\text{Zn}}-2\text{V}_{\text{Zn}}$  acceptor in the film.

When DC power on  $\text{Zn}_3\text{As}_2$  target remained  $2.5\text{W}$ , the As-doped ZnO films were grown at different temperatures from  $250$  to  $500^\circ\text{C}$ , corresponding to Samples I, L, K, M and N, respectively. The electrical properties of the films was shown in Table 12 (Fan&Xie, 2008a). As shown in this table, the conduction type of As-doped ZnO films conversed from n-type to p-type with increasing the substrate temperature. The films grown at  $250$  and  $300^\circ\text{C}$  and the ones grown at  $400$ ,  $450$ ,  $500^\circ\text{C}$  were n-type and p-type, respectively while the film deposited at  $350^\circ\text{C}$  showed unstable electrical behavior between n- and p-type. The change of the conduction type of the films could also be attributed to form more  $\text{As}_{\text{Zn}}-2\text{V}_{\text{Zn}}$  acceptor in the films grown at  $T \geq 400^\circ\text{C}$ . The reduction of carrier concentration from  $7.40 \times 10^{16}$  to  $1.64 \times 10^{16}\text{cm}^{-3}$  with temperature increasing from  $400$  to  $500^\circ\text{C}$  may be due to plentiful  $\text{As}_{\text{Zn}}$ ,  $\text{As}_{\text{Zn}}-\text{V}_{\text{Zn}}$  donors at excessive temperature, such as  $450$  and  $500^\circ\text{C}$ . In addition, the degeneration of crystallinity of the films deposited at excessive temperature may form a large number intrinsic donors, such as Zn<sub>i</sub> and V<sub>o</sub>, compensating for hole in the films.

Samples	Resistivity ( $\Omega\text{cm}$ )	Mobility ( $\text{cm}^2/\text{Vs}$ )	Carrier concentration ( $\text{cm}^{-3}$ )	Type
F	4.17	1.88	$7.95 \times 10^{17}$	n
G	21.8	0.215	$1.33 \times 10^{18}$	n
H	103.5	0.717	$8.42 \times 10^{16}$	p
G+annealing( $350^\circ\text{C}$ )	64.4	0.143	$6.78 \times 10^{17}$	p
G+annealing( $450^\circ\text{C}$ )	57.2	0.565	$1.94 \times 10^{17}$	p

Table 11. Electrical properties of undoped and As-doped ZnO films deposited with different DC powers on  $\text{Zn}_3\text{As}_2$  target at  $350^\circ\text{C}$ .

Substrate temperature ( $^\circ\text{C}$ )	Resistivity ( $\Omega\ \text{cm}$ )	Mobility ( $\text{cm}^2/\text{Vs}$ )	Carrier concentration ( $\text{cm}^{-3}$ )	Type
250	4.71	0.613	$2.16 \times 10^{18}$	n
300	6.54	0.995	$9.59 \times 10^{17}$	n
350	51.1	0.248/0.0482	$4.92 \times 10^{17}/2.53 \times 10^{18}$	n/p
400	103	0.605	$7.40 \times 10^{16}$	p
450	139	0.957	$6.34 \times 10^{16}$	p
500	248	1.53	$1.64 \times 10^{16}$	p

Table 12. Electrical properties of As-doped ZnO films deposited at various temperatures with  $2.5\text{W}$  DC power on  $\text{Zn}_3\text{As}_2$  target. From Ref.(Fan & Xie, 2008a).

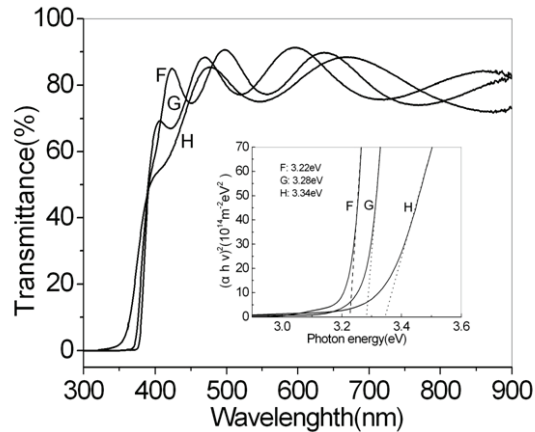


Fig. 31. Transmittance spectra of as-grown ZnO films with different DC powers on  $Zn_3As_2$  target: (F) 0W, (G) 7.6 W, and (H) 9.7 W. The inset is the  $(\alpha h\nu)^2$  vs  $h\nu$  curves for the optical band gap determination in the films. From Ref.(Fan, et al., 2007b).

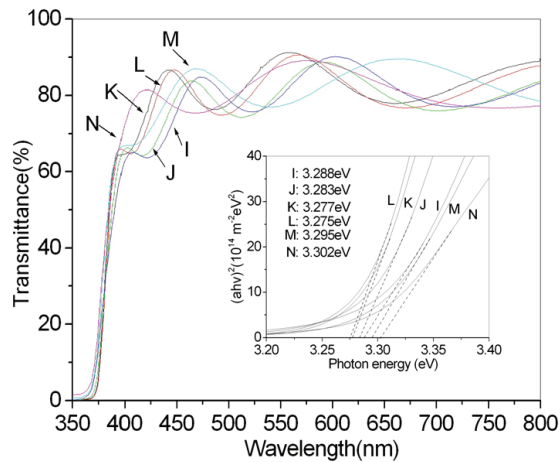


Fig. 32. Transmittance spectra of As-doped ZnO films grown at various temperatures: 250°C(I), 300°C (J), 350 °C(K), 400°C (L), 450 °C (M), and 500 °C(N). The inset is the  $(\alpha h\nu)^2$  vs  $h\nu$  curves for the optical band gap determination in the films. From Ref.(Fan & Xie, 2008a).

Figure 31 shows the optical transmittance spectra of undoped and As-doped ZnO films (Samples F,G and H). The transmittances were over 70% in visible region. The absorption edge of the films shifted to short-wavelength as DC power on  $Zn_3As_2$  target increased, indicating that the  $E_g$  of the films blueshifted, as shown in the inset in Figure 31. From XRD results, the phenomenon was attributed to the effects of As doping on the crystallinity of the films. In a simplified physical model, the structure can be considered as various nanocrystalline islands embedded in a matrix of amorphous ZnO. The absorption of photon was mainly ascribed to amorphous ZnO phase in the films and as the fraction of amorphous ZnO phase in the films increased, the extended localization in the conduction and valence

band increased. For the As-doped ZnO films deposited with different DC power on Zn<sub>3</sub>As<sub>2</sub> target, the c-axis preferred orientation of the films became weaker and the crystallinity of the films degraded with DC power increased (Figure 25), resulting in amorphous ZnO phase in the films increased, therefore, the E<sub>g</sub> value blueshifted from 3.22 to 3.34eV. Similar phenomenon was also observed in the transmittance spectra of As-doped ZnO films grown at various temperature, as shown in Figure 32 (Fan & Xie, 2008a). The shift of E<sub>g</sub> value in Figure 32 was also owned to amorphous ZnO phase in the films. The crystallinity of ZnO films improved and the amorphous ZnO phase in the films decreased when the substrate temperature increased from 250 to 400°C, the E<sub>g</sub> value red-shifted from 3.288 to 3.275eV. For p-type As-doped ZnO films grown at T ≥ 400°C, the crystallinity of the films became poorer and the amorphous ZnO phase in the films increased, the E<sub>g</sub> value blue-shifted from 3.275 to 3.302eV.

## 6. Conclusion

p-Type ZnO:As films with hole concentration 10<sup>16</sup>-10<sup>17</sup> cm<sup>-3</sup> were fabricated on glass and SiO<sub>2</sub>/Si substrates at different temperatures by sputtering Zn<sub>3</sub>As<sub>2</sub>/ZnO target or cosputtering Zn<sub>3</sub>As<sub>2</sub> and ZnO targets, demonstrating two new approaches to obtain p-type ZnO films for the development of ZnO-based optoelectronic devices. We studied the structural, electrical and optical properties of As-doped films with various methods and discussed the changes of conduction type of As-doped ZnO films deposited with different conditions. XPS results revealed that As was in its oxidization state and it occupied the Zn site in ZnO:As films. PL investigation showed that the acceptor binding energy was ~150 meV. Both XPS and PL results were consistent with As<sub>Zn</sub>-2V<sub>Zn</sub> acceptor model about p-type conductivity of As-doped ZnO film proposed by Limpijumnong *et al.*, which helped to understand the microscopic structure of As in As-doped ZnO and the microscopic origin of p-type ZnO by doping large-size-mismatched impurities.

## 7. Acknowledgement

The work was supported by the Fundamental Research Funds for the Central Universities (Contract No.: 531107040334) and the Aid Program for Science and Technology Innovative Research Team in Higher Educational Institution of Hunan Province. The authors would like to acknowledge Yujia Zeng in State Key Laboratory of Silicon Materials (Zhejiang University) for Hall effect measurement.

## 8. References

- Fan J.C.; Xie Z.; Wan Q. & Wang Y.G.(2007a), Dependence of conduction type of ZnO films prepared by sputtering a Zn<sub>3</sub>As<sub>2</sub>/ZnO target on substrate temperature and treatment, *J.Cryst. Growth*304, 295-298.
- Fan J.C.; Xie Z.; Wan Q. & Wang Y.G.(2007b), As-doped p-type ZnO films prepared cosputtering ZnO and Zn<sub>3</sub>As<sub>2</sub> targets, *J. Cryst. Growth* 307, 66-69.
- Fan J.C. & Xie Z. (2008a), Effects of substrate temperature on structural, electrical and optical properties of As-doped ZnO films, *Mater. Sci. and Eng.B* 150, 61-65.
- Fan J.C. & Xie Z. (2008b), As-doped p-type ZnO films grown on SiO<sub>2</sub>/Si by radio frequency magnetron sputtering, *App. Surf. Sci.* 254,6358-6361.

- Fan J.C.; Zhu C.Y.; Fung S. Zhong Y.C.; Wong K.S.; Xie Z.; Brauer G.; Anwand W.; Skorupa W.; To C.K.; Yang B.; Beling C.D.& Ling C.C.(2009), Arsenic doped p-type zinc oxide films grown by radio magnetron sputtering, *J.Appl. Phys.*106, 073709 (6pages).
- Fan J.C.; Ding G.W.; Fung S.; Xie Z.; Zhong Y.C.; Wong K.S.; Brauer G.; Grambole D.&ling C.C.(2010), Shallow acceptor and hydrogen impurity in p-type arsenic-doped ZnMgO films grown by radio frequency magnetron sputtering, *Semicond. Sci. Technol.* 25, 085009(5pages).
- Heo Y. W., Kwon Y. W., Li Y., Pearton S. J.,& Norton D. P. (2003), Transport properties of phosphorus-doped ZnO thin films, *Appl.Phys.Lett* 83,1128(3pages).
- Janotti A. & Van de Walle C.G.(2009), Fundamentals of zinc oxide as a semiconductor, *Rep.Prog.Phys.*72, 126501(29pages).
- Klingshirn C.(2007), ZnO: Materials, Physics and Applications, *Chem.Phys.Chem*8, 782-803.
- Kang H.S.; Ahn B.D.; Kim J.H.; Kim G.H.; Lim S.H.; Chang H.W.& Lee S.Y.(2006), Structural, electrical, and optical properties of p-type ZnO films with Ag dopant, *Appl.Phys.Lett* 88,202108(3pages).
- Limpijumngong S.; Zhang S.B.; Wei S.H.&ParkC.H.(2005), Doping by large-size-mismatched impurities:The microscopic origin of arsenic or antimony-doped p-type zinc oxide, *Phys.Rev.Lett.*92(15),155504 (4pages).
- Look D.C. (2001), Recent advances in ZnO materials and devices, *Mater.s. Sci.and Eng. B* 80, 383-387.
- Look D.C. & Claflin B.(2004),P-type doping and devices based on ZnO, *Phys.Status.Solidi B* 241,264-630.
- Look D.C.; Renlund G. M.; Burgener II R.H.&Sizelove J.R.(2004), As-doped p-type ZnO produced by an evaporation/sputtering process, *Appl.Phys.Lett* 85(2),5269-5271.
- McCluskey M.D. & Jokela S.J.(2009), Defects in ZnO, *J. Appl.Phys.*106,071101 (13pages).
- Minegishi K. et al (1997), Growth of p-type zinc oxide films by chemical vapor deposition, *Jpn J. Appl.Phys.*36, 1453-1455.
- Marfaing Y. & Lusson A.(2005), Doping engineering of p-type ZnO, *Superlattices and Microstructures* 38 , 385-396.
- Madelung O. (Ed.) (1996), *Semiconductors- Basic data* 2<sup>nd</sup> revised Edn, Springer, ISBN: 3540608834, Berlin.
- Norton D.P.; Heo Y.W.; Ivill M.P.; Ip K.; Pearton S.J.;Chisholm M.F.& Steiner T.(2004), ZnO: growth, doping & processing, *Mater. Today* 6, 34-40.
- Özgür Ü.; Alivov C.; Liu C.; Teke A.; Reshchikov A.; Doğan S.; Avrutin V.; Cho S.-J.& Morkoç H.(2005), A comprehensive review of ZnO materials and devices, *J. Appl.Phys.*98, 041301(103pages).
- Petersen J.; Brimont C.; Gallart M.; Crégut O.; Schmerber G.; Gilliot P.; Hönerlage B.;Ulhaq-Bouillet, C.; Rehspringer J. L.; Leuvrey C.;Colis S.; Aubriet H.; Becker C.; Ruch D.; Slaoui A.&Dinia A.(2008), Structural and photoluminescence properties of ZnO thin films prepared by sol-gel process, *J. Appl. Phys.* 104, 113539 (5pages).
- Park C H, Zhang S B., Wei S H.(2002) Origin of p-type doping difficulty in ZnO: the impurity perspective. *Phys. Rev. B*, 66: 073202(3pages).
- Ryu Y.R.; Zhu S.; Look D.C.; Wrobel J.M.; Jeong H.M.&White H.W.(2000), Synthesis of p-type ZnO films, *J.Cryst. Growth* 216, 330-334.

- Shur M. & Davis R F.(2004), GaN-based Materials and Devices: Growth, Fabrication, Characterization and Performance. N. J., London World Scientific Publishing Co.,
- Tsukazaki A.; Ohtomo A.; Onuma T.; Ohtani M.; Makino T.; Sumiya M.; Ohtani K.; Chichibu S.F.; Segawa Y.; Ohno H.; Koinuma H.& Kawasaki M.(2005), Repeated temperature modulation epitaxy for p-type doping and light-emitting diode based on ZnO. *Nat. Mater.*4, 42-46.
- Wang Z. L. (2004), Nanostructures of zinc oxide, *Mater.Today*7,26-33.
- Wenckstern H Von (2008), Doping, contacting, defect levels and transport properties of ZnO (Dissertation).
- Wahl U.; Rita E.; Cooreia J. G.; Marques A.C.; Alves E,& Soares J.C.(2005), Direct evidence for As as a Zn-site impurity in ZnO, *Phys.Rev.Lett.*95,215503(4pages).
- Xiu F.X.; Yang Z.; Mandalapu L.J.; Zhao D.T. & Liu J.L. (2005), Photoluminescence study of Sb-doped p-type ZnO films by molecular-beam epitaxy, *Appl.Phys.Lett.* 88,052106(3pages).
- Yu H.D.; Zhang Z.P.; Han M.Y.; Hao X.T.& Zhu F.R.(2005), A general low-temperature route for large-scale fabrication of highly oriented ZnO nanorod/nanotube arrays, *J.Am.Chem.Soc.*127, 2378-2379.
- Yan Y. F.;Al-Jassim M. M.& Wei S.H.(2006),Doping of ZnO by group-IB elements, *Appl.Phys.Lett.* 89, 181912(3pages).
- Yan Y.F. & Zhang S. B.(2001), Control of doping by impurity chemical potentials: predictions for p-type ZnO, *Phys.Rev.Lett.*86(25), 5723-25726.
- Yamamoto T. (2002), Codoping for the fabrication of p-type ZnO, *Thin Solid Films* 420-421,100-106.
- Yi G.C.; Wang C.R. & Park Won II( 2005), ZnO nanorods: synthesis, characterization and applications, *Semicond. Sci. Technol.*20, 22-34.
- Zhong Y.C.; Hsu Y.F.; Djurišič A.B.; Hsu Y.F.; Wong K.S.; Brauer G.; Ling C.C.& Chan W. K.(2008), Exceptionally long exciton photoluminescence lifetime in ZnO tetrapods, *J.Phys.Chem.C*112 (42),16286-16295.



# Light Intensity Fluctuations and Blueshift

Moon Kyu Choi  
*Hongik University*  
*South Korea*

## 1. Introduction

Chaos-like properties such as noise or fluctuations arising from quantum effects have recently investigated on a single barrier potential and on a one-dimensional periodic potential barrier. They used either the plane wave of light or a wavepacket (pulse) passing through the potential barrier, demonstrating the chaos created by the bounded one-dimensional multibarrier potential (Bar and Horwitz, 2002; Hondou and Sawada, 1995), and proved it is an ordered and periodic phenomenon. Also another group demonstrated unexpected behavior of a dissipative particle in simple multiscale systems subject to chaotic noise and clarified the reason for the particular behavior because it is under a periodic potential (Chialvo et al., 1997). They concluded the occurrence of drift in a symmetric periodic potential would be expected to be a common feature of noise-driven systems. Essentially this effect is quite similar to the problem of a particle placed in a potential well of finite barrier (Cohen-Tannoudji et al., 1977) and the present issue of the photon distribution on a crystallite surface.

When the crystallite size decreases to a few nanometers, the light absorption or photoluminescence in air moves to the direction of smaller wavelength, which is known as the blueshift (Kale and Lokhande, 2000; Nanda et al., 1999; Tsunekawa et al., 2003; Von Behren et al., 2000). The basic theory for this phenomenon is the quantum confinement effect (Andersen et al., 2002; Sharma et al., 2005). According to this theory the number of photons confined in each unit cell increases with the decreasing crystallite size. It is also said to enlarge the band gap between the valence band and the conduction band. Another approach is to take crystalline unit cells as numerical elements and employ different potential energies over a unit cell (Choi, 2007; Choi and Kim, 2007), realizing light intensity fluctuations. The effect of the film thickness on the blueshift was investigated by one of the authors (Choi and Pyun, 2008) about cellular crystalline surfaces with periodic potential, getting the blueshift numerically demonstrated in good agreement with experiments.

In this paper we deal with surface nanostructures and try to prove the blueshift numerically by predicting the location of absorption wavelength. One of the best ways to uphold the present numerical method would be to demonstrate the blueshift phenomenon observed widely experimentally (Lu et al., 2008; Miyake et al., 1999; Tan et al., 2005; Tsunekawa et al., 2000). They demonstrated experimentally the dependence of the blueshift on the crystallite size for CeO and CdS. One of the authors has been studying this problem recently, publishing a few papers (Choi, 2007; Choi and Kim, 2007; Choi and Pyun, 2008), and this paper may be taken as an extension of these consecutive efforts. Another publication (Choi and Choi, 2009) predicting the blueshift with respect to the shell layer thickness has been already accomplished and led the present investigation to be made.

Another possible and not-yet-practiced application from the same technique would be coating a heat radiant or absorbing surface with paint of nanoparticle dispersion. To save energy it is extremely important to have the best emissive or absorptive coefficient of radiation. It is desirable to find the criteria to produce such surfaces with a double layer having nanoparticles dispersed. The average distance between the nanoparticles is one of the important parameters that have a big influence on the emission or absorption. The present technique would be an excellent approach to that problem.

## 2. Theoretical background

We are considering a single-layer microsphere irradiated by monochromatic unpolarized light wave and investigate the realization of light intensity fluctuations at the absorption wavelengths. Figure 1 displays a schematic of the present situation. We want to show numerically the blueshift phenomenon observed experimentally. This is the phenomenon that the absorption (or the luminescence) wavelength decreases with decreasing unit cell or particle sizes (Andersen et al., 2002; Kale and Lokhande, 2000; Nanda et al., 1999; Sharma et al., 2005; Tsunekawa et al., 2003; Von Behren et al., 2000). Since this investigation is an extension of the former ones, most mathematical formulations are omitted here and only essential contents are stated. The details may be referred to in the previous publications (Choi, 2007; Choi and Kim, 2007; Choi and Pyun, 2008). Readers are especially advised that they see Ref. (Choi, 2001) for the modeling details. The electric and magnetic vectors in both the internal and the external regions must satisfy the macroscopic Maxwell equations that govern the behavior of electromagnetic fields. Taking the harmonic time dependence to be  $\exp(-i\omega t)$  for all fields and assuming no free charge, we reduce the Maxwell equations to a set of vector wave equations for the electric field  $\mathbf{E}$  and the magnetic field  $\mathbf{H}$ :

$$\nabla^2 \mathbf{E} + k^2 \mathbf{E} = 0, \quad (1)$$

$$\nabla^2 \mathbf{H} + k^2 \mathbf{H} = 0, \quad (2)$$

where  $k$  is the wave number,  $k = \omega(\epsilon\mu)^{1/2}$ ,  $\epsilon$  is the complex permittivity, and  $\mu$  is the permeability.

It is very difficult to solve Eqs. (1) and (2) numerically. There are three scalar equations coupled to solve simultaneously for each layer, since Eqs. (1) and (2) are separate vector equations. To treat the present case, one has to solve nine equations in general simultaneously. One can derive, however, the governing equations for the Debye potentials, which are equivalent to Schrödinger equations, to represent the TM and TE modes from Eqs. (1) and (2) as done in the Mie method of solution. For the particle or the air outside the particle, the Debye potentials are governed by

$$\nabla^2 u + k^2 u = 0, \quad (3)$$

Note that the scalar governing equations for each layer are separate and independent of each other; this is the great advantage of employing the Debye potentials over solving Eqs. (1) and (2) directly.

One has to note that these transformed equations are, as a matter of fact, Schrödinger equations which govern the quantum behavior of particles, or photons in this case. The wave number,  $k$ , is related to the refractive index of particle or medium,  $N$  as follows.

$$k = \frac{N\omega}{c} \quad (4)$$

Here the frequency,  $\omega$ , and the light speed in vacuum,  $c$ , are constant, but the refractive index changes depending on particle material. We know from the quantum mechanics that the wave number is also related to the potential energy ( $U$ ) as

$$k^2 = (E - U) \frac{8\pi^2 m}{h^2} \quad (5)$$

The significance of bigger wave number or higher refractive index is lower potential energy. In this study we want to treat a single-layer microsphere with crystalline unit cells covered on, so photons should experience different potential energies depending on whether they are placed on the edges of the cells or their inside. Figure 2 shows a typical graph of potential energies in the whole system, which is as similar a situation as finite well potentials in series. For a single photon particle making a harmonic oscillation in a particular coordinate let the displacement from the position of equilibrium be  $q$  (Denbigh, 1981). The potential energy is given by

$$U = \frac{1}{2} b q^2 \quad (6)$$

We need to separate the potential energy into two different regions, the edge and the inside of a unit cell. The edge value of the potential energy leads us to use a specific refractive index on the end points of numerical elements in order to solve Eq. (3). On the other hand, the inside quadratic variation of the potential energy may be approximated by taking linear averages of the endpoint values instead of solving Eq. (3). This approximating method saves us from finding the refractive index of the inside. If the size of a unit cell (or a crystallite) decreases, we may have a different value of  $b$  in Eq. (6), but here in this research we just make an *ad hoc* assumption that the value of  $b$  remains constant. Then with a new smaller unit cell we should have a smaller potential energy on the edge of the cell and thus the refractive index gets bigger (See Fig. 3).

The boundary element method developed recently by the author in a previous investigation (Choi, 2007) is extended to study an absorption problem on a single-layer sphere and suggest a method to predict the light intensities on a  $\text{TiO}_2$  microsphere. Since the governing equations in the present investigation, the Helmholtz type equations, admit of the boundary-element formulation, one need only calculate two integral equations simultaneously for each surface. Since we are dealing with a single-layer microsphere here, we need to make two layers in a coated microsphere the same material.

There are many factors that influence light intensity fluctuations. Some of them are the crystalline size, the shell layer (or film) thickness, the particle size, etc. Besides other chemical and physical properties including chemical compositions, passivation and surface morphology may also be in effect. These implicit properties are represented by the refractive index (or the potential energy). We need to demonstrate blueshift theoretically somehow with one of those causes. The effect of the shell thickness on the blueshift was investigated in a previous research (Choi and Choi, 2009) and the blueshift was proved by the numerical approach. In this paper we especially want to study on the effects of the crystalline size on the blueshift, fixing other parameters. The realization of the blueshift by the boundary element method would be another great proof of the author's recent successive publications.

The properties of any thermodynamic system in macroscopic equilibrium with its surroundings, for instance, the energy, the density, etc., undergo microscopic fluctuations, but give us only average values. The intrinsic fluctuations in matter-density are most easily observed by the scattering of light which they produce in transparent systems. Another well-known example is the critical opalescence with the substance at the critical

point. The fluctuation-dissipation theorem (Chandler, 1987) expresses a relation between the susceptibility of an irreversible response and equilibrium fluctuations. Phenomenologically it is found that the flow of energy in a thermally conducting body is proportional to the gradient of the temperature. Likewise the electric potential difference causes the flow of electrons in a conductor. The phenomenological thermal and electrical conductivities are related to the autocorrelations of fluctuations of some properties. Similarly the energy conversion from one type to another may occur from the fluctuations of energy on the interface. This research area is named as fluctuation-induced transport (Chialvo et al., 1997).

The problem dealt with in the present investigation is about steady-state photon densities inside a microscale single-layer dielectric sphere, given the surface intensities of the incident light. The sphere may be, therefore, considered as a thermodynamic equilibrium system and the fluctuations of light intensities should be related to some kind of energy conversion rates by the fluctuation-dissipation theorem. The electron transfer among microstates can happen after a part of input photon energy is transferred to the particle surface. These excited electrons may contribute to photovoltaic effects, photocatalytic behaviors, and photoluminescence.

### 3. Results and discussion

We studied three cell (i.e., crystallite) sizes in the present investigation. Intuitively if the cell sizes reduce, the potential energy difference between the edges of a unit cell and its inside will be changed according to the Eq. (6). If we assume the parameter,  $b$ , in Eq. (6) remains constant over different crystallite sizes, then we can see that the refractive index on the edge of the smaller crystallite becomes larger. We will show, therefore, the numerical results obtained by increasing the refractive index (or decreasing potential energies) with decreasing cell size. One of the main purposes of this paper is to demonstrate the blueshift numerically. For this purpose Table I and the following set of parameters are employed for typical demonstrations:

- light: 100 – 1100 nm wavelength at 10 nm intervals and unpolarized
- microparticle radius: 500 nm
- microsphere material:  $\text{TiO}_2$
- medium outside the microsphere: air
- incident direction of light: +z-axis

Case	#1	#2	#3
cell size [nm]	3.00	2.52	2.17
refractive index of $\text{TiO}_2$	2.43+i0.01	2.83+i0.01	3.23+i0.01

Table 1. Parameters for modeling.

The numerical results obtained using these data are shown in Fig. 4-7. The angle in the x-axis of graphs is the azimuthal angle measured from the +z-axis, the light propagation direction as shown in Fig. 1. The value of +1 implies the peripheral location where the sphere is exposed to the incident light whereas -1 is the opposite location. The source functions are the ratio of the electric field magnitude of the incident light to that of the absorption light. One may regard this source function as the intensity ratio. Figures 4(a)–(d) display the source functions numerically calculated on the particle surface of crystallite size 3.0 nm. Parts (a) and (b) display surface intensity results at the interval of about 100 nm. As a matter of fact

calculations were done with the interval of 10 nm from 100 nm to 1100 nm in wavelength, but only representative results are shown. As one can see from part (b), fluctuations are remarkable at the wavelength of 700 nm and more detailed data from around it are shown in parts (c) and (d). One can observe fluctuations to occur notably between 680 nm and 720 nm. One may anticipate this wavelength will be the absorption peak when the absorption spectra are taken. If you look at the plots in part (b), you will find a little fluctuations with the wavelengths over 1000 nm. This happens because the ratio of the cell size to the wavelength is small enough in this region of wavelength (Choi and Kim, 2007). Thus we can expect there should be light absorption here too, and it is not related to jumping the bandgap, but to heat dissipation. Moreover, this latter region of wavelength yielding fluctuations is not our concern here because it is infrared (IR).

Then we had the crystallite size reduced to 2.51 nm by increasing the number of numerical elements on the particle surface. When one has two different crystallite sizes, the smaller crystallite may have a higher potential energy on the edge of the crystallite than the bigger one. Therefore, we need to increase the refractive index from the value (or  $2.43 + i 0.01$ ) which corresponds to the case of 3.0 nm crystallite size. The numerical results from the increased refractive index (or  $2.83 + i 0.01$ ) are shown in Fig. 5 (a)–(d) and we can see from part (b) that there are fluctuations around 620 nm (i.e., implying the blueshift), which are more in detail displayed in parts (c) and (d). We can see noticeable fluctuations over 800 nm, but it is as similar a phenomenon as observed in Fig. 4(b) at the wavelengths over 1000 nm with 3.00 nm crystallite size, and they are beyond our wavelength region of concern. Besides since the ratio of crystallite size to wavelength became lower here than in the former case, the incipient wavelength causing heat dissipation to move from 1000 nm to 800 nm.

We decreased the crystallite size further to 2.16 nm by increasing the number of numerical elements. As is the case with the crystallite size of 2.51 nm, the refractive index on the edge of unit cell is increased a little more to be  $3.23 + i 0.01$ . The numerical results from this case are displayed in Fig. 6 (a)–(d). We can clearly see that the location of fluctuations moved to about 570 nm.

The above results of absorption wavelength are summarized in Fig. 7. The solid points are the representative absorption wavelengths yielding the strongest intensity fluctuations while the vertical line segments denote the ranges of wavelength where intensity fluctuations are seen. These representative wavelengths are thought to be the location where light is absorbed and it is, in other words, the bandgap. As was explained in the Introduction, the blueshift has been observed as the crystallite sizes reduce in semiconductor nanomaterials (Kale and Lokhande, 2000). According to the fluctuations-dissipation theorem, one can expect that light absorption happens at the wavelength showing fluctuations. Therefore, we could demonstrate the blueshift numerically by employing three crystallite sizes.

Figure 8 is the comparison of the present numerical results with the experiments (Von Behren et al., 2000) from another research group. This group was arbitrarily chosen since their data were available to be shown for comparison. A few other experimental results from other groups mentioned in the Introduction are in qualitative agreement with our numerical demonstration, but they did not display their results specifically and quantitatively enough to be presented here. Significant agreement can be seen in Fig.8 although the two results came from totally different situations of materials (i.e., refractive indices) and morphology.

#### 4. Conclusion

A single-layer  $\text{TiO}_2$  microsphere where the refractive index of microsphere is adjusted depending on the crystallite size is irradiated by monochromatic unpolarized light. We

could find the wavelength location where light absorption is highly probable because of severe intensity fluctuations. This wavelength location moves toward smaller wavelength (i.e., blueshift) as the crystallite size reduces. Qualitatively, this demonstration agrees with experiments from other research groups.

## 5. Acknowledgments

This work was supported by the 2010 Hongik University Academic Research Support Fund.

## List of Figures

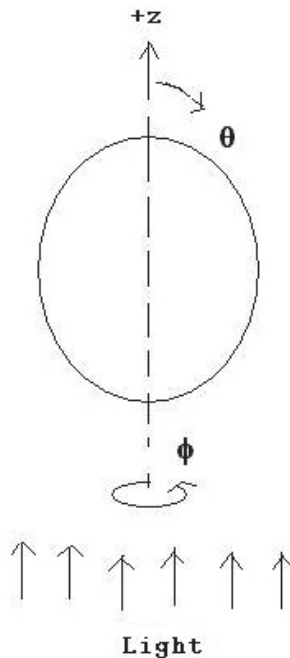


Fig. 1. Schematic diagram of a microsphere. The monochromatic unpolarized light irradiates a single-layer microsphere in the  $+z$  direction.

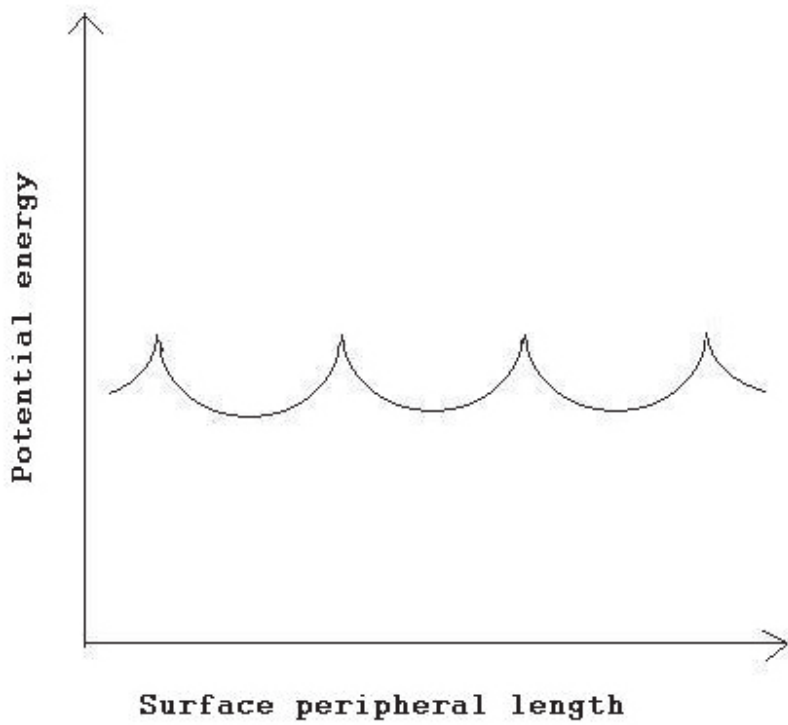


Fig. 2. The potential energy variation along a particle peripheral surface.

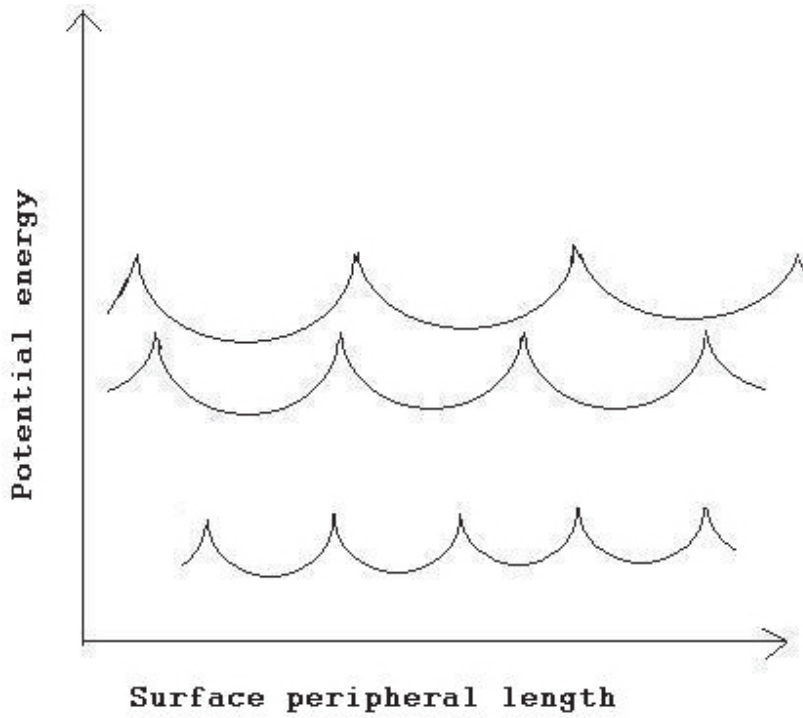


Fig. 3. The potential energy variation with the crystallite size reduction.



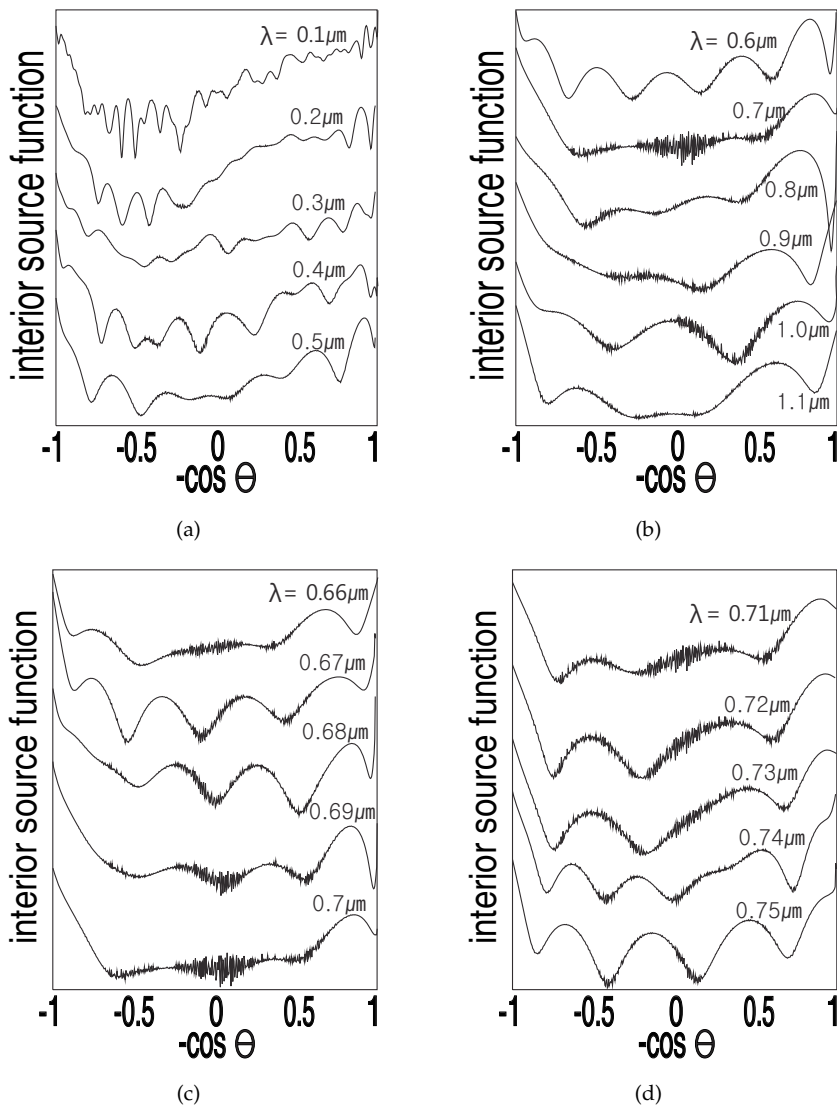


Fig. 4. Source functions vs.  $\cos(\text{angle})$  for a single-layer microsphere of 500 nm radius, the crystal size of 3.0 nm, and many different wavelengths. (a) For the wavelengths from 100 nm to 600 nm. (b) For the wavelengths from 700 nm to 900 nm. (c) and (d) More detailed data for wavelengths between 710 nm and 800 nm. The number of surface peripheral elements were 525. The refractive index on the unit cell edge was chosen to be  $2.43+i0.01$ . The abscissa tic -1 corresponds to a point on the particle surface opposite the incident light (in the forward scattering direction) and +1 corresponds to the point nearest the incident light source (in the back scattering direction).

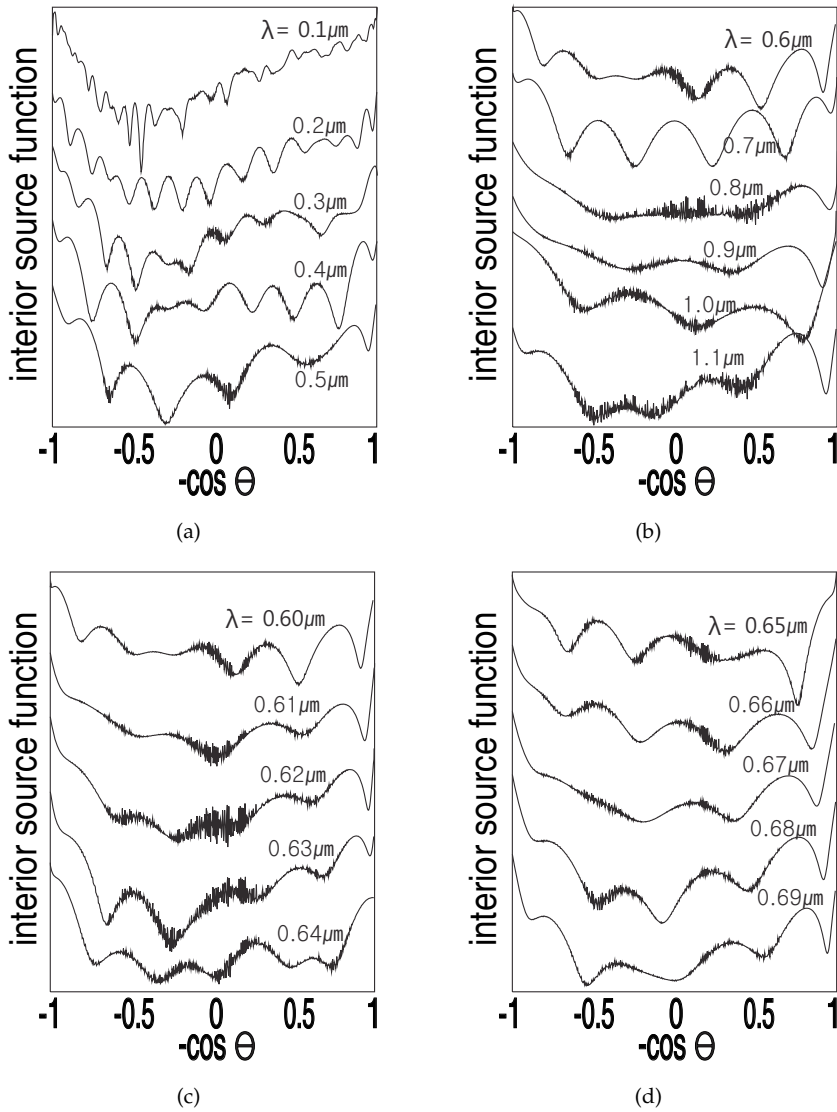


Fig. 5. Source functions vs.  $\cos(\text{angle})$  for a single-layer microsphere of 500 nm radius, the crystal size of 2.52 nm, and many different wavelengths. (a) For the wavelengths from 100 nm to 500 nm. (b) For the wavelengths from 600 nm to 1100 nm. (c) and (d) More detailed data for wavelengths between 600 nm and 690 nm. The number of surface peripheral elements were 625. The refractive index on the unit cell edge was chosen to be  $2.83+i0.01$ .

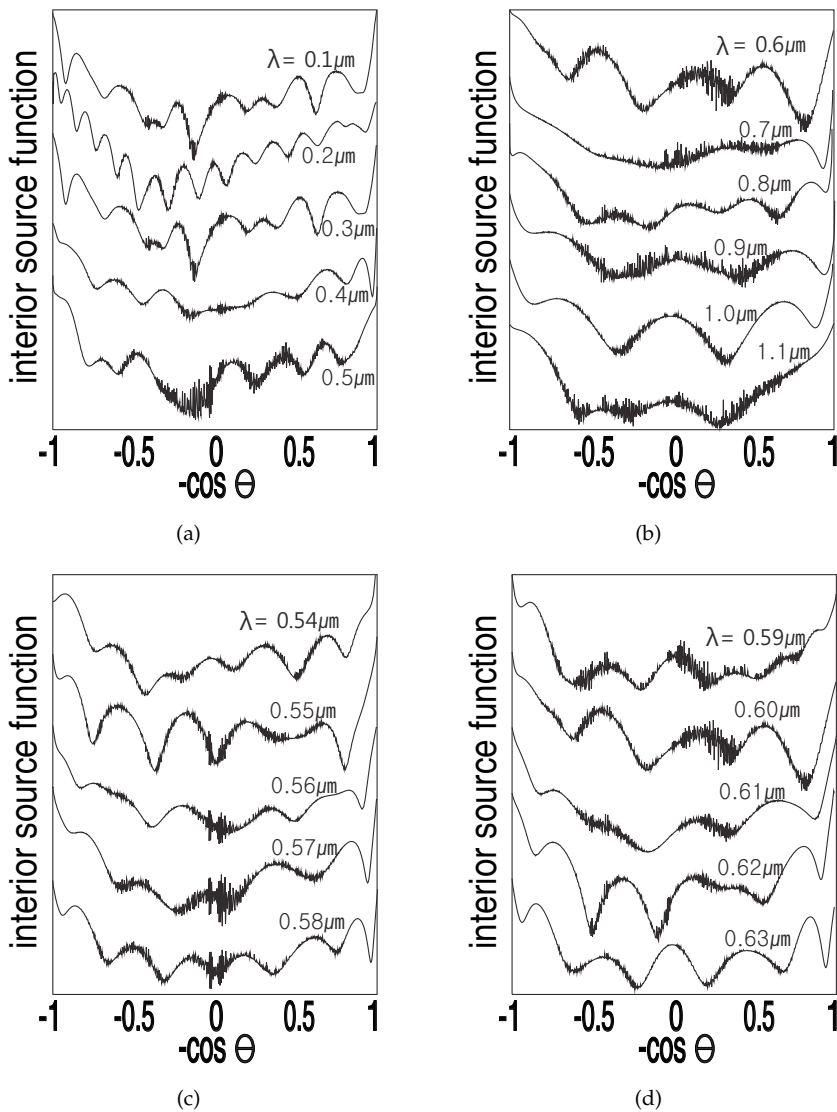


Fig. 6. Source functions vs.  $\cos(\text{angle})$  for a single-layer microsphere of 500 nm radius, the crystal size of 2.17 nm, and many different wavelengths. (a) For the wavelengths from 100 nm to 500 nm. (b) For the wavelengths from 600 nm to 1100 nm. (c) and (d) More detailed data for wavelengths between 540 nm and 630 nm. The number of surface peripheral elements were 725. The refractive index on the unit cell edge was chosen to be  $3.23+i0.01$ .

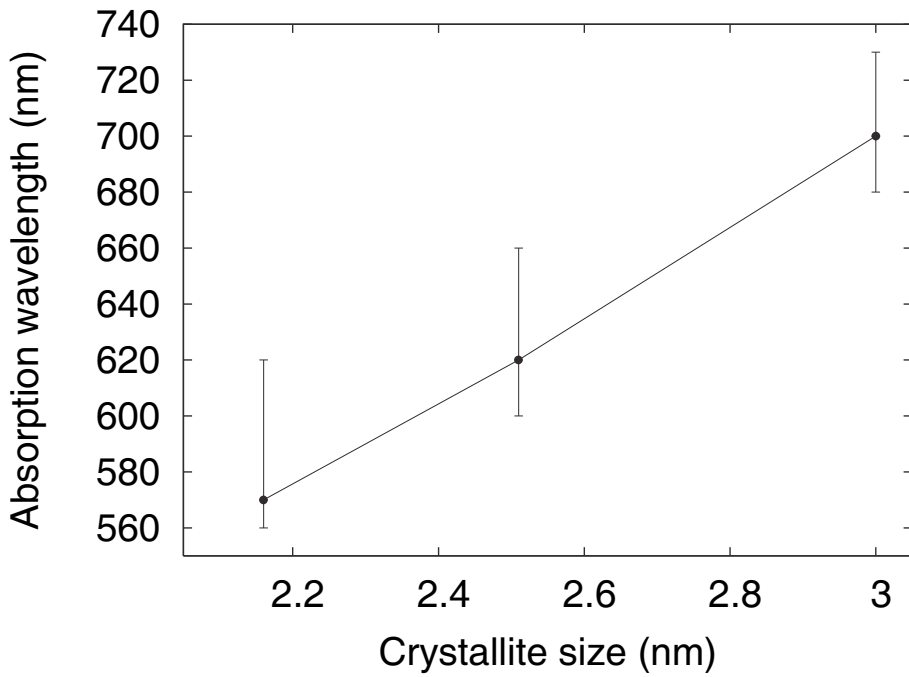


Fig. 7. The absorption wavelengths versus the crystallite sizes are summarized here after their identifications from Figs. 4–6. The points are the exact locations of wavelength for the strongest fluctuations while the vertical bars represent a range where fluctuations are seen.

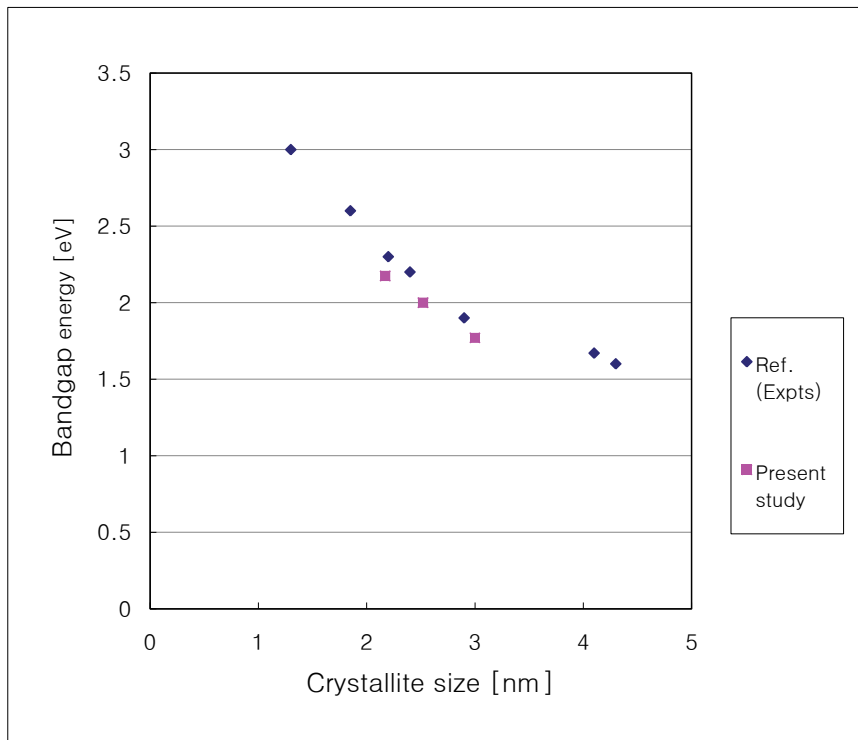


Fig. 8. The bandgap energies and the blueshift from the present numerical demonstrations are displayed together with experimental results reproduced from Ref. (Von Behren et al., 2000).

## 6. References

- Andersen, K. E.; Fong, C. Y. & Pickett, W. E. (2002). Quantum confinement in CdSe nanocrystallites. *J. Non-Cryst. Solids*, Vol. 299-302, 1105–1110.
- Bar, D. & Horwitz, L. P. (2002). Dynamical effects of a one-dimensional multibarrier potential of finite range. *Eur. Phys. J. B*, Vol. 25, 505–518.
- Chandler, D. (1987). *Introduction to Modern Statistical Mechanics*, Oxford University Press, New York.
- Chialvo, D. R.; Dykman, M. I. & Millonas, M. M. (1997). Fluctuation-induced transport in a periodic potential: noise versus chaos. *Phys. Rev. Lett.*, Vol. 78, No. 8, 1605.
- Choi, M. K. (2001). Numerical calculation of light scattering from a layered sphere by the boundary-element method. *J. Opt. Soc. Am. A*, Vol. 18, 577–583.
- Choi, M. K. (2007). Light intensity fluctuations on a layered microsphere irradiated by a monochromatic light wave: Modeling of an inhomogeneous cellular surface with numerical elements. *Mater. Sci. Eng. B*, Vol. 137, 138–143.
- Choi, M. K. & Choi, Y. (2009). Numerical demonstration of the blueshift of the light absorption wavelength for a layered microsphere: Effects of shell thickness on the blueshift. *J. Korean Phys. Soc.*, Vol. 54, No. 6, 2309–2317.

- Choi, M. K. & Kim, J. (2007). Light intensity fluctuations on a semiconductor microsphere calculated by boundary element method. *Curr. Appl. Phys.*, Vol. 7, 622–628.
- Choi, M. K. & Pyun, J. (2008). Light intensity and its fluctuations on a layered microsphere: Effects of shell thickness acting as a quantum well. *Curr. Appl. Phys.*, Vol. 8, 603–611.
- Cohen-Tannoudji, C.; Diu, B. & Lalo, F. (1977). *Quantum Mechanics*, Wiley, New York.
- Denbigh, K. (1981). *The Principles of Chemical Equilibrium*, Cambridge University Press, Cambridge.
- Hondou, T. & Sawada, Y. (1995). Dynamical Behavior of a Dissipative Particle in a Periodic Potential Subject to Chaotic Noise: Retrieval of Chaotic Determinism with Broken Parity. *Phys. Rev. Lett.*, Vol. 75, No. 18, 3269–3272.
- Kale, S. S. & Lokhande, C. D. (2000). Thickness-dependent properties of chemically deposited CdSe thin films. *Mater. Chem. and Phys.*, Vol. 62, No. 2, 103–108.
- Lu, S. G., Mak; C. L., Pang; G. K. H.; Wong, K. H. & Cheah, K. W. (2008). Blue-shift and intensity enhancement of photoluminescence in lead-zirconate-titanate-doped silica nanocomposites. *Nanotechnology*, Vol. 19, 1–4.
- Miyake, M.; Torimoto, T.; Sakata, T.; Mori, H. & Yoneyama, H. (1999). Photoelectrochemical characterization of nearly monodisperse CdS nanoparticles-immobilized gold electrodes. *Langmuir*, Vol. 15, 1503–1507.
- Nanda, K. K.; Sarangi, S. N. & Sahu, S. N. (1999). Visible light emission from CdS nanocrystals. *J. Phys. D: Appl. Phys.*, Vol. 32, 2306–2310.
- Sharma, S. N.; Kohli, S. & Rastogi, A. C. (2005). Quantum confinement effects of CdTe nanocrystals sequestered in TiO<sub>2</sub> matrix: effect of oxygen incorporation. *Physica E*, Vol. 25, 554–561.
- Tan, S. T.; Chen, B. J.; Sun, X. W.; Fan, W. J.; Kwok, H. S.; Zhang, X. H. & Chua, S. J. (2005). Blueshift of optical bandgap in ZnO thin films grown by metal-organic chemical-vapor deposition. *J. Appl. Phys.*, Vol. 98, 013505.
- Tsunekawa, S.; Fukuda, T. & Kasuya, A. (2000). Blue shift in ultraviolet absorption spectra of monodisperse CeO<sub>2-x</sub> nanoparticles. *J. Appl. Phys.*, Vol. 87, 1318–1321.
- Tsunekawa, S.; Wang, J.-T.; Kawazoe, Y. & Kasuya, A. (2003). Blueshifts in the ultraviolet absorption spectra of cerium oxide nanocrystallites. *J. Appl. Phys.*, Vol. 94, 3654–3656.
- Von Behren, J.; Wolkin-Vakrat, M.; Jorne, J. & Fauchet, P. M. (2000). Correlation of photoluminescence and bandgap energies with nanocrystal sizes in porous silicon. *J. Porous Materials*, Vol. 7, 81–84.

# Self-Similarity in Semiconductors: Electronic and Optical Properties

L. M. Gaggero-Sager<sup>1</sup>, E. Pujals<sup>2</sup>, D. S. Díaz-Guerrero<sup>1</sup>  
and J. Escorcía-García<sup>1</sup>

<sup>1</sup>*Universidad Autónoma del Estado de Morelos*

<sup>2</sup>*Instituto de Matemática Pura e Aplicada - IMPA Brasil*

<sup>1</sup>*México*

<sup>2</sup>*Brasil*

## 1. Introduction

Since the first time the human reason glimpse at the subatomic world, the idea that an atom resembles the solar system appear very natural, although wrong. This idea have intrinsically the notion of self-similarity, i. e., the matter organizes in a very similar, but not the same, way at different scales of length. The self-similarity in nature has been considered and searched for by many scientists from different fields of knowledge. But perhaps the most accurate description, as usual, came from mathematics.

The middle third Cantor set  $\mathcal{C}$  is one of the simplest examples of self-similarity and give us the opportunity of emphasize a key feature, self-similarity exist only in sets. So, a function would be self-similar if its image set is self-similar. Although  $\mathcal{C}$  is self-similar it has other interesting properties, e. g., it is a perfect set, it is totally disconnected, and a very astonishing one is that it has the same cardinality as  $\mathbb{R}$ .

Finally it seems appropriate to mention that the study of irregular objects has a very important reason, the world around us is not made of lines, planes and spheres, at least not in the human eye scale. For this reason it is crucial to consider other type of “geometries”. In this spirit the fractal geometry was very promising and visually very spectacular, but has some disadvantages, such as that the very definition of a fractal discard immediately every physical object. Nonetheless, it is worth to mention it because of the relation between fractals and self-similar sets. In the rest of this section we try to give a general overview about the concepts mentioned here as well as the formal definitions of the more relevant ones.

### 1.1 Self-similar sets

As mentioned before, self-similarity is a feature of sets and is more evident in its geometrical representation. So before giving the formal definitions, let us take a look at some illustrative examples.

The first thing that should be notice is the scale invariance of both figures, that is, if you take a part of the Sierpinski’s triangle and zoom in, you should see the whole figure again. In the case of the Koch’s snowflake, you don’t get the whole snowflake when zoom in, instead you

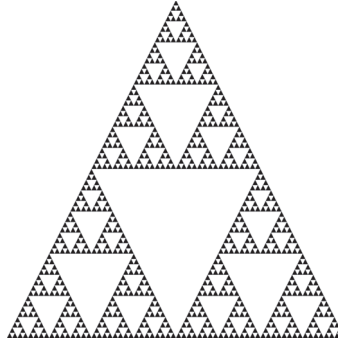


Fig. 1. Sierpinski's triangle.

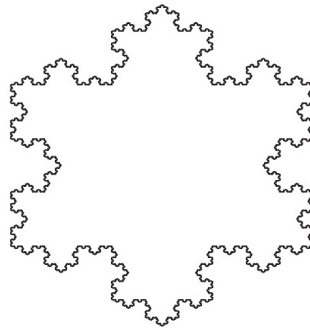


Fig. 2. Koch's snowflake.

get what is called the Koch's curve. This examples shows that the equivalence under scaling is not exact but similar. The case of the Cantor set is more simple and less visually exiting because it 'lives' in (is a subset of) the real line. However we will use the Cantor set in the coming sections so we should give a more detailed description of it, but before we translate this ideas into formal definitions that are more convenient to work with.

**Definition** A map  $S : \mathbb{R}^d \rightarrow \mathbb{R}^d$  is a **similitude** with ratio  $r > 0$  if  $\forall x, y \in \mathbb{R}^d$

$$d(S(x), S(y)) = rd(x, y) \quad (1)$$

where  $d : \mathbb{R}^d \rightarrow \mathbb{R}$  is a distance function. If  $r \in (0, 1)$   $S$  is called a contraction.

**Definition** A set  $F \subset \mathbb{R}^d$  is called **self-similar** if given a family of similitudes  $\{S_1, \dots, S_n\}$  with the same ratio  $r$

$$F = S_1(F) \cup \dots \cup S_n(F) \quad (2)$$

Now we consider the most important example for our purposes, the Cantor's set. The traditional construction of this amazing set can be found in several books, and is based in the geometrical idea of removing the middle third open segment of the interval  $[0, 1]$ , which give us the first generation of the construction. Next, the process is repeated at infinitum for the remaining segments. What is left is the so called middle third Cantor's set  $\mathcal{C}$ . For our purposes



it seems more convenient to take the similitudes  $S_1(x) := x/3$  and  $S_2(x) := x/3 + 2/3$  with ratio  $1/3$ , and to build from them and the segment  $\mathcal{C}_0 := [0, 1]$ . Let  $\mathcal{C}_i := S_1(\mathcal{C}_{i-1}) \cup S_2(\mathcal{C}_{i-1})$  for  $i = 1, 2, \dots$ . So,  $\mathcal{C}_1 := S_1(\mathcal{C}_0) \cup S_2(\mathcal{C}_0)$  and  $\mathcal{C}_2 := S_1(\mathcal{C}_1) \cup S_2(\mathcal{C}_1)$ , etc. From this it is clear that

$$\mathcal{C}_2 = S_1(S_1(\mathcal{C}_0) \cup S_2(\mathcal{C}_0)) \cup S_2(S_1(\mathcal{C}_0) \cup S_2(\mathcal{C}_0)) \quad (3)$$

$$= (S_1 \circ S_1)(\mathcal{C}_0) \cup (S_1 \circ S_2)(\mathcal{C}_0) \cup (S_2 \circ S_1)(\mathcal{C}_0) \cup (S_2 \circ S_2)(\mathcal{C}_0) \quad (4)$$

Now denoting  $S_i \circ S_j$  as  $S_{ij}$  and in a natural way  $S_{i_1} \circ \dots \circ S_{i_n}$  as  $S_{i_1, \dots, i_n}$  where  $i_l = 1, 2$  we could write

$$\mathcal{C}_k = \bigcup_{\pi(i_1, \dots, i_k)} S_{i_1, \dots, i_k}(\mathcal{C}_0) \quad (5)$$

The union runs over all the possible sequences  $i_1, \dots, i_k$ . So we get that

$$\lim_{k \rightarrow \infty} \mathcal{C}_k = \mathcal{C}. \quad (6)$$

This is similar to take the set  $\mathcal{C} = \text{Closure}(\bigcap_k \mathcal{C}_k)$ .

Quasiperiodic or quasiregular heterostructures (henceforth QH) follow an algorithmic sequence based on some self-replicating rule, for example the Fibonacci sequence among others. There is a great deal of current work on QH (see for example Refs. (1; 2)) and numerous references can be found in two recent reviews.(3; 4) In these kind of systems, the question of self-similarity was deeply examined but found to have a very limited range of validity in actual practice(5). In addition, the fractal character (6) of the spectrum of elementary excitations is rigorously proved (7; 8) and confirmed in many numerical calculations (see for example Refs. (3; 5)).

We propose the study of very different systems, inspired by QH and other self-similar systems. In particular, we aim to study semiconductor quantum systems in which the potential is close to a self-similar function (6) defined in a bounded interval. We hope this can be generalized and applied to other problems.

The study of this kind of potentials is motivated by the evidences that the transmittance reflects the self-similar property of the potential through its fractal dimension. In the other hand Lavrinenko et al (10; 11) studied the propagation of classical waves of the optical Cantor filter. This system is not a self-similar system, because the refractive indices are not scaled. The authors observed that the optical spectra has shown spectral scalability. In the last few years, a lot of experimental works concerning the worth noting properties of porous silicon in chemical and biological sensing have been reported (12). Moretti et al have compared the sensitivities of resonant optical biochemical sensor, based on both periodic and aperiodic porous silicon structures, such as Bragg and the Thue-Morse multilayer. They observed that the aperiodic multilayer is more sensitive than the periodic one. Finding other similar systems with larger sensitiveness would be important for applications.

Agarwal et al (13) have reported experimental results on electromagnetic wave propagation in nanostructures porous silicon multilayer where geometrical length follows the Cantor code. For generations higher than six equidistant fringes are observed instead photonic bands. Esaki et al (14)observed that for specific values of wave numbers, transmission coefficients are shown to be governed by the logistic map and, in the chaotic region, they show sensitive dependence on small changes in parameters of the system such as the index of refraction. In

the other hand, Pilevary Salmasi (15) et al studied a fractal shaped antenna using multilayer structure.

A significant number of papers have been also devoted to different mathematical aspects of this problem. See, for example, Refs. (16)-(17), and references therein.

The study of properties material's is due to the research on optimal devices with the goal to improve the present ones. With this in mind, and for methodological purposes, scientists look at the fundamental physical properties of such materials. One of the possibilities is the transmission coefficient, or transmittance, of an electromagnetic wave incident upon a quantum potential, typically barriers or wells. This topic is covered in the college courses for a single rectangular barrier, nevertheless is very interesting to study some more complex systems. Among these, there is the so called superlattices for which the transmittance has been well characterized by their band structure. An even more irregular case is the Cantor-like potential (1; 3), which is inspired in the Cantor set, in this system the height, width and distance of the barriers (or wells) are modified just like in the construction of the Cantor set.

**2. Topological self-similar quantum wells**

In this section, first we are going to introduce the selfsimilar quantum wells; later we show how the selfsimilarity are reflected in terms of the solution of the Schrödinger's equation. This is done formally in subsection 2.2 and in subsection 2.3 from the point of view of semiclassical approximation. In subsection 2.4 we analyze numerically the properties of the discrete spectrum.

**2.1 Definition and properties of the potential**

Let us define the intervals  $I = [0, 1]$  and  $J = [a, b]$ , with  $0 < a < b < 1$ . Let us consider two differentiable functions  $f_0 : [0, 1] \rightarrow [0, a]$  and  $f_1 : [0, 1] \rightarrow [b, 1]$ , such that both are onto and  $0 < |f'_0(x)| < \lambda_0 < 1$ ,  $0 < |f'_1(x)| < \lambda_1 < 1$  for any  $x \in [0, 1]$ . Given  $a_N = (i_1, i_2, \dots, i_N)$  an  $N$ -couple of 0's and 1's, i.e.  $i_j = 0, 1$  for all  $j = 1, 2, \dots, N$ , we define the composition functions

$$f_{a_N}(x) = f_{i_N} \circ \dots \circ f_{i_2} \circ f_{i_1}(x)$$

and the intervals

$$I_{a_N} = f_{i_N} \circ \dots \circ f_{i_2} \circ f_{i_1}(I_0) \tag{7}$$

$$J_{a_N} = f_{i_N} \circ \dots \circ f_{i_2} \circ f_{i_1}(J_0). \tag{8}$$

We consider the particular case that the functions  $f_0, f_1$  are affine; i.e.  $\lambda_0 := |f'_0| = \frac{1}{a}$  and  $\lambda_1 := |f'_1| = \frac{1}{1-b}$ . Observe that the intervals  $I_{a_N}$  has length  $\lambda_0^{a_N^0} \lambda_1^{N-a_N^0}$  where  $a_N^0$  is the number of 0's that appear in the sequence  $a_N$ . In the same way, the intervals  $J_{a_N}$  has length  $\lambda_0^{a_N^0} \lambda_1^{N-a_N^0} (b-a)$ .

To avoid notation, we denote  $\lambda_{a_N} := \lambda_0^{a_N^0} \lambda_1^{N-a_N^0}$ .

An special case of the above defined affine maps are the ones associated to the classical 1/3–middle Cantor set where  $f_0(x) = \frac{1}{3}x$  and  $f_1(x) = \frac{1}{3}x + \frac{2}{3}$ . In this situation, the intervals and functions just defined have a direct interpretation in terms of the standard Cantor construction. See Fig. 3.  $I = [0, 1]$  is the starting interval and  $J = [1/3, 2/3]$  is the central one third interval of  $I$ .

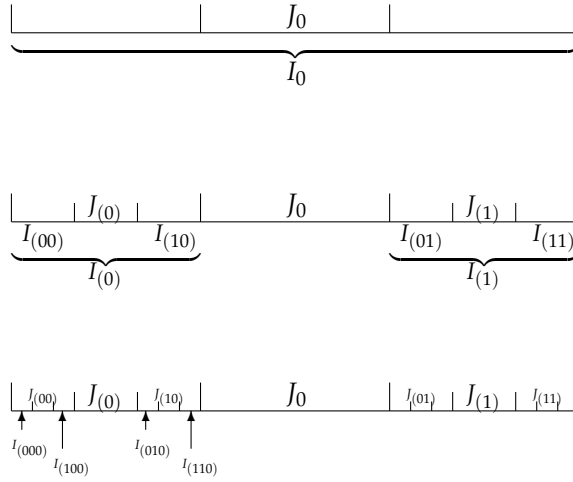


Fig. 3. The three first generations of Cantor construction. For the sake of clarity the starting interval  $I_0$  is only denoted in the upper panel, and intervals  $I_{(0)}$  and  $I_{(1)}$  are only denoted in the middle panel.

For more general and precise construction of cantor’s map and the role that they played in theory of dynamical systems see (18; 19).

Now, we take  $0 < \alpha_0 < 1$  and  $0 < \alpha_1 < 1$  and we denote  $\alpha_{a_N} := \alpha_0^{a_N} \alpha_1^{N-a_N}$ . From that, we define the potential equal to  $V_0 \alpha_{a_N}$  in any of the intervals  $J_{a_N}$  and zero elsewhere.  $V_0$  is some amplitude irrelevant for the following.

Observe that this potential verifies the following property that resembles the classical notion of self-similarity:

$$V(f_{a_N}^{-1}(x)) = \frac{1}{\alpha_{a_N}} V(x) \quad \forall x \in f_{a_N}(I_0). \tag{9}$$

Indeed, this condition would be a full self-similarity if it is fulfilled for all values of the coordinate variable  $x$ . Since it only holds for  $x$  in certain intervals, the arguments in the spirit of Group Theory can not be pursued. However, in the following we call this condition *self-similarity*, or in any case *quasi-self-similarity*, due to the close resemblance with the theoretical pure situation of self-similarity.

**2.2 Formal solution and self-similarity**

We will now explain, in a little more rigorous and general manner, a theorem regarding the self-similarity of the wave functions of the continuous spectrum when the potential is a self-similar function.

Let  $E > 0, k > 0$  ( $k = \hbar^2 / (2m(x))$  where  $m(x)$  is the position-dependent effective mass). In the sequel, we will note with  $\Psi_{E,k}$ , the solution of the problem

$$k\Psi_{E,k}(x) + (E - V(x))\Psi_{E,k}(x) = 0 \tag{10}$$

We want to study how the self-similarity of the potential  $V(x)$  -and the mass  $m(x)$ - is reflected in the eigenfunctions and eigenvalues. More precisely we want to see if there exist some similarity between the eigenfunction restricted to the whole interval, and the same (or another) eigenfunction, when it is restricted to the interval  $f_{a_N}(I_0)$ . In others words, we want to see, if given  $E$  and  $k > 0$ , there exist  $E' > 0$  and  $k' > 0$  such that

$$\Psi_{E,k}(f_{a_N}^{-1}(x)) = \Psi_{E',k'}(x) \quad (11)$$

for any  $x \in f_{a_N}(I_0)$ . In this direction, we obtain the following Theorem which is a renormalization Theorem.

**Theorem 1.** *Let  $E > 0$ ,  $k > 0$  and the eigenfunction  $\Psi_{E,k}$ . Given  $N > 0$  then we get that*

$$\Psi_{E,k}(f_{a_N}^{-1}(x)) = \Psi_{E',k'}(x)$$

for any  $x \in f_{a_N}(I)$ , where  $E' = E\alpha_{a_N}$ ,  $k' = \lambda_{a_N}^2 \alpha_{a_N} k$

Before to give the proof, observe that the Theorem is showing equivalently, that given  $N > 0$  then

$$\Psi_{E,k}(f_{a_N}(x)) = \Psi_{E',k'}(x)$$

for any  $x \in I$ .

Now, let us give the proof.

**Proof:** We have that

$$k\Psi_{E,k}''(x) + (E - V(x))\Psi_{E,k}(x) = 0 \quad (12)$$

with  $x \in [0, 1]$ .

Taking the transformation  $f_{a_N}^{-1} : f_{a_N}(I) \rightarrow I$ , we get that for any  $x \in f_{a_N}(I)$

$$k\Psi_{E,k}'' \circ f_{a_N}^{-1}(x) + (E - V \circ f_{a_N}^{-1}(x))\Psi_{E,k} \circ f_{a_N}^{-1}(x) = 0. \quad (13)$$

Using that  $\Psi_{E,k}'' \circ f_{a_N}^{-1} = \lambda_{a_N}^2 (\Psi_{E,k} \circ f_{a_N}^{-1})''(x)$  and that  $V(f_{a_N}^{-1}(x)) = \frac{1}{\alpha_{a_N}} V(x)$ ,

$$\lambda_{a_N}^2 k (\Psi_{E,k} \circ f_{a_N}^{-1})''(x) + (E - \frac{1}{\alpha_{a_N}} V(x))\Psi_{E,k} \circ f_{a_N}^{-1}(x) = 0 \quad (14)$$

for any  $x \in f_{a_N}(I)$  and equivalently,

$$\alpha_{a_N} \lambda_{a_N}^2 k (\Psi_{E,k} \circ f_{a_N}^{-1})''(x) + (\alpha_{a_N} E - V(x))\Psi_{E,k} \circ f_{a_N}^{-1}(x) = 0 \quad (15)$$

for any  $x \in f_{a_N}(I)$ . This implies that  $\Psi_{E,k} \circ f_{a_N}^{-1}$  is solution of

$$k'Y''(x) + (E' - V(x))Y(x) = 0, \quad (16)$$

where  $k' = \lambda_{a_N}^2 \alpha_{a_N} k$ , and  $E' = E\alpha_{a_N}$ . And this means that

$$\Psi_{E,k}(f_{a_N}^{-1}(x)) = \Psi_{E',k'}(x) \quad (17)$$

for  $x \in f_{a_N}(I)$ . This finishes the proof.

### 2.3 Semiclassical solution and self-similarity

Observe that in the particular case of the standard 1/3 Cantor set for the potential defined above the following properties are satisfied.

$$\text{if } 0 \leq x \leq 1/3 \quad \text{then } V(x) = \frac{1}{3}V(3x) \quad (18)$$

$$\text{if } \frac{2}{3} \leq x \leq 1 \quad \text{then } V(x) = \frac{1}{3}V(3x-2) . \quad (19)$$

Now, let  $E > \text{Max}[V(x)]$ , be a eigenvalue of the continuous spectrum of the Schrödinger equation:

$$\frac{d^2F(x)}{dx^2} + \frac{2m}{\hbar}(E - V(x)) F(x) = 0 . \quad (20)$$

For this eigenvalue, using semiclassical approximation, we get that the associated eigenfunction is (20)

$$F_E(x) = A_E(x) \exp \left[ \frac{i}{\hbar} S_E(x) \right] \quad (21)$$

where

$$A_E(x) = \frac{C_1}{(2m(E - V(x)))^{1/4}} \quad (22)$$

$$S_E(x) = \int_0^x \sqrt{2m(E - V(x))} dx . \quad (23)$$

Using the properties of  $V(x)$ , observe that for any  $x \in [0, 1/3]$

$$\begin{aligned} A_E(x) &= \frac{C_1}{(2m(E - V(x)))^{1/4}} = \frac{C_1}{(2m(E - \frac{1}{3}V(3x)))^{1/4}} \\ &= 3^{1/4}C_1A_{3E}(3x) . \end{aligned} \quad (24)$$

This means that, up to a certain constant, the function  $A_E$  (of the eigenvalue  $E$ ) in the interval  $0 \leq x \leq 1/3$  is equal to the function  $A_{3E}$  (of the eigenvalue  $3E$ ) in the interval  $0 \leq x \leq 1$ . On the other hand, for the function  $S_E$ , we have that for  $x \in [0, 1/3]$

$$S_E = \frac{1}{\hbar} \int_0^x \sqrt{2m \left( E - \frac{1}{3}V(3x) \right)} dx . \quad (25)$$

Changing the integration variable  $x$  by  $x' = 3x$ , we have that for  $x \in [0, 1/3]$

$$\begin{aligned}
 S_E(x) &= \left(\frac{1}{3}\right)^{3/2} \int_0^{3x} \sqrt{2m(3E - V(x'))} dx' \\
 &= \left(\frac{1}{3}\right)^{3/2} S_{3E}(3x).
 \end{aligned} \tag{26}$$

So, for  $x \in [0, 1/3]$

$$\begin{aligned}
 F_E(x) &= C_1 \left(\frac{1}{3}\right)^{1/4} A_{3E}(3x) \cdot \\
 &\quad \cdot \exp \left[ \frac{i}{\hbar} \left(\frac{1}{3}\right)^{3/2} S_{3E}(3x) \right].
 \end{aligned} \tag{27}$$

That is, the eigenfunction corresponding to the state  $E$  in the interval  $[0, \frac{1}{3}]$  is self-similar to the eigenfunction corresponding to the state  $3E$  in the interval  $[0, 1]$ . Arguing in the same way, and using the self-similarity of the potential in  $[\frac{2}{3}, 1]$  we conclude also that the eigenfunction corresponding to the state  $E$  in the interval  $[\frac{2}{3}, 1]$  is self-similar to the eigenfunction corresponding to the state  $3E$  in the interval  $[0, 1]$ . Again, arguing in the same way we get that for any interval  $f_{a_N}(I_0)$  (see previous section for definitions) the semiclassical approximation associated to the eigenvalue  $E$  over the interval  $f_{a_N}(I_0)$  is self-similar over the interval  $[0, 1]$  to the semiclassical approximation associated to the eigenvalue  $3^N E$ .

Since any value of  $E$  is an eigenvalue of the Schrödinger equation, then the self-similarity of the wave function is fulfilled for any value of  $E$ . This implies that for a quantum well with self-similar potential, it affects the wave functions in the whole continuous spectrum, not only the wave functions of the eigenvalues close to the well's limits, as would happen in a normal quantum well. This conclusion is general for any self-similar potential.

#### 2.4 The case of the discrete spectrum

However, our interest is focused on electronic properties. So, we have to look to the discrete levels. For wave functions in discrete levels, it is impossible to find a general formula like those developed in previous sections in the framework of WKB Approximation. So we focus our attention on the resolution of a concrete problem using transfer matrix method (see for example (21) and references therein). Due to the fact that in semiconductors it is possible to grow potentials of different types, we propose the calculation of the discrete levels of the potential given in figure 4, constructed in AlGaAs/GaAs. We calculate the eigenvalues and eigenfunctions of this system in the Envelope Function Approximation (EFA)(22) with an effective mass of  $0.068 m_0$ , where  $m_0$  is the free electron mass and the well width is  $6000 \text{ \AA}$ .

Let us consider a quantum well in AlGaAs/GaAs with a  $1/3$  Cantor-like shape [3] with rigid walls at the ends as shown in figure (1).

We calculate the eigenvalues and eigenfunctions of this system in the Envelope Function Approximation (EFA) with a effective mass of  $0.068 m_0$ , where  $m_0$  is the mass of the free electron, the dielectric constant being  $\epsilon_r = 12.5$  and the well width of  $6000 \text{ \AA}$ .

Let  $\Psi(z)$  be a column vector with two components,

$$\Psi(z) = \begin{pmatrix} F(z) \\ F'(z) \end{pmatrix}$$

and the matrix  $P(z)$ ,

$$P(z) = \begin{pmatrix} 0 & 1 \\ -2m^* / \hbar^2 [E - V(z)] & 0 \end{pmatrix}$$

Thus

$$P(z) \Psi(z) = 0$$

Let  $g_1(z)$  and  $g_2(z)$  be two linearly independent solutions of the Schrödinger equation, then, from the transfer matrix formalism let us take

$$M(z, z_0) = \frac{1}{\Delta} \begin{pmatrix} g_2'(z_0)g_1(z) - g_1'(z_0)g_2(z) & g_1(z_0)g_2(z) - g_2(z_0)g_1(z) \\ g_2'(z_0)g_1'(z) - g_1'(z_0)g_2'(z) & g_1(z_0)g_2'(z) - g_2(z_0)g_1'(z) \end{pmatrix}$$

where

$$\Delta = g_1(z_0)g_2'(z_0) - g_1'(z_0)g_2(z_0)$$

and

$$\Psi(z) = M(z, z_0)\Psi(z_0)$$

Our potential is sectionally constant in all intervals. If we use the trigonometric functions, we obtain the exact result. For the calculation of the eigenvalues we use the boundary conditions, i.e., our potential is infinite in  $z = l_{qw}$  and  $z = -l_{qw}$ , the transcendental equation by calculation of eigenvalues is  $M_{12}(0, -l_{qw}) = 0$ , for odd states and  $M_{22}(0, -l_{qw}) = 0$  for even states, where  $M_{ij}$  are the elements  $ij$  of the matrix  $M(l_{qw}, -l_{qw})$ . Once we have the eigenvalues, the eigenfunctions are calculated in the usual manner, using the transference matrix method [5].

This system is actually a set of coupled quantum wells, therefore, we expect to observe self-similarity for basic states corresponding different wells as for excited states. Even if we did not observe the same structure of self-similarity as the one obtained for continuous spectrum, we do observe some interesting properties in the states of the discrete spectrum. For example, the states  $E_1 = 1.104$  meV,  $E_{46} = 361.9$  meV, and  $E_{58} = 490.7$  meV are self-similar among themselves. In fact, the three states correspond to the basic levels of the different wells. The same thing happens with the first and second excited levels. In figure 5 (top panel) and 5 (bottom panel) the states  $E_{17} = 135.4$  meV and  $E_{49} = 397.0$  meV are observed, which are self-similar and this self-similarity does not respond to the simple coupling between wells. In figure 6 we present the state  $E_{62} = 510.0$  meV, which is self-similar to itself. This occurs whether they are either self-similar or some kind of renormalization property between different states hold. On the other hand, we have observed that the density of the localized charge (the product of the eigenvalue with the eigenfunction) presents self-similarity (9).

## 2.5 Intersubband optical absorption

In Fig. 7 we depict the absorption coefficient due to intersubband transitions as a function of photon energy. The calculation method can be found in many textbooks. See, for example Ref. (22). As expected, the graphics is a sectionally constant function, and consequently, its derivative is a set of delta function peaks. Theoretical and numerical methods tend to

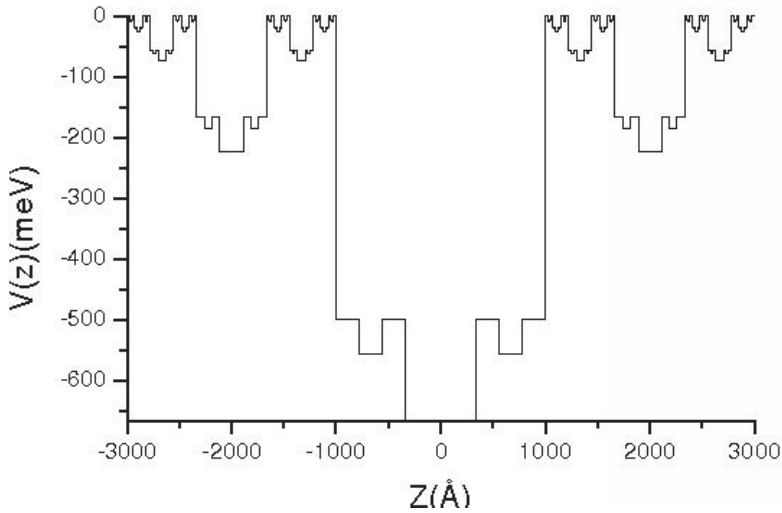


Fig. 4. Self-similar potential profile constructed as a fifth order Cantor function. This potential is scaled by three.

smooth this kind of graphics; this indicates the convenience of using the derivatives instead the original function in order to find the shoulders of the absorption coefficient as a function of energy. The calculation of fractal dimensions  $D(q)$  of this set produces a value of 1 for  $q$  negative or about zero and a value neatly below 0.6 for  $q$  greater than 5. Then, the fractality of the spectrum has been transferred to the absorption coefficient.

### 3. GaAs-AlGaAs like heterostructure

To perform the calculations we used the parameters of the GaAs already mentioned. Assuming parabolic bands, in the low temperature limit, the charge density of the  $i^{th}$  level, is given by:

$$\rho_i(z) = \sum_{j=1}^i |F_j(z)|^2 E_j$$

where the  $F_j(z)$  and  $E_j$  are the eigenfunctions and eigenvalues of the potential presented in Fig.1

In Fig.2 the charge density of the  $i^{th}$  level of the proposed system is presented for the first 100 energy levels. The self-similarity is evident. Then as it can be seen, self-similarity is not an exclusive property of infinite systems. Here we have shown that a self-similar finite quantum system may also exhibit self-similarity. In this case, self-similarity is evident in the charge density and this is a physically clear result. Other physically relevant parameters could in principle exhibit fractal characteristics in finite systems.



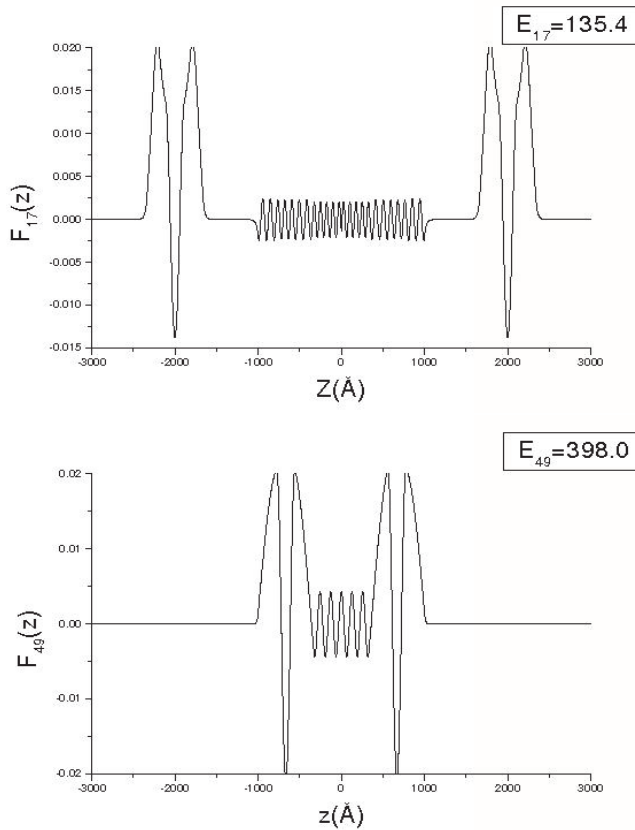


Fig. 5. Top panel: Eigenfunction corresponding to the eigenvalue  $E_{17} = 135.4$  meV. Bottom panel: Eigenfunction corresponding to the eigenvalue  $E_{49} = 397.0$  meV.

## 4. Self-similar barrier systems

### 4.1 Introduction

In this section we present the important case of strict self-similar potentials and their electronic transmission coefficient. These potentials are constructed based on the construction of the Cantor set, i. e., are based on an iterated replacement of the zero potential zones by scaled copies of the main barrier, figure 10.

The set of parameters of this kind of systems are the follows: the value of the main barrier  $H_0$ , the total length of the multibarrier system and the generation of the potential. Let us take a look at the transmission coefficient corresponding to the eighth generation of the self-similar potential with  $H_0 = 500\text{meV}$  and length from  $L_t = 75\text{\AA}$  to  $L_t = 750\text{\AA}$ , figure 11.

This shows that the total length determines the oscillatory behavior of the transmission coefficient, so, if we take this potential isolated, we must focus on lengths greater than  $200\text{\AA}$  in order to obtain some oscillations in our transmission curves.

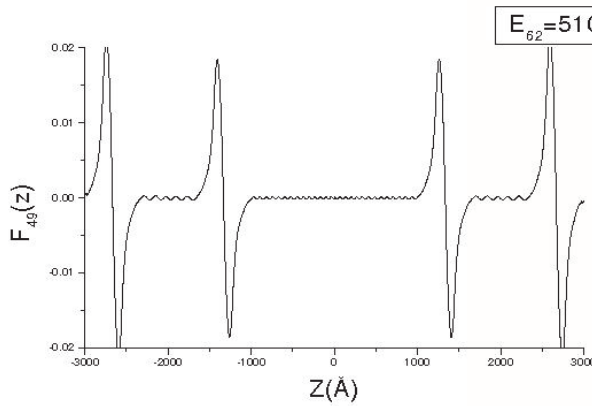


Fig. 6. Eigenfunction corresponding to the eigenvalue  $E_{62} = 510.0$  meV.

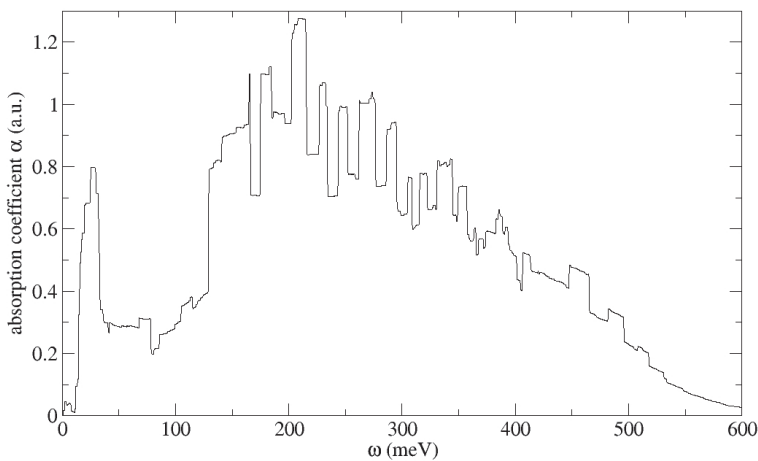


Fig. 7. Intersubband optical absorption coefficient.

It is also important to see what happens when we move from one generation of the potential to the next, in order to determine the effect, if any, of the self-similarity on the transmission coefficient. So in figure 12, we see the transmission coefficient curves for the first four generations of the self-similar potential.

Those curves could suggest that the self-similarity does not make much difference in the transmission coefficient, nevertheless, in the following subsection we will see that it's real contribution is really clear when is "mixed" with another type of structures.

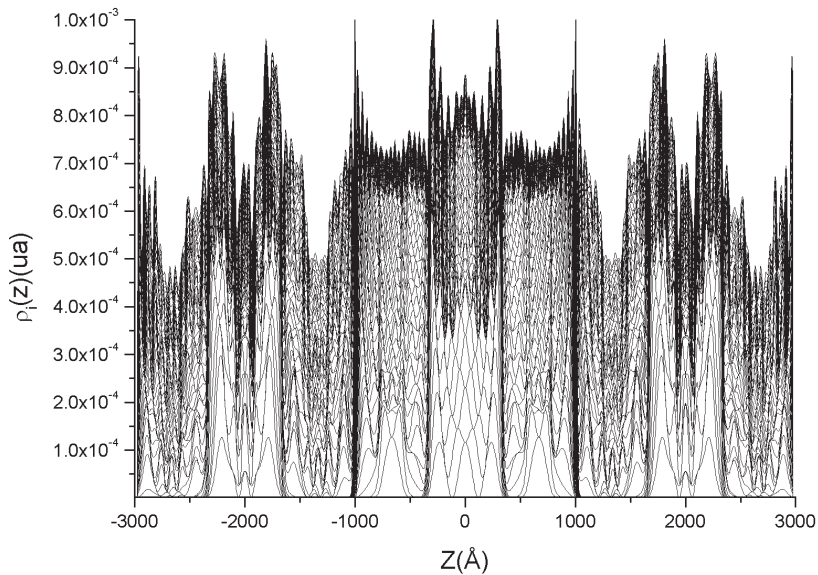


Fig. 8. Charge density.

#### 4.2 Mixed multibarrier potentials

Now we consider a multibarrier system that mix the self-similar potential (henceforth ssp), and a multibarrier periodic potential (henceforth mbpp).

##### 4.2.1 Methodology

An mixed multibarrier potential is built using two mbpp and one ssp. The mixing process is quite simple, in fact it is just an arrangement of the two systems in the following order, first a mbpp, next the ssp and then the other mbpp, see figure 13. It is important to notice that when the generation of the self-similar potential is increased the number of layers in the mbpp is increased linearly. The transfer matrix method is used to calculate the transmittance of the previous systems. These calculations are made in the framework of effective mass theory. In this system a given generation comprehend the same generation for the component systems, i. e., consider the generation three of the mixed multibarrier potential, it has two mbpp of three barriers each and one ssp of the third generation.

It is clear that the generation one corresponds to an mbpp of generation 3 (three layers), which most have the characteristic band structure. The parameters involved in this system are the height and width of the barriers and the distance between them. The parameters that are changed to study its effect on the transmittance are the width and distance. This parameter variation is applied to the mbpp systems. The key parameter for the ssp is the length of the whole structure, in this case 750Å. In figure 14 we present the transmittance for the mixed system. The first thing that one can note is the appearance of transmission peaks in the region between 250 and 350 meV, that seems to correspond to quasibound states for energies above

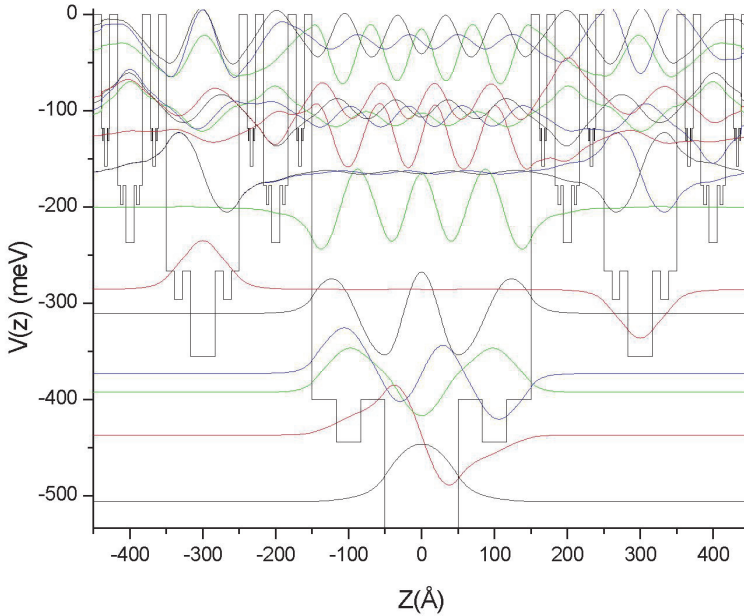


Fig. 9. Potential, energy levels and wave functions with scaling factor for the potential 3/2.

the value of  $V$  for the barriers. Those peaks are placed in the region corresponding to a gap in the mbpp. Finally it is worth to remark the following: it seems that those peaks are equidistant; the addition of the ssp to de mbpp rules out the tunneling region and the gaps in the transmittance are better defined.

Figure 15 shows that the inclusion of the ssp effectively made the tunneling band to disappear. Also, it shows quasibound states in energetic regions corresponding to gaps in the mbpp. Last but not least, it seems that the perfect reflection is obtained for the minimums of the gaps.

### 5. Optical case

#### 5.1 Electromagnetic waves in self-similar multilayer systems

First we generalize the theorem 1 to the case of electromagnetic waves, so in the following we will use the construction of the potential given in section 2.1.

**Theorem 2.** Let  $N > 0$ ,  $\omega > 0$  and  $E(x)$  the frequency and the electric field respectively. Then if  $E(x)$  is solution of then equation

$$E''(x) - \frac{\omega^2}{v(x)^2} E(x) = 0 \tag{28}$$

we get that  $E_\omega(f_{a_N}^{-1}(x)) = E_{\omega'}(x)$

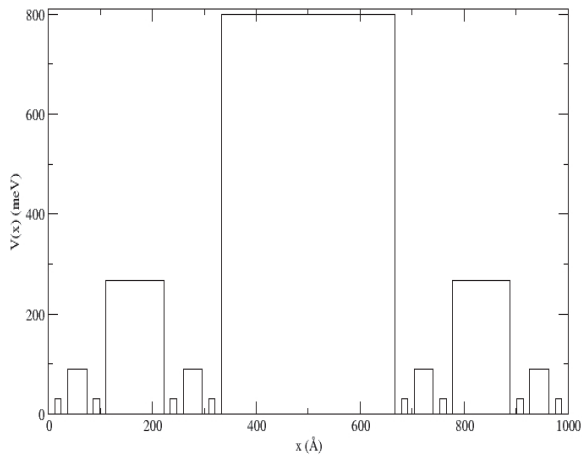


Fig. 10. Strict self-similar potential.

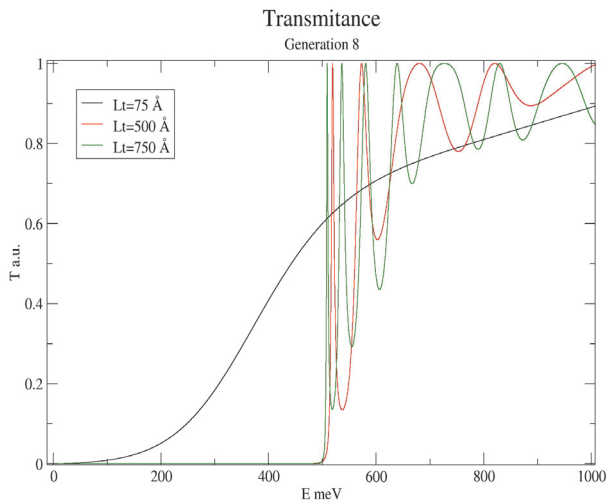


Fig. 11. Comparison of the transmission for the eighth generation of the GP-potential varying the total length of the system.

**Proof:** First we take  $E(x, t) = E(x)e^{i\omega t}$ , which give us the time-independent electric field equation Following the procedure for the quantum case, we consider the effect of the

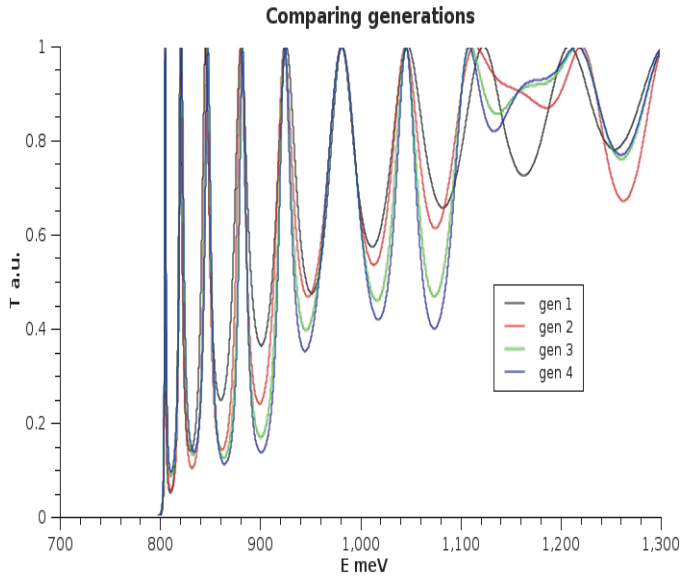


Fig. 12. Comparison of the first four generations of the GP-potential with  $H_0 = 800$  meV and  $Lt = 1000\text{\AA}$  (total length).

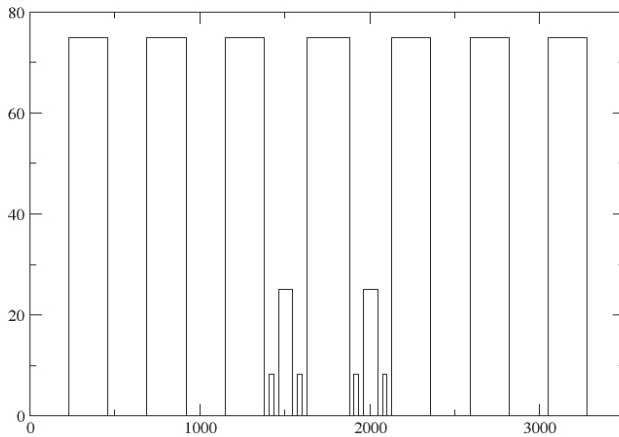


Fig. 13. Mixed Cantor-like potential, generation 3.

transformation  $f_{a_N}^{-1}$  for the preceding equation

$$E'' \circ f_{a_N}^{-1}(x) - \frac{\omega^2}{v(x)^2} E \circ f_{a_N}^{-1} = 0 \quad (29)$$

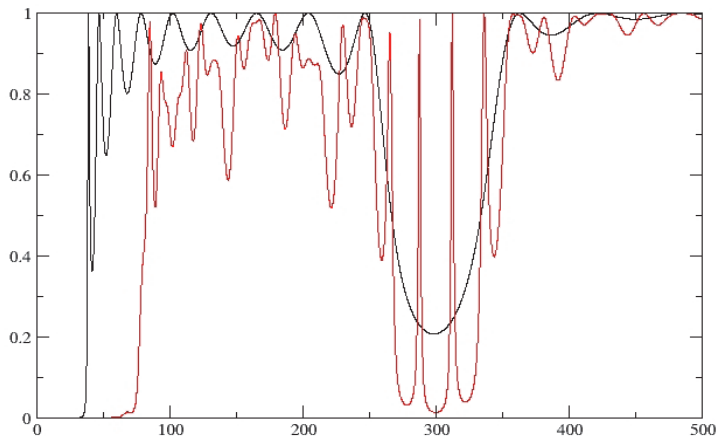


Fig. 14. Transmittance for an width/distance of 23 Å, generation 10.

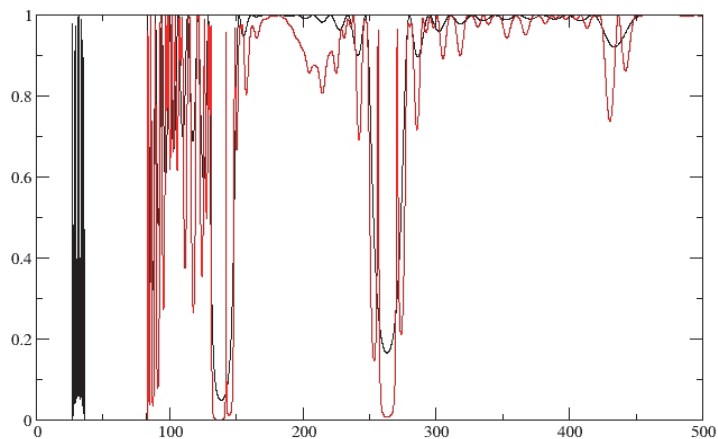


Fig. 15. Transmittance for an width/distance of 75 Å, generation 10.

Once again using that  $E'' \circ f_{a_N}^{-1} = \lambda_{a_N}^{-2} (E \circ f_{a_N}^{-1})''$  we get

$$(E \circ f_{a_N}^{-1})''(x) - \lambda_{a_N}^2 a_{a_N}^2 \frac{\omega^2}{v(x)^2} E \circ f_{a_N}^{-1} = 0 \tag{30}$$

which implies that  $E \circ f_{a_N}^{-1}$  is solution of the equation

$$Y''(x) - \frac{\tilde{\omega}^2}{v(x)^2}Y(x) = 0 \tag{31}$$

where  $\tilde{\omega}^2 = \lambda_{a_N}^2 \alpha_{a_N}^2 \omega^2$ , i. e., if we take the electric field for whole system  $E_T$  and we compares this with the corresponding to a rescaled copy  $E_{\beta T}, \beta \in (0, 1)$ , then  $\omega_{E_{\beta T}} = \lambda_{a_N} \alpha_{a_N} \omega_{E_T}$ . This implies that  $E_{\omega}(f_{a_N}^{-1}(x)) = E_{\omega'}(x)$ .

Finally we consider the case in which  $\lambda_{a_N} \alpha_{a_N} = 1$ , in this case the electric field is self-similar in the space for a given energy, i. e.  $E_{\omega}(f_{a_N}^{-1}(x)) = E_{\omega}(x)$ .

**5.2 Reflectance**

For this case Lavrinenko et al (11) give an excellent analysis and presentation of this kind of systems. And the two main features that they distinguish are the scalability and the sequential splitting of the spectra.

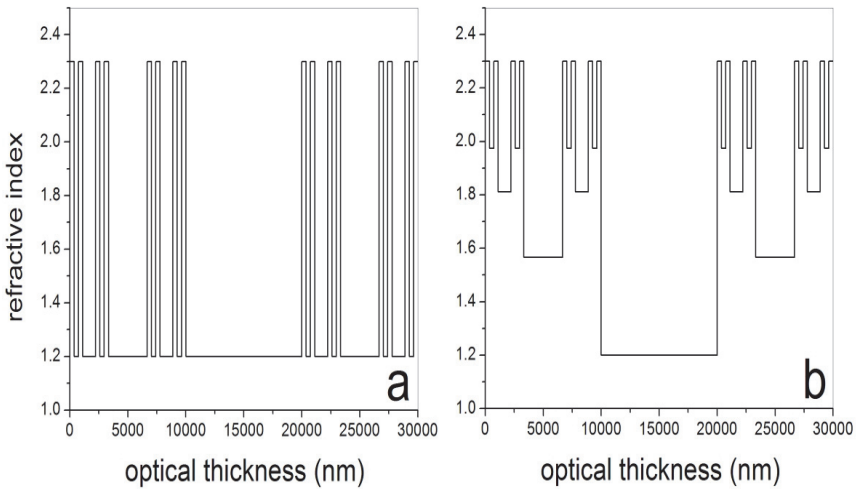


Fig. 16. Two types of fourth Cantor generation structures in which was applied the Cantor rule to a) the optical thickness and b) both the optical thickness as well as the refractive index.

According to the equation 31, it does not exist a limiting condition to find self-similar behavior of the electric field in the whole interval with respect to the restricted interval  $f_{a_N}(I_0)$  of the system. So we generated two types of Cantor structures shown in figure 16 which satisfy the ternary Cantor rule. In the first case we applied the Cantor rule only to the optical thickness (nd) (type-I) while in the second case we applied it to the optical thickness as well as to the refractive index (type-II); both structures retain the same total optical thickness equal to 30  $\hat{\mu}m$ . Since the physical thickness is defined as the rate of the optical thickness divided by refractive index, the physical thickness of the second type Cantor structure is expected to be narrower than the first type in each generation.



Theoretical simulation of transmission spectra of the Cantor structures was performed using transfer formalism (29) (21), in which we assumed that the layers that constitute the Cantor structure are homogeneous, isotropic and infinite in two transverse directions. Figure 17 shows the results obtained for transmission spectra of different type-I Cantor generations. It can be observed that increasing the order of Cantor generation the transmission spectra becomes more complex, exhibiting very pronounced resonance peaks and shifts to short wavelengths due to a finest inner structure of Cantor multilayer, retaining the same total optical thickness in each generation. In order to compare the transmission spectra of each one, we normalize the spectra with respect to the smallest optical thickness ( $\Lambda_0$ ) in each generation as shown in figure 18.

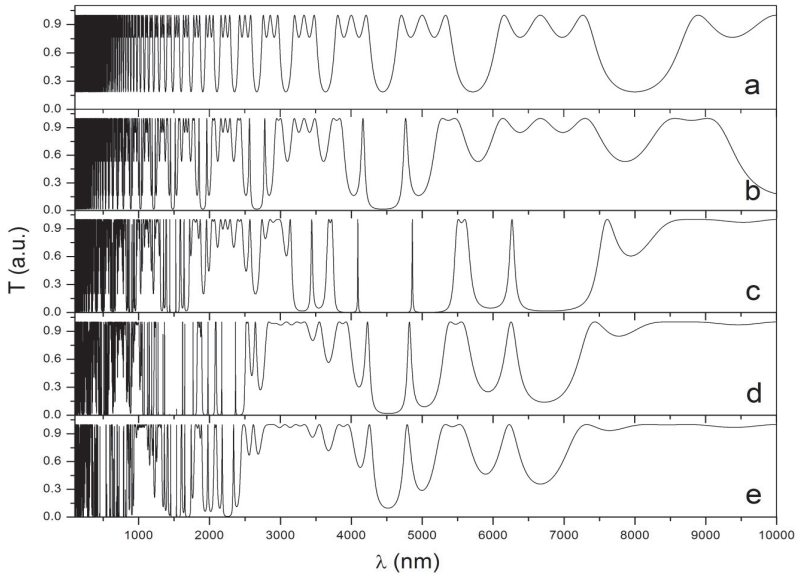


Fig. 17. Theoretical transmittance calculation of the type-I Cantor structures at different orders of generation: a) first, b) second, c) third, d) fourth and e) fifth. The calculation was realized using refractive indices of 2.3 and 1.2 remaining the same optical thickness equal to  $30\mu m$  for all generations.

The normalized results display interesting optical properties of the Cantor structures. First, we observe that the transmittance spectra of the  $i$ th Cantor generation contains the previous  $i - 1$  Cantor generation. For example, the second Cantor generation spectra (Fig. 5.3 b) is present in each one of the following generations (Fig. 18 c, d y e, represented by the shadow area) which indicates that transmittance spectra exhibit self-similarity. Furthermore, the scaling factor required to scale the  $i - 1$  Cantor generation and reproduce the  $i$ th Cantor generation is the same used to scale the spatial thickness, i.e. equal to 3. These facts have been observed in other systems with high refractive index contrast ( $nB/nA=2.3$ )(11). However, the amplitude of the transmittance does not have a unique scale factor.

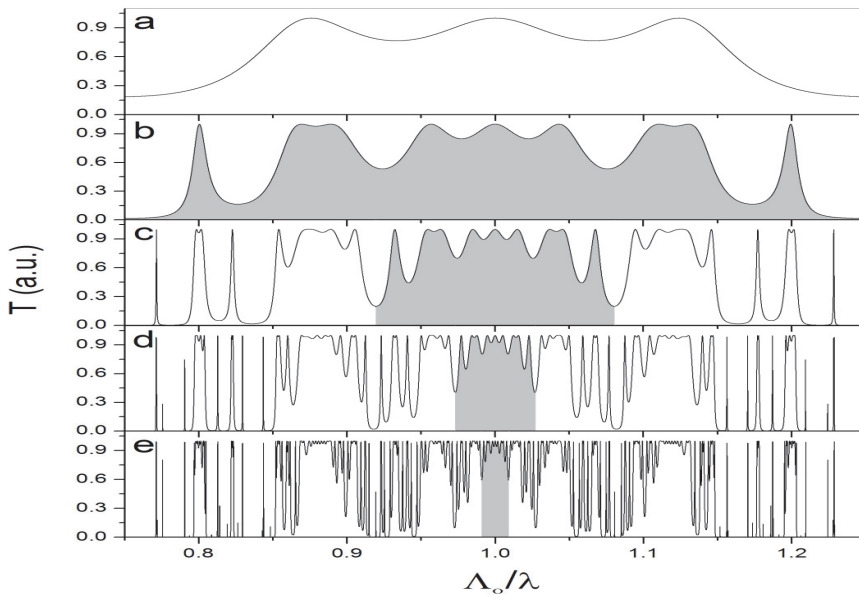


Fig. 18. Theoretical transmittance of the type-I Cantor structures normalized with respect to the optical thickness ( $\Lambda_0$ ) of the smallest layer in each structure. The refractive indices and the whole optical thickness are the same used in the figure 17.

In figure 19 is shown the normalized transmittance spectra of the type-II Cantor structures for various Cantor generations. It is observed that the optical spectra are qualitatively similar to the obtained in type-I Cantor's. However, in this case, more transmission and reflection modes appear due to the multiple splitting of the optical thickness as well as the refractive index. Once more, the  $i$ th spectra is contained in the following generations and it is scaled by a factor of 3. But in this case it is possible to find a scaling factor to rescale the transmission amplitude of the  $i + 1$  Cantor spectra to reproduce the  $i$  Cantor spectra, and so on. This scaling factor was found to be approximately equal to 0.41.

### 5.2.1 Electric field

The distribution of electric field intensity along the structure for each type-I Cantor generation is shown in figure 20. The EF was calculated for a wavelength of 1650.70164 nm which corresponds to a very well defined transmission mode. Increasing the generation order, it follows that the intensity as well as the confinement of the electric field increases drastically reaching a maximum value of  $|E|^2 = 477$  in the fourth generation. A subsequent increment the confinement of EF starts to decrease. Another interesting thing is the fact the confinement occur preferably in the central part of the Cantor structures and can be tuned to a particular wavelength by only scaling the whole Cantor structure, i.e. either increasing or reducing the total optical thickness. This can be exploited to the development of active nucleus in the heating, emitting and lasing applications such as LED's, lasers, etc.

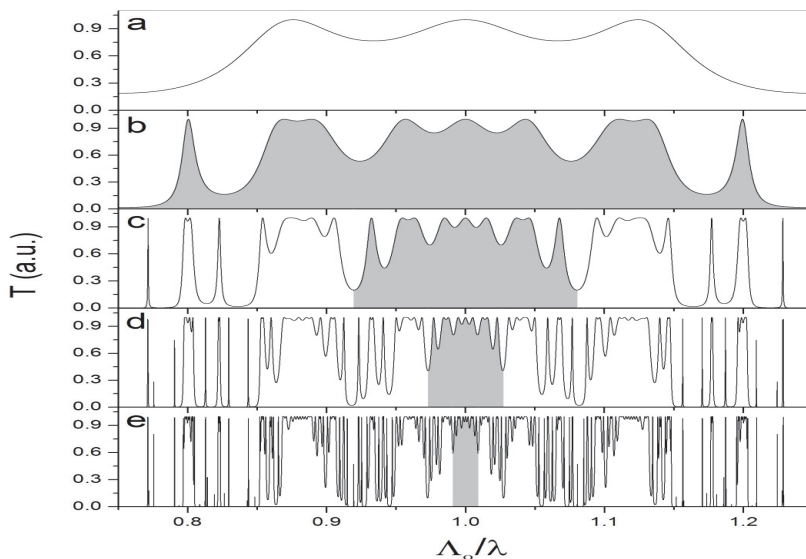


Fig. 19. Theoretical transmittance of the type-II Cantor structures normalized with respect to the optical thickness ( $\Lambda_0$ ) of the smallest layer in each structure. The refractive indices and the whole optical thickness are the same used in the type-I Cantor structures.

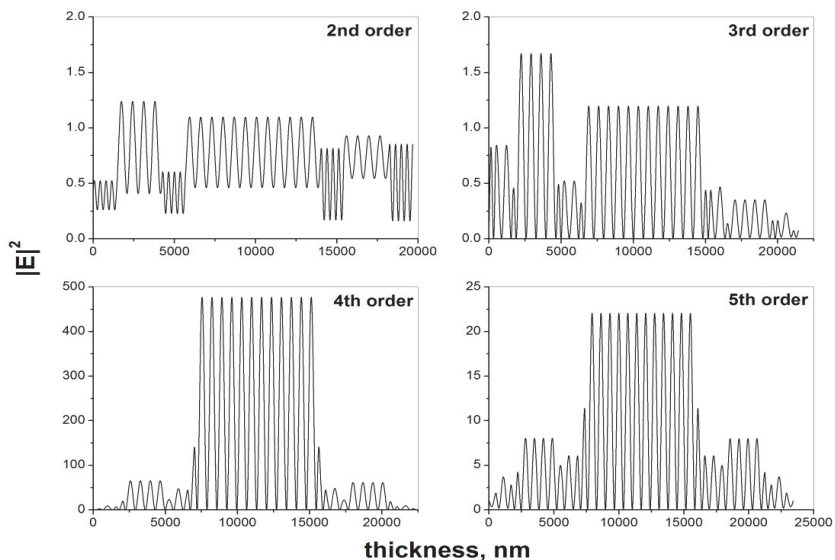


Fig. 20. Electric field intensity calculated at a wavelength of 1650.70164 nm for different type-I Cantor structures.

## 6. Conclusions

First, we have demonstrated that the wave functions exhibit a self-similar property induced by the *self-similarity* condition (9) on the potential. We have given a proof in the framework of quasiclassical approximation. This is true for energy values, no matter how large it could be. This behavior of the self-similar quantum well is radically different from that known from a standard quantum well, which only affects the eigenfunctions of the levels closest to the well top. On the other hand, we have observed some interesting properties for the discrete levels. At first sight, it could be supposed that the system proposed is not different from those that appeared before in the literature. However, the system that we have considered are extremely different from a topological point of view, since the quantum well proposed is self-similar. This property, allows us to show that for any eigenvalues the associated eigenfunction "feels" the presence of the quantum well, despite how large is the eigenvalue. This is a main difference to the standard quantum well, where the eigenfunctions show the presence of the quantum well only for eigenvalues close to the well top.

At this stage of the study, it is more than likely acceptable to suggest that there are other bounded potentials defined in finite intervals also having self-similar wavefunctions. Indeed the standard Cantor construction can be changed in a variety of ways, as can be seen in Ref. (24), all of them having the same analytical properties. In a given Cantor construction one may study non-constant potentials, and the main steps of our analysis are valid as long as the *self-similar* condition (9) remains legitimate.

Other isomorphic problems possess the same properties. Among them we can mention the transversal horizontal elastic modes, the TE or TM electromagnetic modes, both of them in a multilayered system,(21) etc. It is not so evident, on the other hand, that non-isomorphic problems, like those discussed in Ref. (26), share the fractal property of the self-similarity of the corresponding states. But it is worth to mention that in quasiregular heterostructures, elementary excitations exhibit fractality as well as self-similarity of the zero state, despite being isomorphic with onedimensional Schrödinger-like equations.

The properties of the spectrum of different Hamiltonians is a problem of current interest for mathematicians as well as for physicists. A significant number of progresses have been obtained in the last decennials. As a survey the reader can be addressed to Refs. (1; 27; 28) and references therein. However, there remains a number of intriguing questions; one of them is the character of the spectrum for strange potentials as the one we have analyzed in this paper.

Apparently this strange potential could be described as nothing but a curiosity; however, this is not entirely true. In the present days the experimentalists can construct, and in fact they do, finite realizations of these bizarre systems obtaining interesting and applicative properties. We hope the present theoretical lucubration encourages some experimental works.

Furthermore, we have calculated the coefficient of intersubband optical absorption (in the region of the discrete spectrum of energies), but we have found no self-similarity, at least none evident.

We present a formal definition of topological self-similar potentials. These, not only have to show scaling properties in the length but also in the values of  $V$ . In this situation, the eigenfunctions of the discrete spectrum are self-similar by pairs. In this type of systems the eigenfunctions seems to be strongly localized at the small wells. This behavior suggest that the electronic mobility will be greater than the corresponding to traditional quantum wells.

On the other hand, the optical absorption coefficient does not present a remarkable behavior. The electronic transmittance for self-similar barriers shows certain interesting oscillations for high energies. Particularly interesting came to be the case of mixed systems. First, the ssp filters the tunneling transmittance of the mbpp. Also, it shows a gap in a permitted region of the corresponding mbpp. In this gap, it could be observed three quasibound levels. This behavior seems to be particular of these kind of mixing, as it can not be obtained with mbpp or multibarrier quasiregular potentials. The proof of theorem 2, shows that distinct types of selfsimilarity is obtained depending on the similar ratios that is taken for the construction of the potential.

The mixed systems modify the general behavior of the transmittance corresponding to the potential component systems. Also, the transmittance in function of the width of the barriers shows that the contribution of smaller barriers in the ssp is reflected on the whole structure of maximum and minimum. Finally, in the optical reflectance spectrum for a self-similar structure based on porous silicon, the more interesting property is the nesting from one generation to next. Which gives the possibility of characterize this kind of spectrum.

## 7. References

- [1] J.M. Luck, "Cantor spectra and scaling of gap widths in deterministic aperiodic systems", *Phys. Rev.* **B39**:9, 5834-5849 (1998).
- [2] M. Kolár and F. Nori, "Trace maps of general substitutional sequences", *Phys. Rev.* **B42**:1, 1062-1065 (1990).
- [3] R. Pérez-Álvarez and F. García-Moliner, "The spectrum of quasiregular heterostructures", invited chapter in "Some Contemporary Problems of Condensed Matter Physics", Nova Science Publishers, ed. by S. Vlaev and M. Gaggero-Sager (2000), pp. 1-37.
- [4] E. Maciá and F. Domínguez, "Phonons and Excitons in Low Dimensional Aperiodic Systems", Editorial Complutense, Madrid (2000).
- [5] R. Pérez-Álvarez, F. García-Moliner, and V.R. Velasco "Some elementary questions in the theory of quasiperiodic heterostructures", *J. of Phys.: Condens. Matter* **13**, 3689-3698 (2001).
- [6] B.B. Mandelbrot, "The Fractal Geometry of Nature", W.H. Freeman and Company, New York (1983).
- [7] A. Bovier and J.M. Ghez, "Spectral properties of one-dimensional Schrödinger operators with potentials generated by substitutions", *Commun. Math. Phys.* **158**:1, 45-66 (1993).
- [8] A. Bovier and J.M. Ghez, "Remarks on the spectral properties of tight-binding and Kronig-Penney models with substitution sequences", *J. Phys. A:Math. Gen.* **28**:8, 2313-2324 (1995).
- [9] L.M. Gaggero-Sager, E.R. Pujals, and O. Sotolongo-Costa, "Self-similarity in a Cantor-like semiconductor quantum well", *Phys. Stat. Sol. (b)* **220**, 167-169 (2000).
- [10] S.V. Zhukovsky, A.V. Lavrinenko, and S.V. Gaponenko, "Spectral scalability as a result of geometrical self-similarity in fractal multilayers", *Europhys. Lett.* **66**:3, 455-461 (2004).
- [11] A.V. Lavrinenko, S.V. Zhukovsky, K.S. Sandomirski, and S. V. Gaponenko, "Propagation of classical waves in nonperiodic media: Scaling properties of an optical Cantor filter", *Phys. Rev. E* **65**, 036621 (2002).
- [12] L. Moretti, I. Rea, L. De Stefano, and I. Rendina, "Periodic versus aperiodic: Enhancing the sensitivity of porous silicon based optical sensors", *Applied Phys. Lett.* **90**, 191112 (2007).

- [13] V. Agarwal, B. Alvarado-Tenorio, Jose Escorcia-García, and Luis Manuel Gaggero-Sager, "Cantor Dielectric Heterostructures Made of Nanostructured Multilayers of Porous Silicon", *PIERS Online* **4:4**, 451-454 (2008).
- [14] Kenta Esaki, Masatoshi Sato, and Mahito Kohmoto "Wave propagation through Cantor-set media: Chaos, scaling, and fractal structures" *Phys. Rev. E* **79**, 056226 (2009)
- [15] M. Pilevari Salmasi, F.H. Kahani, and M.N. Azarmanesh, "A novel broadband fractal Sierpinski shaped, microstrip antenna", *Progress In Electromagnetics Research C* **4**, 179-190 (2008).
- [16] Massimiliano Berti and Philippe Bolle, "Cantor families of periodic solutions for completely resonant wave equations", *Frontiers of Mathematics in China*, **3:2**, 151-165 (2008).
- [17] Artur Avila, Jairo Bochi, and David Damanik, "Cantor spectrum for Schrödinger operators with potentials arising from generalized skew-shifts", *Duke Math. J.* **146:2**, 253-280 (2008).
- [18] J.Palis and F.Takens *Hyperbolicity and sensitive-chaotic dynamics at homoclinic bifurcations* Cambridge University Press, 1993.
- [19] C. G. Moreira, J-C. Yoccoz, Stable intersections of regular Cantor sets with large Hausdorff dimensions. *Ann. of Math. (2)* **154** (2001), no. 1, 45-96.
- [20] L.D. Landau and E.M. Lifschitz, "Mecanique Quantique", éditions Mir, Moscou (1966).  
"Quantum Mechanics, Nonrelativistic theory", Pergamon, New York (1981).  
"Mecánica Cuántica (teoría no-relativista)", editorial Reverté S.A. Barcelona-Buenos Aires-Mexico (1967).
- [21] D.J. Griffiths and C.A. Steinke, "Waves in locally periodic media", *Am. J. Phys.* **69:2**, 137-154 (2001).
- [22] G. Bastard, "Wave mechanics applied to semiconductor heterostructures", Éditions de Physique, Paris (1989).
- [23] S.N. Rasband, "Chaos dynamics of nonlinear systems", Wiley Professional Paperback Series (1997).
- [24] T.C. Halsey, M.H. Jensen, L.P. Kadanoff, I. Procaccia, and B.I. Shraiman, "Fractal measures and their singularities: The characterization of strange sets", *Phys. Rev.* **A33:2**, 1141-1151 (1986).
- [25] S.Ya. Jitomirskaya and Y. Last, "Dimensional Hausdorff properties of singular continuous spectra", *Phys. Rev. Lett.* **76:11**, 1765-1769 (1996).
- [26] R. Pérez-Álvarez, F. García-Moliner, C. Trallero-Giner, and VR Velasco, "Polar optical modes in Fibonacci heterostructures", *Journal of Raman Spectroscopy* **31:5**, 421-425 (2000).
- [27] B. Simon, "Almost periodic Schrödinger operators: A review", *Adv. Appl. Math.* **3**, 463-490 (1982).
- [28] B. Simon, "Schrödinger operators in the twenty-first century", eds. A. Fokas, A. Grigoryan, T. Kibble, and B. Zegarlinski, Imperial College, London, 283-288 (2000). Also at *J. Math. Phys.* **41**, 3523-3555 (2000).
- [29] M. E. Mora, R. Pérez-Álvarez and C. Sommers, *J. Physique* **46**, 1021-1026 (1985).

# Long-Term Convergence of Bulk- and Nano-Crystal Properties

Sergei L. Pyshkin and John Ballato  
*Academy of Sciences of Moldova and Clemson University,  
Republic of Moldova,  
United States of America*

## 1. Introduction

Single crystals of semiconductors grown under laboratory conditions naturally contain a varied assortment of defects such as displaced host and impurity atoms, vacancies, dislocations, and impurity clusters. These defects result from the relatively rapid growth conditions and inevitably lead to the deterioration of the mechanical, electric, and optical properties of the material, and therefore to degradation in the performance of the associated devices.

Over time, driving forces such as diffusion along concentration gradients, strain relaxation associated with clustering, and minimization of the free energy associated with properly directed chemical bonds between host atoms result in an ordered redistribution of impurities and host atoms in a crystal. In the particular case of GaP, any attempt to accelerate these processes through annealing at increased temperatures cannot be successful because high-temperature processing results in thermal decomposition (due to P desorption) instead of improved crystal quality. Therefore successful thermal processing of GaP can only take place at temperatures below its sublimation temperature, requiring a longer annealing time. Evaluated in the framework of the Ising model, the characteristic time of the substitution reaction during N diffusion along P sites in GaP:N crystals at room temperature constitutes 15-20 years (Pyshkin et al., 1990a). Hence, the observations of highly excited luminescence and some other phenomena in the crystals made in the 1960s-1970s and in the 1980s-1990s were then compared with the results obtained in 2009-2010 under similar experimental conditions.

The pure and doped GaP crystals discussed herein were prepared about 50 years ago (Goryunova et al., 1969). Throughout the intervening decades they have been periodically re-evaluated in order to investigate the change over time in their electro- and photoluminescence (PL), photoconductivity, bound excitons of high density, nonlinear optics, and other phenomena. Accordingly, it is of interest also to monitor the change in crystal quality over the course of several decades while the crystal is held under ambient conditions.

The long-term ordering of doped GaP and other semiconductors has been observed as an important accompanying process, which can only be studied using the same unique set of samples and the interest to observe them over decade time scales. More specifically, since

2005, we have analyzed the optical and mechanical properties of single crystalline Si, III-V semiconductors {GaP (Goryunova et al., 1969)}, and their ternary analog CdIn<sub>2</sub>S<sub>4</sub> (Pyshkin et al., 1990b), all of which were grown in the 1960s. Comparison of the properties of the same crystals has been performed in the 1960s, 1970s, 1980s, 1990s (Goryunova et al., 1969; Ashkinadze et al., 1968; Pyshkin & Zifudin, 1974; Pyshkin, 1975a; Pyshkin et al., 1990a,b; Pyshkin et al., 1993; Pyshkin & Anedda, 1993, 1998), and during 2000s (Pyshkin, 2002a,b; Pyshkin & Ballato, 2005, 2006, 2008, 2010; Pyshkin et al., 2006, 2007a,b,c, 2008, 2009a,b,c,d,e, 2010a,b,c,d; Pyshkin, 2009-2012) along with those of newly made GaP nanocrystals (Pyshkin et al., 2006, 2010b,c; Pyshkin & Ballato, 2010); and freshly prepared bulk single crystals (Pyshkin et al., 2009a,b,c,d,e).

Jointly with the above-noted references this chapter provides a generalization of the results on long-term observation of luminescence, absorption, Raman light scattering, and microhardness of the bulk single crystals in comparison with the same properties of “modern” GaP nanocrystals. We show that the combination of these characterization techniques elucidates the evolution of these crystals over the course of many years, the ordered state brought about by prolonged room-temperature thermal annealing, and the interesting optical properties that accompany such ordering. We demonstrate that long-term natural stimuli that improve the perfection of crystals prevail over other processes, which could lead to novel heterogeneous systems and new semiconductor devices with high temporal stability.

Additionally, it is worth noting, that semiconductor nanoparticles for optoelectronic applications also were synthesized mainly to avoid limitations inherent to freshly grown bulk semiconductors with a wide range of different defects. For instance, different defects of high concentration in freshly prepared GaP single crystals completely suppress any luminescence at room temperature due to the negligible free path for non-equilibrium electron-hole pairs between the defects and their non-radiative recombination, while the quantum theory predicts their free movement in the field of an ideal crystal lattice. The long-term ordered and therefore close to ideal crystals demonstrate bright luminescence equivalent to the best nanoparticles and stimulated emission with pronounced quantum confinement effect. These perfect crystals, due to their unique mechanical and optical properties, are useful for application in high-quality optoelectronic devices as well as they are a new object for development of fundamentals of solid state physics and, nanotechnology and crystal growth.

Lastly, for completeness, during the recent years, since 2005, the authors have continued their efforts on the preparation of GaP nanoparticles in order to improve their quality and to apply their composites with appropriate polymers for advanced light emissive structures (Pyshkin et al., 2006, 2010c, d; Pyshkin & Ballato, 2010; Pyshkin, 2009-2012). Application of the GaP/polymers nanocomposites in device structures for accumulation, conversion and transport of light energy have only recently received attention while bulk and thin GaP films have been successfully commercialized for many years.

## 2. Results and discussion

The discussion of results begins with the synthesis of GaP nanoparticles and nanocomposites such that a comparison can then be made to the properties of bulk single crystals.



## 2.1 GaP nanocrystals and nanocomposites: improvement of quality and properties

### 2.1.1 Nanocrystals

The highest quality GaP nanoparticles have been synthesized using white phosphorus under mild aqueous low temperature conditions. The photoluminescence (PL) and Raman light scattering (RLS) spectra, X-ray diffraction (XRD) and electron microscopy (TEM) of the nanoparticles prepared under different conditions have been compared with each other as well as with those from bulk single crystals. After the relevant investigation of different regimes and components for hydrothermal reactions this type of the synthesis has been chosen as an optimal (Pyshkin et al., 2010b); the other advanced methods are also under elaboration (Pyshkin, 2009-2012).

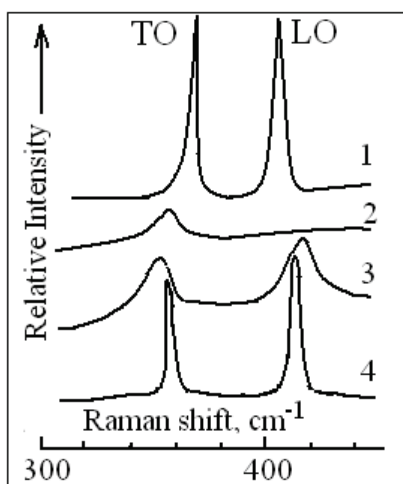


Fig. 1. Raman light scattering from GaP nanoparticles of different treatment (spectra 2-4) and in comparison with perfect GaP bulk crystals (spectrum 1). 2. Not thoroughly treated powder of nanoparticles prepared using red phosphorus at 200°C. 3. Thoroughly treated GaP nanoparticles prepared using red phosphorus at 200°C. 4. Nanoparticles prepared on the base of white P by low temperature syntheses.

Note that according to our investigations of the conditions of the synthesis and data on nanoparticle characterization (TEM, XRD, RLS and PL), only a combination of low temperature synthesis, using white P and thorough ultrasound treatment of the reaction products during the synthesis and after leads to the creation of nanoparticles suitable for high quality light emissive nanocomposites (Pyshkin et al., 2010c) with the controlled broadband and UV shift of luminescence. Further, the use of an ultracentrifuge to separate the nanoparticles based on their dimension provides an opportunity to efficiently change the line-width and spectral position of the luminescent maximum. The suspensions, specially produced for storage of the nanoparticles and preparation of nanocomposites, contain 10 nm single nanoparticles obtained from thoroughly ultrasonicated and washed reaction product, while its powder consists of the particles with the dimensions up to 100 nm and their clusters.

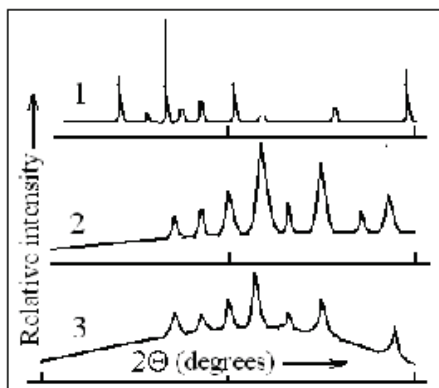


Fig. 2. X-ray diffraction from GaP nanoparticles. 1. White phosphorus, best performance of low temperature syntheses, well-treated powder. 2. White P, not the best performance and powder treatment. 3. Red phosphorus, the best result obtained using red P.

**Figure 1** shows the Raman light scattering spectra from the GaP perfect bulk crystals (**spectrum 1**) and from the nanoparticles prepared using either white or red P by mild aqueous synthesis at increased or low temperatures and ultrasonically treated (**spectra 2-4**). The characteristic Raman lines from the nanoparticles prepared at high temperatures (**spectra 2 and 3**), especially from not thoroughly washed powder (**spectrum 2**), were weak and broad, while the lines from the nanoparticles prepared at low temperature using white P were narrow and intense (**spectrum 1**).

**Figure 2, spectra 1-3**, provides the X-ray diffraction spectra from GaP nanoparticles prepared at different conditions using red or white phosphorus. The nanoparticles obtained by low temperature aqueous synthesis using white phosphorus develop clear and narrow characteristic lines (**spectrum 1**) similar to those obtained of bulk GaP taken from our long-term (more than 40 years) ordered GaP single crystals (Pyshkin et al., 2010b).

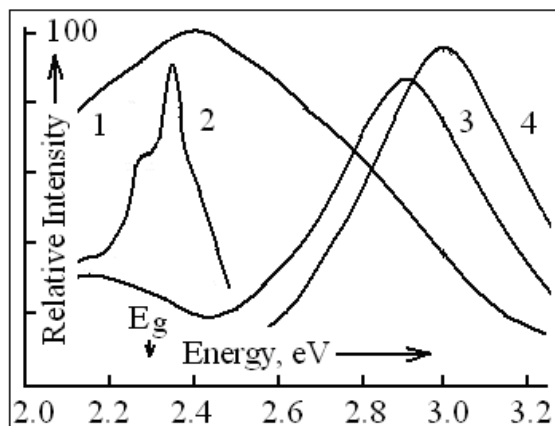


Fig. 3. Luminescence spectra from perfect, long-term ordered GaP single crystals (1) in comparison with the spectra of GaP nanoparticles, prepared in 2005 (2) and now (3, 4).

Initial results on the luminescent properties of GaP nanoparticles (Pyshkin et al., 2006) confirm the synthesis of 10 nm GaP nanoparticles with clear quantum confinement effects. The luminescent spectrum was not bright enough and its maximum was only slightly blue shifted against the 2.24 eV forbidden gap at room temperature (**Fig. 3, spectrum 2**). The nanoparticles obtained from the reaction with white P at low (125 °C) temperature exhibit an intense broad-band spectra considerably blue-shifted (**Fig. 3, spectrum 3, 4**). Note that the original powder contains only a part of GaP particles with nearly 10 nm dimension, which develop quantum confinement effect and the relevant spectrum of luminescence, so the spectrum of luminescence consists of this band with maximum at 3 eV and of the band characterizing large particles with the maximum close to the edge of the forbidden gap in GaP (**Fig. 3, spectrum 3**). A thorough ultrasonic treatment yields a more pure fraction of nanoparticles, shown the **spectrum 4**, having the maximum at 3 eV and no maximum in the vicinity of the GaP forbidden gap.

It is reasonable to use such particles in GaP nanocomposites given the goal to obtain broad band luminescence from UV to the yellow-red region with controlled spectral width and position of maximum.

Thus, it was established that GaP nanoparticles can be prepared from white phosphorus at decreased temperature (125°C), intense ultrasonication during the syntheses and, if necessary, separation based on size using ultracentrifuge. These optimal conditions for GaP nanoparticles syntheses have been chosen in our works on fabrication of the GaP/polymers nanocomposites. The other possibilities to get the nanoparticles of the best quality are discussed in (Pyshkin et al., 2011).

### 2.1.2 GaP/Polymers nanocomposites

In the preparation of the nanocomposites, the fractions of uniform GaP nanoparticles were used following thorough ultrasonic treatment and a number of other operations that yielded the bright broad-band luminescence from UV until yellow-red region with controlled width and position of maximum. It is important to note that the value of the forbidden gap in GaP at room temperature is only 2.24 eV and its bulk freshly prepared single crystals have no luminescence at 300 °K.

Different polymers [Polyglycidyl methacrylate (PGMA), polyglycidyl methacrylate-co-polyoligoethyleneglycol methacrylate (PGMA-co-POEGMA) and biphenyl vinyl ether (BPVE)], compatible with GaP nanoparticles have been used in preparation of the nanocomposites. The details of their fabrication are described in (Pyshkin et al., 2010c).

The nanocomposite films were deposited from a suspension in water-ethanol mixture solution on the surface of a silica substrate via the procedure known as dip-coating. Surface morphology of the nanocomposite films was studied in ambient air by AFM in the tapping mode, on a Dimension 3100 (Digital Instruments, Inc.) microscope. Thickness of the polymer composite film was within 250-300 nm defined from AFM scratch experiment. Luminescence of the nanocomposites films was excited by the N<sub>2</sub> laser nanosecond pulses at wavelength 337 nm and measured at room temperature. AFM imaging demonstrated that no significant aggregation was caused by the polymerization. In general, individual particles were observed.

Thus, the thoroughly washed, ultrasonicated and dried nanopowder obtained by mild low temperature aqueous synthesis from white P may be used for fabrication of quite good blue light emissive nanocomposites (**Figure 4, spectrum 1**), but the best quality and the largest shift of the position of luminescence maximum to the UV side (up to 3, 2 eV) can be obtained only in the case of fabrication of the nanocomposite from similarly prepared

nanoparticles with the dimension of approximately 10 nm and stored as a suspension in a suitable liquid (**Figure 4, spectrum 2**).

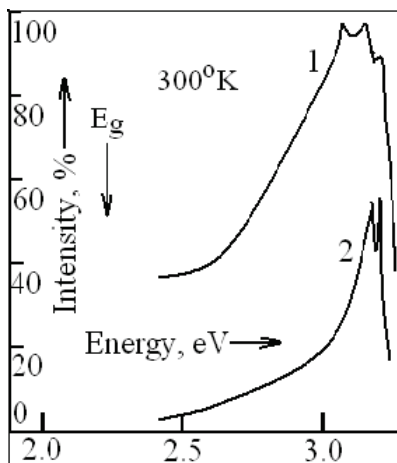


Fig. 4. Luminescence spectra of GaP/PGMA-co-POEGMA nanocomposite prepared on the best GaP nanoparticles synthesized and stored as the dry powder (spectrum 1) or suspension in a liquid (spectrum 2).

**Figure 5** shows the luminescence spectra of 2 nanocomposites produced on the base of 2 batches of GaP nanoparticles obtained under different conditions (temperature, modification of P, etc.). We note that in the GaP/BPVE nanocomposite the position of the luminescent maximum can be changed between 2.5 – 3.2 eV and the brightness is 20-30 more than in the PGMA and PGMA-co-POEGMA matrixes.

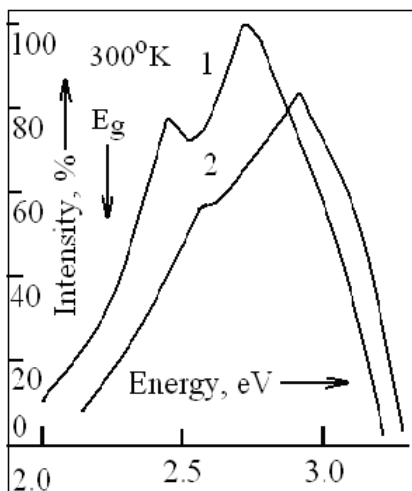


Fig. 5. Luminescence spectra of 2 GaP/BPVE nanocomposites produced on the base of 2 parties of GaP nanoparticles prepared using different conditions.

Initial attempts to prepare GaP nanoparticles, dating from the years 2005-2006 (Pyskhin et al. 2006), yield room temperature luminescence with maximum shifted only to 2.4 eV that in comparison with the new maximum at 3.2 eV confirms serious achievements in technology of GaP nanoparticles and GaP based nanocomposites.

## 2.2 Aged and freshly grown crystals: comparison of properties

We begin by comparing selected properties of pure and doped GaP crystals measured recently to those measured many years ago in order to better understand their luminescence behavior.

Luminescence and Raman light scattering spectra indicate that over a period of about 25 years the zero-phonon line of the exciton bound to nitrogen, A, and its phonon replica LO, TO are narrower in their line widths (Figure 6) and in comparison with freshly prepared single crystals. Further, the zero-phonon line A and its phonon replica of single N impurity-bound excitons in the aged crystals shift according to the existing theory (Allen, 1968) their spectral positions with concentration of N impurities. In comparison with ordered GaP:N, newly grown crystals exhibit broader luminescence line-widths when the nitrogen concentration increases. These findings indicate that a more ordered disposition of N impurities with equal spacing exists between them in the aged crystals.

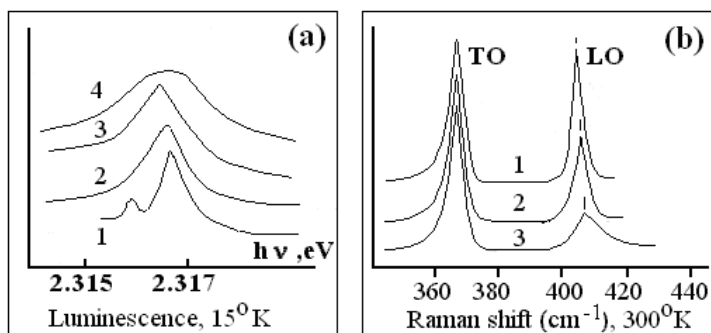


Fig. 6. Evolution of the non-phonon line of bound exciton A in luminescence (a), excitation by Ar<sup>+</sup>-laser at 488 nm, 15K) and its LO (longitudinal optical) and TO (transversal optical) phonon replica in Raman light scattering (b), Excitation by Ar<sup>+</sup>-laser at 514 nm, 300K) as a function of N (nitrogen) concentration. 1-3: ordered crystals. 4: unordered. 1-4:  $N_0 = 10^{17}$ ;  $10^{18}$ ;  $10^{19}$  and  $10^{18} \text{ cm}^{-3}$ .

Figure 7 shows the Raman spectra of pure GaP and GaP:N in 1989–1993 (a) and in 2006 (b, c). It is observed that the line-width and position of transverse optical (TO) modes are largely the same now as in 1989–1993 and do not depend on impurity concentration. In the case of the longitudinal optical (LO) modes, the peaks from the original sample are broad and weak and shift with impurity level. After 40 years, these peaks are now much more intense, possess narrower linewidths and have a spectral position that no longer depends on N concentration. In earlier measurements, the intensity of the LO peak was only a few times less in heavily doped than in the pure disordered crystals. Now the same crystals display a reversal in the ratio between the intensities of these peaks.

A new phenomenon observed in the Raman spectra, that has developed in the crystals over 40 years, are the peaks denoted by us here as LA, 2TO and TO + LO (Figure 7c). Note that the

theory of Raman light scattering in GaP predicts the LO phonon to decay into two longitudinal acoustic (LA) phonons. LA phonons with a frequency  $LO/2$  (Bairamov et al., 1975), and two-phonon processes of 2TO and TO + LO emission can also be observed in perfect crystals (Pyshkin et al., 1990b). This observation of a multi-phonon process and a decay of LO phonon, having a low intensity, confirms the high quality of the host lattice, uniform impurity distribution, and as a consequence, low noise background in the Raman scattering.

**Figures 6-8** demonstrate differences between the disordered, newly prepared single crystals, and crystals ordered for 25 years and 40 years. As can be seen from Fig. 7, differences between the freshly prepared and 25-year ordered GaP crystals are observed in the line-widths and their spectral position with N concentration, which suggests an improvement in ordering of the host lattice and nearly equal spacing between impurities.

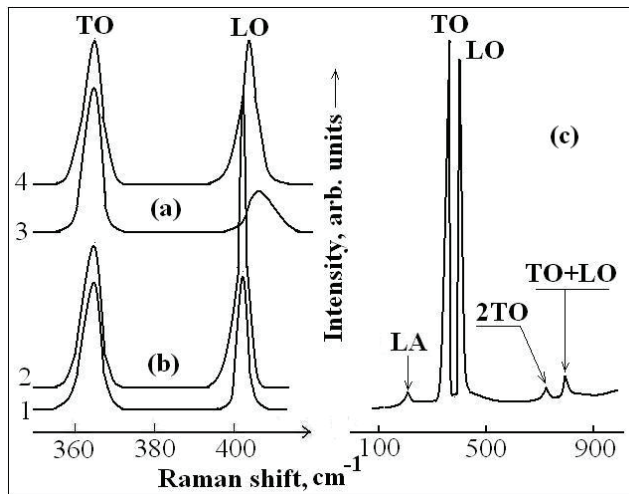


Fig. 7. Raman spectra in GaP and GaP:N in 1989-1993 (a) and in 2006 (b, c). 1, 4 – pure GaP, 2, 3 – GaP heavily doped by N.

**Figure 8** shows the absorption edge as a function of photon energy (a) and provides a comparison of microhardness and density of dislocations as a function of N concentration (b). The position of the absorption edge in freshly prepared GaP:N crystals does not depend on N impurity concentration and it coincides with the position for pure GaP crystals (**Figure 10a, curves 2 and 3**). This N impurity creates the 21-meV energy level under the conduction band for bound excitons both in freshly prepared and 25-year ordered crystals. On the contrary, curve 1, **Figure 8a**, shows that the GaP:N crystals ordered for approximately 40 years demonstrate an increase in the forbidden gap and the clear shift of the absorption edge, which is proportional to the N concentration according to Vegard's law, similar to that in a dilute GaP-GaN solid solution.

Let us discuss now the influence of long-term ordering of the dopants and defects on the optical and mechanical properties of GaP and its ternary analog  $CdIn_2S_4$ . The microhardness and dislocation density in these samples have been evaluated over many decades (Goriunova, 1960; Radautsan et al., 1969; Pushkash et al., 1978; Valkovskaya et al., 1984; Pyshkin, 1967). Taking into account the full 50-year timeframe makes an exact comparison difficult; therefore, only general trends are discussed here.

According to the classical point of view (Kittel, 1978), good plasticity is determined by free movement of dislocations through the crystal under mechanical loading. Impurities act to pin the movement of dislocations. Therefore, the value of microhardness,  $H$ , in GaP should depend on the impurity concentration (Fig. 8b, lines 1 and 2). As can be seen, the relatively pure crystals have minimum microhardness. An increase in the impurity concentration in GaP crystals, with the dopants such as N, Bi, simultaneously N and Sm (Pyshkin et al., 1990a; Pyshkin, 1967), substituting for the host atoms (N, Bi) or occupying the interstitials in the crystal lattice (Sm), leads to an increase in microhardness for the long-term-ordered crystals. The same behavior of microhardness for freshly prepared and long-term ordered single crystals was observed for mono-atomic Si and binary InP, pure and doped by different impurities.

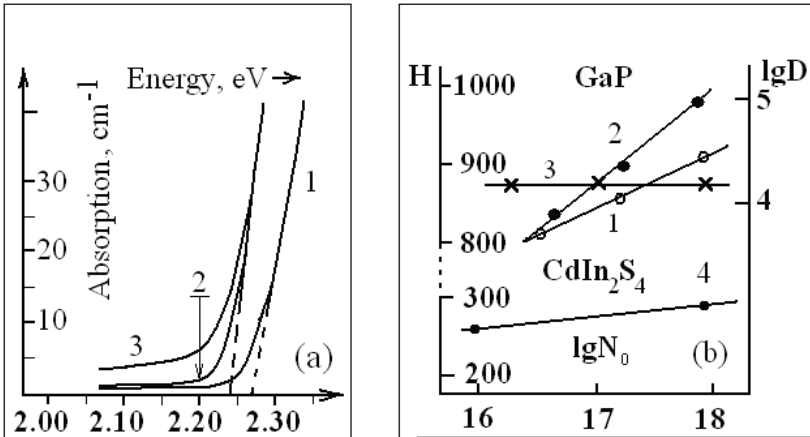


Fig. 8. (a) Absorption coefficient in long-term ordered (40 years) GaP:N (1) and in 25 years old (2) or freshly prepared undoped GaP (3). N concentration is  $10^{18} \text{ cm}^{-3}$ . (b) Microhardness,  $H$ , in fresh unordered GaP crystals as a function of N concentration (1); the same for 40 years ordered crystals (2);  $D$  as a function of N concentration (3);  $H$  in CdIn<sub>2</sub>S<sub>4</sub> at different concentration of defects (4).

The rather large difference in microhardness of the long-term-ordered highly doped crystal relative to the newly grown crystals can possibly be explained by the regular disposition of impurities. This might create a more significant obstacle to dislocation movement than in the newly grown system, in which the impurities form clusters with large distances between them, permitting greater dislocation movement.

Figure 8b, line 3 shows that the density of dislocations  $D$  in GaP does not depend on time (at least over nearly 50 years), concentration of impurities, or the nature of their distribution along the crystal. It is possible that the method of crystal growth determines the density of dislocations. It is worth noting that the high-quality growth conditions for the initial GaP crystals and accurate control over temperature during growth considerably decreased the density of dislocations (Pyshkin, 1967).

As we have shown earlier (Pyshkin, 1971), optical properties and quality of crystal lattice of CdIn<sub>2</sub>S<sub>4</sub> highly depend on position and concentration of intrinsic structural (stoichiometric vacancies of In and Cd cations) and antistructural (In<sub>Cd</sub> and Cd<sub>In</sub> - In replaces Cd and vice versa in partly inverse spinel) defects. CdIn<sub>2</sub>S<sub>4</sub> due to wrong positions of cations has partly

inverse spinel structure instead of normal spinel and antistructural defect ( $\text{In}_{\text{Cd}}$ ,  $\text{Cd}_{\text{In}}$ ) concentration dependently on the growth condition up to  $10^{20} \text{ cm}^{-3}$  (Guzzi & Grilli, 1984). Analysis both of luminescence and Raman light scattering spectra (Pyshkin et al., 1990a; Pyshkin, 1971) shows that due to the long-term ordering the partly inverse spinel  $\text{T}_d^2$  turns into the normal spinel structure  $\text{O}_h^7$ . This implies that the high concentration of the antistructural defects characterizing freshly grown crystals will decrease from app.  $10^{20} \text{ cm}^{-3}$  until their equilibrium level of the order of  $10^{16} \text{ cm}^{-3}$ . As in GaP, where the microhardness highly depends on the concentration of impurities, its ternary analog demonstrates the considerable dependence of microhardness on concentration of the defects (**Figure 8b, the line 4**).

**Figure 9a** shows that the freshly prepared and then slowly cooled as well as the long-term ordered crystals having a small concentration of the antistructural defects, in comparison to quickly cooled crystals, develop fine structure of the luminescence due to interaction of electrons only with lattice phonons.

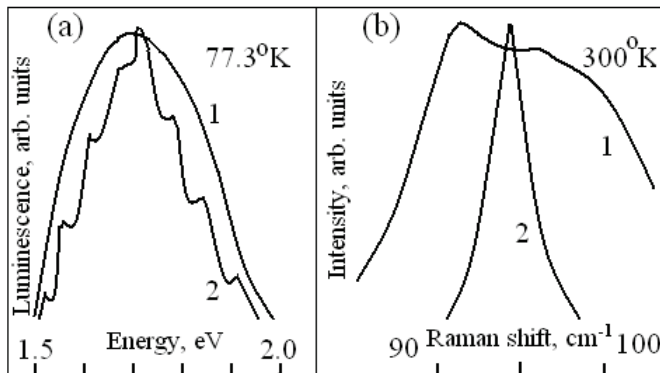


Fig. 9. Luminescence and Raman light scattering in  $\text{CdIn}_2\text{S}_4$ . (a) Luminescence of freshly prepared and long-term ordered  $\text{CdIn}_2\text{S}_4$  crystals. Rapid (1) and slow (2), less than  $5^\circ\text{C}$  per hour, cooling rates. Ordered crystals develop a spectrum like 2. (b) Raman light scattering at  $92 \text{ cm}^{-1}$  of unordered (1) and ordered (2) crystals.

Exactly as in GaP, a phonon mode is broad and weak for freshly prepared  $\text{CdIn}_2\text{S}_4$ , but after the long-term ordering this peak is more intense, has a more symmetric shape and narrower linewidth, characterizing harmonic vibrations in a perfect lattice (**Figure 9b, curves 1 and 2**). Now luminescence phenomena that can be observed only in perfect long-term ordered GaP and  $\text{CdIn}_2\text{S}_4$  single crystals will be discussed.

The 40-year ordered GaP:N crystals have no discrete impurity level in the forbidden gap and demonstrate uniform luminescence from a broad excitonic band (**Figure 10b**) instead of narrow zero-phonon line and its phonon replica in disordered and partly ordered (25-year-old, **Figure 10a**) single crystals. For the first time, to the best of our knowledge, the transformation of a discrete level inside the forbidden gap into an excitonic band (**Figures 10b and 11b**) is observed. In this case the impurity atom of nitrogen regularly is located into host lattice instead of phosphorus and affects the band structure of the crystals, which is now a dilute solid solution of GaP-GaN but not GaP doped by occasionally located N atoms. Note that the increase in the level of excitation of luminescence (**dotted lines in Figure 10**) in the case of partly ordered GaP:N leads to a broad luminescence band as a result of bound



exciton interaction (Pyshkin & Zifudin, 1974), while in the case of perfectly ordered crystals one can see an abrupt narrowing of the luminescence band, probably due to stimulated emission in perfect non-defect crystals as is discussed further below.

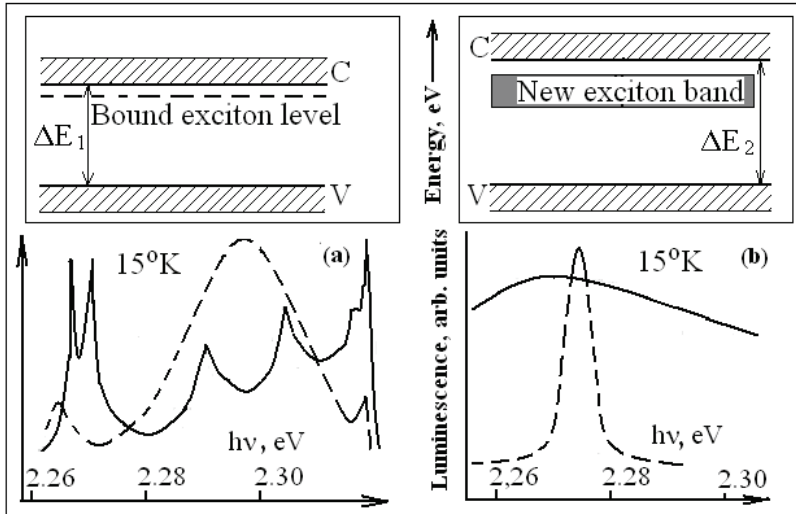


Fig. 10. Luminescent spectra and the view of the forbidden gaps ( $\Delta E_1$ ,  $\Delta E_2$ ) in the partly 25 years ordered (a) and perfect 40 years ordered (b) crystals GaP doped by N. The dotted lines correspond to highly optically excited crystals. C and V - the positions of the bottom of the conductance and the top of valence bands respectively.

Thus, taking into account the above-mentioned results, a model for the crystal lattice and its behavior at a high level of optical excitation for 40-year-old ordered GaP doped by N (**Figure 11**) can be suggested. At relevant concentrations of N, the anion sublattice can be represented as a row of anions where N substitutes for P atoms with the period equal to the Bohr dimension of bound exciton in GaP (approximately 10 nm) (**Figure 11a**). At some level of excitation, all the N sites will be filled by excitons, creating an excitonic crystal (**Figure 11b**) which is a new phenomenon in solid-state physics and a very interesting model for application in optoelectronics and nonlinear optics (Pyshkin et al., 2008).

This new crystal lattice in which the impurities have become its intrinsic component can be corroborated by recent Raman light scattering experiments. The difference in the present ordered state of the crystal lattice, with respect to the data obtained with the same crystals and conditions during 1989–1993 (Pyshkin et al., 1993; Pyshkin, 2002) can be seen in **Figures 7a and b**, which shows the Raman spectra of pure GaP and GaP:N (Pyshkin et al., 2007, 2008). One can see (**Figure 7a, curves 3 and 4**) that, for the longitudinal optical (LO) phonon modes, the peak from the original samples is broad, weak, and shifts with impurity level. After 40 years (**Figure 7a, curves 1 and 2**), this peak is much more intense, has a symmetric (Lorentzian) shape, narrower linewidth, and a spectral position that no longer depends on N concentration.

These results are characteristic of harmonic vibrations in a perfect lattice. The LO phonon line is narrower in the doped crystal (**Figure 7a, curve 2**) than in the undoped (pure) crystals (**Figure 7a, curve 1**) and also is more intense than the TO phonon line. The same results have

been obtained for various impurities (N, Sm, and Bi) in spite of their maximum possible concentrations in GaP and different masses of impurity atoms and different types of substitution (N and Bi impurities substitute P sites in the crystal lattice whereas Sm occupies interstitials) (Pyshkin et al., 2007). These results confirm the important role of the impurities that are periodically located in the host crystal lattice and result in the formation of the new perfect crystal lattice.

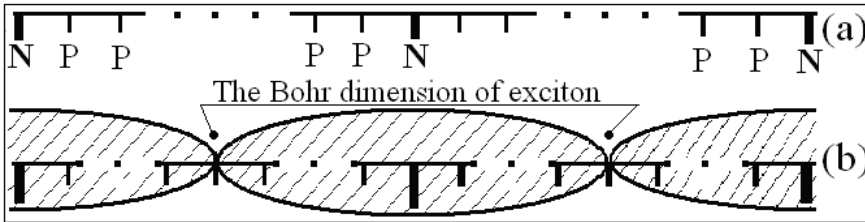


Fig. 11. The models of 40 years ordered GaP doped by N. (a) The new type of crystal lattice where the host P atoms are periodically substituted by N atoms. (b) The exciton crystal on the base of this crystal lattice. The substitution period is equal to the Bohr dimension of exciton (app. 10 nm) and the optical excitation should be sufficient to fill the N sublattice.

As noted previously (Pyshkin et al., 2008), due to a large concentration of defects and a large nonradiative recombination rate for non-equilibrium current carriers, the luminescence of fresh doped and undoped crystals only could be observed at temperatures below 80 °K. The luminescence band and lines were always seen at photon energies less than the value of the forbidden gap (2.3 eV). Now, after 40 years, luminescence of the long-term-ordered bulk crystals similar to the GaP nanocrystals (Pyshkin et al., 2008, 2010c, d,) clearly is detected in the region from 2.0 eV to 3.0 eV at room temperature. We suppose that, in the long-term-ordered bulk crystals, this considerable extension of the region of luminescence at 300 K to the high-energy side of the spectrum is due to: (a) a very small concentration of defects, (b) low contribution of nonradiative electron-hole recombination, (c) considerable improvement of crystal lattice, (d) high transparency of perfect crystals, and (e) high efficiency of so called "hot" luminescence in perfect crystals.

Thirty-five years ago, laser action had been observed only in highly optically excited, high-quality-factor resonators of GaP and at temperatures of 80 K and below. Taken from (Pyshkin, 1975b), **Figure 12** demonstrates that the stimulated emission can be observed only if the excitation light band is located perpendicular to resonator planes (**Figure 12a**). The stimulated emission takes place in the case presented in **Figure 12a** only since this geometry supplies the necessary condition when light losses are less than amplification in the resonator.

The stimulated emission previously observed only at 80 K and below (**Figure 12a**) is due to the radiative recombination of bound excitons that are accompanied by LO phonon emission.

The bright broadband luminescence is observed at room temperature from the long-term-ordered single crystals. In **Figure 13**, the stimulated emission is developed at 300°K and indirect optical transition by radiative recombination of an electron at the bottom of the conduction band with a hole at the top of the valence band and the LO phonon absorption.

The fact that the bright luminescence is seen at photon energies exceeding the energy gap confirms the high degree of perfection of the crystal. Additionally, this "hot" luminescence provides a good opportunity for fabrication and application of interesting light emissive device structures.

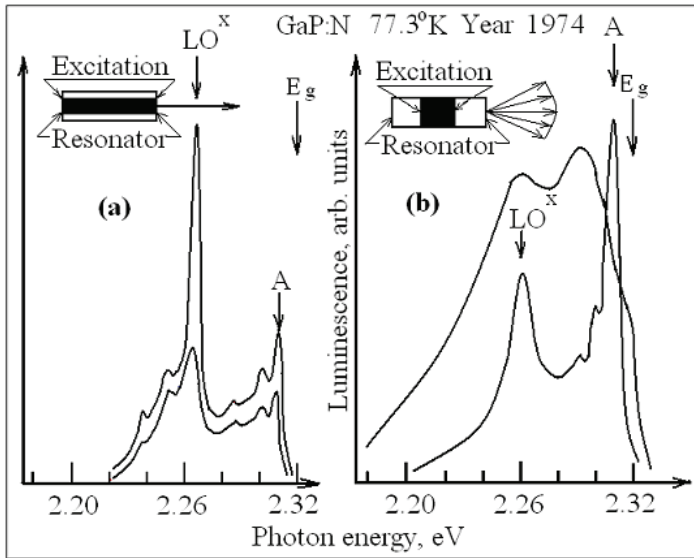


Fig. 12. Year 1974. Emission spectra of GaP excited by the 2nd harmonic of a Q-switched Nd<sup>+</sup> laser at different relation between losses and amplification of the emitted light. (a) Excitation light is perpendicular to the resonator planes, amplification exceeds losses. (b) Excitation light is parallel to the resonator planes, losses exceeds amplification.

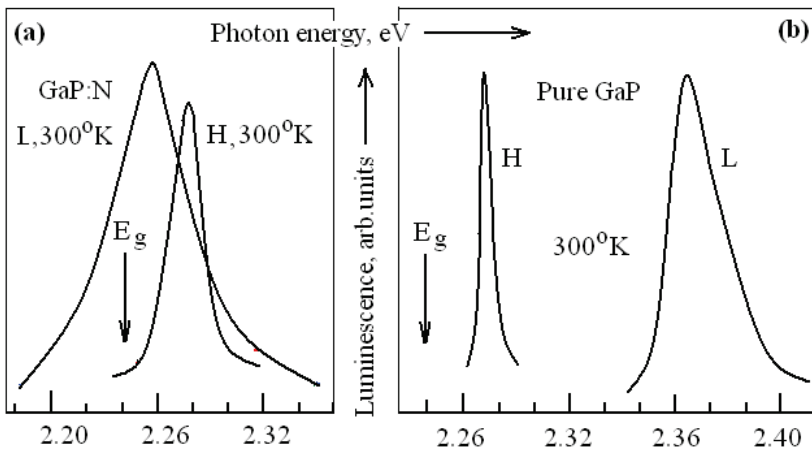


Fig. 13. Year 2007. 300K. Emission spectra of N doped (a) and pure (b) GaP grown in 1965. The letters L and H at the luminescent curves mean low and high level of excitation respectively.

**2.3 Comparison of properties of nanocrystals, aged and freshly-grown bulk crystals**

The high quality of our long-term ordered semiconductor crystals as well as the considerable improvement of their mechanical and optical properties in comparison with

the same freshly-grown crystals are confirmed by investigations of luminescence, light absorption, Raman light scattering, X-ray diffraction, microhardness and discussed in a number of papers and presentations (Pyshkin & Anedda, A., 1993, 1998; Pyshkin, 2002; Pyshkin & Ballato, 2005, 2006, 2008, 2010; Pyshkin et al., 1990, 1993, 2006-2011). The most convincingly this statement can be illustrated by the comparison of luminescence from GaP bulk and nanocrystals.

**Figure 14** presents luminescence spectra of our long-term (up to 50 years) ordered GaP single crystals (**spectrum 1**) in comparison with the spectra of GaP nanoparticles (and their nanocomposites), prepared under different conditions. As already noted, luminescence was absent at room temperature in newly-grown bulk single crystals, but the same crystals, aged app. 50 years, exhibit bright broad band luminescence at 300°K between 1.8 – 3.2 eV with the maximum blue-shifted from the position of the GaP forbidden gap ( $E_g = 2.24$  eV).

Nearly the same spectrum of luminescence is observed from nanocrystals provided that they are not separated on their dimension (**spectrum 2**). Nanocrystals of sizes close to 10 nm and stored as dry powder demonstrate rather broad luminescent band with maximum at 3 eV (**spectrum 3**). At last, nanocrystals of about 10 nm sizes, thoroughly separated and distributed in a suspension, that prevent their coagulation, mechanical and optical interaction, have bright narrow-band luminescence with maximum at 3.2 eV, approximately 1 eV far from the position of the absorption edge in GaP at 300°K (**Spectrum 4**).

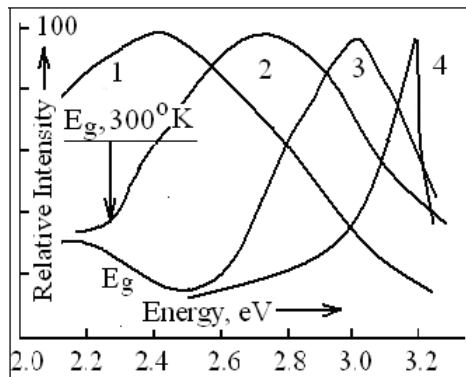


Fig. 14. Luminescence of perfect bulk GaP single crystals (1) in comparison with the luminescence of GaP nanoparticles (2-4). Nanoparticles have been prepared using white P by mild aqueous synthesis at decreased temperature and stored as the dry powders (spectrum 2, 3) or suspension in a liquid (spectrum 4). The other details are in the text.

Thus, perfect GaP bulk crystals as well as nanoparticles have no practical difference in their luminescence behavior, brightness or spectral position. This implies the negligibly small contribution of non-radiative electron-hole recombination and an opportunity for current carriers to move along the more perfect crystal lattice without any essential scattering on the defects inherent to freshly-grown single crystals.

### 3. Conclusion

This study of GaP:N and CdIn<sub>2</sub>S<sub>4</sub> brings a novel perspective to improving the quality of semiconductor crystals. The unique collection of pure and doped crystals of semiconductors

grown in the 1960s provides an opportunity to observe the long term evolution of properties of these key electronic materials. During this almost half-centennial investigation the main trends of the evolution of optoelectronic and mechanical properties have been established. It was shown that these stimuli to improve quality of the crystal lattice are the consequence of thermodynamic driving forces and prevail over tendencies that would favor disorder.

For the first time, to the best of our knowledge, we observe a new type of the crystal lattice where the host atoms occupy their proper (equilibrium) positions in the crystal field, while the impurities, once periodically inserted into the lattice, divide it in the short chains of equal length, where the host atoms develop harmonic vibrations. This periodic substitution of a host atom by an impurity allows the impurity to participate in the formation of the crystal's energy bands. In GaP it leads to the change in the value of the forbidden energy gap, to the appearance of a crystalline excitonic phase, and to the broad energy bands instead of the energy levels of bound excitons. The high perfection of this new lattice leads to the abrupt decrease of non-radiative mechanisms of electron-hole recombination, to both the relevant increase of efficiency and spectral range of luminescence and to the stimulated emission of light due to its amplification inside the crystal. The further development of techniques for the growth of thin films and bulk crystals with ordered distribution of impurities and the proper localization of host atoms should be a high priority.

This long-term evolution of the important properties of semiconductor single crystals promises a novel approach to the development of a new generation of optoelectronic devices. The combined methods of laser assisted and molecular beam epitaxies (Pyshkin, 1995, 1997; Pyshkin et al., 1996) will be applied to fabrication of device structures with artificial periodicity. Using these methods one can grow a multi-layer structure where the monolayer of N atoms will be incorporated in it each 10 nm, creating a one-dimensional periodic structure of N traps for excitons. Preparation of two dimensional perfect sublattice of N impurities along pure GaP film is rather difficult, but also is possible using ion lithography or atomic force microscope built into a growth chamber. Together with classic methods of crystal growth, these methods can be employed to realize impurity ordering that would yield new types of nanostructures and enhanced optoelectronic device performance.

It is worth noting in conclusion that semiconductor nanoparticles have been introduced into materials science and engineering mainly that to avoid limitations inherent to freshly grown semiconductors with a lot of different defects. The long-term ordered and therefore close to ideal crystals discussed herein exhibit equivalent behavior to the best nanoparticles with pronounced quantum confinement effect. These perfect crystals are useful for application in high-quality optoelectronic devices as well as they are a new object for development of fundamentals of solid state physics.

#### 4. Acknowledgment

The authors are very grateful to the US Department of State, Institute of International Exchange, Washington, DC, The US Air Force Office for Scientific Research, the US Office of Naval Research Global, Civilian R&D Foundation, Arlington, VA, Science & Technology Center in Ukraine, Clemson University, SC, University of Central Florida, FL, Istituto di elettronica dello stato solido, CNR, Rome, Italy, Università degli studi, Cagliari, Italy, Joffe Physico-Technical Institute, St.Petersburg State Polytechnical University, Russia, Institute of Applied Physics and Academy of Sciences of Moldova for support and attention to this protracted (1963-present time) research.

## 5. References

- Pyshkin, S. L.; Radautsan, S. I.; Zenchenko. (1990a). Processes of long-lasting ordering in crystals with a partly inverse spinel structure. *Journal of Soviet Physics - Doklady*, Vol. 35, No.4, pp. 301-304
- Goryunova, N.A.; Pyshkin, S.L.; Borshchevskii, A.S.; Radautsan, S.I.; Kaliujnaya, G.A.; Maximov, Yu.I. & Peskov, O.G. (1969). Influence of impurities and crystallization conditions on growth of platelet GaP crystals, *Journal of Crystal Growth*, N.N. Sheftal (Ed.), Vol. 8, pp. 68-72 New York; Symposium on Crystal Growth at the 7th International Crystallography Congress (Moscow, July 1966)
- Ashkinadze, B.M.; Pyshkin, S.L.; Bobrysheva, A.I.; Vitiu, E.V.; Kovarsky, V.A.; Lelyakov, A.V.; Moskalenko, S.A. & Radautsan, S.I. (1968). Some non-linear optical effects in GaP, *Proceedings of the IXth International Conference on the Physics of Semiconductors* (Moscow, July 23-29, 1968), Vol.2, pp. 1189-1193
- Pyshkin, S. & Zifudin, L. (1974). Excitons in highly optically excited gallium phosphide. *Journal of Luminescence*, Vol. 9, pp. 302-308
- Pyshkin, S. (1975a). Luminescence of GaP:N:Sm crystals. *Journal Soviet Physics of Semiconductors*, Vol. 8, pp. 912-13
- Pyshkin, S.; Radautsan, S.; & Zenchenko, V. (1990b). Raman spectra of Cd-In-S with different cation-sublattice ordering. *Journal of Soviet Physics - Doklady*, Vol.35, No. 12, pp. 1064-67
- Pyshkin, S.L. & Anedda, A. (1993). Preparation and Properties of GaP Doped by Rare-Earth Elements, *Proceedings of the 1993 Materials Research Society (MRS) Spring Meeting*, Symposium E, Vol. 301, pp. 192-197
- Pyshkin, S.L. & Anedda, A. (1998). Time-dependent behavior of antistructural defects and impurities in Cd-In-S and GaP, *Institute of Physics Conference Series, Ternary and Multinary Compounds*, Vol. 152, Section E, pp. 785-89, The XI International Conference on Ternary and Multinary Compounds -XI (ICTMC-XI), Salford, UK, 1997)
- Pyshkin, S.L.; Anedda, A.; Congiu, F. & Mura, A. (1993). Luminescence of the GaP:N ordered System. *Journal of Pure and Applied Optics*, Vol. 2, pp. 499-502
- Pyshkin, S.L. (2002a). Luminescence of long-time ordered GaP:N, *ACerS Transaction series*, Vol. 126, pp. 3-10. Invited talk at the 103rd ACerS Annual Meeting (Indianapolis, 2001)
- Pyshkin, Sergei L. (2002b). Bound excitons in long-time ordered GaP:N. *Moldavian Journal of the Physical Sciences*, Vol. 1, No.3, pp. 14-19
- Pyshkin, Sergei & Ballato, John (2005). Advanced light emissive composite materials for integrated optics, *Proc of the 2005 MS&T Conference*, Symposium: The Physics and Materials Challenges for Integrated Optics - A Step in the Future for Photonic Devices, Pittsburgh, TMS, pp. 3-13
- Ballato, J. & Pyshkin, S.L. (2006). Advanced light emissive materials for novel optical displays, lasers, waveguides, and amplifiers. *Moldavian Journal of Physical Sciences*, Vol. 5, No. 2, pp. 195-208
- Pyshkin, S.L.; Ballato, J.; Chumanov, G.; DiMaio, J. & Saha, A.K. (2006). Preparation and characterization of nanocrystalline GaP, *Technical Proceedings of the 2006 NSTI Nanotech Conference*, Vol. 3, pp. 194-197

- Pyshkin, S.L.; Zhitaru, R.P. & Ballato, J. (2007a). Long-term evolution of optical and mechanical properties in gallium phosphide, *Proceedings of the XVII St. Petersburg Readings on the Problems of Durability*, Devoted to the 90th Birthday of Prof. A.N. Orlov, Vol. 2, pp. 174-176
- Pyshkin, S.L.; Zhitaru, R.P. & Ballato, J. (2007b). Modification of crystal lattice by impurity ordering in GaP, *Proceedings of the MS&T 2007 Conference*, pp. 303-310, International Symposium on Defects, Transport and Related Phenomena (Detroit, MI, September 16-20, 2007),
- Pyshkin, S.L.; Ballato, J. & Chumanov, G. (2007c). Raman light scattering from long-term ordered GaP single crystals. *Journal of Optics, A. Pure and Applied Optics*, Vol. 9, pp. 33-36
- Pyshkin, S.L.; Ballato, J.; Bass, M. & Turri, G. (2008). Luminescence of long-term ordered pure and doped gallium phosphide. *Journal of Electronic Materials*, Vol. 37, No.4, pp. 388-395, TMS Annual Meeting (March 9-13, New Orleans, LA), invited talk at the Symposium: Advances in Semiconductor, Electro Optic and Radio Frequency Materials
- Pyshkin, S. & Ballato, J. (2008). Long-term ordered crystals and their multi-layered film analogues, *Proceedings of the 2008 MS&T Conference*, pp. 889-900 (September 2008, Pittsburgh), Symposium on Fundamentals & Characterization, Session "Recent Advances in Growth of Thin Film Materials"
- Pyshkin, S.L.; Ballato, J.; Bass, M.; Chumanov, G. & Turri, G. (2009a). Time-dependent evolution of crystal lattice, defects and impurities in CdIn<sub>2</sub>S<sub>4</sub> and GaP. *Physica status solidi*, Vol. C, No. 6, pp. 1112-15
- Pyshkin, S.; Zhitaru, R.; Ballato, J.; Chumanov, G. & Bass, M. (2009b). Structural characterization of long-term ordered semiconductors, *Proceedings of the 2009 MS&T Conference*, pp. 698-709, International Symposium "Fundamentals & Characterization"
- Pyshkin, S.; Ballato, J.; Bass, M.; Chumanov, G. & Turri, G. (2009c). Properties of the long-term ordered semiconductors, *Suppl. Proceedings of the 2009 TMS Annual Meeting and Exhibition*, Vol. 3, pp. 477-484, (San Francisco, February 15-19, 2009)
- Pyshkin, S.; Ballato, J.; Bass, M. & Turri, G. (2009d). Evolution of luminescence from doped gallium phosphide over 40 Years, *Journal of Electronic Materials*, Vol. 38, No. 5, pp. 640-646
- Pyshkin, S.; Ballato, J.; Chumanov, G.; Bass, M.; Turri, G.; Zhitaru, R. & Tazlavan, V. (2009e). Optical and mechanical properties of long-term ordered semiconductors. *Moldavian Journal of the Physical Sciences*, Vol. 8, No.3-4, pp. 287-295, The 4<sup>th</sup> Int. Conference on Materials Science and Condensed Matter Physics, Kishinev, Sept 23-26, 2008
- Pyshkin, Sergei; Ballato, John; Mura, Andrea & Marceddu, Marco. (2010a). Luminescence of the GaP:N long-term ordered single crystals, *Suppl. Proceedings of the 2010 TMS Annual Meetings*, Vol. 3, pp. 47-54 (Seattle, WA, USA, February, 2010
- Pyshkin, Sergei & Ballato, John. (2010). Evolution of optical and mechanical properties of semiconductors over 40 Years, *Journal of Electronic Materials*, Vol. 39, No. 6, Springer, DOI: 10.1007/s11664-010-1170-z, pp. 635-641
- Pyshkin, S.; Ballato, J.; Chumanov, G.; Tsyntaru, N. & Rusu, E. (2010b). Preparation and characterization of nanocrystalline GaP for advanced light emissive device

- structures. *NSTI, NSTI-Nanotech 2010*, *www.nsti.org*, ISBN 978-1-4398-3401-5, Vol. 1, pp. 522-525, The 2010 Nanotech Conference (Anaheim, CA, June 21-24)
- Pyshkin, S.; Ballato, J.; Luzinov, I. & Zdyrko, B. (2010c). Fabrication and characterization of the GaP/polymer nanocomposites for advanced light emissive device structures. *NSTI, NSTI-Nanotech 2010*, *www.nsti.org*, ISBN 978-1-4398-3401-5, Vol. 1, pp. 772-775, The 2010 Nanotech Conference (Anaheim, CA, June 21-24, 2010)
- Pyshkin, S. (Project Manager). (2009-2012). Joint Moldova/US/Italy/France/Romania STCU (*www.stcu.int*) Project 4610 "Advanced Light Emissive Device Structures"
- Pyshkin, S.; Ballato, J.; Belevschii, S.; Rusu, E; Racu, A. & Van DerVeer, D. (2011). Synthesis, characterization and sampling of GaP nanoparticles for light emissive devices. The 2011 NSTI-Nanotech Conference, Boston, MA, June 13-16, 2011, *Technical Program*, Vol.1, pp 327-330, *www.nsti.org*, ISBN 978-1-4398-7142-3
- Allen, W.J. (1968). Energy levels of nitrogen-nitrogen pairs in gallium Phosphide. *Journal of Physics, C: Solid State Physics*, Vol. 1, pp. 1136-1138
- Bairamov, B; Kitaev, Y.; Negoduiko, V. & Khashkhozhev, Z. (1975). Light scattering by optical phonons and non-linear optical properties of GaP. *Journal of Soviet Physics - Solid State*, Vol. 16, pp. 1323-1327
- Goriunova, N.A. (1960). Chemistry of diamond-like semiconductors. *Journal of the All Union Chemical Society*, Vol. 5, pp. 522-527, (in Russian)
- Radautsan, S.I.; Maximov, Yu.I; Negreskul, V.V. & Pyshkin, S.L. (1969). *Gallium Phosphide*, "Shtiinza", Moldavian Academy of Sciences, Kishinev
- Pushkash, B.M.; Valkovskaya, M.I.; Maximov, Yu.I. & Martynko, D.V. (1978). Influence of temperature on microhardness and structure of dislocations of the GaP single crystals. In: *Deformation of Crystals under Influence of Localized Loading*, pp. 120-125, "Shtiinza", Moldavian Academy of Sciences, Kishinev, (in Russian)
- Valkovskaya, M.I.; Pushkash, B.M. & Maronchuk, E.E. (1984). *Plasticity and Fragility of Semiconductors at the Tests for Microhardness*, pp. 24-29, "Shtiinza", Moldavian Academy of Sciences, Kishinev
- Pyshkin, S.L. (1967). *Preparation and Properties of Gallium Phosphide*, Ph.D. thesis, State University of Moldova, Kishinev
- Kittel, C. (1971). Elastic constants and elastic waves, In: *Introduction to Solid State Physics*, the 4th edition, pp. 133-156, John Wiley & Sons, Inc., ISBN 0471490210, New York
- Pyshkin, S.L. (1971). Some luminescence properties of  $(\text{CdS})_{3x} - (\text{In}_2\text{S}_3)_{1-x}$ . *Physica Status Solidi*, Vol. A 6, pp. 425-429
- Guzzi M. & Grilli, E. (1984). Localized levels and luminescence of  $\text{ab}_2\text{x}_4$  semiconducting compounds. *Journal of Materials Chemistry and Physics*, Vol. 11, No. 3, pp. 295-304
- Pyshkin, S.L. (1975b). Stimulated emission in gallium phosphide. Presented by Nobel Prize Laureate A.M. Prokhorov, *Journal of Soviet Physics - Doklady*, Vol. 19, pp. 845-846
- Pyshkin, S.L. (1995). Heterostructures  $(\text{CaSrBa})\text{F}_2$  on InP for optoelectronics, *Report to the US AFOSR/EOARD on the Contract No. SPQ-94-4098*
- Pyshkin, S.L.; Grekov, V.P.; Lorenzo, J.P.; Novikov, S.V. & Pyshkin, K.S. (1996). Reduced temperature growth and characterization of InP/SrF<sub>2</sub>/InP(100) heterostructure, *Physics and Applications of Non-Crystalline Semiconductors in Optoelectronics*, NATO ASI Series, 3. High Technology, Vol. 36, pp. 468-471
- Pyshkin, S.L. (1997). CdF<sub>2</sub>:Er/CaF<sub>2</sub>/Si(111) Heterostructure for EL displays, *Report to the US AFOSR/EOARD on the Contract No. SPQ-97-4011*



# Micro-Raman Studies of Li Doped and Undoped ZnO Needle Crystals

R. Jothilakshmi  
*Department of Physics,  
Vel Tech University,  
India*

## 1. Introduction

The interest in ZnO structures has increased drastically in recent years as it is a wide band gap (3.4 eV) II-VI compound semiconductor, with a stable wurtzite structure with lattice spacing  $a = 0.325$  and  $c = 0.521$  nm. A prominent feature of ZnO is its large exciton binding energy ( $\sim 60$  meV) at room temperature which results in extreme stability of exciton [Khan,2005]. ZnO has been used as transparent conductors in solar cells, UV light emitters, as components in high power electronics and gas and chemical sensors. ZnO nanostructure has attracted attention for possible applications in optoelectronic and spintronic devices, such as high-emitting and laser diodes with polarized output, spin based memory and logic [Vladimir,2006].

The topic of p-doping is especially difficult and undoped ZnO exhibits n-type conductivity, and resists being doped p-type. This technological issue pulls up the use of ZnO for optoelectronics. p-type ZnO can be hypothetically achieved by doping with either Group-I or Group-V elements. Doping with Group-I elements is possibly more effective than doping with Group-V elements because of more shallow acceptors [Yamamoto,1999]. It was observed that doping with Group-I elements increases donor concentration. This is attributed to tendency of Group-I dopants to occupy the interstitial sites, partly due to their small atomic radii [Park,2002]. The Group-V elements have low solubility in ZnO due to the mismatch in ionic radii. Several works on p-type ZnO doping have been made and however the results are not reproducible or questionable [Look,2002, Look,2004].

It is believed that large difference in ionic radii between the host Zn ( $0.74 \text{ \AA}$ ) and the dopant Li ( $0.60 \text{ \AA}$ ) is very important for the appearance of Ferro electricity in Li-doped ZnO. The electrical resistivity due to carriers can be improved by the introduction of Li ions [Wang, 2003]. The interstice impurity may result in lattice distortion. Therefore the resistivity of the ZnO sample will increase. If the annealing temperature is high, the oxygen vacancy increases which produces more electrons and hence the resistivity of Li-doped ZnO decreases [Min-Rui,2005].

Raman spectroscopy is a non destructive characterization method of choice for many recent studies of the vibrational properties of ZnO nanostructures [Khan,2005, Vladimir,2006, Harish Kumar,2007]. In the present work we have carried out a comprehensive Micro-Raman scattering study of the phonons in Li doped and undoped ZnO needle crystals have been grown using flux growth to ensure good quality and an effective incorporation of the

dopant ions. Flux growth offers the convenience of operating under relatively low temperatures and also it is helpful to obtain crystals with more control on the stoichiometric properties, annealed at 800°C for 1 hour to enhance oxygen vacancy.

## 2. Experimental

Raman spectra were measured from Li doped and undoped ZnO needle crystals using a Dilor XY double spectrometer under 514.5nm excitation from an Ar<sup>+</sup> laser. The samples were placed on a glass plate and the laser beam was focused onto the sample using a 50X objective lens. Before the spectra were recorded the instrument was calibrated using the Raman line of Si wafer. The total power of laser excitation at the sample was about 1.05mw.

## 3. Results and discussion

ZnO is a semiconductor with wurtzite crystal structure, having the space group  $c_{6v}^4$  with two formula unit primitive cell, where all atoms occupy  $C_{3v}$  sites [Roth,1967]. The optical phonons at the  $\Gamma$  point of the Brillouin zone belong to the following irreducible representation.

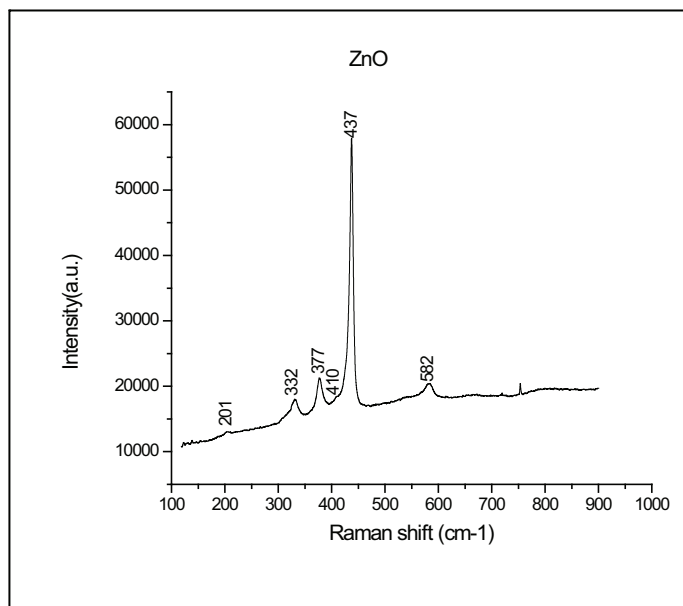
$$\Gamma_{\text{opt}} = 1A_1 + 2B_1 + 1E_1 + 2E_2.$$

Both  $A_1$  and  $E_1$  modes are polar and split into transverse (TO) and longitudinal optical (LO) phonons, all being Raman and infrared active. The two non polar  $E_2$  modes having two wavenumbers,  $E_2$  (high) is associated with oxygen atoms and  $E_2$  (low) is associated with Zn sublattice. Both are Raman active only. The  $B_1$  modes are infrared and Raman inactive that is they are silent modes [Khan,2005, Bundesmann,2003].

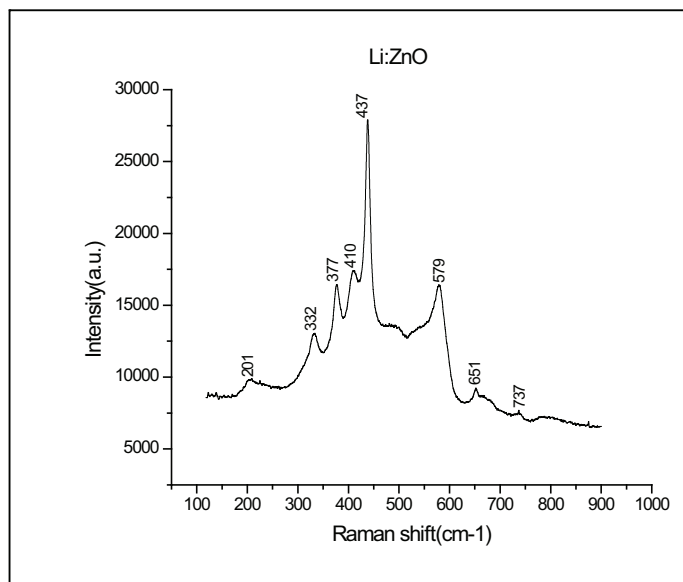
The measured micro-Raman spectra at an arbitrary point of needle ZnO crystal and Li doped needle crystal are shown in Figs. 1(a) and 1(b) respectively.

The wavenumbers of the Raman active phonon modes reported previously for bulk and needles crystals are presented in Table1. [Khan,2005, Tatjana,2007].

Comparison of Fig1 (a) with Table 1, shows that four fundamental and two second-order modes are observed. The only Raman active non polar  $E_2$ (high) mode associated with oxygen atom vibration appears at 437 $\text{cm}^{-1}$  with appreciable intensity and  $E_2$ (low) associated with the heavy Zn sublattice is absent [Khan,2005, Alim,2005]. This fact explains that the low-frequency  $E_2$  mode does not resonate at  $E_o$ . The vibration of the Zn sublattice does not modulate valence-band states of ZnO which compose almost exclusively of oxygen 2p wave functions [Calleja,1977]. 377 $\text{cm}^{-1}$  corresponds to  $A_1$  (TO) and  $E_1$  (TO) mode at 410 $\text{cm}^{-1}$  is not predominant in the spectra due to the chosen scattering geometry. A weak  $E_1$ (TO) band at 410  $\text{cm}^{-1}$  will appear in the spectrum of the sample consisting of tripods which are not c-axis orientated and may be ascribed to the contribution of the polarization due to crystals mixed orientation [Gupta,2006]. Thus the presence of a very weak band at 410 $\text{cm}^{-1}$  corresponding to  $E_1$ (TO) mode indicates that ZnO needle crystals have not grown preferably c-axis perpendicular to the substrate [Tatjana,2007]. A weak peak is observed at 582  $\text{cm}^{-1}$ . This band may be due to  $A_1$ (LO) or  $E_1$ (LO) mode ( see Table 1). It is reported  $E_1$  (LO) can occur at 584  $\text{cm}^{-1}$  as this mode is related to the defects such as oxygen vacancy or interstitial zinc in zinc oxides [Zhang,2006, Zhao,2006]. This is the reason for the appearance of a weak band at 582  $\text{cm}^{-1}$  in our case. The  $A_1$  (LO) mode is not observed shows the absence of resonance of exciting phonon energy with that of electronic interband transition with in the ZnO particle [Rajalakshmi ,2000].



(a)



(b)

Fig. 1. (a) and (b) Micro-Raman spectra of ZnO and Li: ZnO needle crystal.

	First Order	Second Order
Optical Phonon	wavenumber ( $\text{cm}^{-1}$ )	wavenumber ( $\text{cm}^{-1}$ )
$E_2(\text{low})$	102	208
$A_1(\text{TO})$	379	334
$E_1(\text{TO})$	410	540-670
$E_2(\text{high})$	439	986
$A_1(\text{LO})$	574	1050
$E_1(\text{LO})$	591	1084-1149

Table 1. Wavenumber and symmetry of the fundamental and second-order optical modes in ZnO.

The peaks at about 201 and  $332\text{cm}^{-1}$  are attributed to the second-order Raman spectra arising from zone boundary phonons. [Khan,2005, Tatjana,2007].The peak at  $201\text{cm}^{-1}$  corresponds to the wavenumber of  $2E_2$  ( $101\text{cm}^{-1}$ ) at  $\Gamma$ . The peak at  $332\text{cm}^{-1}$  should be ascribed to two phonons from the K-M- $\Sigma$  around  $160\text{cm}^{-1}$ [Calleja ,1977].These processes presumably occur for phonon wave vectors considerably removed from the center of the Brillouin zone. Without the knowledge of critical points and selection rules for various points in the zone, appropriate interpretation cannot be made [Tatjana,2007, Nusimovici,1965].

On comparison of Micro-Raman spectra of Li doped ZnO Fig.1 (b) with that of Fig.1 (a), it is noticed that in the case of undoped ZnO the intensity has been decreased. When Li atoms are introduced there will be a change in the electronic bonding force between the nearest two atoms. This in turn will influence the Raman peak positions and line profile. Moreover a drastic phonon anomaly feature was not observed in our case. Hence it suggests that the electronic effects are predominant than the ionic instability [Ehleeanal, 2002].

The  $E_2$  mode at  $437\text{cm}^{-1}$  of Li doped ZnO does not show the Li-dependence [Ehleeanal ,2002] as it is associated with oxygen atom vibration[Khan, 2005, Alim ,2005].The second order mode at  $201\text{cm}^{-1}$  occurring due to oxygen vacancies is pronounced. The peaks at 332 and  $377\text{cm}^{-1}$  are same in both cases. The peak at  $410\text{cm}^{-1}$   $E_1$  (TO) mode is much intense than undoped crystal. This feature is expected where in the crystals are not grown preferably in c-axis perpendicular to the substrate. This is an evidence of the growth conditions imposed on the system. [Tatjana,2007]. The  $E_1$  (LO) mode is highly intense and broad but shifted to a lower wavenumber side ( $579\text{cm}^{-1}$ ) confirms the point defect density.  $E_1$  (LO) mode is associated with lattice defects, such as oxygen vacancies and zinc interstitials  $E_1$  (LO) mode increases after annealing, so it is possible that defect level such as oxygen vacancies was increased [Tak,2006]. The From fig.1 (b) the origin of two new peaks at 651 and  $737\text{cm}^{-1}$  is not well understood. These peaks could be associated with multiphonon processes [Tatjana, 2007] or unlisted weak plasma lines [Rajalakshmi,2000].

In the present work the micro-Raman spectra was recorded at three different positions (center, tip and wall) of the doped and undoped ZnO needle crystals. The plots are given in Fig.2 (a) and 2(b)

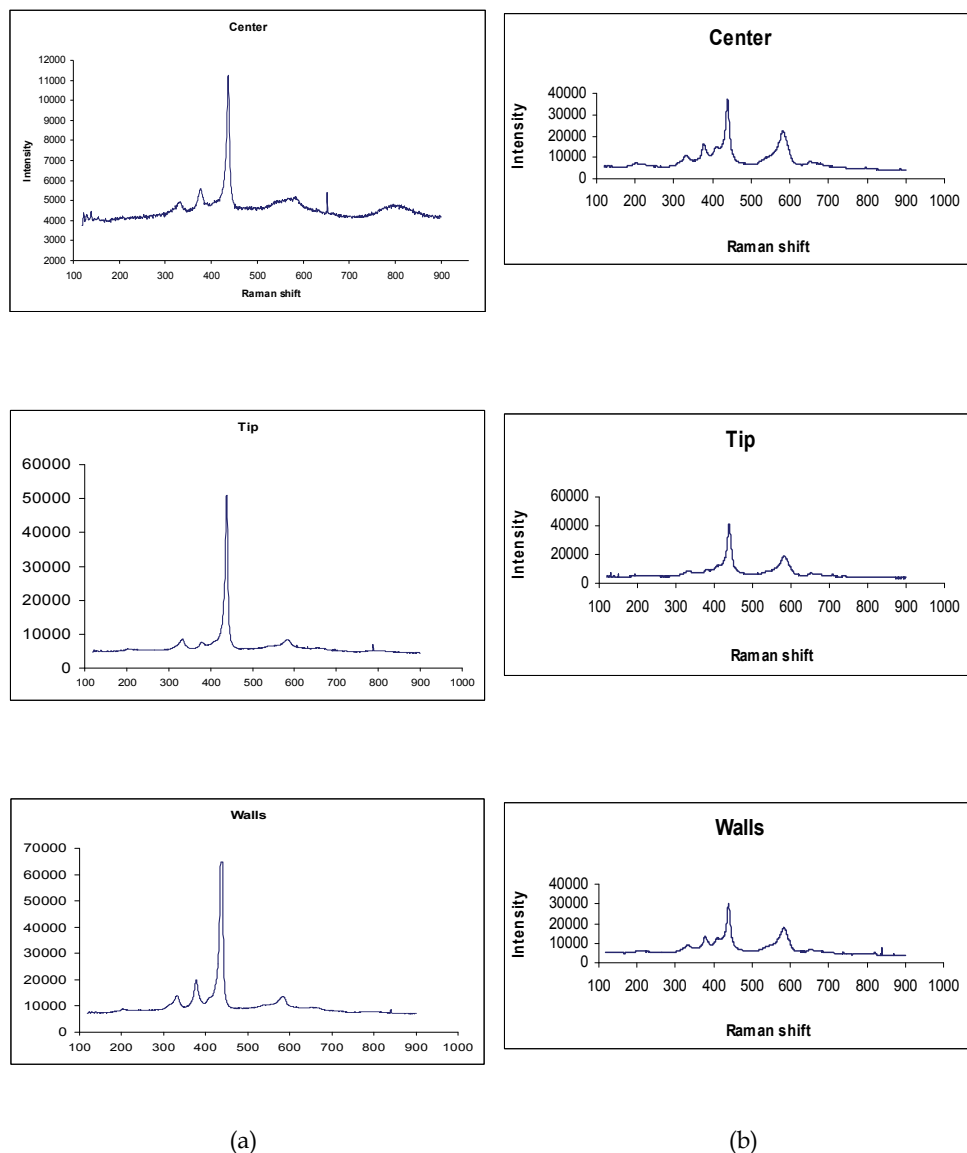


Fig. 2. (a) and (b) are plots of micro-Raman spectra of ZnO and Li: ZnO at different position. To study the quality of the crystal the strongest Raman active peak at 437cm<sup>-1</sup> was intensity normalized and a Gaussian fit was applied to get the area and width under each curve for different regions given in fig. 3(a) and 3(b).

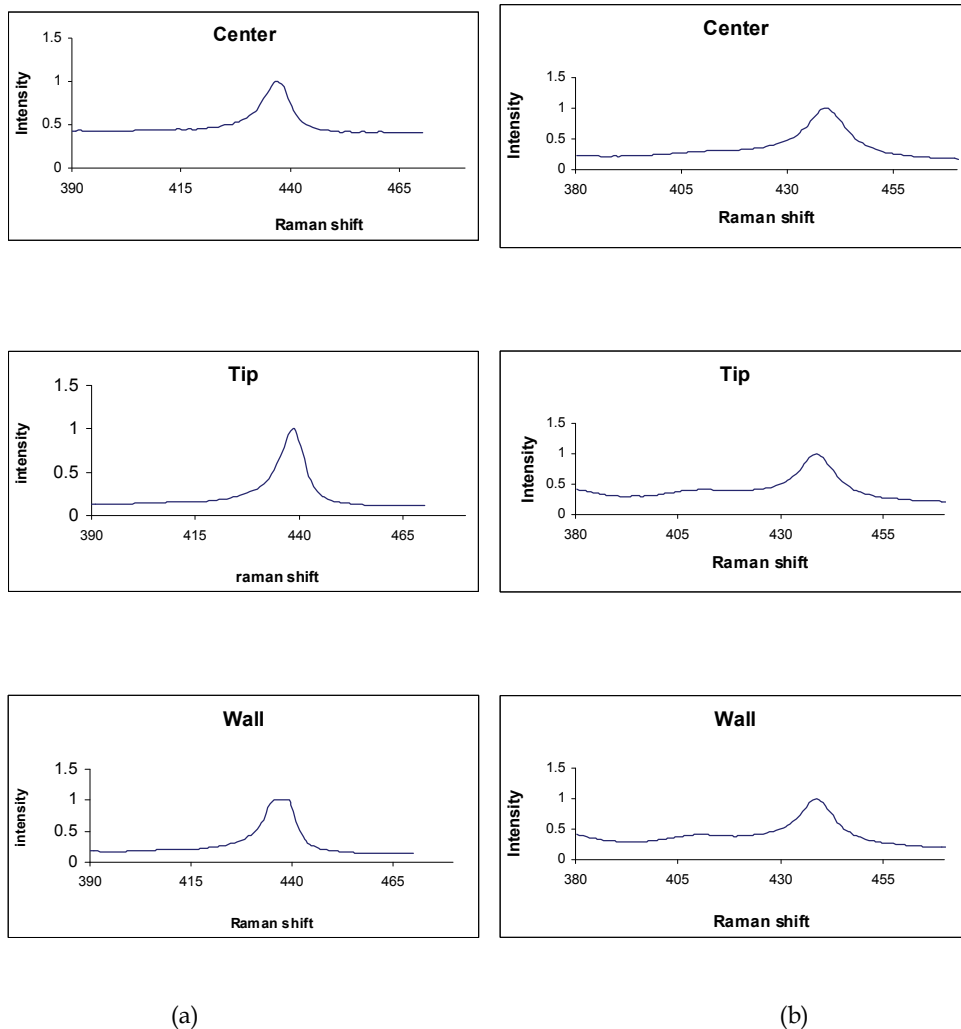


Fig. 3. (a) and (b). Intensity normalized ZnO and Li: ZnO peaks at various positions.

Line width and grain size are inversely proportional to each other [Harish Kumar,2007, Zhang, 2006]. When width decreases grain size increases, a good crystallinity is expected. Similarly area under the peak also shows the same feature as a sharp peak will be observed for a regular degree of structural order. Table 2. presents area and width at center, tip and wall of ZnO and Li doped ZnO needle crystals. On comparison of doped and undoped ZnO needle crystals, it is found that tip of the crystal shows a good crystallinity and high degree of structural order.

	ZnO needle crystal		Li doped ZnO needle crystal	
	Area(cm <sup>-2</sup> )	Width(cm <sup>-1</sup> )	Area(cm <sup>-2</sup> )	Width(cm <sup>-1</sup> )
Center	5.8	7.3	7.6	9.7
Tip	5.0	7.2	7.4	9.6
Walls	8.9	8.4	9.6	11.3

Table 2. Area and Width of doped and undoped needle crystal at different positions

#### 4. Conclusions

We have made a careful Micro-Raman study on ZnO and Li doped ZnO annealed needle crystals. It was found that E<sub>2</sub> phonon mode of doped and undoped ZnO does not show any shift. But E<sub>1</sub> (TO) mode is predominant and two new less intense peaks have been observed in Li doped crystal. The shift in the E<sub>1</sub> (LO) mode to a lower wavenumber confirms that our material shows nano dimensional character. With the intensity normalized plots we can conclude that for both Li doped and undoped ZnO crystals the crystallinity is improving towards the tips of the needle crystals.

#### 5. References

- C. Bundesmann, N. Ashkenov, and M. Schubert, *Appl. Phys. Lett.* Vol. 83, No. 10, 8 September 2003.
- J. M. Calleja, and M. Cardona, *phys. Rev. B* 16, 3753 (1977).
- Ehlee-anul Islam, *J. Phys. Soc. Jpn.* Vol. /No:71, page 1594, 2002.
- V. Gupta, P. Blattacharya, Y. I. Yusuk, K. Sreenivas and R. S. Katiyar, *J. Cryst. Growth* 287, 39 (2006).
- Harish Kumar Yadav and K. sreenivas *Mater. Res. Soc. Symp. Proc.* Vol. 957, 2007.
- Khan A. Alim, *J. Appl. Phys.* 97, 124313(2005).
- Khan A. Alim, *Appl. Phys. Lett.* 86, 053103(2005).
- D. C. Look, D. C. Reynolds, C. W. Litton, R. L. Jones, D. B. Easer and G. Cantweel, *Appl. Phys. Lett.* 81, 1830(2002).
- D. C. Look, B. Clafin, Y. I Alivor and S. J. Park, *Phys. Stat. Sol. (b)* 241, 624(2004).
- Min-Rui Wang. *Journal of Material Science* 40 (2005).
- N. Nusimovici and J. L. Birman, *Bull. Am. phys. Soc.* 10, 616(1965).
- C. H. Park, S. B. Zhang, and S. H. Wei, *Phys. Rev.* B66, 073 202(2002).
- M. Rajalakshmi and A. K. Arora, *J. Appl. Phys.* Vol. 87, No. 5, (2000).
- W. L. Roth, in *The Physics and chemistry of II-VI compounds*, edited by M. Aven and J. S. Prener (north-Holland, Amsterdam, 1967), p. 122.
- Tatjana Dedora, *Mater. Res. Soc. Symp. Proc.* Vol. 957, 2007.
- Tak, Park, and yong, *J. Vac. Sci. Technol. B*, Vol. 24, No. 4, jul/Aug 2006.
- Vladimir A. Fonoberov, *J. Nanoelectron. optoelectron*, 2006, vol-1, No. 1.
- X. s. Wang, *Appl. phys.* A77, 561-565(2003).
- T. Yamomoto and H. Kalayana-Yoshida, *Jpn. J. Appl. Phys.* 38, L166 (1999).
- D. F. Zhang, L. D. Sun and C. H. Yan, *Chem. Phys. Letters* 422, 46(2006).

- A. Zhao, T. Luo, L. Chen, Y. Liu, X. Li, Q. Tang, P. Cai, Y. Qian, *Mat. Chem. Phys.* 99, 50(2006).
- Y. Zhang, *J. Phys. :condens. Matter* 18(2006)957-963.